PRECAST CONCRETE FLOOR SUPPORT AND DIAPHRAGM ACTION

A thesis submitted in partial fulfilment of the requirements for the

Degree of Doctor of Philosophy

by

Michael D Herlihy

Supervised by

Professor R Park

ENGINEERING
LIBRARY
TA
660
.F6
.H549
copy 2

Dedicated to:

My late father
Michael James Herlihy

My wife Marinka and our children
Kate, Dacre and Frances

21 DEC 2000

Contents

Abstract

Experimental research, engineering analysis and theoretical developments comprise a study in which various interactions between ductile moment resisting frames and precast prestressed hollow core flooring have been examined.

The most critical interaction tested involves support behaviour, and the ability of reinforcing details to provide control against loss of support and possible catastrophic flooring collapse under dilation effects. Plastic hinge dilation, also known as elongation or growth, is an inherent property of ductile concrete members when subjected to cyclic plastic deformations. Hence, the performance of floor support details is enveloped by the general design philosophy of seismic resisting structures. In the experimental phase, emphasis was placed on testing support construction joints from contemporary building practice, for direct comparison with special support tie details of known capabilities. The contemporary details were found to exhibit seriously flawed behaviour under monotonic and cyclic loading regimes.

Corroborative experiments were undertaken to establish direct shear capacities between typical composite bond surfaces. In particular, these tests addressed the discrepancy that has emerged between direct shear and shear flow strengths. Also, the continuity response of conventional and proposed support detail types was examined.

A composite section model was analysed to demonstrate the likely influence of prestressing steel on beam bending strength within a ductile frame environment. Likewise, the probable effects of prestressing steel on beam plastic hinge development were examined, but on a more theoretical basis.

Other elements of theory have been presented. These mainly concern the general topic of elastic-plastic response in reinforced concrete elements. The particular focus of this work has been to demonstrate a rational basis to stiffness transition and plastic buckling analysis. The important role of stiffness degradation in dynamic analysis has also been examined.

Although ductile moment resisting concrete frames have been emphasised, it is considered that the findings of this thesis are applicable to other structural systems, such as dry joint "hybrid" precast concrete frames and spring connected steel frame structures.

Acknowledgments

The research presented in this thesis was conducted at the Department of Civil Engineering at the University of Canterbury under the supervision of Professor R. Park. I wish to sincerely thank Professor Park for the support he has given to this project.

The principal financial sponsors of this research were the Earthquake Commission and Firth Industries Ltd. I wish to express my gratitude to these organisations for their invaluable assistance.

Further acknowledgment is due to Firth Industries Ltd for their generous contribution towards the supply of materials, namely the extruded hollow core flooring units and cast-in-place concrete. Pacific Steel Ltd sponsored the supply of reinforcing steel and Golden Bay Cement Ltd the cement bag weights. These contributions are very gratefully acknowledged.

An appreciation must go to each and every one of the technician and laboratory staff. However, particular gratitude is owed to my unwavering technician Paul Murphy for the many hours spent on this project. Thanks also to Messrs G. Hill and G. Clarke (now retired) for their guidance. Others involved in this project were Messrs N. Hickey, G. Harvey, G. Hill, N. Dixon, R. Allen, M. Roestenburg, D. MacPherson, M. Stuart-Jones, R. Newton and P. Coursey. Their assistance is gratefully acknowledged.

My thanks to Mr D. Bull for his support during the early stages of this project, and to Miss C. Price for assisting with the final edit.

Special thanks to Mr Len McSaveney of Firth Industries for his early engineering inspiration and continued support.

My sincere gratitude to the McKendry Brothers and the precasting firm M.J. McKendry Ltd, without whom this thesis would not have happened.

Finally, to Marinka for her assistance and extreme patience throughout this whole exercise.

Notation

Chapter 1

A_c	area of concrete cross-section
A_p	cross-section area of prestressing steel at bottom of the section
A_{ps}	area of prestressed reinforcement in flexural tension zone
A_s	area of non-prestressed tension reinforcement
A_{vf}	area of shear-friction reinforcement
b_w	web thickness
c	clear concrete cover
C	compression in concrete, in equilibrium with T
d	distance from extreme compression fibre to centroid of tension reinforcement
d'	distance from extreme compression fibre to centroid of compression reinforcement
d_b	nominal diameter of prestressing strand or bar
d_c	distance from extreme compression fibre to centroid of prestressing steel
D	the diagonal vector sum reacting against tension components ΣT_X and ΣT_y
e, e_o	eccentricity of prestressing force
f'_c	characteristic concrete cylinder compressive strength
f'_{ci}	concrete compressive strength at transfer of prestress
f_{ccj}	mean concrete cube compressive strength at time j
f_{ck}	characteristic concrete cylinder compressive strength
f_{ckcub}	characteristic concrete cube (150 mm) compressive strength
f_{cki}	concrete cylinder compressive strength at transfer of prestress
f_{cm}	characteristic cylinder strength of mortar in a joint
f_{ct}	mean tensile strength of cast-in-place concrete or grout
f_{ctd}	$f_{ctk} / 1.4$
f_{ctf}	mean concrete tensile flexural strength
$f_{ctfk,0.05}$	the flexural tensile strength below which 5% of all tests may be expected to fall
f_{ctk}	characteristic concrete tensile strength
$f_{ctk,0.05}$	the compressive strength below which 5% of all tests may be expected to fall
f_{ctkf}	characteristic concrete tensile flexural strength
f_{ctkj}	the characteristic concrete tensile strength at time j
f_{ctm}	the mean concrete tensile strength
f_{ctmj}	the mean concrete tensile strength at time of release

f_{pc}	compressive stress in concrete (after allowance for all prestress losses) at centroid of cross-section resisting all applied loads
f_{pu}	ultimate tensile strength of prestressing steel
f_{si}	initial (jacking) stress in prestressing steel
f_y	lower characteristic yield strength of non-prestressed reinforcement
F_{ps}	the effective tensile force of prestressing steel
F_{st}	tensile capacity of tie configuration
h	height, inter-storey height
h	total member depth (thickness)
I	second moment of inertia
I	structural importance factor
I_c	second moment of inertia of the concrete section
k	$2I_c / hA_c$
k	ratio of the distances between beam plastic hinge zones to column centrelines (<1.0)
ℓ_{add}	additional development length in embedded cores
ℓ_b	development length of deformed bar
ℓ_{crit}	a length equal to the transfer length of prestressing strand
ℓ_d	total development length
ℓ_p	plastic hinge length
ℓ_s	support length
ℓ_t	transfer (transmission) length
ln	natural logarithm
L	length of a structure or an element of structure
L_s	limit state factor for the serviceability limit state (=1/6)
L_u	limit state factor for the ultimate limit state (=1.0)
M^*	design bending moment at section at the ultimate limit state
M_o	decompression moment in prestressed member
M_x	bending moment in cross-section at a distance x from support
n	number of pretensioned strands contributing to flexural tension reinforcement
N^*	design axial load at the ultimate limit state normal to the cross section occuring simultaneously with V^* to be taken positive for compression, negative for tension, and to include effects due to temperature and shrinkage
p_w	$(A_s + A_{ps}) / b_w d$
P	prestress force
P_o	prestressing force immediately after release
R	risk factor for a structure
S	static moment of inertia of the section
T	tension in reinforcing steel in equilibrium with C

$T_{x,y}$	tension component in direction x or direction y as given
u	perimeter of core or alternately **2h** if embedded in joint
v_b	basic shear stress
v_{cn}	nominal shear stress provided by concrete when cracking results from combined shear and flexure
v_{cw}	nominal shear stress provided by concrete mechanisms when diagonal cracking results from excessive principal tensile stress.
V_{pc}	shear forces due to prestressing components
V^*	design shear force at section at the ultimate limit state
V_{Rd11}	design value of shear force resistance in region cracked in flexure
V_{Rd12}	design value of shear force resistance in the region uncracked in flexure (i.e., web shear)
V_{tp}	shear force component caused by transfer of pretension force
V_x	shear force in cross-section at a distance x from support
$V_{\tau r}$	horizontal shear strength developed along a cracked construction joint
W_{px}	the weight supported by a diaphragm and the elements tributary thereto at a level
x	distance along member from support or end of member, (x axis)
Z	zone factor
α	reduction factor for prestressing force with regard to end transfer
δ	displacement
Δ_{ct}	proposed limiting measure of free end slip of prestressed strands for quality assurance of flexural bond performance
Δl_b	additional length of bar to allow deformation capacity of $\delta_u = \varepsilon_{lim} \Delta l_b$
ε_c	strain in concrete at extreme compression fibre
ε_{lim}	the limiting steel strain for a tie
ε_s	strain in steel
ε_{sp}	spalling strain of concrete
ε_y	steel strain at yield
ϕ	strand diameter
ϕ	strength reduction factor
γ	factor of safety
γ_c	partial safety factor for concrete (= 1.4 for good quality control)
φ_p	curvature in a plastic hinge
φ_u	curvature in plastic hinge at design level of structural ductility
φ_y	curvature at yield
μ	structural ductility factor
μ_f	coefficient of friction

μ_p	structural ductility factor used for the design of a part
θ	an angle, slope or rotation
θ_u	plastic hinge rotation at design level of structural ductility
θ_y	plastic hinge rotation at yield
ρ_p	prestressed reinforcement ratio
σ	stress
σ_c	compressive stress in concrete or joint
σ_{cp}	average prestress in concrete
σ_p	effective prestress in steel
σ_{po}	stress in tendons immediately after release
σ_{sp}	maximum spalling stress
τ	shear stress
τ_{max}	maximum shear stress in a mortar joint just before initiation of first crack
τ_r	residual shear stress in a cracked mortar joint
τ_{Rd}	design value of resistant shear stress
ξ	depth factor, = 1.6 – d (metres), but not taken less than 1.0 m

Chapter 2

a	acceleration
A	area
$\mathbf{A_c}$	area of concrete cross-section
$\mathbf{A_s}$	area of reinforcing steel
$\mathbf{A_{vf}}$	area of shear-friction reinforcement
b	width of concrete compression block
B	width of a structure or an element of structure (breadth)
c	distance from extreme compression fibre to the section neutral axis
d	distance from extreme compression fibre to centroid of tension reinforcement
d′	distance from extreme compression fibre to centroid of compression reinforcement
e	exponential function (≈ 2.7183)
E	modulus of elasticity
EI*	equivalent flexural rigidity
$\mathbf{E_c}$	elastic modulus of concrete
$\mathbf{E_s}$	elastic modulus of steel
$\mathbf{f'_c}$	characteristic concrete cylinder compressive strength
$\mathbf{f'_{ci}}$	concrete compressive strength at transfer of prestress
$\mathbf{f_c}$	concrete compression stress

f_{cr}	modulus of rupture (stress at first cracking)
f_s	steel stress
f_y	lower characteristic yield strength of non-prestressed reinforcement
F_{ps}	the effective tensile force of prestressing steel
g	gravitational acceleration ($\approx 10 m/s^2$)
h	height, inter-storey height
H	height function, total building height (storeys 0→n)
I_{cr}	second moment of inertia based on cracked elastic section analysis
I_e	effective second moment of inertia
jd	lever arm of moment resisting section
k	ratio of the distances between beam plastic hinge zones to column centrelines (<1.0)
K	structural stiffness, stiffness matrix
K_N	interstorey stiffness after N damaging load cycles have elapsed
K_o	initial interstorey stiffness
l	distance between column centres
l′	effective length of beam between opposing plastic hinges
$l'_{min,\pm}$	minimum effective length of beam (under ± bending moment as appropriate) to maintain compatibility between opposing plastic hinges at a prescribed rotation
ln	natural logarithm
l_p	plastic hinge length
$l_{x,y}$	length along intersecting beams in appropriate x or y direction from connecting column (beams need not be at right angles)
L	length of a structure or an element of structure
m	mass per unit length
M	bending moment
M	mass, mass matrix
M_{oxy}	vector sum of overstrength moments
M_p	bending moment in a plastic hinge zone (corresponding to φ_p)
M_y	bending moment at first yield (corresponding to φ_y)
n	number of strands contributing to flange tension under negative bending moment
n	modular ratio
N	number of successive load cycles causing loss of horizontal stiffness at storey level
N_{oxy}	couple force corresponding to vector sum of overstrength moments M_{oxy}
P	force
q_{sr}	force developed in shear friction per unit length of beam
s	spacing of starter reinforcement
$s_{x,y}$	required spacing of starter reinforcement in respective x or y direction
t	time elapsed

T	a period of vibration
u	strain energy density (strain energy per unit volume of material
U_b	strain energy due to bending
V	shear force
V'	nominal shear force at a plastic hinge
V_{vr}	horizontal shear strength developed along a cracked construction joint
x	distance in direction of x axis
y	distance in direction of y axis
y	distance to neutral axis in cracked elastic section analysis
z	distance from critical section to the point of contraflexure
Z	section modulus
α	structural sway constant (relationship between mass and stiffness)
β	bisection angle of beams intersecting at a column (for beams at right angles, $\beta = 45°$)
δ	displacement
δ_b	maximum amplitude of displacement at base of structure
δ_o	displacement response with nil resonance
Δ	inter-storey deflection
ε_c	strain in concrete at extreme compression fibre
ε_o	concrete strain at peak compression stress
ε_s	strain in steel
ε_{sp}	concrete spalling strain
ε_y	steel strain at yield
ϕ	strength reduction factor
η	shape factor (cumulative distribution of building mass with height)
φ	curvature
φ_Δ	difference between plastic and yield curvatures in plastic hinge zone ($\varphi_p - \varphi_y$)
φ_p	curvature in a plastic hinge
φ_u	curvature in plastic hinge at design level of structural ductility
φ_y	curvature at yield
κ^2	separation constant for solution to PDE
μ_f	coefficient of friction
ν	angle made between force N_{oxy} and the corner bisection angle β
θ	an angle, slope or rotation (building angle of drift)
θ'	angle of beam plastic hinge rotation in side-sway mechanism
θ_u	plastic hinge rotation at design level of structural ductility
θ_y	plastic hinge rotation at yield
σ	stress

ω	circular frequency of vibration
Ψ_{Δ}	strain energy per unit length due to inelastic portion ($= M_p \cdot \varphi_{\Delta}$)
Ψ^*	sum of strain energy per unit length of contributing portions of a section
Ψ_c	strain energy per unit length in concrete portion
Ψ_p	sum of strain energy per unit length at bending moment M_p
Ψ_{se}	elastic strain energy per unit length in steel portion
Ψ_{sp}	plastic strain energy per unit length of steel portion
ς	stiffness reduction coefficient (damping)

Chapter 3

a	
A'_c	transformed area of concrete section
A_b	area of topping bond interface
A_{pc}	gross area of precast section
A_s	area of non-prestressed tension reinforcement
c	depth from neutral axis to extreme compression fibre
d_b	nominal diameter of prestressing strand or bar
e	eccentricity of pretension force
E_c	elastic modulus of concrete
f'_t	principal tensile stress
f_c	concrete stress
f_y	yield stress of reinforcement
f_s	reinforcing steel stress
f'_c	compressive strength of concrete
f_{tx}	axial tensile stress in hollow core section at fracture
F_p	force in prestressing steel
F_s	force in non-prestressed steel
G	modulus of rigidity ($\approx 0.4E$)
h_t	topping thickness
H	overall height (thickness) of member
L	length
L_o	gauge length
M	bending moment
P	axial tension force applied ny test rig
P_f	effective (final) pretension force after losses
P_i	initial pretension force (before transfer)

P_{pc}	force in precast section
t	effective thickness (depth) of shear volume
u	bar bond stress
u	strain energy density (strain energy per unit volume)
$\bar{u}$	average bar bond stress
U_e	external work done
U_i	internal strain energy
U_{pc}	strain energy stored in precast section
V_n	shear force transferred by shear friction across a construction joint
V_{se}	effective embedded volume of reinforcement
$\acute{y}_s$	distance from section bottom fibre to centroid of strands
$\acute{y}_x$	distance from section bottom fibre to neutral axis
Z	section modulus

ΔL	change in length
ε_u	ultimate strain
φ	curvature
θ_p	plane of principal stress, relative to plane of axial tensile stress
τ	shear stress
τ_b	topping bond shear stress

Chapter 5

A	area
A_b	steel bar area
A_s	area of reinforcement
b	width of slab
c	depth from neutral axis to extreme compression fibre
C	end condition constant
d_b	nominal diameter of prestressing strand or bar
E_c	elastic modulus of concrete
E_s	elastic modulus of steel
f_c	concrete stress
f'_c	compressive strength of concrete
f_r	modulus of rupture
f_s	reinforcing steel stress
f_y	yield stress of reinforcement

$\mathbf{h}$	topping thickness
$\mathbf{H}$	overall height (thickness) of member
$\mathbf{I}$	second moment of area
$\mathbf{L}$	Length
$\mathbf{L_{cr}}$	critical buckling length
$\mathbf{L_{Ecr}}$	critical buckling length calculated by Euler theory
$\mathbf{M_{cr}}$	flexural cracking moment
$\mathbf{M_e}$	bending moment corresponding with elastic buckling
$\mathbf{M_p}$	plastic bending moment
$\mathbf{M_{\theta(i)}}$	Moment capacity of the i^{th} plastic hinge
$\mathbf{n_f}$	number of fixed ends
$\mathbf{n_\theta}$	number of plastic hinge rotations in buckling mechanism
$\mathbf{N^*}$	design axial force
$\mathbf{r}$	radius of gyration
$\mathbf{S}$	plastic section modulus
$\mathbf{u_c}$	strain energy density (strain energy per unit volume) of concrete
$\mathbf{u_s}$	strain energy density (strain energy per unit volume) of steel
$\mathbf{U_b}$	strain energy due to bending
$\mathbf{U_c}$	strain energy due to axial compression
$\mathbf{V}$	volume (concrete or steel reinforcement)
$\mathbf{y}$	distance to centroid
$\mathbf{Z}$	elastic section modulus
δ	displacement
δ_{cr}	critical displacement
δ_{ie}	critical displacement of intermediate elastic members
δ_p	critical displacement of plastic members
δ_{se}	critical displacement of slender elastic members
δ^*	design critical displacement
ε_c	concrete strain
ε_o	strain corresponding with peak stress
ε_s	steel strain
ε_u	ultimate strain
ε_y	yield strain of steel
φ	curvature
λ	length division factor: 1 for sway members, 2 for braced members
σ	average stress

Chapter 6

A	bond surface area
f'_c	concrete crushing strength
V_h	horizontal shear force

Chapter 7

A_s	area of reinforcing steel
b	width of concrete compression block
d	distance from extreme compression fibre to centroid of tension reinforcement
E	elastic modulus
f'_c	measured concrete cylinder compressive strength
f_y	measured yield strength of reinforcement
I	second moment of area
K_θ	rotational stiffness (from test data)
l_p	plastic hinge length
L	Length
M	bending moment
M^*	design bending moment in the Ultimate Limit State
M_p	plastic bending moment
M_y	first yield bending moment
w	weight per unit length
z	distance from critical section to the point of applied force (shear span)

δ	displacement
ε_c	strain in concrete at extreme compression fibre
ε_o	concrete strain at peak compression stress
ε_s	steel strain
ε_y	steel strain at yield
φ_p	curvature in a plastic hinge
φ_y	curvature at first yield
φ_Δ	difference between plastic curvature and yield curvature in plastic hinge zone
θ	rotation at support
θ_p	rotation at plastic bending moment
ρ	rotation at simple induced by applied loads
Ψ_p	sum of strain energy per unit length at bending moment M_p
Ψ_Δ	strain energy per unit length due to inelastic portion ($= M_p \cdot \varphi_\Delta$)

Chapter 8

A_b	area of bar
d_b	bar diameter
E	elastic modulus
f_{ck}	cylinder crushing strength
f_s	steel stress
f_y	steel yield stress
I	second moment of area
l_d	development length
L	total embedment length of bar
M	bending moment
M^*	design bending moment in the Ultimate Limit State
n	shape coefficient for bond capacity function
N	normal force due to curvature
q	bond capacity
q_u	ultimate bond capacity
s	slip
T	tension force
T_o	initial tension force
T_{5db}	reduced tension force at five bar diameters ($5d_b$) embedment
	average bond stress
V	shear force
V_o	initial shear force
w	weight per unit length
x	length along bar
α	shape coefficient for bond-slip function
μ	friction coefficient
ρ	rotation at simple induced by applied loads
τ	bond stress
τ_{max}	maximum (peak) bond stress
Σo	sum of surface area of bar per unit length

Thesis Outline

This thesis is comprised of nine chapters. A brief outline of each of these chapters is given as follows:

Chapter 1 **Introduction** **(83 pages)**

The introductory chapter gives a comprehensive background to the development and use of precast prestressed flooring systems in New Zealand. Support tie reinforcement is introduced and comparisons are made with detailing practices of North America and Europe. Various approaches to analysis and deign of structures incorporating floor diaphragms are discussed in general terms. Also discussed are design issues particular to extruded hollow core flooring and the likely response of floor systems when incorporated in ductile seismic resisting structures. The analyses if a simple mechanism concludes that precast prestressed flooring systems may significantly increase the overstrength actions of ductile moment resisting frames.

Chapter 2 **Diaphragm Analysis** **(52 pages)**

Chapter two deals with the fundamental (first mode) seismic response of frame buildings and extrapolates this response to the compatibility requirements ofprecast prestressed flooring units within floor diaphragms. In the development of compatibility equations, other related aspects of flexural rigidity are examined. In particular, an expression is derived for the equivalent flexural rigidity of reinforced concrete sections, based on summations of internal strain energy. Also presented are the more general aspects of diaphragm analysis, such as compression fields.

Chapter 3 **Loss Of Support (LOS) Tests** **(70 pages)**

The most important body of experimental work is presented in this chapter. Typical flooring support details were tested for their ability to withstand dilation type loading as described in the introductory chapter. The systematic premature failure of these details is reported, with many of the conclusions drawn from these tests being fundamental to the whole course of study.

Chapter 4 **Loss Of Support Tests Involving Cyclic Loading** **(22 pages)**

This chapter considers the effects of cyclic loading on support tie details. Two specimens were tested, one involved continuity bars and the other embedded tie bars. The experiments conclude that cyclic loading has the potential to cause delamination and uplift of topping slabs.

Chapter 5 **The Buckling Of Topping Slabs** **(32 pages)**

Based on conservation of energy principles, a buckling theory is developed for the analysis of plastic buckling response typical of reinforced concrete members. To further demonstrate the generality of the proposed model, the elastic-plastic buckling response of steel members is considered and compared to existing methods. The potentially adverse buckling effect from cyclic loading of densely reinforced topping slabs is examined.

Chapter 6 **Composite Topping Bond** **(13 pages)**

This chapter reports the results of eight composite bond tests. These tests were undertaken to establish the likely magnitude of bond capacities that exist between topping slabs and precast surfaces under direct shear loading. The outcomes of these tests indicate that composite bond capacities derived from shear flow tests are not applicable to direct shear-loading regimes.

Chapter 7 **Cantilever Tests** **(27 pages)**

Three cantilever bending tests were performed on hollow core flooring sections with composite topping. The purpose of these tests was to establish both the continuity effects of various support details and to determine whether moment-rotation behaviour could be predicted by calculation. The outcomes indicate that practical levels of continuity can be achieved, and that rotation response can be predicted with reasonable accuracy.

Chapter 8 **Reinforcing Bar Bond** **(20 pages)**

A bar bond model is proposed, in which bond is treated as either cohesive bond, curvature bond or bond induced by dowel action (direct shear). It is shown that dowel action may significantly reduce the bond length required to develop the strength of reinforcing bars. It can also be demonstrated that curvature bond may contribute to bar bond capacity in regions of constant bending moment (zero shear).

Chapter 9 **Summary, Conclusions and Recommendations** **(4 pages)**

1

Introduction

1.1 THE USE OF PRETENSIONED FLOORS IN BUILDINGS

1.1.1 BACKGROUND

The first instance of pretensioned floor slab manufacture appears to be connected with the experimental work of the German engineer E Hoyer at Braunschweig Technical University in the mid 1930s. The technique of long-line prestressing that has since evolved is synonymous with the pioneering work of Hoyer, and is often referred to as the Hoyer system. Typically, this method involves the pretensioning of prestressing steel through a form work that is placed between bulkheads. Concrete is cast into the form around the prestressing steel and is cured until a degree of compressive strength is attained. At this point, the force sustained by the prestressing steel is released and transferred to the formed concrete section. The innovative significance of Hoyers system, in relation to contemporary techniques employed in prestressed concrete, was the method of force transfer. The Hoyer system relies on the establishment of transfer bond stresses at the interface of the prestressing steel and the surrounding concrete matrix without the specific use of anchorages. Provided that sufficient transfer bond between the prestressing steel and concrete elements is attainable, this system becomes ideally suited to the mass production of precast units. With respect to buildings, the Hoyer, or long-line system, is especially suited to the manufacture of modular flooring units of uniform sections and load carrying requirements.

The experimental slabs constructed by Hoyer were 50 mm thick and 1.2 m wide, and a multiple number of 2.0 mm diameter cold-drawn high strength piano wires were used for prestressing steel. Such small diameter wires were necessary because of the high bond stresses demanded by wire with a typical ultimate strength of more than 2400 MPa. The experiments concluded that pretensioned slabs are strong, flexible and durable. Unfortunately, an excessive number of piano wires were required to construct a reasonable span, making this system an interesting concept but rather impractical for economical deployment in construction. However, it is evident that pretensioning was used in Germany during the second world war period in the construction of submarine bases along the Atlantic and North Sea coasts.

1.1.2 THE COMMERCIAL DEVELOPMENT OF PRETENSIONED CONCRETE

It was not until about 1950 that pretensioning began to expand into the commercially successful industry as we know it today. A number of North American engineers had long recognised the potential of this form of construction, and had followed pre-war developments in European

prestressing technology, the work of Freyssinet, Magnel, Hoyer and Abeles. However, it was a United States invention that provided the genuine means of economical and dependable pretensioning, and that was the development of seven wire stress relieved prestressing strand by the John A. Roebling & Sons Corporation.

Concurrently, the building industry across the United States was in a boom situation. The demand for longer floor spans in the absence of a reliable structural steel supply became an influential factor in the creation of a pretensioned concrete industry. As a result of the demonstrated viability and cost effectiveness of pretensioned concrete products, investors were guided towards enhancing the existing concrete industry operations by promoting and undertaking this form of construction. The commercial market remained buoyant and specifiers became increasingly enthusiastic about the use of pretensioned concrete. Thus, engineers were encouraged to diversify and refine applications, and to explore options such as the development and standardisation of sections. Consequently, many pretensioned flooring products were devised that went on to become industry standards such as double tees, single tees, flat slabs and joist-infill systems.

The first extruded hollow core flooring produced in the United States was probably in 1954 and this was achieved using modified German extrusion plant. Early precast concrete manufacturers had also attempted to produce non-extruded hollow core units using either paper voids or systems involving core forming dies that were drawn through the concrete by external machinery. In the late 1950s, successful extruded hollow core plant was in active service but it was mostly in the 1960s that the extruded hollow core flooring products were developed to their potential.

General references on the advent of pretensioning in North America are contained in the book "Reflections on the Beginnings of Prestressed Concrete in America" [PCI, 1981].

Although New Zealand engineers generally recognise that most of the fundamental advances in prestressed concrete technology are European in origin, the development of pretensioned concrete in New Zealand has been more strongly influenced by the North American experience. Moreover, it can be said that the backgrounds of commercial development of pretensioned concrete in North America and New Zealand have a similar economic theme. As neither the North American continent or New Zealand were physically attacked during the second world war, post-war construction was driven almost entirely by boom economy investment in contrast with the immediate civil reconstruction needs of post-war European countries.

Like their counterparts in America, the early entrepreneurs in New Zealand recognised the potential of prestressed concrete as a diverse and competitive construction material. However, pretensioned flooring manufacture in New Zealand did not develop as dramatically as other products such as pretensioned piles, power poles and bridge beams. This was partly due to the small population of New Zealand coupled with a strong tradition of timber frame housing on freehold land titles, which tended to limit the use of precast flooring to projects other than domestic construction. Another very influential factor was that much of the readily accessible money for construction came through local and central government expenditure and not from

the financial backers of private development. This generally resulted in a demand for products that are synonymous with an expanding infrastructure, such as power poles and bridge beams.

By the mid 1960s, pretensioned flooring had gained more momentum in the construction market and during that decade utilisation expanded to include most of the standardised sections that had originated in North America. Extruded hollow core flooring systems, however, did not appear on the New Zealand construction scene until the latter half of the 1970s.

The 1980s saw a major building boom in New Zealand that resulted in a considerable attrition of construction methods, with one of the critical requirements becoming speed of erection on a short lead time. This resulted in a tendency towards multi-storey buildings constructed from precast concrete frame elements and occasionally from precast wall elements; a trend inspired by some creative structural designers that proved to be a very efficient form of construction [O'Grady, 1988; Wood, 1988]. Moreover, the mass production capabilities, cost effectiveness and structural efficiency of hollow core flooring made this product the ideal collaboration in suspended flooring.

The increasing success of pretensioned one-way systems over cast-in-place floors may also be attributed to market forces that have existed in New Zealand for some time. Because of the general non-availability of quick reusable forms and the continual high cost of ordinary formwork and labour, cast-in-place floors appear to have become part of the attrition process. In the authors own experience, the last cast-in-place floor tendered against was in 1988 when a precast alternative of 250 mm double tees was accepted on a medium-rise frame structure that was detailed as a cast-in-place slab with secondary beams.

In the present decade, pretensioned flooring has maintained its strong position in New Zealand construction, and this should continue as such. However, the concrete industry in the 1990s is generally showing more diversity than earlier decades and there also appears to be better integration of ideas than was previously demonstrated. The use of cast-in-place systems will always be an option to designers, and there has been a resurgence of post-tensioned floors in certain parts of the country as well as some proposals of lift-slab construction. The construction industry infrastructure has, though, become very much geared toward the erection of precast flooring systems. In the authors opinion, it would take an impressive swing of the pendulum to change this construction culture in New Zealand.

1.1.3 APPROPRIATE DESIGN STANDARDS

An important ingredient that prompted New Zealand engineers into quickly adopting the American state-of-the-art in pretensioning (besides its suitability and extensiveness) was obviously language. The proceedings from ACI-ASCE committees that produced substantiated code requirements were immediately comprehensible to New Zealand engineers, and the use of English units of measurement was agreeable as well. The ACI 318 codes, in particular ACI 318-63, were to become standard documents that covered concrete design in New Zealand during the 1960s. By 1968, the Standards Association of New Zealand had produced a Standard Recommendation for prestressed concrete NZSR 32:1968 [SANZ, 1968]. Although this

document made extensive use of existing American, British and Australian guidelines, it most importantly established prestressed concrete in context with contemporary New Zealand standards relating to construction materials and key chapters (i.e., chapters 8, 9 and 11) of the then current Model Building Bylaw, NZS 1900.

NZSR 32: 1968 was not superseded until the publication of the comprehensive New Zealand concrete structures standard "Code of Practice for The Design Of Concrete Structures" NZS 3101: 1982, parts 1 and 2 [SANZ, 1982]. This standard devoted a chapter to prestressed concrete and included information in its references from both broader and more specific sources than the previous document. This is indicated by referrals to European (CEB-FIP) material and recommendations from New Zealand research on seismicity in post-tensioned frames that is associated with Professor R Park. The issue of seismicity in the prior standard NZSR 32: 1968 formed perhaps the shortest section in the entire document (section 13) and is quoted thus: "Firm recommendations to cover seismic design of prestressed concrete structures have not yet been established". The use of pretensioned flooring in seismic resisting buildings is implicit in this statement.

The new order of construction that emerged during the 1980s often saw precast frame and wall elements replace cast-in-place construction, and because of cost effectiveness an almost complete preference developed for pretensioned flooring systems. A number of the provisions in the 1982 concrete standard were challenged by precast elements because this standard was, of course, developed on the basis of cast-in-place concrete construction. The cast-in-place design philosophy also embraced many of the assumptions relating to the generalised performance of structural diaphragms. In particular, the requirements for diaphragms were briefly considered in the section of the code that covered structural (shear) wall construction. Although this standard provided reasonable guidance for the consideration of actions that may arise in a diaphragm, the provisions for detailing were not of a comprehensive nature. This has been noted in a compilation text [Booth (Ed.), 1994] that compares United States, New Zealand and Japanese practices, which quotes on diaphragms thus: "The detailing requirements given in the concrete code (i.e., NZS 3101: 1982) are minimal compared with those for other elements".

In recognition that there was a need for some congruity in the use of precast concrete elements as functional parts of seismic resistant structures, a joint study group was appointed by the New Zealand Concrete Society (NZCS) and the New Zealand National Society of Earthquake Engineering (NZNSEE) in the latter 1980s to address this situation. The outcome of this joint study group was the publication of a useful text containing applicable guidelines (though not code requirements) for general precast concrete construction [NZCS-NZNSEE, 1991]. In this publication, separate chapters have been included for both the use of pretensioned flooring and the distinctive role of floor diaphragms in seismic resistant buildings.

In 1995, the revised New Zealand concrete design standard was published [Standards New Zealand, 1995], and this comprehensive document has incorporated standard requirements that are relevant to precast concrete construction. A separate chapter has also been provided for the specific requirements of diaphragms, which includes recommendations for methods of analysis and general considerations of design actions.

Although there is an abundance of design information that is available from standards and other notable references, much of the onus in prestressed concrete design will remain with the designers. It would be extremely difficult, if not impossible, to provide a standardised set of design rules that can encompass all aspects of prestressed concrete design and construction. This is largely due to the nature of prestressed concrete itself. Prestressed components may appear in a multitude of forms with each requiring its own levels of design and manufacturing input, considerations of construction materials, construction procedures on site and considerations of elastic behaviour and ultimate limit state performance. Perhaps due to the reward that comes from extra effort, prestressed concrete has traditionally been associated with those engineers who are willing to work from first principles as the requirements dictate.

1.1.4 PRETENSIONED FLOOR SYSTEMS IN COMMON USE

1.1.4.1 General

The concrete industry in New Zealand has developed and popularised a diverse array of building applications and products in recent years. As a result, a greater proportion of domestic dwellings are constructed from concrete elements such as tilt panels, masonry blocks and expanded polystyrene (EPS) systems with infilled concrete cores.

Table 1.1 Typical simply supported span-to-depth ratios of commonly used pretensioned concrete members [after Collins and Mitchell, 1987]

Type of element	Live load (kPa)	Span/depth ratio (l/h)
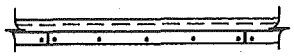	less than dead load	40
	2.4 4.8	40-50 32-42
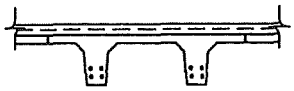	2.4 4.8	20-30 18-28
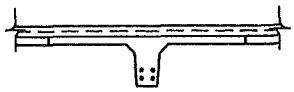	2.4 4.8	23-32 19-24
	less than dead load	30

These forms of wall construction immediately facilitate the use of pretensioned flooring units and in many situations (especially with tilt panels) a suspended concrete floor fully complements the design of the supporting wall structure by providing a rigid diaphragm element. At this lighter end of the construction market the floor requirements are often influenced by the relative geometric complexities of house construction. In this role, pretensioned flat slab units and joist-infill systems have proved most effective.

Flat slabs and joist-infill systems have also been widely used in commercial construction, however, there is a limitation with these systems when significant spans are desired without the additional expense of having to provide temporary shoring. In this role extruded hollow core systems are ideal, allowing longer spans to be achieved at the optimum of economy. Where long spans are required to support more intense loads (especially from shear or impact) either double tee or single tee sections may become the more appropriate option to the designer. Pretensioned tee sections also allow the use of partial prestress techniques which can improve both the flexural performance and economics of the section.

1.1.4.2 Flat Slabs

The typical pretensioned flat slab that is consistently manufactured in New Zealand is commonly known as Unispan and has a section that is 1.2 m wide and 75 mm deep (Figs. 1.1 and 1.2). Various thicknesses of composite topping can be placed to facilitate particular load and span requirements and also the addition of continuity reinforcement over the supports. This system almost always requires either one or two rows (depending on span) of temporary shoring that is positioned before the cast-in-place topping is added (Fig. 1.3). This shoring acts to pre-set a construction camber into the floor for deflection control and alleviation of bottom fibre tension stresses under service loads.

The thickness of flat slabs may be increased to form either stiffer composite floors or pre-finished flooring units that do not require temporary shoring. Where a composite topping is not employed, special detailing must be considered in order to achieve dependable diaphragm performance under seismically induced forces [Standards New Zealand, 1995].

Pretensioned flat slabs are generally favoured in short-span domestic and light commercial construction due to their efficiency in terms of delivered cost, relatively light weight and simplicity to erect. Because they are shored at construction it is not difficult to achieve a uniform soffit that may be either lined, textured or painted, thus permitting a minimum of compartment head-room without compromising fire resistance ratings and sound insulation properties. One of the features of flat slabs is that they permit inexpensive chases and rebates to be formed for floor penetrations. Raked and curved end seatings can also be accommodated without too much difficulty, which adds to flat slab popularity as suspended flooring for architecturally designed houses.

Provided that sensible load-span ratios are chosen and that on-site construction is properly carried out, such as the temporary shoring and cast-in-place topping, pretensioned flat slabs are an ideal flooring element. The upper surface of flat slabs can be broomed to achieve a good

texture for composite bond with the cast-in-place topping, and tie reinforcement (typically R6 spirals) can be incorporated to enhance the interface bond capacity. The generally low magnitude of axial prestress in flat slabs coupled with small internal lever arms results in a composite section that exhibits stable behaviour under long-term creep and shrinkage actions.

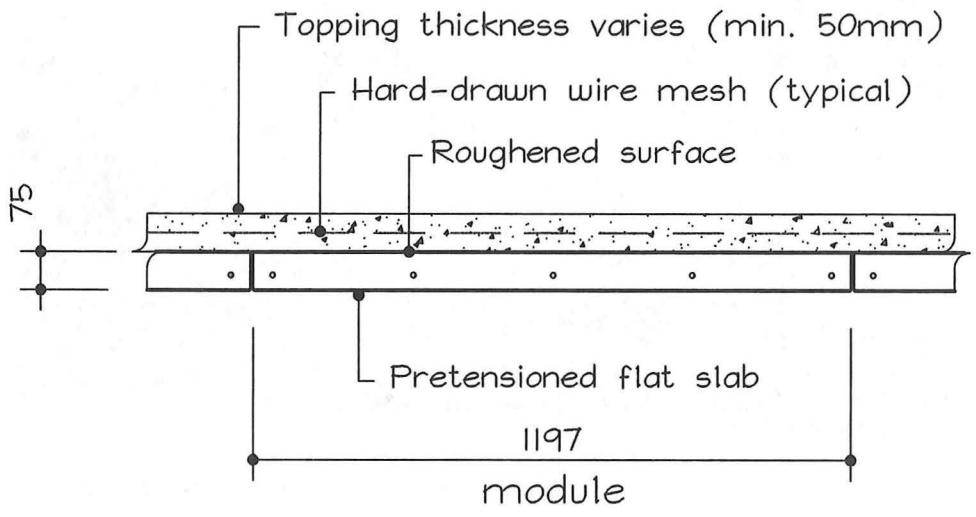

Fig. 1.1 Typical composite section of pretensioned flat slab (Unispan) flooring

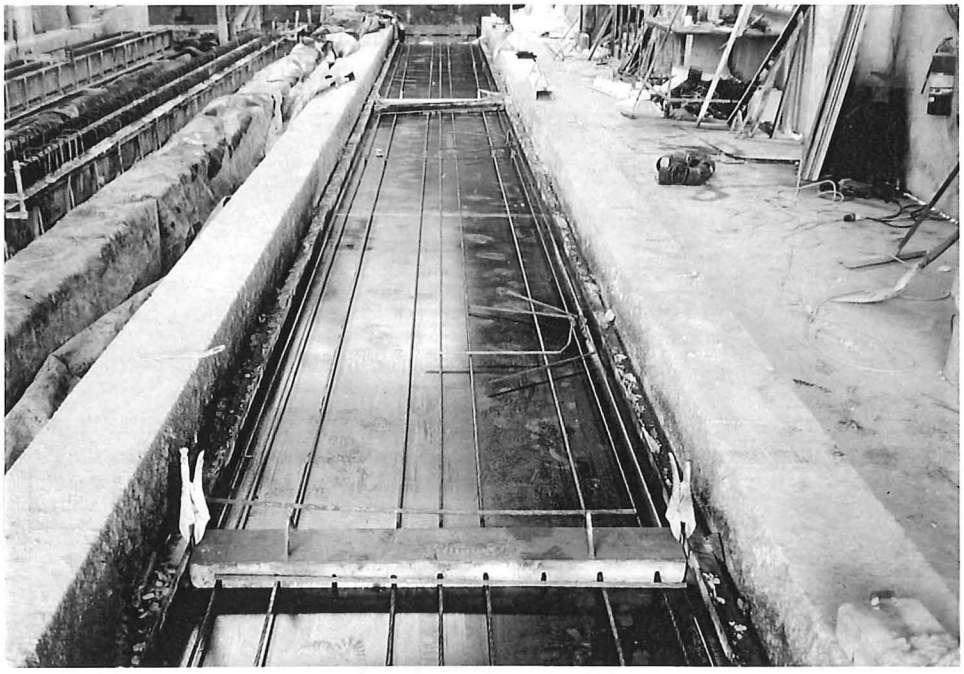

Fig. 1.2 Manufacture of pretensioned flat slabs

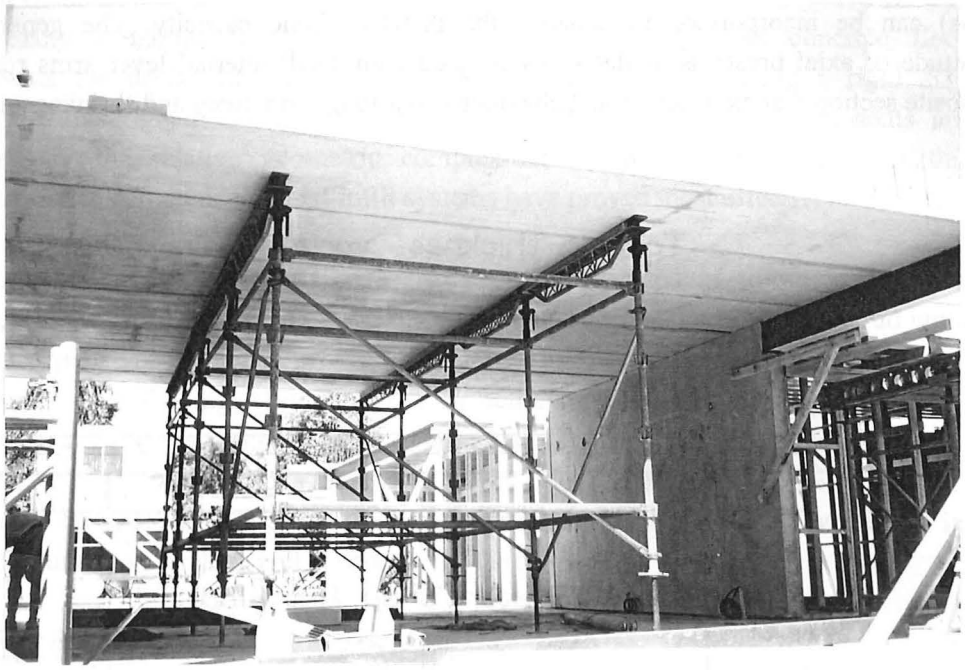

Fig. 1.3 Temporary shoring of a suspended floor constructed from flat slabs

1.1.4.3 Joist-Infill Systems

Although joist systems involving precast concrete infill blocks have been used in New Zealand construction, progressive refinement has led to the general use of pretensioned concrete joists with sawn timber infills in combination with a cast-in-place concrete topping. The sections of pretensioned joists that are commonly manufactured in New Zealand (e.g., Fig. 1.4) only differ in the basic dimensions of the joist units themselves and the nominal configurations of composite ties. These sections are designed on the assumption of a one-way joist flooring system and certain alleviations are permitted for these joist floors with respect to shear reinforcement, provided that specified dimensional and spacing limitations are adhered to [Standards New Zealand, 1995].

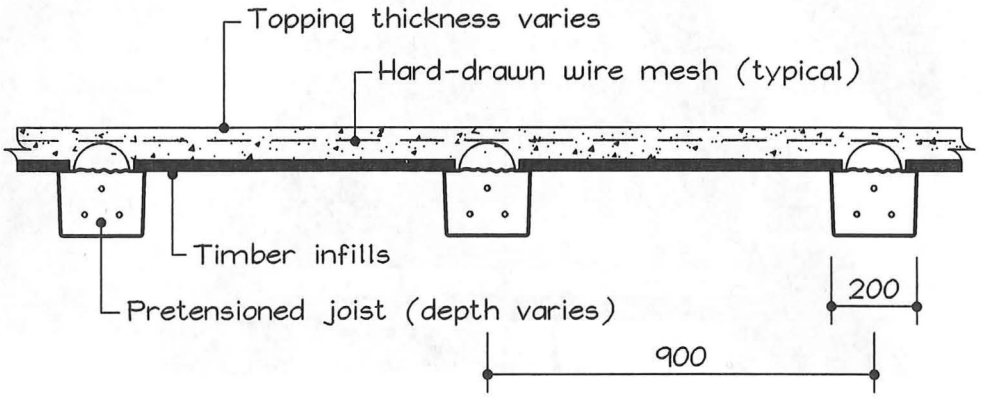

Fig 1.4 Typical joist-infill section used in New Zealand construction

The joist units may be manufactured to any suitable depth which usually ranges between 75 mm and 250 mm deep. At construction, temporary shoring is necessary to pre-set a construction camber and residual compression stresses into the bottom fibre of the precast unit similarly to pretensioned flat slab units. Although joist-infill systems are more efficient than flat slabs in terms of floor self weight and span capabilities, the structural advantage of joist-infill systems is often offset by additional materials and labour costs associated with manufacture and on-site construction.

Joist-infill systems are well suited to floors where difficulties arise from seating layouts, point loads and penetrations. Because only the discrete length of the joist unit needs to be considered, geometrically difficult layouts are often more manageable than with slab systems where a reasonably accurate end seating profile must be formed. Where significant point loads or additional superimposed patch loads are supported by the floor, joists may be conveniently grouped together under the load to provide for the increased demand in floor capacity. Another distinct advantage with joist-infill systems is for floor layouts that require many small and seemingly random penetrations for services, such as with hospital buildings. These types of penetrations can be better managed on-site by simply locating and forming these duct holes through the timber infills before the topping concrete is placed.

An important design consideration with joist-infill systems is the proportion that the composite topping makes to the finished composite section. The ratio of the composite section second moment of inertia to that of the bare prestressed rib may be in the order of twelve or more. The relatively large lever arm that may occur between the centroid of the topping slab and the composite section axis can result in excessive long term deflections due to shrinkage strains in the topping element. The possible effects of these separate section portions must always be considered in the design of joist flooring.

Fig. 1.5 Manufacture of pretensioned joist units (Interspan)

Fig. 1.6 The light unit weight of joists allows for efficient transportation and craneage

1.1.4.4 Double Tee and Single Tee Units

Before the advent of hollow core flooring, tee sections were the most popular pretensioned flooring unit for constructing long spans and for situations involving larger superimposed floor loads without the need for temporary shoring. In New Zealand, the double tee unit has been most commonly used, although single tee units have appeared on occasion and have proven to be an effective unit for longer span applications.

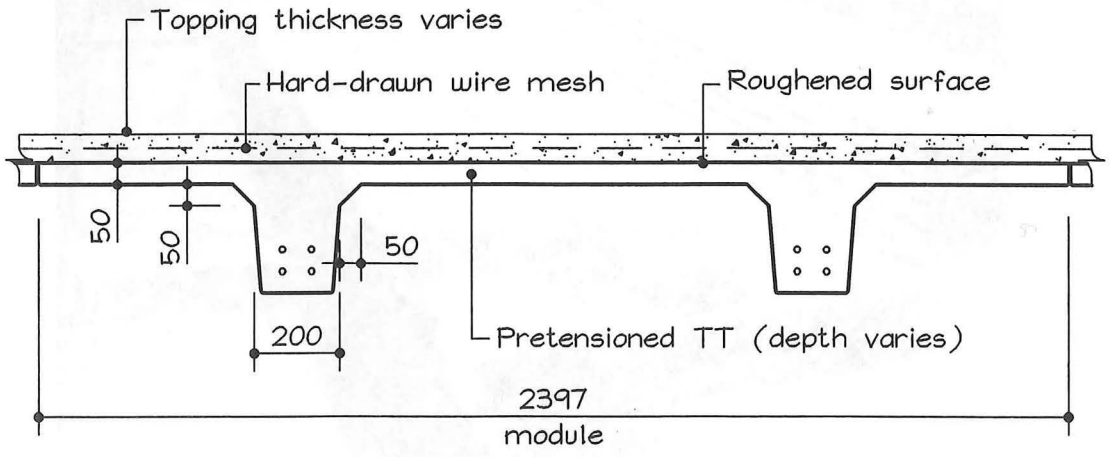

Fig. 1.7 Typical metric double tee section with composite topping

A useful feature of tee sections is that partial prestress methods may be used and this can result in a more efficient design in certain situations. Partial prestressing may also compensate for using less pretension force in the section, thus producing a unit which has less tendency to creep than a fully pretensioned section. This is especially beneficial for longer spans where the impact of volume changes upon the support structure must always be considered. Because of the relative size of tee sections, creep and shrinkage movements in particular have been known to cause problems with relatively flexible support elements such as walls.

With tee floors it is possible to include cast-in connection details, which makes possible the use of these units in untopped floor diaphragms. Additional tie reinforcement may also be included to enhance the composite bond between the precast unit and topping concretes. Because of the end seating configurations available it is not difficult to detail tee units for additional shear force or support restraint actions that may arise.

Many of the major difficulties with double tee units occur at the manufacturing stage. In floor layouts that involve irregular floor penetrations it can be a difficult detailing exercise getting the units to line up with the penetrations without interfering with the tee legs. Placing rebates in these units can likewise cause difficulties at the production stage. The compounding cost of moulding time and the generally higher labour and raw materials content required in tee manufacture can quickly make this type of unit less attractive than hollow core flooring systems. With single tee units, storage and transportation must always involve support frames to keep the units upright. This requirement can cause logistical problems where single tee units are to be stored in the manufacturers yard, and can be especially difficult when units need to be set down on the construction site.

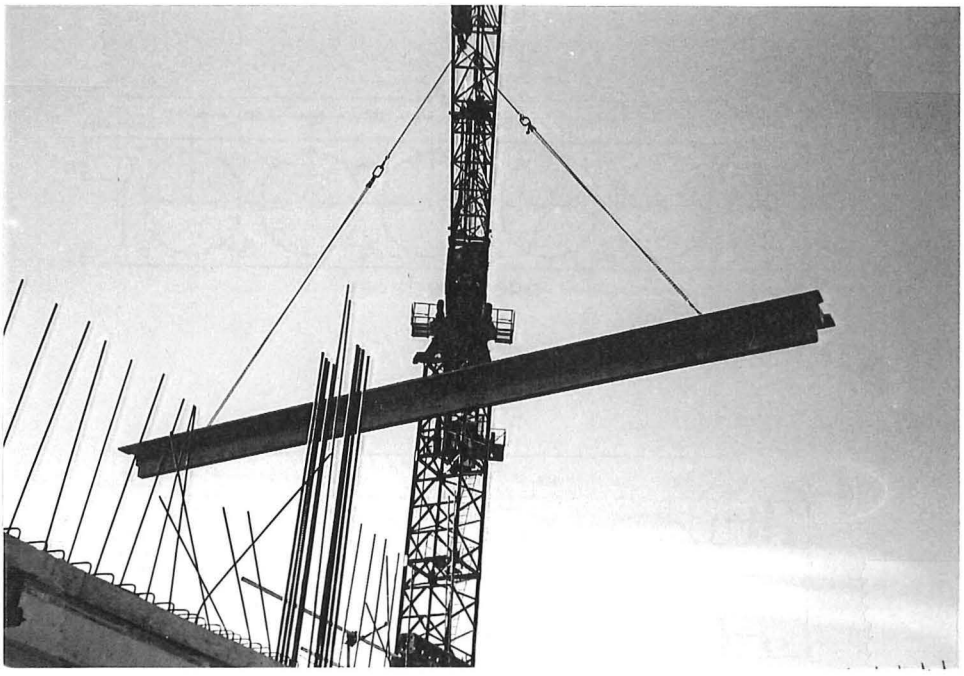

Fig. 1.8 Single tees used in the construction of the new Civil and Mechanical Engineering buildings at the University of Canterbury School of Engineering (1996).

1.1.4.5 Extruded Hollow Core Flooring

Extruded hollow core is probably the most economical of the longer span pretensioned flooring sections available. An automated production process coupled with the flexural efficiency of prestressed hollow core sections results in a flooring element that is ideal for the repetitive production runs demanded by many of the larger building projects. Because of the so called "zero slump" concrete that is required for the extrusion process, early release strengths are obtainable, which adds to the mass production capabilities of hollow core flooring.

There are, however, some aspects of hollow core units that are potentially not so ideal as their raw production advantage. The most obvious is that the extrusion process does not allow for the inclusion of shear reinforcement in the webs of hollow core units, and another important point is that the surface of extruded concrete is difficult to significantly roughen by traditional brooming methods. These characteristics are unique to extruded products and may be either emphasised or discarded (in terms of structural importance) depending on the particular usage that the flooring unit is put to. However, these facets surrounding the construction of hollow core units will always remain as important design considerations and form the basis of much of this thesis. Extruded hollow core flooring is the subject of further discussion in the following section.

1.2 PRECAST PRESTRESSED HOLLOW CORE FLOORING

1.2.1 GENERAL

1.2.1.1 Cross Sectional Sizes

A variety of extrusion machines have been used in New Zealand since hollow core manufacture began in about 1976. The earlier plant tended to be either "Dycore" or "Stresscore" extruders but these brand names have been superseded in recent times by the "International Hollow Core Engineering (IHE)" and "Partek" machines. Differing forms of cross-section may be associated with the individual brands of extrusion plant, however, the fundamentals of concrete extrusion apply in a general way to all of the typical hollow core machines used in New Zealand.

A number of cross-section depths have been made available (Fig 1.9), with the most commonly used sizes being 200 mm and 300 mm deep. However, units as shallow as 150 mm are also manufactured, and a 400 mm deep unit was introduced into the Auckland market by Firth Industries during April of 1996.

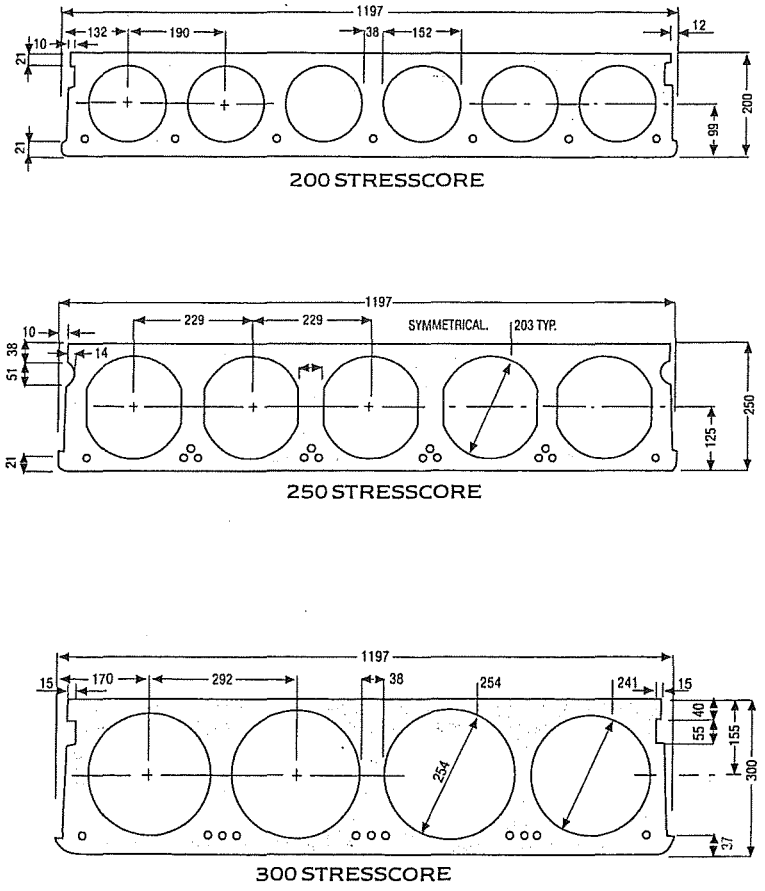

Fig. 1.9 Typical hollow core sections produced by Firth Industries

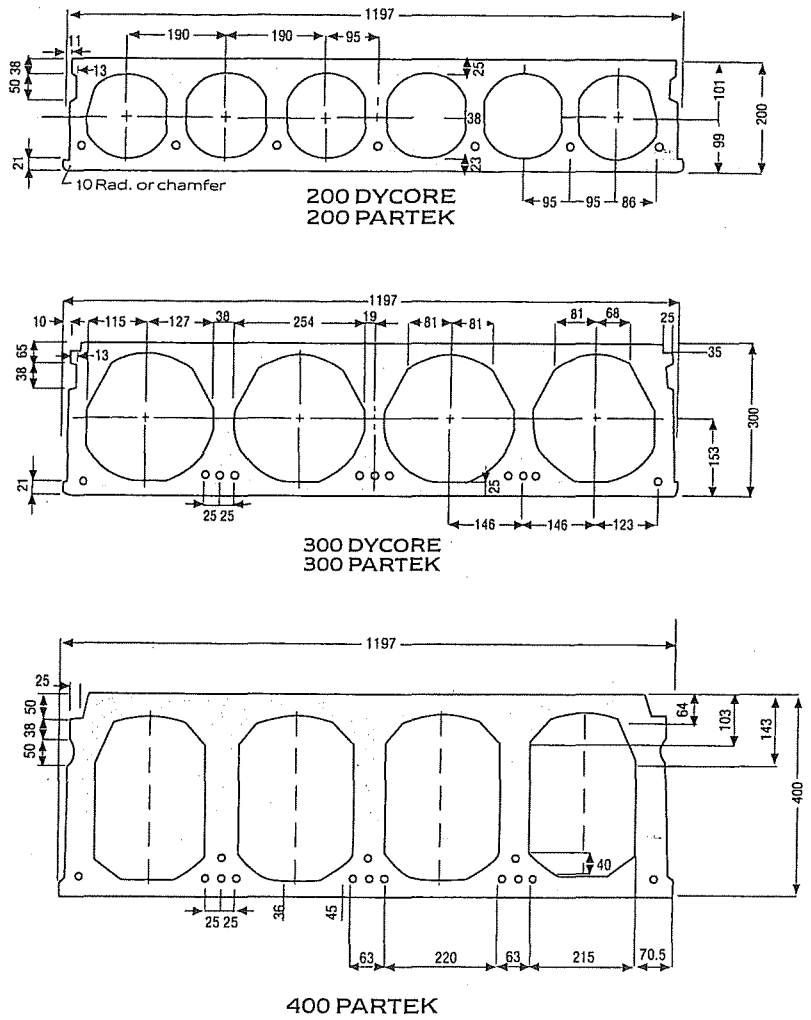

Fig. 1.9 (continued) Typical hollow core sections produced by Firth Industries

Table 1.2 Section properties corresponding to cross-sections shown in Fig. 1.9

Unit	Area (m^2)	Y_b (mm)	I_x (m^4)	Self Wt. (kPa)
200 Dycore/Partek	0.1192	100	0.00065	2.4
200 Stresscore	0.1264	99	0.000629	2.6
250 Stresscore	0.1336	125	0.001123	2.8
300 Dycore/Partek	0.1606	153	0.00204	3.2
300 Stresscore	0.1718	145	0.00199	3.6

As with all flooring systems used in New Zealand, hollow core units are required to satisfy a number of serviceability and ultimate limit state performance criteria. The serviceability requirements associated with pretensioned floors will almost always include such obvious items as the control of flexural stresses and short-term and long-term deflections, although acoustic, thermal and vibration properties may also need to be considered in the serviceability checks [Standards New Zealand, 1992].

1.2.1.2 Design for Comfort and Fire Safety

As part of a building space that is designed for human occupancy, hollow core units need to comply with certain requirements relating to comfort and safety that are distinct from purely structural behaviour considerations. The four main categories involve three serviceability requirements relating to comfort which are Vibration Behaviour, Acoustic Properties and Thermal Properties (ambient), along with the ultimate limit state category of Fire Resistance.

(a) Vibration Behaviour

For typical applications and span lengths of pretensioned flooring systems there appears to be no need to overly consider the problems of vibration due to vertical accelerations caused by foot traffic and seismic actions. This is mainly due to the relative stiffness of the floor component, which is usually achieved in design work by a sensible choice of span-to-depth ratio. However, with pretensioned floors there is a real temptation for the designer to push the span out. Hence, where long design spans employ continuity reinforcement to allow redistribution of design bending moments, care should be exercised to ensure that the floor proportions are not decided on the basis of strength alone. This may be especially true when there is a potential for vibration stimuli within the structure, or there is little by way of effective damping in the form of partition walls, etc.

With longer spans, the natural frequency of hollow core units with composite topping may coincide with the broader range of characteristic frequencies that are generated by human activities (typically 2-8 Hz). In New Zealand it is specified [Standards New Zealand, 1992] that floors with fundamental frequencies of less than 8 Hz will require an investigation based on dynamic analysis if the proposed occupancy involves rhythmic activities, such as with dance venues and gymnasiums. Of course, any situations involving the support of frequently reciprocating loads and vibrating machinery should be treated in the same manner.

Long span hollow core flooring units may also be susceptible to vibration caused by the vertical accelerations associated with earthquakes. A feature of the recent Northridge (1994) earthquake was the propensity of significant vertical accelerations measured in both structures and the free-field. For example, a vertical acceleration of 0.52g was measured in a six storey parking structure and up to 1.83g was recorded on an interchange bridge with a corresponding maximum horizontal acceleration of 1.0g [NZNSEE, 1994]. On several occasions, and with a wide dispersion of epicentral distances, the vertical acceleration components resulting from Northridge were sufficiently manifest to warrant extra consideration when reviewing the performance of structures. The design vertical acceleration due to earthquakes is normally taken

as being two thirds of the horizontal component [Standards New Zealand, 1992]. The Northridge event is justification that measures to avoid unfavourable effects caused by significant vertical accelerations should be embodied in the overall design philosophy.

Simplified approaches to what otherwise can be a complex problem are available for guidance [ACI, 1979; CEB, 1991], which includes useful information on damping ratios and the comparative behaviour of calculated response versus the measured response of floor systems. It is interesting to note that with realistic estimates of flexural stiffness, damping and vertical acceleration, it is feasible that long span hollow core floors could exhibit a deflection amplitude that would be described as "very disturbing" as a subjective measure of human response to the serviceability level earthquake.

Bearing vertical accelerations in mind, it is essential that designers approach longer spans from the point of view of providing enough flexural stiffness over the basic strength and defection requirements under static gravity loads. This is because the vertical response amplitude alone, before the application of a suitable dynamic amplification factor, may already be unacceptable in the serviceability limit state environment. Both the measured and calculated values of damping for floors supporting non-structural partitions point to characteristic values that range between 5% and 10% of critical damping, therefore, the provision of an adequate flexural stiffness may be the most efficient method of amplitude control.

Although vibration problems have traditionally been counteracted by prescribing floor deflection limits under superimposed loads, such as span/360 (1/30 in. per ft. of span), these types of empirical formulae are directed towards controlling vibrations induced by foot traffic and not seismic actions. As shown at Northridge and at other places, there are always elements of uncertainty and magnitude when detailing for seismic response. In the case of long span hollow core floors it is envisaged that open plan floors in stiff low-rise structures may be the most susceptible to the effects of vertical seismic accelerations.

(b) Acoustic Properties

The requirements for noise control are usually most acute when floors act as a partition between different occupancies in a residential building. In New Zealand, a standard for sound transmission is set out in section G6 of the New Zealand Building Code [Building Industry Authority, 1991]. In this document the minimum requirements for a sound transmission classification (STC) between party walls and floors and an impact insulation class (IIC) for floors is given as 55. This figure is supported by recommended practice from other parts of the world that have sufficient experience of noise control in multi-storey apartments. However, emphasis is still placed on the need to plan carefully so that louder sound sources such as laundries are not positioned in near proximity to designated quiet areas, otherwise an STC of up to 70 is recommended [CPCI, 1987].

Since a 200 mm deep hollow core unit with 65 mm topping has an STC of about 54 and an IIC of 30, it is apparent that additional sound proofing of the floor will be required in most structures. In this situation the shortfall of IIC could be overcome by specifying dense carpet

with a soft underlay on the floor unit, giving an additional IIC of 25 to meet the building code requirements.

For qualitative information on the acoustic properties of individual types of hollow core sections the licence holder (precast manufacturer) will have access to specific test data that is the property of the suppliers of the particular brand of hollow core extruder.

(c) Thermal Properties

Similarly to acoustics, the Building Code [Building Industry Authority, 1991] contains section G3 on the requirements for thermal insulation in buildings. The minimum thermal resistance (R) value will usually vary for different compartments within a structure, ranging from a minimum R value of 0.6 for concrete walls to an R value of 1.5 for roofs. When designing for thermal requirements, the prescribed R value is achieved, in its simplest form, by the addition of the R values of individual components (including air gaps) that make up the thermal barrier. It is evident that hollow core units with composite topping alone are not adequate to achieve the required external R value. For 300 mm hollow core with 65 mm topping, this value is only about 0.5 [CPCI, 1987].

There are methods for improving the thermal resistance of bare hollow core units from within, such as applying insulation materials to the hollow core voids. Again, the precast manufacturer will have access to proprietary information on the thermal properties of particular extruded hollow core units and methods for improving their thermal properties. With one of the larger manufacturers of hollow core machinery being a Finnish company, this is hardly surprising.

(d) Fire Resistance

Many tests have been performed on the fire resistance properties of pretensioned flooring units including hollow core flooring [CPCI, 1987]. The standard for practice in New Zealand relating to the fire resistance rating (FRR) of hollow core flooring [Standards New Zealand, 1995] has been developed around the findings of European (CEB-FIP) and North American test laboratories. Based on an equivalent thickness, it is apparent that a simply supported 200 mm deep hollow core unit without topping and with normal height of pretension strand will achieve the prescribed integrity, insulation and stability end point criteria when exposed to a 90 minute fire. Because the vast majority of new buildings in New Zealand have a required FRR of 60 minutes or less [Building Industry Authority, 1991] there should be no foreseeable problems with the fire safety aspect of composite topped and partially continuous hollow core floors.

For applications where abnormally high fire loads are present or other concerns may exist within the fire compartment with regards to unusual geometry and combinations of building materials, consultation should be made with a Fire Engineer [Thomas, 1996].

1.2.1.3 The Flexural Behaviour of Hollow Core Flooring

(a) Serviceability Limit State

The combination of a dry-mix concrete and the high frequency vibration that is required for extruded concrete manufacture results in a concrete constituent that is dense with good binding between the aggregate and cement paste. This is beneficial to the flexural cracking modulus of these elements and it is anticipated that the allowable tensile stress values for uncracked pretensioned members as given in standards [Standards New Zealand, 1995] will be conservative for hollow core units (although this may be affected by aggregate source). Well compacted and dense concrete coupled with a characteristically high release strength will also benefit the pretension strand transfer bond performance when control is achieved through radial tension inducing mechanisms such as Hoyers effect [Lin and Burns, 1982].

Referring to Fig. 1.10, it can be seen that hollow core slabs are flexurally efficient as an unpropped flooring system. This efficiency is partly due to the comparatively large pretension eccentricity that can be utilised in cored slab systems without exceeding the allowable combined stress parameters (compressive or tensile) at the prestress transfer stage. Because most of the deeper hollow core units shown in Figs. 1.9 are pretensioned at eccentricities that are well outside the middle third kern of the section, tensile stresses will result in the top flanges at the ends of these members. Under a non-continuous support configuration (i.e., at a true simple support) and after term losses of prestress force, the top fibres of these units may continue to act in tension throughout the service life of the structure.

Due to flexural proficiency, the provision of continuity reinforcement is not a strict requirement for the satisfactory strength performance of hollow core flooring under either service or ultimate limit state loadings. For longer spans, however, the allowable deflection criteria will become an increasingly relevant consideration and the full use of continuity bars should be specified for these applications.

Full scale gravity load tests conducted on both a simple span [Scott, 1973] and continuous spans [Rosenthal, 1978] indicate that much of the flexural behaviour of hollow core slabs can be predicted by established principles of analysis. In his paper, Scott concluded that the methods prescribed by the ACI building codes [ACI 318-71, 1971] will, with sufficient accuracy, predict the flexural behaviour of a hollow core slab at all the critical phases in a test-to-failure. These observations are supported by other references in which the more precise moment-curvature analysis techniques are also presented [Lin and Burns, 1982. Collins and Mitchell, 1987].

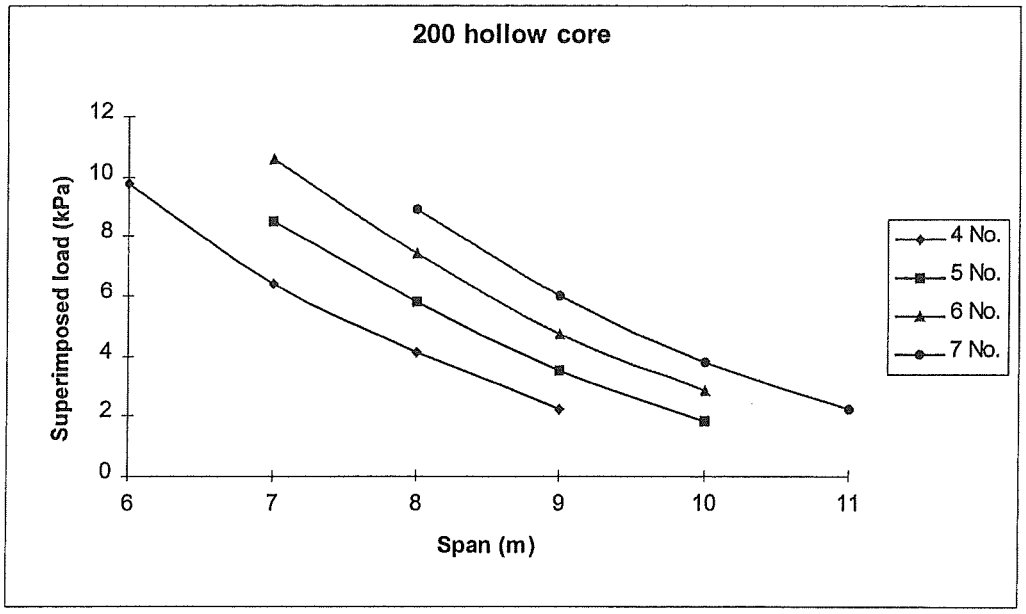

(a)

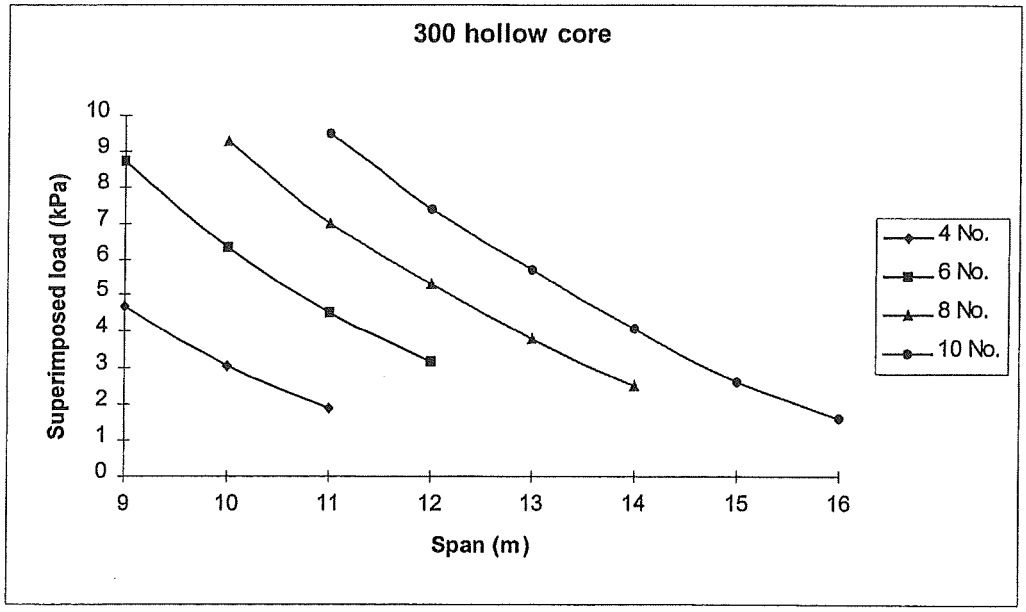

(b)

Figs 1.10 Load-span relationships of hollow core flooring with 65 mm thick composite topping and differing levels of prestress force. The numbers of 12.7 mm diameter strand are indicated in the legend.

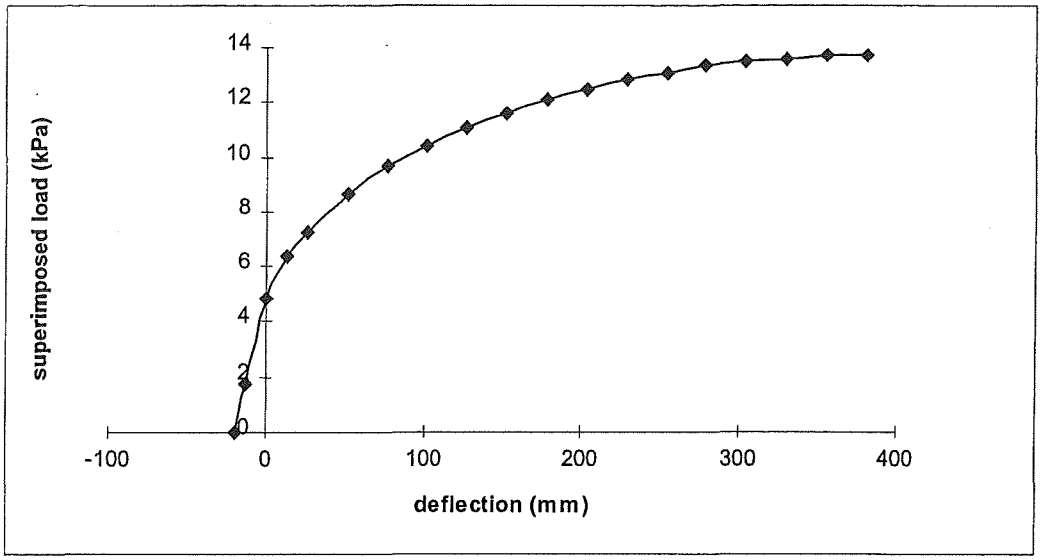

Fig. 1.11 Typical load-deflection curve for a simply supported hollow core slab with composite topping [after Scott, 1973]

The European recommended [FIP, 1988] approach to flexure in hollow core flooring is perhaps the most discriminating (ultimately due to shear implications) in that it tends to regard extruded hollow core units as a non-generic form of pretensioned floor construction. In the FIP publication on hollow core, emphasis is placed on eliminating flexural cracks that may otherwise occur in zones that involve the development of prestress force. This is due to the likelihood that cracks generated in these regions, without the benefit of reinforcing ties, will penetrate the full depth of the section resulting in reduced aggregate interlock and a reliance on prestressing steel dowel action to sustain shear forces.

The FIP recommends that flexural tension allowed in the extreme fibre of hollow core sections over the prestress transfer zone should be limited to an average of about 85% of the flexural tensile stress that is allowed in zones of full prestress force, as derived from Equation 1.1 for common depths of hollow core section. The FIP recommendations for flexural stress in extruded hollow core systems are somewhat more restrictive than those adopted by the New Zealand standard because the tensile stress used in calculations is limited to the lower five percentile value, which is about 71% of the mean value of concrete tensile strength taken from tests (refer columns 3 and 4 in Table 1.5). In accordance with Table 1.4, this leads to a maximum allowable flexural tension stress of approximately 70% of the ACI building code values in zones of full prestress force at a given strength of concrete. In the aforementioned zones of prestress development, allowable flexural tension stress will reduce to about 60% of that allowed by ACI building codes (see Table 1.3).

The FIP publication [FIP, 1988] provides another example where flexural tensile strength and axial tensile strength have been made distinct. This is in the limits that are placed on flexural tensile stresses that may occur due to bending in the transverse direction. The lesser axial tensile stress value has been employed in this situation because the presence of cores in the section does not support assumptions regarding flexural tension.

Table 1.3 shows the maximum allowable concrete stress for uncracked sections at the serviceability limit state used in New Zealand. The corresponding FIP values are shown in Table 1.4.

Table 1.3 Maximum allowable concrete stresses for uncracked sections at the serviceability limit state [after Table 16.1, Standards New Zealand, 1995]

	Load category			
	I	**II**	**III**	**IV**
Stress case	Immediately after transfer before time dependant losses	Permanent loads plus variable loads of long duration or frequent repetition	Specified service loads for buildings where load category II does not apply	Permanent loads plus infrequent combinations of transient loads
Compression	$0.6f'_{ci}$	$0.4f'_c$	$0.45f'_c$	$0.55f'_c$
Tension	$0.5\sqrt{f'_{ci}}$	zero	$0.5\sqrt{f'_c}$	$0.5\sqrt{f'_c}$

For calculation of the effective flexural tensile stress, the axial tensile stress is modified as a function of the section depth. For the application of stresses given in Table 1.4, the concrete flexural tensile stress f_{ctf} is related to the axial tensile strength f_{ct} by:

$$f_{ctf} = f_{ct}\left(0.6 + \frac{0.4}{d^{0.25}}\right) \qquad (1.1)$$

where the effective section depth d is in metres, and is not taken greater than 1.0 m.

Table 1.4 Maximum allowable concrete stresses for uncracked hollow core sections at the serviceability limit state [after FIP, 1988 and CEB-FIP, 1978]

	Load category		
	I	**II**	**III**
Stress case	Stress in concrete at transfer	Stress at top or bottom fibre in transfer zones for any load combination	As for load category II in zones of full prestress development
Compression	$0.6f_{cki}$	$0.6f_{ck}$	$0.6f_{ck}$
Tension	$f_{ctmj}/1.3$	$f_{ctk,0.05}/1.3$	$f_{ctfk,0.05}/1.3$

From the FIP recommendations, the tensile stress values referred to in Table 1.4 may either be obtained directly or derived from the values given in table 1.5 below:

Table 1.5 Relationships between ①cube strength, ②cylinder strength, ③lower limit tensile strength and ④mean tensile strength of concrete, used in Table 1.4 [FIP, 1988]

① $f_{ckcub.\ 150mm}$	② f_{ck}	③ $f_{ctk,0.05}$	④ f_{ctm}
30	25	1.8	2.5
35	30	2.0	2.8
40	35	2.2	3.1
45	40	2.4	3.4
50	45	2.6	3.7
55	50	2.8	4.0
60	55	3.0	4.3

(b) Ultimate Limit State

For the ultimate limit state the FIP approach to composite hollow core flooring is less specific and follows general provisions [CEB-FIP, 1978] that are applied on the basis that adequate composite bond is maintained between the precast and cast-in-place components of the section [FIP, 1982].

For calculation of section capacity the New Zealand Standard and the ACI building codes treat hollow core units identically to other prestressed construction. By simplified methods, the stress in the strand at the flexural strength of the unit is obtained by making a suitable reduction to the ultimate tensile capacity of the strand to allow for the characteristic stress-strain curve of the prestressing steel. Alternatively, moment-curvature analysis may be used with strain compatibility assumptions being applied over the actual stress-strain characteristics of the constituent materials in the section. For hollow core floors the simplified method of analysis has proved adequate for design purposes [Scott, 1973].

Another consideration that has been of interest in the flexural strength design of hollow core flooring is the establishment of flexural bond in the prestressing strand. This pertains mainly to highly loaded short spans where flexural bond demands may extend into the transfer bond regions at the ends of a unit. Tests have shown that sudden collapse of these types of members is unlikely. However, important conclusions were drawn on quality control aspects at manufacture [Anderson and Anderson, 1976].

1.2.1.4 The Shear Behaviour of Hollow Core Flooring

(a) Flexure-Shear

Hollow Core slabs have demonstrated adequate shear capacity to resist the customary levels of uniformly distributed load that are associated with the floors of buildings [Scott, 1973]. In situations where concentrated loads occur near the ends of units, the support details may require extra attention if the allowable shear and bond stresses are not to be exceeded. If required, the shear capacity can be greatly enhanced by specifying concrete infilled voids and embedded reinforcing bar details for end seatings that are subjected to increased shears [Mejia-McMaster and Park, 1994].

It is widely considered that extruded hollow core slabs should not be used in structural applications that involve large shear forces, especially large shear forces in combination with impact such as is caused by heavy motor vehicles.

In keeping with section 1.2.1.3, a comparison drawn between New Zealand practice [Standards New Zealand, 1995] and the recommendations of the FIP [FIP, 1988] indicates that a more conservative stance has been taken by the Europeans with respect to shear in hollow core flooring. However, the New Zealand standard approach to shear in prestressed concrete does concur with CEB-FIP methods, and some important qualifications on shear formulae given in the New Zealand standard are outlined in the commentary (part 2) of the standard.

Although the FIP recommendations could appear to be conservative with respect to flexure-shear in hollow core systems, this document has only existed as a recommendation against a large background of European national codes. Written along the lines of a guide to good practice, it is understandable that the authors would advocate design criteria that can guarantee absolute performance for expressly "precast prestressed hollow core flooring".

Flexure-shear due to predominant point loads would appear to be an acute consideration for extruded hollow core units because of the likelihood that flexural cracks will coincide with the development of shear mechanisms as the ultimate limit state of loading is approached. Because there is an absence of shear reinforcement, longitudinal splitting cracks may be expected to propagate along the hollow core webs, possibly resulting in a catastrophic shear failure (see Fig. 1.12). This peeling effect is caused by dowel action on vertically unrestrained longitudinal reinforcement as part of the shear resistance mechanism and has been widely observed in many flexure-shear tests involving beam sections without web reinforcement [Park and Paulay, 1975].

To avoid flexure-shear problems the FIP recommendations place extra limitations on the shear capacity of extruded hollow core members that are cracked in flexure. It should also be noted that the allowable flexural tension stresses have already been restricted for the serviceability limit state, as discussed in the previous section on hollow core flexure. The CEB-FIP model code method is followed [CEB-FIP, 1978] for calculation of flexure-shear capacity. However, the design values of resistant shear stress (as a function of design concrete compressive

strength) have been scaled to an average of 73% of those calculated by the model code formula, and are listed in Table 1.6.

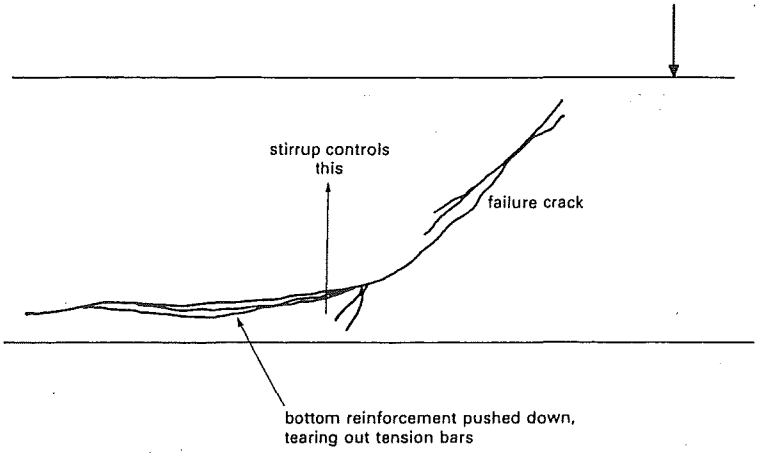

Fig. 1.12 Longitudinal peeling in flexure-shear zones caused by the dowel action of principal reinforcement in the absence of stirrups [BS 8110: 1995 Handbook, 1995]

Table 1.6 FIP recommended values of resistant shear stress for use in flexure-shear capacity calculations (Eq. 1.2) involving extruded hollow core flooring [after FIP, 1988]

f_{ck} (MPa)	τ_{Rd} (MPa)
25	0.27
30	0.29
35	0.31
40	0.33
45	0.34
50	0.36
55	0.36
60	0.36

Thus, the flexure-shear capacity in the ultimate limit state is given by:

$$V_{rd11} = \tau_{Rd} b_w d \xi \left(1 + 50 \rho_p\right) + \frac{0.9 M_0 V_x}{M_x} \qquad (1.2)$$

Actually, both terms of this equation differ from the treatment of flexure shear in the CEB-FIP model code because an additional factor of 0.9 placed on the proportion of shear resistance that can be utilised in relation to the section decompression moment. In the CEB-FIP model code, the resistant shear stress is given by:

$$\tau_{Rd} = 0.068 \sqrt{f_{ck} + 5/\gamma_c} \qquad (1.3)$$

where the partial safety factor γ_c is taken as 1.4 for well placed concrete. If Eq. 1.3 is substituted in Eq. 1.2 and the factor of 0.9 is ignored in the second term, a very similar value of flexure shear capacity will result to that calculated by the corresponding equation in the New Zealand standard [Standards New Zealand, 1995]. Equation 9-9 in this document gives the nominal shear stress provided by concrete in regions subject to flexure-shear cracking for non-composite uniformly loaded beams as:

$$v_{cn} = v_b + \frac{V^* M_0}{b_w d_c M^*} \tag{1.4}$$

The basic shear stress v_b is applied identically to all members incorporating tension reinforcement or prestress steel in a flexural tension zone, and is given by:

$$v_b = \left(0.07 + 10\, p_w\right)\sqrt{f'_c} \tag{1.5}$$

For situations where the section is of composite construction and does not support a uniform load (which usually infers a live load) a fundamental approach to flexure and shear interaction must be adopted. This allows for a more exact analysis to be performed with regards to predicting the shear force that corresponds with the designated critical moment in the section. In Eq. 1.4, the critical moment is taken as the decompression moment for the prestressed section and is that which will cause an extreme fibre stress of zero after consideration of all losses. Consequently, this equation is conservative for some sections because the mechanics of flexure-shear are such that first cracking due to flexural bending stresses is the point from which a shear failure is instigated. The ratio of first cracking moment to decompression moment will vary with differing configurations, and is most significant for members with light, concentric prestress and reduces with increased prestress force and eccentricity.

The development of flexure-shear equations for specific load configurations is discussed in various publications [ACI, 1968] where the dead and live load components are isolated and treated accordingly. Analysis of flexure-shear capacity for composite topped and shored flooring systems involves extra steps with the separation of components and this has been discussed in relation to the shear design of pretensioned joists [Herlihy, 1995].

(b) Web Shear

For web shear capacity, the formula given in the FIP recommendations [FIP, 1988] is described as the shear capacity for a region that is uncracked in flexure. Because the critical section for web shear is at the interior face of the end support, the FIP method directly modifies the beneficial effect of axial prestress force over the transfer length of the pretensioning steel. The shear capacity formula is given as:

$$V_{Rd12} = \frac{I b_w}{S}\sqrt{f_{ctd}^2 + 0.9\alpha\sigma_{cp} f_{ctd}} \tag{1.6}$$

where the average prestress in the concrete is:

$$\sigma_{cp} = A_p \sigma_p / A_c \tag{1.7}$$

and the reduction factor α is based on a parabolic prestress force transfer distribution, given as:

$$\alpha = 1 - \left(\frac{\ell_t - \ell_s}{\ell_t} \right)^2 \tag{1.8}$$

It will be recognised that the FIP equation is a manipulation of the classic formula for shear flow and, therefore, the section is indeed assumed to be uncracked.

Further information on the shear and transverse loading performance of hollow core flooring is presented in a comprehensive FIP Technical Report [FIP, 1982].

Equation 9-11 in the New Zealand standard [Standards New Zealand, 1995] works along the same lines as the FIP equation in that allowances are made for the effects of axial prestress and the contribution of concrete principal tensile stress, however, these are then incorporated into a shear index (V/bd) format:

$$v_{cw} = 0.3\left(\sqrt{f'_c} + f_{pc} \right) \tag{1.9}$$

The New Zealand standard also permits calculation on the basis of limiting the principal tensile stress at the centroid of the composite section to $0.33\sqrt{f'_c}$. In this regard, the classic elastic shear formula may also be used with due considerations being made for axial prestress effects and other such stresses that may bear an influence under Mohrs circle failure criterion.

Attention to secondary transverse stresses is also important because the phenomena of bursting and splitting stresses are notable side-effects that also exist in the transfer zone. These and other aspects relating to production technique are discussed in the following subsection on hollow core manufacture.

1.2.2 THE MANUFACTURE OF HOLLOW CORE FLOORING

1.2.2.1 Machinery and Concrete

There are two recognised modern processes for automated hollow core flooring production, these are the extrusion and slip-forming methods. There are some notable differences between these processes, and there has also been some opinion as to the performance of each.

The slip-form method utilises a higher slump concrete than the extrusion process but also requires a higher cement content in the mix. A direct benefit with slip-forming is that less formidable vibration is required to form deep sections, which until recently has been a limiting factor with the extrusion process. Many slip-forming machines also allow the manufacture of a diverse range of industry products by means of an interchangeable profile forming insert.

Almost all the hollow core flooring produced in New Zealand have been manufactured using the extrusion process. The combination of a "zero slump" dry-mix concrete with high frequency vibration has produced perhaps the most cost effective and reliable hollow core sections available. Because extruded mixes require a comparatively small amount of cement and use a low water-cement ratio, yet achieve a well compacted high modulus concrete, there is good control of creep and shrinkage effects. This has proven to be a very important factor with hollow core flooring because the pretensioned hollow section is otherwise poorly conditioned to resist actions that cause volume changes.

The "shear compaction" machinery that has recently appeared in New Zealand symbolises the state-of-the-art in hollow core manufacture. This improved method makes the extrusion of deep hollow core sections possible without the problems of suitable high frequency vibration, and has greater tolerance of concrete slump variations.

When producing dry-mix concrete the proportion of water can be critical, with the mix being sensitive to within 10 litres of the ideal quantity of added water per cubic metre batched. Anything in excess of this limit can result in a mix that is too dry to be properly extruded or one that will tend to collapse. The batching part of the operation is therefore of utmost importance with extruded products and to achieve a workable dry-mix concrete requires carefully graded aggregates, selective use of plasticisers and an industrial strength pan mixer.

In New Zealand, the mix design will be strongly influenced by the regional availability of mineral aggregate. The main centres in New Zealand where hollow core flooring has been produced are the Auckland region, Hamilton (discontinued), Wellington region and Christchurch. In the Auckland and Wellington regions the predominant aggregates are crushed basalt and greywacke and crushed greywacke respectively. Although of differing geological derivation, these are very commendable aggregates for hollow core production, being hard, inert and angular stone [C&CA, 1990].

In the Hamilton area, the aggregate source has been either crushed basalt or andesite. Andesite is a least preferred aggregate for use in concrete, generally having inferior crushing and abrasion resistance than basalt and greywacke. Nevertheless, the porous texture of andesite can promote bond between the aggregate and cement paste components of a mix, thus benefiting concrete tensile properties.

Canterbury province in the South Island has benefited from good quality river run greywacke aggregate. However, it is common for these mixes to contain comparatively small percentages of crushed coarse aggregate. Although this does not necessarily affect the compressive strength of concrete, the assumed flexural tensile strength (when taken as a function of compressive strength) may not be so consistently high in practice. Production experience suggests that mixes containing a large proportion of smooth rounded stones (also known in the vernacular as "ball-bearing mixes") can show limitations with regards to tensile strength properties. This observation is somewhat under-researched but logically it would suggest that unlike the andesite aggregates mentioned earlier, it is difficult to establish good bond between a hard, polished stone surface and cement paste (see Fig. 1.13).

The incidence of reduced bond strength that is attributed to rounded aggregate does not go without mention in the literature, and the reasoning given is similar: " There is little influence of the type of the aggregate on the direct and splitting tensile strengths, but the flexural strength of concrete is greater when angular crushed aggregate is used than with rounded natural gravel. The explanation is that the improved bond of crushed aggregate holds the material together but is ineffective in direct or indirect tension " [Neville and Brooks, 1987].

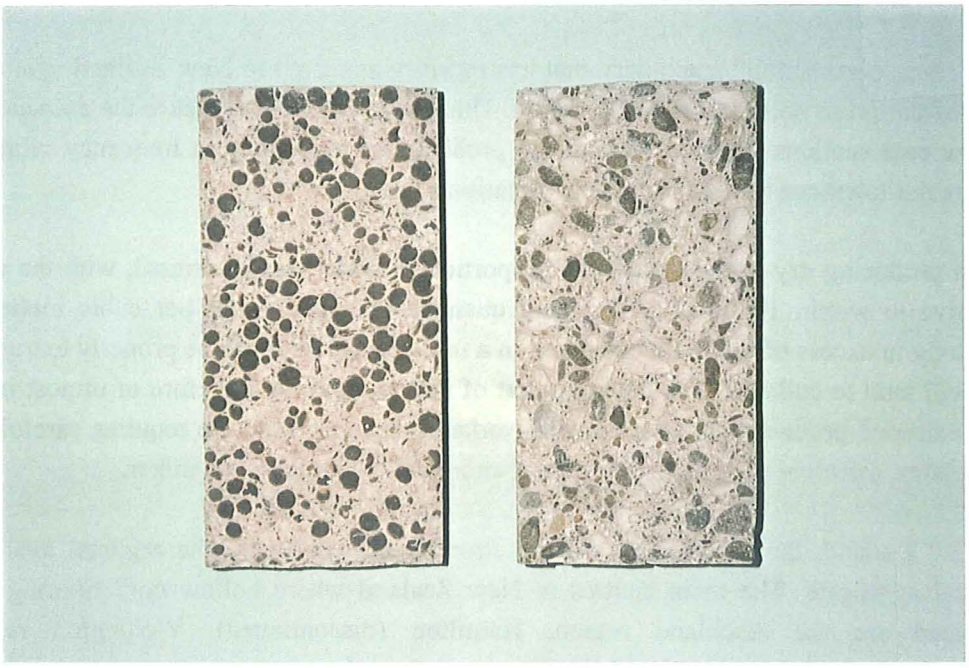

Fig. 1.13 Differing failure modes of the aggregate component in concrete cylinders subjected to the standard splitting test. Fractured light-weight expanded clay shale aggregate (at left) and debonded greywacke smooth pebble aggregate.

In the context of hollow core performance, units comprised of mainly smooth round aggregates as those described could have a reduced shear capacity. In particular, flexure-shear capacity is determined by first flexural cracking followed by aggregate interlock across an inclined flexure-shear crack that is subjected to further opening. These actions invoke the exact elements of performance that have been found lacking in rounded stone mixes through research and production experience.

No special guidance is given by the manufacturers of hollow core machinery on the derivation or geometry of aggregates, which is understandably a topic that is beyond their professional obligation.

A mix design for extruded concrete may typically have a ratio of about 2:1 by weight of aggregate to sand, and a ratio of 5:1 by weight of aggregate plus sand to cement (see Table 1.7).

Table 1.7 Typical proportions of solid components in an extruded hollow core mix per cubic metre batched

Constituent	kg/m³
15 mm agg.	590
7 mm agg.	390
Sand	460
Cement	280

An incorrect concrete mix or faulty machinery can result in a product that may typically exhibit collapsed flanges over the hollow core voids or tearing of the concrete along the outer webs of the unit. In accordance with what has been discussed earlier on flexure-shear, tearing cracks in the outside webs may be detrimental to the performance of hollow core units.

Insufficient concrete compaction at manufacture has also been revealed as a prime cause of strand pull-in. Under flexural testing, the strands that exhibited a large pull-in at transfer were observed to undergo a premature flexural bond failure. An important conclusion from these tests was that: "good workmanship and proper maintenance of production equipment are vital for quality assurance" [Anderson and Anderson, 1976]. In their research paper, an empirical quality assurance method was proposed for flexural bond on the basis of measured strand pull-in, Δ_{ct} :

$$\Delta_{ct} \leq \frac{f_{si}\, d_b}{6500} \qquad (1.10)$$

which for the most commonly used supergrade (1860 MPa) strand is equal to $0.2d_b$.

1.2.2.2 Production Process and Quality Control

(a) Surface Roughening

From a composite construction perspective, one criticism that has often been directed at extruded flooring is the problem of achieving a significantly roughened bond surface. In ordinary precasting, obtaining good surface roughening is a simple exercise that is usually accomplished with a clean yard broom [SANZ, 1987]. The hard, compacted surface of extruded zero-slump concrete is not conducive to brooming and excessive pressure applied to the surface to achieve this will cause a cave-in over the hollow core voids (see Fig. 1.14).

The degree of surface roughening specified for extruded flooring in the New Zealand standard is a minimum of 2 mm peak to trough. Reliance is placed on the shear keys between units to assist the composite bond and the specified minimum key width is 20 mm. It has been proven by tests that smooth bond surfaces without the keys are adequate for the development of composite bond under gravity loads [Scott, 1973. CTA, 1976]. Although automated roughening

of the top surface of extruded systems is feasible, this may seem an excessive measure in view of results from the composite bond tests reported.

Fig. 1.14 Brooming of an extruded hollow core surface

The information reported by Concrete Technology Associates [CTA, 1976] is quite thorough. A number of deleterious practices were imposed on the bond surface to cause variations in performance and reduce the composite bond capacity. Of these, it was found that a heavy coating of oil or unvibrated low slump concrete produced the lowest bond strengths. Putting these observations in context with the construction environment, it is insufficient vibration of topping concrete that would be of greatest concern.

(b) Saw Cutting and Transfer of Prestress

Saw cutting is the necessary method of separating extruded units from the bed and transferring the prestress force into the section. With deeper units, pre-cutting is often done through the upper half of the section with a cross-cut blade to prevent the mechanical saw blade from jamming when cutting the strands. Care must be exercised when pre-cutting plastic concrete not to disturb the bond between strands and concrete, hence, a maximum depth of pre-cut should be specified.

The effects of shock release that are associated with saw cutting of strands have been suitably well researched. It is concluded that sudden release by saw cutting has no obvious effects on the flexural bond capacity of strands provided that the pull-in limits prescribed by Equation 1.10 are not exceeded [Anderson and Anderson, 1976]. Where the prescribed limit is exceeded, some downgrading of the unit capacity should be considered in accordance with the observed pull-in of individual strands.

The most fundamental parameters used for defining prestress transfer length are the diameter of strand, the initial prestress and the crushing strength of the surrounding concrete at the time of release [Zia and Mostafa, 1977]. More elaborate models have also been developed in which fuller representation is made of variations in the prestress force, strand slippage and bond stress distributions over the transfer length [Balázs, 1992]. However, it remains difficult to determine what the actual transfer bond length will be for a given situation. Analysis of research indicates that there is considerable scatter in experimental results for both sudden and gradual release. Therefore, a simple approximation for transfer length is satisfactory for design purposes.

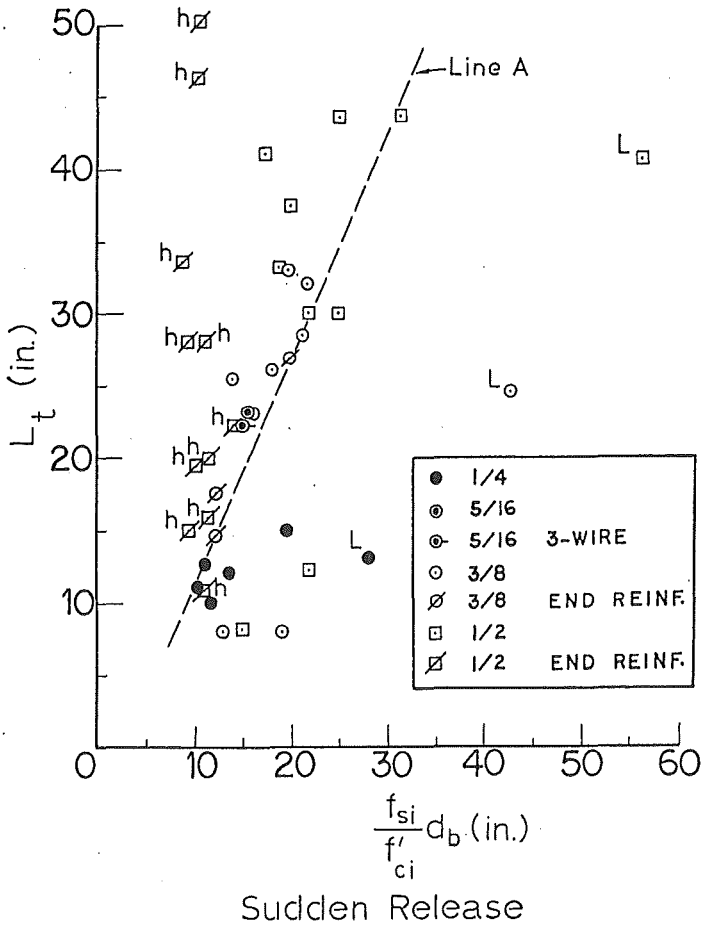

Fig. 1.15 Transfer length versus $f_{si}d_b / f'_{ci}$ for sudden release [Zia and Mostafa, 1977]

What appears to be consistent is that the maximum expected transfer length for typical configurations of strand and concrete strengths of hollow core units is about 80 times the strand diameter. The transfer length for sudden release has been proposed as a linear relationship based on regression analysis of a body of experimental results (Fig. 1.15) [Zia and Mostafa, 1977]. Substituting typical values into equation 1.11 (the metric equivalent of line A in Fig. 1.15) the ratio of maximum transfer length to the average transfer length under sudden release will be in the order of 4/3.

$$\ell_t = 1.5 \frac{f_{si}}{f'_{ci}} d_b - 120 \qquad (1.11)$$

The design figure for transfer length under sudden release is often taken as a factor of 1.2 to 1.3 times that for gradual release [Libby, 1977], which results in an estimated range of 60 to 65 strand diameters.

For design purposes, the distribution of force over the transfer length is either taken as being linear over 50 strand diameters [ACI, 1991; Standards New Zealand, 1995] or parabolic over usually about 60 strand diameters (Equation 1.8) [FIP, 1988]. As a result, the calculated strand force at a fraction of the transfer length is not particularly sensitive to the chosen method. For in-depth analyses a power curve relationship has proved to correlate well with test results, as well as facilitating a solution to the governing second order differential equation [Balász, 1992; Bruggeling and Huyghe, 1991].

Part of the significance of transfer length and the force distribution over this length is the resulting component of shear force generated in the support zone. Since the bending moment induced in a section by prestress force is given as the product of force $P_{(x)}$ times the eccentricity $e_{(x)}$ (which is constant in x for hollow core), the induced shear force may be calculated from the slope of the non-uniform bending moment [Lin Yang, 1994]:

$$V_{pc_{(x)}} = \frac{d}{dx}(P \cdot e)_{(x)} = P\frac{de}{dx} + e\frac{dP}{dx} \qquad (1.12)$$

The vertical component of the force P may be taken into account in the shear capacity design of prestressed members with sloping tendons, and is termed the transverse component of effective longitudinal prestress [Standards New Zealand, 1995]. As mentioned, the eccentricity is constant over the length of a hollow core unit and this component (i.e., the first term in Equation 1.12) disappears. The second term which relates to the shear component induced through transfer bond is not recognised in the standards, although its contribution has been successfully employed in the exact formulation of hollow core web shear capacity for comparison with the results of FEM analysis.

For an estimate of the shear capacity development due to transfer bond, some knowledge of the bond envelope is required. A reasonable approximation of strand force distribution over the transfer length is given by the parabolic FIP equation:

$$P_{(x)} = P\left[1 - \left(\frac{\ell_t - \ell_s}{\ell_t}\right)^2\right] \qquad (1.13)$$

Hence, the shear force induced by transfer of prestress force via equation 1.12 is:

$$V_{tp_{(x)}} = 2Pe\left(\frac{\ell_t - x}{\ell_t^2}\right) \qquad (1.14)$$

The magnitude of this force depends on the prestress force, the eccentricity of prestress and the length terms as expressed in the equation. The direction in which this force acts is entirely

dependent on the position of the eccentricity above or below the neutral axis of the section. For a positive eccentricity (i.e., below the neutral axis) the bottom fibre will be subjected to increasing compression with distance from the end of the member. This corresponds with an upward and decreasing component of shear force in the section over the transfer length.

(c) Spalling and Splitting Stresses

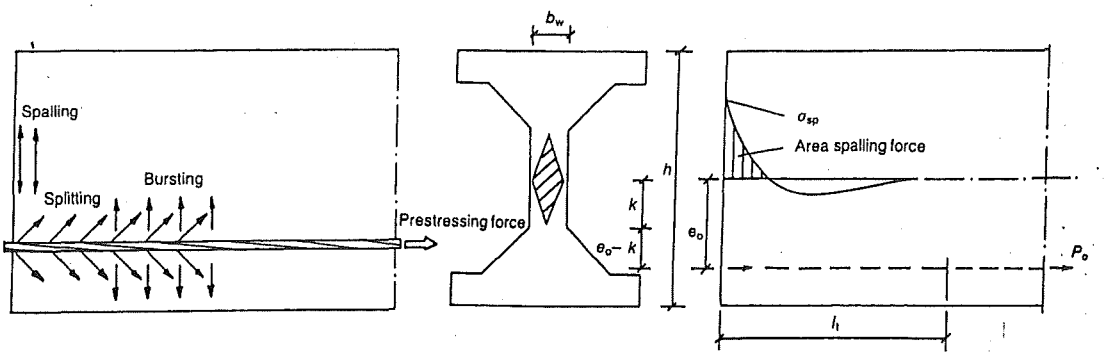

Fig. 1.16 Spalling, splitting and bursting stresses in hollow core sections [FIP, 1988]

Cracks caused by spalling and splitting stresses (and to a lesser extent bursting stress) (see Fig. 1.17) need to be considered at the manufacture stage. Typically, the type of crack propagated by spalling stresses will occur horizontally along the hollow core web and results in a direct reduction to the shear capacity of the member. For standardised hollow core sections that conform to dimensional limitations imposed to counter splitting problems in the transfer zone [FIP 1988], spalling cracks will usually be the result of insufficient tensile strength of concrete at release.

It can be seen from Fig. 1.15 that comparatively short transfer lengths have also been measured for 3/8 inch (9.5 mm) and 1/2 inch (12.7 mm) diameter strands. For hollow core units the abscissa on this graph will fall at about 22, which corresponds with a minimum recorded transfer length of 12 inches (305 mm). Lower bound values such as this need to be taken into account for evaluation of potential spalling stresses in the webs of hollow core sections at release.

The maximum spalling stress is a function of web thickness, the eccentricity and magnitude of prestress force and transfer length. Spalling stress should be checked in the web for which the most effect is generated, and can be done either by a calculation method or by use of Fig. 1.17 which have been partly derived by finite element analyses [FIP, 1988]. In this, the transfer length is taken as a lower bound value which is about 40 strand diameters for hollow core units, or 80% of the mean transfer length nominated in codes or standards.

The spalling stress σ_{sp} as derived from the FIP recommended method should be limited to less than f_{ctkj} ; the characteristic concrete tensile strength at time j.

Control of splitting and bursting stresses is provided by sufficient concrete cover to the strands. In respect of this, the FIP recommendations state that clear cover should be provided of:

$$c \geq \frac{0.05\phi\sqrt{\sigma_{po} f_{ccj}}}{f_{ctkj}} \qquad (1.15)$$

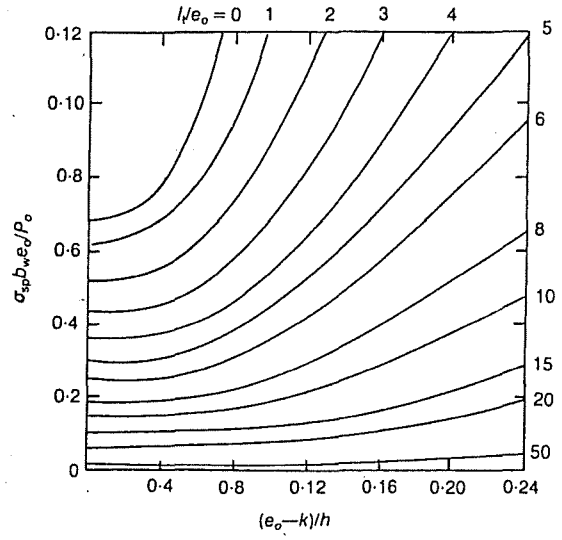

Fig. 1.17 Spalling stress as a function of eccentricity and transfer length [FIP, 1988]

(d) Cleaning, Stacking and Handling

Adequate cleaning of units is perhaps one of the most important operations in the quality control process at manufacture. As discussed in quality assurance literature [e.g., FIP, 1992], unwashed hollow core units may have acute difficulties with composite bond performance, and the problem is not one that is likely to be rectified at the construction site.

The need for thorough washing stems from the fact that saw cutting generates a fine slurry that settles into the slumping depressions over the hollow core voids (Fig. 1.18). If this slurry is not washed away it dries to form an obstructive caked layer that inhibits composite bond.

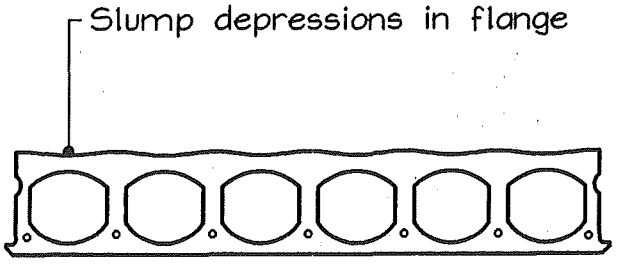

Fig. 1.18 Slurry from saw cutting settles into slump depressions and must be washed off

As with all slender pretensioned products, careful stacking of hollow core units is important, and especially if they are to be stored for some time or uniform deflections are required. A limit must be placed on the height of stacks and because of the eccentricity of prestress the length of overhang must be restricted and placement of stacking spacers must be uniform. Consideration must also be made for the position of slab cut-outs both when handling the unit and at storage.

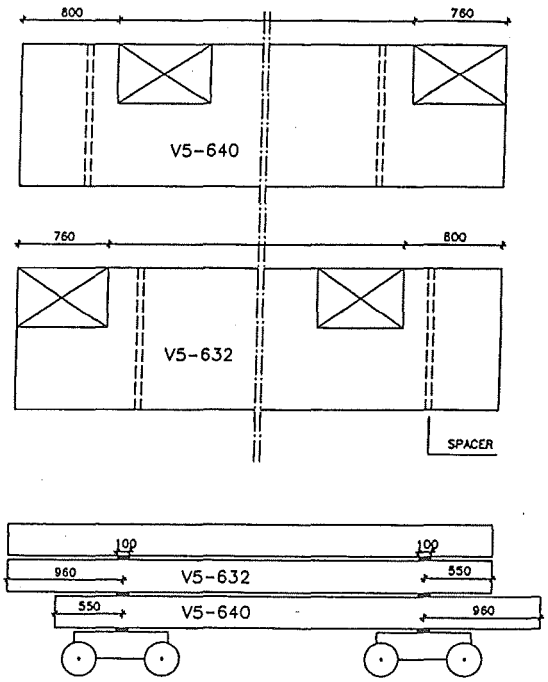

Fig. 1.19 Transportation of hollow core slabs with openings [FIP, 1992]

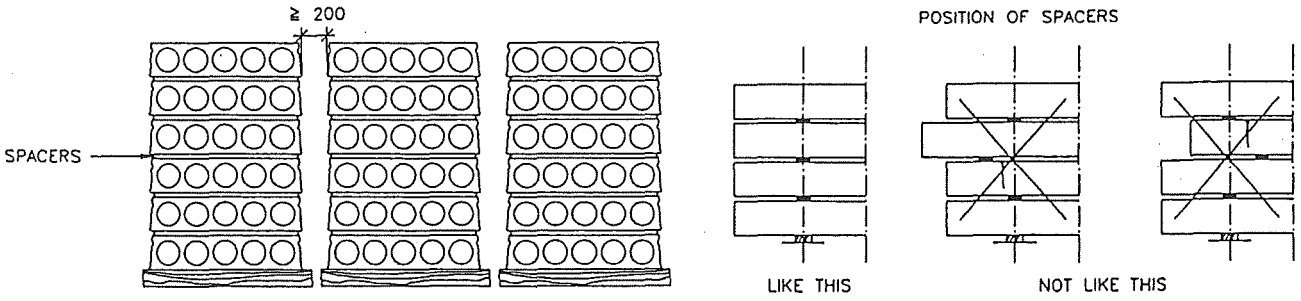

Fig. 1.20 Storage of hollow core slabs [FIP, 1992]

Most issues relating to production are largely a matter of care, common sense, training and experience. Useful and readable guidelines on production process are given by authorities on prestressed concrete [FIP, 1988; FIP, 1992; PCI, 1985].

1.2.3 SUPPORT DETAILS FOR HOLLOW CORE FLOORING

1.2.3.1 General

In this section, current support details that are associated with hollow core flooring are presented. The specific role of connection details in diaphragm action is deferred until the following section.

The nature of support details adopted for hollow core units should be influenced by the governing conditions of structural design. These conditions can be categorised on the basis of a reasonable expectation of the overall performance of the structure. For example, either a bomb blast that results in loss of support or strong seismic forces may cause serious and irreparable damage to structures. Nevertheless, a properly designed earthquake resistant structure should not lose entire support members, nor will a blasted building be subjected to prolonged and intense cyclic base shears. Hence, although cross-crediting of respective diaphragm and support details that arise from these separate design philosophies is acceptable, some rationalisation must be involved to effect a good design.

In a build-up to the analysis of existing and prospective support details, consideration must be given to contemporary construction culture and the underlying requirements of design. From this point onward, optimisation or avoidance of known causes and effects (depending on the consequences of their influence) should result in an appropriate solution. Much of this can only be accomplished with particular knowledge that is gained from experimental research.

1.2.3.2 European Details

In primarily aseismic European building design there is strong emphasis placed on avoiding structural failure through progressive collapse caused by impact, explosion, fire or other effects including unlikely seismic events [FIP, 1986]. As a result, wording in the FIP Recommendations for hollow core flooring is such: "The hollow core units should be directly or indirectly tied to the support structures at both ends. The structural connections, especially the connections at the supports, should be designed and detailed aiming at structural integrity and ductility during collapse" [FIP, 1988].

In effect, these statements set a benchmark for the typical configuration of support details that are recommended by the FIP. Because earthquake risk is quite low over most of Europe there is a general tendency to avoid structural toppings. However, toppings are advocated in Europe for situations where difficulties arise in detailing for the transfer of diaphragm forces in untopped floors, which is usually at the corner connections of strut and tie fields [Bruggeling and Huyghe, 1991].

The principle of tie connections for the purposes of resisting progressive collapse is that they have sufficient strength and ductility to allow full redistribution of the gravity load support mechanism. There are obvious preferences in the type of detail employed to accomplish this because the performance of ties is influenced by a number of geometric and material

parameters. The requirement is for: "high deformability, high force transferring capacity and high energy absorption" (Fig. 1.21) [FIP, 1982]. It is also desirable that an even force-displacement relationship is obtained, as this helps with predicting the net results for systems that involve the interaction of a group of support details under varying rotations (Fig 1.22).

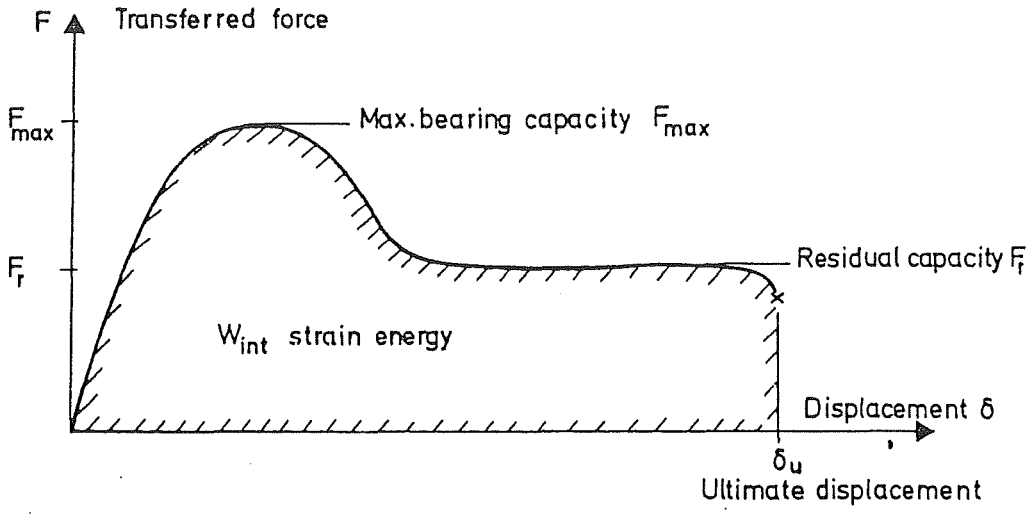

Fig. 1.21 Properties of a force-displacement curve for support connection details that are of interest: ultimate deformation, maximum force transferred, internal strain energy and the initial stiffness [FIP, 1982]

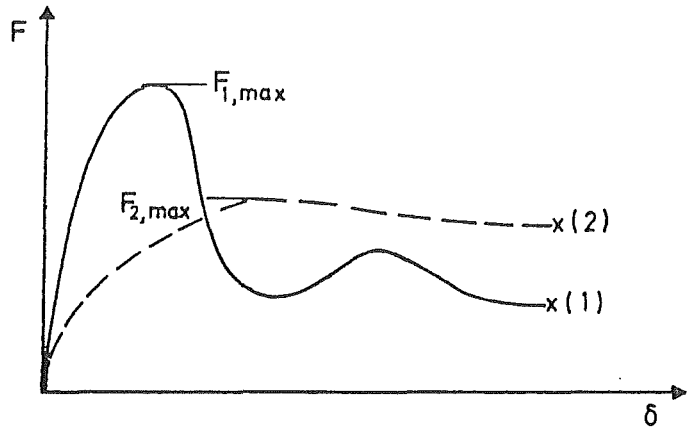

Fig. 1.22 The force-displacement relationship should be as even as possible. Connection detail (2) is preferable despite it having a lower peak strength [FIP, 1982]

One of the important properties of tie connections is their ability to absorb a quantity of internal strain energy. This becomes a critical design parameter when sudden loss of support causes a downward movement, with the potential energy of the total vertical shear force being converted into kinetic energy. The internal potential energy capacity provided by the support tie details must then equal or exceed the maximum kinetic energy that results from this action. This is referred to as the condition of energy equilibrium for the system, and is an important criterion in connection design under sudden loss of support.

A comprehensive body of research has been undertaken on the performance of ductile tie connections for hollow core flooring systems, in particular [Engström, 1992]. In this research, verifications were made of the typical material and construction configurations that appear in the FIP recommendations on hollow core flooring [FIP, 1988]. Further, general information is provided on the performance expectations of reinforcing bar tie connections.

Details from European Literature:

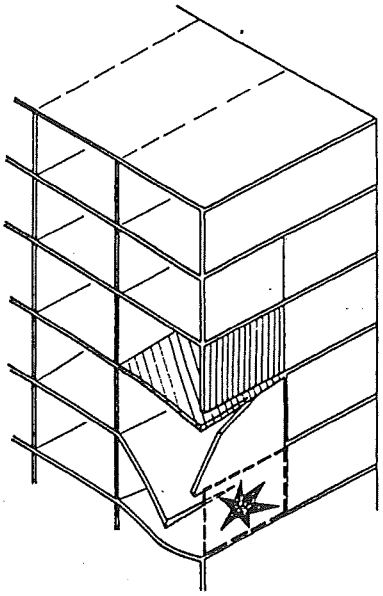

Fig. 1.23 The wall structure is damaged by accidental loading. In order to prevent an extension of the damage and total collapse, the damaged structure must remain stable and an alternative load-bearing system must bridge over the damaged area. [Engström, 1992]

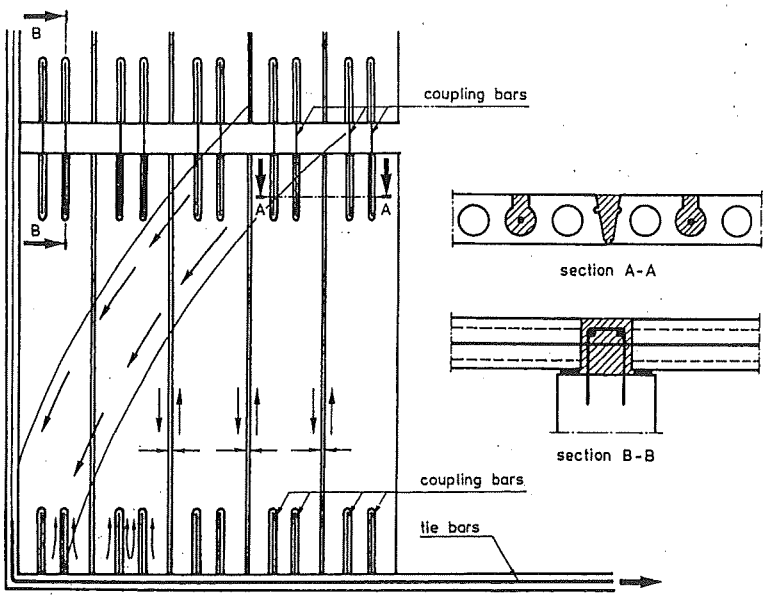

Fig. 1.24 Tie-to-compression arch detail for an untopped hollow core floor slab involving grouted cores [Bruggeling and Huyghe, 1991]

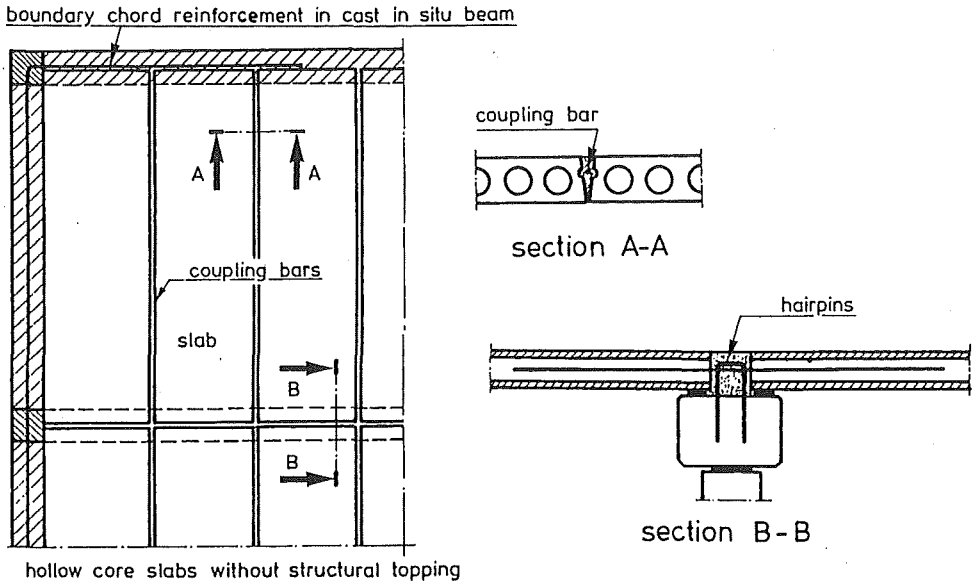

Fig 1.25 Grouted key tie bar details (coupling bars) [Bruggeling and Huyghe, 1991]

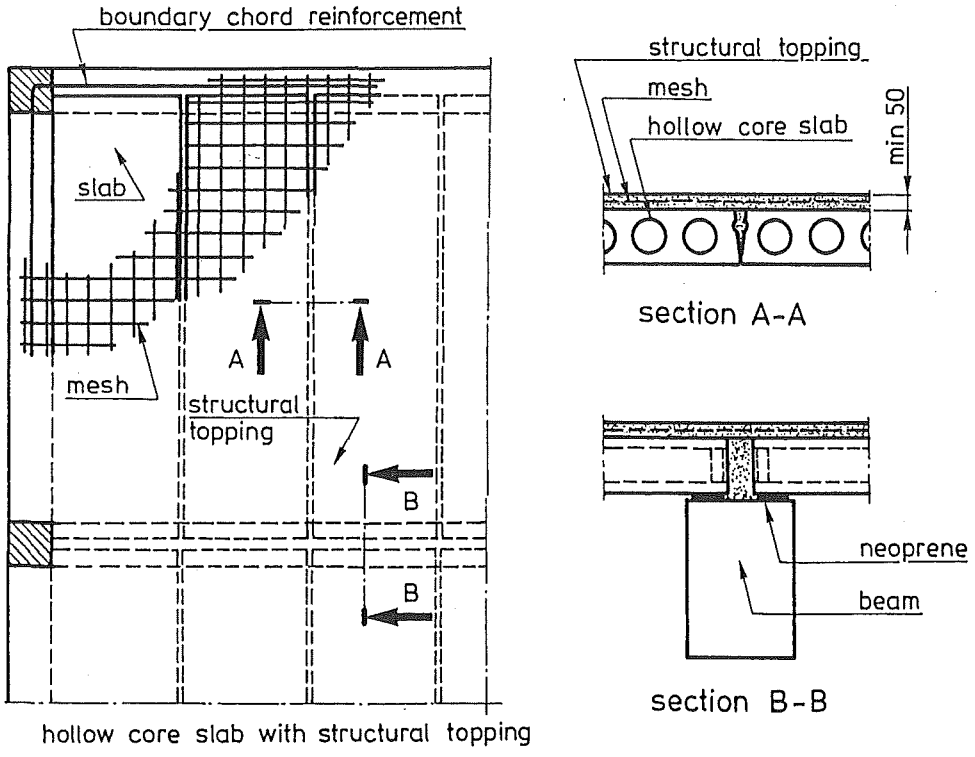

Fig. 1.26 Hollow core floor construction with composite reinforced structural topping [Bruggeling and Huyghe, 1991]

The anchorage length and allowable forces of tie (coupling) bar details shown in Figs 1.24 to 1.26 is also referenced in the comprehensive and all encompassing FIP Recommendations handbook [FIP, 1988].

(a) Bars grouted into shear keys

For straight deformed bar ties, the total development length is the basic development length of the bar l_b plus a margin Δl_b to allow for full plastic deformation over a utilised length. It should be noted that these quantities are additional to the minimal requirement of the prestress transfer length l_{crit} , and hence, the total embedment will be:

$$\ell_d = \ell_{crit} + \ell_b + \Delta\ell_b \tag{1.16}$$

Of the straight ribbed bar details tested [Engström, 1992] it was found that 12 mm diameter bars could develop their full tensile strength over an embeddment length of 50 bar diameters (i.e, 600 mm) at a corresponding ultimate force of about 70 kN. The displacements at fracture were measured between 7.1 and 20.3 mm, however, an average of about 18.5 mm at fracture is a more typical value. The reinforcing steel in question had a measured yield strength of 525 MPa, an ultimate strength of 725 MPa and 13.9% elongation at fracture. It was not possible to develop the tensile strength of 16 mm diameter bars in this way over a 50 bar diameter (i.e, 800 mm) embedment length.

The provision of a specific transverse clamping action is essential for the reliable deployment of key embedment details. In the above tests, pull-out and shear interface failure of the 16 mm bar tests and one pull-out failure involving a 12 mm bar was synonymous with rupture of the transverse tie-beam joint. Premature rupture of the transverse tie joint was caused by pre-cracking of the longitudinal (tie embedment) joint and was a common denominator for all the tie details that failed below the expected load.

It was observed that the quality of grout fill had an important effect on the performance of these details. Deformed bars of 150 to 200 bar diameter anchorage lengths were observed to pull out if the grouting did not fully encase this reinforcement. It was thus concluded that even deformed bars should be provided with hook ends when used in this form of detail [Engström, 1992]. Some straightening of hook ended bars was observed at the plastic stage and it is considered that this was the result of insufficient hook cover. Because of the accumulation of tie force in the hook region, it is particularly important that sufficient end cover is provided for smooth bar details.

(b) Bars grouted into cores

For bars that are grouted into cores, the embedment is taken as the prestress transfer length l_{crit} plus an additional length that is determined by the type of anchorage employed. For hook returns, this additional length can be determined by:

$$\ell_{add} = \frac{F_{st}}{f_{ct}\, u} \tag{1.17}$$

To avoid fracture of the section (see Fig. 1.27) the allowable magnitude of tie force for embedment in individual cores has been provisionally recommended at 80 kN, with a maximum of 160 kN per end for 265 mm deep hollow core units [FIP, 1988]. Subsequent testing has shown that considerably larger forces may be developed by these details, but considerations must also be made for concurrent stresses acting in the ends of units that may contribute to section fracture [Engström, 1992]. It is indicated that forces of up to 100 kN may be safely resisted by a single core with a maximum of 200 kN per end of the member. There was no indication of shear failure between the hollow core and the infill grout interface.

In the role of embedded ties, smooth bars with hook ends have demonstrated greater endurance than deformed bars and there is less concern with secondary effects that may cause failure of the detail. Due to the efficient nature of deformed bar bond, the ensuing shorter embedded gauge length results in a combination of higher splitting stresses and lower deformability than with properly anchored smooth bars (Fig. 1.28). Neither of these characteristics are desirable for the environment in which ductile tie connections for hollow core units must act. Conversely, smooth bar details have demonstrated the potential of strength and dutility required to perform the ultimate limit state task (Fig. 1.29) [Engström, 1992; Mejia-McMaster and Park, 1994].

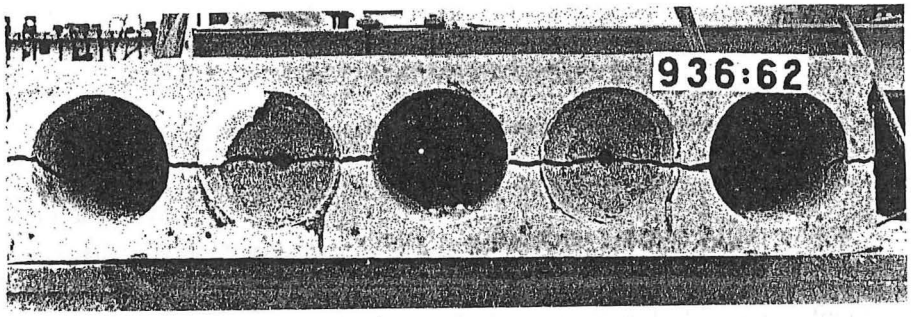

Fig. 1.27 Splitting of hollow core webs due to high strength embedded deformed bars under tension [after Engström, 1992]

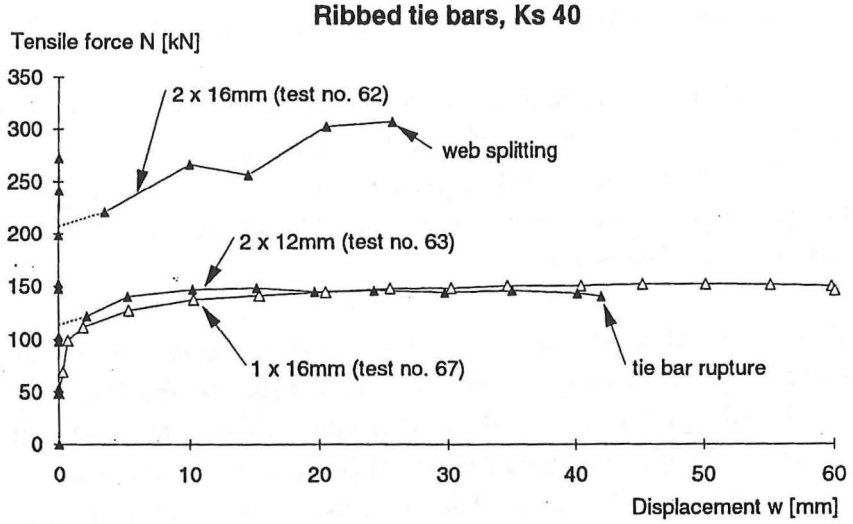

Fig. 1.28 Force-displacement charactersitics of deformed bars embedded in hollow core units [Engström, 1992]

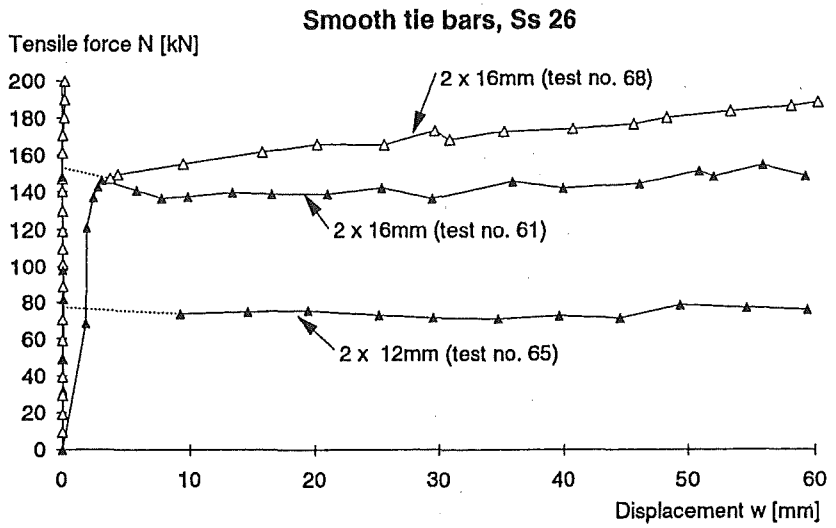

Fig. 1.29 Force-displacement characteristics of smooth bars embedded in hollow core units [Engström, 1992]

1.2.3.3 North American Details

Both composite topped and untopped hollow core floors have been advocated for use in the seismic regions of North America and a variety of connection details have been considered [ATC-8, 1981]. Unlike European practice, more emphasis has been placed on the development of strength and stiffness for floor diaphragm purposes (strong connections) than the potential loss of support to flooring units. As a result, North American details do not appear to exhibit the general requirement of ductility that is prescribed by FIP literature [FIP, 1982. FIP, 1988]. For example; of nine typical North American support connection details reported to the ATC-8 workshop, all were expressly designed on the basis of strength and stiffness. Although attention was drawn to the fact that some "strong" connections may exhibit ductility, no intimation of this quality was attached to any of the details presented [Becker and Sheppard, 1981].

Because a degree of strength development is rudimentary to all connection details, the issue of ductile performance is usually only a matter of specific detailing practice (i.e., the way that strength is developed *and* maintained under foreseeable actions). In review of typical North American details there is no evidence of the ductile embedded bar-in-core type details that have been tested and endorsed by the Europeans.

However, it would be incorrect to suggest that potential loss of support actions in precast flooring has been overlooked by American engineers. In a paper to the PCI, the precast construction pioneer Alfred Yee has discussed the detailing necessary to resist collapse of precast floor slabs caused by support damage [Yee, 1991] (see Fig. 1.30). Moreover, a number of design aspects that are covered in his paper relate to the basis of the present study in a more direct way than European design criteria. The emphasis is on the effects of seismicity with

regards to connections in particular. Also, the type of precast construction that is referred to can be identified as similar to New Zealand practice.

The importance of compatibility of connections for precast components in seismic resisting diaphragms (and hence, ductility requirements) has also been stated in American literature. Based on the findings of ATC-8, it was reported that to preserve stability: "precast diaphragms should be designed to maintain their in-plane stiffness, even after the lateral force resisting system has entered the inelastic range" and furthermore, that: "Sufficient ductility should be provided in inter-element connections to prevent brittle failure of the diaphragm due to out-of-plane deformations imposed in the vertical subsystems. Similarly, connections between diaphragms and vertical subsystems must be ductile and tough enough to sustain inelastic, cyclic rotations of a magnitude consistent with the lateral yielding of vertical subsystems" [Clough, 1982].

With regards to ductile connections between diaphragms and vertical subsystems, there are no actual recommendations given by either ATC-8 or in the PCI journal of how details that meet the stated requirements might look. Some information is given on ductile inter-element connections (i.e., connections between flooring units), however, it must be remembered that the details presented in ATC-8 were given as a representation of contemporary connection practice and of proposed connections only. Of the fifteen diaphragm connection details reported [Becker and Sheppard, 1981] only four had supporting test data, none of which was for expressly ductile connections. It would appear (and is a reasonable expectation) that the onus should lie with practising engineers and research institutions to verify that existing and proposed connection details can perform in a manner conducive to the recommendations from ATC-8. After all (as stated in the preface of the document) the purpose of ATC-8 was to: "summarise the current state-of-practice and research and to prioritise research needs...". The wholesale condonation of an arbitrary group of mostly untested connection details would not be the objective of an astute American research council. Examples of the various diaphragm connection details that were reported by ATC-8 are shown in Figs 1.31 to 1.32.

Details from North American Literature:

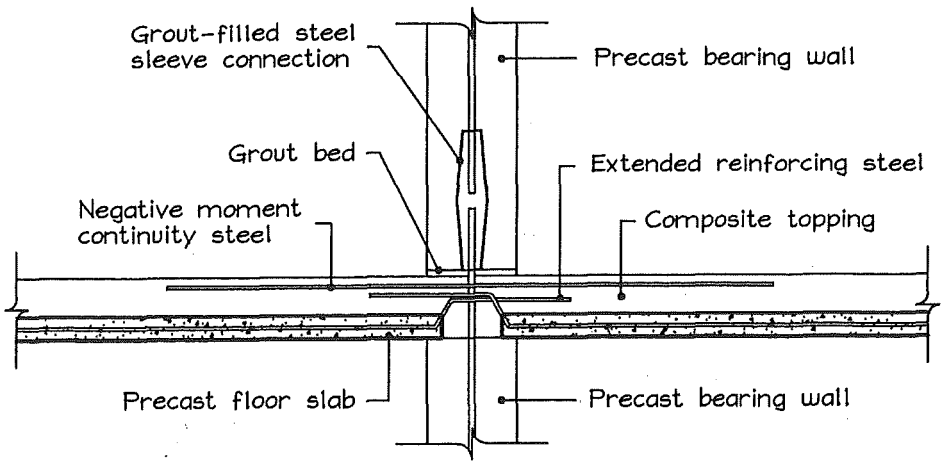

Fig. 1.30 Slab seating connections designed to prevent collapse [after Yee, 1991]

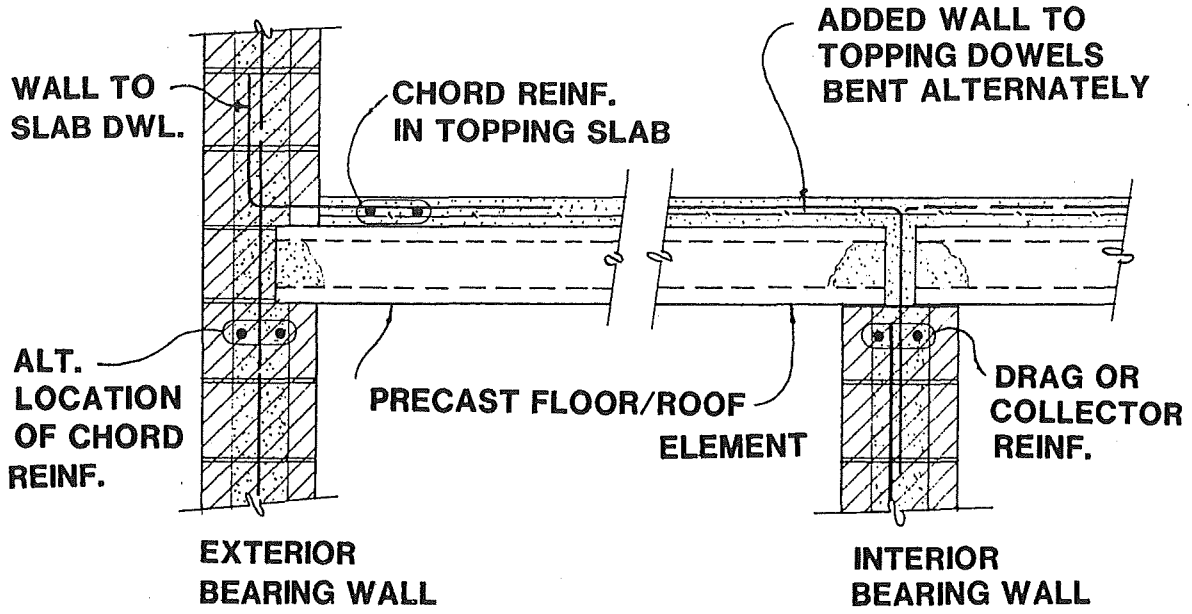

Fig. 1.31 Connection of floor slab to perimeter shear (structural) wall [ATC-8, 1981]

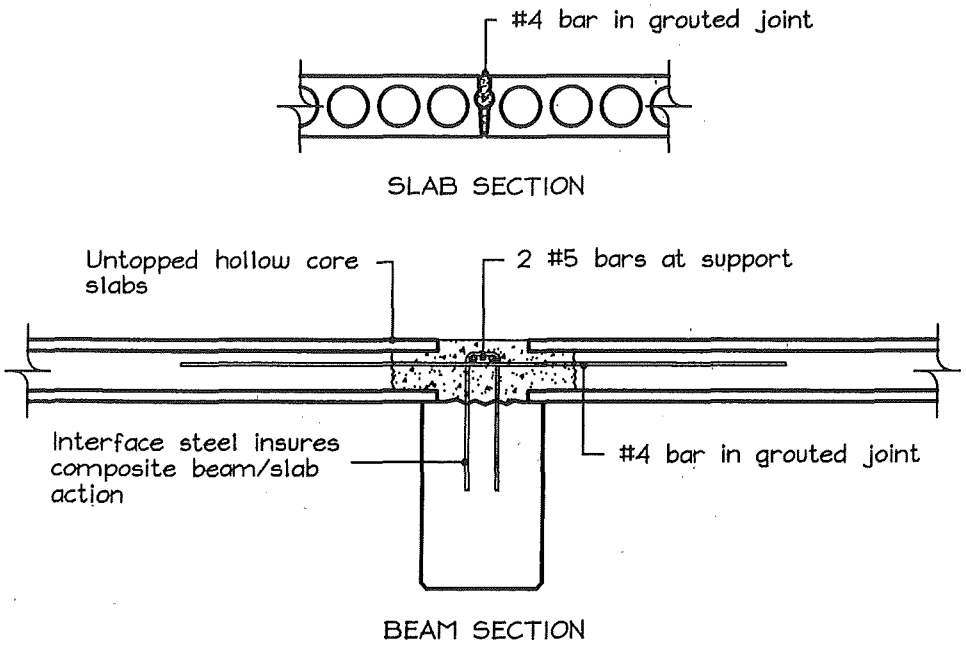

Fig. 1.32 Untopped hollow core floor diaphragm connection detail utilising chord-tie reinforcement and grouted tie bars [after Moustafa, 1981]

1.2.3.4 New Zealand Details

Composite topping of floor diaphragms has been a basic New Zealand code requirement for seismic resisting buildings, and floor diaphragm actions are assumed to be carried by this structural topping alone. The typical connection details employed between precast hollow core and support elements are very similar to those used for composite topped slabs in North America (see Figs 1.35 and 1.36). A special support detail that involves tie reinforcement has been used on occasions where precast units have been supplied undersized (Fig. 1.34). This detail has only been employed for situations that involve short seatings and gravity loadings, it has rarely been used to mitigate the potential of floor collapse caused by imposed actions of support structures.

Unlike North America, the overall seismic performance of New Zealand structures is governed by the principles of capacity design. Capacity design is described as the procedure whereby: "elements of the primary lateral force resisting system are chosen and suitably designed and detailed for energy dissipation under severe deformations. All other structural elements are then provided with sufficient strength so that the chosen means of energy dissipation can be maintained" [Standards New Zealand, 1995]. Until recently, the need to maintain deformation compatibility between the interconnected components of floor diaphragms and members of the seismic resistance system has not been stated in so many words.

The end support zones of simply supported precast flooring units frequently coincide with regions of supporting members that have been detailed to partake in energy dissipation through inelastic deformation. A proportion of the composite floor slab is considered to contribute to the strength and stiffness of the post-elastic section of the support element; a width that is derived from the total thickness of the floor element (see Fig. 1.33). This places more emphasis on the reliability aspect of connection details; especially with regards to the toughness requirements, in the likelihood that deformation compatibility is expected in the vicinity of flooring members supports.

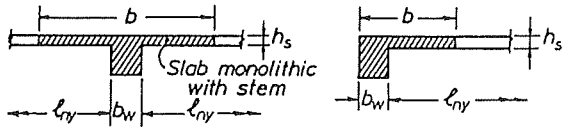

For (*) Flexural strength	Stiffness
$\leq b_w + 16h_s$	$\leq b_w + 8h_s$
$\leq b_w + \ell_{ny}$	$\leq b_w + \ell_{ny}/2$
$\leq \ell_x/4$	$\leq \ell_x/8$

For (*) Flexural strength	Stiffness
$\leq b_w + 6h_s$	$\leq b_w + 3h_s$
$\leq b_w + \ell_{ny}/2$	$\leq b_w + \ell_{ny}/4$
$\leq b_w + \ell_x/12$	$\leq b_w + \ell_x/24$

ℓ_x = span length of beam
ℓ_{ny} = clear distance to the next web
(*) = flange in compression

Fig 1.33 Assumed effective widths of beam flanges used in seismic design [Paulay and Priestley, 1992]

In order to achieve the strength capacity that is provided by starter bars embedded into composite topping, a positive composite bond must exist between the precast flooring element and the topping slab. This is fundamental to the performance of the typical New Zealand support detail and, as a result, composite ties between the precast unit and topping concrete have occasionally been specified for regions of diaphragms where stress concentrations may occur. However, many designers have been reluctant to include devices that will improve or ensure composite bond unless the allowable value of topping slab shear given in the concrete design standard is likely to be exceeded. This is probably an adequate approach for many situations provided that non-exceedance of the given limiting shear value of $0.33\sqrt{f'_c}$ can actually be verified. In reality, this may not be so straightforward as generalised topping slab shear stresses calculated on the breadth of flooring might suggest. At floor supports of ductile structures, the likely sources of critical shear and bond demand will come from localised interactions between the diaphragm element and ductile members of the primary seismic resistance system.

Many of the requirements for precast floor support connections are either directly referenced in (or are inferred by) various sections of the current New Zealand concrete design standard [Standards New Zealand, 1995] and the loadings code [Standards New Zealand, 1992]. The current concrete standard recognises specific interactions between floor elements and the primary resistance members, the importance of maintaining load paths and the restraint that may be applied to vertical systems via the floor element. A number of prescriptive measures of support control have also been introduced for precast flooring, such as minimum seating lengths.

Details from New Zealand Literature:

The following details are for hollow core units as used in New Zealand Construction. The support detail for insufficient seating (Fig. 1.34) is a widely accepted method for overcoming disparities between supplied lengths of precast members and support dimensions:

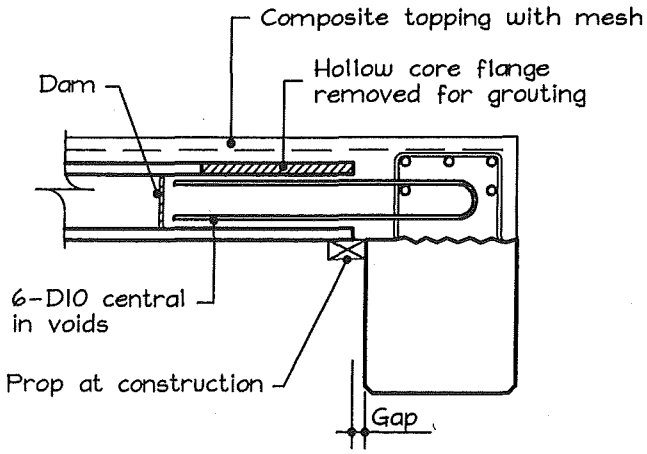

Fig. 1.34 Embedded bar detail for situations where sufficient seating length is unobtainable

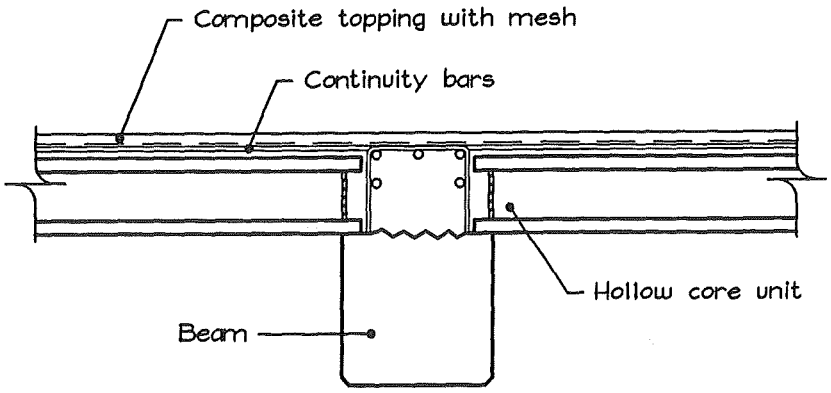

Fig. 1.35 Typical interior support detail

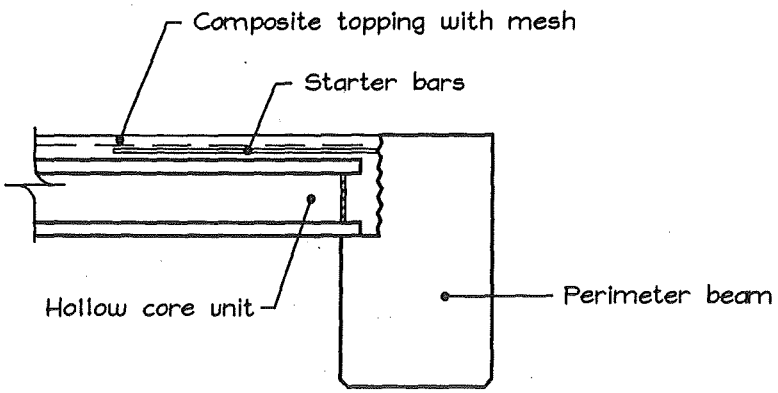

Fig. 1.36 Typical external support detail

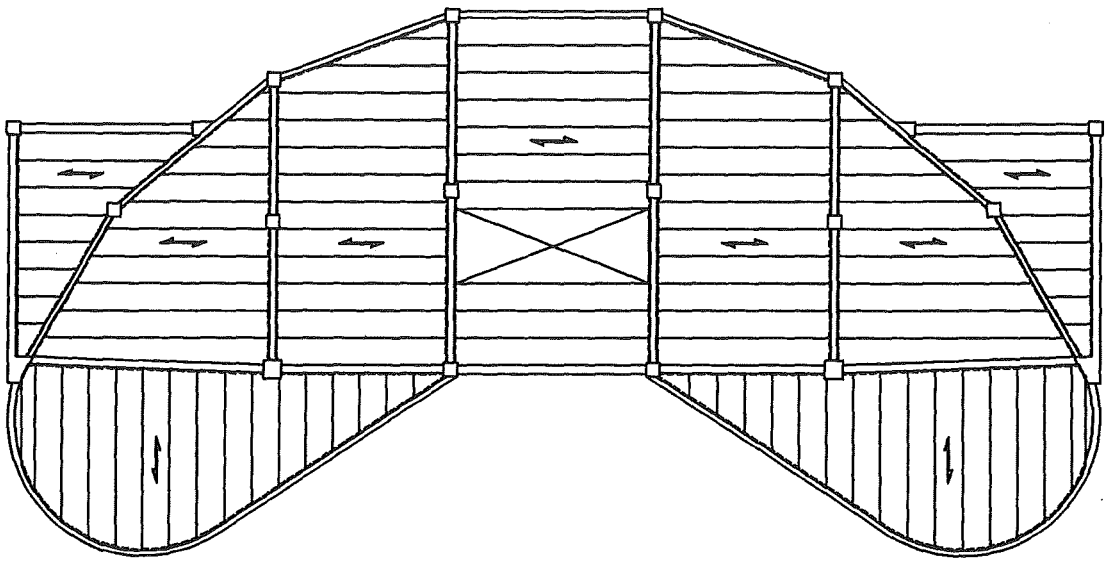

Fig. 1.37 Hollow core flooring layouts may take many forms

1.3 DESIGN ASSUMPTIONS ASSOCIATED WITH FLOOR DIAPHRAGMS IN SEISMIC RESISTING STRUCTURES

1.3.1 GENERAL

As structural entities, diaphragms have generally demanded somewhat less detailed analysis, design and construction effort than other massive critical path elements of a building. In general deployment, the flooring members that make up diaphragms are required to perform a variety of simply defined serviceability and ultimate limit state functions. As described earlier (Section 1.2.1) these functions relate to deflection control, minimum durability, fire safety requirements and ultimate limit state gravity load carrying capacity.

In addition to transferring gravity loads, diaphragms are laterally stiff and dominant components within the structure that may generally (and conveniently) permit simplified assumptions regarding in-plane force transfer. Yet, in broad terms of seismic resistance, diaphragms are usually considered as passively interacting horizontal plate elements that subscribe to the actions of primary seismic resistance members.

Hence, the most crucial function of a diaphragm will be the performance spectrum during a severe earthquake. It is generally recognised that this function will amount to numerous combinations of simultaneously occurring complex actions. Simply described, it will involve the distribution of horizontal in-plane self-weight (inertia) and transfer forces into the primary seismic resisting system via perimeter connections (i.e., the support interface) and the receipt of forces (often large planar reactions in the case of transfer forces) and deformations imposed by the primary resisting system through the same connections. Historically, the observed failure of connections between these elements has proved to be a major concern with so-called seismic resisting diaphragms [Gupta (Ed.), 1981].

From a developers perspective, it should be noted that diaphragms (pertaining to the precast elements) are expected to consistently maintain an economic margin in building construction. In the author's experience, the floor elements of a structure can be the only large portions where the most (apparently) favourable cost and convenience may wholly governs the consultants selection process.

1.3.2 THE SOURCES OF IN-PLANE DIAPHRAGM FORCES

1.3.2.1 General

The basic sources of horizontal in-plane forces that are associated with fundamental diaphragm actions in seismic resistant buildings are separated into two classes; namely, simple and transfer diaphragm actions. The relative magnitudes and incidence of these actions within a structure will mainly depend on the overall configuration of the primary seismic resisting system. In general, seismic resistant structures are categorised as either moment resisting frames, structural (shear) wall systems or dual systems (hybrid structures) comprised of both structural walls and

frame elements. The deformation response of each of these structure types to earthquake induced ground motions will be somewhat different (Fig. 1.38). Because diaphragms subscribe to actions imposed by primary seismic resisting members, the characteristic in-plane force components of diaphragms in each of these systems will also be different.

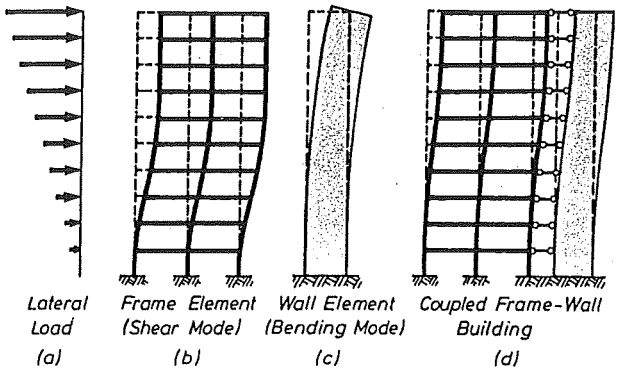

Fig. 1.38 Deformation patterns due to lateral forces of a frame, a wall element, and a dual system [Paulay and Priestley, 1992]

1.3.2.2 Simple Diaphragm Actions

Simple diaphragm actions will occur in all diaphragms and are due to the inertia forces that result from earthquake induced ground motions. The magnitude of these actions is determined by mass-acceleration relationships at the given levels that diaphragms occupy within a structure. Since the self-weight and payload of floor diaphragms may typically be around 70% of a building's total weight, simple diaphragm action is the instigator of most of the horizontal shear forces that are caused by ground shaking.

The forces developed in simple diaphragms are distributed into members of the vertical primary seismic resisting system in accordance with relative stiffness, relative proximities and the availability of suitable load paths. Hence, strut and tie models are widely accepted as being the most pragmatic method for representing the flow of forces in these diaphragms. Analysis of typical strut and tie models will immediately indicate that force concentrations occur in the peripheral regions between the floor plate and vertical members.

Although simple diaphragms subjected to in-plane forces can usually be designed to behave as predominantly elastic elements, it is possible under severe actions that redistributions in force transfer capabilities will occur due to support member elongation and yielding of connections at the floor supports. For this reason it has been recommended that alternative load paths are considered for the inclusion of a viable tension resisting mechanism (Figs 1.39 and 1.40) [Paulay, 1999].

For the purposes of determining design forces, simple diaphragms are usually modelled as deep beams that react against uniformly distributed inertia forces derived from seismic response analysis. The interstorey shears resisted by vertical primary resisting elements (as well as secondary gravity systems) should have already figured in the derivation of horizontal inertia forces at given levels, and need not be considered further. However, the distribution of horizontal in-plane forces within the diaphragm itself must still be resolved. Because diaphragms account for such a large share of the overall seismic weight, it is important that their inertia forces can be distributed into vertical resisting members in near proportion to the stiffnesses attributed to these members in the response analysis. If suitable load paths cannot be secured, the contributions (actions and reactions) of potentially stiff primary resisting members at floor level may need to be reviewed. If load paths are not robust then damage (in the form of inelastic deformation) could be expected to occur within nominally elastically behaving diaphragms and result in the redistribution of load paths. A situation that warrants attention in this regard is where a sizeable floor opening lies adjacent to a vertical member.

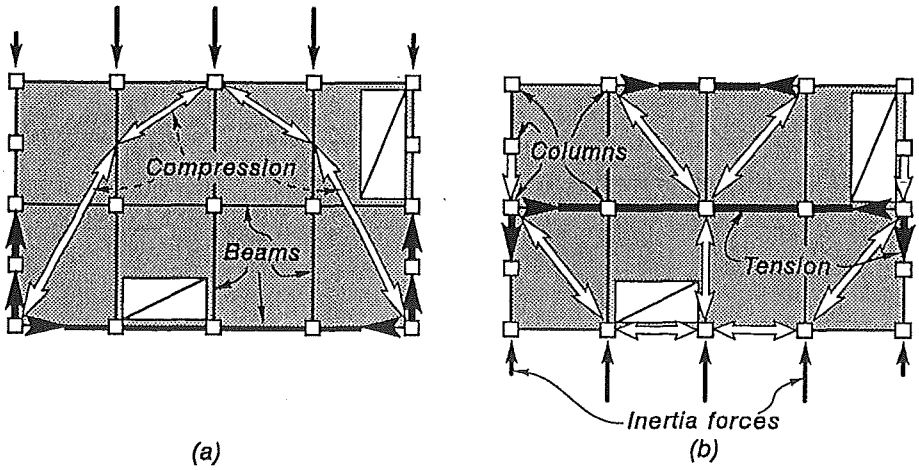

Fig. 1.39 Resistance of a diaphragm to alternate directions of inertia forces using diagonal compression fields [Paulay, 1999]

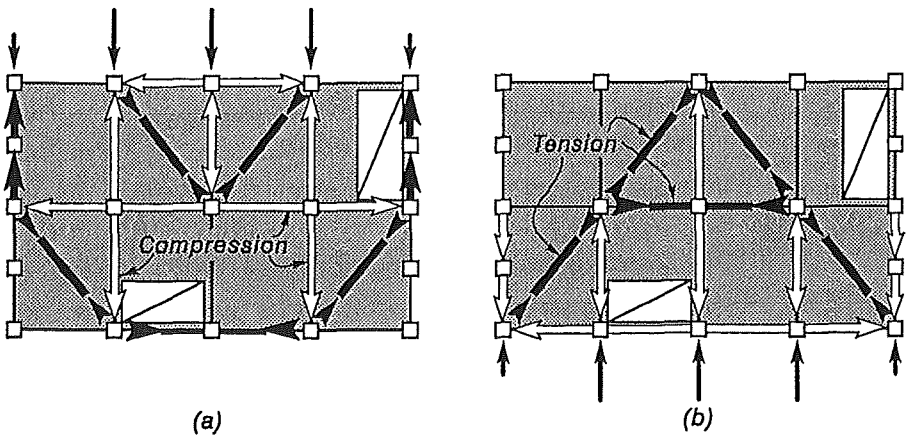

Fig. 1.40 Resistance of a diaphragm to alternate directions of inertia forces using diagonal tension fields [Paulay, 1999]

1.3.2.3 Transfer Diaphragm Actions

Acute variations in the stiffness of primary seismic resisting systems over the height of a structure introduce large in-plane forces. These forces will need to be transferred to the locations of other primary seismic resisting members via the floor diaphragm plate at the level affected by the stiffness change. The typical such case is where a structure is comprised of a monolithically connected tower and podium (Fig. 1.41). The accumulated seismic shears from levels above the podium height will be distributed into the perimeter members of the podium through the transfer diaphragm at podium level.

Obviously some very large forces can be generated, and it is not uncommon for special detailing measures to be incorporated to assist (and direct) force transfer in these floors. These generally appear in the form of well reinforced infill strips that interconnect the vertical elements involved in the force transition (Fig. 1.42). Depending on the magnitudes of forces, additional reinforcement has often been included in the topping slabs as drag bars to achieve tensile force transfer capacity within transfer diaphragms. For the inclusion of any special reinforcing steel to be fully effective, some inelastic deformation within the diaphragm element must occur. Hence, the assumptions of ductile design may need to be applied to some portions of the diaphragm, in particular if concurrent rotations in the horizontal floor plane are likely to occur. For example, yielding of reinforcement may be expected where a floor plate containing drag bars connects with a ductile structural wall.

A similar situation that requires significant force transfer capabilities is where diaphragms interconnect between the structural walls and frame members that make up dual systems (Fig. 1.38). As indicated, the diaphragms of these systems act as in-plane restraints between two dissimilar structural systems so that deformation compatibility is maintained. The result is that net in-plane tension and compression forces must be developed through the floor slab over the height of the wall-frame interface (Fig. 1.43).

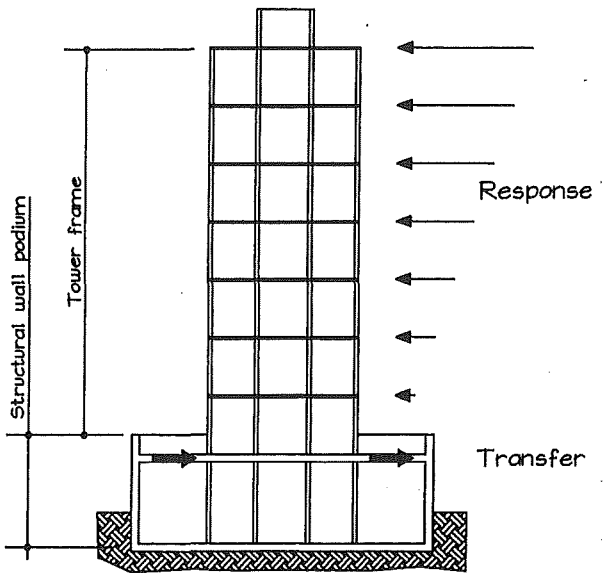

Fig. 1.41 Typical case requiring a transfer diaphragm at podium level

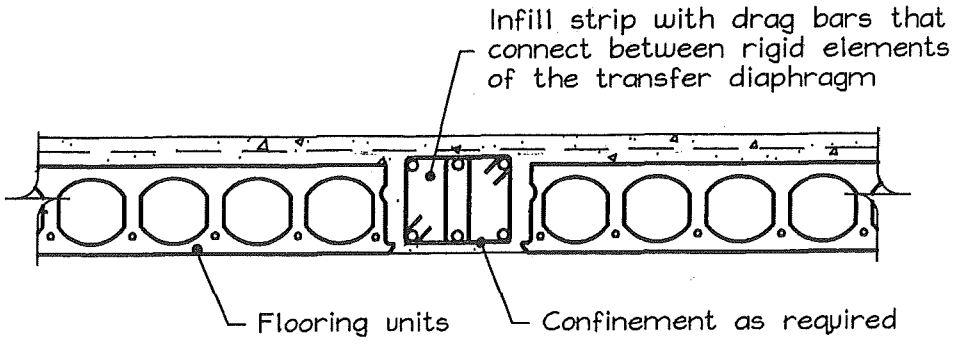

Fig. 1.42 Infill strips and drag bars in a typical transfer diaphragm

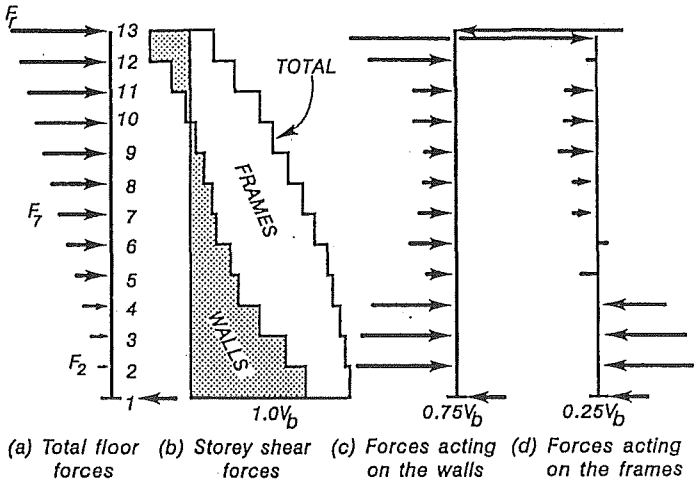

Fig. 1.43 Restraint provided by the diaphragms of dual systems structures [Paulay and Priestley, 1992]

1.3.3 ANALYSIS AND DESIGN PROCEDURES FOR SEISMIC DIAPHRAGMS

1.3.3.1 General

In order to obtain design forces for either simple or transfer diaphragms, some reasonable estimates must first be made of the horizontal shears that may be attributed to the inertia forces of simple diaphragms within a structure. These shears have been described as estimates because it is generally agreed that even the most elaborate procedures for the seismic response analysis of primary seismic resisting systems are only approximations [Paulay and Priestley, 1992]. Hence, diaphragm response, which is derived as a next step from the same global response approximations, can only be taken as an estimate.

The following is a generalised overview of code provisions and methods of analysis used for the determination of diaphragm actions and detailing purposes:

1.3.3.2 The Uniform Building Code (UBC:94) Approach to Diaphragms

Unlike earlier editions of this document, floor diaphragms are treated as being different to shear walls. The requirements of UBC:94 are mainly directed at local inertia forces and structural irregularities as given by section 1631.2.9, and special detailing in accordance with section 1921.6:

Local inertia forces are distributed over the height of a structure by a special formula which gives a lower limit of $0.35ZIW_{px}$ and need not exceed $0.75ZIW_{px}$. Because the lower limit is independent of both structural period and ductility, it will govern for tall ductile structures. Inertia forces calculated in this way are then directly added to forces that may arise from transfer diaphragm actions.

Special requirements are given for structures of irregular plan shape, which may experience differing responses within the same storey level and thus produce out of phase actions. For these diaphragms, drag bars and chords of reinforcing will need to be introduced unless a three dimensional analysis model can demonstrate that the configuration is otherwise sufficient. Limits are placed on the allowable stresses of connector elements in diaphragms that are subject to torsional response, or which contain re-entrant corners or abrupt discontinuities in geometry or stiffness.

Most of the detailing requirements of section 1921.6 are identical to the ACI code provisions for diaphragms that are subject to seismic forces. The method for calculating boundary forces in diaphragms is also as specified by the ACI code.

1.3.3.3 The ACI-318.95 Code of Practice

Section 21.5 of the ACI code [ACI-318, 1995] gives some special requirements for stiff structural systems, which specifically includes diaphragms, struts, ties, chords and collector members used to transmit forces induced by earthquake.

With regards to diaphragms, emphasis is placed on limiting extreme fibre stresses which are calculated using a linear elastic model and gross floor section properties. Unless the entire diaphragm already contains substantial transverse reinforcement (section 21.4.4), boundary members must be provided at diaphragm edges and at the perimeters of openings where extreme fibre stresses under factored loads exceed $0.2f'_c$. Boundary members required as such must also contain the transverse reinforcement specified by section 21.4.4 of the code. Where the calculated compressive stress is less than $0.15f'_c$, these boundary members may be discontinued.

Boundary members are proportioned to resist the sum of factored axial forces acting in the plane of the diaphragm plus the couple force that corresponds with the factored moment acting at the diaphragm section. The lever arm of the couple force is taken as the perpendicular distance between boundary members.

In review of the above requirements, boundary members containing a minimum of transverse reinforcement and fully anchored longitudinal reinforcement are prescribed for the control of seismically induced diaphragm forces. The code provisions appear to be straight forward in their implementation and should achieve a good level of protection for diaphragm elements. Because boundary members at the diaphragm perimeter may also form part of a primary seismic resisting system, the requirements for both transverse and longitudinal reinforcement given in section 21.4.4 of the code should be checked against the minimum requirements for members in potential plastic hinge zones.

1.3.3.4 The New Zealand Standards Approach to Diaphragms

The two documents associated with seismic diaphragm design for concrete structures are the Loadings Standard [Standards New Zealand, 1992] and the Concrete Structures Standard [Standards New Zealand, 1995]. In the Loadings Standard, diaphragm response is considered (as it has been traditionally) along with the "Requirements for parts" of a structure. The Concrete Structures Standard has introduced a section that specifically treats diaphragms as elements with separate detailing requirements.

The Loadings Standard advocates the use of the equivalent static, modal response spectrum and numerical integration time history methods of seismic response analysis. For structures that do not meet horizontal regularity requirements, three dimensional analysis methods are necessary to determine seismic response behaviour.

With regard to diaphragms and structural regularity, the Loadings Standard gives relevant precautions on avoiding geometric and stiffness irregularities within diaphragms that may result in unfavourable response behaviour. Likewise, it is stated that diaphragms of a potentially flexible nature should be investigated to establish whether significant force redistributions may occur. In this way, the Loadings Standard emphasises the need for designers to recognise the areas of concern with diaphragms, and to devise solutions which are consistent with seismic analyses. Ultimately, the design process should incorporate the use of detailing methods such as those provided for diaphragms in the Concrete Structures Standard [Standards New Zealand, 1995]. With the general availability of powerful analysis software, this type of approach may be more in keeping with contemporary design practice than the prescriptive requirements of code documents.

Floor coefficients can be calculated from the "Requirements for parts" section of the Loadings Standard for corresponding equivalent static and response spectrum methods of analysis. For the ultimate limit state, the floor coefficient taken at or below the base of the structure is $0.25RZL_u$, which incidentally may exceed the floor coefficient at the adjacent first floor level. Thus, values taken from the ductile seismic response of the primary structure are scaled by appropriate factors to give a design envelope of floor coefficients that will generally correspond with fully elastic ($\mu = 1$) global response.

The application of elastic diaphragm response, as determined by a floor coefficient, should warrant some consideration. It is essential to fully consider diaphragm response if any inelastic behaviour is expected to occur, as permitted for parts by table C4.12.1 of the Loadings

Standard. The reason is that unlike the true "parts" of a structure, yielding diaphragms can cause a redistribution in the transfer of forces which could in turn influence the response behaviour of the structure. Furthermore as already mentioned, greater ductility demands than the allowable specified ($\mu_p = 3$) for diaphragms under the "Requirements for parts" may occur in certain regions of diaphragms. This ductility demand will not necessarily be due to the proposed inertia forces, but rather through the accompaniment of inelastic deformations that are characteristic of ductile support members. The Concrete Structures Standard [Standards New Zealand, 1995] states that a special study or theoretical analysis is required for diaphragms that may exhibit inelastic deformations. However, this is only a requirement for inelastic deformations that are due to in-plane forces.

Based on the above, it is the author's opinion that the Loadings Standard [Standards New Zealand, 1992] may not go far enough to distinguish diaphragms from their traditional classification as a "part" of a structure. This assertion is supported by the fact that the definition of a "part" of a structure does not encompass the broader function of diaphragms.

A "part" is described in the Loadings Standard as: "An element which is not intended to participate in the overall resistance of the structure to lateral displacement under earthquake conditions in the direction being considered". This definition is contradictory of diaphragms when we consider, for example, the essential coupling role of diaphragms in dual system structures or the major stiffness modifications effected on beam elements due to their rigid connection to diaphragms. These influences are neither unintentional or unquantifiable at the initial design stage. Hence, the influence of diaphragms may be well integrated into both the response analysis and the impending assumptions on post-elastic behaviour of the primary structure. Because the disposition of true parts (e.g., cable train hangers, stand alone partition walls and coffee machines) is far more simply defined than as for diaphragms, it seems logical that diaphragms should be identified by the Loadings Standard as distinct elements with their own detailed requirements.

The new diaphragms section of the Concrete Structures Standard [Standards New Zealand, 1995] summarises the ordinary structural requirements for diaphragms such as minimum topping concrete thickness and maintaining composite tie action. These requirements are essentially identical to those of the preceding concrete design standard [SANZ, 1982]. However, the new section places direct emphasis on providing details that can perform to a level characterised by particular structural actions. This is indicated by the content of section 13.3.7.4 where it is stated that: "Connections by means of reinforcement and shear transfer mechanisms from precast concrete diaphragms to components of the vertical primary lateral force resisting systems shall be adequate to resist the relevant design forces". This requirement becomes fundamental to the present course of study when we consider the full ramifications of the term "relevant". The commonly employed tie connection detail (see Fig. 1.36) for floor construction has had no supporting data from tests involving actions that are characteristic of seismic resisting diaphragms.

In summary, the Concrete Structures Standard has introduced a section which gives useful guidelines for achieving structural control through diaphragms. The commentary (part 2) should

be read in conjunction with the standard to gain an understanding of some of the given requirements. Yet, it is evident that on the subject of seismic resistant diaphragms there is a lack of the gritty underlying experimental data that has been a hallmark of the New Zealand Standard. The diaphragms section of this document is more descriptive than prescriptive, which, for the greater part, may actually be the most pragmatic approach to the design of diaphragms. Nevertheless, the remaining issue is to resolve the capabilities of diaphragm connections that have been based on strength design parameters, but which must perform in context with a capacity design philosophy.

1.3.3.5 Rigid Diaphragms in Response Spectrum Analysis

Modal response spectrum analysis has been by far the most common form of computer analysis used in New Zealand. Until recently, most modal analysis software packages, such as ETABS, have modelled diaphragms as infinitely rigid plates. Thus, only three degrees of freedom feature in the floor analysis, which amounts to two translations and one rotation of the entire floor plate in the horizontal plane at a given level. This modelling infers that the floor portions of diaphragms do not accompany support member rotations through the horizontal plane, which is not even partially correct (otherwise floor serviceability deflections would not require checking under mere gravity loads). However, because diaphragms are such a dominant element under in-plane actions, the assumption of a rigid diaphragm has generally been considered adequate for analysis.

Assuming a rigid diaphragm may result in a lower estimated value of structural period, for use with basic seismic hazard spectra, than would result if floor deformations were included. For the majority of cases, the predominant first (fundamental) mode of vibration will therefore correspond with a higher estimate of spectral acceleration for the determination of seismic shears, which produces a conservative design. This is especially the case for many of the medium-rise structures that are common in this country. In the New Zealand Loadings code, the basic seismic hazard acceleration coefficient for subsoil category (a) (i.e., rock or very stiff soils) increases by more than a factor of two for fully elastic response as natural periods move between 1.0 seconds and 0.45 seconds [Standards New Zealand, 1992]. An overestimate of seismic shears should (albeit indirectly) result in the use of larger magnitude actions for the design of diaphragms.

Where higher mode effects such as significant torsion response of tall or irregular structures may be of concern, a diaphragm that is detailed to maintain structural compatibility and survive the concurrent overstrength actions of support members (particularly in the lower storeys of frames) under first mode response is likely to be adequate to endure higher mode actions. At any rate, extra care with the analysis and detailing for interactions between the diaphragms and support members of torsionally sensitive structures is an implicit requirement of contemporary design practice [Standards New Zealand, 1995]. In many cases, this will involve such measures as introducing seismic gaps in diaphragms of irregular shape to produce a series of well conditioned sub-elements (Fig. 1.44).

The assumption of an infinitely rigid diaphragm can cause a potentially dangerous oversight, as it tends to produce an underestimate of horizontal storey deflections. This is mainly of concern with taller frame structures detailed for ductility in that P-delta effects will start to influence behaviour if limits on inter-storey drift are exceeded [Standards New Zealand, 1992]. In the analysis, the effects of diaphragm flexibility can sometimes be allowed for by reducing the stiffness of primary seismic resisting members that receive forces at the floor level connections [NZCS-NZNSEE, 1991].

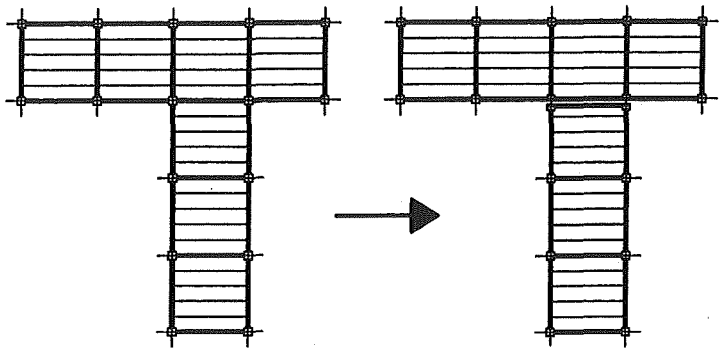

Fig. 1.44 Plan configuration simplified by introducing a seismic break

1.3.3.6 Flexible Diaphragms in Response Spectrum Analysis

More recently, Response Spectrum Analysis programs that allow flexible diaphragm modelling have been made commercially available (e.g., ETABS version 6.0). The term "modelling" has been applied because only rigid elements can have mass assigned to them for purposes of generating diaphragm inertia forces. Therefore, if the effects of diaphragm response are to be incorporated, the designer must construct a grid (checker board) model of rigid elements that are interspersed with flexible elements [Robertson, 1996]. Obviously in doing so, some care must be exercised with how the model is formed, especially with regards to such matters as maintaining compatibility at the boundaries of floor plate elements.

With flexible diaphragm analysis, the results should be subjected to a careful reckoning procedure because a large body of data is extracted giving only the absolute magnitudes of induced actions. The actual task of collating output data to the point of distinguishing concurrent principal actions can be time consuming and may also expose the analyses to interpretation errors (making post-processing an advisable option). Furthermore, the output of response spectrum analysis gives the envelopes of peak response as derived from the global response of the structure. Consequently, it is not feasible to check the equilibrium of diaphragm forces against the structural action envelopes generated for other (primary resistance) structural members.

Response spectrum analysis incorporating flexible diaphragms is generally considered to be a useful design tool for examining the elastic response behaviour of certain types of structures,

especially for deflections criteria. Nevertheless, the detailing of reinforcement for diaphragms will usually need to follow more straight forward methods that involve basic equilibrium equations, such as with the strut and tie methods. This is partly because modal response spectrum analysis does not present the simultaneous coalition of forces and moments which act through a particular plane of reference, making it difficult to keep track of equilibrium in structural interactions. More importantly, response spectrum analysis cannot incorporate the influence of post-elastic behaviour nor the effects of overstrength actions in primary seismic resisting members. To remain consistent with the situation that exists in real members of the primary resistance structure during a severe earthquake, force transfer in diaphragms may best be accomplished by using equilibrium models and the capacity design approach to detailing [Hare, 1996].

1.3.3.7 Numerical Integration Time History Methods of Analysis

Both the linear and non-linear time history methods may be utilised to determine the particular response of primary seismic resisting elements and diaphragms. However, because of the computational effort involved, these methods are generally limited to checking the response of either unique or important structures. The Loadings Standard [Standards New Zealand, 1992] requires that at least three appropriately selected and scaled earthquake accelerograms are used, and that at least 15 seconds of strong motion shaking is featured in the analysis.

Like response spectrum analysis, the linear elastic time history method is strictly limited to linear elastic structural behaviour. Hence, an informed choice of initial stiffness values for the various structural elements is important. It is apparent that some care and foresight must be exercised when selecting nominal member stiffness for use in what are essentially elastic analyses. It must also be appreciated that alternating combinations of direct-axial forces and sway actions will continuously alter the stiffness of concrete members during an earthquake event.

The linear time history analysis method has a major advantage over response spectrum analysis in that it provides definitive information on structural performance, such as the likely magnitude and frequency of damage cycles caused to key structural elements. Because of the equilibrium equations which must be satisfied as part of the analysis, it is also possible to directly extract a particular regime of forces and moments acting in a member at a given interval.

Non-linear time history analysis involves much computational effort and is probably not appropriate for the routine analysis of diaphragms. Furthermore, the analysis procedure relies on elasto-plastic stiffness models which in turn rely on a predetermined configuration of reinforcing steel, both longitudinal and transverse in effect. Hence, a sensible choice of reinforcement configuration is normally required before the analysis can proceed without the risk of doing costly re-runs. As such, non-linear time history analysis is often considered as a useful devise for checking the performance of existing designs, and ultimately as a tool for researchers [Paulay and Priestley, 1992]. The reinforcing details in diaphragms of structures so examined will probably have been based on simple equilibrium models and the principles of capacity design.

1.3.3.8 Strut and Tie Methods (Simple Equilibrium Models)

Design is always an iterative process that involves progressive refinement, and as inferred by the preceding paragraph, even the most elaborate analysis methods may require fairly accurate input. Thus, a designer armed with this ability should at least have the skill to envisage the format of an acceptable engineering solution. In this regard, strut and tie methods form an extremely useful approach to resolving force transfer within diaphragm elements. Strut and tie methods (Fig. 1.45) are strongly advocated for the practical detailing of diaphragms.

A fundamental requirement of correct detailing practice is that equilibrium is achieved through viable load paths. Moreover, the capacity of reinforcing steel provided for this must be adequate to sustain the overstrength actions associated with the inelastic behaviour of supporting primary seismic resisting systems. Good detailing practice requires that continuous chords are developed by the tension reinforcement in an otherwise brittle medium. Hence, it is often more expedient for the designer to exercise this option in the first instance by using strut and tie methods.

It is widely recognised that a potential danger of designing the density of reinforcing steel placement to exactly defined zones of peak stress as derived from elastic analysis, is that consideration is not given to tension shift effects. Considering both response spectrum analysis and linear time history analysis: being purely elastic methods that are subject to the selective nature of input data, the peak actions derived at nominally selected node points within a flexible diaphragm are only discrete results (in the statistical sense of a result). Regardless of how much value the designer may place on the derived planar forces, it is fundamentally important that variations in the magnitude and location of tensile forces can be accommodated within the diaphragm element. The only safe and practical way that this requirement can be accomplished in ordinary reinforced concrete is by implementing a continuous distribution (chord) of fully anchored reinforcing steel. This naturally returns the designer to using simplified detailing practice that is based on strut and tie models.

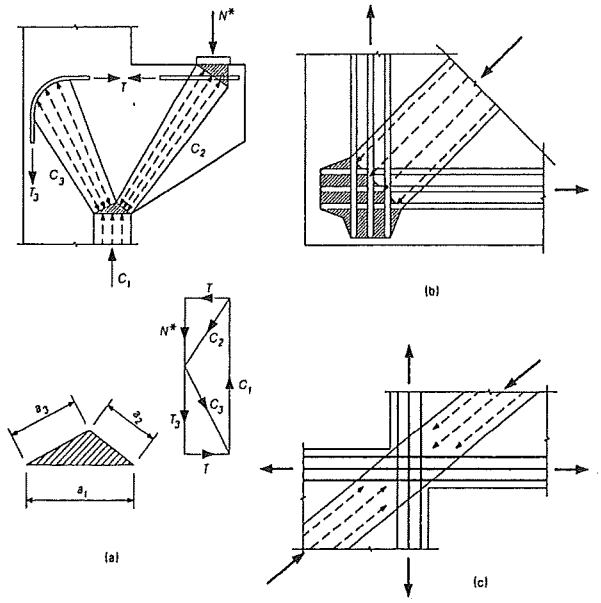

Fig. 1.45 Strut and Tie models [Standards New Zealand, 1995]

1.4 PRECAST FLOORING AND SUPPORT MEMBER INTERACTION

1.4.1 GENERAL

As briefly discussed in section 1.2.3.4, much of the concern with the seating of precast flooring units can be attributed to their interaction with ductile members of the support structure. As a consequence, many of the assumptions used in the analysis of diaphragms may be of secondary importance to the present study, other than to help provide an overall basis for designs that will not exacerbate the problem. Actually, for the diaphragms of most buildings it is considered that variations in analysis input parameters (e.g., diaphragm flexural and shear stiffness) should not significantly affect the output [NZCS-NZNSEE, 1991]. With flooring unit support, the critical factor is global ductility demand and the need to maintain deformation compatibility with ductile members of the primary seismic resisting system.

The ductility demand of supporting members may set up patterns of inelastic deformation that induce certain reactions in flooring units. The deformations of members of the support structure are a by-product of the means by which seismic energy is dissipated through the formation of plastic hinges. As such, the nature of these actions is somewhat absolute and the flooring system is obliged to maintain deformation compatibility with the support structure.

1.4.2 THE INFLUENCE OF STRUCTURAL SYSTEMS

1.4.2.1 General

The manner in which plastic hinge formations may affect floor connections is a direct function of the type of structure involved. There are three main categories of ductile seismic resisting structural systems to consider: ductile moment resisting frames, structural wall systems and dual systems which utilise both frames and structural walls.

1.4.2.2 Ductile Moment Resisting Frames

Medium sized and tall moment resisting frames are designed in accordance with capacity design principles and the provision of beam sidesway (strong column-weak beam) mechanisms [Park and Paulay, 1975]. Accordingly, the structure is analysed and designed on the basis that plastic hinges will only form in beam members (usually where they connect to columns) and at the column bases as necessary (Fig. 1.46). The column sections above the base of the structure are designed to remain elastic or (ultimately) not to allow the formation of plastic hinges under severe seismic actions. For a given structure geometry, the degree of plastic hinge rotation generated in the beams is a function of the global displacement ductility demand and plastic hinge lengths. Analyses of frames has indicated that the displacement ductility factor of a frame is of the same order as a single degree of freedom system having the same force displacement characteristics and designed for the same fraction of elastic response loading [Park and Paulay, 1975]. Subsequently, the curvature ductility factor at beam plastic hinges may be estimated from Equation 1.18:

$$\frac{\varphi_u}{\varphi_y} = 1 + \frac{\ell}{6\ell_p}\left(\frac{\theta_u}{\theta_y} - 1\right) \qquad (1.18)$$

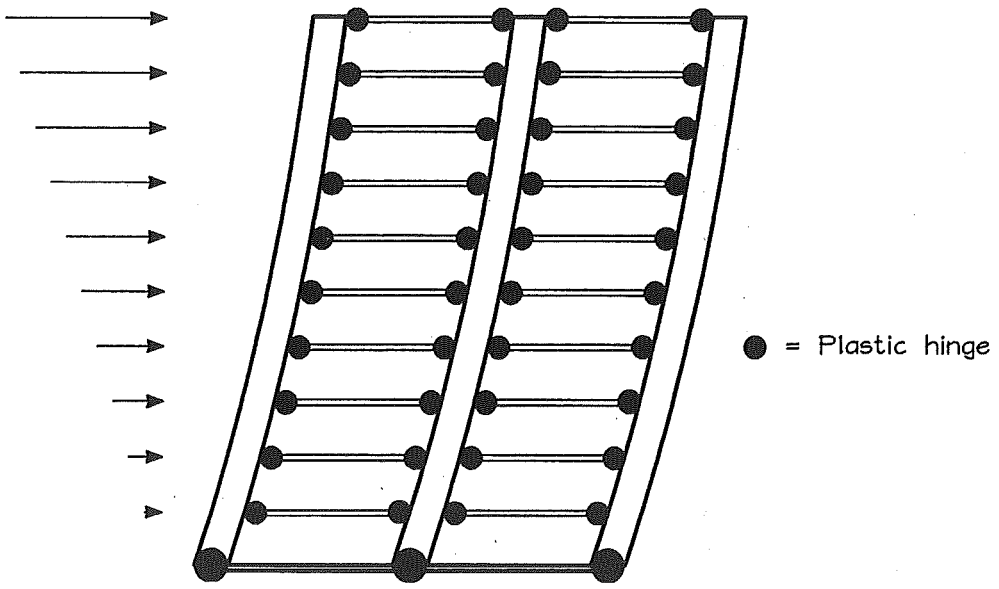

Fig. 1.46 Beam sway mechanism of a building frame

For a symmetrical beam side-sway mechanism, the rotational ductility factor at the beam ends θ_u/θ_y is usually found to be about twice the displacement ductility ratio μ. The ratio of beam length to plastic hinge length l/l_p may typically be about nine. Based on these parameters, the curvature ductility ratios φ_u/φ_y that must be attained in plastic hinge zones for given displacement ductility ratios μ may be estimated for ductile moment resisting frames (Table 1.8):

Table 1.8 Typical estimates of curvature ductility ratios corresponding with displacement ductility factor ratios of frames, as calculated by Equation 1.18

μ	2	3	4	5	6
φ_u/φ_y	5	8	11	14	17

The relationship between curvature ductility factor ratios and strength development in plastic hinge zones of beams may not only depend on the quantity and effective depth of beam reinforcement but also on the layout of precast prestressed flooring elements. Figure 1.47 shows the formation of plastic hinges adjacent to the corner columns of a ductile frame structure.

Because of the complexity of earthquake ground motion, structural elements as such (Fig. 1.47) are designed to resist seismic forces acting independently along each axis of the structure

[Standards New Zealand, 1992]. Under combinations of oblique earthquake motion and induced torsion, it is anticipated that a severe earthquake will cause the simultaneous formation of plastic hinges in each frame axis [Park and Paulay, 1975].

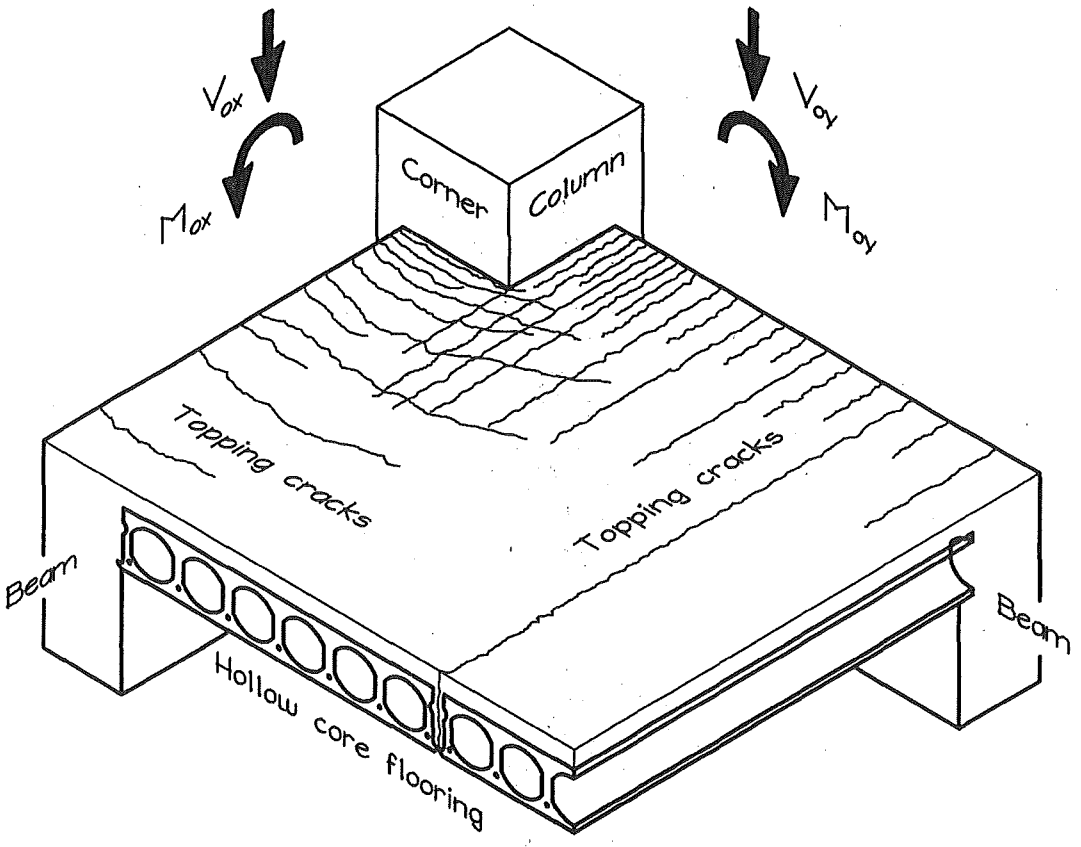

Fig. 1.47 Plastic hinge formation at the junction of perimeter beams, indicating the likely floor plane fracture pattern of a composite hollow core flooring unit

A detailed study of the mechanism of cast-in-place floor slabs acting as beam flanges has been conducted at the University of Canterbury [Cheung, 1991]. However, because of the very different nature of flooring systems involved there is a limit to the applicability of results from this research to the present study. The work of Cheung is based on traditional cast-in-place (two-way slab) floor systems, which for flexural reasons [Park and Gamble, 1980] contain a considerable amount of (often continuous) slab reinforcement that is well anchored into the support elements, including beam plastic hinge zones. Furthermore, a monolithic cast-in-place slab approaches a state that is both homogeneous and isotropic in its original unloaded condition, which is certainly not the case for modular pretensioned flooring systems.

By contrast, one-way prestressed flooring (especially hollow core) systems are generally designed as simply supported members, and tend to contain the minimal amount of "starter" reinforcement needed to form construction joints between the composite topping and beam members. This reinforcement is typically lapped with hard-drawn wire mesh in the composite topping slab and thus curtailed within 600 mm from the support (see Fig. 1.36). Moreover, the likely response of prestressed flooring units to the formation of beam plastic hinges will depend on the obvious differences in section for each direction of floor span (Fig. 1.47). Subsequent behaviour will be conditioned by the type of prestressed flooring sections involved, the strength and stiffness of shear connections between the beam and flooring elements and the actual position along beams where plastic hinges form.

Although the influences described in the foregoing paragraph may appear to present complications, they actually allow for simplifications in modelling the interactions between prestressed flooring systems and ductile beam members. Based on what are considered to be admissible simplifications, comparisons are made below with the findings of research into the contribution to beam tension of cast-in-place slabs [Cheung, 1991].

(a) Orthotropic (Orthogonally Anisotropic) Pretensioned Flooring

The orthotropic nature of modular pretensioned flooring is almost certain to limit the effective floor section contributing to beam tension in plastic hinge zones to the width of one unit module. This also results from inelastic curvature φ_p of the end support beam, which may produce a fracture along the weak joint between unit modules (Fig. 1.47). The result is a structural discontinuity that will interrupt the shear flow between prestressed units (i→j) and also the spread of flexural cracks into the sections of consecutive (i→j→k...) prestressed units (Fig. 1.48). It is a reasonable expectation that cracks will develop in the prestressed section (i.e., unit i) adjacent to a beam plastic hinge, in direct coalition with beam cracking. However, the ensuing degree of crack propagation and participation of flooring units in developing flange tension will be strongly influenced by the configuration of the prestressed floor section in relation to the adjacent beam (Fig. 1.48).

The section of composite topping over the adjoining edges of prestressed units is most often only lightly reinforced with hard drawn wire mesh. Tensile strains developed in the topping slab due to plastic hinging of the end support beam will quickly engage the mesh reinforcement and draw it to strains that correspond with tensile fracture. The elongation capacity of New Zealand

manufactured hard drawn wire mesh has been shown by tests as generally less than 5% [Mejia-McMaster and Park, 1994; Herlihy, 1994]. Obviously, significant crack openings will occur and spread along the joints between prestressed units, causing a marked decrease in shear transfer across this region.

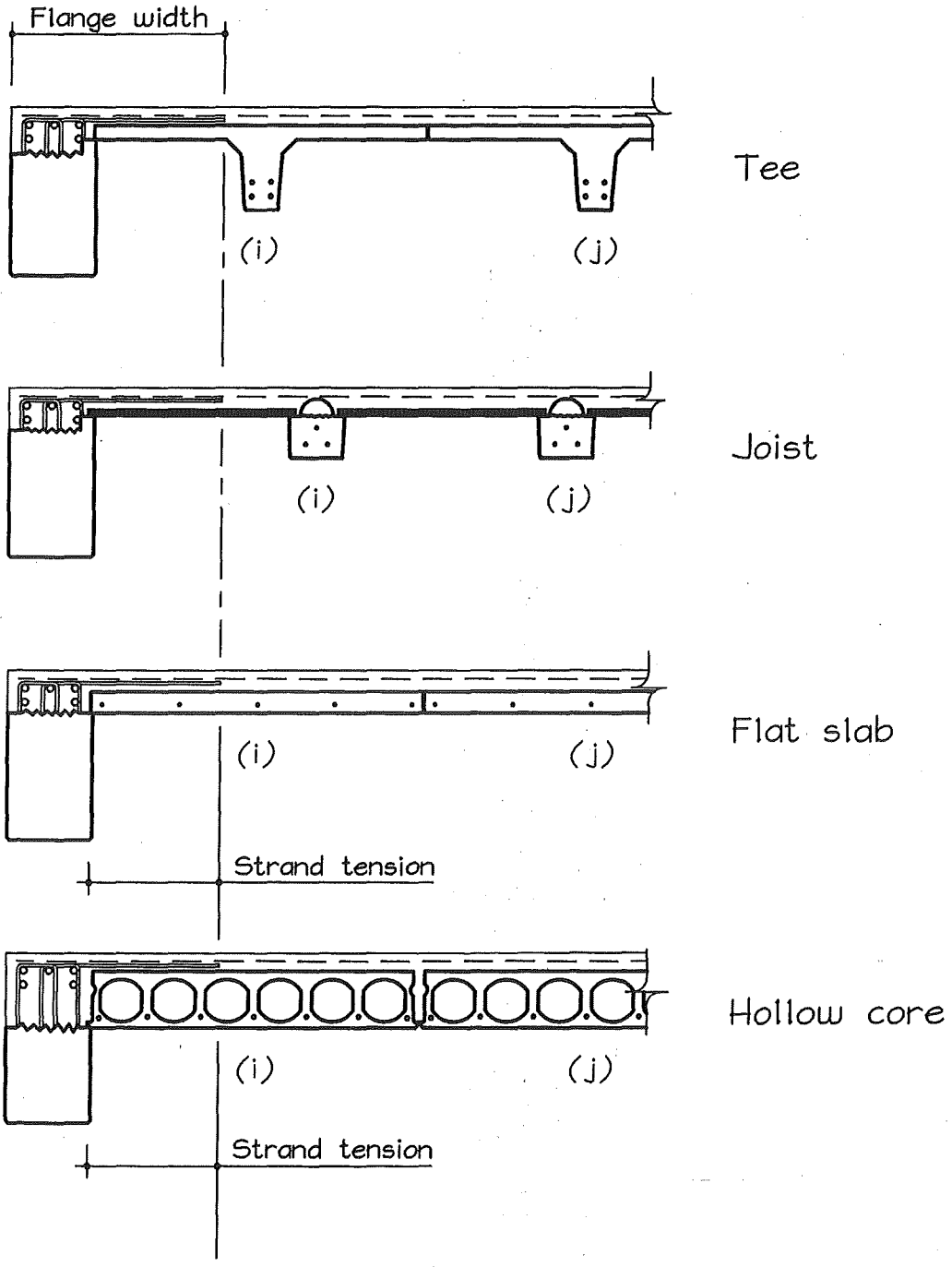

Fig. 1.48 Likely effective widths of tension flange for prestressed flooring systems with nominal side seatings onto ductile perimeter beams

The flange tension mechanism associated with cast-in-place slab systems (Fig. 1.49) relies on developing orthogonal tension components to react against concrete strut segments. To achieve this, similar capacities of reinforcing steel ΣT_X and ΣT_Y must act in each direction to satisfy equilibrium with the vector sum D of the diagonal components (Fig. 1.50). The relatively small proportion of slab starter reinforcement involved with composite toppings coupled with short embedment lengths would not support the formation of this type of mechanism in pretensioned flooring systems. Furthermore, the axial component of prestress force would oppose the development of radial patterns of strut segments in pretensioned slab systems with adequately bonded toppings, as would the discontinuity caused by prestressed stems in tee and joist construction. Hence, the development of cracks in an orthotropic floor system will be most strongly influenced by the initial controlling factors of concrete section properties and relative stiffness in the orthogonal directions.

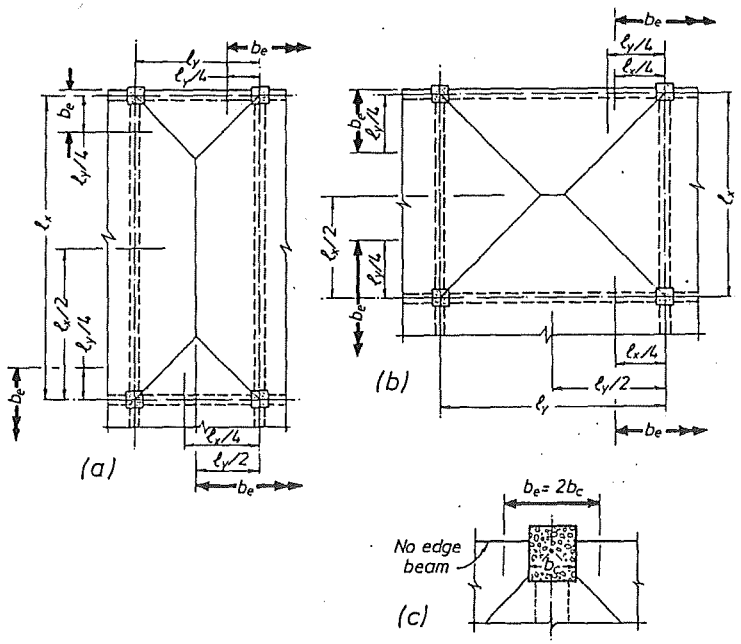

Fig. 1.49 Effective widths of tensile flanges for cast-in-place floor systems [Cheung, 1991]

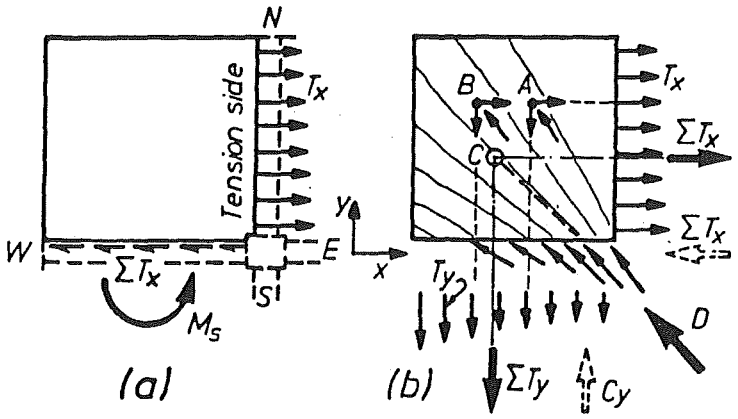

Fig. 1.50 Equilibrium criteria for the mechanism of tension flanges in cast-in-place slabs [Cheung, 1991]

(b) Shear Flow and Construction Joints

The shear transfer across construction joints in diaphragms is normally based on the principles of shear friction [Kolston and Buchanan, 1980], in which the required area of shear friction reinforcement should be calculated by Equation 1.19 [Standards New Zealand, 1995]:

$$A_{vf} = \left(\frac{V^*}{\phi \mu_f} - N^* \right) \frac{1}{f_y} \qquad (1.19)$$

In the case where no external force is acting, Equation 1.19 assumes that a sufficient dislocation has occurred along the opposing faces of the construction joint to develop the yield force of shear reinforcement $A_{vf} f_y$. An amount of shear resistance can also be attributed to the dowel mechanisms of shear friction reinforcement, which become increasingly important at larger shear displacements (Fig. 1.51). However, the shear stiffness across typical floor construction joints is likely to be somewhat reduced at the stage when contributions from dowel action become significant [Paulay, Park and Phillips, 1974].

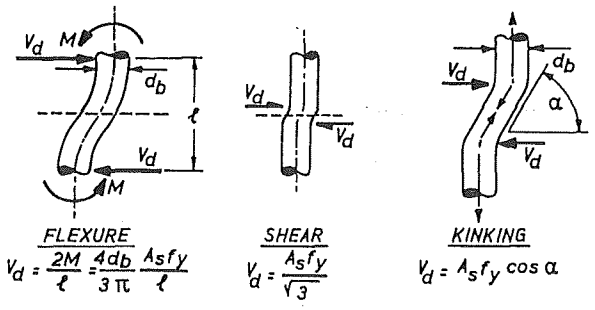

Fig. 1.51 The mechanisms of dowel action across a shear face [Park and Paulay, 1975]

As indicated by tests, the strength and stiffness of shear planes will not reduce until cracking has occurred and degradation of the joint concrete ensues. When crack widths are relatively small and maintained constant along the shear plane, it has been shown that appreciable shear stresses can be developed through aggregate interlock [Paulay and Loeber, 1974]. Under cyclic actions, it is recognised that the rate of stiffness degradation is more sensitive to the magnitude of prior loading cycles than the frequency of loading. This is because the mechanism of aggregate interlock, an important component of shear resistance, tends to become ineffective due to aggregate dislodging under intense cyclic forces (also see section 1.2.2.1).

For the edge shear keys of hollow core members (Fig. 1.52), equations are recommended for estimating the shear capacity of joints in both the uncracked and cracked states (Equations 1.20 and 1.21) [Bruggeling and Huyghe, 1991]. Similar to other such methods, the maximum and residual shear stresses are taken as a function of mortar strength at the interface f_{cm} and the presence of a normal clamping stress σ_c. A safety factor of $\gamma = 2.5$ has been applied in these equations. Hence, the respective maximum τ_{max} and residual τ_r shear strengths may be taken as:

Before cracking: $$\tau_{max} = 0.9\sigma_c^{0.7}(\ln f_{cm})^{0.18} + 0.05 f_{cm} \quad (1.20)$$

After cracking: $$\tau_r = 0.95\sigma_c(\ln f_{cm})^{0.25} \quad (1.21)$$

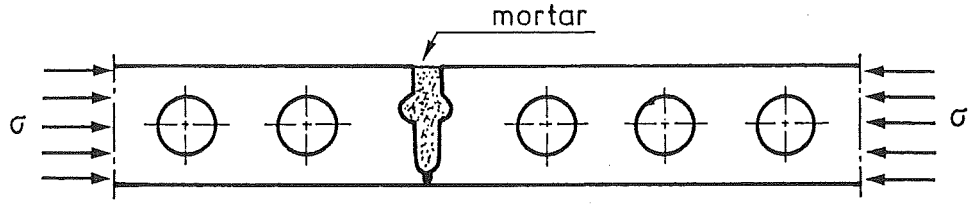

Fig. 1.52 Joint geometry and normal clamping stress [Bruggeling and Huyghe, 1991]

Due to volume changes, a topping crack may develop at the interface between the perimeter beam and the edge of first flooring unit (i) (Fig. 1.48). However, in one-way flooring construction this should remain as a hairline crack and significant concrete tensile capacity will exist across the edge joint under service loads. Hence, if the normal stress σ_c is taken as the tensile capacity of topping concrete (the key infill mortar in composite construction) downgraded to $0.33\sqrt{f'_c}$, then Equation 1.20 will give a τ_{max} of at least 2.5 MPa.

For most situations, a resisting shear stress of 2.5 MPa would be adequate to develop shear flow forces between the perimeter beam and floor unit. The value of τ_{max} calculated as such should be considered conservative because a more effective shear strength will be developed across the monolithic portion of the composite topping, and a generous safety factor has been applied.

As the ultimate limit state is approached during a severe earthquake, extensive cracking is expected to occur in and around the perimeter region of the structure and Equation 1.21 will become more appropriate. An important consideration is that the effective clamping stress σ_c will be continually changing throughout the seismic attack, and this should reflect on the participation of flooring units in beam actions. Clamping stresses that occur in a construction joint during the compression run of a load cycle will overshadow the tensile contributions from starter reinforcement in developing shear capacity. Thus, assuming that the composite topping remains adequately bonded to the precast units, starter reinforcing will provide the base level of clamping stress to the adjacent construction joint, similarly as provided by $A_{vf}f_y$ in Equation 1.19.

Combinations of structural actions will produce tension T and compression C in the top fibres (the floor plane) of beam plastic hinges in regular ductile frames (Fig. 1.53). The combinations shown are all likely events during an earthquake, and are as induced by components of translation only as caused by ground motion that is oblique to the axes of the structure, and translation with torsion. Therefore, these combinations are characteristic of seismic response in all such structures, regardless of (but strongly influenced by) eccentricity of mass and building height etc.

At each of the corner columns (①,②,③ and ④ in Fig. 1.53) there are four combinations of actions to consider due to the formation of plastic hinges in beams under two-way frame actions. Because of the orthotropic nature of pretensioned flooring systems, each combination of plastic hinging in a specific column region will produce a different effect on the horizontal shear capacity of floor construction joints. For an isolated corner column region, which is taken at column ① in Figure 1.53, the effects of combined actions under the given modes of frame displacement are presented in Table 1.9:

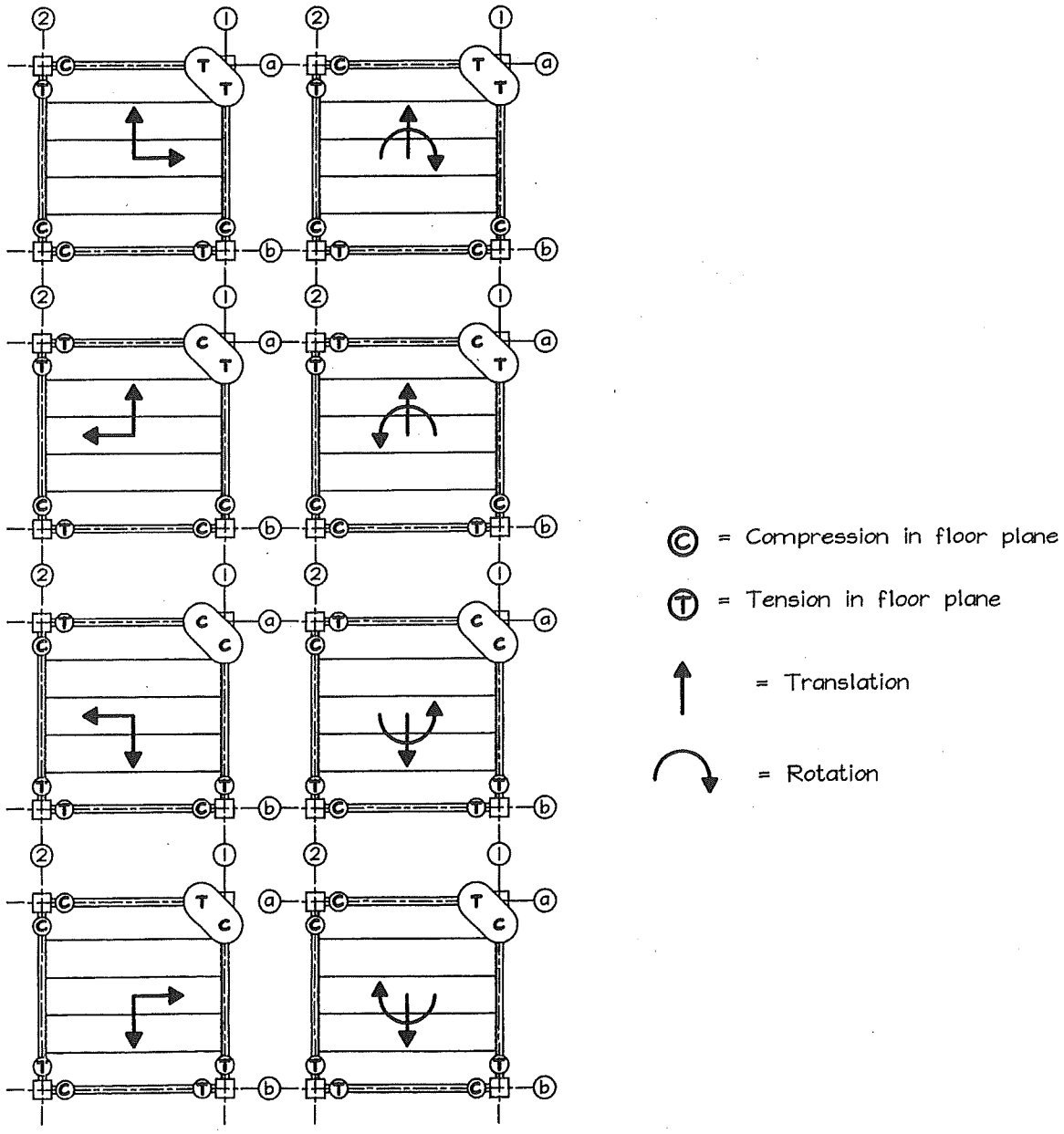

Fig. 1.53 Modes of frame displacement causing tension T and compression C in the floor plane adjacent to plastic hinges

Table 1.9 Combinations of two-way frame actions at column ① (Fig. 1.53) producing tension T or compression C in the top fibre of floor slabs constructed from modular pretensioned units with composite topping

Frame displacement translations only & translation+rotation		**At beam plastic hinges** column ①		**Effect produced in flooring units adjacent to respective beam plastic hinges**		**Combined effect on floor system**
		grid	grid	along grid line	along grid line	along grid lines
T	T + R	a	b	a	1	a,1
(a-1)	(a-1)	T	T	cracks open through precast floor section, unit (i), unit (j)?	cracks open along adjoining edges of floor units & tension across support construction joint	two-way cracking of floor slab & general degradation of joint shear capacity
(a-2)	(a-2)	C	T	cracks close in floor section and potential buckling of topping reinforcement	cracks open along adjoining edges of floor units	opposing shears in floor slab plus potential bar buckling promotes loss of composite topping bond
(b-2)	(b-1)	C	C	cracks close in floor section and potential buckling of topping reinforcement	cracks close along adjoining edges of floor units	buckling of topping reinforcement
(b-1)	(b-2)	T	C	cracks open through precast floor section, unit (i), unit (j)?	cracks close along adjoining edges of floor units & tension across support construction joint	opposing shears in floor slab plus potential bar buckling promotes loss of composite topping bond

Although real seismic response may involve somewhat more complexity than graphic models of translation and rotation, certain fundamental elements of behaviour can be postulated from these. Referring to Figure 1.53 and Table 1.9, it can be concluded that tension should exist in the floor plane of a corner column region during three out of every four seismic response displacements and that response cycles will change the sign (sense) of each force. Thus, regions of in-plane compression C-C or tension T-T will tend to directly alternate, as will regions where the floor plate is subjected to vertical shears, C-T and T-C. This has important implications on providing sufficient capacity in the floor connections and construction joints to withstand recurring alternations of forces, be they in-plane axial forces or shears.

(c) Strength Development in Pretensioned Flooring Tension Flanges

As discussed, the magnitude of flange tension will be influenced by various aspects which relate to the type of pretensioned section involved and the affected shear capacities of construction joints under seismic actions. Another very important factor is the actual location where plastic hinges are formed along the frame members.

Where plastic hinges occur close to column faces, the tension developed by prestressing steel in an adjacent floor section will be limited by strand bond capacity with the surrounding concrete. From a design standards perspective, the length L_d that is required from the free end of a member to develop the full tensile strength of prestressing strand is defined by envelopes of distance versus steel stress (Fig. 1.54).

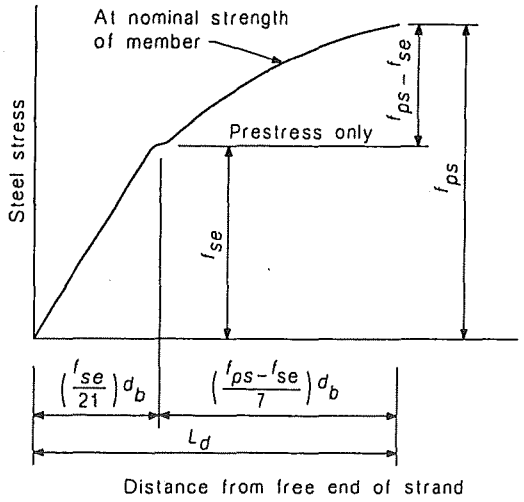

Fig. 1.54 Variation in steel stress with distance from the free end of a pretensioned unit [Standards New Zealand, 1995]

Accordingly, the length in the transfer zone $f_{se}d_b/21$ corresponds with a bond strength of 5.2 MPa and the interior portion $(f_{ps} - f_{se})d_b/7$ with a bond strength of 1.7 MPa [Collins and Mitchell, 1987]. The greater bond strength in the transfer zone is attributed to the Hoyer effect, which is not effective in the interior portion. However, it is important to note that significantly higher bond stresses, in the range of 3 to 5 MPa, have been obtained in tests where the Hoyer effect has been absent [Stocker and Sozen, 1970]. Other tests specifically performed on saw cut pretensioned hollow core units showed that an average of 85% of the design tensile strength of ½ inch 270 ksi (12.7 mm 1860 MPa) strand could be developed over a bond length of 48 inches (1.22 m) [Anderson and Anderson, 1976]. This length is about 60% of L_d as derived from Figure 1.54 for the full strength development of strand, and indicates an average bond strength of 3.2 MPa over the bond length.

When flexural cracking occurs at a distance along the member which is less than required to develop the tensile strength of strand through bond, it is expected that strand slippage will result. This slippage will produce a mode of plastic mechanism which is characterised by

increasing slip displacement at peak bond stress (Fig. 1.55), and will therefore depict the upper limit of strand contribution to the development of flange tension.

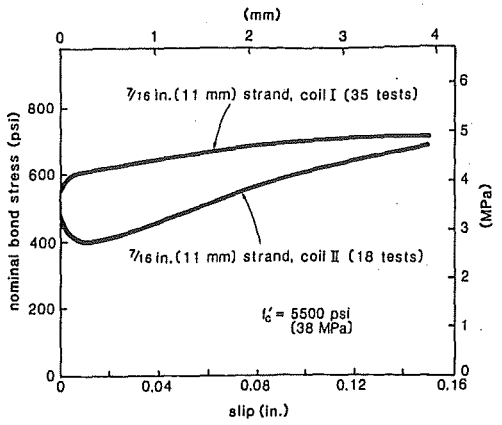

Fig. 1.55 Force-slip relationship of prestressing strand [Collins and Mitchell, 1987]

As the location of plastic hinges move away from columns, as is commonly achieved by bar curtailment and beam haunches (Fig. 1.56), the strength development of strands in the adjacent floor slab will tend towards the tensile capacity of prestressing steel. Furthermore, increased length into the floor section will facilitate shear flow bond between the pretensioned unit and the frame element. Thus, the full tensile strength of prestressing steel may contribute to the strength development in plastic hinges located away from column faces.

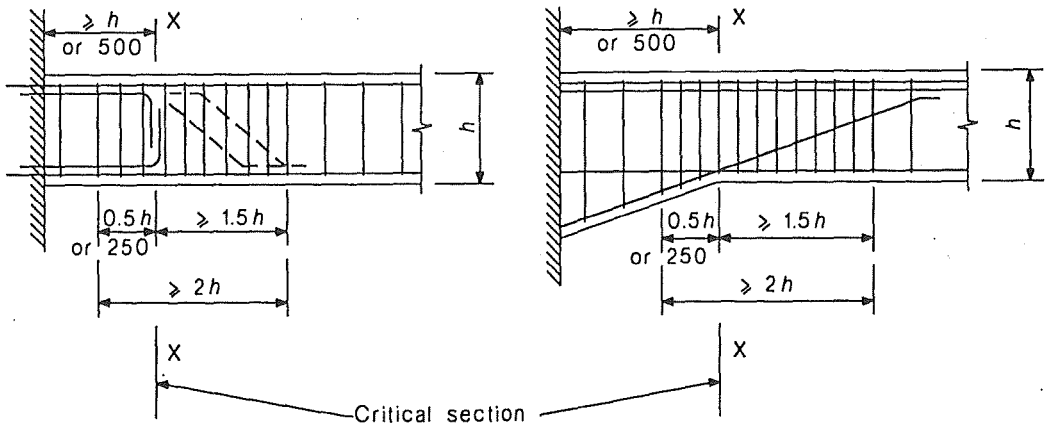

Fig. 1.56 Plastic hinges located away from the columns [Standards New Zealand, 1995]

For hollow core flooring, the contribution of individual strand numbers to tensile flange strength may be estimated from a simple model that is based on the diameter and grade of strand most commonly used and the results from equations and tests as referenced. Assuming that the tensile capacity of 12.7 mm supergrade (1860 MPa) strands is resisted by a uniform horizontal shear stress τ_r (see Equation 1.21) acting along the construction joint between the hollow core flooring unit and edge beam, then equilibrium of forces is achieved by:

$$V_{\tau r\,(x)} = F_{ps\,(x)} \qquad (1.22)$$

Accordingly, the number n of strands considered effective in developing the design ultimate tensile strength of prestressing steel (186 kN) at distances 600 mm, 1.2 m and 1.8 m from the unit end may be calculated:

over transfer length at 600 mm: $$n_{0.6} = \frac{\tau_r h}{200} \quad (1.23)$$

average bond failure at $0.85f_{pu}$: $$n_{1.2} = \frac{\tau_r h}{130} \quad (1.24)$$

where strand bond will not fail: $$n_{1.8} = \frac{\tau_r h}{100} \quad (1.25)$$

Thus, for example, if τ_r is taken as 1.5 MPa ($0.33\sqrt{f'_c}$ for 20 MPa topping concrete) and nominal side seating is provided giving a construction joint depth h of 265 mm (200 unit + 65 topping). The number of strands contributing to flange tension are estimated (Equations 1.23, 1.24 and 1.25) as two at 600 mm, three at 1.2 m and four at 1.8 m from the unit end.

The contribution of prestressing steel to the strength developed at plastic hinges will obviously be significant since a 12.7 mm supergrade strand has about the equivalent tensile strength of a 24mm Grade 430 bar at yield. For comparison, the negative bending moment capacity has been calculated for a typical configuration of perimeter beam plus bonded floor section (Fig 1.57) at first yield and at displacement ductility factors of $\mu = 3$ and $\mu = 6$ (see Table 1.8 and Fig. 1.58). The analysis has allowed for n = 0,1,2,3 and 4 strands to participate in flexure.

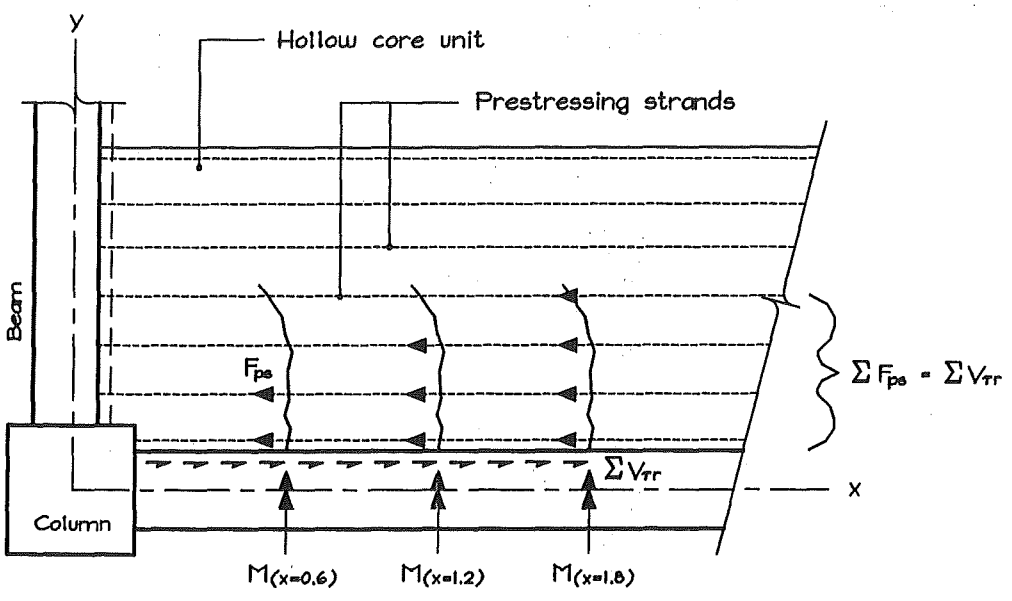

Fig. 1.57 Plan of beam junction in a ductile moment resisting frame incorporating a pretensioned hollow core floor unit, indicating progressive development of strand tension forces with distance from unit end

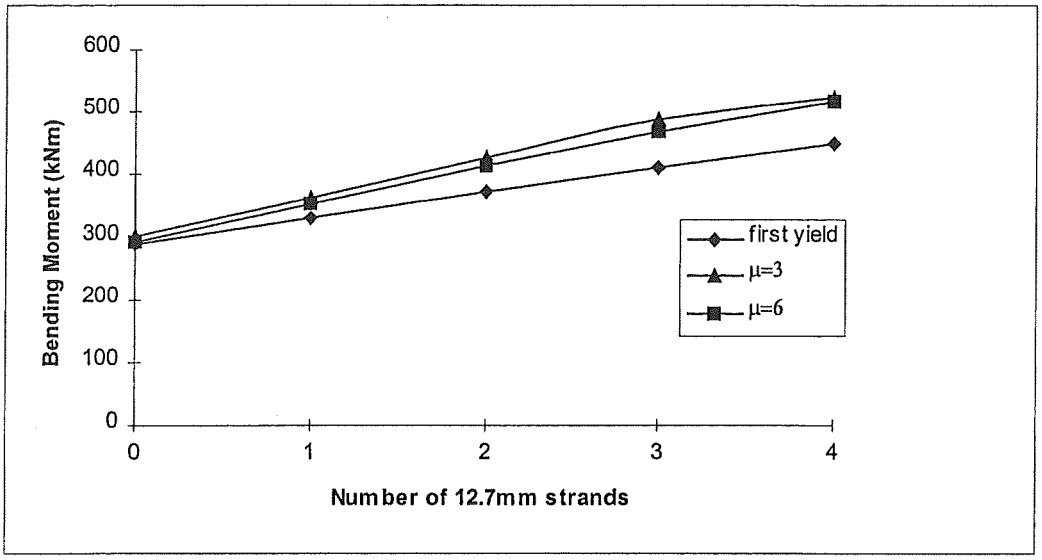

Fig. 1.58 Negative bending moment development corresponding to the number of prestressing strands participating in flange tension at given structural displacement ductility factors (see Table 1.8 and Fig. 1.57).

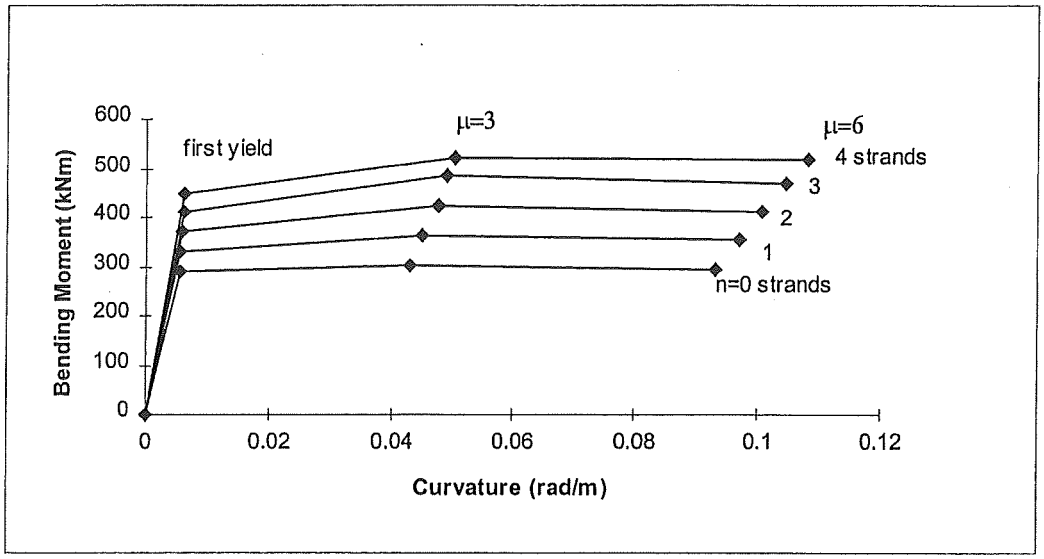

Fig. 1.59 Moment-curvature relationships corresponding to the number of prestressing strands participating in flange tension at given structural displacement ductility factors (see Figures 1.57 and 1.58).

For the chosen section geometry and configuration of reinforcing bars and strand, the increase in bending moment capacity is 40 kNm per strand at first yield and around 57 kNm per strand at $\mu = 3$ and $\mu = 6$.

In the derivation of bending moment capacity the concrete spalling strain ε_{sp} was limited to 0.004. Hence, the bending moment capacity decreases slightly due to the physical loss of section under curvature ductility factor demands corresponding with $\mu = 6$ (Fig. 1.59). The maximum concrete strain obtained from this analysis was 0.0146 ($3.65\varepsilon_{sp}$) for n = 4 strands at $\mu = 6$. The maximum concrete strain obtained at $\mu = 6$ for this section with n = 0 strands (i.e.,

no tensile contribution from strands) was 0.00595 ($1.49\varepsilon_{sp}$). This difference in maximum concrete strain is quite pronounced, making it essential that effective confining reinforcement is provided in the plastic hinge zones of these structures. It should be noted that there has been no allowance in the analysis for the overstrength effects of reinforcement. The overstrength contributions of reinforced cast-in-place slabs have been summarised with similar conclusions by Cheung [Cheung, 1991].

(d) Frame Dilation

One of the recognised by-products of cyclic plastic hinge deformations of beams is the phenomenon of plastic hinge dilation, which involves the incremental elongation of beams (growth) due to the non-closure of cracks. Although documented in many research reports over the years, the actual effects of elongation on the performance of frame structures has only been postulated in fairly recent times. Many of the assumptions regarding the probable effects of plastic hinge dilation on frame structures (i.e., frame dilation) would appear to be upheld by the findings of several bodies of research work [Fenwick, 1990; Fenwick, Ingham and Wuu, 1996].

The magnitude of beam plastic hinge dilation may be estimated as a function of beam depth and the degree of hinge rotation, and is given as [NZCS-NZNSEE, 1991]:

$$\text{extension} = \frac{\theta(d - d')}{2} \tag{1.26}$$

The combined elongations of more than one plastic hinge within a frame may depend on several factors, especially the level of axial restraint. For reversing plastic hinges (see Fig. 1.60), the rotation θ applied at the hinge zone can be related to the interstorey deflection of the building by the expression:

$$\theta = \frac{\Delta}{h\,k} \tag{1.27}$$

where k is the ratio of the distances between the hinge zones in a beam to a column centreline and h is the storey height.

Because cracks in the compression zone of reversing plastic hinges essentially remain open unless appreciable axial restraint is applied, the total storey level extension based on two plastic hinges forming in each beam is:

$$\text{extension} = \frac{2\,n\,\Delta}{h\,k}(d - d') \tag{1.28}$$

where n is the number of bays in the frame.

For the case of unidirectional plastic hinges forming in beams (see Fig. 1.61), the total of extension is given by:

$$\text{extension} = \frac{n\sum\theta}{2k}(d - d') \qquad (1.29)$$

where $\sum\theta$ is the sum of plastic hinge rotations occurring in each bay of the structure. Although $\sum\theta$ cannot be directly related to inter-storey drift in the straightforward manner of reversing plastic hinges, it has been tentatively suggested that $\sum\theta$ should be taken to equal $5\Delta/h$.

Although it is considered that uni-directional plastic hinges will cause the greatest beam elongations, it is reversing plastic hinges that are likely to be synonymous with the type of frame elongation that can cause loss of support to pretensioned flooring units. This is because uni-directional hinges form in beams that are subjected to considerable positive bending moments under gravity loads, and include effects from end moment actions generated by frame sway during an earthquake. Where such a beam lies adjacent and parallel to the span of pretensioned flooring units, the pretensioned units will already have been designed to carry their entire self weight plus all superimposed loads assigned to them, and at a limited midspan deflection. Hence, there will generally be little gravity load distributed into beams that span parallel to pretensioned flooring units, and the development of uni-directional plastic hinges seems very unlikely.

Conversely, the beams that support the ends of pretensioned flooring units will be subjected to a considerable line load and unidirectional plastic hinges are much more a possibility. The consequence of plastic hinge dilation occurring along the axis of these beams is that openings may appear in the construction joints between flooring units, but there should not be a direct loss of support to flooring units through dilation effects. Again, because pretensioned flooring is designed on a modular basis, the degradation of construction joints between units will not normally jeopardise gravity load carrying capacity. However, designers should bear this in mind where hefty point loads have been distributed over more than one modular flooring unit. These units should be effectively tied together by ductile transverse reinforcement in the topping slab that extends at least a development length beyond the outermost contributing floor units.

Tests have shown that the total longitudinal elongation of a plastic hinge is in the order of 2% to 8% of beam depth, and depends on the degree of axial restraint provided. For the general case of beams in a frame configuration, extensions in the order of 2% to 4% are probably realistic considering the variability of axial loads along beam lines as larger ductility ratios are approached during a severe earthquake. Where this causes concern is with the seating of precast flooring when long spanning pretensioned units cover more than one span of ductile beams. The accumulated elongation of each beam span needs to be considered. Although it is evident that an amount of the accumulated elongation will be absorbed at crack openings occurring in the flooring unit adjacent to plastic hinges, it is likely that these actions will also weaken the shear capacity over the construction joint between the flooring unit and beam. Thus, it is feasible that much of the flooring unit length will be mobilised and net elongation will occur at one end of the unit. This, when combined with seating loss through the spalling of support beam cover concrete, gives sufficient reason for the review of construction practice.

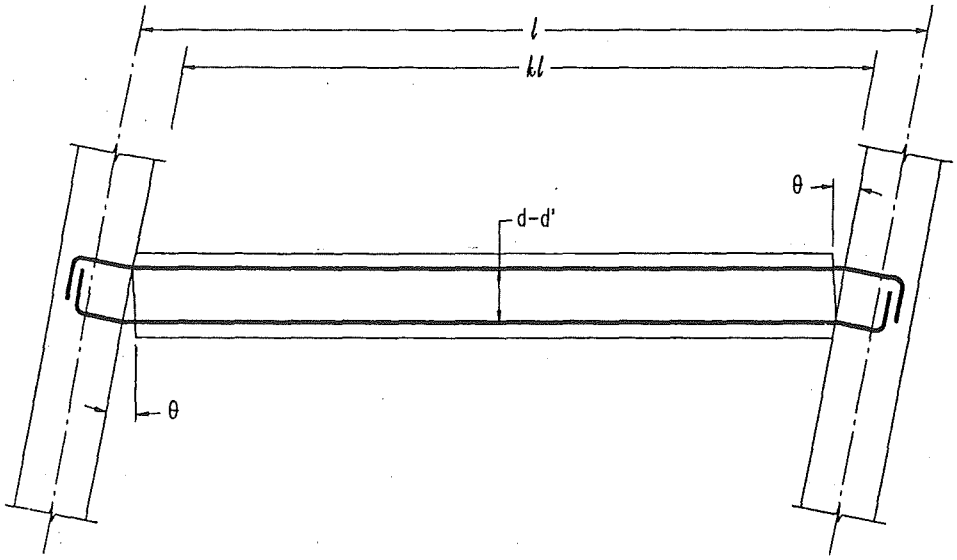

Fig. 1.60 Reversing plastic hinges in a frame bay [NZCS-NZNSEE, 1991]

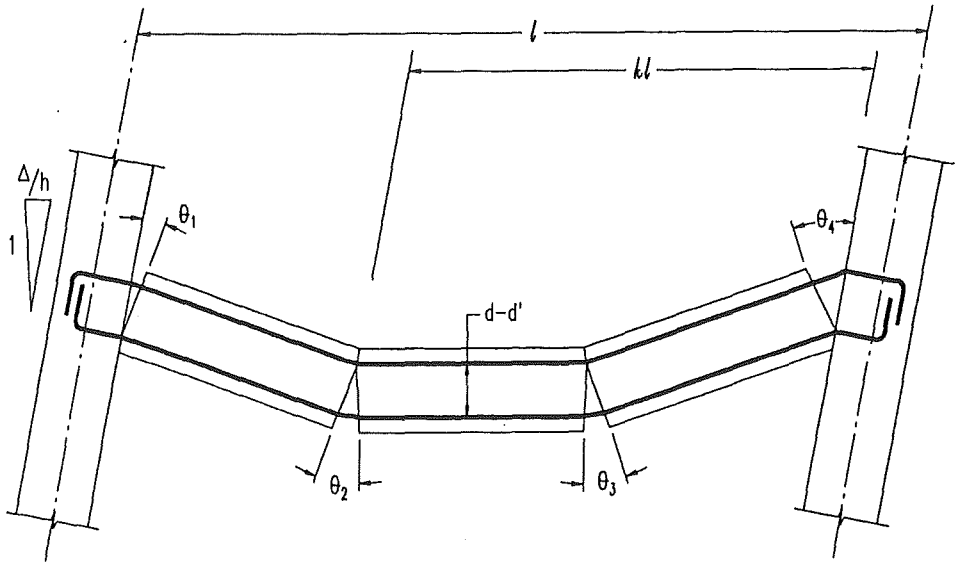

Fig. 1.61 Uni-directional plastic hinges in a frame bay [NZCS-NZNSEE, 1991]

1.4.2.3 Structural Wall Systems

The main consideration with ductile structural wall systems is that a severe earthquake will cause dilation effects in plastic hinge zones at the bases of large vertical wall elements. Although there has not been much specific research done on structural interactions resulting from wall elongation, there are accounts of wall dilation causing coupling effects in a full scale building test [Wight, 1985]. In the referenced test, coupling resulting from wall elongation was observed to cause an overall increase in structural stiffness and exerted an appreciable influence of the response behaviour of the building. By default, the flooring system is incorporated in these actions which may involve a number cyclic rotations about the horizontal plane of the floor plate (Fig. 1.62).

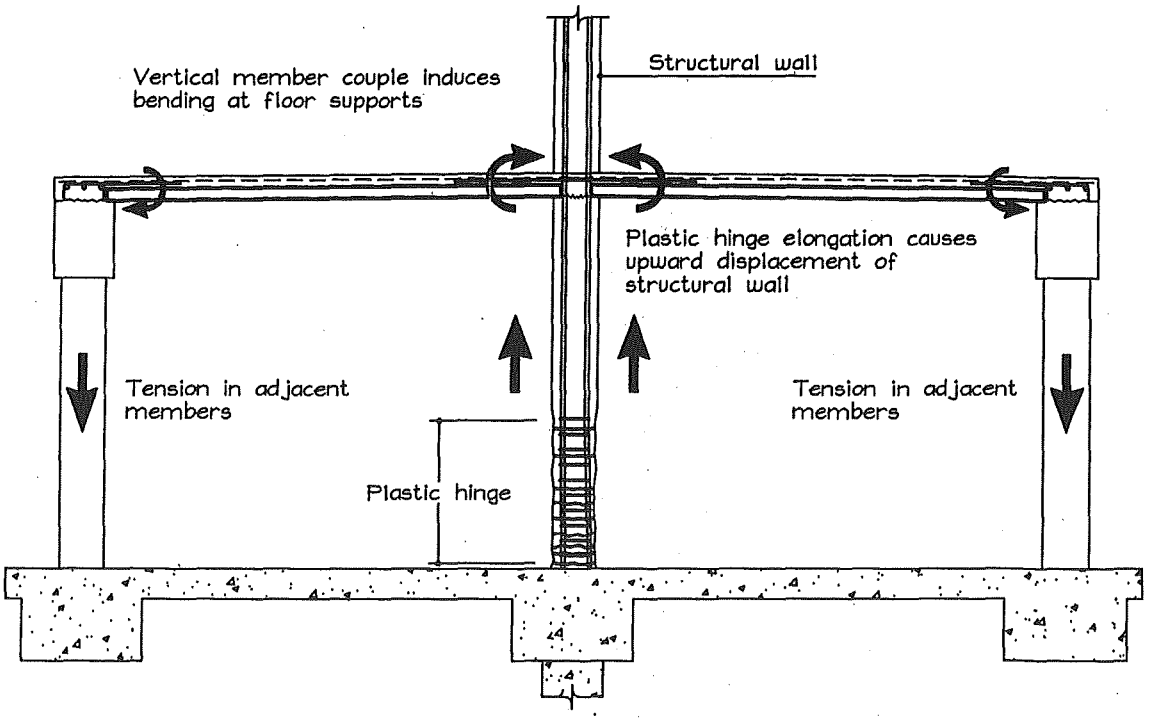

Fig. 1.62 Coupling of the floor elements due to elongation of shear walls

The immediate implication of coupling rotations about the floor slab is that bending moment and shear demands are placed on the support details of flooring units (Fig. 1.62). A cantilever test that was conducted on a typical hollow core specimen with composite topping (see section 7.3.1) showed that the yield strength of deformed starter reinforcement was developed at a slab rotation of about 0.004 radians. If it is feasible that the elongation of a wall which resists both seismic forces and gravity loads will be around 1% of the wall length, then for a 6 m long wall the expected elongation is 60 mm. Typical floor spans are less than 16 m between supports (see Figs. 1.10), which strongly suggests that wall elongations of the aforementioned magnitude may cause starter bars strains which are well in excess of yield strain.

Hence, it is clear (Fig. 1.62) that for pretensioned floor spans which couple between ductile wall elements, there is a basic requirement that the wall support details are able to sustain cyclic

inelastic deformations. Furthermore, for the opposing supports, some consideration should be given to the potential spalling off of concrete in the seating regions.

1.4.2.4 Dual Systems

In the case of dual systems, there is an obvious hybridisation between moment resisting frame and structural wall systems. For ductile seismic resisting structures, both of these systems will integrally resist seismic shears, with deformation compatibility being maintained by coupling forces which act through the planes of the floor diaphragms [Goodsir, 1985](see Fig. 1.43).

With regards to dilation effects in primary seismic resisting members, consideration needs to be given to the characteristic elongation effects of both ductile frames and walls, as discussed in the previous sections. The added consideration is that the various tensile and compressive transfer (coupling) forces acting through the floor slab are essential to achieve dual system response. Consequently, the floor slabs in these structures need to be considered as an integral part of the primary seismic resisting system, and not as elements destined for little more than passive interactions. Hence, depending to a large degree on building configuration, sizeable axial forces will need to be developed concurrently with dilation effects which may arise either from frame members or structural walls, or both.

1.4.3 METHODS OF CONTROL FOR FLOORING-SUPPORT INTERACTIONS

1.4.3.1 General

The most important single attribute of support details which may be subjected to dilation type loadings is the ability to withstand axial deformation without appreciable loss of strength or viability of load carrying capacity. In brief, this is a prerequisite which may be classically termed a ductile support tie detail. Also, in developing such details, due consideration must be given to the mechanics by which ductility can be achieved. From a capacity design point of view, ductile tie details bear a fairly direct resemblance with the "weak link in the chain" analogy which is often used to explicate capacity design philosophy (Fig. 1.63). In using this type of approach, the various ductile and brittle components will need to be identified. The first caution is that a simple extrapolation from the common engineering perception which considers all steel reinforcement as ductile, is not sufficient for implementing fully effective tie details in modular flooring units.

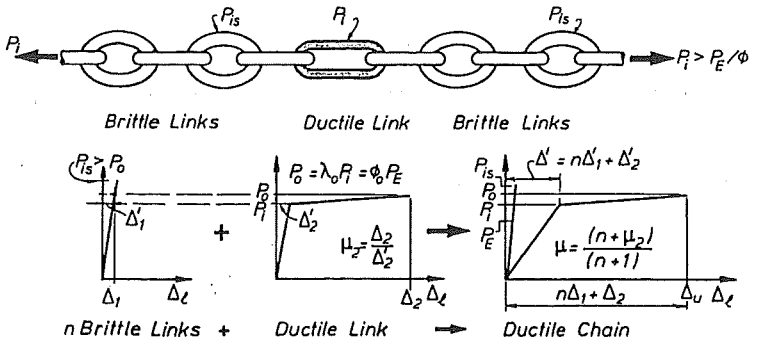

Fig. 1.63 Chain analogy for illustrating capacity design [Paulay and Priestley, 1992]

Because tie details for hollow core units will involve embedment into a flexurally efficient section that contains no transverse reinforcement, simple but important rules for reinforcement type, reinforcement detailing and embedment length need to be carefully observed:

1.4.3.2 The Brittle Concrete Element

(a) Splitting Stresses

Due to the thin unreinforced webs of hollow core flooring units, the potential for splitting due to reinforcing bond stresses needs to be addressed. Experiments [Engström, 1992] have shown that the tensile extension of high strength deformed bars embedded in the cast-in-place concrete in the cores of hollow core units can cause web splitting. Since this is a highly unfavourable effect, the potential for web splitting must be eliminated from details that are required to perform in a ductile manner.

(b) Direct Tensile Fracture

The only necessary concrete fracture to form a ductile tie mechanism is that which occurs between the floor element and the support. The fracture line will be naturally instigated by the transition that occurs in materials and stiffness of the floor section where the precast unit meets the support. It is obvious that the propagation of further tensile fracture in the precast units should be avoided.

1.4.3.3 The Ductile Reinforcing Element

(a) Extendibility

Because of the potentially large ductility demand required in an extreme event, reinforcing steel must be of a ductile type with known qualities. Furthermore, tie reinforcement should be detailed so that large extensions can be obtained by yielding over a length where bond has broken down, and to undergo cyclic loadings without causing additional damage to the surrounding concrete. To achieve these requirements, straight, plain (i.e., non-deformed) reinforcing bar details are a necessity.

(b) Anchorage

Tension forces developed by tie reinforcement in hollow core units will need to be fully anchored in concrete zones where a sufficient compressive reaction exists. Plain bars will require a full hook at the end to achieve anchorage, with due care given to providing sufficient cover concrete to the end hook to avoid bursting and pullout at the hook.

1.5 OBSERVATIONS OF FAILURE

1.5.1 GENERAL

Although diaphragms are generally regarded as presenting less risk of serious failure than other components within seismic resisting structures, there have been occasions where considerable damage has been observed, sometimes resulting in complete or partial collapse.

There are records of multiple structural collapse involving untopped hollow core flooring, such as the Armenian earthquake of 1988. The Armenian disaster (as with earthquakes in similar regions) may have been somewhat predisposed, considering the low (often less than 0.05g) design base shear and general lack of ductile design attributed to the primary seismic resisting members. However, a number of important (if a touch primordial) observations were made regarding connections between floor diaphragm elements and support structures in Armenia. The following paragraphs are reproduced from a section titled "Many very old lessons relearned" taken from a paper which discusses the Armenian earthquake [Wyllie and Filson, 1989].

"Exterior walls must be tied to diaphragms. The complete lack of ties in the masonry buildings...has been seen in many earthquakes. Apparently they (i.e., the designers) relied on friction between precast plank (i.e., hollow core unit) and masonry at the bearings or they ignored the calculation for wall anchorage". Furthermore "A structure must be tied together. The lack of building ties with the untopped precast hollow core floor planks without connections clearly illustrated this old lesson."

Another observation of failure occurred in the Northridge earthquake of 1994, in which a section of the hollow core floor of a single storey car park building collapsed (Fig 1.64).

Fig 1.64 Failure of a single storey car park floor at Northridge

In the case of the Northridge structure, a hollow core floor with structural topping fell from steel beams which were supported on pin ended steel columns. Although exact details of this failure do not appear to have been reported, reconnaissance team photographs indicate that a chord tie failure may have played a part in the eventual collapse. The continuous reinforcing across the supports was comprised of wire mesh which appeared to fracture in tension and offer little resistance to the eventual collapse.

With respect to seismic design, the Northridge structure may have been of substandard construction when compared with other structures in California. The overall building layout consisted of an open fronted perimeter masonry wall with pin-ended steel columns supporting spans of steel beams onto which the hollow core was seated (Fig 1.65). The pin-ended columns would have offered little seismic resistance, and photographs indicate that the structure swayed outwards toward the open fronted side. There was no apparent damage to the masonry perimeter wall.

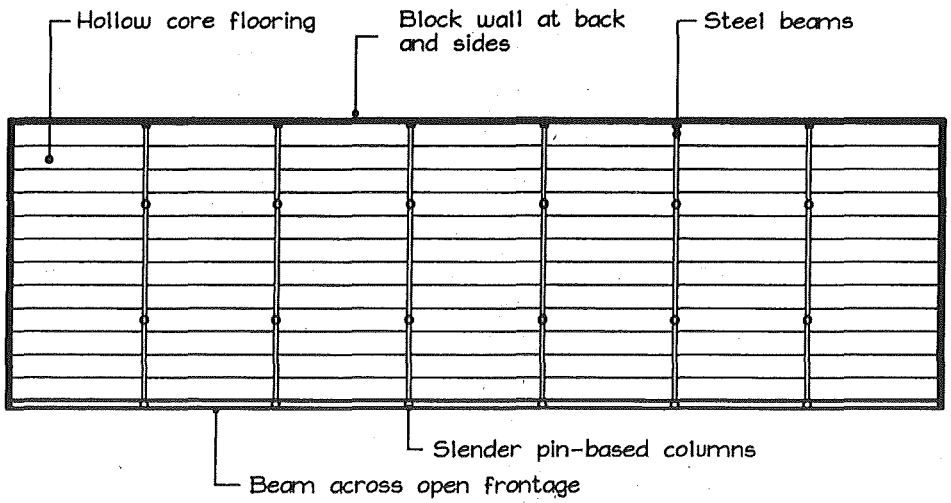

Fig. 1.65 Illustrative layout plan of the Northridge car park building

It is feasible that the chord tie then failed in tension, thus allowing the support beams to move apart and the collapse of the hollow core units to progress into the floor. Under such a loading regime it is possible that a deep block rotation would have occurred in the floor section, similar to the block rotations associated with flexural zones of deep beam sections. As already mentioned, the topping mesh appears to have provided little resistance against the actions which resulted in failure.

1.5.2 WELL ENGINEERED STRUCTURES

The relevance of observed failures in poorly designed and constructed buildings to well engineered buildings will depend on the comparative levels of demand placed on critical elements within the respective buildings. For example, in the Armenian and Northridge structures it is evident that certain details may have been present, but they were inadequate details for the localised levels of demand. In well engineered ductile structures, it is expected

that very high levels of demand will be placed on localised zones of key structural elements during a severe earthquake; this is the very basis of capacity design.

As such, demand may be roughly divided into two areas, strength demand and ductility demand. An idealistically safe seismic resisting structure would have a full compliment of both strength and ductility, however, alleviations in one of these qualities is usually permitted in design codes on the proviso that the other quality remains infallible.

It is perceived as being uneconomic to design structures which contain a full array of design features based on optimal strength and ductility, and this is justified in most cases. The general understanding is that the geometry of a structure will largely determine whether strength or ductility should be the governing criterion. However, the fact remains that individual designers often exercise differing views on acceptable building performance, meaning that a concession of strength in favour of ductility and vice verse is sometimes a fundamental topic of debate. The upshot is that many designers have preferences for particular building systems, such as the structural wall, dual systems and structural frames as discussed in the previous section.

Structures of dubious design and construction fail because the strength and/or ductility demand is exceeded. The obvious question with regards to floor construction joints is whether starter bar details provide adequate demand capacity in terms of strength and ductility to meet a very high local demand in the ductile moment resisting support structure.

1.6 AIMS OF THIS RESEARCH

The broad aim of this research is to provide additional knowledge relating to support tie details for hollow core flooring, and in such a manner that this knowledge may be interpreted by practising engineers for the betterment of seismic resisting construction. Consequently, the experiments conducted are of a rudimentary nature in that they are designed to establish basic facts which will reflect relatively straightforward but admissible assumptions.

Some analysis and theory is offered, and as always, it is to the disposition, experience, and discretion of those who interpret such workings as to their applicability and merit. It is the author's own belief that attempts should be made to present some form of theoretical development or analytical models. The reason is that, although the results of differing theoretical developments or analyses may vary, provided that they are based on reasonable assumptions and concur with the findings of others, they help to define the levels of confidence with which practising civil engineers may administer an otherwise approximate science.

The fundamental aims of this research are as follows:

- To examine the effects of dilation type loadings on support tie details employed in hollow core flooring construction joints.
- To examine the effect of dilation type loadings on the structural integrity of hollow core sections.
- To isolate the aspects of tie detail design which either mitigate or enhance their effectiveness as a support tie detail, under both monotonic and cyclic loading.
- To recommend tie details based on the findings which will withstand dilation type loadings and fully maintain the integrity of hollow core flooring systems.
- To examine related aspects such as moment continuity developed by ties, buckling of tie reinforcement under cyclic loading and bar bond development in topping slabs.

2

Diaphragm Analysis

2.1 GENERAL

In order to define the nature of interactive forces within flooring members that make up structural diaphragms, it is important to be able to predicate certain critical design actions. It is also important to be able to isolate the various components that may be become crucial to the performance of flooring units in this role. In the introductory chapter, a number of fairly generalised concepts have been put forward, such as frame elongation, flooring participation in design seismic design actions and the likelihood of associated carry-over effects on flooring units. It is the purpose of this chapter to present analytical evidence of key structural actions that may be derived from the response of a tall building to earthquake ground motion. The chain of cause and effect is followed from base motion to the interaction between support and flooring members to diaphragm forces and the performance of individual materials within the diaphragm element.

2.2 RESPONSE BEHAVIOUR OF TALL BUILDINGS

2.2.1 BUILDING DEFORMATION AND PLASTIC HINGES

2.2.1.1 General

The development of plastic hinges in beams and walls is almost certain to have a direct influence on adjacent pretensioned flooring units, and probably vice versa depending on the structural configuration at floor level. The patterns of plastic hinge formation in a building will be largely influenced by structural geometry and the relative stiffness of primary seismic resisting members (see Section 1.4.2.). In order to design for such actions, methods acceptable to the engineering profession are employed, which generally involve recognised computer software packages (e.g., Response Spectrum Analysis and the ETABS family of programs). An alternative approach to the estimation of structural response has been derived, and is based on an equation of equilibrium. As a tool for precursory analysis, this approach has the advantage of directly defining structural displacement as a function of ground motion, distribution of storey mass and/or inter-storey stiffness, and the scheme is not necessarily limited to elastic assumptions. Once displaced shapes are ascertained, various important aspects of diaphragm behaviour can be determined by further considering structural interactions within the flooring support region.

2.2.1.2 Frame Displacement Model

The basis of Modal Response Spectrum Analysis is the dynamic response of a multistorey shear building, for which the equilibrium of an applied force, inertial mass, acceleration and vertical stiffness effects are considered at each floor level (Fig. 2.1). By equating equilibrium at respective levels, and noting that typical seismic response only involves free vibration (i.e., no applied force terms), the well-known system of linear equations for an undamped structure may be formulated:

$$[M]\{y''\} + [K]\{y\} = \{0\} \qquad (2.1)$$

where [M] and [K] are the respective mass and stiffness matrices, {y"} and {y} are the respective horizontal acceleration and displacement vectors at storey height.

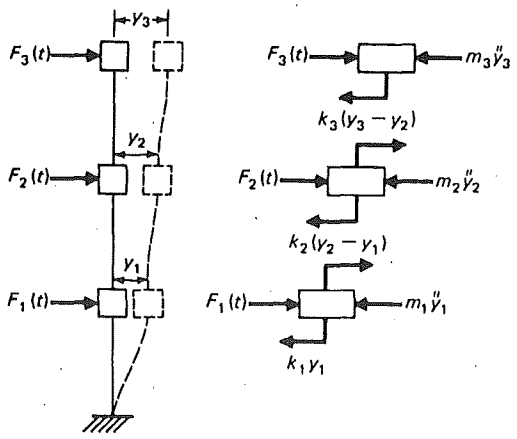

Fig. 2.1 Single column model representation of a shear building [Paz, 1985]

This model can be elaborated to give the discrete system for the equilibrium of forces in a single bay of an arbitrary floor level (j) of a multi-storey building (Fig. 2.2).

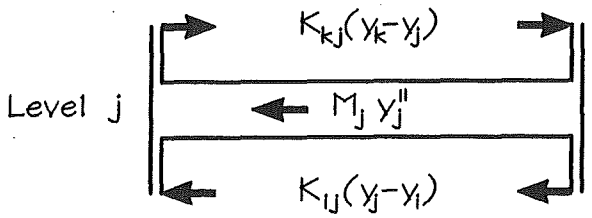

K = Interstorey stiffness
M = Storey mass
y = Relative storey displacement
y" = Acceleration

Fig 2.2 Equilibrium of forces at storey j in single bay of multi-storey building

For this model, the global horizontal storey displacements are denoted by δ_i , δ_j and δ_k for the respective levels i, j and k, and δ''_j is the horizontal acceleration at level j. For most well conditioned seismic resisting multi-storey buildings, it is reasonable to assume that the initial stiffness K of primary resistance members will be reasonably constant over the building height. Hence, by ignoring equivalent viscous damping (the effects of which can be approximated later) the requirements for equilibrium are that:

$$\mathbf{M}_j\delta''_j + \mathbf{K}\left(\delta_j-\delta_i\right) = \mathbf{K}\left(\delta_k-\delta_j\right) \tag{2.2}$$

Noting that the terms in brackets represent interstorey displacements, this may be written as:

$$\mathbf{M}_j\delta''_j + \mathbf{K}\left(\Delta_{ji}\right) = \mathbf{K}\left(\Delta_{kj}\right) \tag{2.3}$$

which gives:

$$\mathbf{M}_j\delta''_j = \mathbf{K}\left(\Delta_{kj}-\Delta_{ji}\right) \tag{2.4}$$

This is an equilibrium model for discrete values, however, if the above was to be defined by a continuous function over the building height then the mass and displacements terms would need to be written in terms of the building height. By considering a distributed building mass $m_{(h)}$ as a function of height and in units of mass per unit length, Equation 2.4 may be written in differential form as:

$$\mathbf{m}_{(h)}\mathbf{dh}\frac{\partial^2\delta}{\partial t^2} = \mathbf{K}\frac{\partial\delta}{\partial\mathbf{h}}\mathbf{dh} \tag{2.5}$$

This derivation may also be verified by assuming a differential element of height (Fig. 2.3). Hence, the partial differential equation for the approximation of building displacements as a function of time and height ($\delta = \delta_{(t,h)}$) is:

$$\frac{\partial\delta}{\partial\mathbf{h}} = \frac{\mathbf{m}_{(h)}}{\mathbf{K}}\frac{\partial^2\delta}{\partial t^2} \tag{2.6}$$

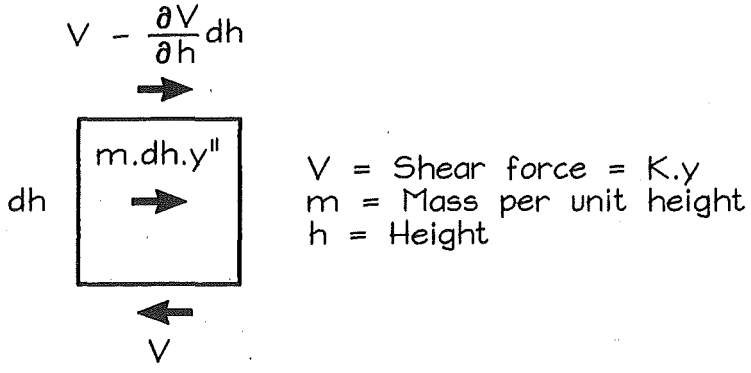

Fig 2.3 Equilibrium of forces for a differential element of height

Incidentally, Equation 2.6 is of very similar form to the one-dimensional diffusion equation, for which many solutions exist. However, special consideration needs to be given to applying relevant initial conditions and boundary conditions.

The initial condition will essentially describe the initial or base ground motion (a displacement function) which will subsequently influence the general response of the structure. For brevity, it may be shown that a sinusoidal base motion of maximum amplitude δ_b will afford a simple solution and may also be regarded as consistent with general assumptions on seismic ground motion, therefore:

$$\delta_{(t,0)} = \delta_b \sin\left(\frac{2\pi t}{T}\right) = \delta_b \sin \omega t \qquad (2.7)$$

Of the boundary conditions, the two important constraints are determined by the generic nature of seismic resisting building structures. Assuming (i) that the building is regular and vertical with no externally applied horizontal forces, and (ii) that the vertical resistance members will form plastic hinges at a rigid base:

$$\begin{aligned} \delta_{(0,h)} &= 0 \\ \frac{\partial \delta}{\partial h}_{(t,0)} &= 0 \end{aligned} \qquad (2.8)$$

The building mass per unit height $m_{(h)}$ may be determined from the slope of the accumulated mass diagram for levels $0 \rightarrow n$ (Fig. 2.4). Since a constant initial stiffness has been assumed over the building height, the envelope of cumulative mass over height becomes an important parameter in the analysis. For well-conditioned seismic resisting structures, it is feasible that variations in inertial mass over the height of a building may be a more important design parameter than variations in initial stiffness (especially where significant superimposed floor loads are involved). Some forethought should always be given to possible variations in the distribution of occupancy loads in seismic resisting multi-storey buildings, but as a design principle, stiffness variations are avoided where possible. Nonetheless, it is evident that initial stiffness variations could have been treated similarly, with mass held constant over unit height.

An envelope for the cumulative mass $\sum M_{(h)}$ from 0 at foundation level to the j^{th} storey level may be expressed as:

$$\sum_{h=0}^{j} M_{(h)} = \sum_{h=0}^{H} M \left(\frac{h_j}{H}\right)^{\eta} \qquad (2.9)$$

where η is a shape factor that is determined by fitting a power curve to the ordinates of the cumulative mass diagram (see Fig. 2.4).

It can be seen that $\eta = 1$ is the shape factor for a building with a uniform distribution of mass over total vertical height H, with $\eta > 1$ for top-heavy distributions and $\eta < 1$ for bottom-heavy distributions of mass.

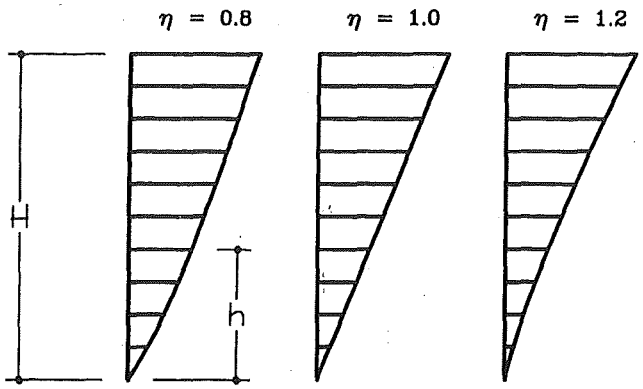

Fig. 2.4 Cumulative mass over building height for determination of shape factor η

Hence, the mass per unit height may be calculated as the derivative of the cumulative mass model:

$$m_{(h)} = \frac{d}{dh}\sum_{h=0}^{j} M_{(h)} = \sum_{h=0}^{H} M\frac{\eta h^{\eta-1}}{H^{\eta}} \tag{2.10}$$

and the relationship of $m_{(h)}/K$ in Equation 2.6 becomes:

$$\frac{m_{(h)}}{K} = \sum_{h=0}^{H} M\frac{\eta h^{\eta-1}}{KH^{\eta}} = \alpha^2 h^{\eta-1} \tag{2.11}$$

Solution of the PDE (Equation 2.6) is approached using the separation of variables method [Greenberg, 1988], which will yield two ordinary differential equations, one in time (T) and the other in height (H):

$$\begin{aligned} T'' + \kappa^2 T &= 0 \\ H' + \kappa^2\alpha^2 h^{\eta-1} H &= 0 \end{aligned} \tag{2.12}$$

where κ^2 is the separation constant, which is not yet determined.

Respective general solutions to the ODEs in Equation 2.12 are:

$$\begin{aligned} T &= A\cos\kappa t + B\sin\kappa t \\ H &= Ce^{-\kappa^2\left(\alpha^2 h^{\eta-1}\right)\frac{h}{\eta}} = Ce^{-\kappa^2\alpha^2\frac{h^{\eta}}{\eta}} \end{aligned} \tag{2.13}$$

where A, B and C are arbitrary constants. By considering the cases for $\kappa = 0$ and $\kappa \neq 0$, and because the governing PDE is linear, the solutions may be summed to give:

$$\delta_{(t,h)} = G + Ht + \left(I \cos \kappa t + J \sin \kappa t\right) e^{-\kappa^2 \alpha^2 \frac{h^\eta}{\eta}} \tag{2.14}$$

where again, G,H,I and J are arbitrary constants.

Applying the boundary conditions given by Equation 2.8 results in the form of the equation for displacement as a function of time and height. To satisfy the boundary conditions without restricting the solution to the null result of $J = 0$, κ is made equal to $n \cdot \pi / T$ which gives:

$$\delta_{(t,h)} = Ht + J \sin \frac{n\pi t}{T} e^{-\left(\frac{n\pi}{T}\right)^2 \alpha^2 \frac{h^\eta}{\eta}} \tag{2.15}$$

In dealing with the arbitrary constant J, it can be shown [Greenberg, 1988] that:

$$\delta_{(t,h)} = Ht + \sum_{n=1}^{N} J_n \sin \frac{n\pi t}{T} e^{-\left(\frac{n\pi}{T}\right)^2 \alpha^2 \frac{h^\eta}{\eta}} \tag{2.16}$$

As mentioned, the initial condition (Equation 2.7) is a reasonable approximation to base displacement during an earthquake that also easily satisfies Equation 2.16. However, more complex initial conditions could have been applied by constructing a Fourier series. Hence, Equation 2.16 becomes:

$$\delta_{(t,h)} = Ht + \delta_b \sin\left(\omega t\right) e^{-\omega^2 \alpha^2 \frac{h^\eta}{\eta}} \tag{2.17}$$

In order to establish the velocity component H, Equation 2.17 is differentiated with respect to time and suitable boundary and initial conditions are applied. The boundary condition for velocity at zero height ($h = 0$) is that the structure velocity is equal to the base velocity. Thus, the arbitrary constant H must equal zero at $h = 0$. By considering the velocity component at the initial condition of $t = 0$, the following is applicable:

$$\begin{aligned} \frac{d\delta}{dt_{(0,h)}} &= \omega \delta_b \cos(0) = H + \omega \delta_b \cos(0) e^{-\omega^2 \alpha^2 \frac{h^\eta}{\eta}} \\ \therefore H &= \omega \delta_b \cos \omega t \left(1 - e^{-\omega^2 \alpha^2 \frac{h^\eta}{\eta}}\right) \end{aligned} \tag{2.18}$$

When combined into Equation 2.17, the characteristic solution for horizontal structure displacement as a function of time and building height becomes:

$$\delta_{(t,h)} = \delta_b \left[\left(\sin \omega t - \omega t \cos \omega t\right) e^{-\omega^2 \alpha^2 \frac{h^\eta}{\eta}} + \omega t \cos \omega t \right] \tag{2.19}$$

Thus, Equation 2.19 describes the undamped motion of a structure subjected to a sinusoidal ground motion, starting from an at-rest initial condition at $t = 0$. Undamped deformation

response according to Equation 2.19 is shown (Table 2.1 and Fig.2.5) for a hypothetical ten storey frame with an estimated natural period of T = 1 second and total mass of 3200 tonnes. The frame is subjected to a constant sinusoidal base motion with peak acceleration of 0.3g. The interstorey height is 3m and interstorey stiffness K_o is constant at 500 MN/m. The deformed response is shown for three different cumulative distributions of building mass of η = 0.8, 1.0 and 1.25. A uniformly distributed mass of 320 tonnes per level applies when η = 1.0.

Table 2.1 Undamped displacement response at each level of a hypothetical 10 storey shear building subjected to a sinusoidal base motion with peak acceleration of 0.3g

Horizontal Displacement at Storey Level: $\delta_{(t,h)}$ (mm)									
storey level	**η = 0.8**			**η = 1.0**			**η = 1.2**		
	time elapsed ($t-t_0$)			**time elapsed ($t-t_0$)**			**time elapsed ($t-t_0$)**		
	1 sec.	**5 sec.**	**9 sec.**	**1 sec.**	**5 sec.**	**9 sec.**	**1 sec.**	**5 sec.**	**9 sec.**
Base	0	0	0	0	0	0	0	0	0
1	18	92	166	12	59	106	7	33	60
2	32	159	286	23	116	209	16	78	141
3	43	217	390	34	172	310	26	129	231
4	54	269	485	45	226	408	36	182	328
5	64	318	573	56	280	503	47	237	427
6	73	364	656	66	331	597	59	294	530
7	82	408	734	76	382	686	70	352	633
8	90	449	808	86	431	776	82	410	738
9	98	488	879	96	479	863	94	468	843
10	105	526	947	105	526	947	105	526	947

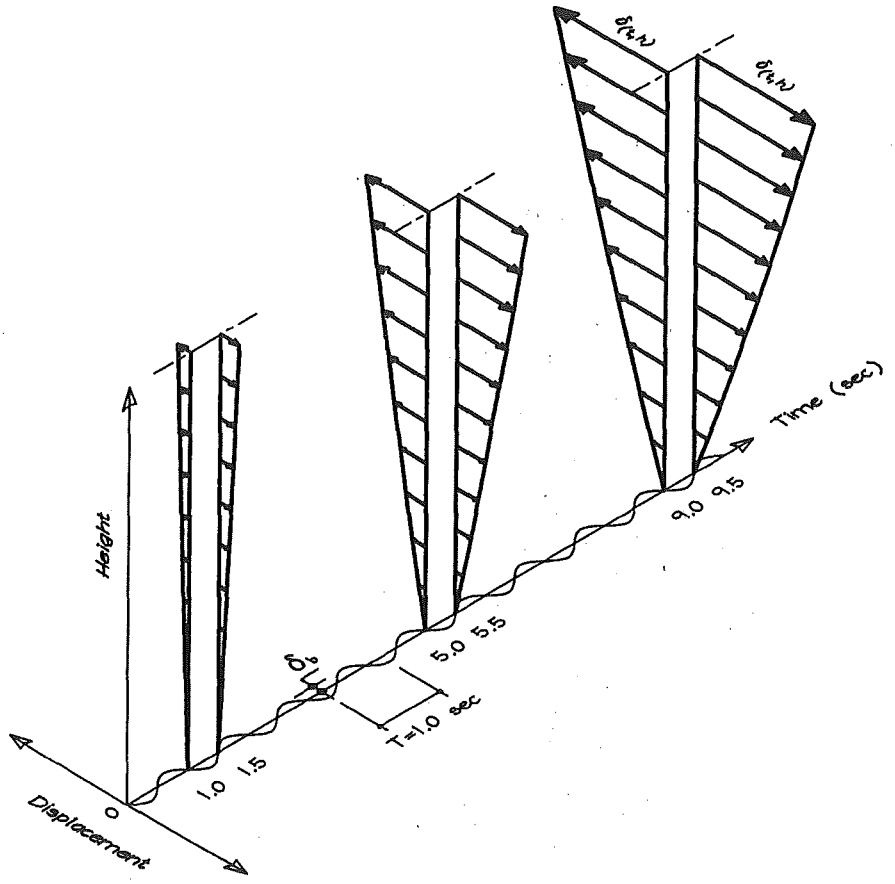

Fig. 2.5 Displacement response, as described by equation 2.19, for a hypothetical 10 storey building (see Table 2.1)

With regard to estimating the effects of damping, an overview is required of the terms in Equation 2.19. If the velocity based terms in Equation 2.19 are removed (i.e., $\omega t \cos\omega t = 0$ for all t), the residual Equation 2.20 satisfies the equilibrium of forces as prescribed by Equation 2.6 and describes the motion of a structure that effectively has nil resonant response, thus:

$$\delta_{o\,(t,h)} = \delta_b \sin \omega t \, e^{-\omega^2 \alpha^2 \frac{h^\eta}{\eta}} \qquad (2.20)$$

This may be regarded as the steady-state response for this model. With the cosine terms included, dynamic amplification occurs and Equation 2.19 will no longer satisfy the dynamic equilibrium requirements of Equation 2.6. However, since the response of the undamped structure will tend towards infinity, an imbalance of forces is anticipated because the system does not approach a state of equilibrium (which is consistent with harmonic response at or near resonance). Furthermore, the model assumes that the structure will participate regardless of the particular acceleration imparted by the selected base motion, and that the degree of participation depends on the absolute acceleration associated with the base motion (note that ω in the foregoing equations applies to the actual frequency of base motion, it does not infer the natural frequency of the superstructure). Consequently, the model requires that a plausible estimate is made of the shortest fundamental period of vibration that might be applicable to the structure, as this becomes the critical base shear parameter.

It is well understood that real structures cannot achieve the levels of resonant response implied by theoretical considerations of elastic dynamic response models. The reasons for this are partly analytical, such as the predictable yielding of materials, and partly empirical, such as the attributed levels of equivalent viscous damping within the structure. In the above model, the yielding of material can be allowed for by reducing the stiffness coefficient. This modification will not affect the validity of the steady state solution (Equation 2.20) and is therefore seen as applicable to Equation 2.19. However, degrading stiffness will also result in reduced resonant response, and this can be applied to the model semi-empirically be considering the reduction in initial stiffness (i.e., the stiffness at elastic levels of displacement) as a function of load cycles. A general observation of tests on elements of building frames displaced inelastically to large percentages of interstorey drift, is that the initial stiffness of a load cycle decreases at a decreasing rate until an almost constant residual value is reached (see Fig. 2.6). Applying reduced stiffness to response analysis has been advocated as a realistic method for modelling the effects of damping [Paulay and Priestley, 1992] and a general observation suggests that a suitable model could take the form of an exponential decay function. The reduction in initial stiffness can be taken as the ratio of the tangents of the angles relating load to displacement after a series of load cycles. Figure 2.6 indicates that the initial stiffness may decrease from peak to a near static value by a factor of about 1/15 after about seven post-elastic load cycles.

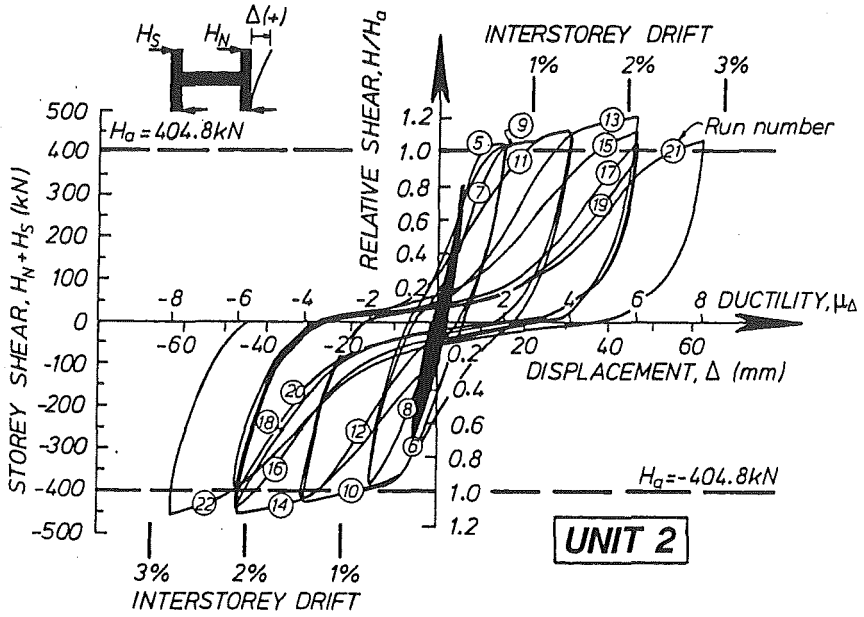

Fig. 2.6 Lateral load displacement response of ductile frame element [Restrepo, 1993]

Hence, if the a stiffness reduction coefficient ζ is adopted and applied to the resonance terms of Equation 2.19, a progressive diminishing will occur in the amplitude of response as time (and the corresponding number of load cycles) increases. For the development of such a coefficient (see Fig. 2.7) values of initial stiffness K_0 , eventual stiffness K_N and the corresponding number of damaging load cycles N to achieve the eventual stiffness are required. The coefficient also represents the level of force activity in the structure, with greater forces resulting in greater

degradation in the plastic hinge zones. As a result, the rate of change of the stiffness reduction coefficient after n cycles is also a function of the coefficient, hence:

$$\zeta - \left(\zeta + \frac{d\zeta}{dn}\cdot dn\right) = \zeta\frac{(K_o - K_N)}{NK_o}\cdot dn \qquad (2.21)$$

Integrating over the interval n and applying the initial condition of $\zeta = 1.0$ at $n = 0$ gives:

$$\zeta_{(n)} = e^{\frac{K_N - K_o}{NK_o}n} \qquad (2.22)$$

A further assumption is made that the fundamental mode of vibration is critical, with $n = t/T$:

$$\zeta_{(t)} = e^{\frac{K_N - K_o}{NK_o}\frac{t}{T}} \qquad (2.23)$$

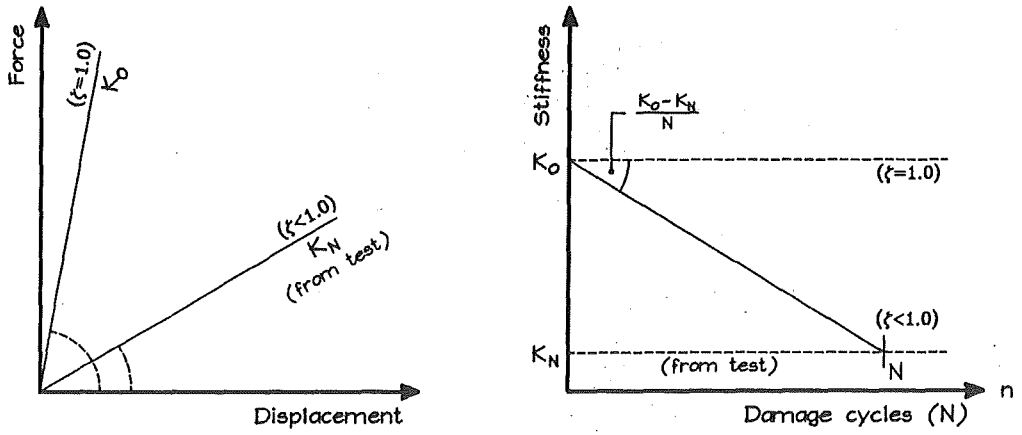

Fig. 2.7 Parameters utilised in the development of stiffness reduction coefficient $\zeta_{(t)}$

In application of the stiffness reduction coefficient, Equation 2.19 is rewritten as:

$$\delta_{(t,h)} = \delta_b\left[\left(\sin\omega t - \zeta\,\omega t\cos\omega t\right)e^{-\omega^2\alpha^2\frac{h\eta}{\eta}} + \zeta\,\omega t\cos\omega t\right] \qquad (2.24)$$

The effect of the reduction coefficient on resonant response behaviour is shown (Fig. 2.8) for a hypothetical ten storey frame with an estimated natural period of T = 1 second that supports 320 tonnes at each storey and is subjected to a constant sinusoidal base motion with peak acceleration of 0.3g. The initial interstorey stiffness K_0 is taken as 500 MN/m, which degrades to K_N = 50 MN/m over N cycles. N has been varied to show the effect of differing rates of stiffness degradation; a larger value of N corresponds with a prolonged elastic response:

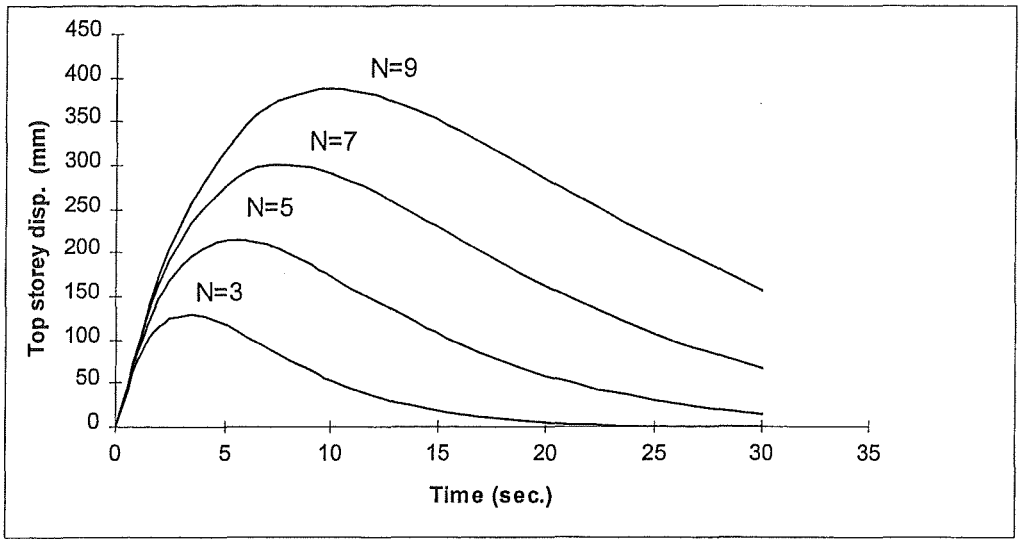

Fig. 2.8 Influence of stiffness reduction coefficient ζ (according to Equations 2.23 and 2.24) on first mode response at differing rates of degrading stiffness

Because Equation 2.24 describes the displaced shape of the responding structure, from this we can obtain an estimate of building slope at given storey levels through differentiation, thus:

$$\frac{d\delta}{dh} = \theta_{(t,h)} = \delta_b \omega^2 \alpha^2 \frac{h^\eta}{h}\left(\sin \omega t - \zeta \cos \omega t\right) e^{-\omega^2 \alpha^2 \frac{h^\eta}{\eta}} \qquad (2.25)$$

For the conceptual ten storey frame, variation in slope with height is shown (Fig. 2.9) at peak response for three differing configurations of distributed mass (i.e., $\eta = 0.8$, $\eta = 1.0$, $\eta = 1.25$) (see Fig. 2.4) at an assumed stiffness degradation rate that corresponds to N = 7 (see Fig. 2.7):

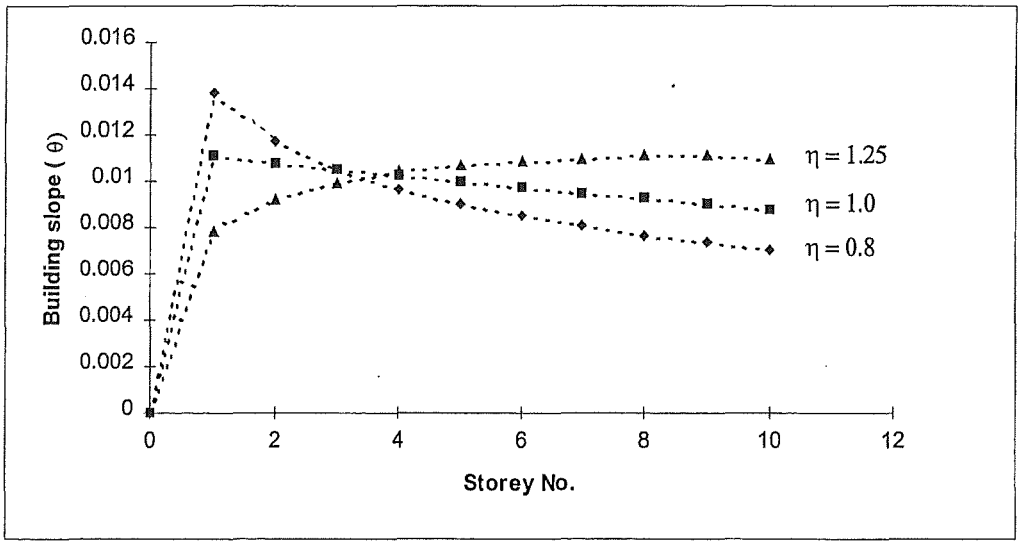

Fig. 2.9 Building slope $\theta_{(t,h)}$ from vertical at storeys one through ten, showing the influence of differing vertical distributions of building mass

With regard to diaphragm analysis, the building slope at storey level (angle of drift) gives an apparent indication of the local rotational demand on support members. As discussed in section 1.4.2.2(c), consideration may then be given to the advent of flexural strength contributions from prestressed flooring units as a result of participation in plastic hinge rotations. Moreover, an estimate of the interstorey drift angle allows estimates to be made as to the potential effects of frame elongation, as described in section 1.4.2.2(d).

In order to relate the angle of drift at storey level with the bending strength development of prestressed flooring units, inelastic structural displacements need to be associated with the curvature ductility ratio demands in plastic hinge zones. The initial approach is to geometrically relate the rotation of vertical members to the average magnitude of rotation in support member plastic hinge zones (Fig. 2.10). Although the determination of curvature ductility ratios and member elongation may initially be separate issues in routine design, the two are fundamentally linked and this geometric model of rotation may be assumed as equally relevant to each. Uni-directional plastic hinges are not examined because of the reasons stated in section 1.4.2.2(d) regarding beam members spanning parallel to self-supporting pretensioned flooring units.

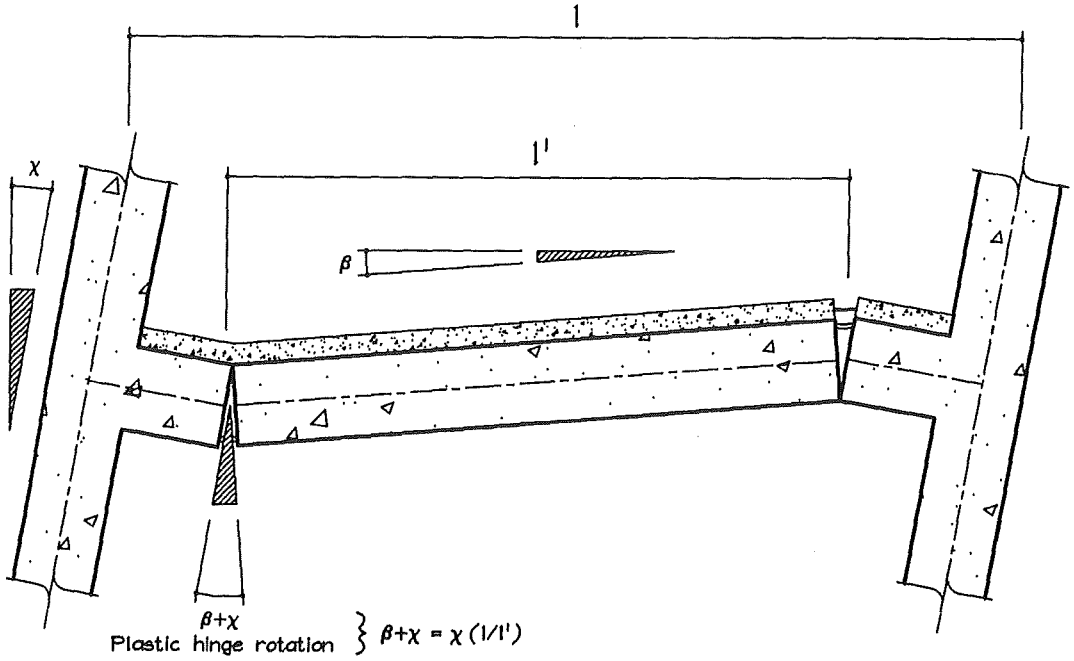

Fig. 2.10 Geometric model relating plastic hinge rotations within a frame assembly [after Restrepo, 1993]

2.2.1.3 Strain Energy and Equivalent Flexural Rigidity

For ductile beam members in seismic resisting structures detailed to code specified dimensions and reinforcement configurations [Standards New Zealand, 1995], the far greatest proportion of member rotation will result from deformations within plastic hinge zones. As such, detailed analysis of elastic bending deformations is not considered critical in establishing rotational magnitudes of seismic resisting members; the relationship between plastic and elastic portions of a member may be generally accounted for by use of correctly modified member stiffness. Likewise, it is usually sufficient to assume an effective plastic hinge length in order that curvature ductility ratios can be calculated. However, it is also a reasonable expectation that pretensioned flooring sections incorporated in plastic hinge rotations will exert unique influences on the characteristics of plastic hinge development. Although the consideration of overstrength capacity is an underlying statement in capacity design, specific analysis of effects arising from beam and pretensioned floor member interaction (see section 1.4.2.2(c)) does not appear in design literature. Thus, it is important to determine what variations may occur in frame displacement characteristics as a result of floor slab participation. The initial consideration has been to demonstrate that increased moments (and the associated shears) are fundamental in this process. The following examines the likely influence of a prestressed component on beam plastic hinge functions that subsequently effect displacement capacity and effective frame stiffness:

By considering an approach in which internal strain energy is equated, it can initially be shown for any beam section subjected to bending that:

$$U_b = \int_L M_{(x)}\, \varphi_{(x)}\, dx \tag{2.26}$$

where U_b is the total bending strain energy, M is bending moment and φ is curvature, and both are functions of length (x). In the case of a reinforced concrete beam, this may be written in terms of the constituent materials, where u_c and u_s are the respective strain energy densities per unit volume of concrete and reinforcing steel:

$$U_b = \int_L M_{(x)}\varphi_{(x)}\,dx = \int_{vol} u_{c(x)}\,dV + \int_{vol} u_{s(x)}\,dV \tag{2.27}$$

The volume element dV is equal to dA·dx; f_c and f_s are the concrete and steel stresses that correspond with respective strains ε_c and ε_s to give strain energy densities. These energy density quantities are most commonly denoted as the areas under characteristic material stress-strain curves (see Fig. 2.11):

$$U_b = \int_L M_{(x)}\varphi_{(x)}\,dx = \int_L \int_{\varepsilon_c} f_c A_c\, d\varepsilon_c\, dx + \int_L \int_{\varepsilon_s} f_s A_s\, d\varepsilon_s\, dx \tag{2.28}$$

Equation 2.28 is a general summation. Because the strain energy stored in an effective length of plastic hinge may be taken as approximately constant over the hinge length, the equation may

be simplified to consider only the strain energy per unit length within the beam plastic hinge zone. Also, since the plastic hinge zones of seismic resisting beam members should maintain a constant area of principal reinforcement, the strain energy per unit length Ψ^* due to bending becomes:

$$\frac{\partial U_b}{\partial x} = \Psi^* = \int_{\varepsilon_c} f_c A_c \, d\varepsilon_c + A_s \int_{\varepsilon_s} f_s \, d\varepsilon_s \tag{2.29}$$

Equation 2.29 can be easily verified for a homogeneous prismatic section such as an uncracked plain concrete beam that is subjected to a bending moment M, as strain energy per unit length is directly proportional to applied moment (Fig. 2.12). Hence, if stress is proportional to strain and elastic modulus ($f = \varepsilon \cdot E$), strain is proportional to curvature and distance ($\varepsilon = \varphi \cdot y$, $d\varepsilon = \varphi \cdot dy$) and area $dA = b \cdot dy$. The elastic bending strain energy per unit volume is generally expressed as:

$$u_{(y)} = \frac{\sigma_{(y)}^2}{2E} \tag{2.30}$$

then for a section of total depth h:

$$\frac{\partial U_b}{\partial x} = M\varphi = 2 \int_0^{h/2} u_{(y)} b \, dy = Eb\varphi^2 \int_0^{h/2} y^2 \, dy \tag{2.31}$$

which gives the elastic bending strain energy relationship of:

$$M\varphi = E b \varphi^2 \left[\frac{y^3}{3} \right]_0^{h/2} = \varphi^2 E \frac{b d^3}{24} \text{ or } \frac{\varphi^2 EI}{2} \tag{2.32}$$

or the more familiar form (since in elastic bending $\varphi = M/EI$):

$$M\varphi = \frac{M_{(x)}^2}{2EI} \tag{2.33}$$

Equation 2.31 can be used for evaluation of cracked sections provided that the actual (or characteristic) material stress-strain relationships are used. Thus, as is typical to plastic bending analysis of reinforced concrete members, strain is generally considered proportional to curvature and distance but stress is not necessarily proportional to strain, etc. Hence, as bending stresses exceed the material proportional limits, strain energy per unit length is no longer directly proportional to bending moment and therefore the symbol Ψ^* has been adopted, instead of the product $M\varphi$, to represent strain energy per unit length.

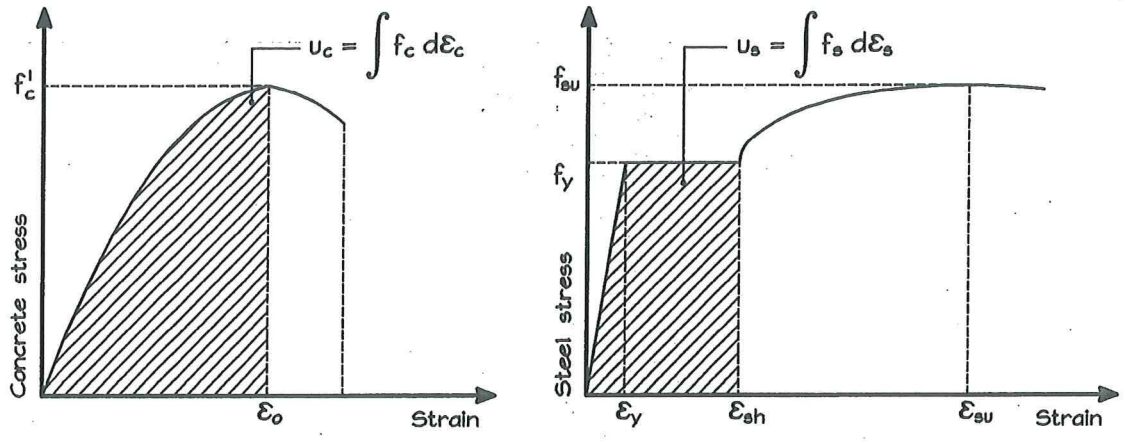

Fig. 2.11 Strain energy densities for concrete and steel as a function of one dimensional (axial) strain

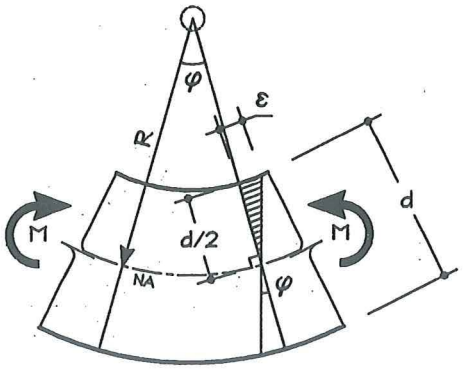

Fig. 2.12 Elastic bending assumptions of a prismatic section

If a simple parabolic stress-strain model is assumed for the concrete component, Equation 2.31 may be written as:

$$u_{(\varepsilon)} = \int_0^{\varepsilon} f_{(\varepsilon)} \, d\varepsilon \quad \text{or} \quad u_{(y)} = \int_0^{y} f_{(y)} \, \varphi \, dy \tag{2.34}$$

where, for the concrete stress block:

$$u_{(y)} = f'_c \, \varphi \int_0^{y} \left[\frac{2 \varphi y}{\varepsilon_o} - \left(\frac{\varphi y}{\varepsilon_o} \right)^2 \right] dy \tag{2.35}$$

Integrating over the element of concrete area dA = b·dy between the limits of zero and the neutral axis depth c, and combining with the steel component gives:

$$\Psi^* = b f'_c \, \varphi \int_0^{c} \left[\frac{\varphi y^2}{\varepsilon_o} - \left(\frac{\varphi}{\varepsilon_o} \right)^2 \frac{y^3}{3} \right] dy + A_s \int_{\varepsilon_s} f_s \, d\varepsilon_s \tag{2.36}$$

and because $\varphi = \varepsilon_c / c$, after integration and substitution this can be reduced to:

THE LIBRARY
UNIVERSITY OF CANTERBURY
CHRISTCHURCH, N.Z.

$$\Psi^* = \frac{b f_c' \varepsilon_c^3}{\varphi \varepsilon_o}\left(\frac{1}{3} - \frac{\varepsilon_c}{12\varepsilon_o}\right) + A_s \int_{\varepsilon_s} f_s \, d\varepsilon_s \qquad (2.37)$$

For practical application, the second term in Equation 2.37 is treated as a discrete summation of individual reinforcing steel (including prestressing steel) components. Equation 2.37 simply expresses a summation of strain energy per unit length of composite materials, and for the preliminary analysis of beam plastic hinges, two typical cases emerge (see Fig. 2.11):

(a) compression steel has not yielded:

$$\Psi^* = \frac{b f_c' \varepsilon_c^3}{\varphi \varepsilon_o}\left(\frac{1}{3} - \frac{\varepsilon_c}{12\varepsilon_o}\right) + \sum_i A_{s_i}' \frac{E_s}{2}\left(\varepsilon_c - \varphi d_i'\right)^2 + \sum_i A_{s_i} f_y \left(\varphi d_i - \varepsilon_c - \frac{\varepsilon_y}{2}\right) \qquad (2.38)$$

(b) compression steel has yielded:

$$\Psi^* = \frac{b f_c' \varepsilon_c^3}{\varphi \varepsilon_o}\left(\frac{1}{3} - \frac{\varepsilon_c}{12\varepsilon_o}\right) + \sum_i A_{s_i}' f_y \left(\varepsilon_c - \frac{\varepsilon_y}{2} - \varphi d_i'\right) + \sum_i A_{s_i} f_y \left(\varphi d_i - \varepsilon_c - \frac{\varepsilon_y}{2}\right) \qquad (2.39)$$

In Equations 2.38 and 2.39, the first term relates to concrete, the second to compression steel and the third term to tension steel. It should be noted that Equations 2.38 and 2.39 do not allow for the effects of strain hardening and maximum steel strain is taken as equal to or less than strain at strain hardening. However, it is considered that the dimensional characteristics of plastic hinges will have developed before the onset of strain hardening. Strain hardening will effectively allow more strain energy to be stored in a given length of plastic hinge, resulting in a concentration of plastic hinge rotation under increased bending moment. This is a significant effect with regard to the participation of flooring units in plastic hinge rotations, however, the principal field of rotation (plastic hinge zone) will already be evident in the section.

It is proposed that the above model and summation may be utilised to establish the equivalent flexural rigidity (EI value) of a concrete section at various stages of flexural response. The equivalent flexural rigidity, denoted EI*, may be derived by considering the general summation provided by Equation 2.37, and re-arranging the terms of Equation 2.32 so that:

$$EI^* = \frac{2\Psi^*}{\varphi^2} \qquad (2.40)$$

Verification of the foregoing equation is made by examination of a simple reinforced concrete structural wall element that is subjected to combinations of axial force and out-of-plane bending moment. The wall is 120 mm thick and reinforced by HD12 bars at250 mm centres (Fig. 2.13), and the following assumptions are made with regard to materials (Table 2.2). Material stress-strain relationships are assumed to behave in accordance with Figure 2.11. The customary

parabolic stress-strain relationship for unconfined concrete has been adopted, as depicted by Equation 2.35.

Table 2.2 Material parameters for derivation of equivalent flexural rigidity of wall element

f'_c (MPa)	f_{cr} (MPa)	ε_0	E_c (GPa)	f_y (MPa)	E_s (GPa)
25	3.0	0.00213	23.5	430	200

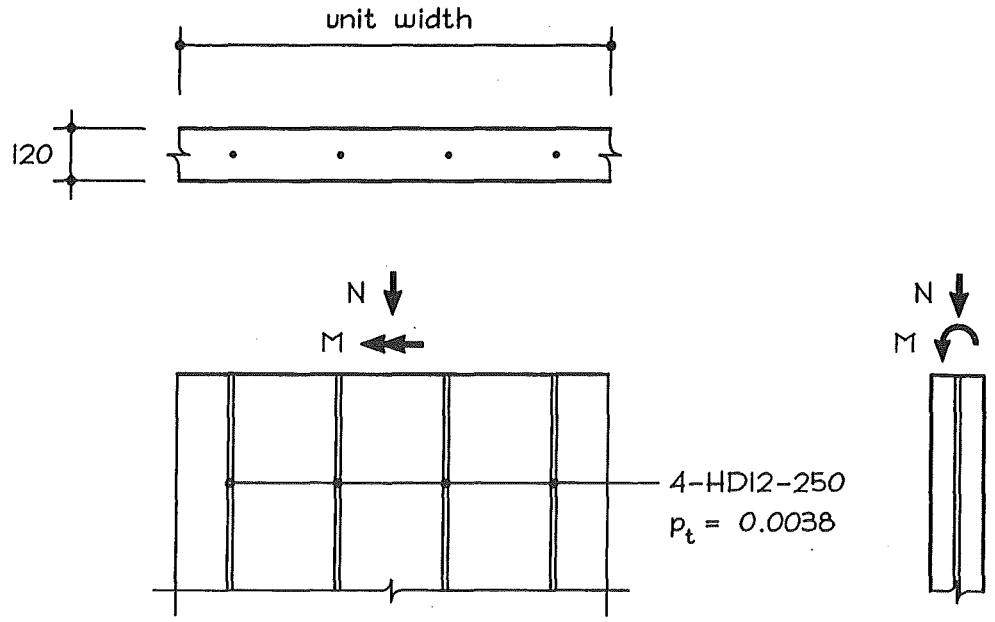

Fig. 2.13 Singly reinforced wall element subjected to combinations of axial force and bending moment

The equivalent flexural rigidity EI* per meter length is derived for three axial force regimes: (i) 50 kN axial tension, (ii) zero axial load and (iii) 50 kN axial compression. An elastic phase is exhibited between zero bending moment and first cracking moment M_{cr}. At first cracking moment, the equivalent flexural rigidity is compared with the same property calculated by elastic cracked section methods. Beyond first cracking, the equivalent rigidity is traced up to the ideal flexural capacity M_i at an ultimate concrete strain of 0.003.

(a) Flexural Rigidity at First Cracking

The cracked elastic section properties are calculated by initially locating the neutral axis of the cracked section. Hence, first moments of area must be taken, and for a singly reinforced element, this will effectively balance the area of concrete in compression $b \cdot y$ with the transformed area of reinforcement $n \cdot A_s$. The resulting formulation for neutral axis depth y may be written as:

$$y = \frac{1}{b}\left(\sqrt{nA_s}\sqrt{nA_s + 2bd} - nA_s\right) \tag{2.41}$$

and the second moment of inertia about the neutral axis:

$$I_{cr} = \frac{by^3}{3} + nA_s(d - y)^2 \tag{2.42}$$

For the given configuration of section and materials (see Fig. 2.13 and Table 2.2), it follows that:

$$y = 17.98 \text{ mm}$$
$$EI_{cr} = 205.15 \times 10^9 \text{ Nmm}^2$$

The equivalent section rigidity is obtained by consideration of Equation 2.37, and observing that the solution by Equations 2.41 and 2.42 is not sensitive to concurrent levels of bending curvature. It is also evident that the solution in accordance with Equation 2.40 may only converge with the traditional section analysis, since curvature cannot equal zero. This is not to say that the equivalent flexural rigidity is less accurate. In fact, the contrary is true because the EI* approach allows for the actual response of materials to be modelled through all stages of loading, and bending curvature will always be present. Likewise, the EI* method will allow section analysis for situations where reinforcement has yielded and/or where prestressing steel is present. However, section analysis based on cracked elastic properties is often an approximation because, as typified by the given wall example, concrete compressive stress increased from 3.0 MPa to around 15 MPa at the instant of cracking. At this level of stress (i.e., 60% of crushing strength), there is certainly a departure from elastic behaviour within the concrete compression block.

Hence, for comparison with elastic analysis a nominally small level of concrete strain is adopted so that departure from linear elastic behaviour is negligible. As such, the same neutral axis depth y used in elastic analysis is applicable:

$$\varepsilon_c = 1 \times 10^{-10} \quad \text{and} \quad y = 17.98 \text{ mm}$$
$$\varphi = 5.562 \times 10^{-12} \text{ θ/mm}$$

The summation of strain energy per unit length will involve the concrete compression block and unyielded tension reinforcement:

$$\Psi^* = \Psi_c + \Psi_{se} = \frac{bf_c'\varepsilon_c^3}{\varphi\varepsilon_0}\left(\frac{1}{3} - \frac{\varepsilon_c}{12\varepsilon_0}\right) + \frac{f_s^2}{2E_s}A_s \tag{2.43}$$

which gives:

$$7.0422 \times 10^{-13} + 2.4687 \times 10^{-12} = 3.1729 \times 10^{-12} \text{ Nmm/mm}$$

and the equivalent flexural rigidity is calculated as:

$$EI^* = \frac{2 \times 3.1729 \times 10^{-12}}{\left(5.5617 \times 10^{-12}\right)^2} = 205.15 \times 10^9 \text{ Nmm}^2$$

Closer examination will show that at the selected level of concrete strain, the two solutions converge to within an accuracy of 8 decimal places, i.e.:

$$EI_{cr} = EI^* = 2.05149397 \times 10^{11} \text{ Nmm}^2$$

(b) Flexural Rigidity in the Plastic State

Subsequently, the EI* value has been calculated (Equations 2.40 and 2.44) for the wall element subjected to each of the three axial force regimes (see Tables 2.3, 2.4 and 2.5):

$$\Psi^* = \Psi_c + \Psi_{se} + \Psi_{sp} = \frac{b f_c' \varepsilon_c^3}{\varphi \varepsilon_o}\left(\frac{1}{3} - \frac{\varepsilon_c}{12\varepsilon_o}\right) + \frac{A_s f_s^2}{2E_s} + A_s f_s\left(\varepsilon_s - \frac{f_y}{E_s}\right) \qquad (2.44)$$

Table 2.3 Equivalent flexural rigidity EI* of wall element resisting 50 kN axial tension

Wall Element with (i) 50 kN Axial Tension						
ε_c =	0.00067	0.001	0.0015	0.002	0.0025	0.003
M (kNm)	6.209	7.928	8.107	8.182	8.210	8.207
φ (θ/mm)	4.141e^{-5}	6.863e^{-5}	1.401e^{-4}	2.235e^{-4}	3.094e^{-4}	3.881e^{-4}
Ψ_c (N)	26	50	78	107	144	181
Ψ_{se} (N)	149	209	209	209	209	209
Ψ_{sp} (N)	NA	188	924	1800	2700	3520
Ψ^* (N)	175	447	1211	2116	3053	3910
EI* (Nmm²)	204.1e^9	189.9e^9	123.4e^9	84.7e^9	63.8e^9	51.9e^9
EI*/EI$_{cr}$	1.000	0.930	0.605	0.415	0.313	0.254

Table 2.4 Equivalent flexural rigidity EI* of wall element without axial load

Wall Element with (ii) Zero Axial Force						
ε_c =	0.00068	0.001	0.0015	0.002	0.0025	0.003
M (kNm)	7.196	10.18	10.66	10.79	10.84	10.84
φ (θ/mm)	$3.611e^{-5}$	$5.189e^{-5}$	$1.041e^{-4}$	$1.660e^{-4}$	$2.298e^{-4}$	$2.885e^{-4}$
Ψ_c (N)	31	67	105	143	184	240
Ψ_{se} (N)	100	202	209	209	209	209
Ψ_{sp} (N)	NA	NA	504	1130	1780	2360
Ψ^* (N)	131	269	818	1482	2173	2809
EI* (Nmm²)	$201.3e^9$	$199.4e^9$	$151.0e^9$	$107.6e^9$	$82.3e^9$	$67.5e^9$
EI*/EI$_{cr}$	1.000	0.991	0.750	0.535	0.409	0.335

Table 2.5 Equivalent flexural rigidity EI* of wall element under 50 kN axial compression

Wall Element with (iii) 50 kN Axial Compression						
ε_c =	0.00068	0.001	0.0015	0.002	0.0025	0.003
M (kNm)	8.218	11.16	13.07	13.29	13.37	13.36
φ (θ/mm)	$3.099e^{-5}$	$4.662e^{-5}$	$8.278e^{-5}$	$1.320e^{-4}$	$1.829e^{-4}$	$2.294e^{-4}$
Ψ_c (N)	36	74	131	181	235	302
Ψ_{se} (N)	63	146	209	209	209	209
Ψ_{sp} (N)	NA	NA	256	733	1230	1670
Ψ^* (N)	99	220	596	1123	1674	2181
EI* (Nmm²)	$207.0e^9$	$202.5e^9$	$174.1e^9$	$128.9e^9$	$100.1e^9$	$82.9e^9$
EI*/EI$_{cr}$	1.000	0.978	0.841	0.622	0.483	0.400

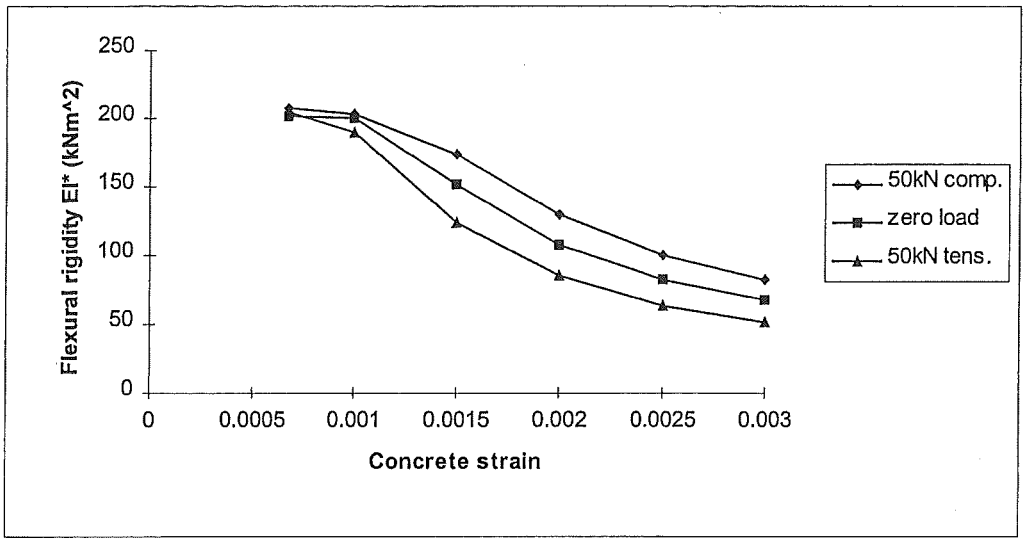

Fig. 2.14 Equivalent flexural rigidity EI* of a singly reinforced wall (see Fig. 2.13) in response to increasing bending curvature, as described by Equations 2.40 and 2.44

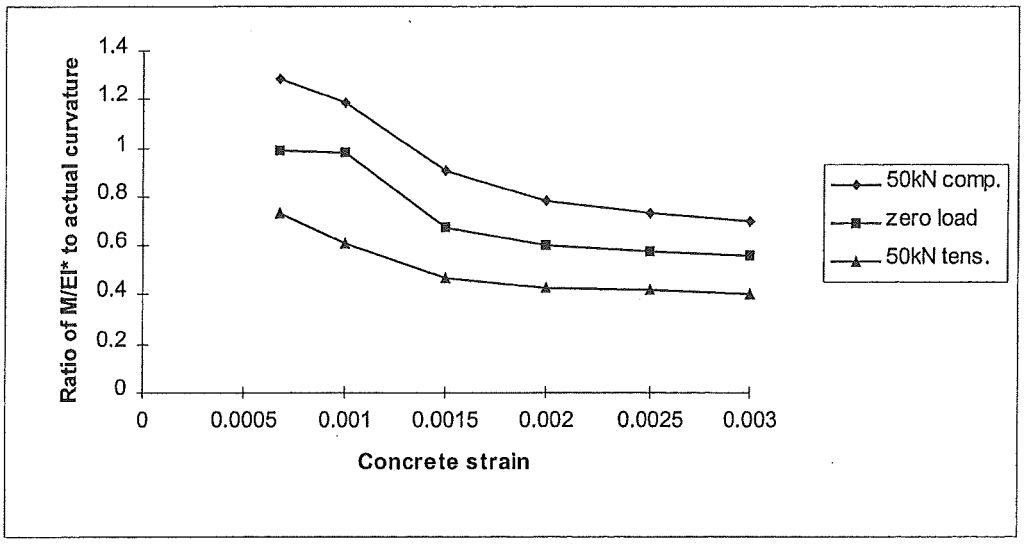

Fig. 2.15 Ratio of M/EI* to the actual curvature φ for a singly reinforced wall with varying levels of axial load and increasing bending curvature

For further comparison, a more flexurally efficient section is examined. Figure 2.16 shows a pretensioned 300 mm deep double tee section without composite topping. The tee is prestressed by eight 12.7mm diameter supergrade strands, giving a prestressing steel area of 800 mm² centred at 75 mm above the leg soffit. The prestress force after losses is 967 kN. The flexural rigidity of the gross section is $EI_g = 55.84 \times 10^{12}$ Nmm².

Table 2.6 Material parameters for derivation of equivalent flexural rigidity of double tee

f'_c (MPa)	f_{cr} (MPa)	ε_o	E_c (GPa)	f_{pu} (MPa)	E_{ps} (GPa)
40	3.8	0.00287	27.9	1900	195

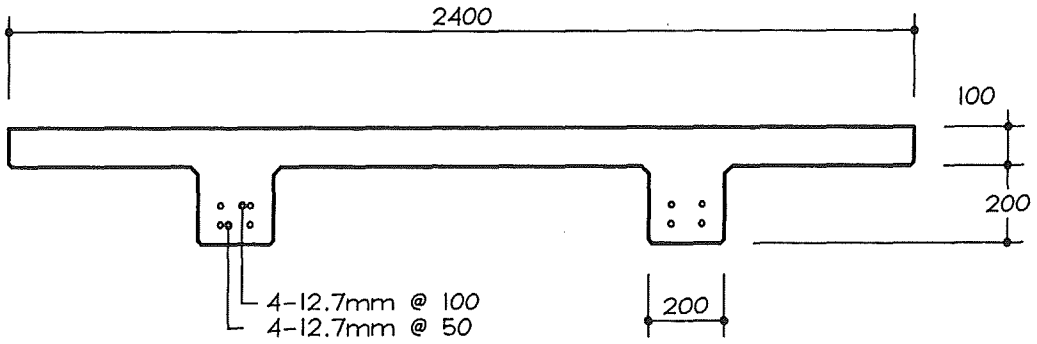

Fig. 2.16 Pretensioned double tee section

Table 2.7 Equivalent flexural rigidity EI* of a pretensioned double tee section in response to increasing bending curvature, as described by Equations 2.40 and 2.44

300 mm deep Pretensioned Double Tee						
ε_c =	0.00026	0.0005	0.00075	0.001	0.0015	0.002
M (kNm)	186.2	228.6	270.2	309.7	377.6	412.0
φ (θ/mm)	$2.131e^{-6}$	$6.443e^{-6}$	$1.084e^{-5}$	$1.513e^{-5}$	$2.351e^{-5}$	$3.195e^{-5}$
Ψ_c (N)	94	209	443	764	1649	2850
Ψ_{ps} (N)	3210	3990	4850	5770	7785	9910
Ψ^* (N)	3304	4199	5293	6534	9434	12760
EI* (Nmm²)	$1.459e^{15}$	$202.2e^{12}$	$90.12e^{12}$	$57.1e^{12}$	$34.1e^{12}$	$25.0e^{12}$
EI^*/EI_g	26.13	3.62	1.62	1.02	0.61	0.45

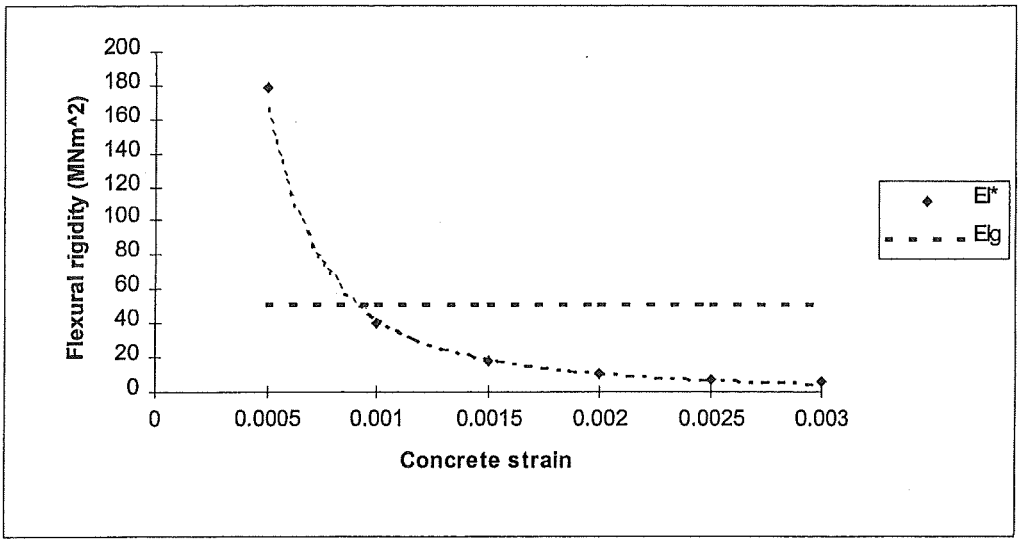

Fig. 2.17 Relationship between EI* and the gross section rigidity EI_g for a pretensioned double tee section (see Fig. 2.16) subjected to increasing bending curvature

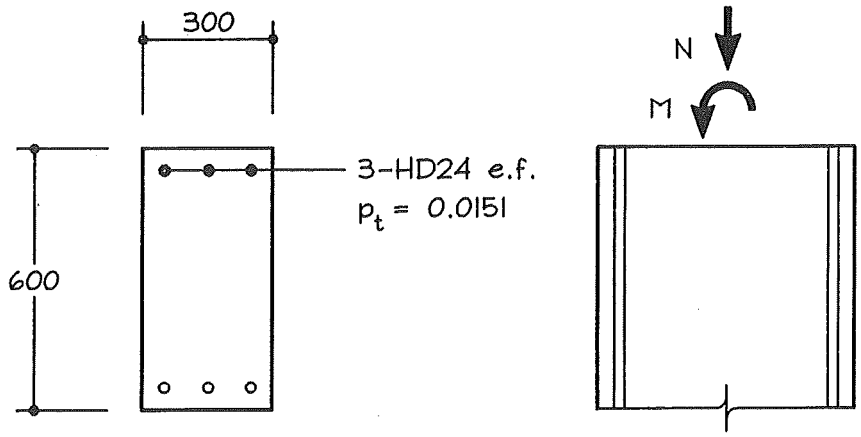

Fig. 2.18 600 mm x 300 mm column section

Table 2.8 Material parameters for derivation of equivalent flexural rigidity of a column

f'_c (MPa)	f_{cr} (MPa)	ε_0	E_c (GPa)	f_y (MPa)	E_{ps} (GPa)
30	3.3	0.00239	25.1	430	200

The equivalent flexural rigidity EI* of the column element (see Fig. 2.18) is analysed for three axial force regimes: (i) 250 kN axial tension, (ii) zero load and (iii) 1000 kN axial compression:

Table 2.9 Equivalent flexural rigidity EI* of a column section resisting 250 kN axial tension

600 mm x 300 mm Column with (i) 250 kN Axial Tension						
ε_c =	0.0005	0.001	0.0015	0.002	0.0025	0.003
M (kNm)	201.7	234.9	236.7	237.9	238.7	239.0
φ (θ/mm)	$4.421e^{-6}$	$1.333e^{-5}$	$2.513e^{-5}$	$3.704e^{-5}$	$4.864e^{-5}$	$5.976e^{-5}$
Ψ_c (N)	34	84	142	212	293	393
Ψ_{sy} (N)	516	642	635	630	627	627
Ψ_{sp} (N)	NA	2439	5929	9458	12890	16160
Ψ^* (N)	550	3165	6706	10300	13810	17180
EI* (Nmm²)	$56.29e^{12}$	$35.61e^{12}$	$21.25e^{12}$	$15.02e^{12}$	$11.68\ e^{12}$	$9.62e^{12}$
EI*/EI$_g$	0.42	0.26	0.16	0.11	0.09	0.07

Table 2.10 Equivalent flexural rigidity EI* of a column section with zero axial load

600 mm x 300 mm Column with (ii) Zero Axial Load						
ε_c =	0.0005	0.001	0.0015	0.002	0.0025	0.003
M (kNm)	177.7	293.8	298.8	300.7	301.7	302.0
φ (θ/mm)	$1.001e^{-6}$	$7.764e^{-6}$	$1.665e^{-5}$	$2.685e^{-5}$	$3.731e^{-5}$	$4.754e^{-5}$
Ψ_c (N)	4	144	214	297	384	491
Ψ_{sy} (N)	24	678	687	685	681	679
Ψ_{sp} (N)	NA	653	3211	6189	9255	12240
Ψ^* (N)	28	1475	4112	7171	10320	13410
EI* (Nmm²)	$54.44e^{12}$	$48.95e^{12}$	$29.67e^{12}$	$19.90e^{12}$	$14.83\ e^{12}$	11.87^{12}
EI*/EI$_g$	0.40	0.36	0.22	0.15	0.11	0.09

Table 2.11 Equivalent flexural rigidity EI* of a column section resisting 1000 kN axial compression

600 mm x 300 mm Column with (iii) 1000 kN Axial Compression						
ε_c =	0.0005	0.001	0.0015	0.002	0.0025	0.003
M (kNm)	146.8	302.9	437.6	508.2	522.4	529.6
φ (θ/mm)	$9.843e^{-7}$	$3.272e^{-6}$	$5.869e^{-6}$	$9.302e^{-6}$	$1.400e^{-5}$	$1.914e^{-5}$
Ψ_c (N)	151	343	608	854	1034	1214
Ψ_{sy} (N)	28	182	602	946	1066	1193
Ψ_{sp} (N)	NA	NA	NA	563	1778	3137
Ψ^* (N)	179	525	1210	2363	3878	5544
EI* (Nmm²)	$369.0e^{12}$	$98.03e^{12}$	$70.29e^{12}$	$54.61e^{12}$	$39.58\ e^{12}$	$30.25e^{12}$
EI*/EI$_g$	2.72	0.72	0.52	0.40	0.29	0.22

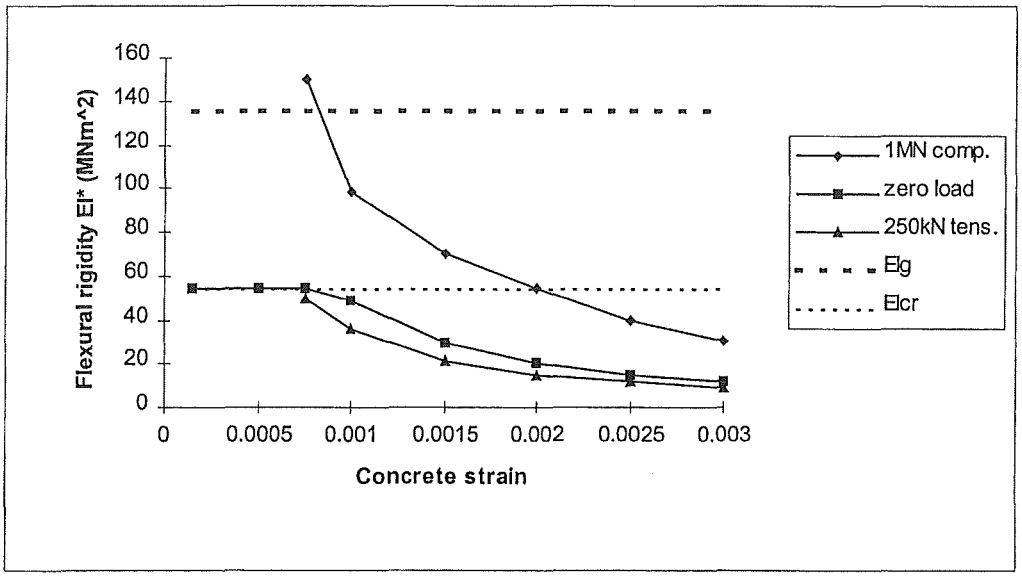

Fig. 2.19 Relationship between EI*, gross section rigidity EI_g and cracked section rigidity EI_{cr} for a column section (see Fig. 2.18) subjected to increasing bending curvature

2.2.1.4 Plastic Hinge Rotations and Compatibility

The plastic hinge regions of typical beam sections that incorporate a proportion of pretensioned floor section will naturally exhibit different moment capacities and rotational characteristics under alternating positive and negative bending actions. In order to rationally deduce the likely magnitude of beam plastic hinge rotations, strain energy quantities obtained through the preceding equations may be applied on the basis that internal strain energy will equal the work done by an external force moving through a distance (i.e., $M \cdot \theta = P \cdot \delta$). As discussed, beams spanning parallel to pretensioned flooring members usually support little more than self weight. Therefore, the predominant bending moment and shear force envelopes are easily defined in relation to the point of contraflexure for frame elements subjected to horizontal sway actions (Fig. 2.20).

The displacement δ (Fig.2.20) is comprised of respective elastic and inelastic components, and from the distribution of bending curvature may be calculated as:

$$\delta = \frac{\varphi_y z^2}{3} + (\varphi_p - \varphi_y)\ell_p\left(z - \frac{\ell_p}{2}\right) \qquad (2.45)$$

Equating the external work done to the quantity of internally stored strain energy, the following may be written in terms of respective elastic and inelastic components (see Fig. 2.20):

$$V\delta = \tfrac{1}{2}\int_z M_y \varphi_y \, dx + \Psi_p \ell_p \qquad (2.46)$$

By expanding this equation, noting that $V = M_p/z$ for the frame sway model and simplifying so that (see Fig. 2.20):

$$\varphi_\Delta = \varphi_p - \varphi_y \qquad (2.47)$$

then:

$$M_p\left[\frac{\varphi_y z}{3} + \varphi_\Delta \ell_p\left(1 - \frac{\ell_p}{2z}\right)\right] = \frac{M_y^2 z}{6E_c I_e} + \Psi_p \ell_p \qquad (2.48)$$

In the first term on the right hand side of Equation 2.48, which relates to nominally elastic strain energy, the full length of beam segment has been used without subtracting the plastic hinge length. This simplifies the equation and semi-empirically accounts for additional internal strain energy due to strain penetration into the section beyond the plastic hinge zone, as well as shear displacements. Ψ_p is the sum of strain energy per unit length that occurs under bending moment M_p. From the above, it can be shown that:

$$\frac{\ell_p^2}{2z} + \left(\frac{\Psi_p}{M_p \varphi_\Delta} - 1\right)\ell_p - \frac{\varphi_y z}{M_p \varphi_\Delta}\left(\frac{M_p}{3} - \frac{M_y}{6}\right) = 0 \qquad (2.49)$$

and solving for the equivalent length of plastic hinge required to meet the constraints of Equations 2.45 and 2.46 gives the exact solution of:

$$\frac{\ell_p}{z} = \frac{\frac{1}{\sqrt{3}}\sqrt{3\Psi_p^2 - \Psi_\Delta\left[6\Psi_p - 3\Psi_\Delta - \varphi_y\left(2M_p - M_y\right)\right]} + \Psi_\Delta - \Psi_p}{\Psi_\Delta} \qquad (2.50)$$

where: $$\Psi_\Delta = M_p\,\varphi_\Delta \qquad (2.51)$$

By considering that in general the plastic hinge moment M_p is not significantly greater than first yield moment M_y, Equation 2.50 can usually be simplified with negligible error to:

$$\frac{\ell_p}{z} = \sqrt{\left(\frac{\Psi_p}{\Psi_\Delta} - 1\right)^2 + \frac{M_p}{3M_y\left(\frac{\varphi_p}{\varphi_y} - 1\right)}} - \left(\frac{\Psi_p}{\Psi_\Delta} - 1\right) \qquad (2.52)$$

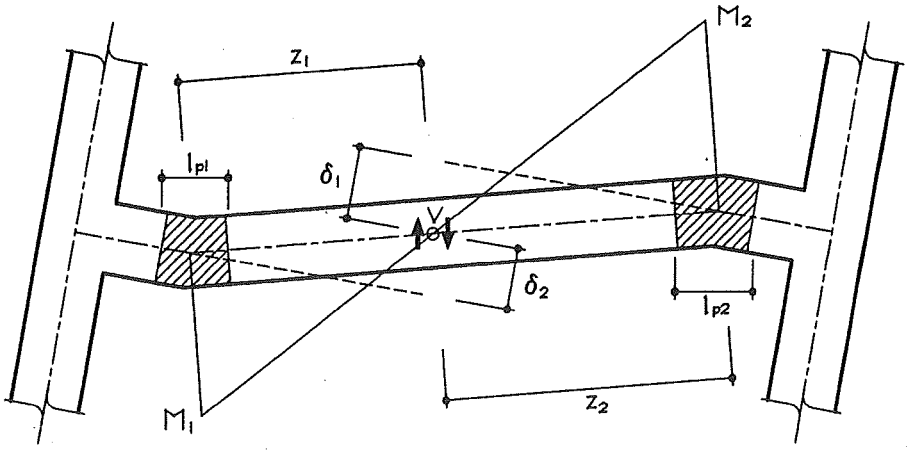

Fig. 2.20 Bending moment and displacement model of frame element under sway action

Equation 2.52 would be seen as applicable to most ordinarily reinforced sections. However, where prestressing steel and possible overstrength is involved, the ratio of M_p to M_y can become significant and (especially where φ_y is relatively small) Equation 2.50 may be (but is not necessarily) more appropriate. For applications involving typical sections, Equation 2.52 will give only a marginally larger estimate of equivalent plastic hinge length than Equation 2.50.

In order to assess the influence of plastic hinge development as determined by the foregoing equations, further reference is made of the hypothetical perimeter beam element, Figure 1.57 of Section 1.4.2.2(c). Using this beam model for dimension and reinforcement, estimates of effective plastic hinge lengths and subsequent plastic hinge rotations (as a proportion of flexural length z) are calculated for alternate positive and negative bending (see Table 2.12, Figs 2.21 and 2.22). For each bending case, the effective plastic hinge lengths and hinge rotations have been plotted against concrete strain in the extreme compression fibre. In keeping with Figs 1.58 and 1.59 of Section 1.4.2.2(c), the characteristic plastic hinge lengths correspond to varying numbers of participating 12.7 mm Supergrade strands (from n = 0 to n = 4) over the strain interval.

Table 2.12 Calculation (Equation 2.50) of effective plastic hinge lengths under negative (b = 300 mm) and positive (b = 1500 mm) bending moments for a hypothetical perimeter beam in a ductile moment resisting frame with pretensioned hollow core flooring (see Fig. 1.57 and Section 1.4.2.2 (c))

Strands (n)	ε_c	Bending	M_p (kNm)	M_y (kNm)	φ_p (θ/m)	φ_y (θ/m)	Ψ_p (kNm/m)	EI^*/EI_g	l_p/z (m/m)
0	0.002	-ve	301	289	0.0267	0.00545	7.116	0.081	0.206
2	0.002	-ve	420	372	0.0170	0.00591	6.289	0.176	0.217
4	0.002	-ve	506	449	0.0124	0.00635	5.830	0.304	0.197
0	0.002	+ve	325	307	0.0625	0.00463	19.060	0.039	0.155
2	0.002	+ve	391	348	0.0500	0.00479	18.640	0.060	0.152
4	0.002	+ve	457	387	0.0408	0.00491	17.940	0.087	0.157
0	0.003	-ve	302	289	0.0476	0.00545	13.430	0.048	0.165
2	0.003	-ve	425	372	0.0333	0.00591	13.230	0.096	0.182
4	0.003	-ve	541	449	0.0236	0.00635	11.800	0.170	0.203
0	0.003	+ve	331	307	0.0938	0.00463	29.310	0.027	0.143
2	0.003	+ve	396	348	0.0811	0.00479	30.890	0.038	0.134
4	0.003	+ve	462	387	0.0682	0.00491	30.520	0.053	0.137
0	0.004	-ve	301	289	0.0667	0.00545	19.180	0.035	0.140
2	0.004	-ve	424	372	0.0494	0.00591	20.040	0.066	0.156
4	0.004	-ve	542	449	0.0364	0.00635	18.700	0.114	0.178
0	0.004	+ve	331	307	0.1210	0.00463	38.410	0.021	0.124
2	0.004	+ve	396	348	0.1050	0.00479	40.480	0.029	0.119
4	0.004	+ve	460	387	0.0909	0.00491	41.000	0.040	0.118

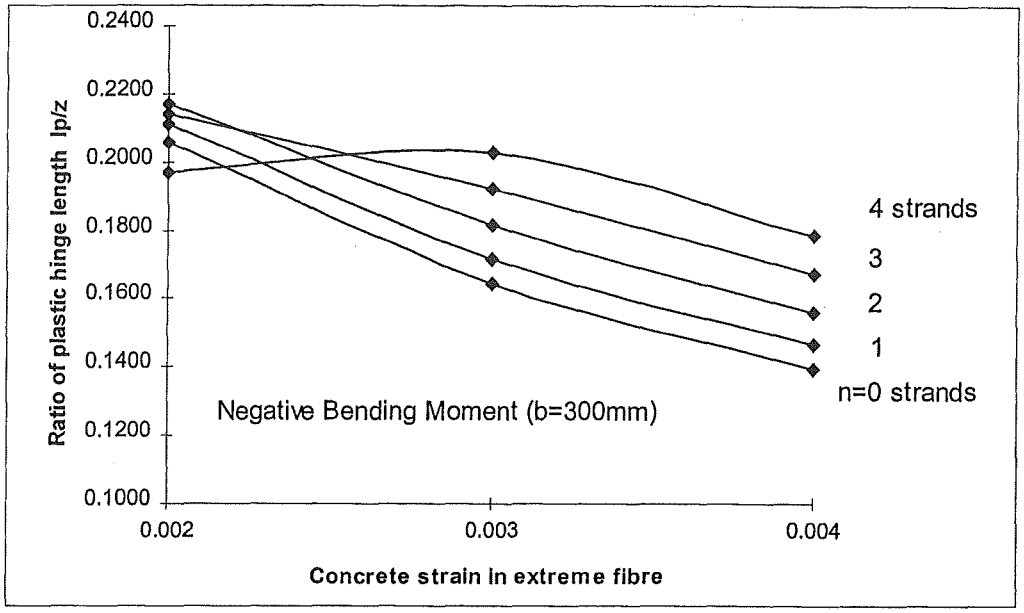

Fig. 2.21(a) Ratio of negative bending equivalent plastic length l_p to contraflexure distance z as a function of concrete compressive strain and the number of strands (n) contributing as flexural tension reinforcement

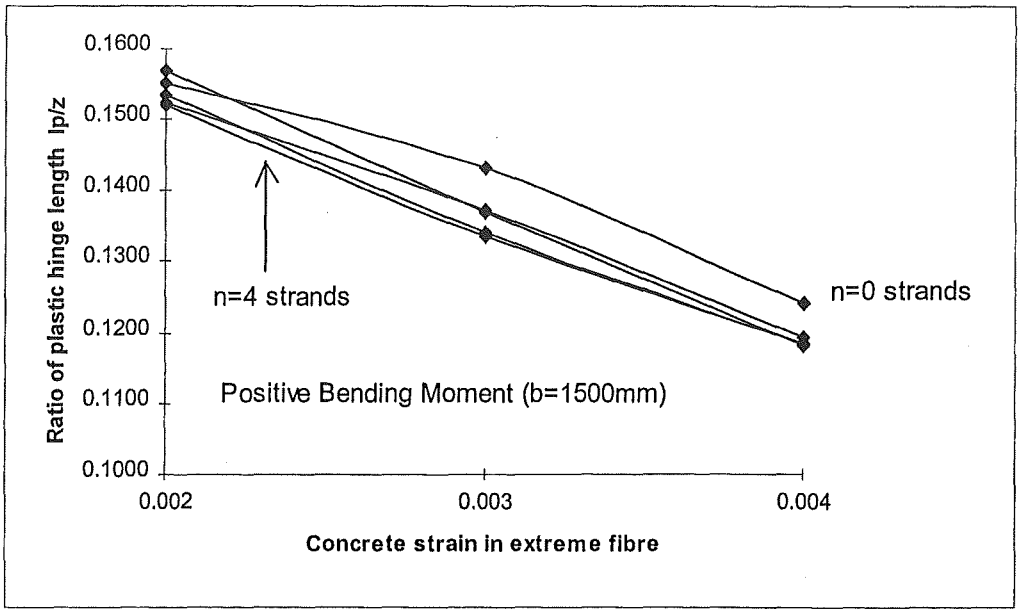

Fig 2.21(b) Ratio of positive bending equivalent plastic length l_p to contraflexure distance z as a function of concrete compressive strain and the number of strands (n) contributing as flexural tension reinforcement

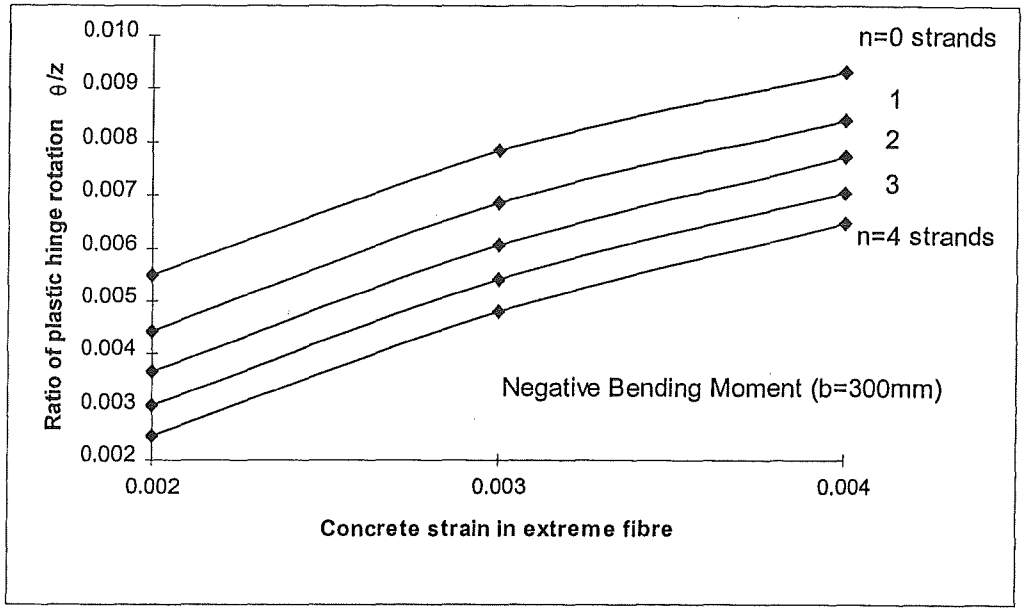

Fig. 2.22(a) Ratio of negative bending plastic hinge rotation θ to contraflexure distance z (metres) as a function of concrete compressive strain and the number of strands (n) contributing as flexural tension reinforcement

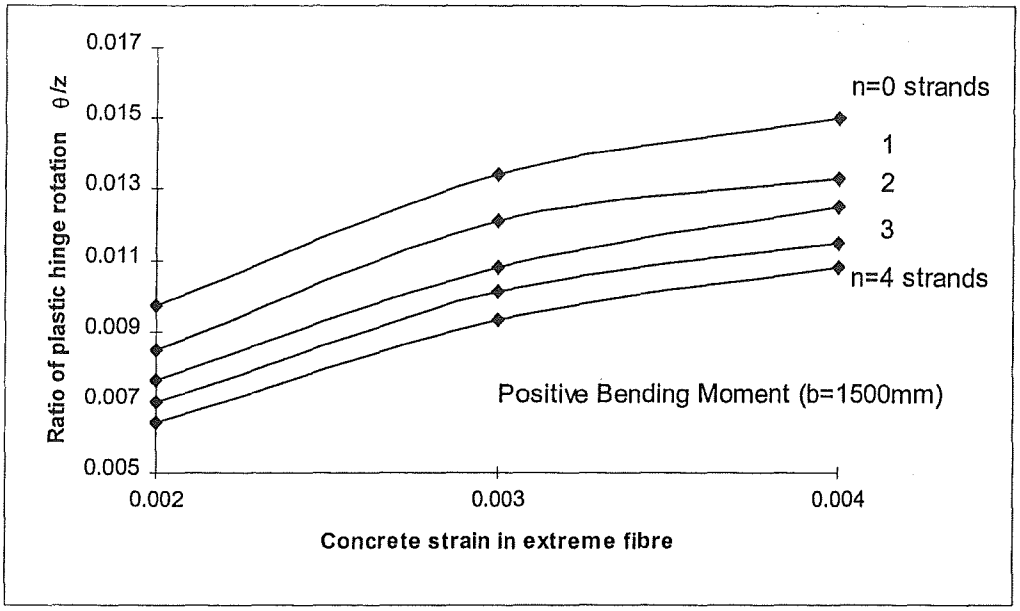

Fig. 2.22(b) Ratio of positive bending plastic hinge rotation θ to contraflexure distance z (metres) as a function of concrete compressive strain and the number of strands (n) contributing as flexural tension reinforcement

In order to determine the deformation capacity of an element of building frame under sway actions, we may observe (see Fig 2.20) that there is almost constant shear force on the beam member. Hence, for practical purposes there is a direct proportion between the magnitude of plastic hinge bending moments M_{p1} and M_{p2} , and their respective distances to the points of contraflexure, z_1 and z_2. Also, because the angle of beam rotation θ' is equally applicable to both beam-end plastic hinges (Fig. 2.20) then the relationship may be written:

$$\frac{|M_{p1}|\theta'}{z_1} = \frac{|M_{p2}|\theta'}{z_2} \tag{2.53}$$

Subsequently, by multiplying the plastic hinge rotations derived in Figures 2.22(a) and 2.22(b) by their corresponding plastic hinge bending moments, a direct reckoning can be made between concrete compressive strain in opposing plastic hinges and a prescribed level of beam rotation θ' (see Figs 2.23). Thus, it is possible to estimate the ability of a beam to meet sway compatibility requirements in relation to building slope $\theta_{(t,h)}$ without exceeding a limiting parameter of concrete compressive strain:

The total strain energy required of two opposing beam plastic hinges in a frame at a prescribed rotation is:

$$U^* = |M_{p1} + M_{p2}|\theta' \tag{2.54}$$

Directly calculated from Table 2.12 (as the product of $M_p \cdot \varphi_p \cdot l_p/z$), Figures 2.23 show quantities of strain energy per unit length as influenced by varying numbers of participating prestressing strands. These are given for positive and negative bending moments at various levels of concrete strain. Typical of plastic moment-curvature relationships, it may also be noted from Table 2.12 that variation in moment capacity under positive and negative bending is small (and often imperceptible) over the plastic bending curvature interval.

Hence, the limiting value of strain energy per unit length may be applied as the basis for estimating a minimum compatible beam length for a given rotation:

$$l'_{min,\pm} = \frac{|M_{p1} + M_{p2}|\theta'}{\left(\frac{M_p\,\theta}{z}\right)_{\pm}} \tag{2.55}$$

Based on Table 2.12, the exact data for calculation of minimum compatible beam lengths has been tabulated in Table 2.13.

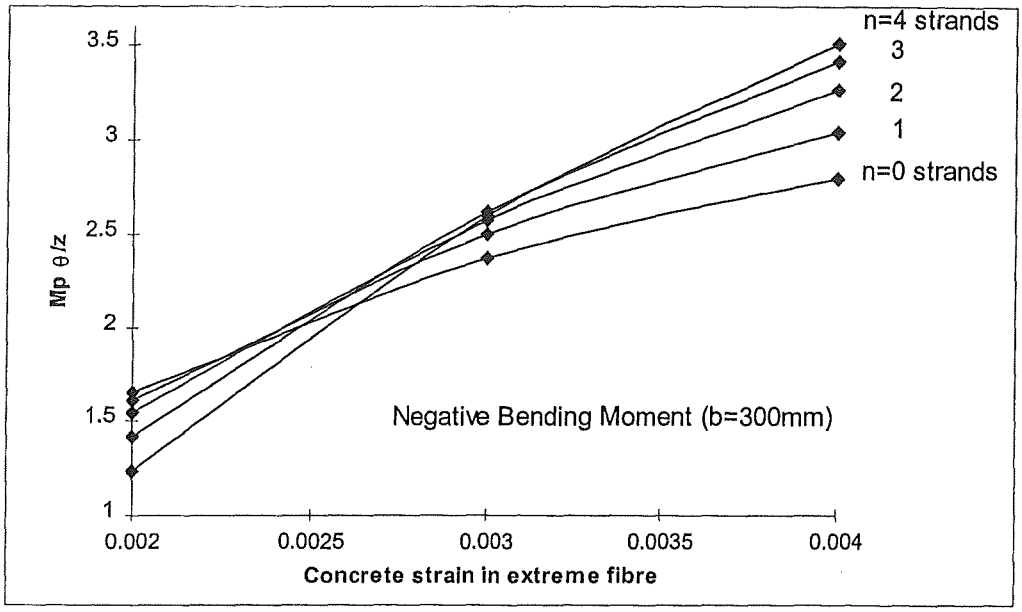

Fig. 2.23(a) Ratio of negative bending strain energy $M_p \cdot \theta$ (kNm) to contraflexure distance z (meters) as a function of concrete compressive strain and the number of strands (n) contributing as flexural tension reinforcement

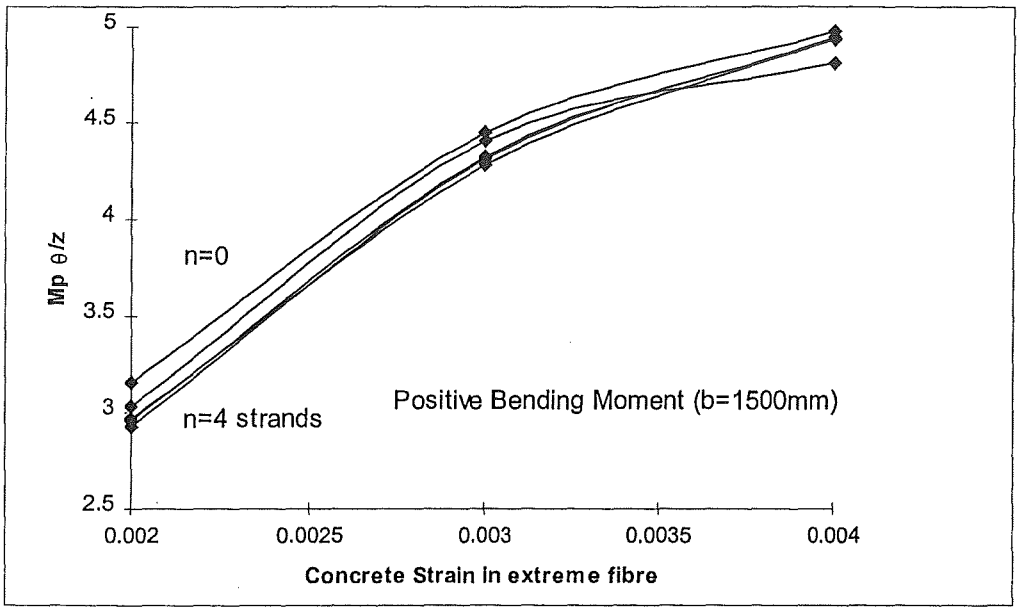

Fig. 2.23(b) Ratio of positive bending strain energy $M_p \cdot \theta$ (kNm) to contraflexure distance z (metres) as a function of concrete compressive strain and the number of strands (n) contributing as flexural tension reinforcement

Table 2.13 Strain energy per unit length $M_p\theta/z$ under negative (b = 300 mm) and positive (b = 1500 mm) bending moments (see Fig. 1.57 and Section 1.4.2.2(c)) for use with Equation 2.55 to estimate minimum compatible beam lengths at a limiting concrete strain and prescribed rotation

Strands (n)	ε_c	Bending	M_p (kNm)	φ_p (θ/m)	l_p/z (m/m)	$M_p\theta/z$ (kNm/m)
0	0.002	-ve	301	0.0267	0.206	1.650
2	0.002	-ve	420	0.0170	0.217	1.550
4	0.002	-ve	506	0.0124	0.197	1.237
0	0.002	+ve	325	0.0625	0.155	3.152
2	0.002	+ve	391	0.0500	0.152	2.973
4	0.002	+ve	457	0.0408	0.157	2.924
0	0.003	-ve	302	0.0476	0.165	2.365
2	0.003	-ve	425	0.0333	0.182	2.572
4	0.003	-ve	541	0.0236	0.203	2.588
0	0.003	+ve	331	0.0938	0.143	4.430
2	0.003	+ve	396	0.0811	0.134	4.287
4	0.003	+ve	462	0.0682	0.137	4.320
0	0.004	-ve	301	0.0667	0.140	2.803
2	0.004	-ve	424	0.0494	0.156	3.272
4	0.004	-ve	542	0.0364	0.178	3.518
0	0.004	+ve	331	0.1210	0.124	4.970
2	0.004	+ve	396	0.1050	0.119	4.927
4	0.004	+ve	460	0.0909	0.118	4.947

The following is an example of the compatibility application which gives comparisons of ductile beams with varying numbers of participating prestressing strands (i.e., n = 0, 2, 4):

Referring to Figure 2.9, the building slope at level 1 with $\eta = 1$ is given as $\theta = 0.011$. With the ratio of column spacing to effective beam length taken as $l/l' = 1.25$, then rotation $\theta' = \theta \cdot l/l' \approx 0.014$, which is constant for the given configuration of building slope and effective beam length. Therefore, both sides of Equation 2.53 may be divided by this value without prejudice to the equality inferred by the expression.

It is assumed that the limiting concrete compression strain is $\varepsilon_c = 0.003$, and that this will first occur under negative bending. Hence, the corresponding positive bending (flange) compression strain in the opposing plastic hinge will be somewhat less. However, the exact determination of flange compression strain is not necessary, and may be assumed to be in the order of $\varepsilon_c = 0.002$ with little variation in bending moment capacity.

If it is considered that two prestressing strands of the adjacent floor section will participate in flexural actions, then Table 2.13 is entered at $\varepsilon_c = 0.003$, n = 2 strands and negative (-ve) bending. The corresponding moment is $M_p = 425$ kNm and strain energy per unit length is $M_p\theta/z = 2.572$. The opposing moment at n = 2, $\varepsilon_c = 0.002$ and positive (+ve) bending is $M_p = 391$ kNm and strain energy per unit length of $M_p\theta/z = 2.973$. According to Equation 2.55, compatibility between plastic hinge rotation capacity and the limiting value of compression strain will not be exceeded in the span, provided that the effective beam length is no less than:

(a) $$\frac{|425 + 391| \times 0.014}{2.572} = 4.45\,\text{m}$$

Alternatively, if it was considered that flange compression strain should not exceed $\varepsilon_c = 0.002$ and that the beam soffit strain could approach spalling, then the appropriate SE per unit length is substituted to give a reduced minimum length of:

(b) $$\frac{|425 + 391| \times 0.014}{2.973} = 3.85\,\text{m}$$

Likewise, if the number of participating strands is increased to n = 4, and the same regime of limiting strains are applied, the minimum effective lengths become:

(c) $$\frac{|541 + 457| \times 0.014}{2.588} = 5.40\,\text{m}$$

and with flange compression critical at $\varepsilon_c = 0.002$ as in the above case (b):

(d) $$\frac{|541 + 457| \times 0.014}{2.924} = 4.80\,\text{m}$$

Based on the above, variations in compatible beam lengths are shown in Figure 2.24.

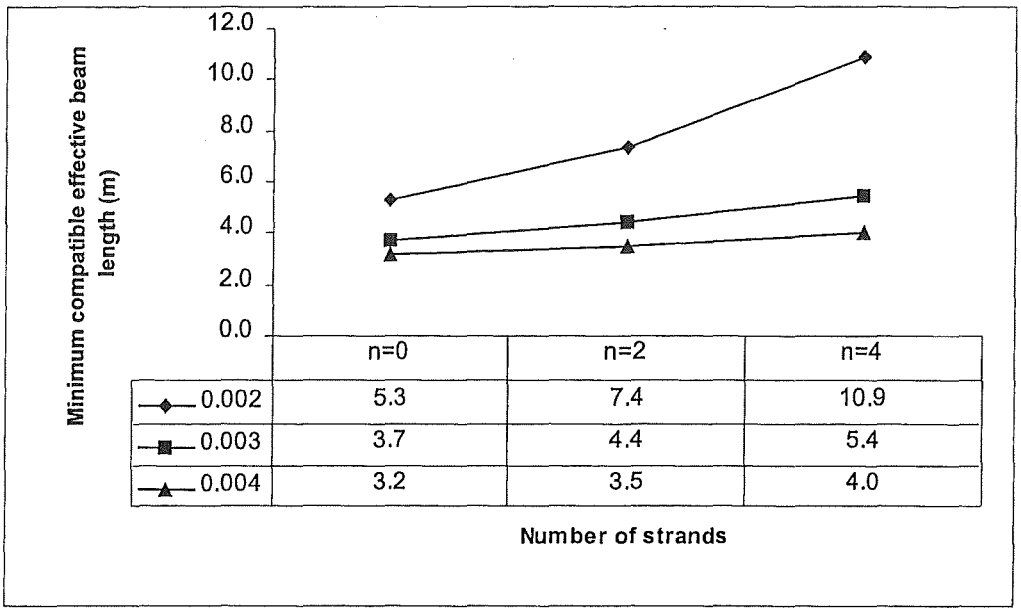

	n=0	n=2	n=4
0.002	5.3	7.4	10.9
0.003	3.7	4.4	5.4
0.004	3.2	3.5	4.0

Fig. 2 24 Minimum compatible effective beam lengths between opposing plastic hinges under a prescribed rotation of $\theta' = 0.014$; at limiting values of concrete compressive strain ($\varepsilon_c = 0.002$, 0.003 and 0.004) and numbers ($n = 0$, 2 and 4) of participating prestressing strands

2.2.2 PLASTIC HINGE LOCATION AND DILATION EFFECTS

2.2.2.1 General

In Section 1.4.2.2(d), frame dilation due to beam plastic hinge rotations was discussed in a general way and mostly reflected the considerations of elongation effects as given in current New Zealand design guidelines [NZCS-NZNSEE, 1991]. In addition to these guidelines there are other aspects that need to be examined, especially with regard to the floor unit and beam interactions. In the preceding Sections, it has been shown that plastic hinges incorporating a sufficient length of pretensioned flooring strands are likely to exhibit significantly greater bending moment and less plastic hinge rotation capacity at a limiting value of concrete compressive strain. Hence, it is important to determine what factors may influence the formation of principal flexural cracks in potential regions of plastic hinging. It is also important to appreciate that the floor component forms a large portion of the elastic section properties. Therefore, it is conceivable that in the initial stages of frame sway, the state of stress within the floor element itself may determine where and when the principal cracks occur.

2.2.2.2 State of Stress in a Hollow Core Flooring Unit

The state of stress in the support region of a pretensioned hollow core flooring unit is likely to have a direct influence on principal crack formation when subjected to negative bending moment (i.e., flange in tension). This is because a disparity exists in the stress states of the pretensioned member and the adjacent beam member. Unless very shallow hollow core sections

are involved, the centre of prestress force in hollow core sections is usually near or outside the middle third kern. Therefore, due to prestress eccentricity, the end regions of hollow core units are often designed to have a limited amount of top fibre tension stress in the end region. When incorporated into the composite section, the residual state of stress in the pretensioned hollow core component may exert some influence on the general propagation of flexural cracks (see Fig. 2.25).

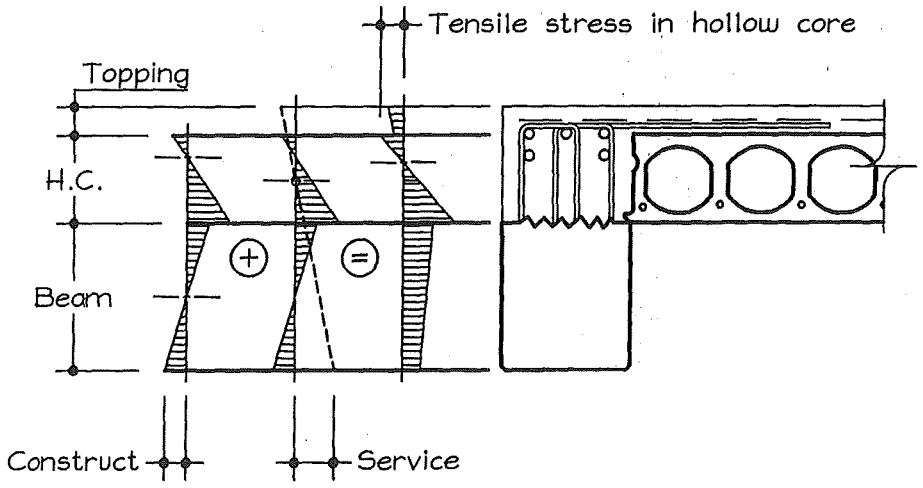

Fig. 2.25 Stress states at a short distance from end support of a beam and pretensioned hollow core unit (both simply supported at construction), plus composite effect.

2.2.2.3 Bar Curtailment and Plastic Hinge Development

Additional to a conducive state of stress in the floor section, the tendency for cracks to originate in the floor is very likely to be augmented by the curtailment of topping starter reinforcement. As such, this portion of the composite member may be susceptible to tension shift effects, and it is feasible that topping cracks will have already formed at the starter curtailment point due to shrinkage induced tension at the discontinuity of topping reinforcement.

By contrast, the formation of cracks in the same composite member subjected to positive bending (i.e., flange in compression) will be more strongly influenced by the discontinuity at the beam-column intersection. Hence, under reversing bending moments, the resulting origins of cracks will facilitate the development of inclined flexure-shear cracks in a plastic hinge zone (see Fig. 2.26). The implication of plastic hinge elongation is that much of the dilation effect could occur at a location that is remote from the actual floor unit end seating. From an analysis point of view, this introduces some complexity into the required design approach. However, it also suggests that some options may be examined for providing an effective means of control within the broad context of plastic hinge actions.

Hence, when developing comprehensive support tie details, consideration should also be given to the effects of curtailment. In particular, the bond relationship between the pretensioned floor unit, composite topping and beam element becomes an important aspect of the overall design.

For example, Equation 1.22 in Section 1.4.2.2(c) relates the development of pretensioned strand force (through strand bond capacity within the extruded section) to the shear friction force developed in the joint between the flooring unit and adjacent beam. The basis of this equation is re-emphasised (Fig. 2.27) by the likelihood that the location of principal cracks will be influenced by bar curtailment in the topping slab. Thus, if a point of curtailment is provided within the domain of a beam plastic hinge and relatively close to the end seating, it may be possible to mitigate the unfavourable effect of developing a large pretensioned strand force through strand bonding. Consequently, this would reduce the likelihood of strands in the pretensioned section causing problems with overly strong beam members (see Figs 1.58 and 1.59). Alternatively, if continuous topping reinforcement is extended well beyond the potential plastic hinge zones, it may be possible to gain more control of composite topping behaviour and reduce the occurrence of premature cracking.

Where the actual beams have been detailed to form plastic hinges sufficiently far from the column face (Fig. 1.56), it would appear difficult to avoid the full potential contribution of prestressing strands to the flexural capacity of the composite member.

2.2.2.4 Maintaining a Composite Section

What is strongly implied by the above is that the curtailment of topping reinforcement (starters and/or continuity bars) should occur either well within the plastic hinge zone, or well past the plastic hinge zone. In addition to the reasons already given, there is an important issue of detailing. If a principal crack occurs through the topping under negative bending, then this crack will almost certainly extend down into the hollow core section due to the conducive state of stress (Fig. 2.25). Because the large concurrent shear force acting on the section produces a rotation such as indicated by Figure 2.26, tie capacity is also required between the topping and floor unit to avoid the potential of delamination or tearing. Hence, it is desirable that an embedded tie force can be developed between the pretensioned floor unit and the cast in place topping slab over a distance that is no shorter than the beam plastic hinge zone, and preferably somewhat greater.

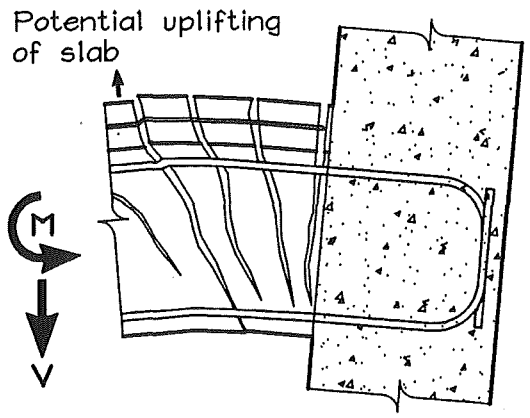

Fig. 2.26 Crack pattern induced by concurrent flexure and shear in side-sway members

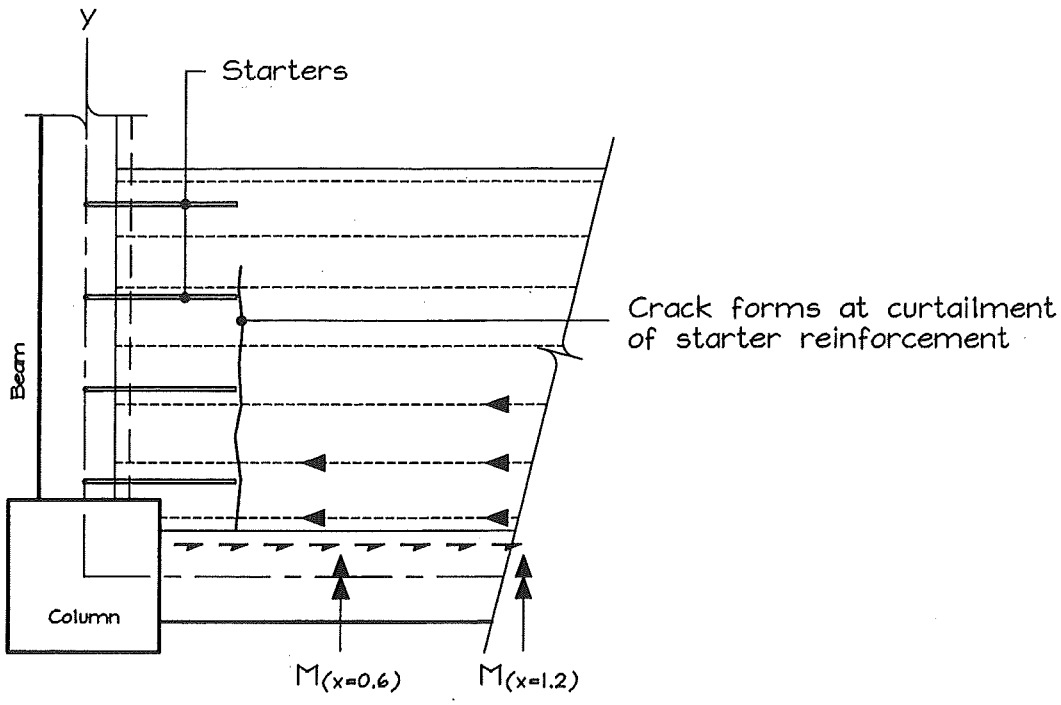

Fig. 2.27 Formation of topping cracks at the curtailment of starter reinforcement

2.3 FORCES ENTERING A DIAPHRAGM

2.3.1 REACTIONS AT COLUMNS AND WALLS

2.3.1.1 General

It is widely recognised that for forces entering building diaphragms, a reliable mechanism is required to achieve force transfer between the floor plate and members of the vertical resistance system. In the case of diaphragms of structures that may need to resist severe seismic actions, the ability to effect reliable force transfer between these structural members is imperative.

The way in which forces arise in relation to particular diaphragms has been discussed in Section 1.3, along with generalised procedures for the treatment of diaphragms in analysis and design. As noted (Section 1.3.3.8), design for force transfer by strut and tie methods has become an increasingly accepted method for establishing viable load paths within diaphragms. Based on established principles, the method revolves around constructing a system of nodes that will facilitate the equilibrium of tensile and compressive axial forces in a manner similar to simple truss analysis.

Regardless of whether critical design actions for diaphragms are based on strut and tie models or the more traditional notion of a uniform shear stress [Kolston and Buchanan, 1980], starter type reinforcement must be provided so that reactions can be developed through shear friction between the floor plate and support members. It is a feature of all well developed design standards and codes of practice that starter type reinforcement should be considered for this purpose. The European design recommendations give an actual minimum value of tensile force capacity per unit length of building in the transverse and longitudinal directions [FIP, 1988].

With regard to capacity design procedures, it can be reasoned that the provision of starter reinforcement should be based on an approach that is consistent with associated overstrength actions. From earlier deliberations (see Section 1.4.2.2), it was established that plastic hinge mechanisms may generally impose the most critical forces on the support regions of simple diaphragms during a severe earthquake. It follows that an in-plane reaction force at floor level will form one component of the bending moment couple generated by plastic hinges. In this Section, the components of forces entering diaphragms are considered from the perspective of immediate reactions at node points (which coincide with column locations and walls) and the flow of forces away from node points into the floor plate in response to diaphragm inertia.

2.3.1.2 Reactions at Node Points

To determine the components that result from plastic hinge zones of ductile beams subjected to oblique frame actions, the vector sum of moments may be considered (see Fig. 1.47 and Fig. 2.28). The magnitude of coupling force resisting the vector sum of overstrength moment M_{oxy} is the resulting component of in-plane reaction, N_{oxy}. The directional sum of this force component is perpendicular to the plane of the maximum bending moment. Hence, starter reinforcement may be proportioned in accordance with the maximum force component as it acts in relation to the orientation of beams. At the intersection of beams, it can be shown that the maximum and minimum components of force resisted by shear friction along the interface of beam and floor are:

$$V_{\tau r(max)} = \frac{N_{oxy}}{2}\left(\frac{\cos \nu}{\cos \beta} + \frac{\sin \nu}{\sin \beta}\right), \quad V_{\tau r(min)} = \frac{N_{oxy}}{2}\left(\frac{\cos \nu}{\cos \beta} - \frac{\sin \nu}{\sin \beta}\right) \tag{2.56}$$

where β is the bisection angle and $\pm\nu$ is the angle made between the force N_{oxy} and the bisection angle (see Fig. 2.29). The force $V_{\tau r}$ can be related to shear friction capacity per unit length by:

$$\frac{V_{\tau r}}{\ell} = q_{\tau r} = \frac{A_{vf} f_y \mu \phi}{s} \tag{2.57}$$

from which the required spacing of starter reinforcement may be calculated as:

$$s_{x,y} = \frac{2 A_{vf} f_y \mu \phi \ell_{x,y}}{N_{oxy}\left(\frac{\cos \nu}{\cos \beta} \pm \frac{\sin \nu}{\sin \beta}\right)} \tag{2.58}$$

The length $l_{x,y}$ is the effective length over which shear friction may be developed in the applicable x or y direction, and should not be taken larger than the actual beam length.

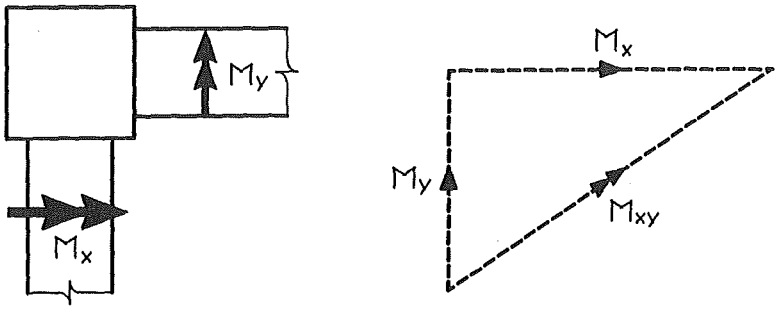

Fig. 2.28 Vector sum of overstrength moments in beam plastic hinges near a corner column

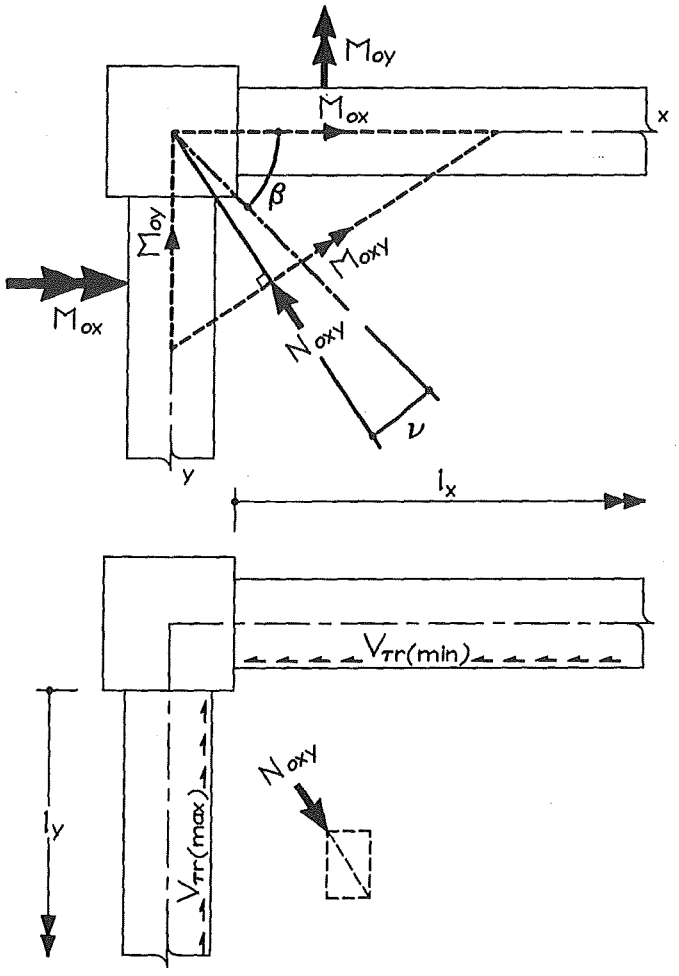

Fig. 2.29 Model application of Equations 2.56 to 2.58

Equation 2.58 may be implemented for any configuration where beams intersect at a column. In accordance with Equation 2.56, the shear force $V_{\tau r}$ is shown as a proportion of the resultant N_{oxy} at different beam intersections (Figs 2.30). The indicated beams have equal bending moment capacity, hence, the deviation angle $\nu = 0°$ and $V_{\tau r(max)} = V_{\tau r(min)}$.

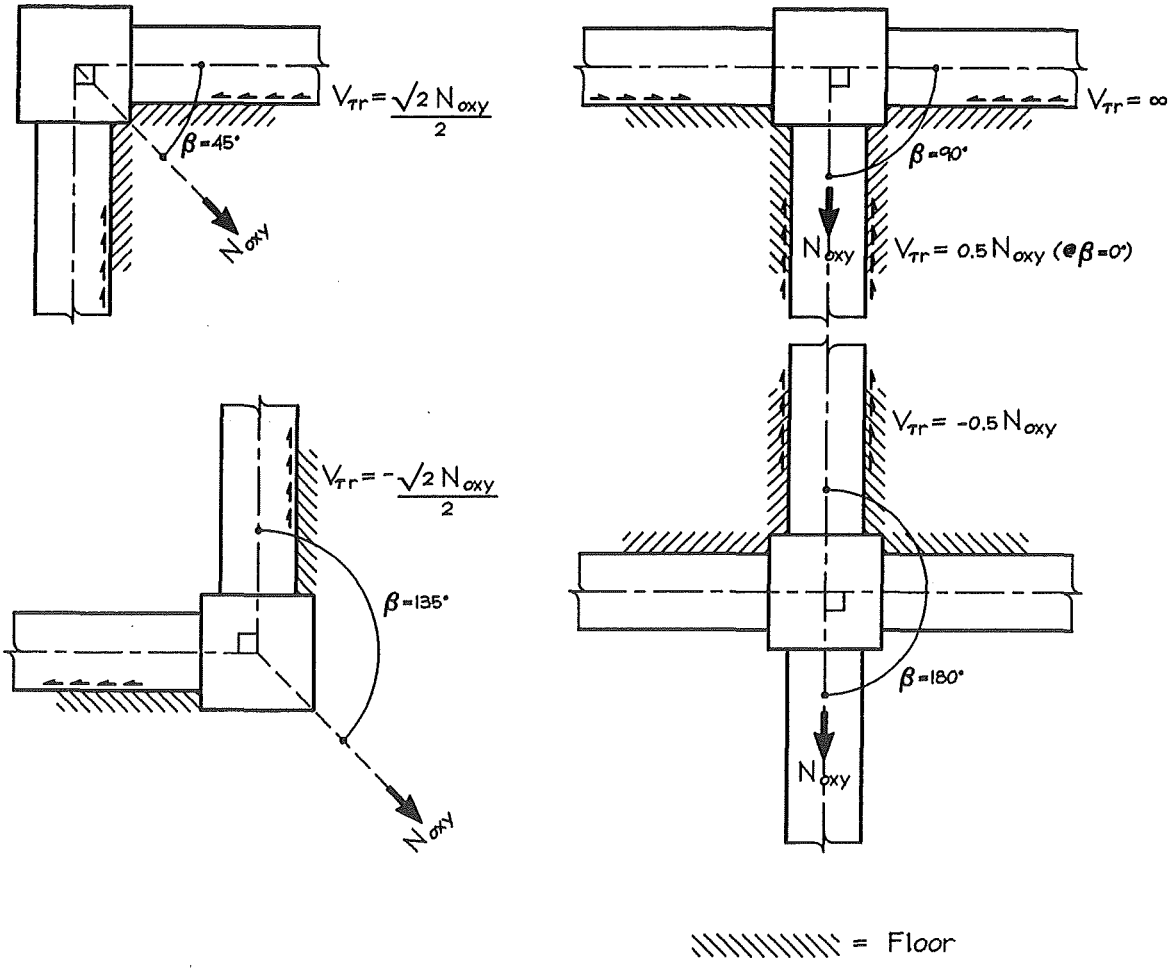

Figs. 2.30 Forces Q (according to Equation 2.56) as a proportion of resultant N_{oxy} , resisted in shear friction by starters at the interface of respective beams and floor slab

Considering the case where a corner column is intersected by two beams at right angles (see Fig. 2.31). The beams concurrently develop respective plastic hinge moments of M_{ox} = 400 kNm and M_{oy} = 300 kNm with jd = 0.5m. Hence, the vector sum of moments is M_{oxy} = 500 kNm, the couple component of force N_{oxy} = 500/0.5 = 1000 kN and acts through the floor plane at approximately 37 degrees to the x-axis. Thus, the bisection angle β = 90/2 = 45° and the deviation angle ν = 45 – 37 = 8°. If HD10 starters (Grade 430) are selected and the construction joint is cast monolithically, then the required spacing in millimetres in accordance with Equation 2.58 and based on 6 metre beam lengths in the x and y directions is:

$$s_{x,y} = \frac{2\times 79\times 430\times 1.4\times 0.75\times 6}{1000\left(\frac{\cos 8}{\cos 45} \pm \frac{\sin 8}{\sin 45}\right)}$$

$$s_x = \frac{428}{1.2} \approx 350\,\text{mm}$$

$$s_y = \frac{428}{1.6} \approx 250\,\text{mm}$$

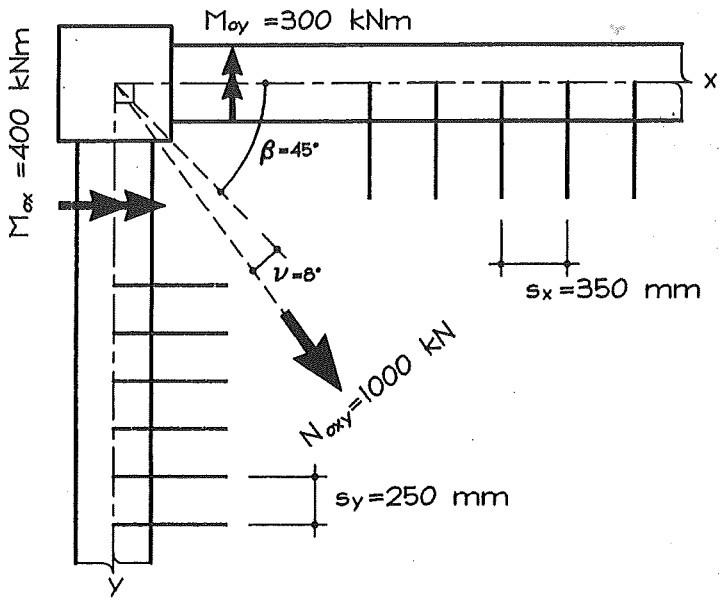

Fig. 2.31 Resistance to plastic hinge bending moments at the intersection of beams through the shear friction developed by starters along construction joints

2.3.2 COMPRESSION FIELD IN A SIMPLE DIAPHRAGM

2.3.2.1 General

As discussed in Section 1.3.2.2, all floor diaphragms may be subjected to a degree of simple diaphragm action and possibly transfer actions. With regard to simple diaphragm actions, there are two forms to consider; those associated with externally applied forces (e.g., wind) and those that may be associated with body forces (e.g., seismically induced inertia forces). For design purposes, the actual mechanism of force development in simple diaphragms is generally considered to be negligible. Thus, for the design of diaphragms it is usually considered sufficient to apply floor level inertia forces as uniformly distributed loads acting along one side of the structure and determine bending moments and shear forces from simple beam theory. In this way, inertia forces are treated identically to a uniform wind load applied to the windward face of a structure (Fig. 2.32). The above assumption would appear very reasonable for routine design applications. For instance, the calculation of maximum bending moments is unlikely to be much affected if inertia forces are treated as externally applied loads.

However, as it stands, a simplified model of bending and shear is not of great assistance if we are to envisage the likely path of principal strut action. Furthermore, on the assumption that a strut force of appreciable magnitude does occur, it should be consistent with boundary conditions of shear and bending moment. The simplified model would indicate that tension cord reinforcement is not critical in regions of lower bending moment, which does not agree with the formation of principal strut and tie nodes at corner columns. Consequently, a model of strut action is examined, based on development of a strut force that remains compatible with concurrent bending moment and shear.

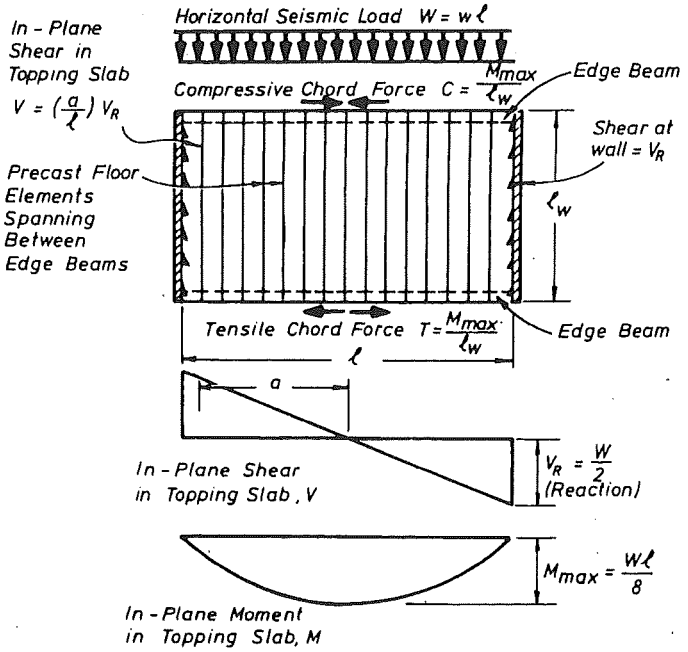

Fig. 2.32 Calculation of diaphragm actions in a cast-in-place topping slab [NZCS, 1983]

2.3.2.2 Diaphragm Strut Model

The object of the model is to obtain an effective strut force in response to concurrent bending moment and shear forces. Thus, the component of this principal strut must satisfy the concurrent conditions of bending and shear. The principal strut force is envisaged as a compression field that exists within the diaphragm plate under the effects of seismically induced inertia. The horizontal component of the strut force couples with the tension cord forces to produce bending moment equilibrium, the vertical component of the strut force produces shear equilibrium (see Fig. 2.33).

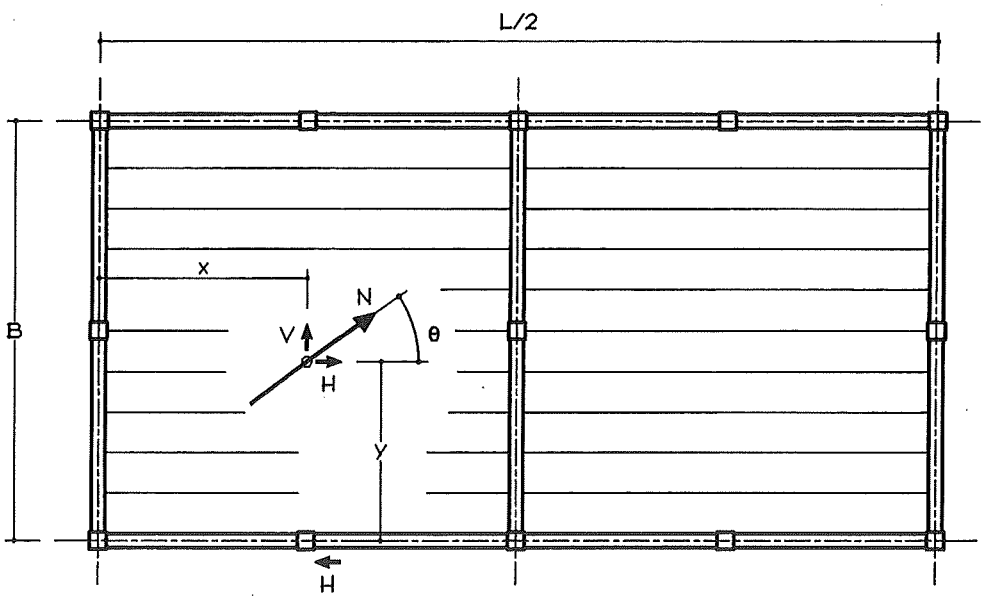

Fig. 2.33 Model used for development of an equivalent principal strut

It is reasonable to assume that bending and shear equilibrium can be achieved through the action of an equivalent principal strut field. For example, the tension forces in the tension cord will form a moment couple with the nearest component of compressive reaction from where an equal and opposite force is obtainable. With the strut force taken as N, the coupling moment becomes (see Fig. 2.33):

$$M_{(x)} = N\cos\theta \cdot y_{(x)} \tag{2.59}$$

and the corresponding shear force V is:

$$V_{(x)} = N\sin\theta \tag{2.60}$$

Rearranged, the above may be written as:

$$\frac{\sin\theta}{\cos\theta} = \tan\theta_{(x)} = \left[\frac{Vy}{M}\right]_{(x)} \tag{2.61}$$

The underlying assumptions to this equation are quite straightforward, and the solution for distance ordinate y involves a first order differential equation that is easily solved:

$$\frac{dy}{dx} - \left[\frac{V\,y}{M}\right]_{(x)} = 0 \tag{2.62}$$

and may be written in terms of separated variables so that:

$$\frac{dy}{y} = \left[\frac{V}{M}\right]_{(x)} dx \tag{2.63}$$

Hence, the position and inclination of the principal strut field may be defined according to the relationship between shear and bending moment, written as a function of the distance variable, x. In the general analysis of seismic resisting floor diaphragms there are only a few important flexural cases to consider, of which the two most fundamental cases are shown (Figs 2.34). The relationship between shears and bending moments for these cases, when applied in Equation 2.63, produce elementary parabolic stress fields.

(a) Uniformly Loaded Simple Beam

$$\frac{dy}{y} = \frac{2\left(\frac{L}{2} - x\right)}{Lx - x^2} dx \;\Rightarrow\; \ln(y) + \ln\left(Lx - x^2\right) + C \tag{2.64}$$

The constant C is also treated as logarithmic, therefore $C = \ln(\chi)$ and the general solution is:

$$y = \chi\left(Lx - x^2\right) \tag{2.65}$$

To obtain a characteristic solution, a boundary condition is applied. The obvious boundary condition concerns the stress field location at mid-span, which is generally taken as the width between tension and compression cords, B. Hence, the characteristic solution is:

$$y = \frac{4Bx}{L^2}(L - x), \quad \text{and} \quad \tan\theta = \frac{4B}{L^2}(L - 2x) \tag{2.66}$$

(b) Uniformly Loaded Cantilever Beam

$$\frac{dy}{y} = \frac{2}{x} dx \;\Rightarrow\; \ln(y) = 2\ln(x) + C \tag{2.67}$$

$$y = \chi x^2 \tag{2.68}$$

Again assuming that the coupling distance is the width of diaphragm, B:

$$y = \frac{B\,x^2}{L^2}, \quad \text{and} \quad \tan\theta = \frac{2Bx}{L^2} \tag{2.69}$$

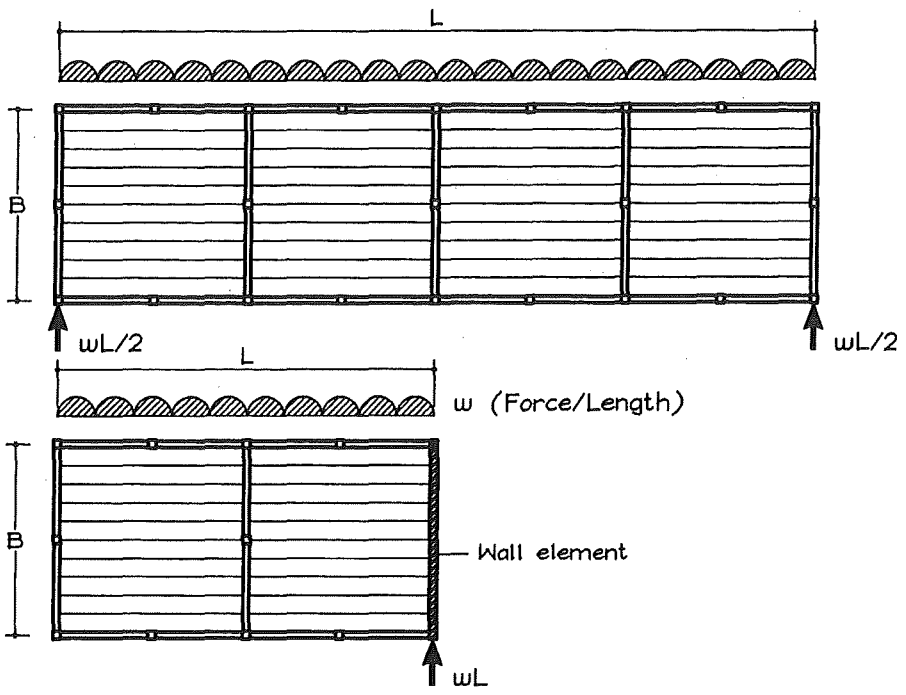

Figs. 2.34 Fundamental load cases for routine analysis of seismic resisting diaphragms

In order to assess diaphragm forces under simple response actions, information is required of inertia forces at the given floor level. Inertia force is produced by the mass-acceleration relationship at floor level, and therefore, both an estimate of effective weight and peak floor accelerations are required. The hypothetical 10-storey building configuration (see Section 2.2.1.2) has a total occupied building weight of 32000 kN. The corresponding floor accelerations $a_{(t,h)}$ result from the second derivative of Equation 2.24:

$$a_{(t,h)} = \delta_o \omega^2 \left[\zeta \omega t \cos \omega t \left(e^{\frac{-\omega^2 \alpha^2 h^\eta}{\eta}} - 1 \right) + \sin \omega t \left((2\zeta - 1) e^{\frac{-\omega^2 \alpha^2 h^\eta}{\eta}} - 2\zeta \right) \right] \qquad (2.70)$$

For the case where the number of load cycles to residual frame stiffness is N = 7, and the building is assumed to have a uniform weight of 3200 kN at each floor level (η = 1) (also see Fig. 2.8), the corresponding storey accelerations are shown in Table 2.14 and Fig. 2.35.

If the building plan is assumed to have plan dimensions of L = 25m and B = 12.5m (see Fig. 2.36), then it follows that the maximum simply supported bending moment (at level 10) resulting from the storey acceleration is 1.21 × 3200 × 25/8 = 12100 kNm. The maximum simply supported shear force is therefore 1.21 × 3200/2 = 1936 kN. From Equation 2.66, the initial strut angle at x = 0 is $\tan\theta = 2.0 = 63.4°$. Since the model requires that the cord tie force is constant along the tension cord, then the maximum strut force is 12100 kNm/(12.5 m× $\cos\theta$) = 2165 kN at x = 0. The vertical component at x = 0 is 2165 kN × $\sin\theta$ = 1936 kN, which equals the simply supported shear force, etc.

storey	$a_{(t,h)}$ (m/s²)	seismic force
10	11.88	1.21g
9	10.82	1.10g
8	9.74	0.99g
7	8.63	0.88g
6	7.49	0.76g
5	6.32	0.64g
4	5.12	0.52g
3	3.88	0.40g
2	2.62	0.27g
1	1.33	0.14g
ground	0	0g

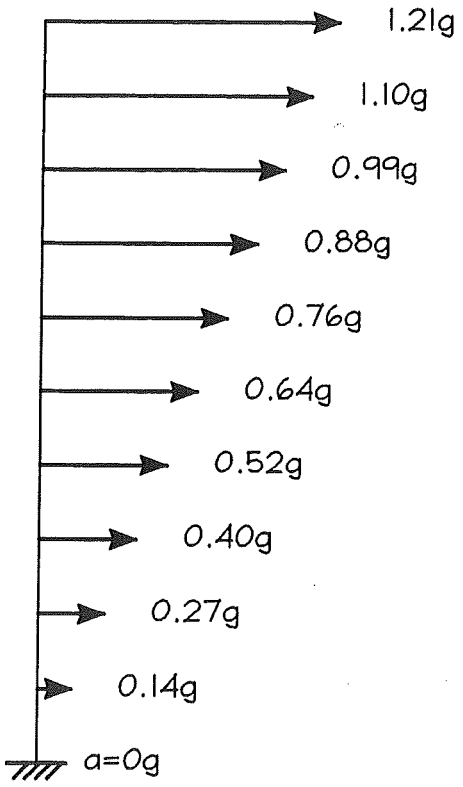

Table 2.14 & Fig. 2.35 Storey accelerations $a_{(t,h)}$ according to Equation 2.70, for hypothetical 10-storey building described in Section 2.2.1.2 with N = 7 and $\eta = 1$.

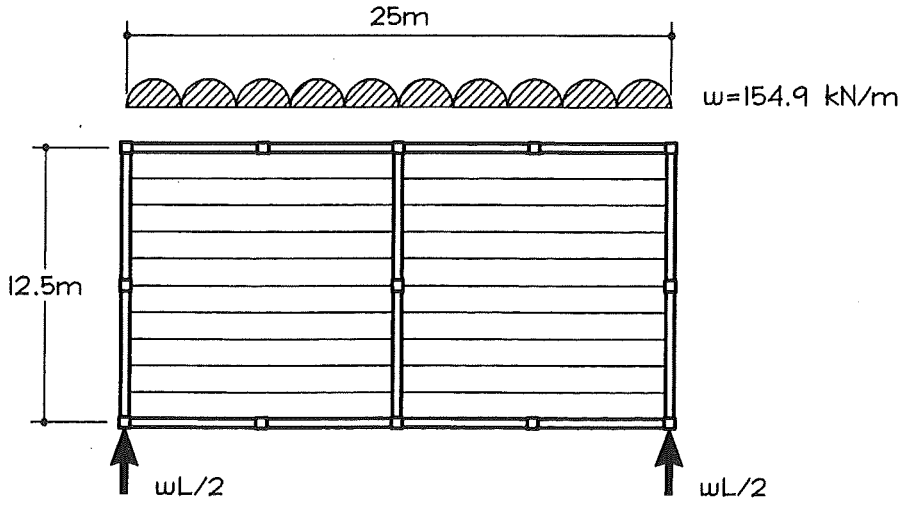

Fig. 2.36 Simple diaphragm actions at level 10 of a hypothetical 10-storey frame building

2.3.3 OPENINGS IN DIAPHRAGMS

2.3.3.1 General

One of the recognised advantages of using strut and tie methods is the treatment of openings in diaphragms. Strut and tie models allow the designer to establish viable load paths, and can be adapted to situations that involve load paths where openings occur and alternate actions may apply (see Section 1.3.2.2 and Figs 1.39 and 1.40). However, there are instances where the predominant strut or tie action is of less significance than the immediate distribution of stresses produced by concurrent bending moment and shear force. One such situation is cantilevered portions of diaphragms, described as case (b) in the preceding Figure 2.34. As shown, (Fig. 2.38) openings may occur in regions of high shear and bending without interrupting the viability of a simple principal strut field for resisting the associated forces.

2.3.3.2 Elastic Design of Beams with Openings

Since diaphragms are initially designed as elastic beam elements, it is consistent to adopt methods for elastic beams with openings. A recognised method for the analysis of slotted elastic beams is based on combined stresses with an allowance for coupling and shear effects [Young, 1989]. Referring to Figure 2.37, extreme fibre stresses are given as:

$$\sigma_a = -\frac{M_A}{Z} - \frac{V_A x I_1/(I_1+I_2)}{Z_1} \quad \text{(compression)}$$
$$\sigma_b = \frac{M_A}{Z} + \frac{V_A x I_2/(I_1+I_2)}{Z_2} \quad \text{(tension)} \qquad (2.71)$$

In these formulas, it is assumed that all forces acting to the left of line A may be replaced by an equivalent couple M_A and shear V_A at line A. The couple M_A produces stress due to bending moment in the net beam section, as provided by the first term in the equations. The shear force V_A is proportioned to parts 1 and 2 in accordance with their respective stiffness, as given by second moments of inertia, I_1 and I_2. Thus, the bending moment resulting from the shear $V_A \cdot x$ produces an increment or decrement in stress at points a and b in accordance with the respective section moduli, Z_1 and Z_2.

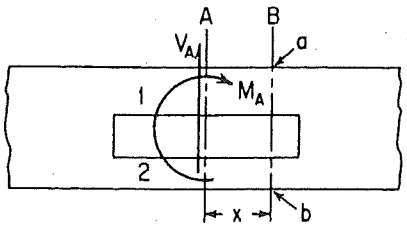

Fig. 2.37 Model of coupling and shear for derivation of Equations 2.71 [Young, 1989]

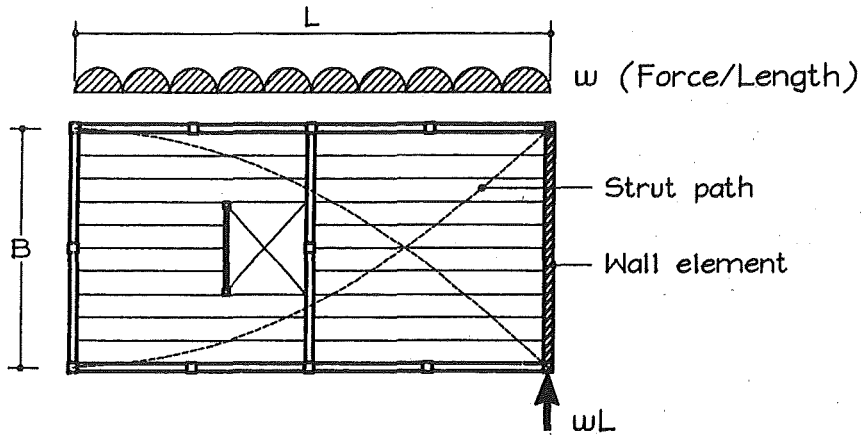

Fig. 2.38 Principal strut actions unaffected by an opening in cantilever diaphragm

The increment of extreme fibre stress caused by the above configuration is calculated in accordance with Equation 2.71. The seismic weight and storey accelerations are as assumed in the simply supported diaphragm example of Section 2.3.2.2. Likewise, the overall plan dimensions of the diaphragm are length L = 25m and width B = 12.5m. The various requisite section properties are shown in Table 2.15:

Table 2.15 Member properties of the slotted diaphragm portion in Fig. 2.38. The effective thickness of 200 hollow core plus 65mm topping is taken as 165mm

I (mm^4)	Z (mm^3)	I_1, I_2 (mm^4)	Z_1, Z_2 (mm^3)	x (mm)
32.2e12	5.15e9	2.07e12	938e6	6250

The weight over the slotted portion is reduced in proportion to the area of flooring removed. Therefore, the seismic weight per unit length of building is calculated as $1.21 \times (1 - 2.4/12.5) \times$ (3200 kN/25m) = 125 kN/m. If the slot is ignored and simple cantilever bending assumed, the bending stress at point b (Fig. 2.38) will be:

$$\sigma_b = \frac{M_b}{Z} = \frac{125 \times 12500^2}{2 \times 5.13e^9} = 1.9 \text{ MPa}$$

Incorporating the slot effect in accordance with Equation 2.71, the stress at point b is:

$$\sigma_b = \frac{125 \times 6250^2}{2 \times 5.15e^9} + \frac{125 \times 6250 \times 6250 \times 1/2}{938e^6} = 3.1 \text{ MPa}$$

Hence, in an elastic diaphragm, the slot effect increases bending stresses by more than 60% and approaches the concrete modulus of rupture at point b.

2.4 DISCUSSION

2.4.1 GENERAL

In this chapter, a number of analytical methods have been developed to assist with the rationalised design of structural frames and floor diaphragms. With the developed models, emphasis has been placed on relatively tangible concepts that recognise plasticity effects on building seismic response and member compatibility functions. As such, some exercise has been given to the subject of elastic-plastic transition and plastic hinge development in ordinary reinforced and prestressed concrete members.

2.4.2 BUILDING DEFORMATION

The solution to a partial differential equation describes the fundamental mode of deformed shape of a building frame as a function of time and building height (Equation 2.19). Essentially, the derived structural deformations are the diffused shapes of a prescribed base motion, which is displacement as a function of time. For both simplicity and relative correctness, the selected base motion has been taken as sinusoidal in the examples (Equation 2.7).

The effects of plasticity are applied to the model by use of a semi-empirical stiffness reduction coefficient based on the observed stiffness degradation of beam-column elements under cyclic loading (Equations 2.23 and 2.24). Consistent with increasing plasticity and reduced stiffness in the structure, the coefficient effectively dampens elastic response by reducing the activity of resonance terms in the transient solution. In this way, the nil resonance or steady-state response deformation of an inelastic structure is approached (Equation 2.20).

The displaced shape is described by a continuous function in both time and height. Thus, the respective velocities and accelerations (Equation 2.70) are obtained by differentiation with respect to time. Likewise, differentiating with respect to height (Equation 2.25) approximates the beam-column rotation at storey level; noting that the displaced shape describes the relative displacements between storey levels and not the curvature of columns.

The natural period of structure does not feature in the analysis, since response is derived from inertia forces that react against directly imputed ground motion. Consequently, the geotechnical aspect of site-specific input motion is more relevant to the model than an assumed natural period of vibration. Yet, although from a differing perspective, the outcomes generally concur with those of traditional dynamic (harmonic) analysis. As a preliminary design tool, it is considered that the model would best be applied to compare response at both the upper (critical displacement) and lower (critical acceleration) bounds of natural period that characterise a structure (i.e., a response period envelope).

For example: considering two sinusoidal input ground motions of equal accelerations, one of short period and small amplitude motion, the other of long period and large amplitude. It is assumed that periods, displacement amplitudes and acceleration are interrelated by the expression: $\delta = a\,(T/2\pi)^2$. The following observations result from the various equations:

- At equal input accelerations; the response accelerations resulting from short period ground motion are significantly higher than for long period ground motion, but the corresponding structural displacements are small. Hence, the model suggests that a structure subjected to distinct short period ground motion (generally mitigated in real structures by damping) is more susceptible to shear failure at foundation level than structural damage at higher levels.

- Long period ground motion results in lower response accelerations but larger structural displacements, suggesting that long period ground motion is synonymous with larger inter-storey deflections and ductility demands.

With regards to variations in initial structural stiffness and stiffness degradation due to plastic deformation, the following are observed from the model for structures of equal mass:

- Structures with a large initial stiffness tend towards small response accelerations and displacements. Hence, rigid ground block motion is approximated by very stiff structures.

- Initially stiff structures are influenced to a lesser extent by stiffness degradation than flexible structures.

- Flexible structures may be concurrently subjected to significant response accelerations and displacements, especially if stiffness degradation requires an appreciable number of load cycles.

- For effective damping of resonant elastic response by plasticity mechanisms, the early occurrence of stiffness degradation is significantly more effective than the actual degree of degradation. Hence, judicious and well-distributed placement of ductile fuse mechanisms would appear beneficial in flexible structures.

General conditions that are implicit in the model:

- The fundamental pattern of displacement response is governed by the vector components (i.e., direction and amplitude) of input ground motion.

- Resonant response is governed by the velocity components of input ground motion.

2.4.3 EQUIVALENT FLEXURAL RIGIDITY (EI*)

The equation for equivalent flexural rigidity (Equation 2.40) is a rigorous derivation of the flexural stiffness response of concrete members through the elastic-plastic transition. Hence, the equation provides reasonable estimates of rigidity values for plastically deformed members under varying load conditions. As such, the stiffness variations of critical members in a typical elastic analysis may be modified on a rational basis.

For members subjected to simply supported bending moments, the variation in equivalent flexural rigidities of a prestressed tee and reinforced beam are indicated by Figures 2.39 and 2.40 respectively.

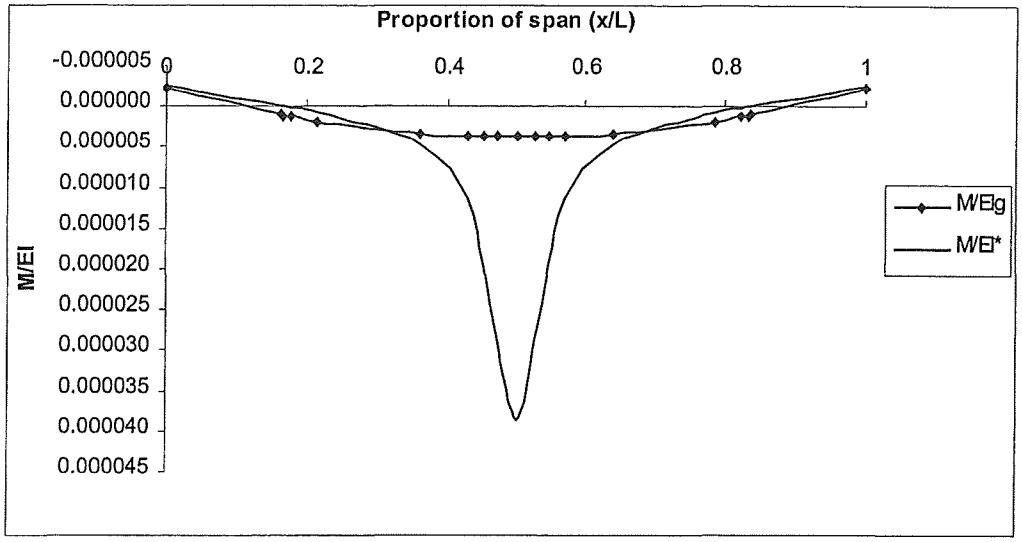

Fig. 2.39 Relationship between simply supported bending moment and flexural rigidities EI_g (gross section) and EI* (Equation 2.40) for prestressed tee beam (see Fig. 2.16) at a mid-span concrete compressive strain of $\varepsilon_c = 0.003$.

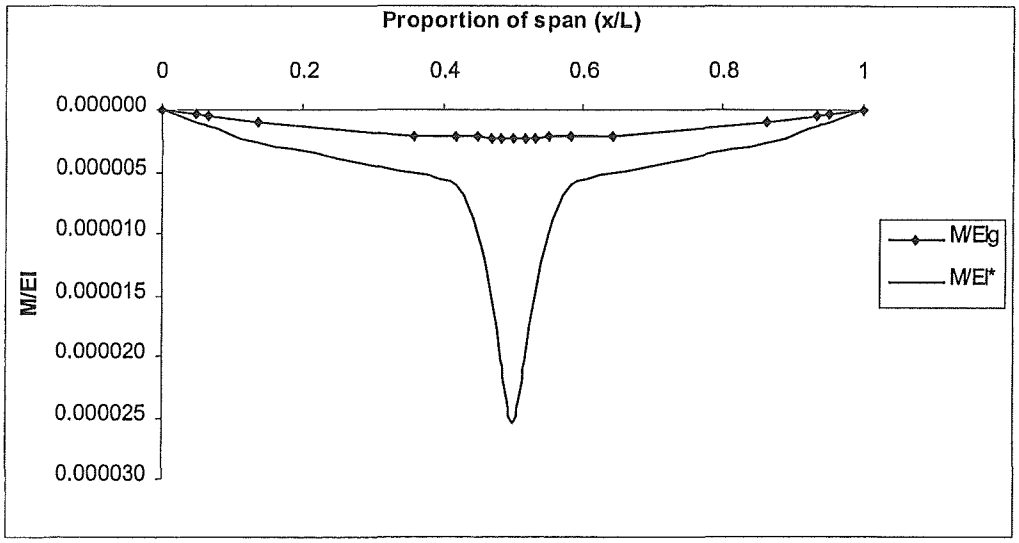

Fig. 2.40 Relationship between simply supported bending moment and flexural rigidities EI_g (gross section) and EI* (Equation 2.40) for reinforced beam (see Fig. 2.18) at a mid-span concrete compressive strain of $\varepsilon_c = 0.003$.

2.4.4 PLASTIC HINGE ROTATIONS AND COMPATIBILITY

An equation for equivalent plastic hinge length (Equation 2.52) has been derived for the purpose of estimating compatible rotations in sway members. For ductile beam members that incorporate boundary elements of pretensioned flooring, the compatibility equations (Equations 2.53 to 2.55) indicate that increased effective beam lengths are required to achieve prescribed levels of rotation at limiting values of concrete compressive strain.

Based on the above, reasonable estimates can be made regarding the compatibility of beam-column joint rotations with the development of beam plastic hinges within an effective span length. Hence, preliminary design may be approached from the point of view of maintaining beam rotation compatibility with a prescribed displaced shape of structure.

2.4.5 PLASTIC HINGE LOCATION AND DILATION

Practical aspects are discussed, relating to the likely effects of flooring member configuration and local reinforcement detailing on the development of beam plastic hinges. Further consideration is given to the ability of details to maintain composite action.

2.4.6 DIAPHRAGM FORCES

Equations are presented for practical detailing of diaphragm boundary elements to resist the various forces that may develop during a severe earthquake. The equations provide consideration of:

- The distribution of starter reinforcement along floor construction joints to resist, in shear-friction, the reactions derived from couple forces in the floor plane. The couple forces are those derived from concurrent bending actions at beam-column joints (nodes). (Equation 2.58).

- The geometric developments of principal strut actions in common diaphragm elements (Equations 2.66 and 2.69) that are compatible with boundary assumptions. The described strut geometry is a means of determining the viability of force transfer.

2.4.7 DIAPHRAGM OPENINGS

A calculation method is presented (Equation 2.71) for estimating the effects of openings on flexural stresses generated at extreme tension fibres of elastic diaphragms.

3

Loss Of Support (LOS) Tests

3.1 GENERAL

One of the fundamental aims of this research project is to establish the ability of support tie details to withstand displacements caused by the effects of frame dilation. Hence, an important initial criterion is to determine the performance of contemporary support details. Without doubt, the most common form of support tie detail used when composite topping is placed involves simple starter bars. This type of detail was discussed in Sections 1.2.3.3 and 1.2.3.4, where it was also noted that there is no documented evidence that starter bar details can provide ductile tie capacity. Hence, the inaugural part of the experimental programme has been mainly directed at ordinary starter bar details subjected to dilation effects.

3.2 TEST METHODOLOGY

3.2.1 GENERAL PROCEDURE AND SUMMARY OF TEST SPECIMENS

To remain consistent with the earlier experiments of Mejia-McMaster and Park, the same basic methodology of testing was adopted. As such, the general emphasis of testing is to apply an axial tension force across the support interface so to extract the flooring unit from its seating. In this way, an effective force causing elongation is applied directly to the flooring unit and resistance to this force is provided by reinforcement details in the support region.

As discussed in Section 1.4.2.2(d), it is considered feasible that there may be sufficient accumulated elongation of plastic hinges to cause physical loss of support. Thus, in accordance with the earlier experimentation, a total axial displacement of 55 mm was adopted. This value is sufficient to give a clear loss of support (support length is generally taken as 50 mm minimum) without the beneficial effects provided to shear resistance through aggregate interlock.

On the assumption that support tie details will sustain an axial displacement of 55 mm, a vertical force can then be applied to examine residual support capacity. Perhaps the singularly most important criterion for the success of such details is residual tie capacity after the physical loss of support.

The details tested, LOS 1, LOS 2, LOS 3 and LOS 4 are summarised as follows:

Test LOS 1:
Involved a 200 mm hollow core unit with 65 mm composite topping. The support detail featured a typical configuration of 4-HD12 starter bars plus 665 hard-drawn wire mesh. The hollow core edge keys were fully integrated with the support block concrete. A superimposed load of 3.25 kPa was applied at testing.

Test LOS 2:
Involved a 200 mm hollow core unit with 65 mm composite topping. The support detail featured a special tie bar configuration of 6 HD10 hairpin ties, one grouted into each of the hollow core voids. No superimposed loads were applied at testing.

Test LOS 3 and LOS 4:
Involved a 200 mm hollow core unit with 65 mm composite topping. The support detail featured the typical configuration of starters and mesh used in LOS 1. The hollow core edge keys were debonded from the support block concrete. No superimposed loads were applied at testing.

3.2.2 DESCRIPTION OF TEST EQUIPMENT

3.2.2.1 General

Test equipment, divided into three major categories, was comprised of:

- Test specimens and associated structural support elements, which generally involves full scale concrete specimens and reinforcement to represent an actual portion of building construction.

- Actuating system that involves hydraulic rams, pumps, heavy steel reaction members and positive methods of attachment to the concrete test members.

- Electronic and mechanical componentry for the general measurement and logging of forces and displacements as derived from testing.

Of these three basic categories, the first may vary in principal with different tests. However, the equipment used for the general application of forces and the logging of results essentially remains unchanged throughout the LOS test programme. Hence, the description of structural mechanisms governing particular tests is deferred to the actual descriptions of individual tests. The basic support beam, actuating equipment and measuring apparatus is described as follows:

3.2.2.2 Precast Support Beams

A precast concrete support beam was constructed for each test (see Figs. 3.1). The fundamental beam design remained unchanged throughout the test programme. The actual reinforcement configuration of the support beam (other then attached starter bars) is not considered to have any influence on test results. The beam was designed to essentially remain uncracked

throughout the tests. Any cracks migrating into the beam section from the floor support region were intercepted by sufficient principal and shear reinforcement to prevent them from becoming significant.

Provision was made for locating sole plates attached to 250 UC 73 steel reaction members by bolting through the beam section. To achieve cyclic loading capacity (tests LOS5 and LOS6), this detail was enhanced by adding two extra bolts to each sole plate and matching anchor plates on the opposite face of the precast support beam.

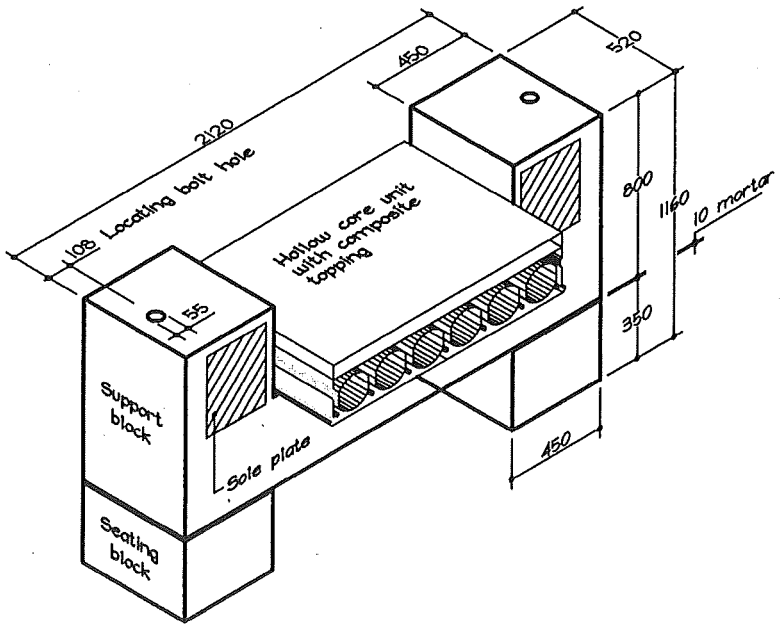

Fig. 3.1(a) Detail of precast concrete support beam and seating blocks

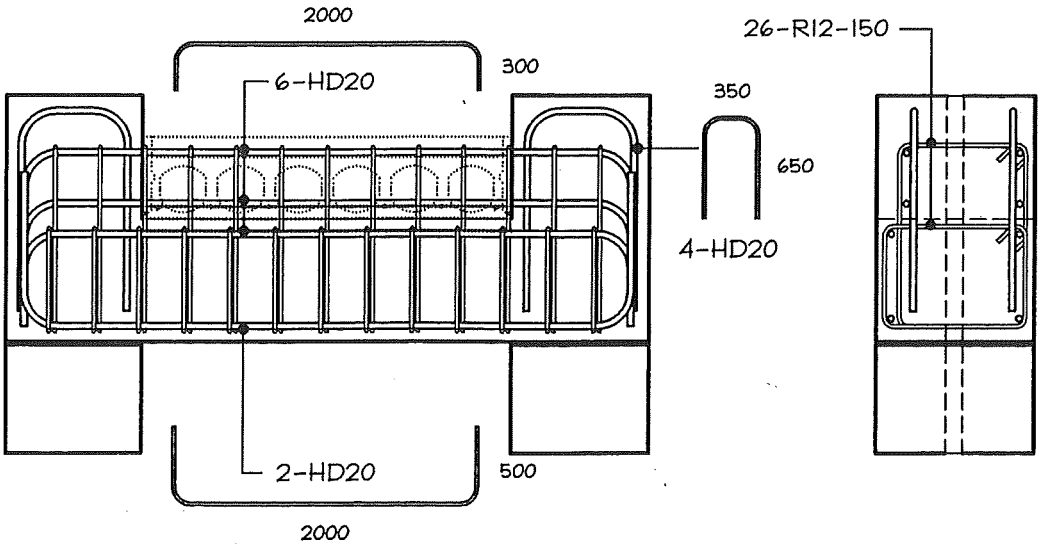

Fig. 3.1(b) Reinforcement details of precast support beams

3.2.2.3 Horizontal Displacement

(a) Actuating System

Horizontal displacement was applied to the test specimens by two parallel acting hydraulic rams, each rated at 43 tonnes (see Figs 3.2). These rams were attached directly to the support beam blocks, were self-equilibrating and had no reliance on external reactions. At the other end, the rams were each connected to a hinging carriage that permitted both horizontal and rotational displacements. In each case, hydraulic pressure was applied to the rams by two identical hand operated pumps acting in unison.

The hollow core flooring unit was secured onto the support carriages by two 310 UC 97 beams placed above and below the precast section, and bolted to it by eight 24 mm diameter threaded rods. The threaded rods were incorporated into the section by filling the adjacent hollow core voids with topping concrete, over a distance of 600 mm from the end of the member. Additional reinforcement was placed at the topping interface, sufficient to develop the resulting horizontal reaction force through shear friction.

(b) Measurements

Principal horizontal displacements were measured by placing two 100 mm linear displacement potentiometers near each support carriage, which connected between target plates mounted on the hollow core unit and rigidly braced uprights bolted to the laboratory strong-floor. Potential slip between the topping and precast concretes was monitored by two sets of potentiometers placed on isolated stands that were epoxied into the top flange hollow core unit (see Fig. 3.4). Further potentiometers were attached to the concrete support block to monitor movement of the test rig in relation to the floor. Force measurements were accorded by 44 tonne load cells positioned between the respective hydraulic rams and support carriages.

3.2.2.4 Vertical Force

(a) Actuating System

The provision of vertical force was made available by a vertical reaction frame supporting a hydraulic ram with 130 tonnes capacity (see Fig. 3.3). The ram acted into the floor section via a series of spreader beams. The spreader beams were each seated onto a bedding layer of either plaster of Paris or cement-sand mortar. Hydraulic pressure was provided by a hand operated pump.

(b) Measurements

Two 300 mm linear displacement potentiometers were connected to the hollow core unit near the support to measure vertical displacements. A 100 tonne load cell was placed between the vertical ram and spreader beams for vertical force measurement.

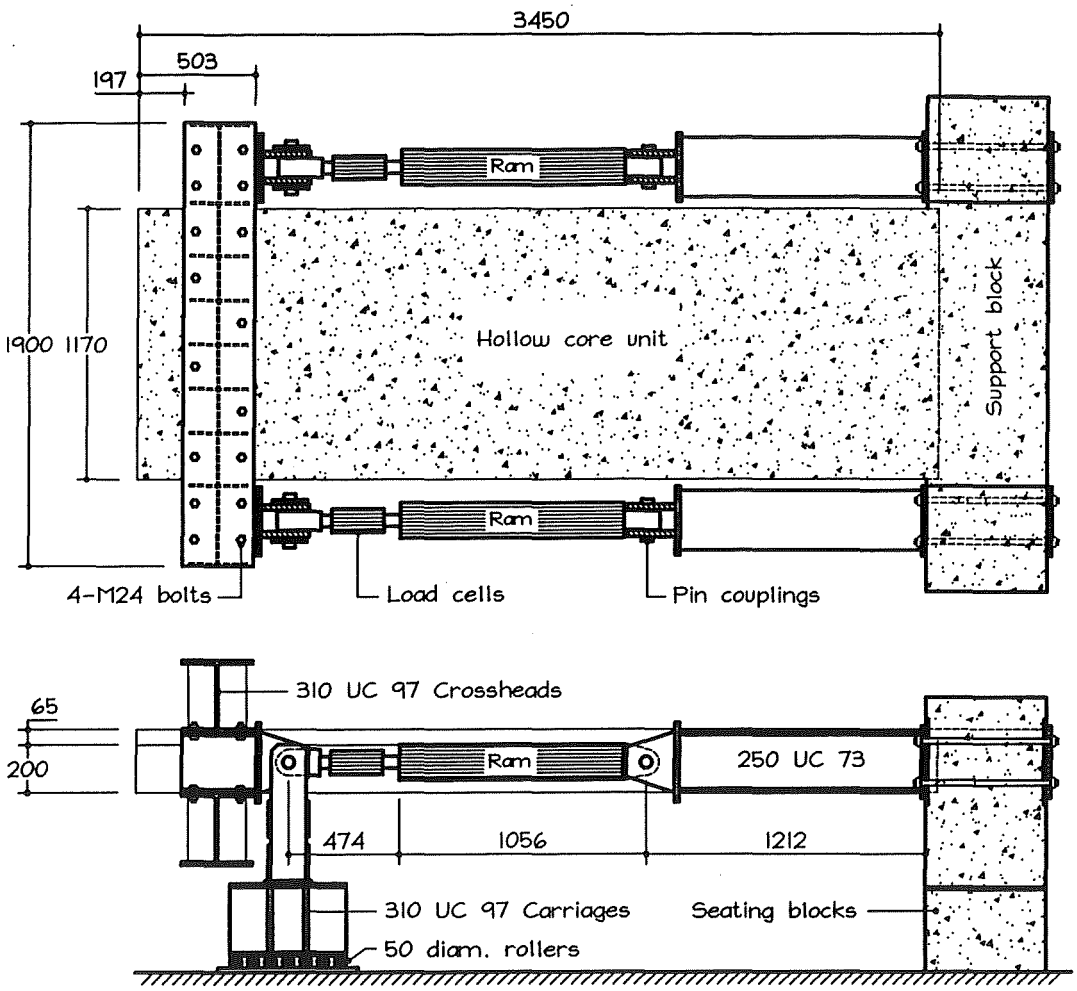

Fig. 3.2(a) Method for applying horizontal displacements

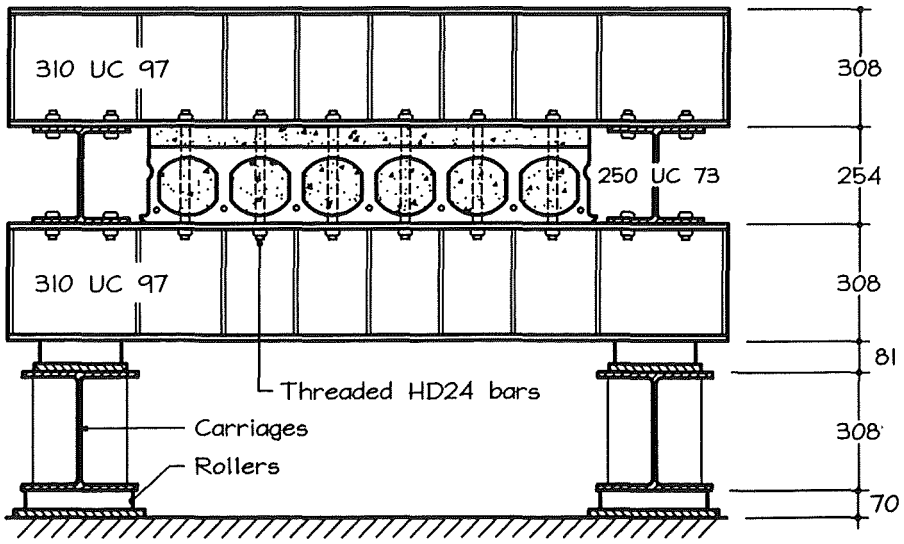

Fig. 3.2(b) End elevation of loading carriage and hollow core section

(a) Set-up immediately prior to test LOS 1

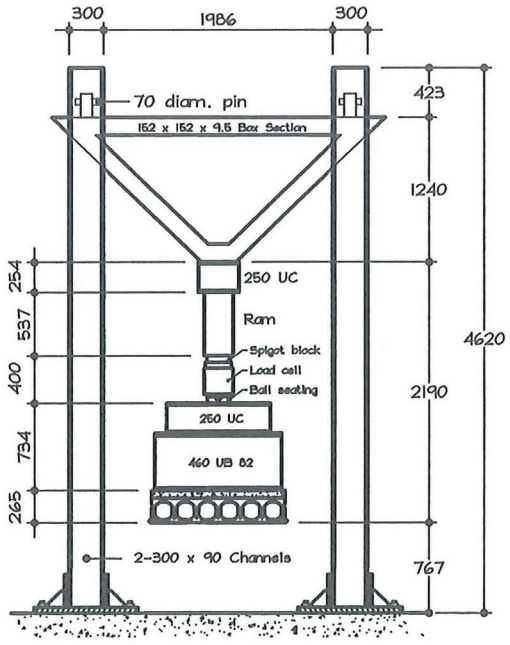

(b) Method for applying vertical force

Fig. 3.3 Test rig assembly

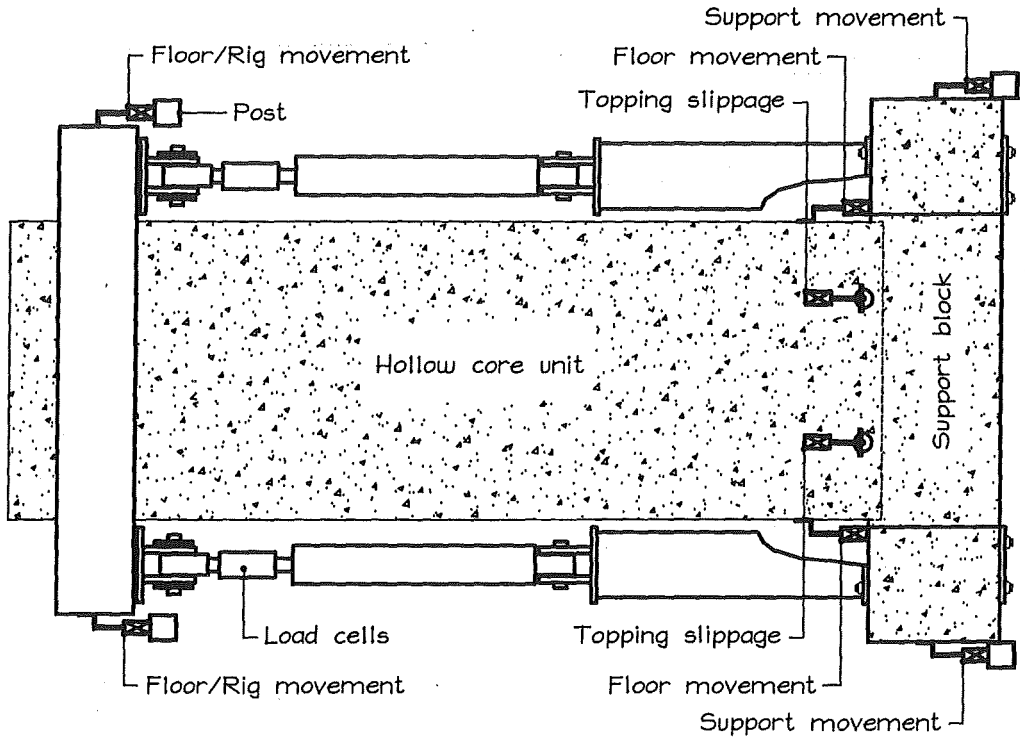

Horizontal Displacements

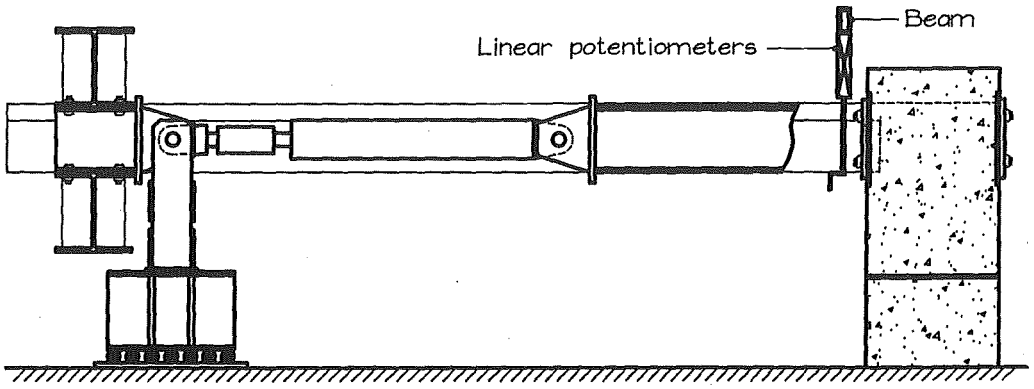

Vertical Displacements

Linear Potentiometers & Load Cells

Fig. 3.4 Methods for obtaining measurements of forces and displacements

3.2.2.5 Reinforcing Bar Strain Gauges

Electrical resistance strain gauges were connected to principal reinforcement to establish bar strain characteristics. Two types of electrical resistance strain gauges were considered for these tests. In the locations where principal cracking was expected to occur, 20% extension gauges were attached to the bar. These gauges were supplied by the Tokyo Sokki Kenkyujo Co. and were gauge type YL-5, with 120Ω resistance and 5 mm gauge length. Because of the large strain involved, a suitable adhesive is required to secure the gauge to the reinforcing bar. A recommended adhesive for use with large extensions is Armstrong A-12 epoxy. This adhesive is applied as a bedding for the gauge, and requires oven drying to achieve strength in a reasonable time frame. Previous tests at the University of Canterbury showed that 19% extensions could be attained with the YL-5 gauge [Mejia-McMaster and Park, 1994].

At bar positions away from the expected critical section, ordinary 3% extension strain gauges were used. These were supplied by Tokyo Sokki Kenkyujo Co. gauge type FLA-5-11, with 120Ω resistance and 5 mm gauge length.

Surface preparations and the method of fixing electrical resistance strain gauges was carried out in accordance with the departmental guidelines for these procedures [Hill, 1992].

3.2.2.6 Data Logger Unit

The load cells, potentiometers and strain gauges were all connected to the Metrabyte logger which converted voltage changes caused by linear displacement into digital values. These values were recorded against respective scan numbers that were manually taken throughout the tests. At the conclusion of a test, the logged information was converted to an ASCII file that was then imported into Excel (spreadsheet program) for subsequent editing and data extraction.

3.2.3 MATERIALS AND CONSTRUCTION

3.2.3.1 General

The emphasis of this experimental programme was to reflect the general performance of pretensioned floor construction. As such, no special efforts were made to embellish or unduly influence the characteristics of materials provided. As may be assumed in regular commercial construction practice, a competent manufacturer supplied the pretensioned hollow core flooring and a Special Grade batch plant supplied the topping concrete.

Subsequently, there was general avoidance of the idealised concrete construction that can result in a laboratory placing and curing environment. With regard to construction practice, it is easy to appreciate that a single precast hollow core unit set in a loading frame inside a laboratory will automatically receive more detailed attention than perhaps 50 such units as part of a typical floor layout. Hence, the construction practice adopted for the preparation of LOS tests specimens was respectful, though not of a flattering nature.

3.2.3.2 Precast Pretensioned Hollow Core Units

The hollow core units were supplied by Firth Stresscrete Ltd out of their Auckland Hollow Core Factory at Papakura. All units were standard 200 mm deep by 1197 mm wide extruded Dycore/Partek profile hollow core sections (Fig. 3.5). It should be noted that the section profile was not a criterion for selection and it is considered that the actual section profile will not have had a measurable influence on subsequent test results. The only dimension stipulated to the precasting factory was for 200 mm deep extruded pretensioned hollow core flooring units of varying lengths with clean but unroughened top flange surfaces.

Variations in prestress force was an additional requirement, namely, units with four, five and seven 12.7 mm diameter Supergrade strands. In all cases, the centre of prestress was 45 mm above the unit soffit. Inspection of the actual strand centres indicated positions that were sufficiently close to the design value so that the variation was negligible.

The hollow core units were inspected upon arrival and it was evident that they were all of good quality. The concrete matrix was dense and uniform with no indication of the type of irregularities that may result from incorrect mix design or insufficient vibration. The average strand slippage was in the order of three millimetres, which is comfortably within the acceptance criteria for the development of flexural bond strength [Anderson and Anderson, 1976] (see Section 1.2.2.1).

From data provided by the precasting factory, the hollow core units were released from the casting pallet at a concrete compressive stress of around 35 MPa (as indicated by impact hammer) and had a design concrete compressive stress of 45 MPa.

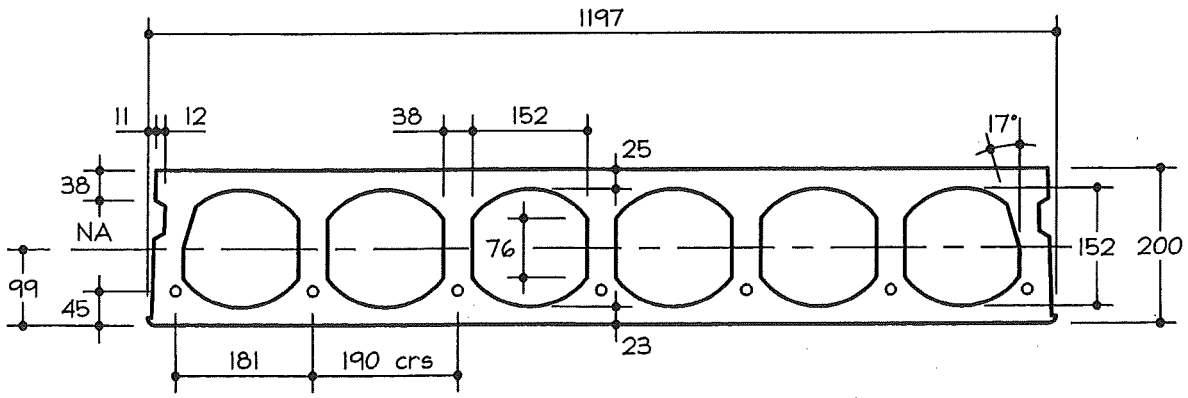

Fig. 3.5 Section profile of hollow core of units incorporated in the LOS test programme

3.2.3.3 Prestressing Strand

The hollow core units were pretensioned with 12.7 mm diameter Grade 1860 strands supplied from Australia by BHP Industries. Strand of the LRSS type (ie., low relaxation, stress relieved, super-grade) directly complies with the requirements of the New Zealand standard [SAA, 1987], and is probably the most common source of pretensioning strand used in New Zealand at present.

The mechanical characteristics of strand used in the precasting factory at the time the hollow core units were manufactured is as follows (Table 3.1 and Fig. 3.6):

Table 3.1 Mechanical properties of prestressing strand used in the manufacture of hollow core test specimens

Coil Number	Cross section area (mm^2)	Proof Load (0.2%) (kN)	Ultimate tensile strength (kN)	Strain at Fracture (%)
3506	98.4	190	200	5.5
3532	99.2	189	198	5.0
3533	99.2	189	198	5.0

Average E = 196 GPa

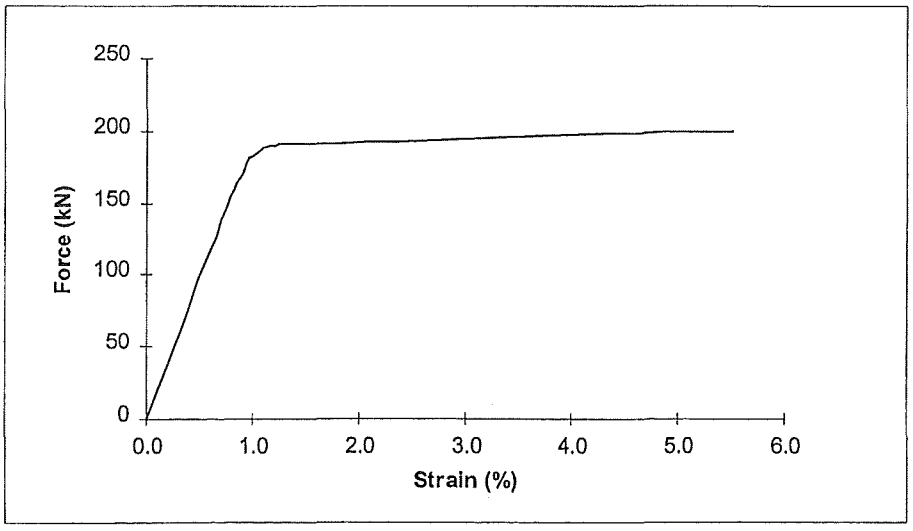

Fig. 3.6 Typical stress-strain characteristics of prestressing strand employed in the manufacture of hollow core units that were subsequently used in the LOS test programme

3.2.3.4 Cast-In-Place Topping Concrete

Because the LOS series of tests would involve direct tension applied to a built-up floor section, some care needed to be exercised in relation to specifying concrete compressive strength within a testing time frame. The most important consideration was that concrete tensile strength will generally develop at a slower rate than compressive strength. Hence, it was concluded that concrete with a target compressive strength higher than may normally be used should be applied as cast-in-place topping. This measure was adopted to ensure that a reasonable magnitude of topping tensile strength would be exhibited at testing.

Obtaining the actual direct tensile strength of concrete at testing was not considered because of the difficulty in establishing this value with certainty. Hence, the result would be meaningless in the context of general floor construction. Furthermore, it was expected that topping cracks would occur during testing and that micro-cracks would have already developed at an earlier stage due to typical shrinkage effects.

In accordance with recommended construction practice, the top of the hollow core unit was lightly dampened before the topping was placed. In order to ensure sufficient moist curing of the topping concrete, wetted hessian cloth was applied to the slab area for at least five days after casting. For each specimen, a minimum of three representative concrete test cylinders were cured in the same environment, adjacent to the topping slab.

The actual descriptions of topping concrete that was specified and tested are deferred to the reporting of individual LOS tests.

3.2.3.5 Reinforcing Steel

(a) Starter and Tie Bars

12 mm diameter Grade 430 (HD12) starter bars and 10 mm diameter Grade 300 (D10) tie bars complying with the appropriate New Zealand standard [Standards New Zealand, 1989] were supplied cut and bent from recognised reinforcing steel merchants. Specifically manufactured for use in ductile seismic resisting structures, the New Zealand standard specifies that these steels must exhibit minimum elongation capacities of 15% and 20% respectively before fracture. Subsequent tensile tests indicated that all reinforcement met with these requirements (see Fig. 3.7). The actual tensile characteristics of starter and tie reinforcement are deferred to individual LOS tests.

(b) Welded Wire Fabric (Mesh)

665 mesh (5.3 mm diameter) complying with the appropriate New Zealand standard [Standards New Zealand, 1975] was supplied by recognised reinforcing steel merchants. A minimum elongation capacity for hard drawn wire mesh has not been a feature of the New Zealand standard. Earlier tests conducted on 665 mesh [Mejia-McMaster and Park, 1994] indicated that

hard drawn wire mesh exhibited very poor elongation capacity, with an average of only 2.7% elongation over a 50 mm gauge length before fracture.

Tests were conducted on mesh used in the LOS programme with elongations based on 100 mm gauge lengths (see Table 3.2 and Fig. 3.7). Although the extensions so obtained were greater than those obtained by Mejia-McMaster and Park, they are still very small when placed in context with the requirements of ductile design. It is immediately evident that hard drawn wire mesh will exhibit no more than one third the elongation capacity of ductile reinforcing bars which are manufactured to the New Zealand standard.

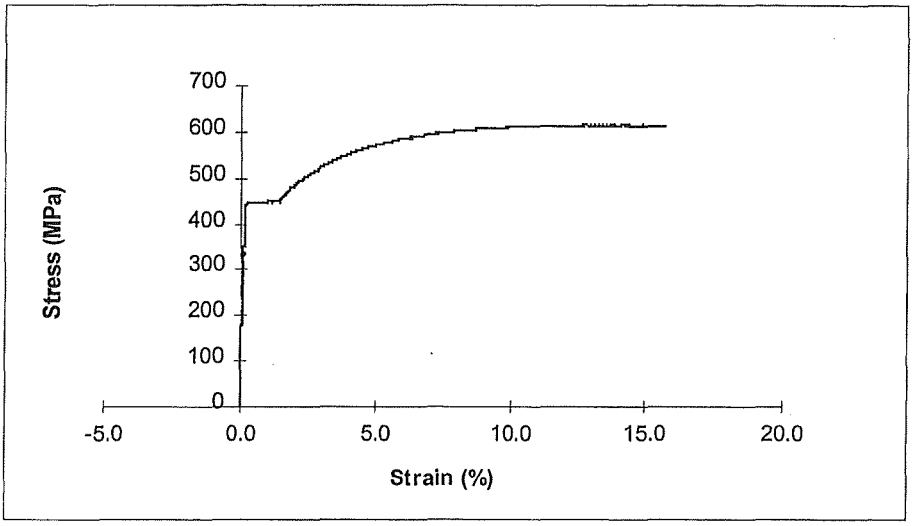

Fig. 3.7 Typical stress-strain relationship of 12 mm diameter Grade 430 bars employed as starters in the LOS test programme

Table 3.2 Characteristics of 5.3 mm diameter (5 gauge) hard drawn wire comprising the 665 mesh used in the LOS test programme

665 Mesh Specimen	Proportional Limit (MPa)	Ultimate tensile strength (MPa)	Strain at Fracture (%)
1	529	657	6.4
2	532	671	4.1
3	523	648	5.6
average:	528	660	5.4

Average E = 196 GPa

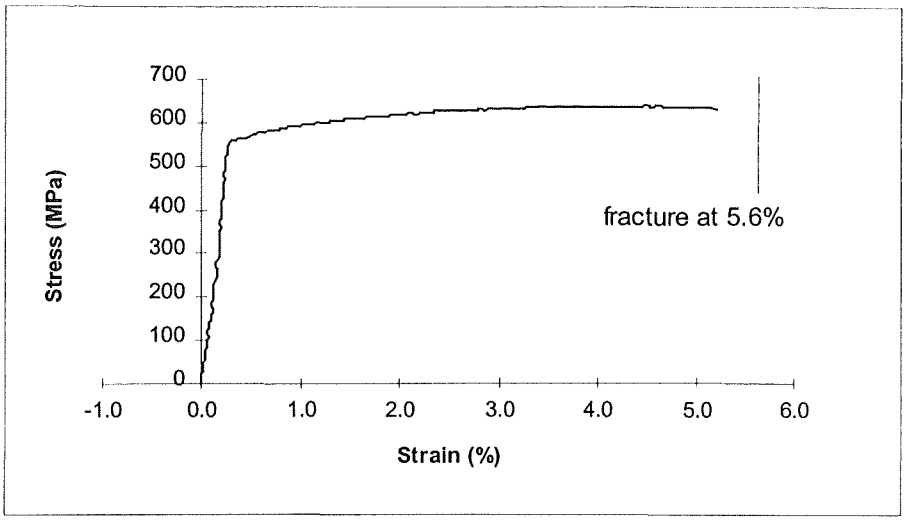

Fig. 3.8 Typical stress-strain relationship of 5.3 mm diameter (5 gauge) hard drawn wire comprising the 665 mesh used in the LOS test programme

3.3 RESULTS OF EXPERIMENTS

3.3.1 LOS 1

3.3.1.1 General

The initial LOS test was directed at the typical starter bar detail (Figs 3.9 and 3.10). The floor configuration involved 65 mm of cast-in-place topping over a 200 mm hollow core extruded flooring unit that was pretensioned with five 12.7 mm diameter Supergrade strands. A total of four 12 mm diameter Grade 430 (HD12) starter bars were placed at 300 mm centres, and extended 600 mm into the topping slab. 665 mesh was placed over the hollow core unit, and was continued beyond the end of the seating length, thus contributing to the tensile strength across the construction joint (assumed to be the critical section).

The mechanics of this detail clearly depend on the development of horizontal shear strength between the precast unit and composite topping concretes. For this detail to successfully perform under dilation type loading, the shear strength developed at the interface of concrete surfaces must at least match the full tensile strength of starter bar reinforcement.

The initial assumption with regard to composite bond capacity was based on the composite bond strength of chapter eight (ie., Composite Concrete Flexural Members) of the then current (June 1994) New Zealand design standard [SANZ, 1982]. Section 8.4.1.4 of this document states that "When ties are not provided, but the contact surfaces are clean and intentionally roughened, permissible v_h = 0.55 MPa. Allowing an overstrength factor of 1.25 for reinforcement, and considering a development length l_d that is 100 mm shorter than the embedment length (ie., 500 mm), the design horizontal shear stress corresponding to one starter was calculated as:

$$v_{\tau h} = \frac{f_{su} A_s}{\phi s \ell_d} \quad \text{and} \quad v_h \geq v_{\tau h} \tag{3.1}$$

Based on the above properties and dimensions, the calculated horizontal shear stress becomes: (1.25 × 430) × 113/0.75 × 300 × 500 = 0.54 MPa < 0.55 MPa. Hence, a literal interpretation of "permissible horizontal shear stress" would suggest that starter bar forces could be resisted by this mechanism. Note that the tensile contribution of mesh does not need to be considered in the numerator of Equation 3.1. This is because the mesh is continuous throughout the topping, enabling it to develop tensile strength independently of the interface shear mechanism.

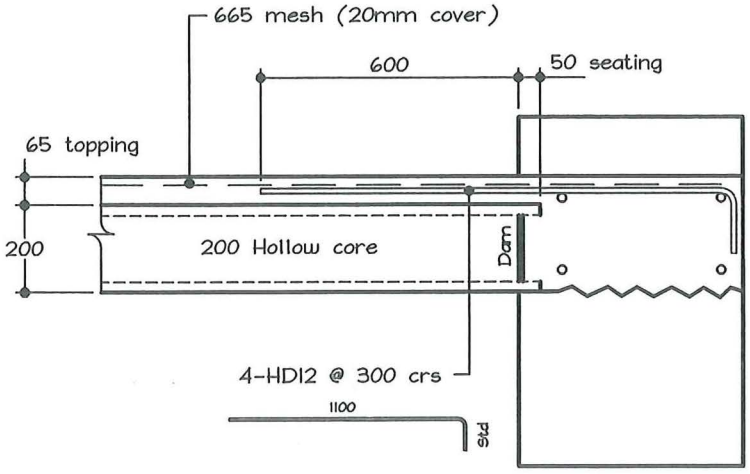

Fig. 3.9 Support configuration of LOS tests that involved typical starter bar details

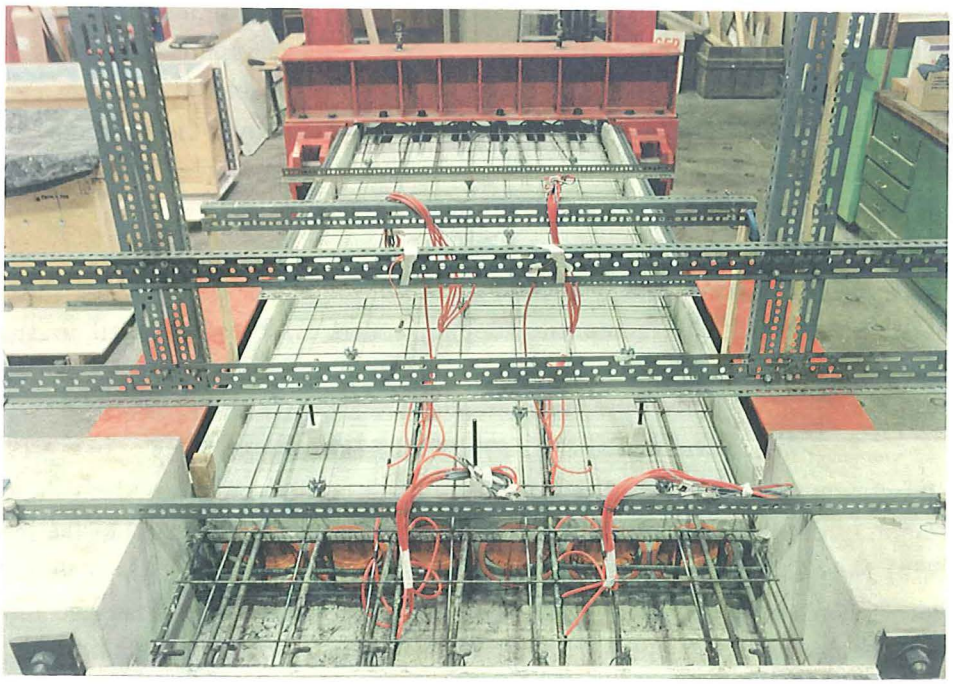

Fig 3.10 Typical LOS test set-up before the addition of topping concrete

3.3.1.2 Instrumentation

(a) Forces and Displacements

Forces and displacements were measured in accordance with the methods described in Section 3.2.2 (also Fig. 3.4).

(b) Reinforcement

Both 20% and 3% extension electrical resistance strain gauges (as described in Section 3.2.2) were employed on two individual items of starter reinforcement. These gauges were configured so that the 20% extension varieties were situated directly over the expected plane of cracking, at the end of the hollow core section and 50 mm into the support block. The 3% strain gauges were set at 100 mm centres about the expected cracking zone (see Fig. 3.11).

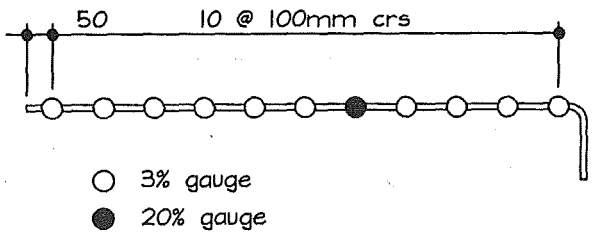

Fig. 3.11 Strain gauge positions on starter bars used in the LOS test series

3.3.1.3 Cast-In-Place Topping Concrete

Some difficulty surrounded the supply of concrete at the specified slump of 100 mm. The initial delivery was measured at 160 mm, which was outside the snatch sample upper tolerance value of 140 mm. The replacement delivery was measured at 60 mm slump, and was accepted as just inside the minimum tolerance level of 60 mm (see Table 3.3). Although this slump was just within tolerance and was accepted for casting over a single specimen, it is unlikely that this slump could have been used on a construction site without the addition of a workability agent.

Hence, because of the small volume of material involved and the high labour input it was possible to cast and compact this concrete to an adequate standard at 60 mm slump

Table 3.3 Characteristics of cast-in-place topping concrete for test LOS 1

Design Strength (MPa)	Max. Aggregate Size (mm)	Ordered Slump (mm)	Received Slump (mm)	Test Strength (MPa)
35 at 28 days	13	100	60	38 at 23 days

3.3.1.4 Reinforcement

(a) 665 Mesh

The characteristics of hard drawn wire mesh were identical to those described in Table 3.2.

(b) HD12 Starters

Tensile tests were performed on three specimens of 12 mm diameter Grade 430 bars, and the following was recorded (Table 3.4):

Table 3.4 Characteristics of HD12 starters used in test LOS 1

Average yield strength (MPa)	Average ultimate tensile strength (MPa)	Average strain at ε_{sh} (%)	Average strain at ultimate tensile strength (%)	Average strain at fracture (%)
445	613	1.35	12.74	20.90

Average E = 205 GPa

3.3.1.5 Results of Testing

(a) Initial Response

The initial response to horizontal loading showed a very stiff system (Fig. 3.12) that allowed only 0.27 mm of horizontal displacement at the peak load of 352 kN. The first cracks appeared across the topping above the end of the hollow core unit at 250 kN, with a maximum crack width of around 0.3 mm occurring in this region at a force of 350 kN.

(b) Fracture

At 352 kN a sudden and resonant fracture occurred, resulting in a fracture through the hollow core section along the support line, and a crack of 0.6 mm width through the topping slab at an average distance of 650 mm from the face of the support. This topping fracture was located just beyond the curtailment point of the starter reinforcement.

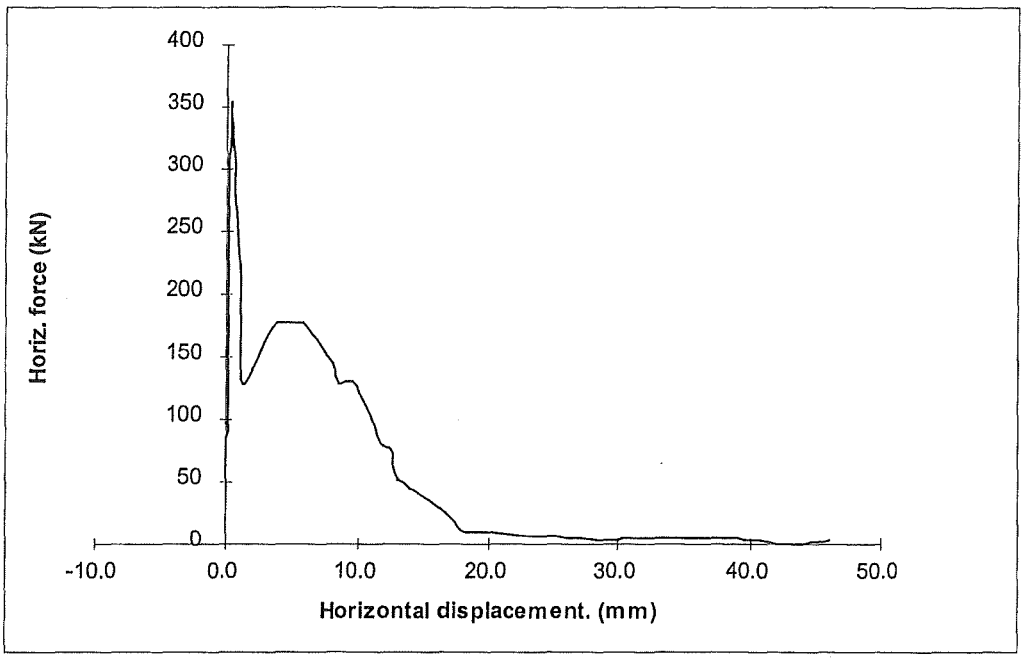

Fig. 3.12 Force-displacement response of test LOS 1

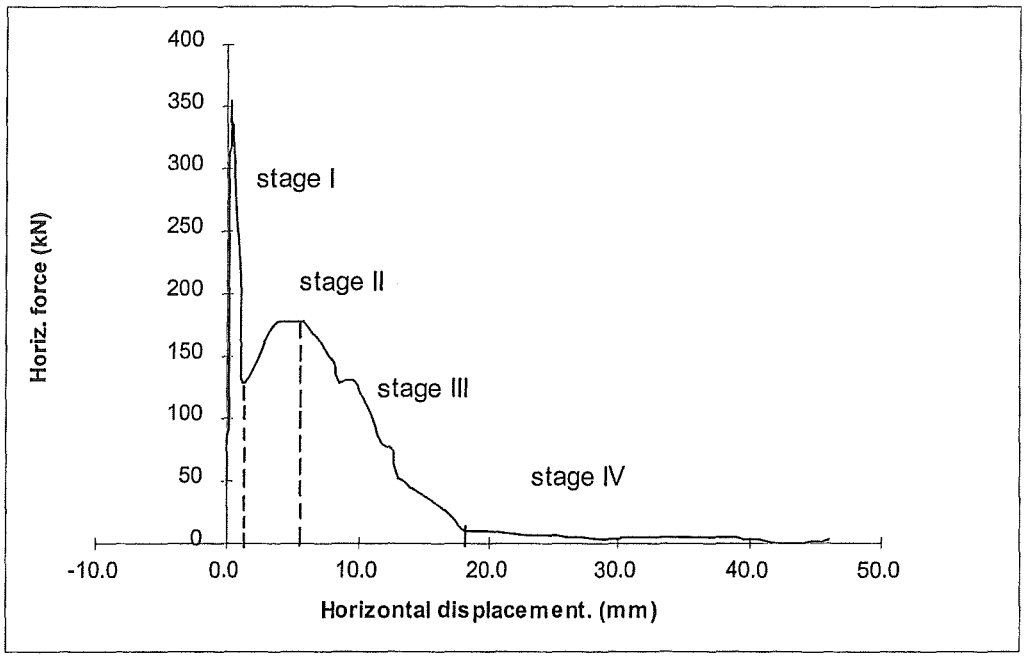

Fig. 3.13 Force-displacement diagram divided into regions of significance in terms of resistance mechanisms

From this point onwards, the whole nature of the test changed. The horizontal force dropped to 130 kN, and reached a post-fracture maximum of 178 kN at 5 mm displacement. Horizontal

restraint capacity progressively diminished, out to 18 mm displacement. Throughout this phase there was intermittent tensile fracturing of topping mesh wires. Once the restraint provided by mesh wires was completely overcome, only residual sliding friction was observed.

Although all eight mesh wires were fractured during the test, not all the wires failed along the principal crack that had developed through the topping. Three wires fractured a short distance inside the topping, away from the crack face. Assisted by the largely unaffected state of the transverse wires, this reinforcement was able to develop a degree of catenary action at the latter stages of the test. This support action tended to peel the topping slab away from the hollow unit on the mid-span side of the principal crack.

(c) Displacements

There was an instantaneous loss of bond between the precast and topping concretes at the initial point of fracture. At 18 mm displacement, this had progressed to a vertical separation of 4 mm between these elements. At 25 mm displacement, the hollow core section had dropped to 7 mm below the projection of the topping slab as a result of support concrete spalling. At 32 mm displacement, this distance had increased to 12 mm. The test terminated when the hollow core section slipped from the support at a displacement of 43 mm.

3.3.1.6 Analysis of Test Results

In order to analyse the response of test LOS 1, the force-displacement diagram has been divided into the four distinct regions that were reflected in the test outcome (Fig. 3.13). Each of these regions (i.e., stages) indicates a basic change in the resistance mechanism against imposed horizontal displacements. As a whole, the diagram clearly indicates the differing contributions of respective steel reinforcement and concrete components.

(Stage I) Peak Load and Fracture

The initial response showed an average axial stiffness of 1825 kN/mm, with resistance provided by the entire composite section. At 300 kN (ie., 85% of peak load), only 0.14 mm of horizontal displacement was registered, with topping cracks appearing across the entire unit above the interface between the hollow core unit and the support beam.

Initial cracking had appeared at about 250 kN and just under 0.1 mm horizontal displacement. This introduced a predictable tensile response in the starter reinforcement (Figs 3.17 and 3.18). As displacement increased beyond 0.1 mm towards fracture at 0.27 mm, the tensile contribution of the reinforcement continued to increase, but at a sharply decreasing rate. This is significant, and indicates that the reinforcing steel would not reach a particularly high degree of tension at the point of fracture. At peak load, reinforcement contributed to only 28% of the total measured horizontal reaction (Fig. 3.14).

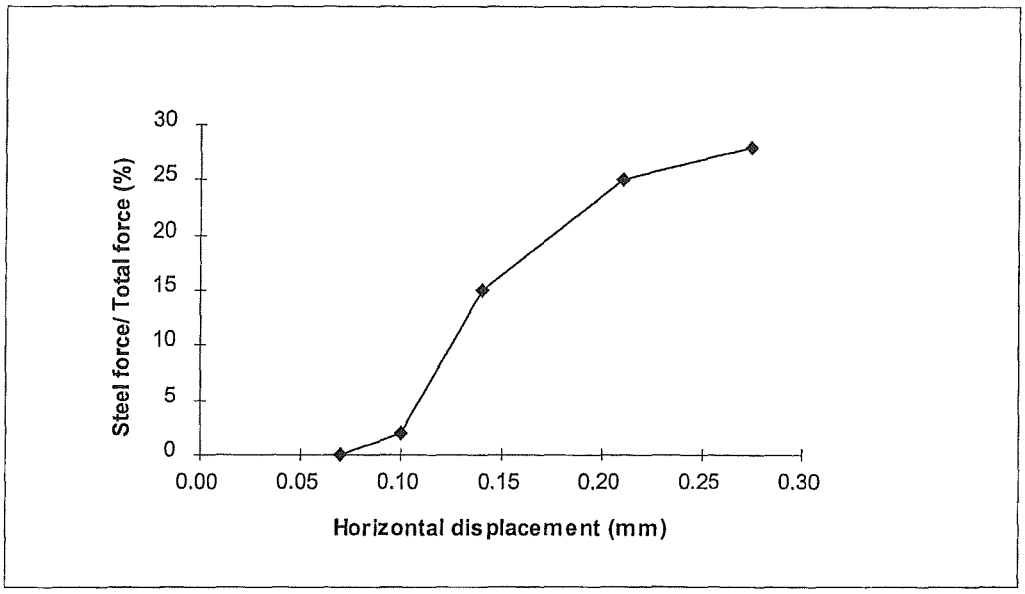

Fig. 3.14 Proportion of total horizontal force resisted by starter bars and mesh in the support region, up to sudden fracture at 0.27 mm displacement

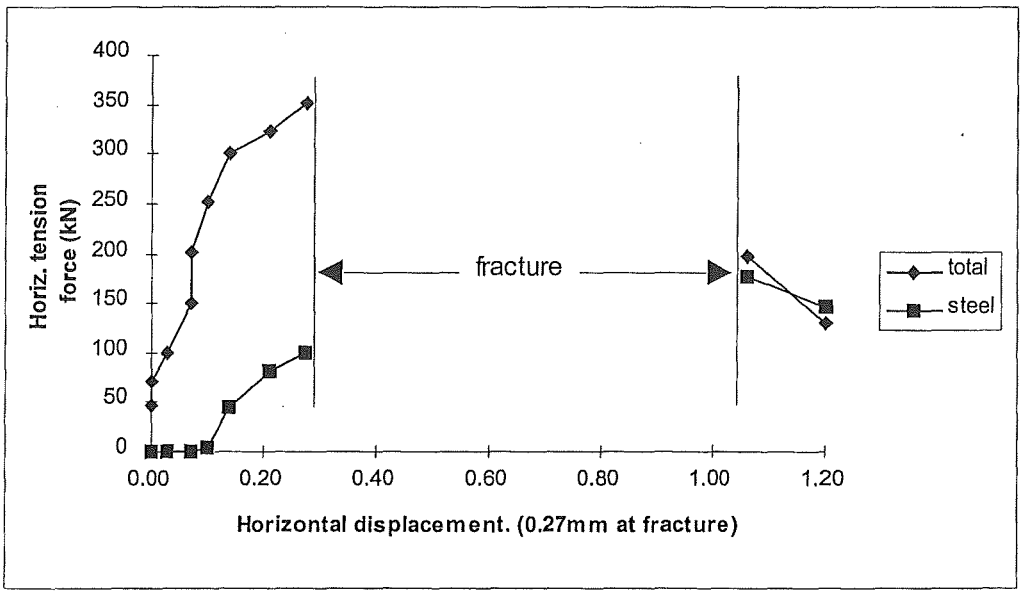

Fig 3.15 Total force and reinforcing steel force (starters and mesh) across the support region, before and immediately after sudden fracture

With reference to Figure 3.15, the force resisted by concrete alone is the difference between the total force and the force resisted by steel reinforcement. It can be deduced that an almost constant force of 250 kN was carried by the concrete section from around 0.1 mm horizontal

displacement up to fracture at 0.27 mm (see Fig 3.16). This implies that the concrete section was mobilised in a plastic manner, showing no increase in resistance under increased displacement. However, the small displacements involved may not have been sufficient to fully overcome the post-cracking tensile strength of infill concrete around the hollow core voids. It is certain that the influence of edge effects augmented as fracture displacement was approached, in particular, resistance from wedging between the sides of the hollow core unit and the support block. Analysis of Table 3.5 indicates that starter reinforcement was not the element providing critical restraint in the support region at the pre-fracture stage.

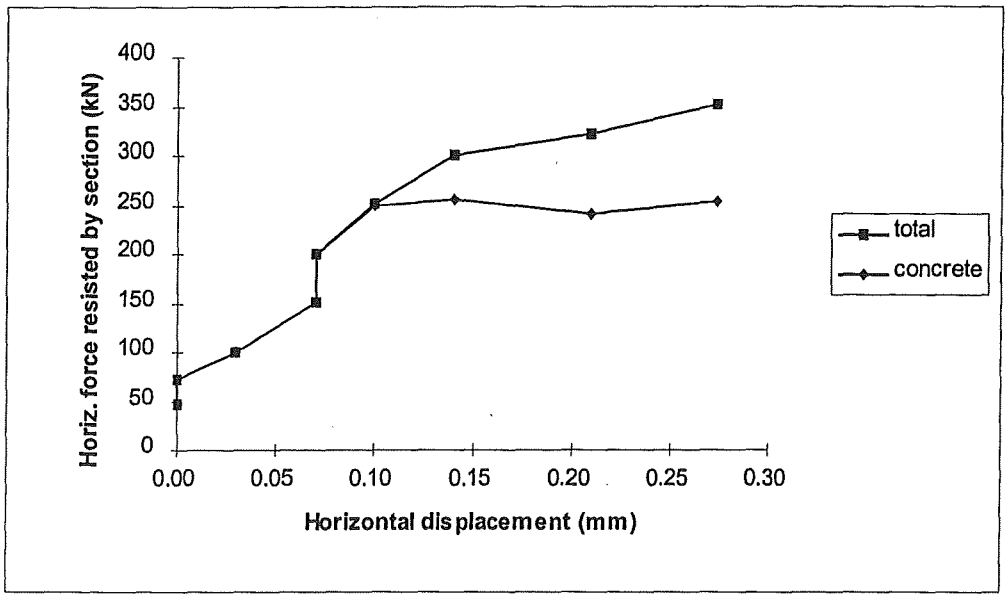

Fig 3.16 Total horizontal force and force resisted by concrete section prior to fracture

Table 3.5 The average measured tensile stresses in the starter bars and mesh over the support immediately before and after fracture

Reinforcing Element	Average stress before fracture (MPa)	Proportion of total reaction (%)	Average stress after fracture (MPa)	Proportion of total reaction (%)
HD12 starters	134	17	253	58
665 mesh	216	11	350	31
		Σ 28%		**Σ 89%**

The maximum starter bar stress at this stage of the test was 59% of the nominal yield stress of 430 MPa. The corresponding maximum stress in the mesh was 73% of the nominal proportional limit. The respective distributions of tensile stress in the HD12 starter bars and 665 mesh are shown in Figures 3.17 and 3.18, and indicate that yield stress was not approached in either the starter bar or mesh reinforcement during the decisive first stage of this test.

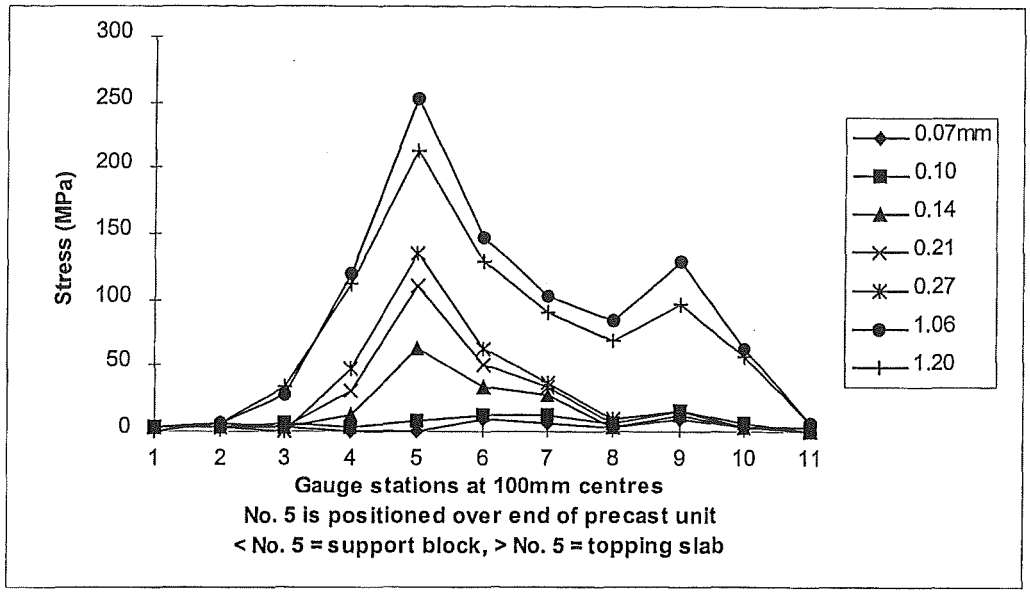

Fig. 3.17 Average stress distributions along HD12 starter bars at the indicated horizontal displacements during Stage I of test LOS 1

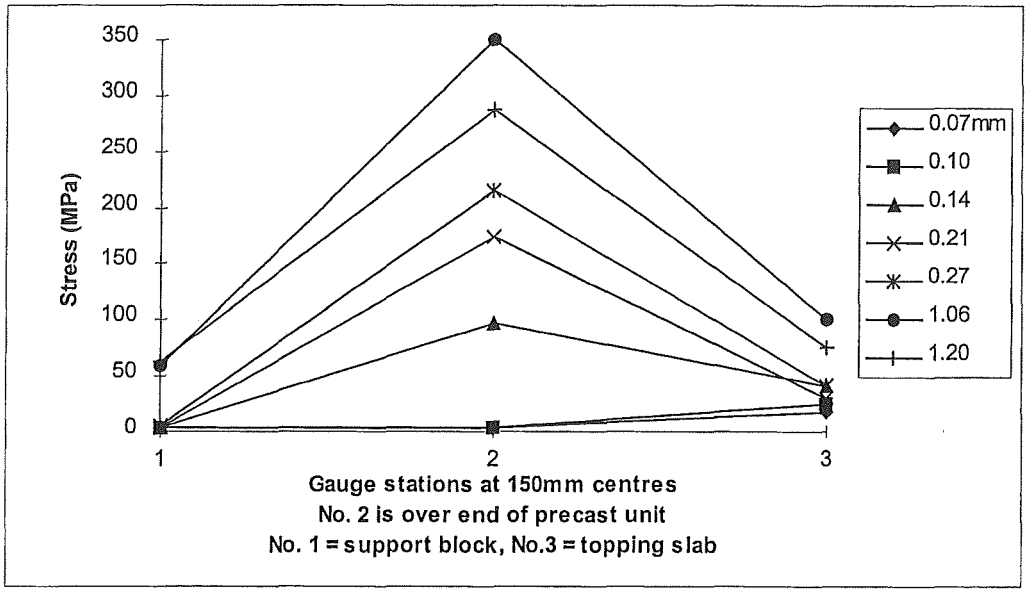

Fig. 3.18 Average stress distributions along 665 mesh wires at the indicated horizontal displacements during Stage I of test LOS 1

Figure 3.17 indicates a sudden increase in starter bar tension at gauge station number 9 after the section had fractured. This increase was due to a sizeable crack that developed through the topping slab. It is apparent that this crack was forming prior to the section fracture, as implied by the small preceding increase in bar strain.

Inspection of Figure 3.17 suggests that starter bar bond efficiency was greater in the cast-in-place support beam region than in the topping slab over the hollow core unit. This is indicated by the respective slopes of bar strain distributions on either side of the pivotal gauge station number 5.

The strength development of starter bar and mesh elements was not in proportion to their respective areas. The area of HD12 starters was 452 mm² (ie., 72% of total topping steel area) and the area of mesh was 176 mm². In the pre-fractured section, the meshed developed 40% of the total steel reaction force, decreasing to 35% of the total steel reaction after fracture. It is evident that the mesh developed proportionally greater tensile stresses than the starters, and this difference could be due to the characteristic bond efficiencies of each of these materials at small displacements.

The sudden fracture of the concrete section resulted in two principal cracks through the hollow core unit. These cracks extended through the entire hollow core section and were generally focused along the face of the support beam. The cracks started near the termination point of the concrete support beam at the edges of the hollow core unit and propagated back towards the centre-line of the hollow core section. Hence, this pattern of cracking further suggests that shear stresses were developed between the edge of the hollow core unit and the cast-in-place infill concretes (Fig. 3.19). The crack width along the line of the support was about 1.0 mm, and corresponded with the measured post-fracture horizontal test displacement of almost 1.1 mm.

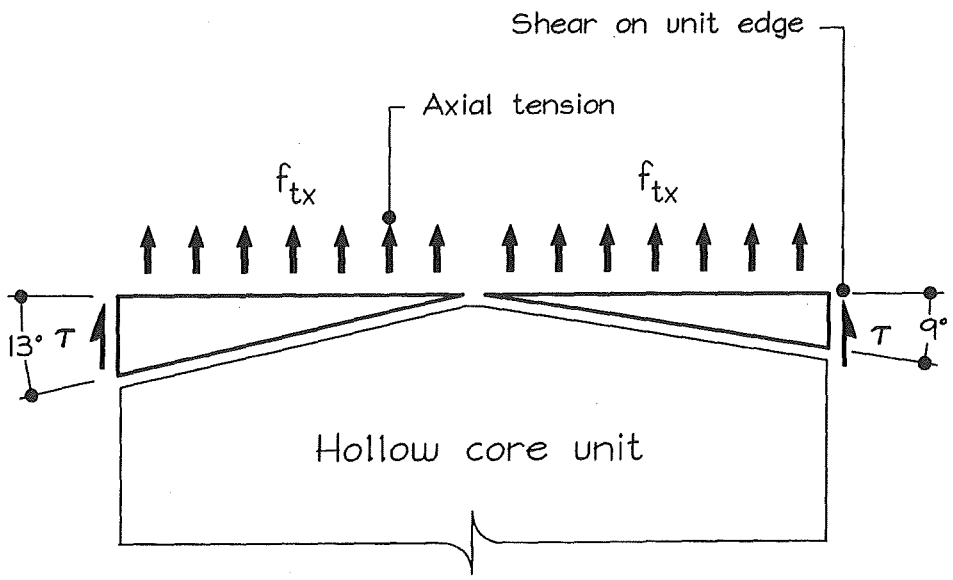

Fig. 3.19 Planes of fracture through the topping slab and hollow core section in the vicinity of the support region, as influenced by cast-in-place mortar joint

(Stage II) Post-Fracture to Post-Fracture Peak Force

From a static position at post-fracture, further horizontal displacement resulted in an increased reaction up to the post-fracture peak force of 178 kN, one half of the peak pre-fracture force. Throughout this stage of the test, resistance was provided by a complex combination of mechanisms. Although it was clear that complete separation had occurred between the hollow core unit and the support, prestressing strand stubs were still embedded in the support beam near the edges of the unit. The maximum embedment length of strand stub was 60 mm, and although pullout effects may have initiated, it is considered that the embedded stubs may have developed an appreciable tensile resistance. An amount of resistance was also developed through aggregate interlock and friction between the precast unit and the support, however, it is very difficult to estimate the magnitudes of these constituent forces.

At the end of this loading phase, the maximum developed force was mostly dependant on the integrity of mesh wires which bridged the principal topping crack, 650 mm from the face of the support (see Fig. 3.19). Assuming that the mesh wires were near their maximum tensile capacity of 660 MPa, the tensile contribution of reinforcing steel was about 116 kN, or 65% of the post-fracture peak force.

The maximum starter bar stress recorded during test LOS 1 was 292 MPa, which is two-thirds of the nominal yield stress of reinforcement. The maximum stress occurred over the support line of the hollow core unit (gauge station 5), and concurrently with the peak post-fracture force at 5.5 mm horizontal displacement (Fig. 3.20). The maximum mesh wire stress in the support region was 338 MPa, a reduction from the 375 MPa that was recorded at this location during Stage I of the test.

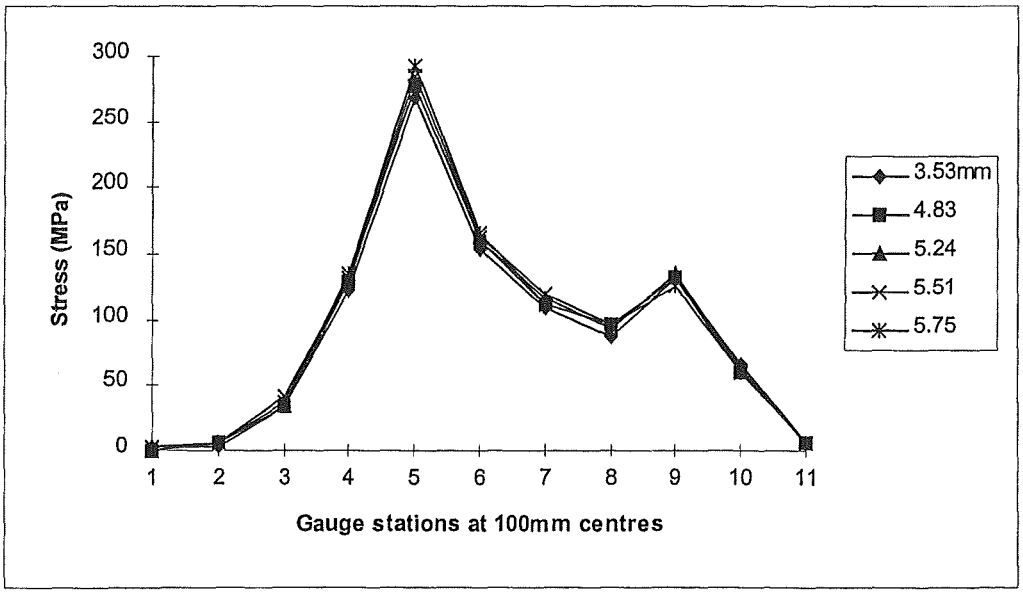

Fig 3.20 Average stress distributions along HD12 starter bars at the indicated horizontal displacements during Stage II of test LOS 1

(Stage III) Post-Fracture Peak Load to Full Loss of Steel Reaction

Once the peak load displacement of 5.5 mm was exceeded, a steady loss of reaction resulted from the serial tensile fracture of mesh wires. Likewise, the initially significant effects of residual concrete bond and friction were completely diminished during this stage of loading. Because the mesh wires were the only form of reinforcement offering resistance across the principal topping crack (see Fig. 3.19), the entire contribution of reinforcement was lost with fracture of the last wire at 18 mm displacement. Beyond 18 mm displacement it was clear that the only resistance provided was due to sliding friction between the soffit of the hollow core unit and the seating ledge.

Sliding resistance between the hollow core unit and its seating caused the support ledge tospall, resulted in a 4.0 mm downward dislocation of the hollow core section by the end of this stage. Visible separation had occurred between the precast and topping concretes prior to loading Stage III. Therefore, it is considered that significant frictional resistance could not have been developed along the precast-to-topping interface over this stage.

(Stage IV) Loss of Reaction to Collapse

For the reasons discussed earlier, the final stage of the test registered almost negligible reaction force. The final stage of the test involved displacing the unit until the eventual collapse occurred. Of particular interest was the amount of downward movement displayed by the precast section as a result of support spalling (Fig. 3.21). During the later stage of the test, the unit was supported primarily by dowel action provided by the prestressing strand stubs (as referred to in Stage II). At 43 mm displacement, the unit effectively slipped off the support.

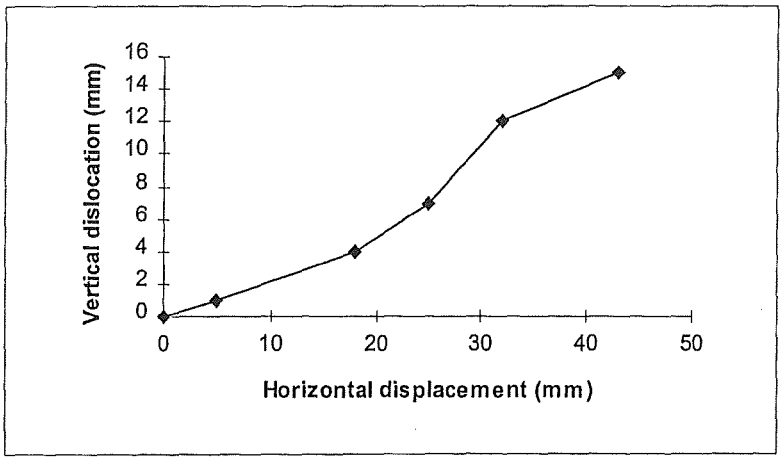

Fig. 3.21 Vertical dislocation of the hollow core section due to spalling of the support ledge, measured in relation to horizontal displacement up to collapse

Fig. 3.22 Soffit of hollow core unit showing fracture at the support

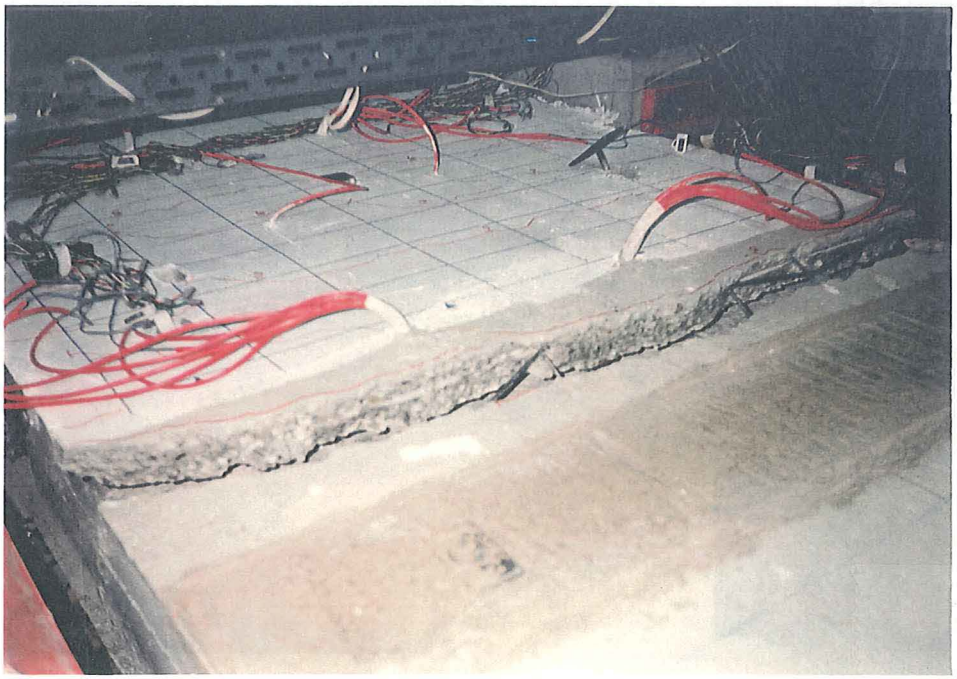

Fig. 3.23 Separation of the principal topping crack immediately prior to collapse

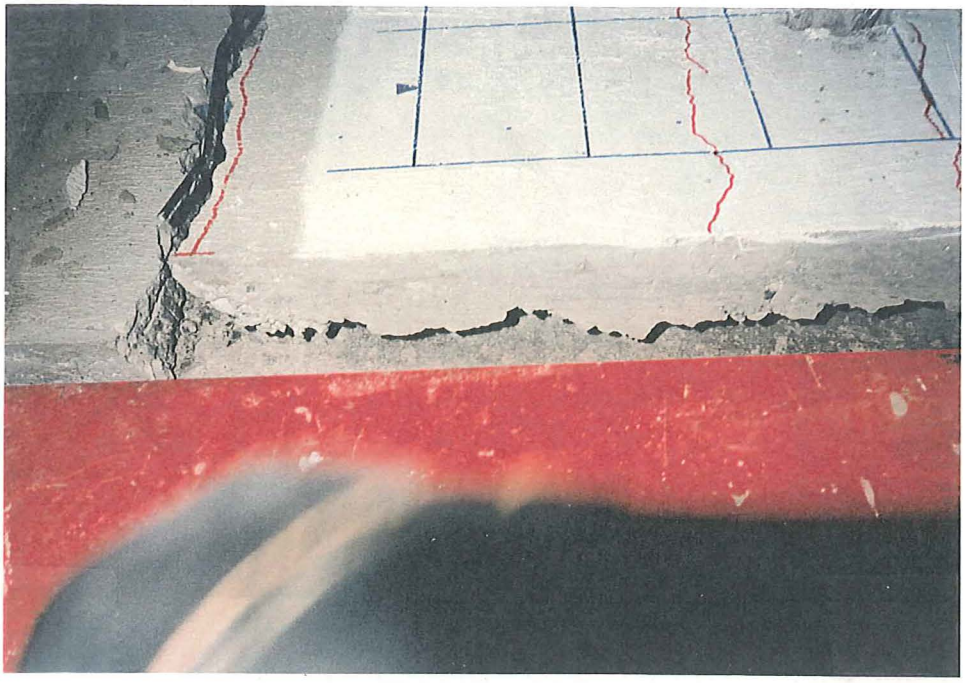

Fig. 3.24 Topping separation caused by downward dislocation of the hollow core unit

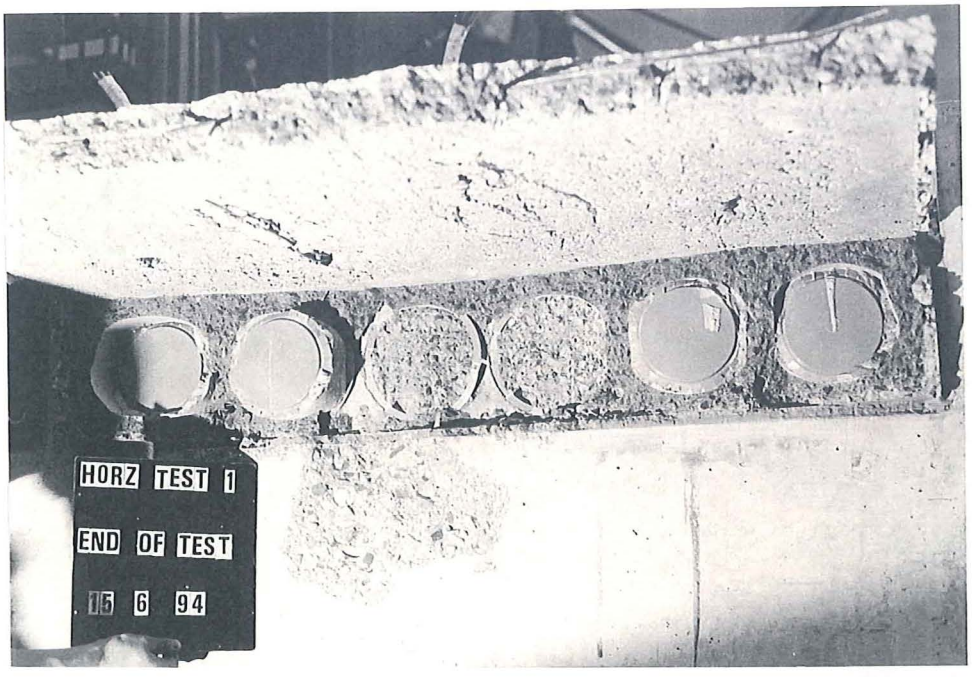

Fig. 3.25 View of support at the end of testing, showing intact plastic dams in outer voids and spalling along the support ledge

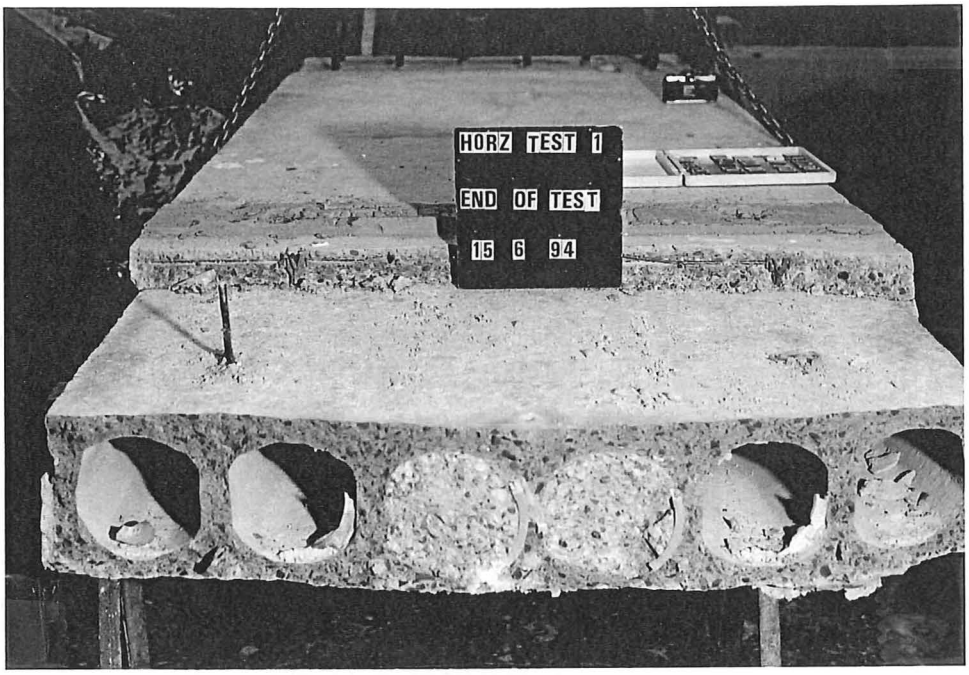

Fig. 3.26 Fractured hollow core section after removal, showing intact plastic dams in two inner voids

3.3.1.7 Specific Analysis

(a) Fracture of the Hollow Core unit at the Support

Before the section fractured, substantial topping cracks had established over the support region. Therefore, the tensile contribution of the topping slab would have been largely depleted at that stage. Assuming the reinforcing and precast section alone resisted the total horizontal reaction at fracture, the proportions of resistance were approximately as follows (Table 3.6):

Table 3.6 Reaction provided by reinforcement and precast section immediately prior to sudden fracture

Element	Horiz. Reaction (kN)	Proportion of Total (%)
665 mesh	38	11
HD12 starters	61	17
hollow core section	253	72
Total	**352**	**100**

Hence, the average axial tensile stress in the hollow core unit at fracture was $f_{tx} = P_{pc}/A_{pc} = 253$ kN/0.119 m², which gives f_{tx} as 2.1 MPa. Considering the effect of shear stresses acting on the two key edges of the hollow core section (see Fig. 3.19), it can be shown that the principal tensile strength of concrete was reached at fracture.

The shear capacity of uncracked mortar joints may be estimated by Equation 1.20. Since there is no apparent normal component of stress, the maximum shear that may be developed as such is $0.05f'_c$. Referring to Table 3.3, this would indicate a potential resisting shear stress value at the time of testing of 0.05×38 MPa = 1.9 MPa.

For an element with combined mono-axial tensile stress and shear stress τ, the equation for the principal tensile stress under brittle failure criterion is given as:

$$f'_t = \frac{f_{tx}}{2} + \sqrt{\left(\frac{f_{tx}}{2}\right)^2 + \tau^2} \qquad (3.6)$$

and the principal stress plane θ_p is located in relation to the plane of axial stress:

$$\theta_p = \frac{1}{2}\tan^{-1}\left(\frac{2\tau}{f_{tx}}\right) \qquad (3.7)$$

The ACI recommended value for the principal tensile capacity of concrete is $0.33\sqrt{f'_c}$ [Lin and Burns, 1982], hence, Equations 3.6 and 3.7 may be rearranged and combined to give the principal stress plane as:

$$\theta_p = \frac{1}{2}\tan^{-1}\frac{2\sqrt{\left(0.33\sqrt{f'_c} - \frac{f_{tx}}{2}\right)^2 - \left(\frac{f_{tx}}{2}\right)^2}}{f_{tx}} \qquad (3.8)$$

Substituting the appropriate values of $f'_c = 45$ MPa and $f_{tx} = 2.1$ MPa into Equation 3.8 yields a principal tensile fracture plane at 12.7° relative to the support line.

The actual fracture planes of the test unit are shown in Figure 3.25. The inclinations of the left and right side fracture planes, as caused by combined shear and tension, were respectively about 13° and 9° relative to the cross section of the unit. Fracture occurred through the entire hollow core section, with the exception of a small portion of web which measured 30 mm (web width) by 40 mm high.

(b) Vertical Reaction at the Support

A static superimposed load of 3.25 kPa was applied to 60% of the hollow core unit plan area by adding two layers of 40 kg cement bags. The superimposed load in combination with the unit self weight and various items of rigging resulted in a support reaction of 9.8 kN. This is not a

particularly large reaction for a hollow core flooring unit, and may be only about one third of the service load reaction of a typical floor member.

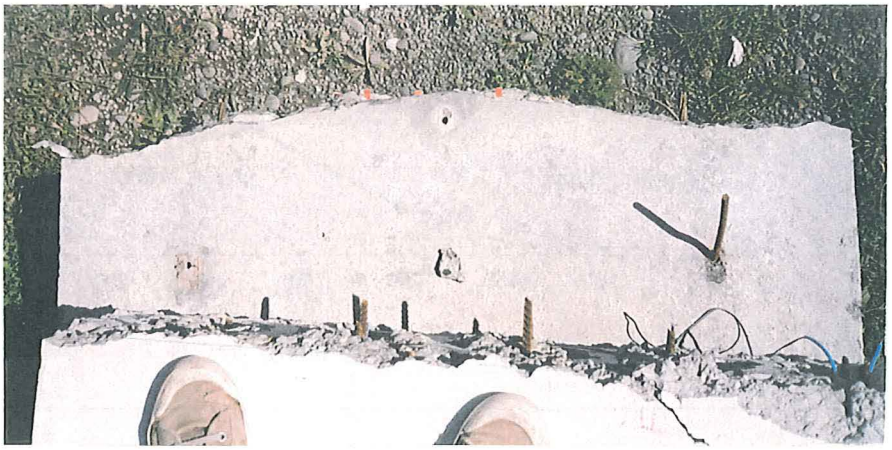

Fig. 3.27 End view of hollow core unit, showing inclined planes of fracture caused by combined shear and tension at the support

It is evident, however, that a greater magnitude of vertical support reaction would have had little influence on the fundamental result of test LOS 1. It is presumed that a greater vertical reaction could have accelerated the vertical dislocation of the hollow core unit as collapse displacement was approached (see Fig. 3.22). Therefore, the test configuration may be considered as producing non-conservative test results in terms of applied loading and apparent behaviour.

(c) Bar Bond in the Support Region

Bar bond stresses may be calculated by considering stress distributions along the bar, as shown in Figure 3.18. Fitted curves of stress distribution are shown in Figures 3.28(a) and 3.28(b) for gauge stations 1 to 5 (over support block) and stations 5 to 9 (in topping slab). It is evident that the fitted parabolas provide strong correlations with measured stresses.

Hence, this would indicate a linear variation in bond stress alone the starter bars at the given magnitudes of stress. Equations 3.1 and 3.2 are the fitted equations for support block and topping slab bar stresses, in megapascals as functions of distance x (where $0 \leq x \leq 400$ mm).

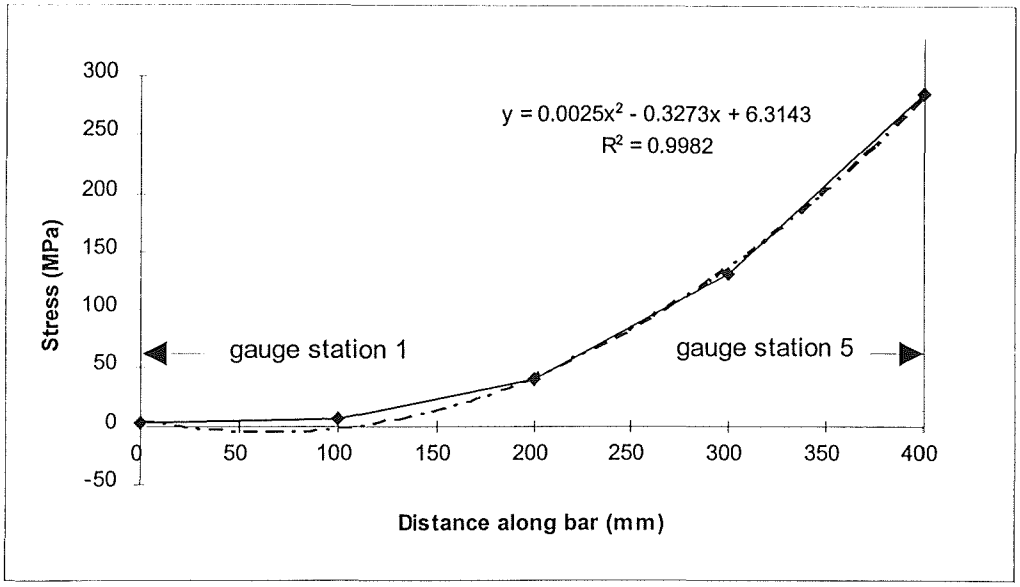

Fig. 3.28(a) Fitted curve of starter bar stress distribution in the support beam at post-fracture peak force (5.5 mm horizontal displacement)

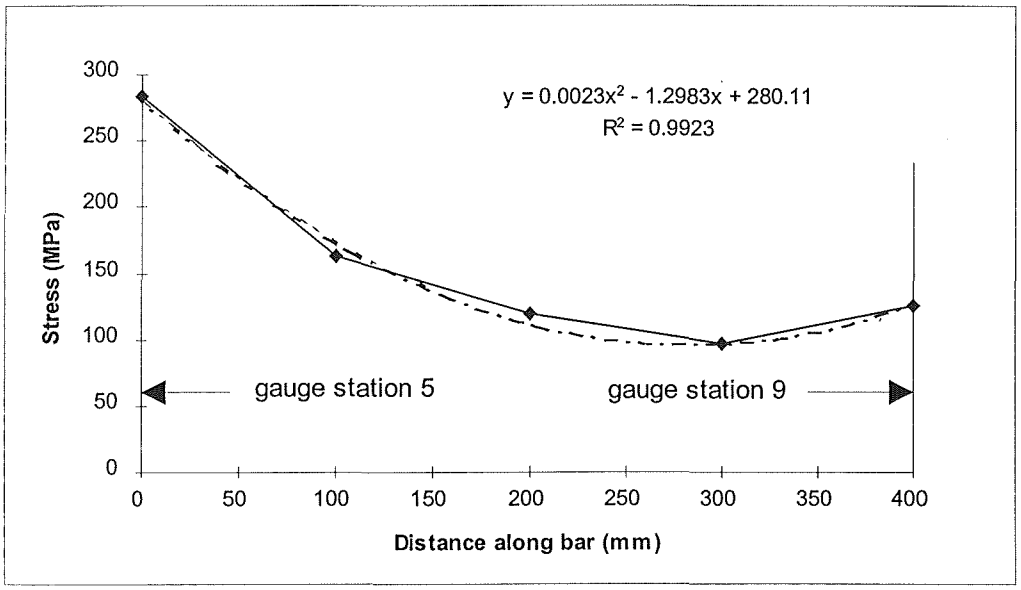

Fig. 3.28(b) Fitted curve of starter bar stress distribution into the topping slab at post-fracture peak force (5.5 mm horizontal displacement)

Support block (gauges 1 to 5): $f_s = 0.0025x^2 - 0.33x + 6$ (3.1)

Topping slab (gauges 5 to 9): $f_s = 0.0023x^2 - 1.3x + 280$ (3.2)

For round bars, the concrete bond stress u may be expressed as:

$$u = \frac{d_b}{4} \cdot \frac{df_s}{dx} \tag{3.3}$$

hence, for 12 mm diameter reinforcement the respective bar bond stresses are:

Support block (gauges 1 to 5): $u = 0.015x - 1$ (3.4)

Topping slab (gauges 5 to 9): $u = 0.014x - 4$ (3.5)

From these Equations 3.4 and 3.5, maximum bond stresses may be calculated adjacent to the initial support-to-precast interface crack located at gauge station number 5 (see Fig. 3.18). Therefore, substituting x = 400 mm into Equation 3.4 yields bond stress of 5.0 MPa. Likewise, substituting x = 0 into Equation 3.5 yields – 4.0 MPa, the negative sign indicating the direction at which the bond stress acts. These values indicate that adequate starter bond stresses were developed under the given conditions of bar stress and adjacent concrete cover [Park and Paulay, 1975].

(d) Work Done

The performance of ductile tie connections is characterised by the measured quantity of work done by the connection detail in the form of internal strain energy (see Figs 1.22 and 1.23). In establishing this value, it is assumed that the conservation of energy principles apply. Thus, the quantity of internal strain energy is equal to the sum of external work done, written as:

$$U_i = U_e \tag{3.9}$$

The external work done by a connection detail is simply the summation of area under the force-displacement curve produced by the test. The support detail exhibited primarily elastic behaviour up to the point of sudden fracture (see Fig. 3.12). Hence, the internal strain energy in this detail up to fracture would have been mostly conservative (ie., recoverable). Beyond the point of fracture, the detail exhibited non-conservative modes of energy dissipation through the plastic deformation of mesh wires and frictional forces. Energy dissipation through secondary effects is not a warranted consideration in practical concrete research.

The summation of external work may be found with sufficient accuracy by taking small increments of displacement:

$$U_e \approx \sum_{\delta} \tfrac{1}{2}\left[P_{\delta i} + P_{\delta i+1}\right]\cdot\left[\delta_{i+1} - \delta_i\right] \qquad (3.10)$$

Referring to Figure 3.13, the summation of total work done through each loading Stage (I to IV) is shown in Table 3.7:

Table 3.7 Summation of external work done by the connection detail of test LOS 1 over each loading stage. Note that stage I exhibited mainly elastic deformation up to peak force, and likewise, plastic deformation beyond sudden fracture:

Stage	I	II	III	IV	Total
Work Done (kN-mm)	277 (69 pre-fracture)	307	1006	120	**1710**
Proportion (%)	16	18	59	7	**100%**

(e) Internal Strain Energy

The nature of developed internal strain energy up to sudden fracture was characterised by the primary materials involved. There were three essential groups of materials to consider, namely steel reinforcement, precast concrete section and cast-in-place concrete section. It is apparent that these respective materials exhibited decreasing relative proportions of conservative strain energy at the point of sudden fracture.

It has been demonstrated that the steel reinforcement remained fully elastic over the support zone, and based on the magnitude of bond stresses, there would have been negligible bar slippage. However, with regard to the elasto-plastic behaviour of the concrete elements, it is difficult to fully deduce the individual pre-fracture contributions of the precast and cast-in-place portions. For prior analyses, it has been assumed as reasonable that the effective tensile contribution of topping was negligible at the point of sudden fracture. Hence, it is certain that the topping concrete portion would have at most exhibited plastic force-deformation characteristics at this point.

Figure 3.16 indicates that the combined concrete section became mobilised and exhibited plastic behaviour prior to sudden fracture. A transition phase from elastic to plastic deformations occurred between 0.1 mm and 0.14 mm displacement, and it is evident that fully plastic behaviour was maintained between 0.14 mm and sudden fracture at 0.27 mm displacement.

The total quantity of elastic strain energy stored in the combined elements immediately before sudden fracture must approximately equal the total energy change in the post-fracture system. Thus, large force at small displacement corresponds with lesser force at increased displacement, etc. The internal strain energy may be calculated and compared to the external work done up to sudden fracture, based on section properties, reasonable assumptions of material parameters and information derived through measurements. Written in terms of the primary reserves of internal

strain energy, respectively the composite section, starter bars and mesh, corresponding with external work done in accordance with Equation 3.9:

$$\frac{P_{max}^2 L}{2A_c' E_c} + \frac{A_s}{2E_s}\int_{l_d} f_s^2\,dx + \frac{A_{sm}}{2E_{sm}}\int_{l_d} f_{sm}^2\,dx = \sum_{\delta=0}^{\delta_{cr}} \tfrac{1}{2}\left[P_{\delta i} + P_{\delta i+1}\right]\cdot\left[\delta_{i+1} - \delta_i\right] - U_{\delta p} \quad (3.11)$$

Immediately prior to sudden fracture, the fitted stress curves for starter bars and mesh expressed in megapascals as functions of distance x over the effective development lengths l_d were:

f_s	$= 0.66x - 135$	$200 < l_d \le 400$mm
f_s	$= 0.0011x^2 - 0.72x + 132$	$0 < l_d \le 400$mm
f_{sm}	$= 1.4x + 6$	$0 < l_d \le 150$mm
f_{sm}	$= 1.2x + 40$	$0 < l_d \le 150$mm

Because of the described inelastic displacements, elastic displacement corresponding with the maximum horizontal force is less than the total displacement. This effect has been allowed for in Equation 3.11 by incorporating the subtractive term $U_{\delta p}$ to account for plastic displacement. Thus, $U_{\delta p}$ is the product of the average force carried by the concrete section over the extent of plastic displacement up to sudden fracture. It is evident from Figure 3.16 that the concrete section exhibited fully plastic behaviour from 0.14 mm displacement onward. Hence, the phase of fully plastic displacement has been taken as 0.27 – 0.14 = 0.13 mm. Associated with this plastic displacement is the average horizontal force resisted by the concrete section, which was 250 kN.

Taking the density of extruded concrete as 2400 kg/m³, the estimated moduli of elasticity of the hollow core section and topping slab are respectively 31 GPa and 27 GPa. (Section 3.8.1.2 of the Concrete Structures Standard) [Standards New Zealand, 1995]. Therefore, the modular ratio of the topping slab concrete to precast concrete is n = 27/31 = 0.87, and the effective elastic section area A'_c becomes 119200 + (0.87 × 1160 × 65) ≈ 185000 mm². The length of composite slab between the support block and the actuating frame was 3120 mm. Subsequently, the elastic internal strain energy evaluated in accordance with terms of Equation 3.11 is:

$$U_i = \frac{1}{2}\left(\frac{(352\text{kN})^2 \times 3120}{185000 \times 31000} + \frac{452 \times 2.44e^6}{205e^3} + \frac{176 \times 5.26e^6}{196e^3}\right)$$

$$= \quad 33.7 \quad + \quad 2.7 \quad + \quad 2.4 \qquad = 38.8 \text{ kN-mm}$$

The corresponding elastic external work done is the total work done (see Table 3.7) less $U_{\delta p}$:

$$U_e = \quad 69.0 - (250 \text{ kN} \times 0.13 \text{ mm}) \qquad = 36.5 \text{ kN-mm}$$

Hence, this summation would indicate that on the basis of materials response, a comparison can be drawn between the conservative portions of internal strain energy and external work done.

(f) Composite Topping Bond

At sudden fracture, the horizontal force was transferred to three planes of resistance. The resulting system involved two vertical fracture planes and one horizontal bond surface (Fig. 3.22). Of the vertical fracture planes, only the principal topping fracture contained fully bonded reinforcement. From available measurements, it is impossible to ascertain the proportions of horizontal force resisted by each of the three primary surfaces throughout the post-fracture phase of Stage I. However, the general test observations suggest that bond contributions from the precast-to-topping interface were negligible at the beginning of Stage II.

The sudden brittle nature of fracture and its radical effect on the entire configuration would strongly suggest that initial rupture occurred through the hollow core section along the support line (see Figs 3.19 and 3.22). Since 72% of the horizontal force was resisted by the hollow core section (Table 3.6), the majority of force was transferred to the available resistance mechanisms in an instant. It is certain that the dynamic aspect of this release diminished the prospect of a suitable mechanism developing through composite bond between the topping and precast concretes.

Assuming that the tensile contribution of the composite concrete section was transferred to a resistance mechanism in the form of composite bond, it is evident that the average static topping bond shear stress τ_b required to maintain equilibrium would not have been very large. Taking the force resisted by the precast concrete element and dividing over the total bond interface area gives:

$$\tau_b = \frac{P_{pc}}{A_b} \qquad (3.12)$$

The topping bond shear stress required to resist a equivalent static horizontal force was:

$$\tau_b = \frac{253\,\text{kN}}{(1160\times 660)\,\text{mm}^2} = 0.33\,\text{MPa}$$

However, dynamic considerations involve the ability of the bond surface to absorb elastic internal strain energy associated with the hollow core section at fracture. If the bond surface was unable to conserve this quantity of strain energy as an alternative elastic mechanism (neglecting secondary effect losses) then plastic deformation would result. In conclusion, plastic deformation would immediately imply a complete loss of bond strength due to the customarily brittle behaviour of unreinforced shear mechanisms.

The required peak bond stress capacity over the tributary bond surface area may be postulated by considering the elastic strain energy per unit volume of material deformed by shear stress. Since only the bond surface area A_b is known, an effective depth of material is required so as to obtain a deformable volume. Considering the hollow core surface as infinitely rigid, the distance between the topping-to-precast interface and the centre-line of the starter bars would

form a distance between opposing bond forces, thus forming a shear depth of $t = h_t/2 = 32$ mm (Fig. 3.29).

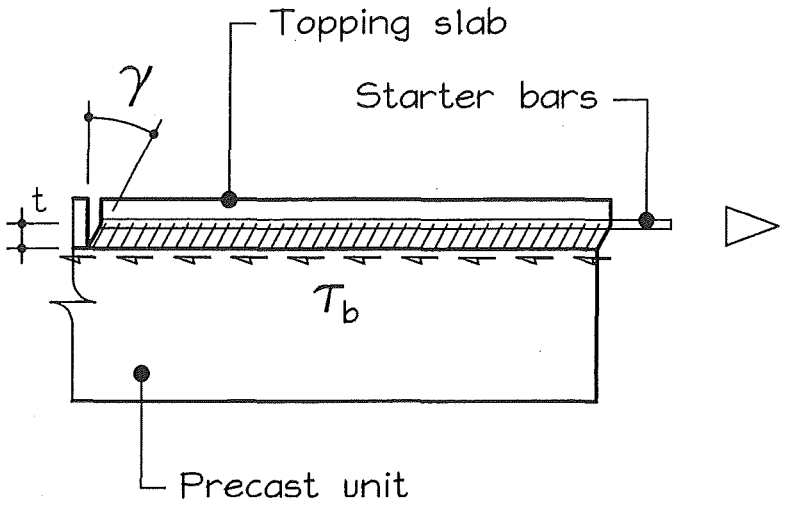

Fig. 3.29 Assumed mechanism for the development of elastic strain energy in shear

The proportion of elastic internal strain energy stored in the hollow core section alone is taken as a ratio of the section area of precast to the total transformed concrete area A'_c in Equation 3.11. Hence, the energy stored in the precast section alone was $U_{pc} = (119200/185000) \times 33.7$ kN-mm = 21.7 kN-mm.

The elastic strain energy density for shearing stress may be written as:

$$u = \frac{\tau_b^2}{2G} \tag{3.13}$$

Equating the stored strain energy in the precast section to the shear mechanism and rearranging gives the required peak shear stress of:

$$\tau_b = \sqrt{\frac{2GU_{pc}}{A_b t}} \tag{3.14}$$

Based on the prior established values and taking the concrete modulus of rigidity G as 10 GPa gives a required elastic peak bond shear stress of:

$$\tau_b = \sqrt{\frac{2 \times 10000 \times 21700}{(1160 \times 660) \times 32}} = 4.2 \text{ MPa}$$

Direct-shear (as opposed to shear flow) topping bond tests conducted as part of this study and reported in Chapter 6 confirm that shear stress of this magnitude will not be sustained by

ordinary bond surfaces. In-fact, it was shown that relatively smooth bond surfaces, such as extruded hollow core, might not even develop the static bond stress as given by Equation 3.12. It is apparent that a bond shear mechanism cannot be considered as a reserve of elastic strain energy in response to sudden tensile fracture of a hollow core section.

3.3.2 LOS 2

3.3.2.1 General

Test LOS 2 was directed at a special support tie detail (Figs 3.30 and 3.31) that entails embedded D10 tie bars. The detail has been specifically developed by industry to overcome short seating problems that may occur with modular precast flooring. The floor configuration involved 65 mm of cast-in-place topping over a 200 mm hollow core extruded flooring unit that was pretensioned with five 12.7 mm diameter Supergrade strands. A 10 mm diameter Grade 300 (D10) tie bar, in the form of a hairpin detail, was placed in each of the six voids of the hollow core section. The hollow core flanges were removed from above the voids to allow grouting with cast-in-place topping concrete. 665 mesh was placed over the hollow core unit, and was continued beyond the end of the seating length, thus contributing to the tensile strength across the construction joint (assumed to be the critical section). There were no starter bars placed in the topping concrete.

For the serviceability limit state, the mechanics of this detail depend on the development of shear friction across the construction joint between the end of the precast unit and the support. With the proper implementation of unit layout (Fig. 3.32), this detail has been successfully employed in practice for many years. However, for the detail to perform successfully under dilation type loadings that may involve significant structural ductilities, the tie reinforcement must have the fundamental capacity to endure the maximum predicted elongation. With increased displacement, the mechanics of support shift from purely shear friction to combined shear friction and the catenary support associated with bar kinking (Fig. 3.33) and eventually to purely catenary support. Because small diameter deformed bars are necessary for the given detail, there is a general concern regarding the elongation capacity of this reinforcement.

3.3.2.2 Instrumentation

(a) Forces and Displacements

Forces and displacements were measured in accordance with the methods described in Section 3.2.2 (also Fig. 3.4).

(b) Reinforcement

Both 20% and 3% extension electrical resistance strain gauges (as described in Section 3.2.2) were employed on two individual items of hairpin reinforcement. These gauges were arranged

so that the 20% extension variety was situated directly over the expected plane of cracking, at the end of the hollow core section. The 3% strain gauges were set at 100 mm centres about the expected cracking zone (see Fig. 3.34).

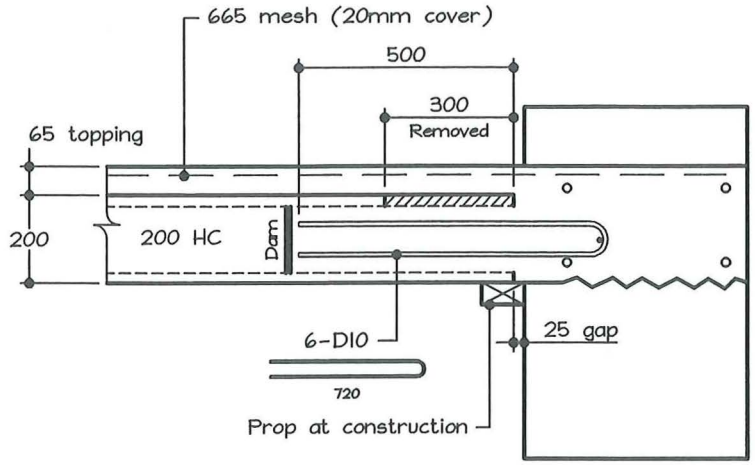

Fig. 3.30 Support configuration of test LOS 2 involving a hairpin tie detail

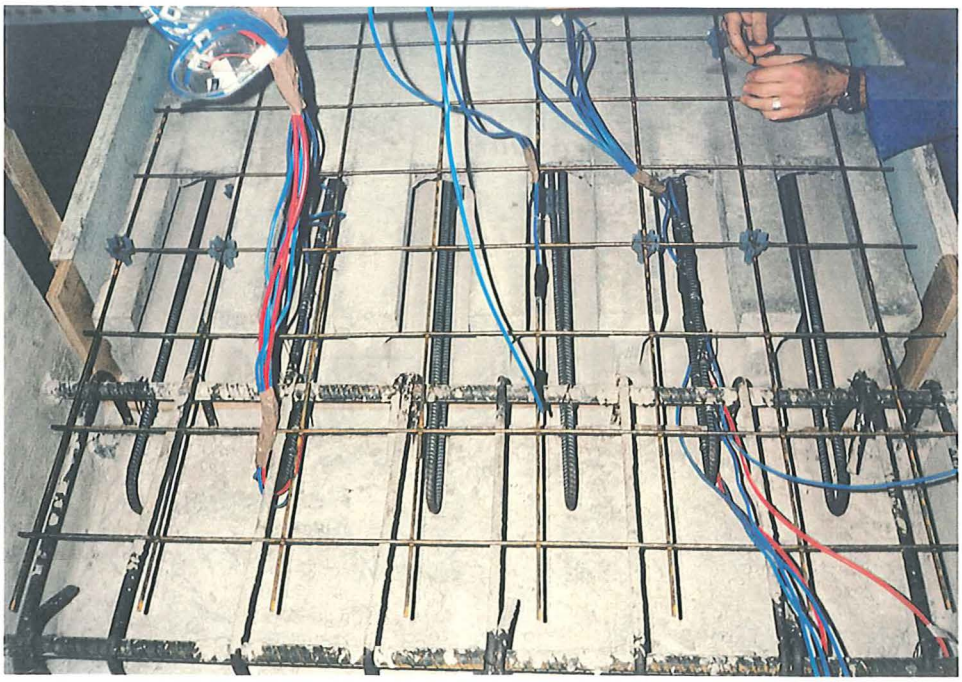

Fig 3.31 LOS 2 test set-up before the addition of topping concrete

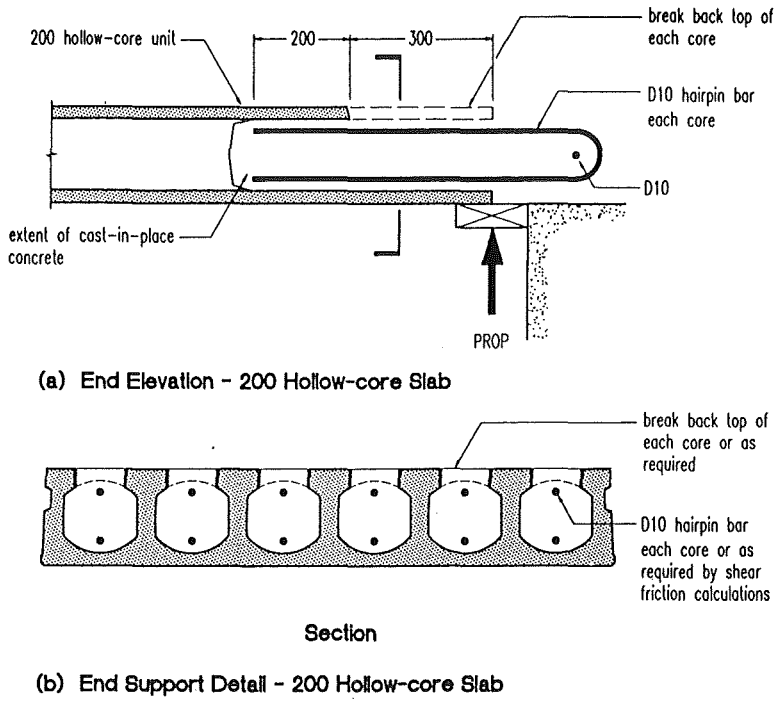

Fig 3.32 End support detail where embedded hairpin ties are employed for units with inadequate seating [NZCS-NZNSEE, 1991]

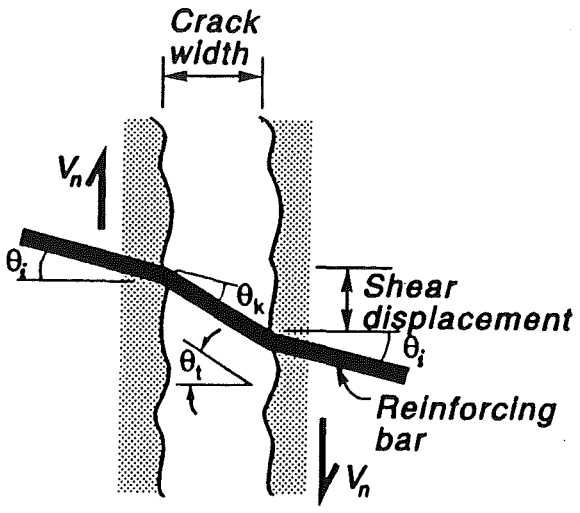

Fig. 3.33 Shear transferred by interface friction across a narrow gap [Mejia-McMaster and Park, 1994]

3.3.2.3 Cast-In-Place Topping and Infill Concrete

The pre-mixed concrete for this test was received at a slump that was well within tolerances for a snatch sample and would be described as a good workable mix (Table 3.8).

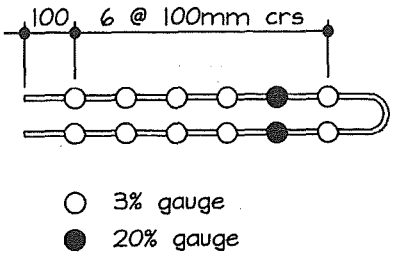

Fig. 3.34 Strain gauge positions on hairpin bars used in the LOS 2 test

Table 3.8 Characteristics of cast-in-place topping and infill concrete used in test LOS 2

Design Strength (MPa)	Max. Aggregate Size (mm)	Ordered Slump (mm)	Received Slump (mm)	Test Strength (MPa)
35 at 28 days	13	100	85	31 at 11 days

3.3.2.4 Reinforcement

(a) 665 Mesh

The characteristics of hard drawn wire mesh were identical to those described in Table 3.2

(b) D10 Hairpins

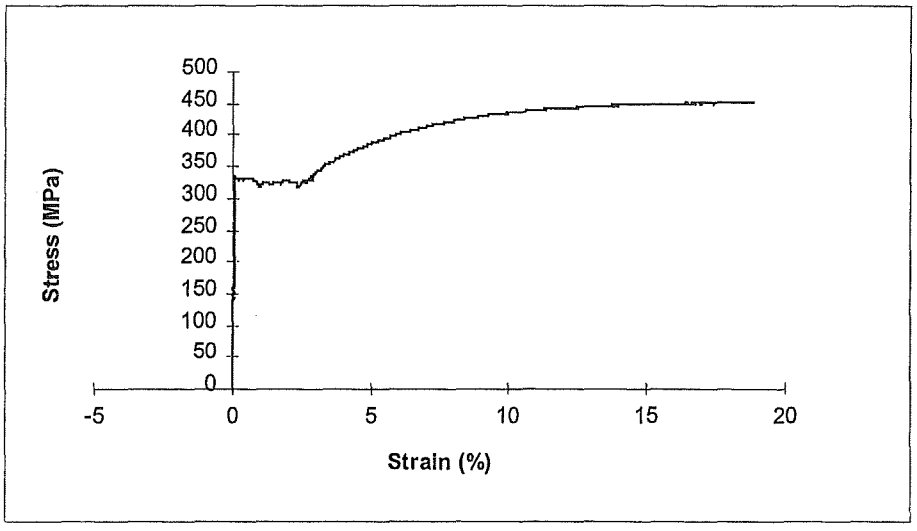

Fig. 3.35 Typical stress-strain relationship of 10 mm diameter Grade 300 bars employed as hairpin ties in test LOS 2

Tensile tests were performed on three specimens of 10 mm diameter Grade 300 bars, and the following was recorded (Table 3.9):

Table 3.9 Characteristics of D10 Hairpins used in test LOS 2

Average yield strength (MPa)	Average ultimate tensile strength (MPa)	Average strain at ε_{sh} (%)	Average strain at ultimate tensile strength (%)	Average strain at fracture (%)
312	434	2.53	16.3	23.6

Average E = 196 GPa

3.3.2.5 Results of Testing

(a) Initial Response

The initial response to horizontal loading showed a stiff system (Fig. 3.36). The first cracks, measuring approximately 0.1 mm, appeared in the infill strip between the precast unit and support block at a force of 250 kN. At a force of 441 kN a small plateau occurred in the force displacement response, with an increment in displacement from 0.85 mm to 1.4 mm. This plateau signalled the loss of notable concrete tensile contribution. From this point the horizontal resistance increased at a steady rate up to peak reaction of 520 kN at 7.2 mm displacement.

(b) Fracture

Immediately beyond the peak horizontal reaction, mesh wires began to fracture in a serial fashion and this continued out to displacement of 21 mm. From 25 mm displacement a plateau occurred at which the D10 hairpins approached fracture elongation. Failure of the hairpins commenced at 38 mm displacement, and between 38 mm and 43 mm displacement, seven of the twelve hairpin legs had fractured. A second smaller plateau featured until 49 mm displacement when a further three legs fractured. The remaining two legs were still intact at the terminal displacement of 55 mm. However, these legs failed under the small additional weight of the technician who had climbed onto the test specimen to place the vertical ram load cell. Hence, complete fracture of the tie reinforcement was achieved without the addition of a significant vertical point load.

(c) Displacements

Section cracks were concentrated in the construction joint region and developed progressively under applied force. The principal crack was fully developed at around 200 kN and 0.4 mm displacement. The latter stages of the test were characterised by increasing downward vertical displacement at the support. The vertical dislocation measured 11 mm when horizontal loading was terminated at 55 mm displacement.

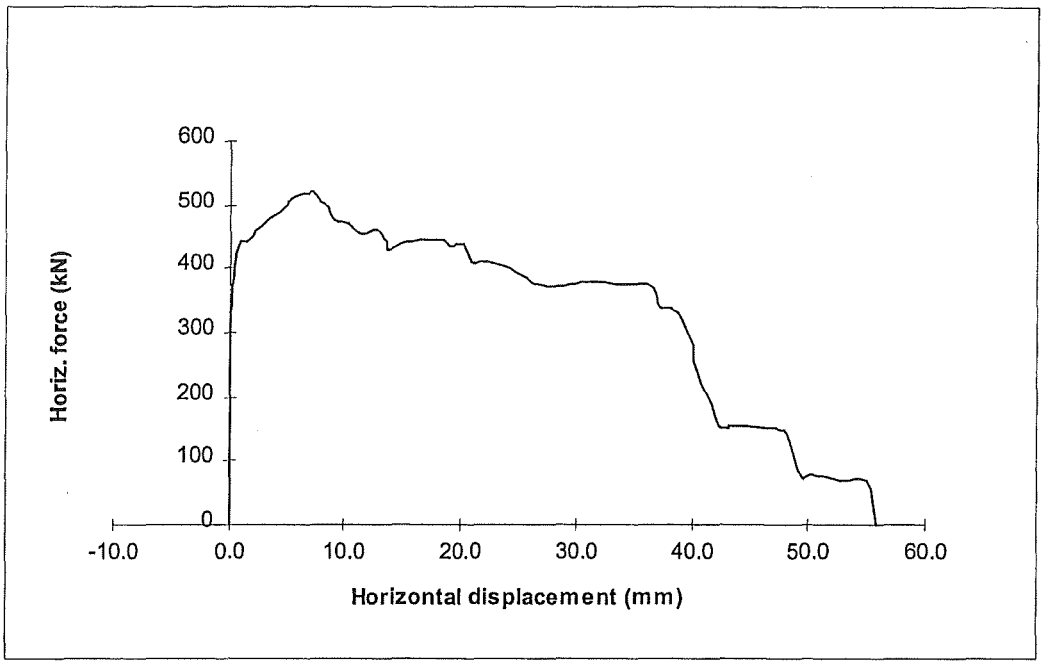

Fig. 3.36 Force-displacement response of test LOS 2

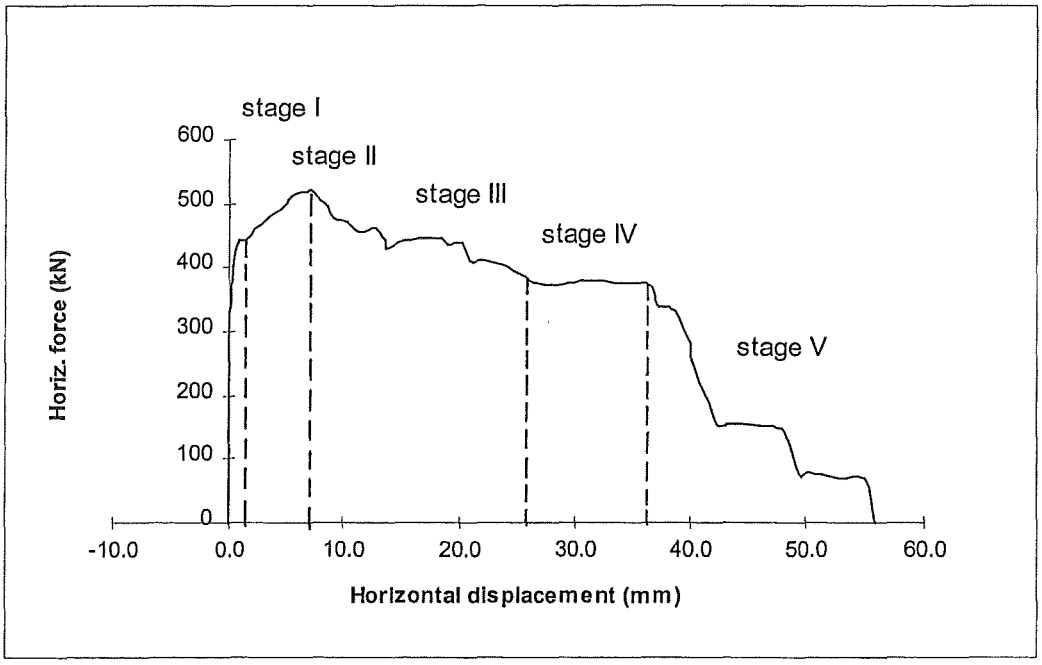

Fig. 3.37 Force-displacement diagram divided into regions of significance in terms of resistance mechanisms

3.3.2.6 Analysis of Test Results

In order to analyse the response of test LOS 2, the force-displacement diagram has been divided into the five distinct regions that were reflected in the test outcome (Fig. 3.37). Each of these regions (Stages) indicates a basic change in the resistance mechanism against imposed horizontal displacements. As a whole, the diagram clearly indicates the differing contributions of respective steel reinforcement and concrete components.

(Stage I) Section Yield

Tensile stresses had begun to register in both the hairpin ties and 665 mesh between 0.1 mm and 0.15 mm displacement. At 0.4 mm displacement the D10 hairpins had typically reached yield stress of just over 300 MPa. Hence, the section response was essentially elastic up to the point where the D10 hairpins began to yield. Strain hardening had commenced in the D10 hairpins by the end of Stage I (Fig. 3.38). The 665 mesh had achieved 150 MPa of tensile stress at 0.2 mm displacement and 400 MPa at 0.4 mm displacement. The mesh reached the proportional limit just prior to the onset of plastic deformation near the end of Stage I. (Fig. 3.39).

From zero to 0.4 mm displacement, the section exhibited elastic properties with a stiffness of 1025 kN/mm. Immediately beyond 0.4 mm displacement, the tensile response rapidly softened to a stiffness of 90 kN/mm. At 0.85 mm displacement the section commenced a short plateau of plastic displacement. During this stage of the test, the 25 mm wide construction joint had fully ruptured and it was evident that the tensile contribution of the concrete section was lost (Fig. 3.40).

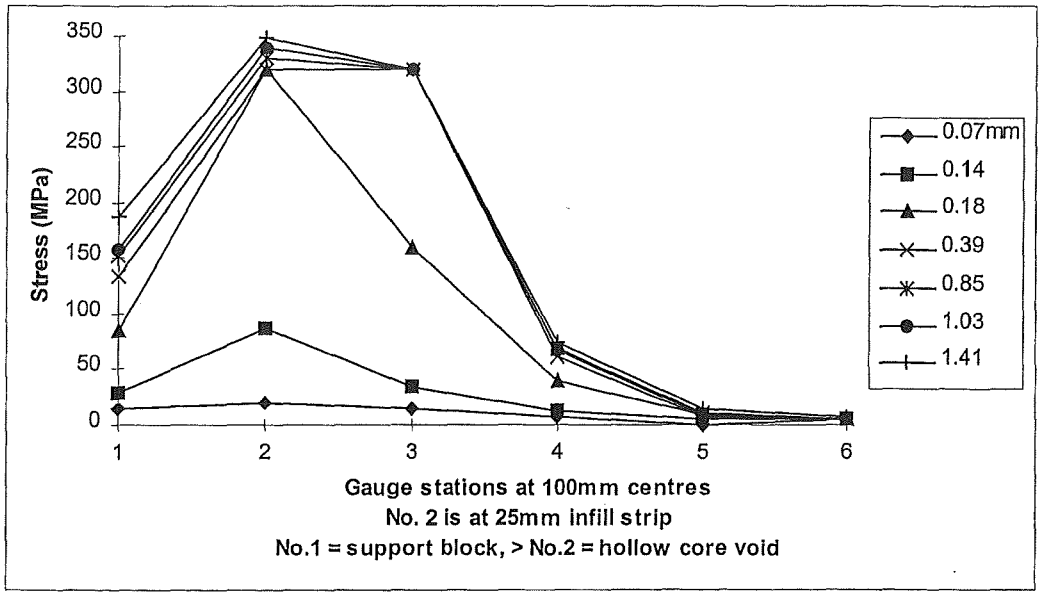

Fig. 3.38 Average stress distributions along D10 hairpin bars at the indicated horizontal displacements during Stage I of test LOS 2

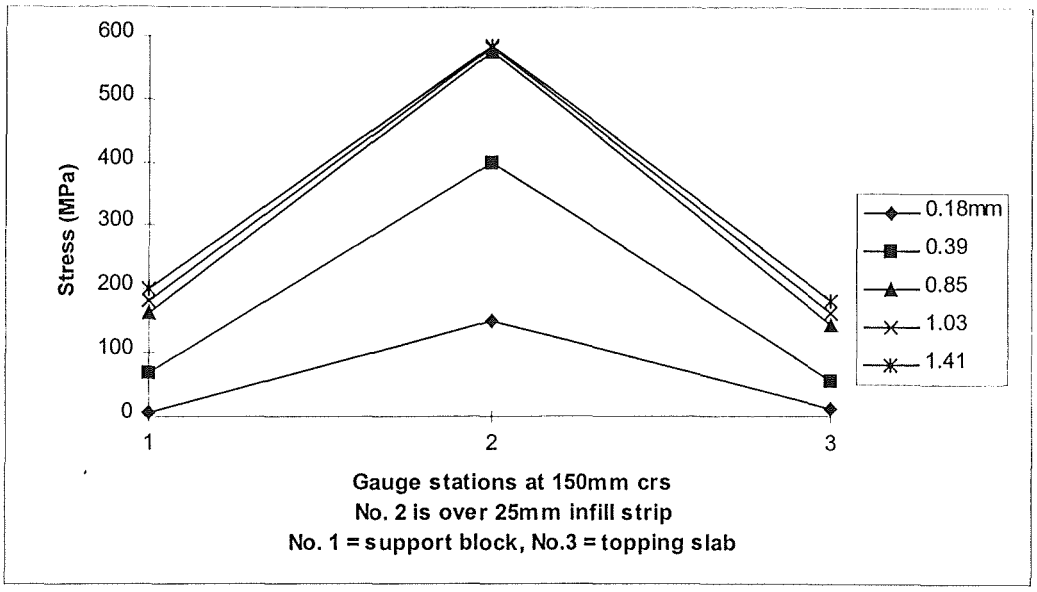

Fig. 3.39 Average stress distributions along 665 mesh wires at the indicated horizontal displacements during Stage I of test LOS 2

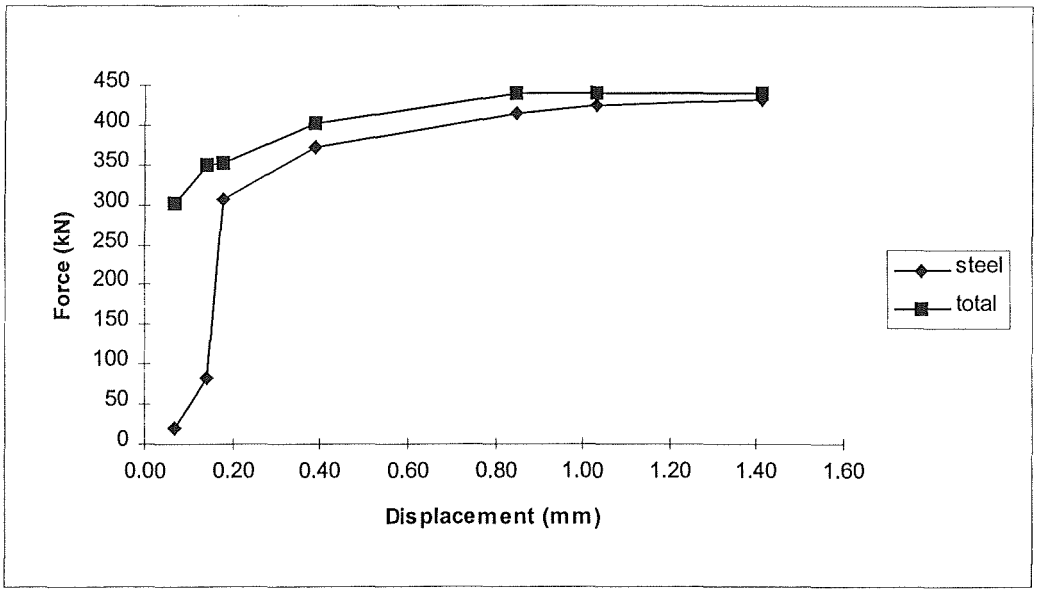

Fig. 3.40 Proportion of force resisted by reinforcing steel during Stage I of test LOS 2

(Stage II) Section Yield to Peak Force

From 1.4 mm displacement to peak horizontal force at 7.2 mm displacement, the 665 mesh provided its maximum contribution to tensile strength. At the end of Stage II, the mesh contributed 22% of the 520 kN total reaction force. The D10 hairpins had all reached strain hardening by 2.0 mm displacement, and by the end of Stage II had attained an average of 5.9% elongation at the critical section.

A crack that had initiated late in Stage I became more pronounced during Stage II. Situated in the hollow core unit (Fig. 3.41), the crack opened at approximately the same rate as the principal crack in the 25 mm wide infill strip. During Stage II, the section crack reached a maximum of 5.0 mm opening at the top of the unit, and averaged 4.0 mm opening through the depth of the section.

It is evident that the placement of prestressing strand exerted some influence on the formation and behaviour of this crack. Since there were no pretensioned strands located at the edge of this particular hollow core unit, the crack propagated from the edge, starting 165 mm from the end of the unit at the side and extending toward the centre-line of the unit at an initial angle of 16°. It appears that the course of the crack was affected by the interception of the first strand located 220 mm from the side of the unit.

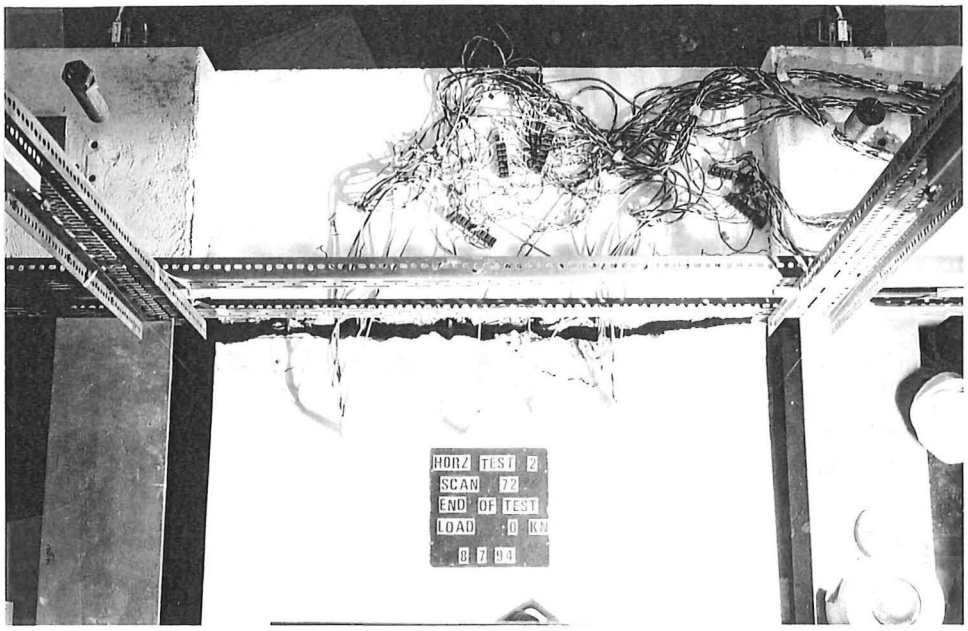

Fig. 3.41 Crack through section of hollow core slab

(Stage III) Peak Force to Fracture of Mesh

From peak force at 7.2 mm displacement through to 22 mm displacement, the reaction force diminished in two notable steps from 520 kN to 412 kN due to fracture of the topping mesh. Between 22 mm and 26 mm displacement, the reaction decreased gradually as the extension of D10 hairpins began to exceeded the ultimate tensile strength plateau of the stress-strain relationship. The peak steel stress (UTS) elongation was first reached during this stage of the test at about 15 mm displacement. Toward the end of Stage III, bar slippage had occurred and significant strain penetration was apparent (Fig. 3.42).

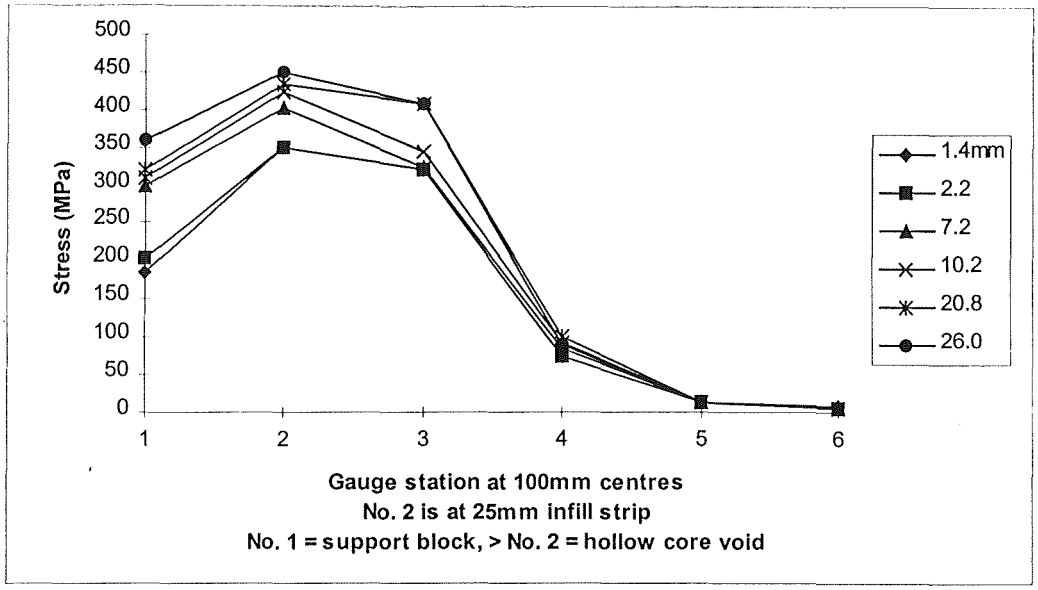

Fig 3.42 Average stress distributions along D10 hairpin bars at the indicated horizontal displacements to the end of Stage III of test LOS 2

(Stage IV) Plateau Region to Onset of Hairpin Fracture

This region indicates a plateau between 26 mm and 37 mm displacement. The plateau was likely to have been symptomatic of the state of stress within the hairpins coupled with an increasing incidence of slippage and strain penetration. It is certain that the hairpin legs were extended into the range of the stress-strain curve between the peak tensile stress and fracture elongations. The net effect of bar slippage was an increasing gauge length that would offset the falling tensile resistance of reinforcement and resulted in a distinctive plateau over several millimetres of displacement. Inspection of the specimen clearly indicated that significant penetration into the section had occurred, with cleanly fractured pull-out cones measuring an average of 10 mm to 15 mm deep (ie., 1.0 to $1.5d_b$) along most of the bars.

(Stage V) Hairpin Fracture and End of Test

Starting at 37 mm displacement, the hairpins failed in quick succession. Seven of the twelve legs fracturing in almost a single volley. This occurred over an increased extension of 5.0 mm, in which the reaction fell from 375 kN to 155 kN. Between 42 mm and 48 mm displacement, a second brief plateau was sustained until a further three of the ties failed. The final small plateau went from 48 mm to 55 mm on the remaining two tie legs. At this point, the reaction had fallen to 68 kN and failure of these ties was imminent. The detail had survived just to the end of the prescribed 55 mm displacement, and failed under the small additional weight of the technician.

Immediately before failure, the end of the unit had dropped an average of 11 mm below the original support level and was apparently supported by the two remaining tie legs.

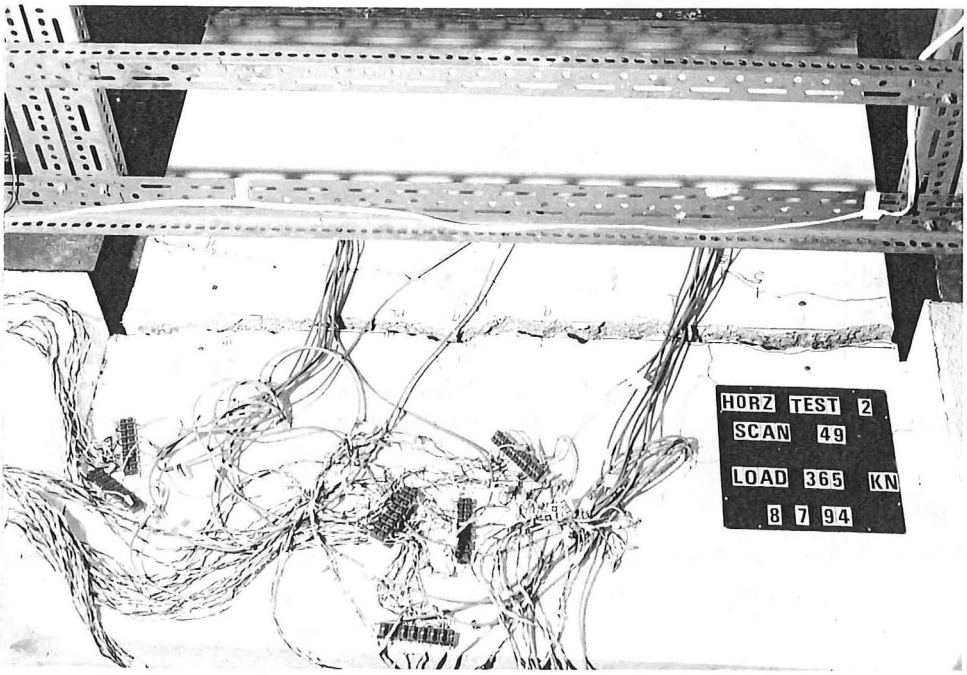

Fig. 3.43 Well defined crack opening through the support construction joint

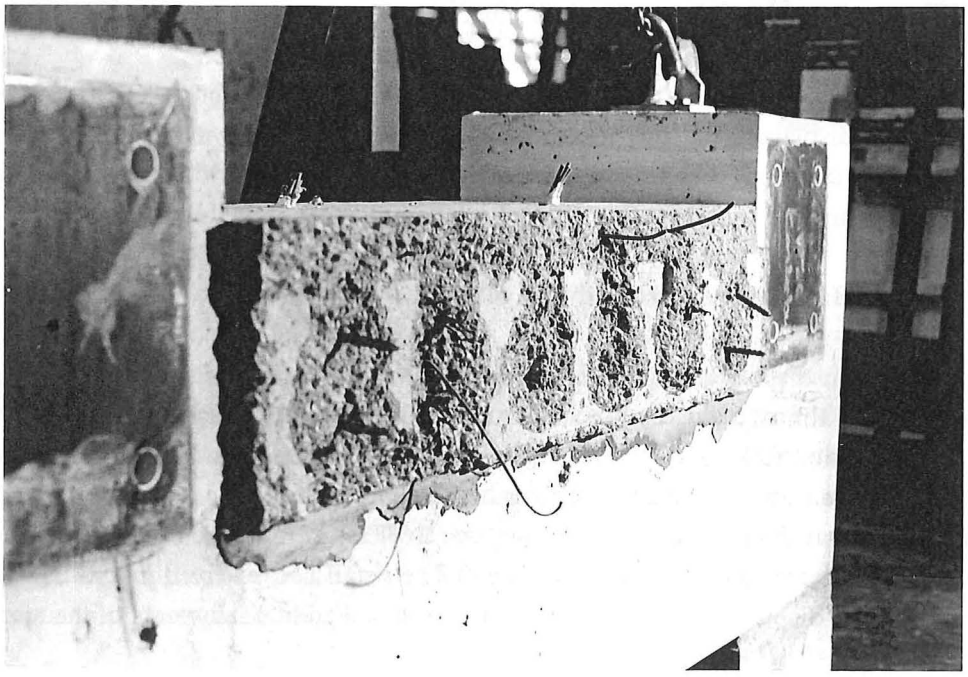

Fig. 3.44 Fractured D10 support ties at end of test

3.3.2.7 Specific Analysis

(a) Work Done

The quantity of work done by this detail over the prescribed 55 mm displacement totalled 18,700 kN-mm.

(b) Ductility

From Figure 3.42, it is evident that the tensile overstrength capacity of a straight length of well confined reinforcing bar can be developed in less than $20d_b$. At the hook end, the strength capacity would probably have developed in an even shorter distance. Hence, most of the strength development and slippage would have occurred between the critical section and the tangent of the hook return.

In effect, the gauge length of the hairpins would have changed continuously due to progressive strain penetration and bar slippage. However, a reasonable estimate of the effective gauge length would be to take the distance to bar yield on either side of the critical section at peak bar stress. The total extension capacity is the product of fracture strain and effective gauge length:

$$\Delta L = \varepsilon_u L_o \tag{3.15}$$

Referring to Figure 3.42 and Table 3.4, the respective lengths on either side of the critical section are 100 mm and 130 mm at 21 mm displacement, giving an extension capacity of ΔL = 23.6% × 230 mm = 54 mm.

(c) Bar Bond in the Support Region

In this detail, the straight embedment length grouted into the hollow cores, will determine the critical bond capacity of reinforcement. From Figure 3.42, peak bond stress was clearly developed in the bond region between gauge stations No. 3 and No. 4.

The average bar bond may be calculated by taking the difference between stress readings at successive gauge stations and dividing the net axial force over the bond surface area between stations:

$$\bar{u} = \frac{A_s\left(f_{si} - f_{sj}\right)}{\pi d_b L} = \frac{d_b\left(f_{si} - f_{sj}\right)}{4L} \tag{3.16}$$

Hence, with reference to Figure 3.45, the average peak bar bond stress is:

$$\bar{u} = \frac{10\left(407 - 91\right)}{4 \times 100} = 7.9 \text{ MPa}$$

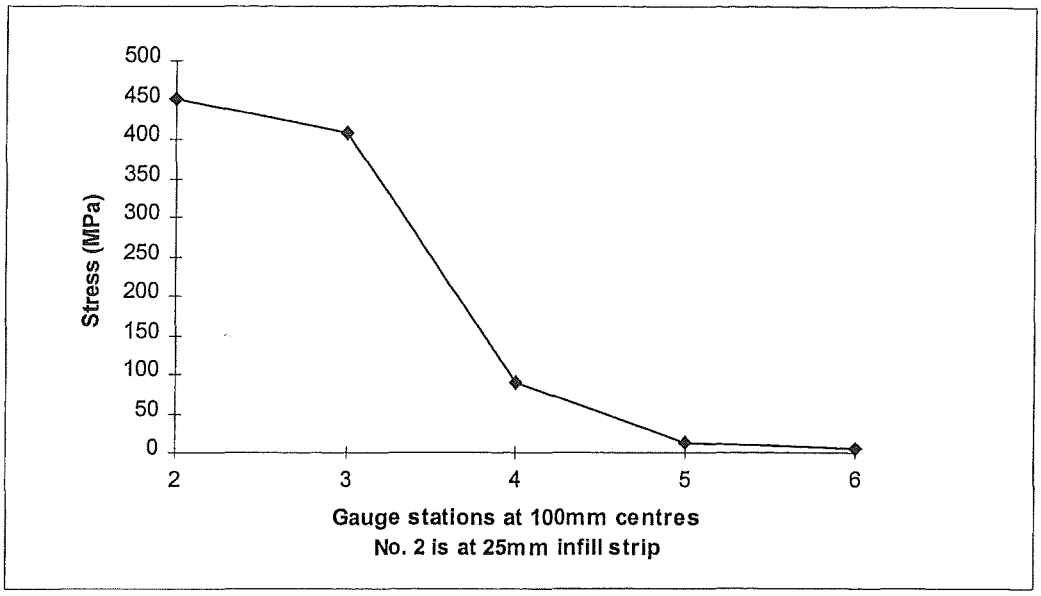

Fig. 3.45 Peak stress distribution along hairpin tie bars embedded in grouted hollow core voids (26 mm horizontal displacement)

(d) Dowel Action at the Support

The support reaction on the test specimen was calculated to be 12.2 kN. At the end of testing the measured bar angle was $\theta_i = 8°$ (see Fig. 3.33). Because there was no friction component at full extension, the shear force was transferred entirely by dowel action, given as:

$$V_n = A_{vf} f_s \sin\theta_i \qquad (3.17)$$

The average ultimate tensile strength of reinforcement was measured at 434 MPa (Table 3.4). Immediately before collapse the end support was provided by two tie legs, giving a calculated vertical reaction of $V_n = 2 \times 79\ mm^2 \times 434\ MPa \times \sin 8° = 9.5\ kN$.

The difference between the calculated dowel reaction of 9.5 kN and the abovementioned support reaction of 12.2 kN was due to interactions between the fractured hairpin legs and the face of the concrete section. As the unit deflected and rotated, a number of the fractured tie legs were effectively thrust into the concrete support face, thus providing a degree of shear resistance.

3.3.3 LOS 3

3.3.3.1 General

Test LOS 3 was the second of three tests directed at the typical starter bar detail (Figs 3.9 and 3.10). The floor configuration involved 65 mm of cast-in-place topping over a 200 mm hollow core extruded flooring unit that was pretensioned with four 12.7 mm diameter Supergrade strands. Four 12 mm diameter Grade 430 (HD12) starter bars were placed at 300 mm centres, and extended 600 mm into the topping slab. 665 mesh was placed over the hollow core unit, and was continued beyond the end of the seating length, thus contributing to the tensile strength across the construction joint (assumed to be the critical section). Unlike the first test involving this detail (ie., LOS 1) a superimposed dead load was not applied to the test specimen.

3.3.3.2 Instrumentation

(a) Forces and Displacements

Refer to the methods described in Section 3.2.2 (also Fig. 3.4).

(b) Reinforcement

Electrical resistance strain gauges were employed as described in Section 3.3.1.2(b).

3.3.3.3 Cast-In-Place Topping Concrete

The concrete supplied for test LOS 3 was exactly on the target slump of 100 mm. This was a good consistent mix that showed ease of placement and good workability (Table 3.10).

Table 3.10 Characteristics of cast-in-place topping concrete for test LOS 3

Design Strength (MPa)	Max. Aggregate Size (mm)	Ordered Slump (mm)	Received Slump (mm)	Test Strength (MPa)
30 at 28 days	13	100	100	25 at 17 days

3.3.3.4 Reinforcement

(a) 665 Mesh

The characteristics of hard drawn wire mesh were identical to those described in Table 3.2.

(b) HD12 Starters

The characteristics of 12 mm diameter Grade 430 starter bars were as given in Table 3.4.

3.3.3.5 Results of Testing

(a) Initial Response

The initial response to horizontal loading showed a stiff system (Fig. 3.46) up to about 200 kN. At this stage a crack appeared through the topping slab at 620 mm from the support, just beyond the point of starter bar curtailment. Under increased force the topping crack widened and slippage occurred between the precast and topping concretes.

(b) Fracture

At just over 2.0 mm displacement and at a force of almost 300 kN, the hollow core section suddenly fractured. The resulting crack occurred across the section at 570 mm from the support, adjacent to the principal topping crack, and extended 135 mm downward into the hollow core section. The resistance of the section fell to 215 kN, and under continued displacement reached the post-fracture peak force of 231 kN at a displacement of 6.5 mm.

(c) Displacements

Slippage between the precast and topping concretes was observed in the very early stages of this test. The magnitude of net topping slippage closely matched the horizontal unit displacement throughout the pre-fracture stage, as recorded in Figure 3.46. The post-fracture stages were characterised by upward (ie., hogging) displacement resulting from the moment couple formed between the prestressing strand reaction in the fractured hollow core section and the centroid of applied force at the support carriage. Eventually, this rotation began to affect the test procedure and the experiment was terminated at 15 mm horizontal displacement. At this stage the rotation had lifted the unit by about 11 mm at the position of the section fracture.

3.3.3.6 Analysis of Test Results

In order to analyse the response of test LOS 3, the force-displacement diagram has been divided into the four distinct regions that were reflected in the test outcome (Fig. 3.47). Each of these regions (Stages) indicates a basic change in the resistance mechanism against imposed horizontal displacements. As a whole, the diagram clearly indicates the differing contributions of respective steel reinforcement and concrete components.

(Stage I) Peak Load and Fracture

The initial response showed an average axial stiffness of 1980 kN/mm, with resistance provided by the entire composite section. At about 200 kN (ie., 67 % of peak load), the response softened markedly to an average of 71 kN/mm up to sudden fracture at just under 300 kN. The reduced stiffness is attributed to the propagation of cracks through the topping slab, especially at the point of starter bar curtailment and over the support region. The subsequent loss of topping

shear bond (see Fig. 3.48) and mobilisation of the precast section contributed to stiffness reduction.

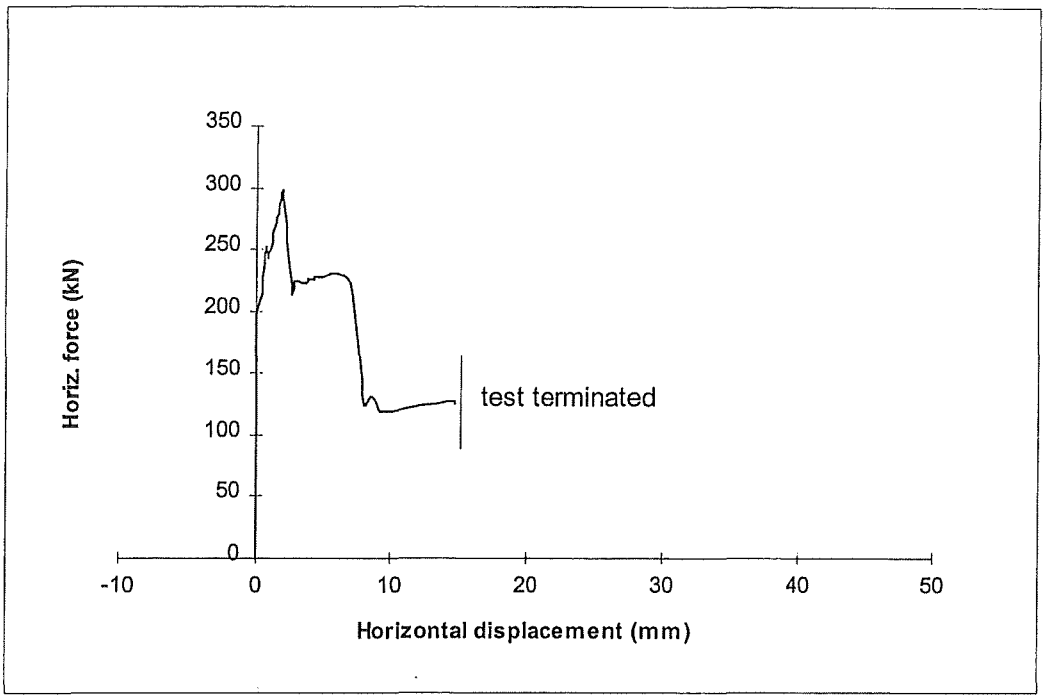

Fig. 3.46 Force-displacement response of test LOS 3

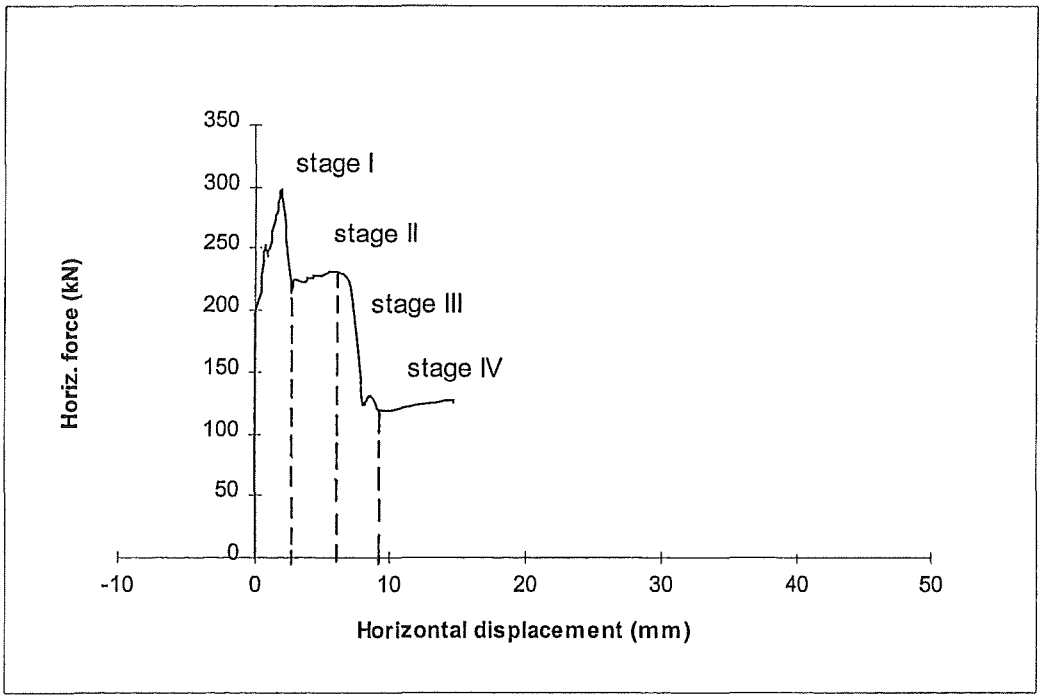

Fig. 3.47 Force-displacement diagram divided into regions of significance in terms of resistance mechanisms

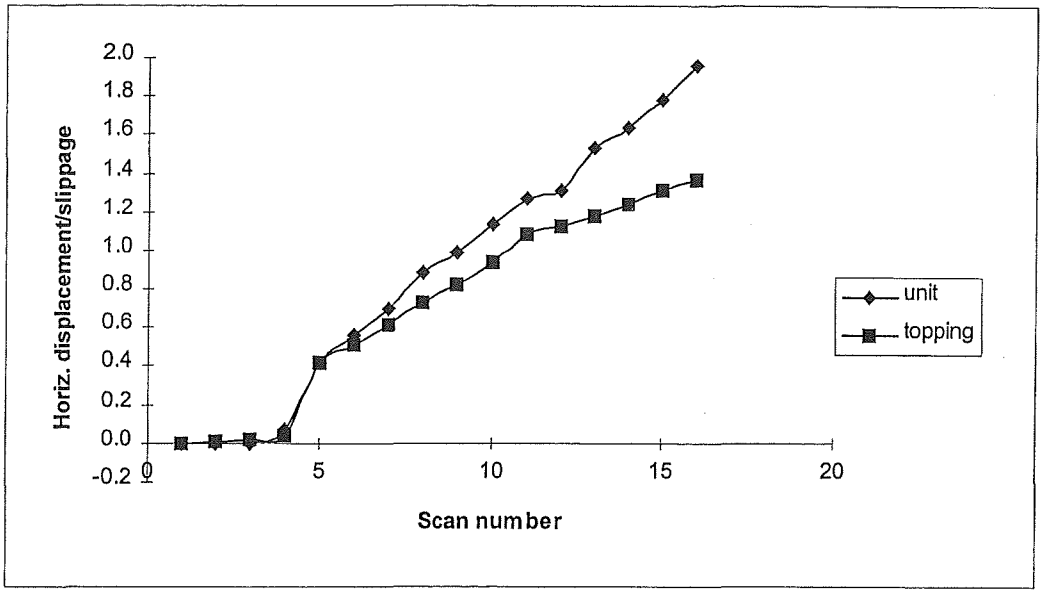

Fig 3.48 Pre-fracture relationship between the unit and topping slippage displacements in the support region, indicating significant shear bond loss between precast and topping concretes

The decrease in stiffness between 200 kN and sudden fracture corresponded with an increase in starter bar and mesh strains. Reinforcement stresses generally increased in direct proportion to applied horizontal force. Analysis of reinforcement stresses indicates that reinforcement provided the majority of axial restraint in the immediate vicinity of the support (Fig. 3.49). Peak starter bar stresses also occurred over the support region, reaching first yield at about 1.3 mm horizontal displacement.

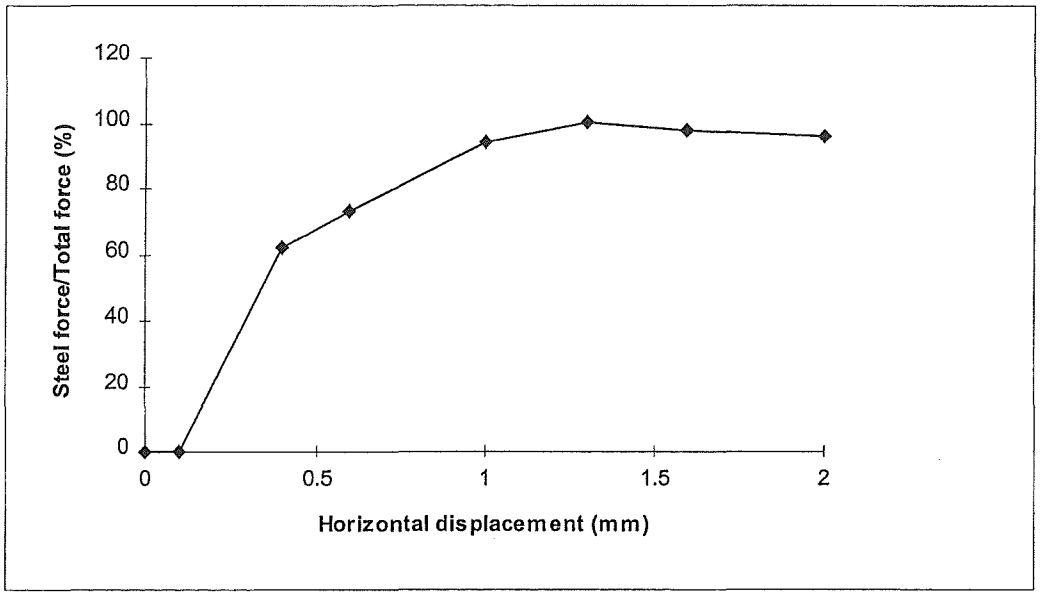

Fig. 3.49 Proportion of total horizontal force resisted by starter bars and mesh in the support region, up to sudden fracture at 2.2 mm displacement

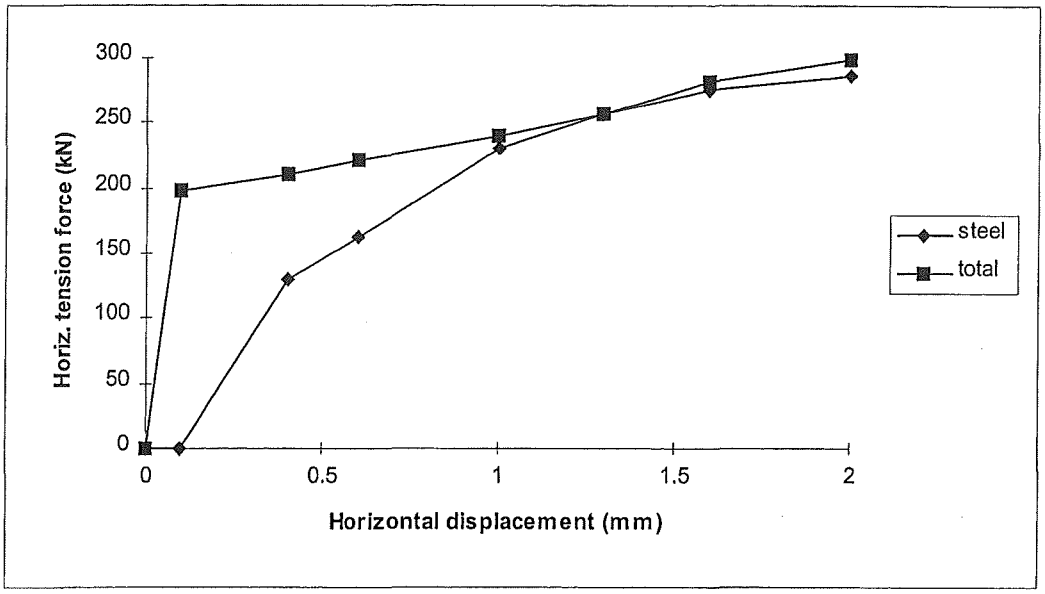

Fig 3.50 Total force and reinforcing steel force (starters and mesh) across the support region, up to sudden fracture of the hollow core section

Analysis of Figures 3.49 and 3.50 would suggest that the sudden fracture of the hollow core section might have been instigated by an increase in precast section tension in the support region. At the location of the hollow core fracture (ie., 650 mm from the support region) the proportion of tension force resisted by the precast section would have been substantially greater than indicated by Figures 3.49 and 3.50. The section force can be estimated by subtracting the force resisted by topping mesh at the proportional limit from the total force, giving 300 kN– (528 MPa × 176 mm²) = 207 kN. Hence, a slight increase in direct restraint applied to the precast section at the support could have been sufficient to cause fracture at a location resisting a much greater proportion of the total force.

It is most likely that the increase in precast section restraint was due to wedging effects in the support region under increasing displacement. Unlike test LOS 1, the sides of the hollow core unit in test LOS 3 were deliberately debonded from the cast-in-place support block concrete so as to avoid the wedging restraint that contributed to the sudden fracture in test LOS 1. However, it was expected that significant wedging forces would develop between the displacing precast section and the typical aberrations that occur in topping slab and support block surfaces.

The distribution of starter bar stresses (Fig. 3.51) shows that bar bond efficiency was greater in the cast-in-place support block than in the topping slab, as indicated by the respective slopes on either side of gauge number 3.

The strength development of starter bar and mesh elements was almost in direct proportion to their respective areas (Fig. 3.52). The area of HD12 starters was 452 mm² (ie., 72% of total topping steel area) and the area of mesh was 176 mm². Immediately before fracture, the starters had developed 70% of the total steel reaction force.

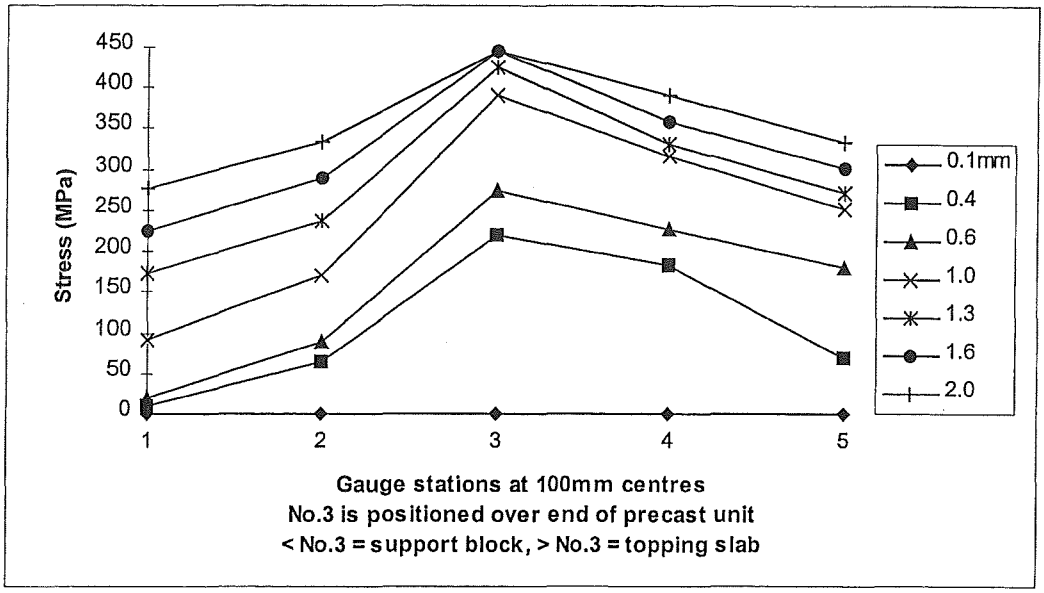

Fig. 3.51 Average pre-fracture stress distributions along HD12 starter bars at the indicated horizontal displacements during Stage I of test LOS 3

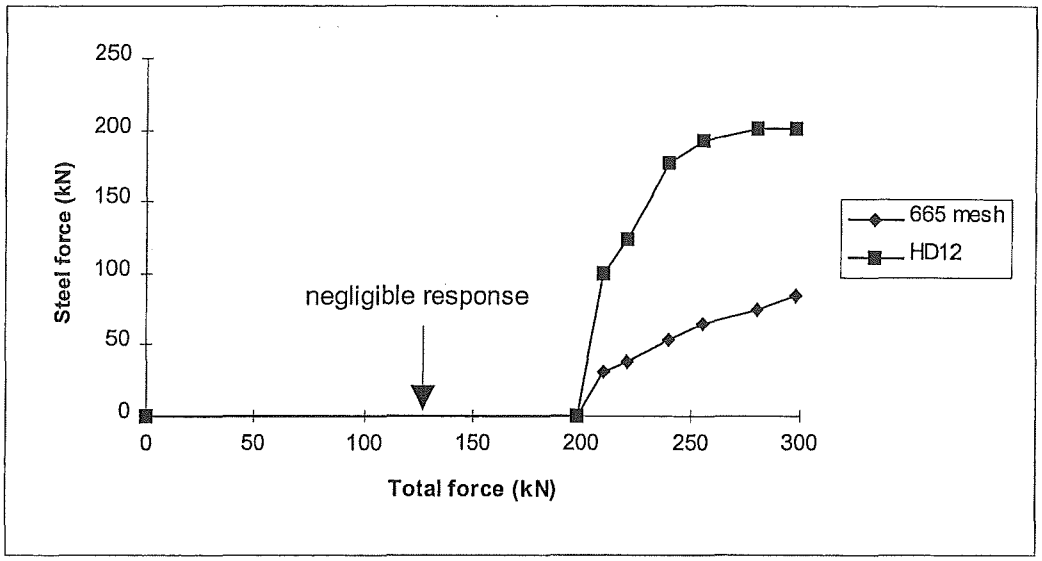

Fig. 3.52 Average pre-fracture restraint forces provided by HD12 starter bars and 665 mesh in the support region

The sudden fracture of the precast concrete section resulted in a principal crack through the entire width of the hollow core unit which extended about two thirds of the section depth. The sudden fracture was accompanied by a horizontal displacement of 0.6 mm, over which horizontal resistance force fell from the peak value of 298 kN to the post-fracture resistance of 215 kN at the end of loading stage I.

It is feasible that the effect of eccentric prestress in the hollow core section (ie., prestressed outside the middle third kern of the section) may have contributed to the precast section fracture by reducing tensile resistance in the section top fibre. The crack occurred immediately beyond the curtailment point of the topping starter bars, at a location of intensified section stresses.

(Stage II) Post-Fracture to Post-Fracture Peak Force

At the beginning of loading stage II the topping crack opening ranged from 1.2 mm to 1.5 mm, which was about one half of the total unit displacement. From a static position at post-fracture, further horizontal displacement resulted in an increased reaction up to the post-fracture peak force of 231 kN (78% of the peak pre-fracture force) with 6.5 mm total displacement. Throughout this stage of the test, resistance to horizontal force was manifested in a combination of tension and bending, with tensile reactions respectively provided by prestressing strand in the fractured precast section and mesh wire in the topping slab. The bending moment resulted from the force couple produced between applied force acting through the centroid of the elastic composite section at the support carriage, and the centroid of tensile reaction in the fractured section.

During this loading stage, the average starter bar and mesh stresses in the support region (see Fig. 3.53) generally behaved in relative proportion to the overall force displacement response (Fig. 3.46). This would suggest that although significant bond loss had occurred between the precast and topping concretes, the wedging mechanism described in the prior section was still apparent in the post-fracture stages.

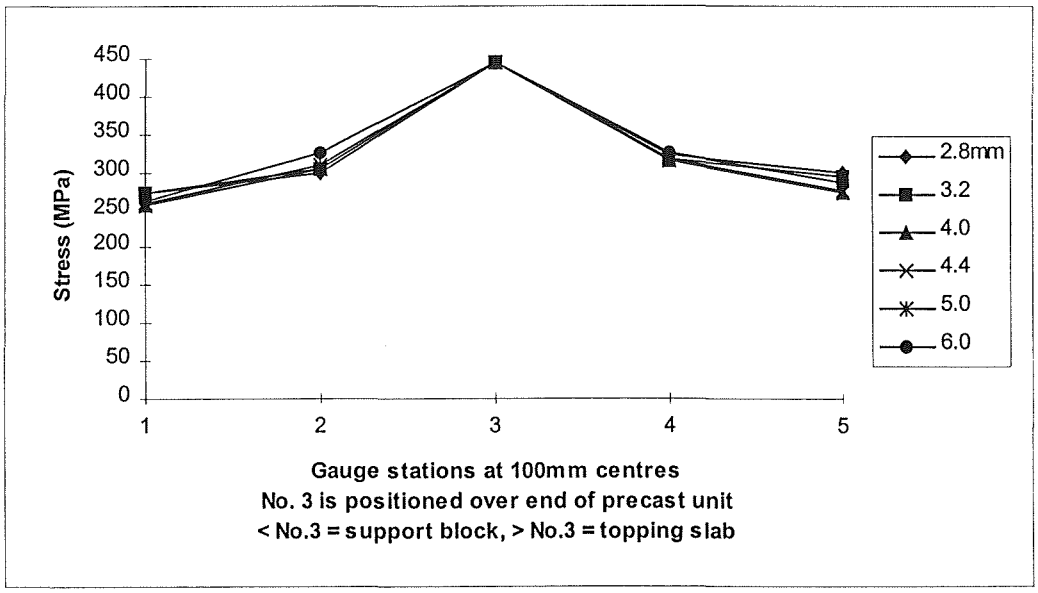

Fig 3.53 Average stress distributions along HD12 starter bars at the indicated horizontal displacements during Stage II of test LOS 3

(Stage III) Post-Fracture Peak Load to Fracture of Mesh Wires

An important feature of this loading stage was the upward rotation caused by the force couple. At the beginning of load stage III, the rotation had caused an upward deflection of 3.0 mm at the location of the section fracture. It is evident that this effect influenced the duration of mesh wire resistance to applied force. Between 6.5 mm and 7.0 mm horizontal displacement, the reaction fell slightly to 224 kN and was followed by the simultaneous fracture of seven out of the eight mesh wires that bridged the topping crack. Further applied force from the residual of 118 kN at 8.0 mm displacement caused fracture of the last mesh wire at 129 kN and 8.7 mm displacement.

(Stage IV) Fracture of Mesh Wires to Termination of Test

Loading Stage IV was characterised by a modest increase in horizontal reaction and significant rotation. Since resistance to bending moment was lost with fracture of the mesh, the rate of upward deflection had accelerated. From the beginning of Stage IV to termination of the test at horizontal displacement of 15 mm, the upward deflection progressed from 8.0 mm to 11 mm. Hence, it became necessary to terminate the test because this magnitude of rotation began to impinge on test rig equipment (Fig. 3.54).

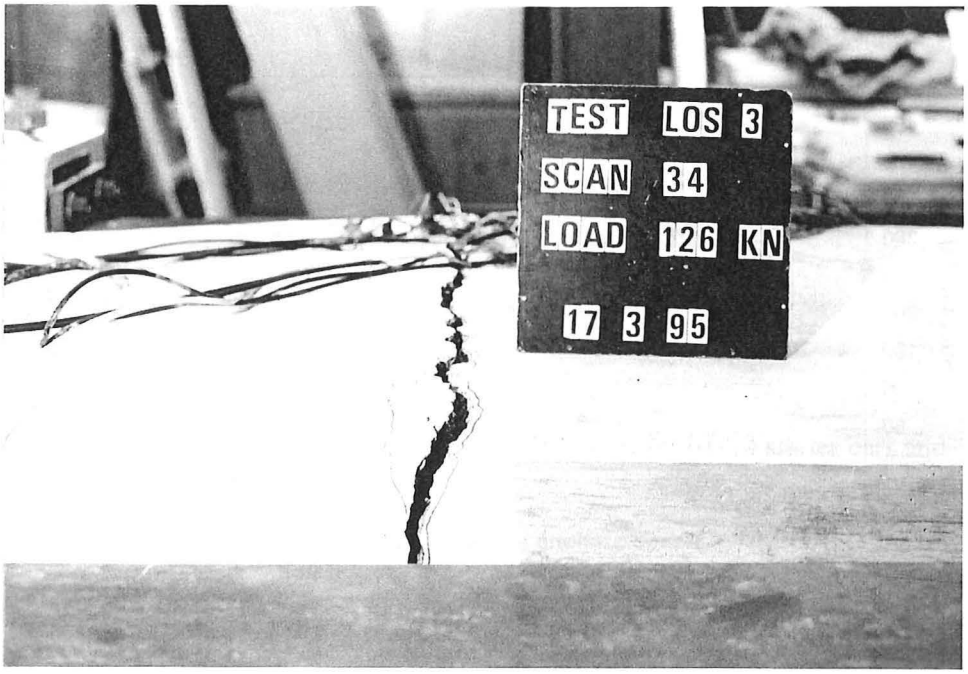

Fig. 3.54 Accentuated crack opening and unit rotation at the end of testing

3.3.3.7 Specific Analysis

(a) Section Fracture

The combination of direct tension, eccentric prestress and small positive bending moment is likely to have had a direct influence on the formation of the hollow core section fracture. At the time of testing, the stress state in the hollow core extreme top fibre is estimated as follows (Fig. 3.55) (also see Fig. 3.2a).

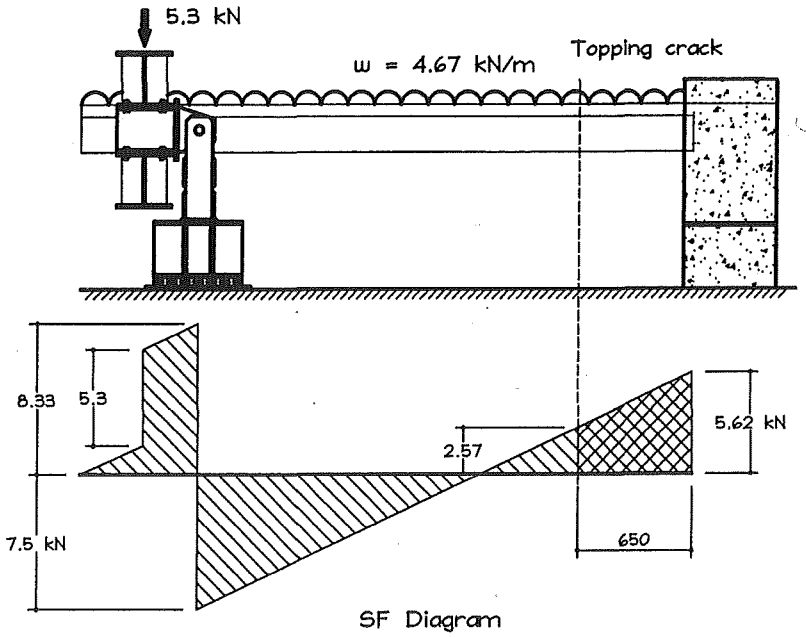

Fig. 3.55 Loads and reactions on test specimen

Hence, bending moment at distance x from the support is equal to $5.62x - \frac{1}{2}wx^2$ (kNm). With x = 0.65 m to the end of the starter bars and a weight per unit length of w = 4.67 kN/m (precast section plus topping concrete), the calculated bending moment $M_{(x)}$ at the point of starter curtailment is +2.7 kNm. This was the bending moment resisted by the precast section from the time that composite topping was placed, since there was no temporary shoring applied to the system at construction.

The effective prestress force P_f is taken to be the initial prestress P_i less 20 % losses. As such, the assumed losses are above average to account for strand slippage incurred by relatively short members with saw-cut tendons. Hence, the estimated effective pretension force is $P_f = (0.8 \times 0.72 \times 184 \text{ kN}) \times 4 = 424$ kN. The prestress eccentricity is the normal distance between the neutral axis and the centroid of strands. Thus, $e = \acute{y}_x - \acute{y}_s$, which equals $(100 - 45) = 55$ mm.

Ignoring short-term effects, the section stress at the time of testing may be calculated under the usual format of combined stresses:

$$f_c = -\frac{P_f}{A_{pc}} \pm \frac{P_f \cdot e}{Z} \pm \frac{M_{(x)}}{Z} \qquad (3.18)$$

Thus, for the test specimen top fibre:

$$f_c = -\frac{424\,\text{kN}}{119300} + \frac{(424\times 0.055)\,\text{kNm}}{6.4e^6} - \frac{4.8\,\text{kNm}}{6.4e^6} = -0.66\text{MPa}$$

Under direct axial tension during testing, a uniform tensile stress is considered to apply across the section. It was noted in the early stages of testing (see Stage I) that cracks had formed in the topping slab at the starter curtailment point, in the vicinity of the section fracture. Hence, it is certain that tensile resistance of the topping slab was significantly reduced at an early stage.

The variation in hollow core geometry precludes straightforward analysis of section stresses based on cracked elastic section properties. Consequently, the principles of equilibrium analysis have been used in an iterative calculation. In this procedure, the topping mesh reaction is treated as a constant force, equal to the characteristic yield strength of mesh (ie., 530 MPa) and independent of section curvature. Because of the small curvatures involved under predominantly axial load and the observed topping slab slippage, this is a reasonable assumption. The configuration of forces and moments and the effective cross section are shown in Figure 3.56.

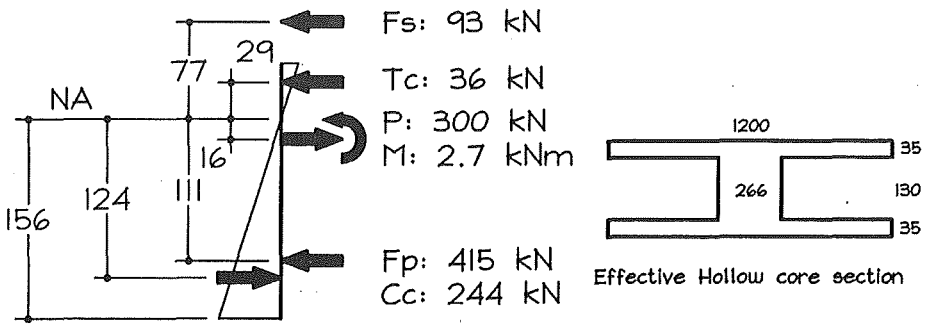

Fig. 3.56 Internal forces with applied force P and moment M acting on section, and effective cross section assumed for hollow core unit

As previous, the peak axial force is taken as P = 300 kN and the concurrent section bending moment as $M_{(x)}$ = +2.7 kNm. With an initial pretension force of F_p = 425 kN and constant mesh tension of F_s = 93.3 kN, section equilibrium is satisfied at a neutral axis depth of c = 156 mm and corresponding curvature of $\varphi = 1.0 \times 10^{-6}$ rad/mm.

With an assumed concrete elastic modulus of E_c = 32000 MPa, the hollow core top fibre tension stress at fracture is calculated as 1.4 MPa from the relationship $f_c = E_c \cdot \varphi \cdot (H-c)$. Based on 45 MPa concrete, this is equal to a tensile rupture strength of $0.21\sqrt{f'_c}$ under predominantly axial loading.

(b) Topping Mesh Fracture

At the fracture of topping mesh, strain-equilibrium principles are likewise applied. However, the mesh force is increased to fracture strength (ie., 660 MPa) and the tensile contribution of hollow core section is ignored (Fig. 3.57).

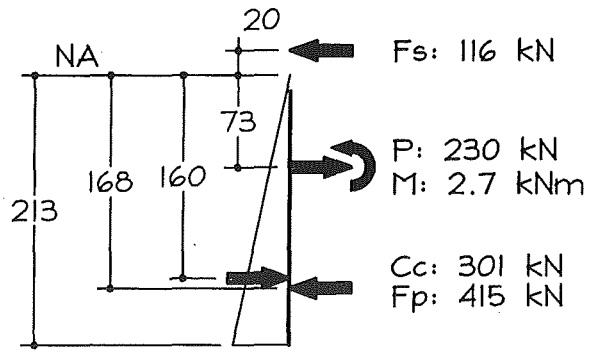

Fig. 3.57 Internal forces with applied force P and moment M acting on the section

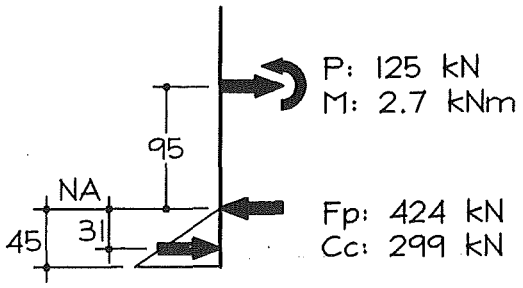

Fig. 3.58 Internal forces with applied force P and moment M acting on section

The peak post-fracture axial force is taken as P = 230 kN and the concurrent section bending moment as $M_{(x)}$ = +2.7 kNm. With an initial pretension force of F_p = 425 kN and constant mesh tension of F_s = 116.2 kN, section equilibrium is satisfied at a neutral axis depth of c = 213 mm and corresponding curvature of $\varphi = 7.14 \times 10^{-7}$ rad/mm.

(c) End Of Test

At the end of test there is no tensile contribution from topping mesh and the tensile contribution of hollow core section is ignored (Fig. 3.58). The peak post-fracture axial force is taken as P = 125 kN and the concurrent section bending moment as $M_{(x)}$ = +2.7 kNm. With an initial pretension force of F_p = 425 kN, section equilibrium is satisfied at a neutral axis depth (corresponding with strand height) of c = 45 mm and curvature of $\varphi = 8.33 \times 10^{-6}$ rad/mm.

3.3.4 LOS 4

3.3.4.1 General

Test LOS 4 was the third of three tests directed at the typical starter bar detail (Figs 3.9 and 3.10). The floor configuration involved 65 mm of cast-in-place topping over a 200 mm hollow core extruded flooring unit that was pretensioned with four 12.7 mm diameter Supergrade strands. Four 12 mm diameter Grade 430 (HD12) starter bars were placed at 300 mm centres, and extended 600 mm into the topping slab. 665 mesh was placed over the hollow core unit, and was continued beyond the end of the seating length, thus contributing to the tensile strength across the construction joint (assumed to be the critical section). Similarly to the second test involving this detail (ie., LOS 2) a superimposed dead load was not applied to the test specimen.

3.3.4.2 Instrumentation

(a) Forces and Displacements

Forces and displacements were measured in accordance with the methods described in Section 3.2.2 (also Fig. 3.4).

(b) Reinforcement

Electrical resistance strain gauges were employed as described in Section 3.3.1.2(b).

3.3.4.3 Cast-In-Place Topping Concrete

The concrete supplied for test LOS 4 was considerably above the target slump of 100 mm. However, the concrete was accepted on the basis that it had good consistency and did not exhibit bleeding when worked (Table 3.11).

Table 3.11 Characteristics of cast-in-place topping concrete for test LOS 4

Design Strength (MPa)	Max. Aggregate Size (mm)	Ordered Slump (mm)	Received Slump (mm)	Test Strength (MPa)
30 at 28 days	13	100	165	30 at 25 days

3.3.4.4 Reinforcement

(a) 665 Mesh

The characteristics of hard drawn wire mesh were identical to those described in Table 3.2

(b) HD12 Starters

The characteristics of 12 mm diameter Grade 430 starter bars were as given in Table 3.4

3.3.4.5 Results of Testing

(a) Initial Response

The initial response to horizontal loading showed a stiff system (Fig. 3.59) up to about 251kN. At this stage, a crack of average 0.25 mm width had appeared through the topping slab across the line of the support. There was a correspondingly small loss of horizontal reaction, ranging from 251 kN to 230 kN.

(b) Fracture

At 230 kN and 1.4 mm displacement, a sudden fracture occurred through the topping slab at an average distance of 840 mm from the support line. This resulted in a significant loss of reaction from 230 kN to 150 kN, and 2.0 mm horizontal displacement. Under increased force the principal topping crack continued to widen, with pronounced slippage occurring between the precast and topping concretes. The post-fracture peak force of 172 kN was recorded at 3.9 mm displacement, with a plateau occurring up until the beginning of topping mesh fracture at around 7.0 mm horizontal displacement.

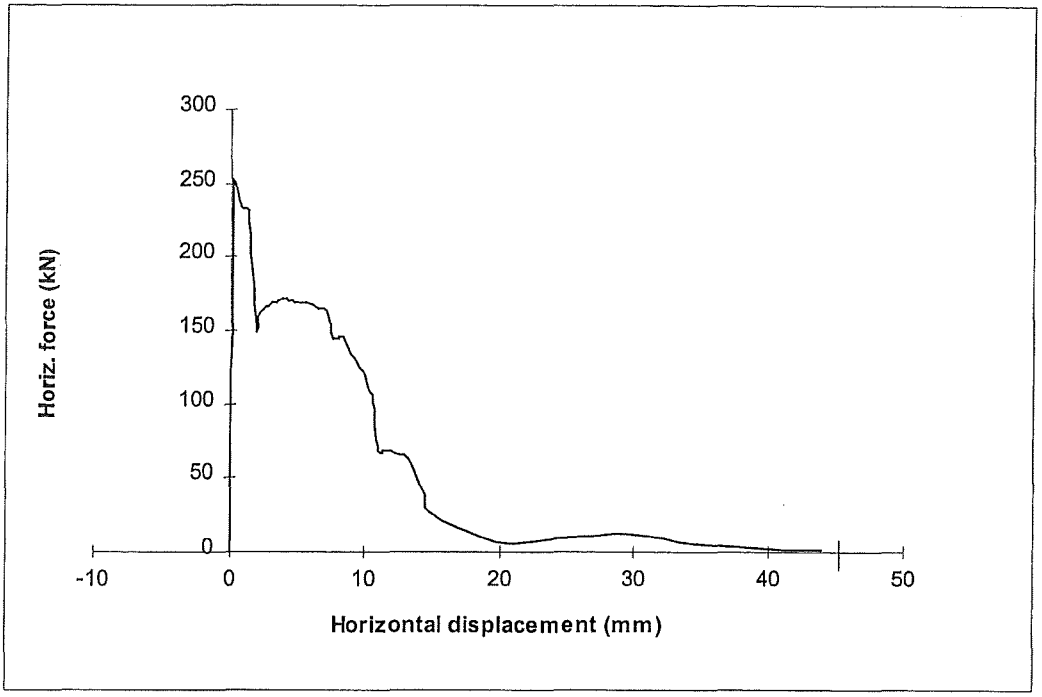

Fig. 3.59 Force-displacement response of test LOS 4

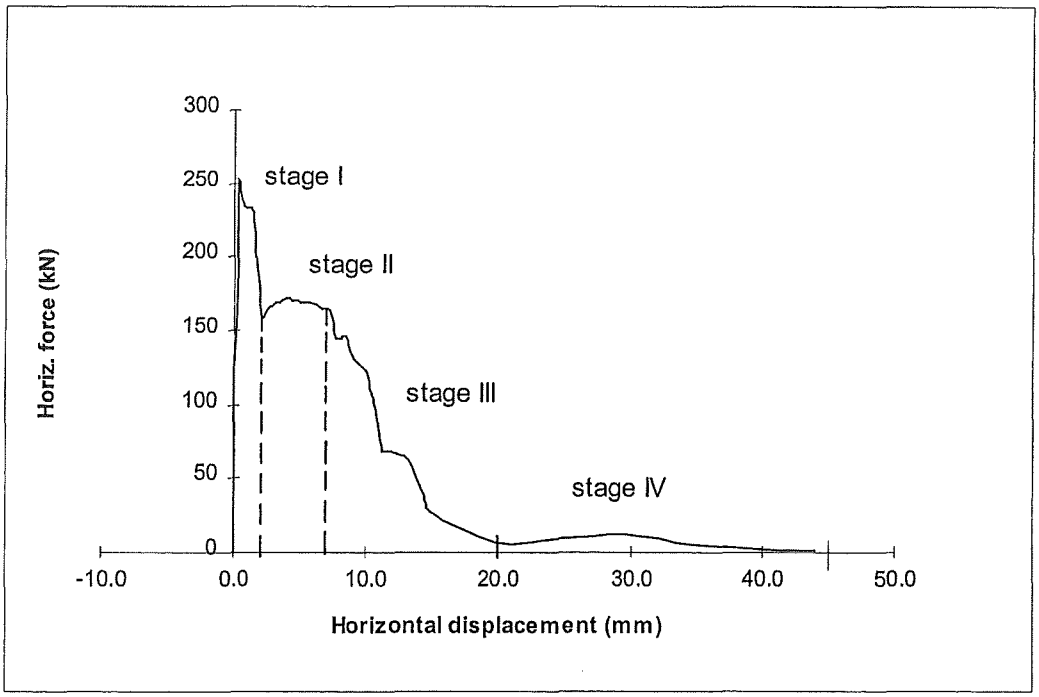

Fig. 3.60 Force-displacement diagram divided into regions of significance in terms of resistance mechanisms

Horizontal restraint capacity progressively diminished between 7.2 mm displacement and the completion of topping mesh fracture at 20 mm displacement. Throughout this phase there was intermittent tensile fracturing of mesh wires, similar to observations in test LOS 1. Once the restraint provided by mesh wires was fully overcome, only the component of residual sliding friction was recorded.

Drying shrinkage cracks had developed in the topping slab during the curing period, and it is certain that these cracks exerted an influence on unit behaviour during testing. Shrinkage cracks observed before testing are shown in Figure 3.64, with crack widths measuring between 0.1 mm and 0.2 mm. The principal topping crack that eventuated under applied load was propagated by an initial drying shrinkage crack situated close to the curtailment of starter bars (see Fig 3.61).

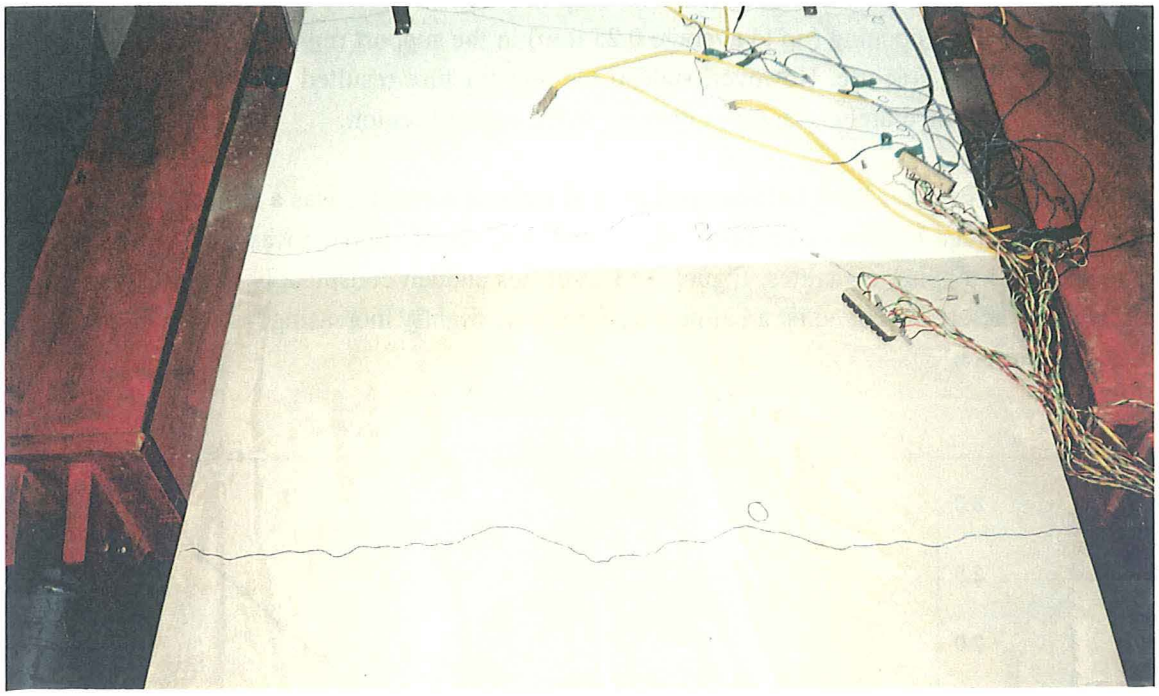

Fig. 3.61 Drying shrinkage cracks in topping slab immediately prior to testing. Under applied axial force, a shrinkage crack (indicated) developed into the principal topping fracture

(c) Displacements

A very small amount of slippage was observed between the precast and topping concretes in the early stages of this test, up to the point of topping fracture. Just prior to topping fracture (approximately 1.4 mm displacement) a considerable increase occurred in the rate of slippage. The post-fracture stages were characterised by continued and increasing slippage. Towards the final stages of the test, the only resistance to axial force was provided by residual sliding friction between the precast section and support block. As a result of support block spalling, the hollow core unit was effectively pulled off the support at a horizontal displacement of 45 mm.

3.3.4.6 Analysis of Test Results

In order to analyse the response of test LOS 4, the force-displacement diagram has been divided into the four distinct regions that were reflected in the test outcome (Fig. 3.60). Each of these regions (Stages) indicates a basic change in the resistance mechanism against imposed horizontal displacements. As a whole, the diagram clearly indicates the differing contributions of respective steel reinforcement and concrete components.

(Stage I) Peak Load and Fracture

The initial response showed an average axial stiffness of 1405 kN/mm, with resistance provided by the entire composite section. The initial stiff response endured until the peak horizontal force of 251 kN and 0.3 mm displacement. The drop in reaction directly beyond peak force was due to gradual crack opening (up to average 0.25 mm) in the support region, and was not caused by sudden topping fracture. However, sudden topping fracture resulted from the reapplication of axial force, immediately after crack opening in the support region.

Sudden loss of shear bond between precast and topping concretes was a feature of post-fracture in loading stage I. Prior to fracture, only a small amount of slippage was recorded between the precast and topping concretes. Figure 3.63 indicates sudden conspicuous slippage just prior to topping fracture, followed by an almost uniform (but slightly increasing) rate of slip in the post-fracture range.

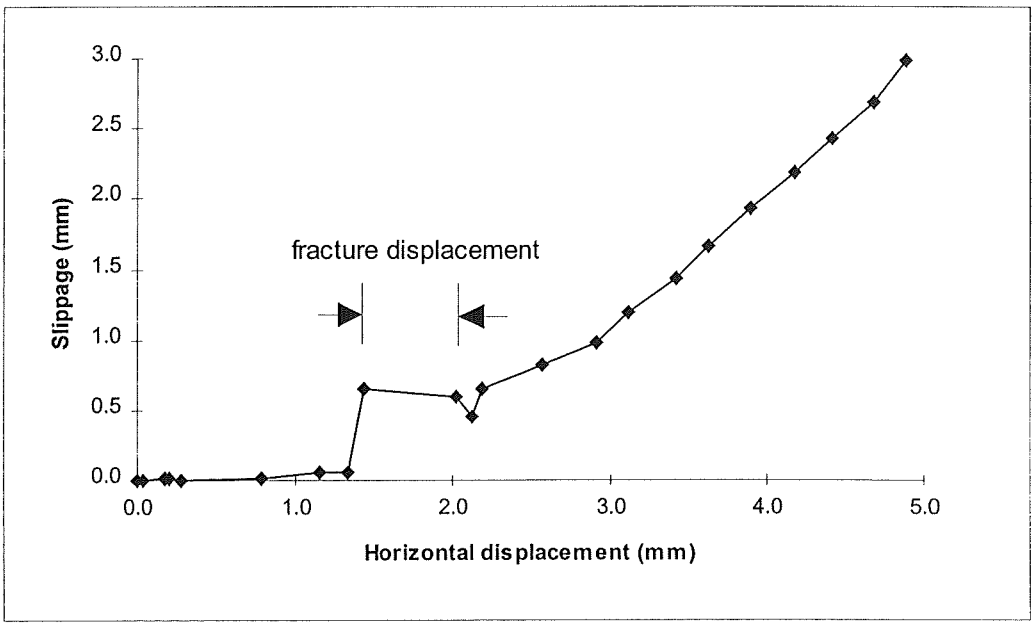

Fig. 3.62 Relationship of precast unit and topping slippage displacements in the support region, showing a step in slippage immediately prior to topping fracture at 1.4 mm displacement

The appearance of topping cracks over the support region corresponded with a marked increase in starter bar and mesh strains. Reinforcement stresses generally increased in proportion to applied horizontal force up to the maximum starter stress of 448 MPa at 1.3 mm displacement, immediately prior to topping fracture. The stress gradients in Figure 3.63 indicate that bar bond stresses were generally more efficient in the topping slab region than in the support block.

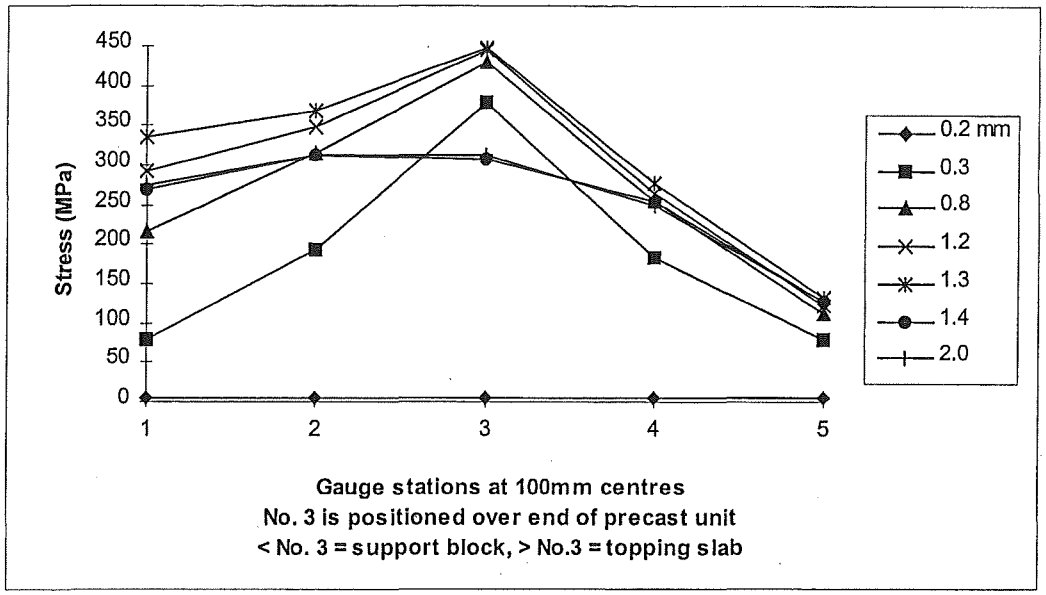

Fig. 3.63 Average pre-fracture stress distributions along HD12 starter bars at the indicated horizontal displacements during Stage I of test LOS 4

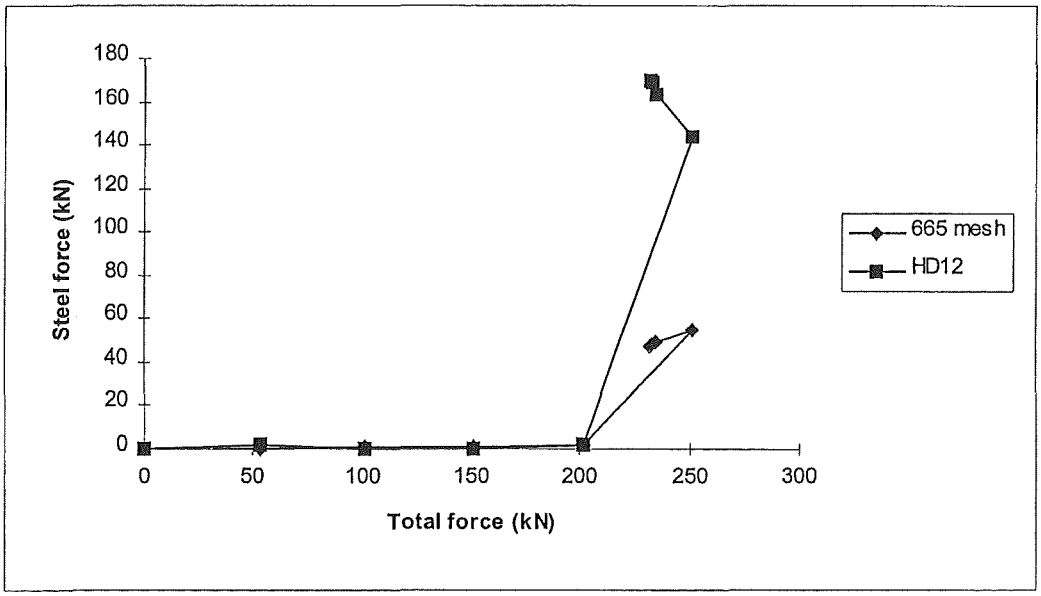

Fig. 3.64 Average pre-fracture restraint forces provided by HD12 starter bars and 665 mesh in the support region

(Stage II) Post-Fracture to Onset of Mesh Fracture

Beyond topping fracture and up to the onset of mesh fracture (ie., between 1.4 mm and 7.2 mm displacement), starter bar strains in the support region maintained almost static levels of tensile stress under continued loading (see Fig. 3.63).

The post-fracture peak force of 172 kN was attained at 3.9 mm displacement, and gradually decreased to 163 kN prior to first mesh fracture.

(Stage III) Onset of Mesh Fracture to Full Loss of Steel Reaction

Once the peak load displacement of 7.2 mm was exceeded, a steady loss of reaction resulted from the serial tensile fracture of mesh wires. Likewise, the initially significant effects of residual concrete bond and friction were completely diminished during this stage of loading. Because the mesh wires were the only form of reinforcement offering resistance across the principal topping crack, the entire contribution from reinforcement was lost with fracture of the last wire at 20 mm displacement. Beyond 20 mm displacement it was clear that the only resistance provided was due to sliding friction between the soffit of the hollow core unit and the seating ledge.

(Stage IV) Loss of Reaction to Collapse

The final stage of the test registered almost negligible reaction force. The final stage of the test involved displacing the unit until the eventual collapse occurred at 45 mm displacement. A degree of downward movement of the precast section resulted from support spalling. Immediately prior to collapse, the unit had slipped to 6.0 mm below the original support level (Fig. 3.65).

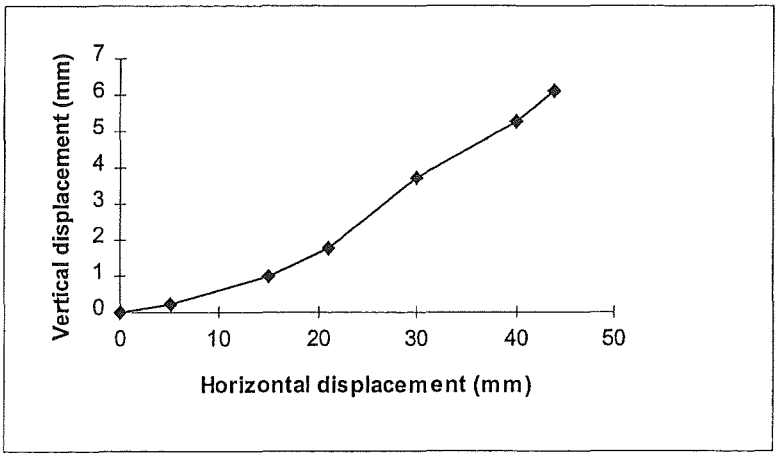

Fig. 3.65 Vertical dislocation of the hollow core section due to spalling of the support ledge, measured in relation to horizontal displacement up to collapse

3.3.4.7 Specific Analysis

(a) Work Done

Referring to Figure 3.60, the summation of total work done through each loading Stage (I to IV) is shown in Table 3.12:

Table 3.12 Summation of external work done by the connection detail of test LOS 4 over each loading stage. Note that stage I exhibited mainly elastic deformation up to peak force, and likewise, plastic deformation beyond sudden fracture:

Stage	I	II	III	IV	Total
Work Done (kN-mm)	415 (182 pre-fracture)	862	791	152	**2220**
Proportion (%)	18	39	36	7	**100%**

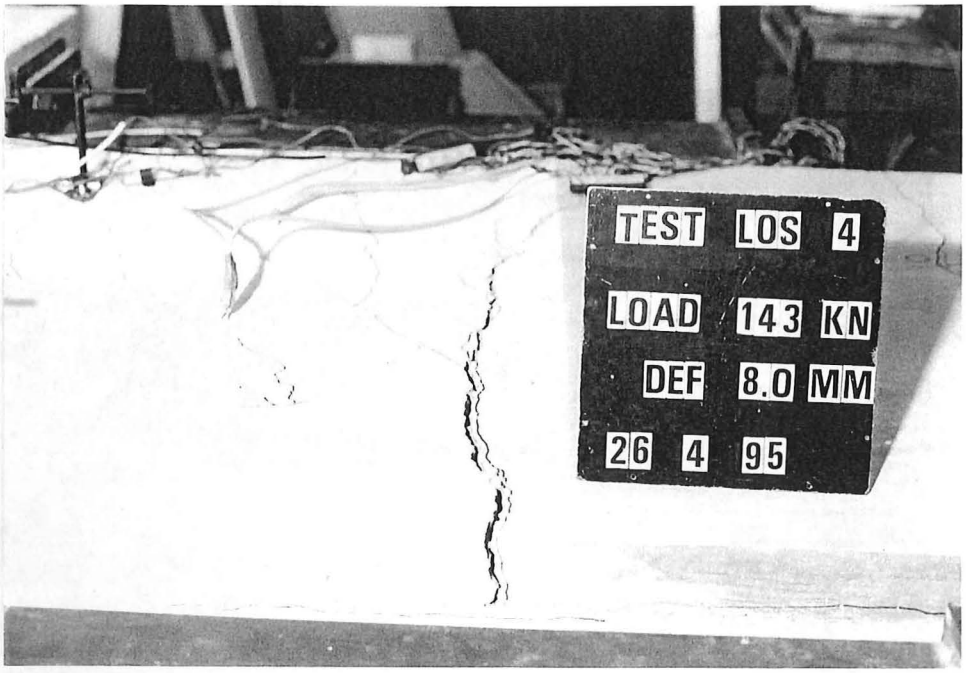

Fig. 3.66 Crack through composite topping at 8mm horizontal displacement, corresponding with the onset of topping mesh fracture

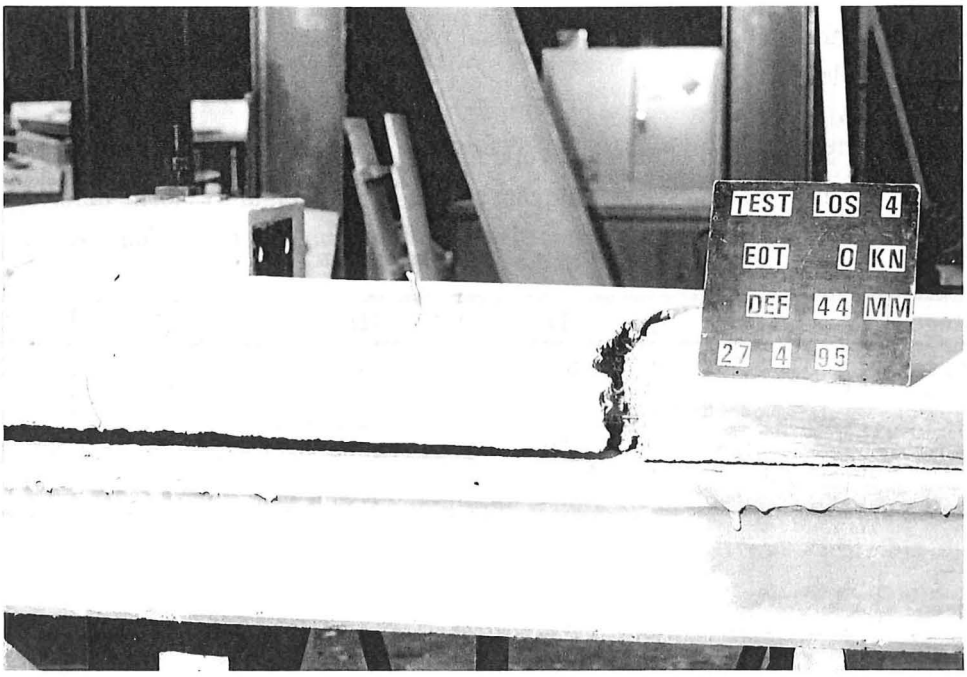

Fig. 3.67 Side view at end of test, showing separation between topping and precast concretes

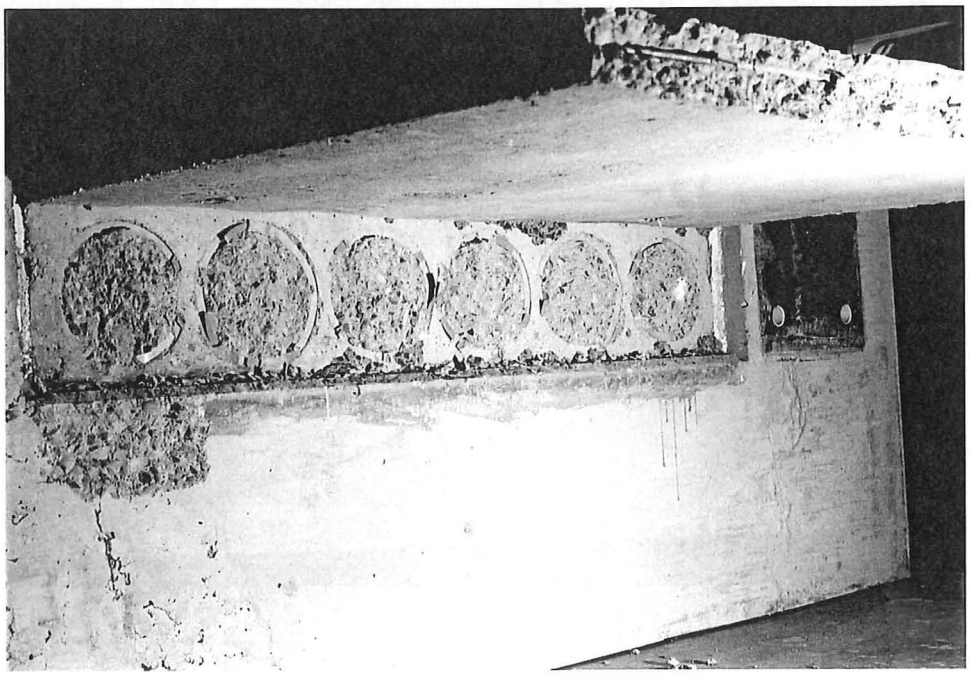

Fig. 3.68 View of support block after removal of hollow core section. Note smooth soffit of cantilevered topping slab

3.4 DISCUSSION ON TEST RESULTS

3.4.1 TYPICAL STARTER BAR DETAIL (Tests LOS 1, LOS 3, LOS 4)

The results of tests performed on the typical starter bar detail (see Sections 1.2.3.3 and 1.2.3.4) provide sufficient evidence of detail performance under dilation type loading. The response behaviours of the three test specimens are shown in Figure 3.69.

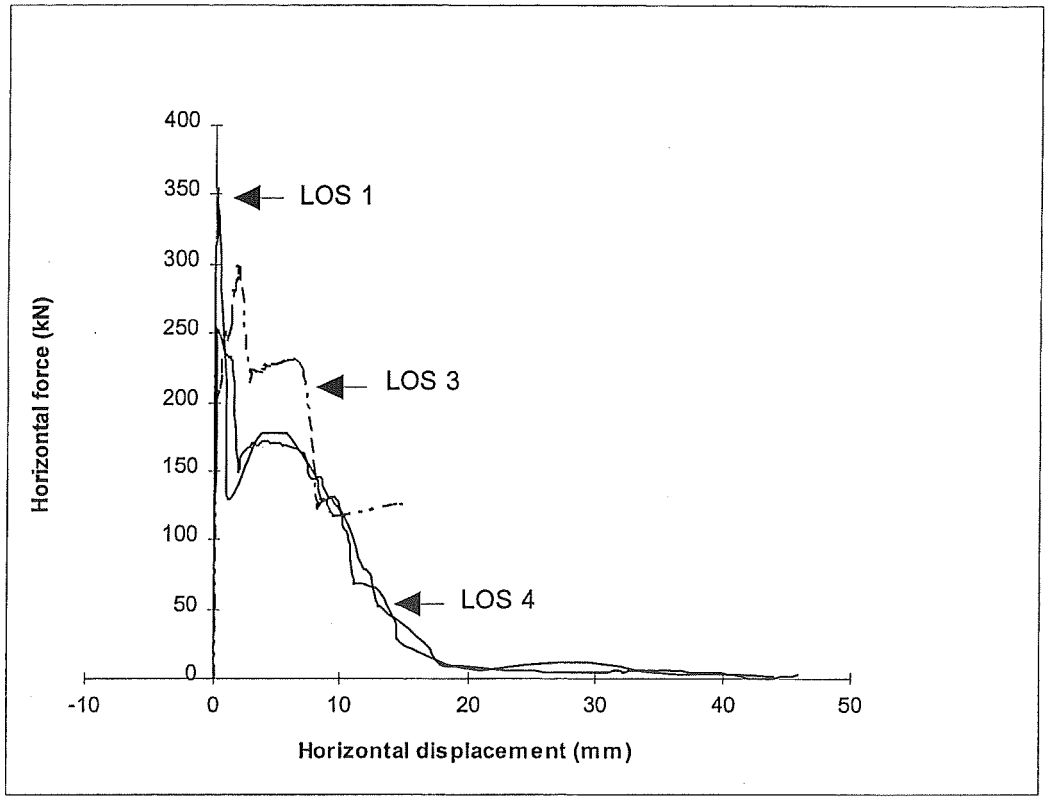

Fig. 3.69 Comparison of force-displacement responses of tests LOS 1, LOS 3 and LOS 4

A comparison of test results indicates that a characteristic mode of failure may occur with starter bar details subjected to axial loading. The relevant observations are as follows:

- In each case, the topping slab fractured a short distance beyond the point of starter bar curtailment. It would appear that the transition in topping stiffness and the reduced ability for crack control directly influences topping fracture.

- Topping fracture is accompanied by a rapid breakdown in composite bond strength between the topping slab and hollow core unit. It is likely that composite bond capacity will have begun to deteriorate prior to the sudden topping fracture.

- The onset of topping mesh fracture can be expected to occur at around 6 mm horizontal displacement. The tensile resistance of mesh will be fully depleted at about 20 mm displacement. Hence, a useful rule of thumb for the ductility of topping mesh under a dilation loading regime is 1 + 2 = 3, in terms of quarter inch increments.

- It is likely that collapse of the hollow core unit will occur at a lesser horizontal displacement than the seating length. This is due to spalling of the support ledge, but may also be result from tensile fracture at the end of the hollow core section. In each case, the actual configuration of seating is important, especially with regard to restraint provided by cast-in-place concrete in unit shear keys.

3.4.2 HAIRPIN DETAIL (Test LOS 2)

The results from this test indicate the following:

- Support tie details involving bars embedded into the support and grouted into the hollow core voids can provide a controlled ductile response to dilation forces.

- From the test, it is apparent that efficient bond capacity associated with deformed bars can mitigate ductile capacity. Hence deformed bars are not suited to applications where significant ductility may be required.

- Details involving cutback hollow core flanges and fully grouted voids result in much improved topping bond capacity.

3.4.3 COMPARISON OF WORK DONE

Table 3.13 shows the comparison of work done by the completed tests (test LOS 3 was terminated at 15 mm displacement). The efficiency of the embedded reinforcement is calculated as the ratio of work done U (N-mm) to the product of the effective volume of embedded bar V_{se} (mm^3) and actual yield stress f_y (N/mm^2). Hence, the dimensionless ratio that results may be regarded as resistance mechanism efficiency index. Based on strain gauge readings taken from the tests (see Figs 3.38 and 3.39) the effective length of embedment has been taken as 300 mm for each case.

Table 3.13 Comparison of external work done by the connection detail of tests LOS 1, LOS 2 and LOS 4, and efficiency index of each

Test	Resistance Mechanism	$V_{se} = 300$ A_s (mm^3)	f_y (N/mm^2)	Work Done (kN-mm)	$U/(V_{se} f_y)$
LOS 1	665 topping mesh	52800	528	1710	0.061
LOS 2	6-D10 hairpins	282600	312	18700	0.212
LOS 4	665 topping mesh	52800	528	2220	0.080

From the last column table 3.13 it is evident that the average work efficiency of the 665 topping mesh mechanism was one third that of the embedded D10 hairpins.

4

Loss Of Support Tests Involving Cyclic Loading

4.1 GENERAL

It has been said: "Engineering is an exact science based on assumptions". In the context of seismic design, perhaps the most important concern is that a given set of details will not compromise fundamental design assumptions when subjected to severe cyclic loading. Hence, to effect good designs, the engineers of (especially) seismic resisting structures must repeatedly and systematically defer "exact science" and concentrate on managing the assumptions.

Considering fundamental design assumptions, a particular case is the behaviour of starter bar and embedded bar details subjected to pronounced cyclic loading. It was observed in the earlier tests (test LOS 2) that efficient bar bond resulted in large strains, and was apparent that cyclic loading would cause bar buckling. This observation may be projected into the topping slab, where dilation and cyclic loading could adversely affect the performance of starter and continuity bars. In view of poor topping bond performance, it was considered that the components of bar buckling might completely dislodge the composite topping slab. Such a result would directly affect assumptions regarding consistent load path networks in seismic resisting floor diaphragms.

Two tests were conducted to observe the relative effects of cyclic dilation loading on both topping bars and embedded bars. In the first test, topping bars were designated as 8-HD12 at 150 mm centres, which may typically appear as continuity reinforcement over the ends of long flooring units. A selection of embedded tie details were then tested in parallel cores to establish if bar buckling tendencies may be induced by tie bar placement and geometry.

4.2 TEST METHODOLOGY

4.2.1 GENERAL PROCEDURE

To remain consistent with earlier experiments, the same basic methodology of previous tests was adopted, but with provision for applying cyclic tension and compression forces. As such, the general emphasis of testing was to apply axial tension force across the support interface so to extract the flooring unit from its seating. At a point when the reinforcing bar strain had exceeded strain at strain hardening ε_{sh}, compressive force was applied in order to close the

cracks caused by dilation loading and to compress reinforcement that crossed the principal crack.

4.2.2 DESCRIPTION OF TEST EQUIPMENT

4.2.2.1 General

Test equipment, including the three categories of test specimens, actuating system and logging componentry was essentially identical to that described in Chapter 3.

4.2.2.2 Precast Support Beams

A precast concrete support beam was constructed for each test (see Figs 3.1) as described in Section 3.2.2.2. To achieve cyclic loading capacity (tests LOS5 and LOS6), this detail was enhanced by adding two extra bolts to each sole plate and matching anchor plates on the opposite face of the precast support beam.

4.2.2.3 Horizontal Displacement

(a) Actuating System

Horizontal displacement was applied to the test specimens by two parallel acting hydraulic rams, each rated at 43 tonnes (see Figs 3.2). The hollow core flooring unit was secured onto the support carriages by two 310 UC 97 beams placed above and below the precast section, and bolted to it by eight 24 mm diameter threaded rods, as described in Section 3.2.2.3.

(b) Measurements

Principal horizontal displacements were measured by placing two 100 mm linear displacement potentiometers near each support carriage, connecting between target plates mounted on the hollow core unit and rigidly braced uprights bolted to the laboratory strong-floor. Potential uplift of the topping slab was monitored by two sets of potentiometers placed on isolated stands that were epoxied into the top flange hollow core unit (see Fig. 3.4). Further potentiometers were attached to the concrete support block to monitor movement of the test rig in relation to the floor. Force measurements were accorded by 44 tonne load cells positioned between the respective hydraulic rams and support carriages.

4.2.2.4 Reinforcing Bar Strain Gauges

Electrical resistance strain gauges were connected to principal reinforcement to establish bar strain characteristics. Ordinary 3% extension strain gauges were used. These were supplied by Tokyo Sokki Kenkyujo Co. gauge type FLA-5-11, with 120Ω resistance and 5.0 mm gauge length.

Surface preparations and the method of fixing electrical resistance strain gauges was carried out in accordance with the departmental guidelines for these procedures [Hill, 1992].

4.2.2.5 Data Logger Unit

The load cells, potentiometers and strain gauges were all connected to the Metrabyte logger which converted voltage changes caused by linear displacement into digital values. These values were recorded against respective scan numbers that were manually taken throughout the tests. At the conclusion of a test, the logged information was converted to an ASCII file that was then imported into Excel (spreadsheet program) for subsequent editing and data extraction.

4.2.3 MATERIALS AND CONSTRUCTION

4.2.3.1 General

The emphasis of this experimental programme was to reflect the general performance of pretensioned floor construction. The construction methods and curing was of a standard that might be expected on a well-supervised construction site.

4.2.3.2 Precast Pretensioned Hollow Core Units

Hollow core units were of the same type, dimensions and quality as described in Chapter 3.

4.2.3.3 Prestressing Strand

Prestressing strand properties were identical to those described in Section 3.2.3.3.

4.2.3.4 Cast-In-Place Topping Concrete

Topping concrete was selected and cured as described in Section 3.2.3.4.

4.2.3.5 Reinforcing Steel

(a) Starter and Tie Bars

12 mm diameter Grade 430 (HD12) continuity bars and 12 mm and 16 mm diameter Grade 300 (R12 and R16) plain round tie bars complying with the appropriate New Zealand standard [Standards New Zealand, 1989] were supplied cut and bent from recognised reinforcing steel merchants. The actual tensile characteristics of continuity and tie reinforcements are deferred to individual LOS tests.

(b) Welded Wire Fabric (Mesh)

665 mesh (5.3 mm diameter) complying with the appropriate New Zealand standard [Standards New Zealand, 1975] was placed in the topping slab, but was not included in the principal crack region.

4.3 RESULTS OF EXPERIMENTS

4.3.1 LOS 5

4.3.1.1 General

The initial cyclic LOS test was directed at a typical continuity bar detail (Fig. 4.1). The floor configuration involved 65 mm of cast-in-place topping over a 200 mm hollow core extruded flooring unit that was pretensioned with seven 12.7 mm diameter Supergrade strands. A total of eight 12 mm diameter Grade 430 (HD12) starter bars were placed at 150 mm centres, and extended the full length of the topping slab to avoid topping fracture at the curtailment. 665 mesh was placed over the hollow core unit and terminated before the end of the seating length (assumed to be the critical section).

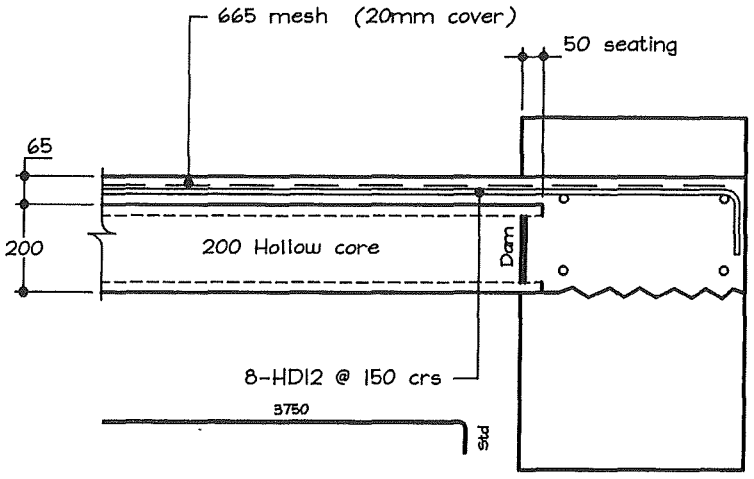

Fig. 4.1 Support configuration of LOS 5 test that involved a typical continuity bar detail

4.3.1.2 Instrumentation

(a) Forces and Displacements

Forces and displacements were measured in accordance with the methods described in Section 3.2.2 (also Fig. 3.4).

(b) Reinforcement

Standard 3% extension electrical resistance strain gauges (as described in Section 3.2.2) were employed on two individual items of starter reinforcement. These gauges were configured so that a gauge was situated directly over the expected cracking plane, at the end of the hollow core section. The strain gauges were set at 50 mm centres about the expected cracking zone (Fig. 4.2).

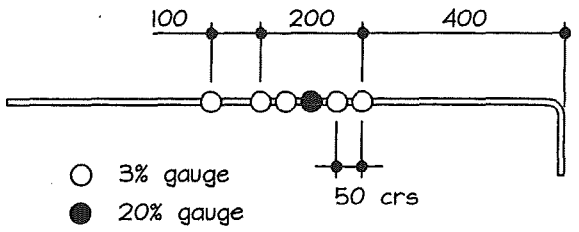

Fig. 4.2 Strain gauge positions on continuity bars used in the LOS 5 test

4.3.1.3 Cast-In-Place Topping Concrete

Concrete was ordered at a specified slump of 120 mm and accepted at a snatch sample slump of 150 mm (Table 4.1). The mix would be described as workable and generally good for topping concrete, although some very early bleed water was observed.

Table 4.1 Characteristics of cast-in-place topping concrete for test LOS 5

Design Strength (MPa)	Max. Aggregate Size (mm)	Ordered Slump (mm)	Received Slump (mm)	Test Strength (MPa)
30 at 28 days	13	120	150	28 at 21 days

4.3.1.4 Reinforcement

(a) 665 Mesh

The characteristics of hard drawn wire mesh were identical to those described in Table 3.2

(b) HD12 Continuity Bars

The characteristics of HD12 bars were identical to those described in Table 3.4

4.3.1.5 Results of Testing

(a) Initial Response

The initial response to horizontal loading showed a very stiff system (Fig. 4.3) with first cracking over the support region observed at around 150 kN and 0.07 mm displacement. The peak elastic response occurred at 0.27 mm horizontal displacement and a force of just over 300 kN. This was followed by a sudden increase in displacement due to tensile fracture of the concrete, resulting in 0.8 mm displacement at 320 kN of applied force. From this point onward, continuity bars in the topping slab governed the section tensile strength.

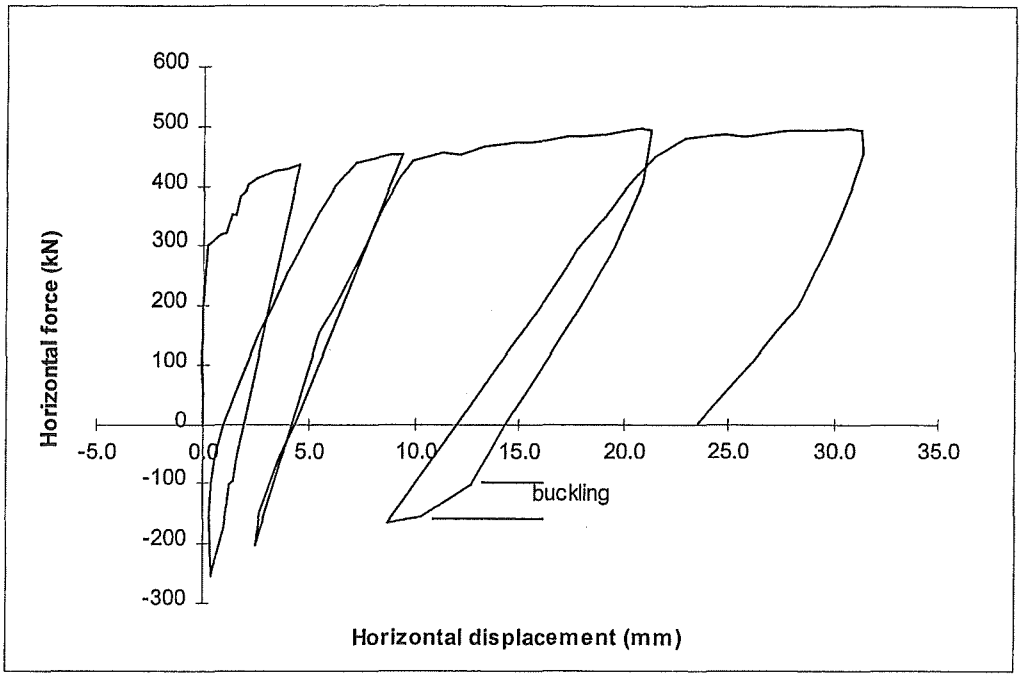

Fig. 4.3 Force-displacement response of continuity bar detail under cyclic loading

(b) First Compression Cycle

The first compression cycle was initiated at 4.5 mm displacement. This displacement was selected due to the relatively uniform distribution of bar strains at gauge stations, apart from those under the critical section (i.e., N4 and S4). The distributions of bar strains at this point are shown in Figure 4.4(a), from where it can be seen that all gauge stations indicate yield strain had been exceeded ($\varepsilon_y = 0.22\%$).

The first compression cycle did not result in noticeable buckling, although it was apparent that a degree of topping bond loss and uplift had occurred during this phase (see Fig. 4.6).

(c) Second Compression Cycle

The second compression cycle was initiated at about twice the displacement of the first cycle (i.e., 9.4 mm). The distributions of bar strains at this point are shown in figure 4.4(b), where it can be seen that several gauges indicate strains well in excess of strain hardening (with ε_{sh} taken as 1.35%). Similar to the first compression cycle, there was no noticeable tendency for the slab to buckle. However, the debonding and uplift that had been observed during the first cycle became more apparent.

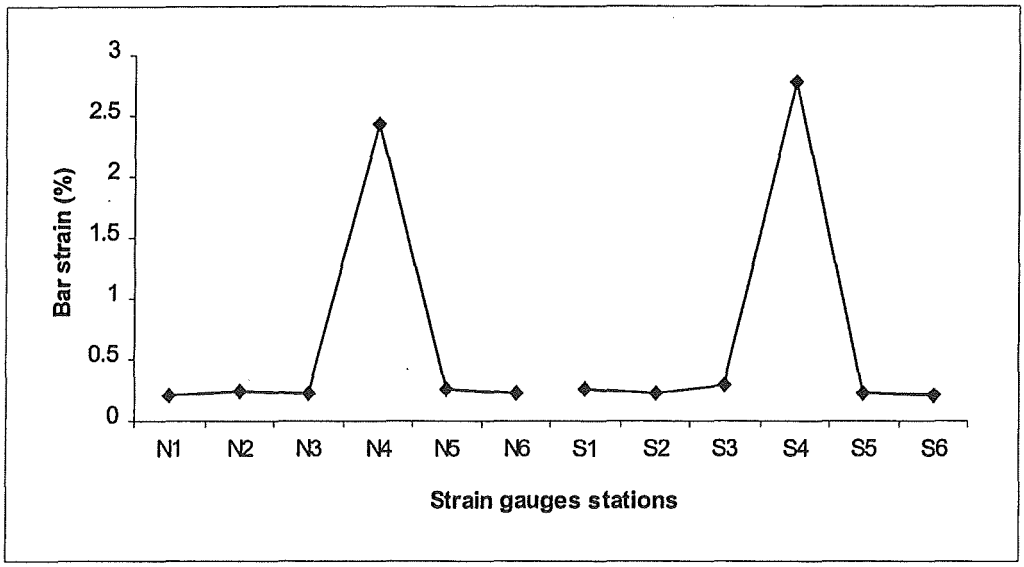

Fig. 4.4(a) Strain in continuity bars at start of first compression cycle (also see Fig. 4.2)

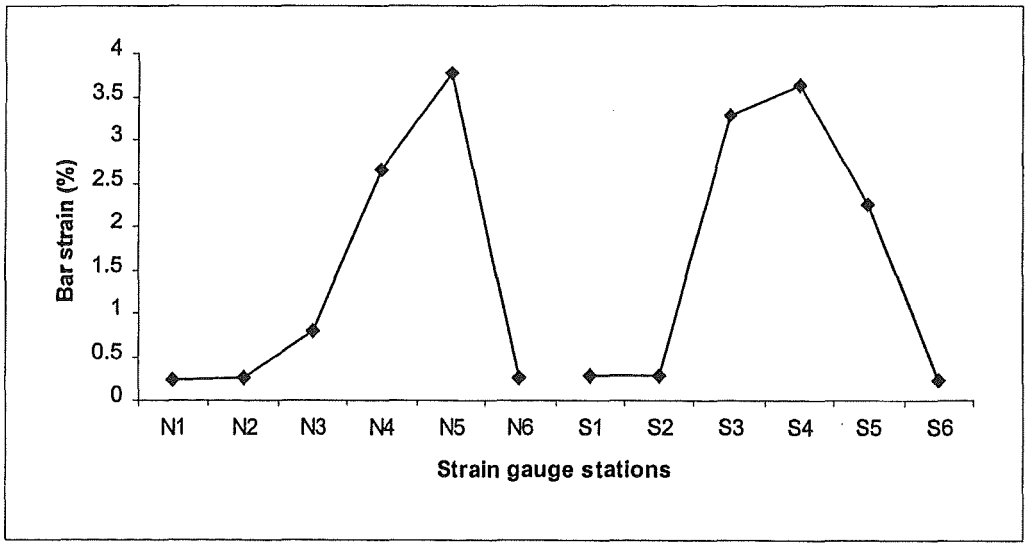

Fig. 4.4(b) Strain in continuity bars at start of second compression cycle

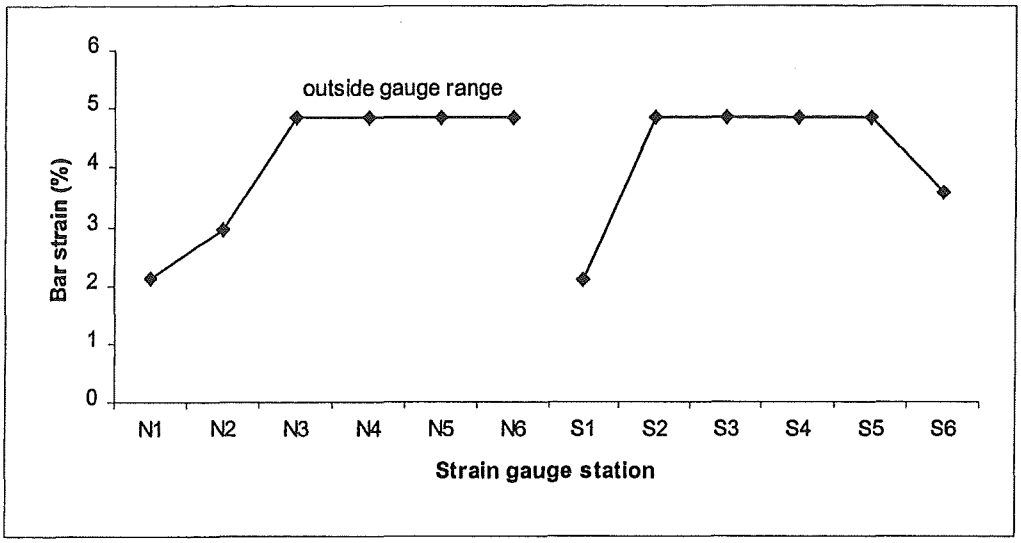

Fig. 4.4(c) Strain in continuity bars at start of third (buckling) compression cycle

(d) Third (Buckling) Compression Cycle

The third compression cycle was commenced at approximately five times the initial compression cycle (i.e., 21.3 mm). The recovery of tension force involved a closing displacement of 7.0 mm, followed by stiffening of the response at the start of the compression run. At 12.7 mm displacement (a further closing of 1.6 mm) and compression force of 103 kN, the slab buckled and completely lifted from the precast unit. The compression run was terminated at 8.7 mm displacement and 167 kN. At this stage, the slab had lifted to a height of 11.5 mm at the position of the linear potentiometer (see Fig. 4.5) and approximately 30 mm at the highest point.

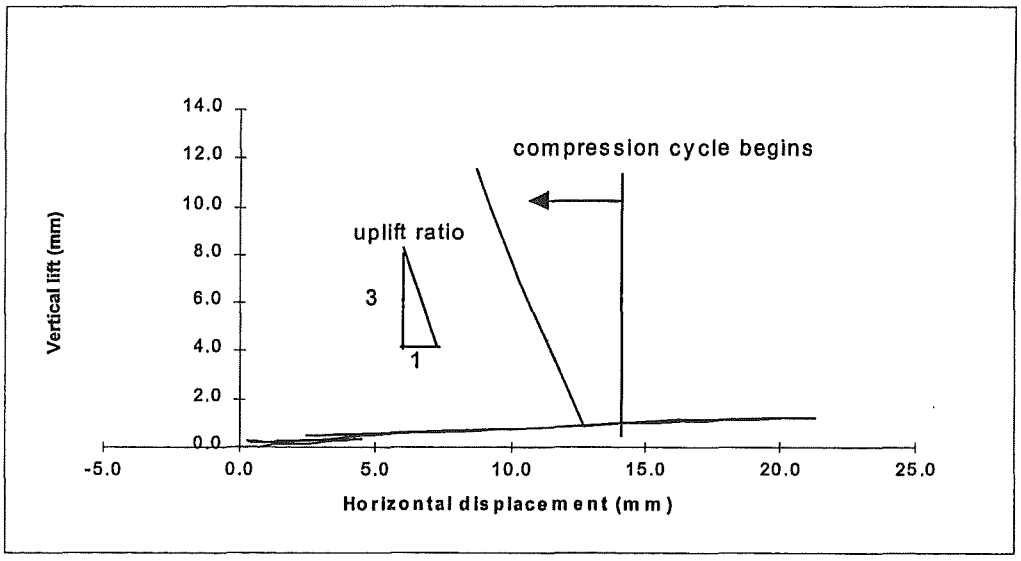

Fig. 4.5 Ratio of vertical uplift of buckled slab to horizontal displacement

It is clear from Figures 4.6 and 4.7 that the topping slab had separated from the precast unit well in advance of buckling, with 0.4 mm uplift recorded at the initiation of the first compression cycle and 0.7 mm at the initiation of the second.

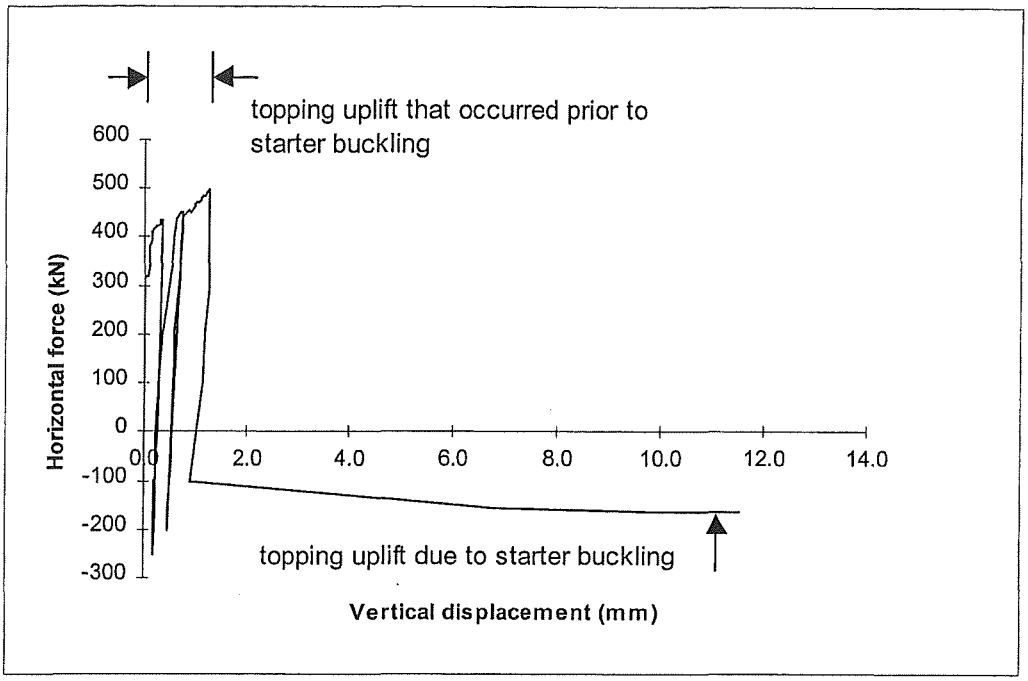

Fig. 4.6 Vertical uplift of topping slab in relation to applied horizontal force

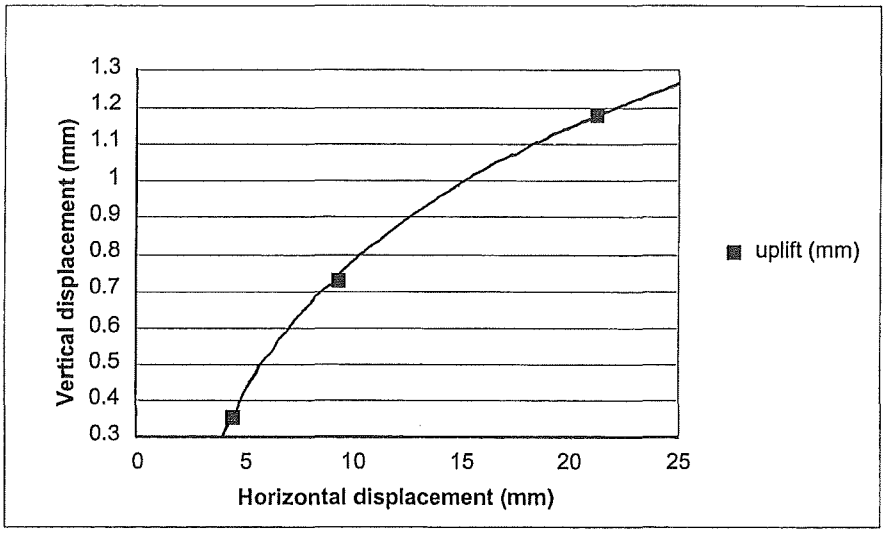

Fig. 4.7 Slab uplift that occurred before buckling, indicated at the initiation of each compression cycle

4.3.1.6 Analysis of Test Results

As expected, the sum of topping slab crack openings approximately equalled the total measured test rig displacement at the end of each tension cycle. Consequently, the topping slab buckling that occurred under compression loading was instigated by bar buckling within the crack spaces. In this situation, the mechanism that initiates slab uplift is derived as the shear components V of plastic bending moments that develop in the buckling zones of reinforcing bars (Fig. 4.8).

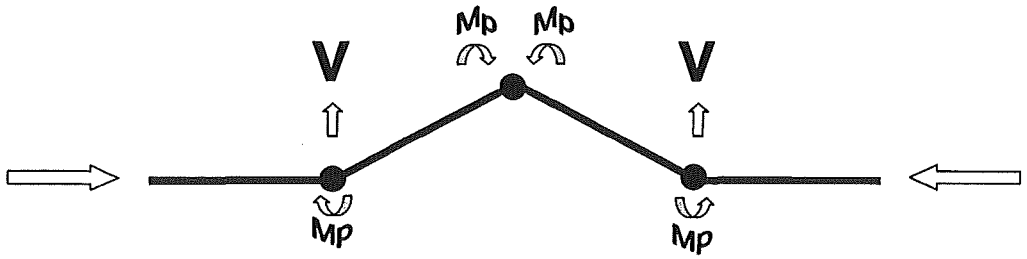

Fig. 4.8 Uplift components caused by formation of plastic hinges in a buckling bar

From this perspective, it is apparent that the cyclic amplitude and frequency of displacements, the size and strength of topping slab reinforcement and composite bond capacity will directly influence the potential for slab buckling.

Immediately prior to failure, the principal topping slab cracks were mostly concentrated within a distance of around 300 mm from the line of support. At failure, plastic hinges formed at two primary crack locations about 150 mm apart, allowing rotation and uplift of the topping slab. It was evident that the stiff portions of topping slab between these principal cracks would also influence the eventual buckling displacement pattern (Fig. 4.9).

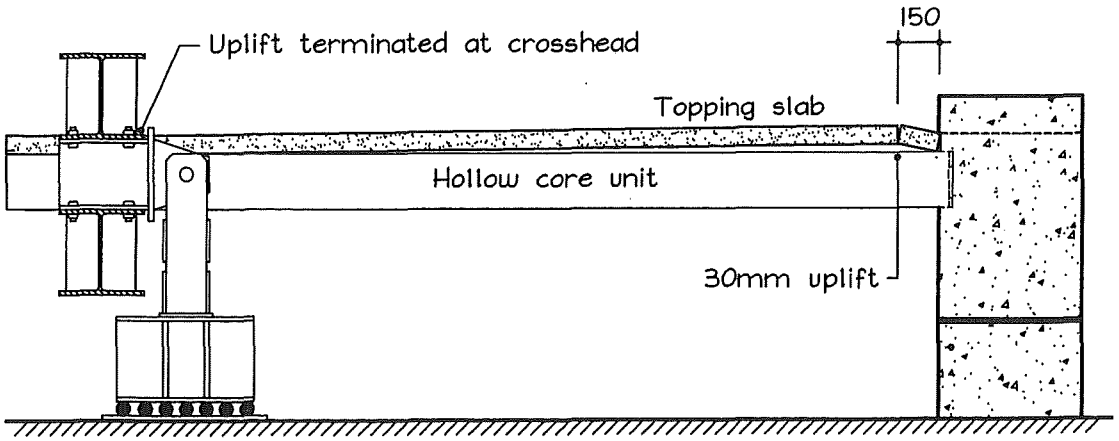

Fig. 4.9 Displaced shape of buckled topping slab at end of third compression run

Referring to Fig. 4.3, it is evident that slab buckling caused in a significant decrease in axial compression stiffness. In the third load cycle between zero axial load and 103 kN compression the axial stiffness determined from the graph was 64.4 kN/mm. The axial compression during buckling had reduced to an average of 13.3 kN/mm, approximately 20% of the pre-buckling stiffness value. This indicates that the topping slab (or at least the topping slab reinforcement) resisted a significant proportion of the axial force.

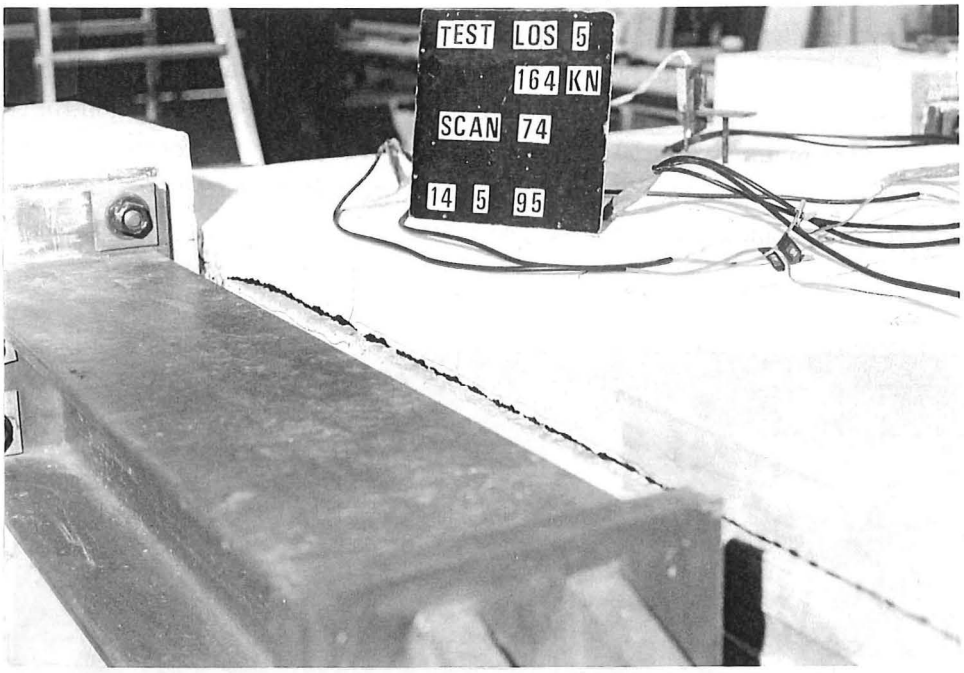

Fig. 4.10 Buckled slab at the end of compression run

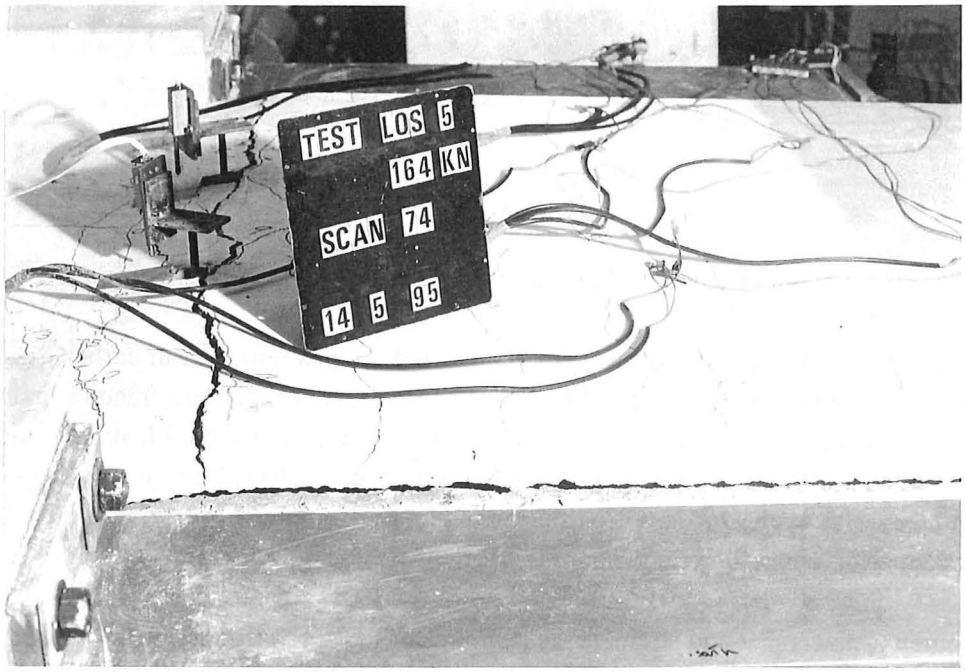

Fig 4.11 Buckled slab at end of compression run

4.3.2 LOS 6

4.3.2.1 General

The intention of the second cyclic LOS test was to establish the extent to which bar geometry and placement might affect tie bar behaviour. The floor configuration involved 65 mm of cast-in-place topping over a 200 mm hollow core extruded flooring unit that was pretensioned with seven 12.7 mm diameter Supergrade strands. The top flanges of the six cores of the hollow core unit were removed and a plain bar tie detail was placed and grouted into each (Fig. 4.12). All the tie details involved plain round bars, however the diameters and configurations of each were varied so as to highlight variations in performance under uniformly applied cyclic displacements. 665 mesh was placed over the hollow core unit and terminated before the end of the seating length (assumed to be the critical section).

Fig. 4.12 Layout of embedded support tie details for test LOS 6

Performance variations arising from tie bar configuration was observed in earlier experiments, in which the geometry of a particular tie detail caused serious concrete fracture under tensile loading [Mejia-McMaster and Park, 1994]. From this, it was considered that particular details that performed well in monotonic tensile tests might cause deterioration in the support region when subjected to cyclic loads. Of particular interest were details involving inclined ties that would produce an upward force component when placed in compression.

The geometry, placement and strain gauge positions of the six tie variations are shown in Figure 4.13. Details A, D, E and F were single leg R16 ties. Details B and C were double leg R12 ties. Detail C differed from all other details in that it was anchored directly around the upper HD20

bar of the support beam. This was purposely done to examine the effects of anchoring ties directly to support member reinforcement, as may be required in some construction situations.

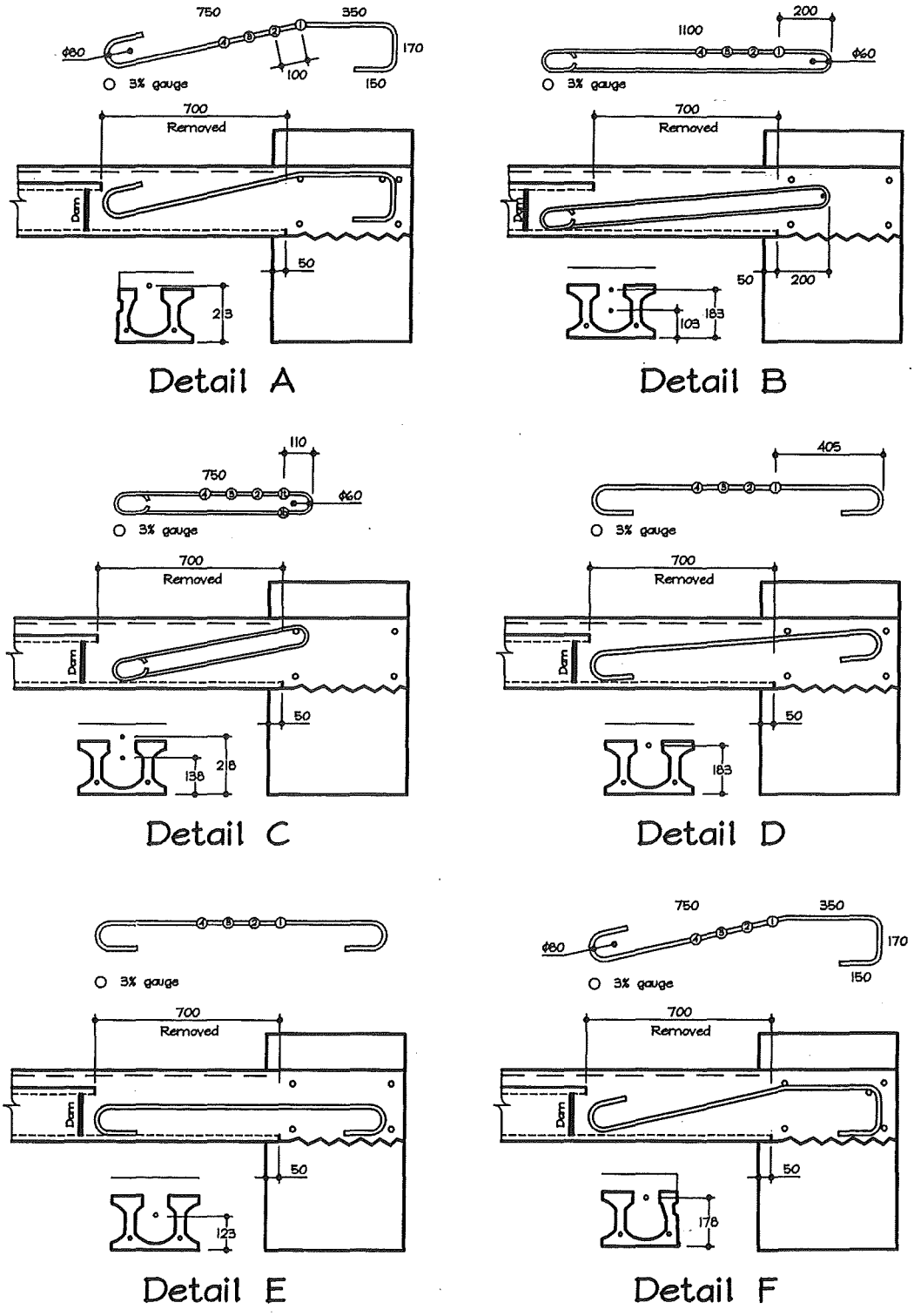

Fig 4.13 Tie detail configurations examined in test LOS 6

4.3.2.2 Instrumentation

(a) Forces and Displacements

Forces and displacements were measured in accordance with the methods described in Section 3.2.2 (also Fig. 3.4).

(b) Reinforcement

Standard 3% extension electrical resistance strain gauges (as described in Section 3.2.2) were employed on individual tie details (see Fig. 4.13). These gauges were configured so that a gauge was situated directly over the expected cracking plane, at the end of the hollow core section. The strain gauges were set at 100 mm centres about the expected cracking zone.

4.3.2.3 Cast-In-Place Topping Concrete

Concrete was ordered at a specified slump of 100 mm and accepted at a snatch sample slump of 85 mm (Table 4.2). The mix would be described as having sufficient workability and well suited for topping concrete, showing very little bleeding or segregation.

Table 4.2 Characteristics of cast-in-place topping concrete for test LOS 6

Design Strength (MPa)	Max. Aggregate Size (mm)	Ordered Slump (mm)	Received Slump (mm)	Test Strength (MPa)
25 at 28 days	13	100	85	34 at 34 days

4.3.2.4 Reinforcement

(a) 665 Mesh

The characteristics of hard drawn wire mesh were identical to those described in Table 3.2

(b) R16 Tie Reinforcement

The tensile characteristics of R16 bars used in test LOS 6 are shown in Table 4.3

Table 4.3 Characteristics of R16 reinforcing steel

Avg. Yield Stress (MPa)	Avg. UTS (MPa)	Avg. Strain at Fracture (%)
313	488	28.9

(c) R12 Tie Reinforcement

The tensile characteristics of R12 bars used in test LOS 6 are shown in Table 4.4

Table 4.4 Characteristics of R12 reinforcing steel

Avg. Yield Stress (MPa)	Avg. UTS (MPa)	Avg. Strain at Fracture (%)
343	486	27.7

4.3.2.5 Results of Testing

(a) Initial Response

The initial response to horizontal loading showed a stiff system (Fig. 4.14) with first cracking over the support region observed at around 200 kN and 0.1 mm displacement. The peak elastic response occurred at 0.25 mm horizontal displacement and a force of just over 280 kN. This was followed by a sudden increase in displacement due to tensile fracture of the concrete, resulting in 0.97 mm displacement at 247 kN of applied force. From this point onward, tie bars in the hollow core voids governed the section tensile strength.

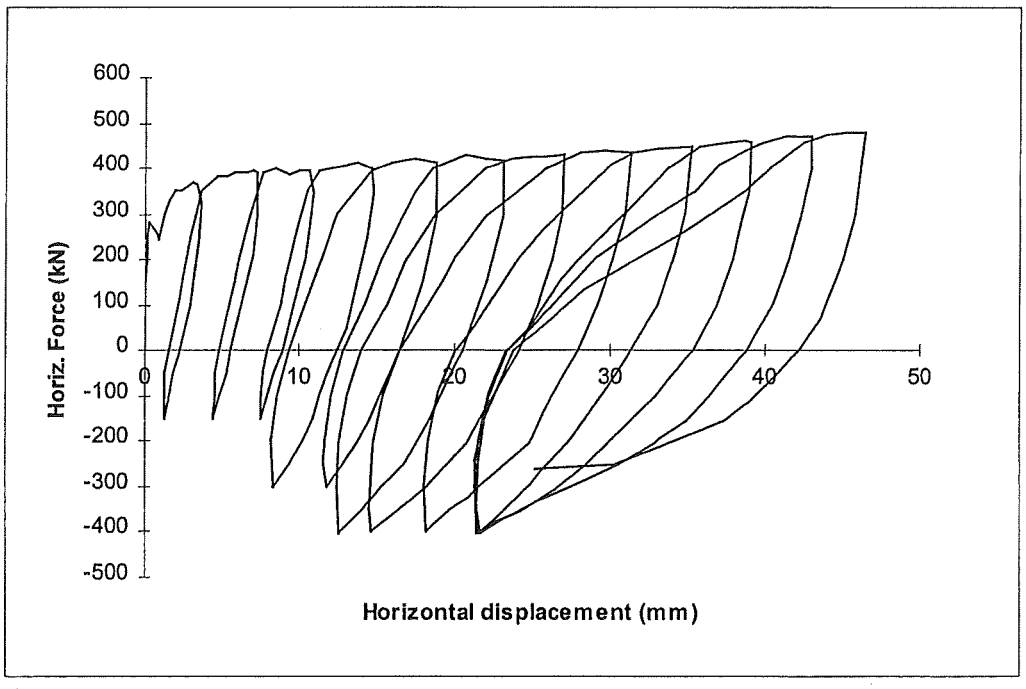

Fig. 4.14 Combined force-displacement response of tie bar details under cyclic loading

(b) Compression Cycles

The first compression cycle was initiated at 3.7 mm displacement. Successive compression cycles were initiated at increments of around 4.0 mm (see Table 4.5), with a total of 12 load reversals being applied during the experiment.

Table 4.5 Horizontal displacement (mm) at the initiation of each of the twelve load cycles

1	2	3	4	5	6	7	8	9	10	11	12
3.7	7.3	10.9	14.8	18.9	23.1	27.1	31.2	35.2	39.1	43.0	46.5

4.3.2.6 Specific Analysis

(a) General

For each of the six details tested, reinforcing bar strains were recorded from the strain gauge positions illustrated in Figure 4.13. The strains recorded from test LOS 6 show considerable variation, with an interesting general tendency for bar strains to dwell in compression after the application of a number of load reversals. Because of the complexity of loading on individual bars, it is difficult to establish the significance of a predominance of compression strain readings at bar positions away from the critical section. However, for the exercise of comparing the performance of various tie details, it is considered sufficient to draw conclusions based on relative behaviours, such as load response at a particular gauge position of a detail towards the latter stages of the test.

Understandably, a number of strain gauges failed at various stages during the test. Strain gauge failure is indicated by a simple termination of the plot line on the graph of strain versus scan number.

(b) Detail A (Fig. 4.13)

Detail A was the only detail that caused rupture of the topping slab during a compression run (Fig. 4.15). However, this did not occur until the eleventh load cycle, and after a closing displacement of 21 mm. It was fully expected that Detail A could cause such a topping slab rupture due to the diameter and inclination of the tie leg, coupled with a lack of effective confinement.

The topping rupture was accompanied by a localised buckling failure of the tie bar. Bar buckling was predestined to occur at the bend between horizontal and inclined portions, which formed a shape conducive to buckling. Hence, bar buckling was concentrated in the immediate vicinity of this bend.

It was apparent from the following load cycle that concrete spalling was unlikely to progress much further, largely due to the facilitated nature of tie bar buckling.

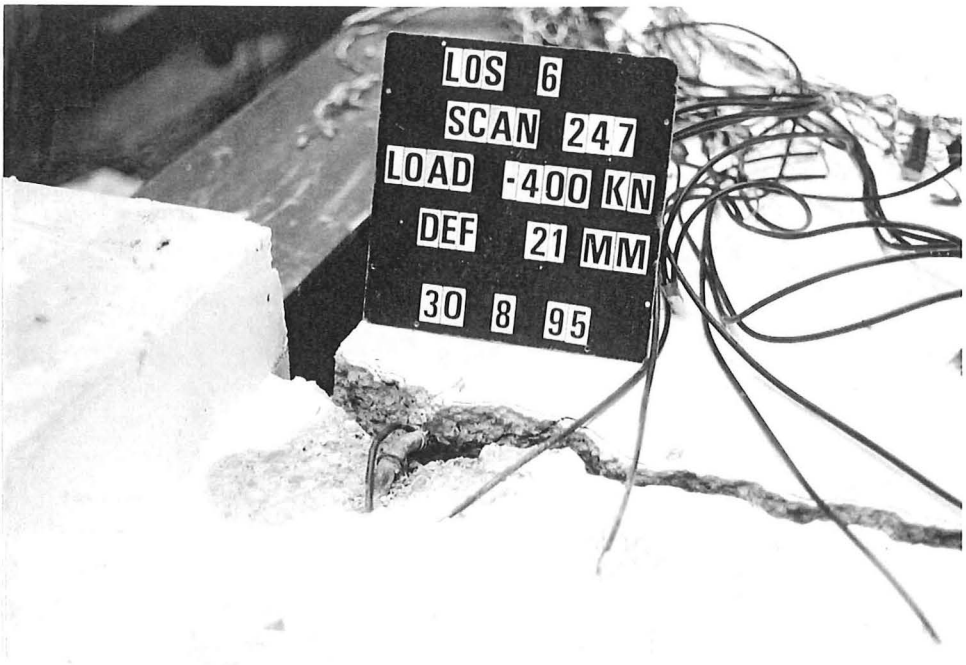

Fig. 4.15 Spalled topping slab concrete caused by buckling of Detail A

Referring to Figure 4.16, it is evident from gauges #3 and #4 that a degree of strain penetration had occurred. The relative amplitude of gauge #2 suggests that the majority of strain penetration had been experienced at around scan number 139, half way through the test. The loss of cyclic response amplitude recorded by gauge #3 at scan 199 coincides with the onset of bar buckling, which suggests a rapid softening of the detail due to formation of the buckling mechanism.

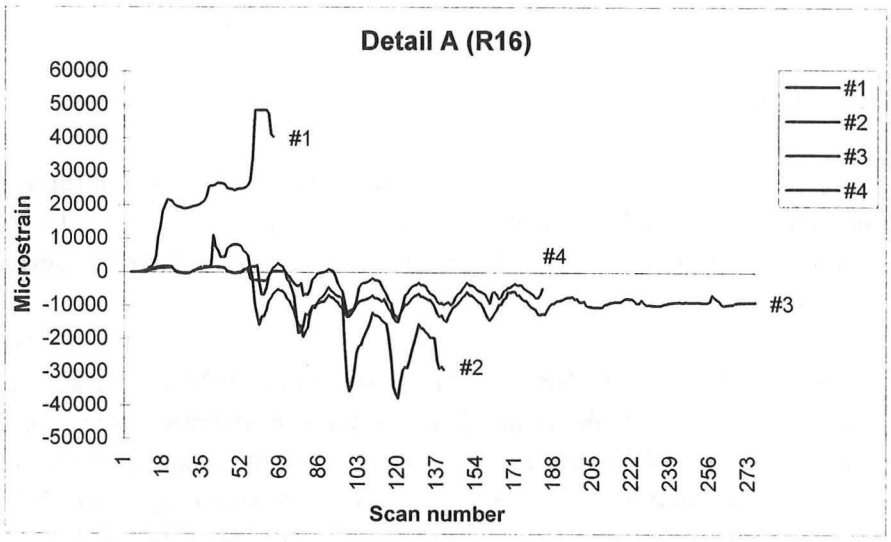

Fig. 4.16 Strain gauge recordings for Detail A

(c) Detail B (Fig. 4.13)

Detail B was one of two R12 double leg ties (paperclip ties) tested. With this particular detail, bar anchorage was achieved by providing 200 mm of embedment into the support block.

The results (Fig. 4.17) indicate an active response to loading along the extent of the upper tie leg during the early stages of testing. The increasing response at gauges away from the critical section suggests that an appreciable amount of strain penetration occurred. The gradual fall in response amplitude at gauge stations #2 and #3 over the latter two thirds testing most likely indicates bond degradation between the strain gauge and bar elements. It is considered that the gradual dampening of response at gauge #4 was due to the onset of bar buckling at the critical section, which was clearly observed during the latter stages of the test.

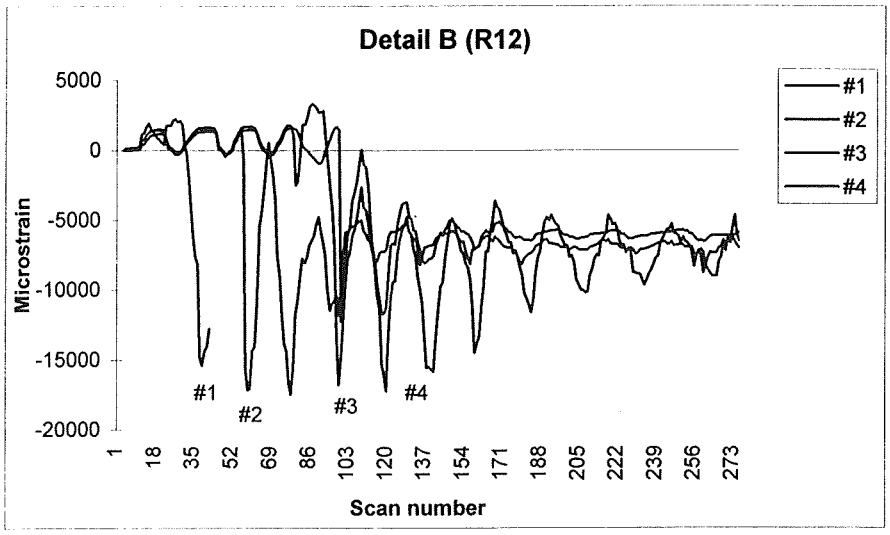

Fig. 4.18 Strain gauge recordings for Detail B

(d) Detail C (Fig. 4.13)

The second R12 paperclip detail was anchored around an upper HD20 bar of the support block, which was nominally confined by R12 stirrups at 150 mm centres (see Figs 3.1). An additional strain gauge was placed on the bottom tie leg (denoted as gauge #1B) to compare response across the section depth.

The results of testing showed considerable deformation of the HD20 anchorage bar (Fig. 4.19), and is reflected in Figure 4.20 by the generally diminished tie response after about scan number 65. As the test progressed, subsequent concrete spalling and deformation of the anchorage bar allowed an increasing amount of free tie movement about the anchorage point. This is indicated by the lag effect shown at the latter stages of testing, in particular, the reducing frequency of cyclic straining from around scan number 161 onwards. Another feature of this detail that

became evident toward the latter stages of testing is the sharp increase in response magnitude. This was most likely caused by the positive form of restraint afforded by an anchored connection at a stage when the stiffness of adjacent details had diminished due to the breakdown of bar bond mechanisms.

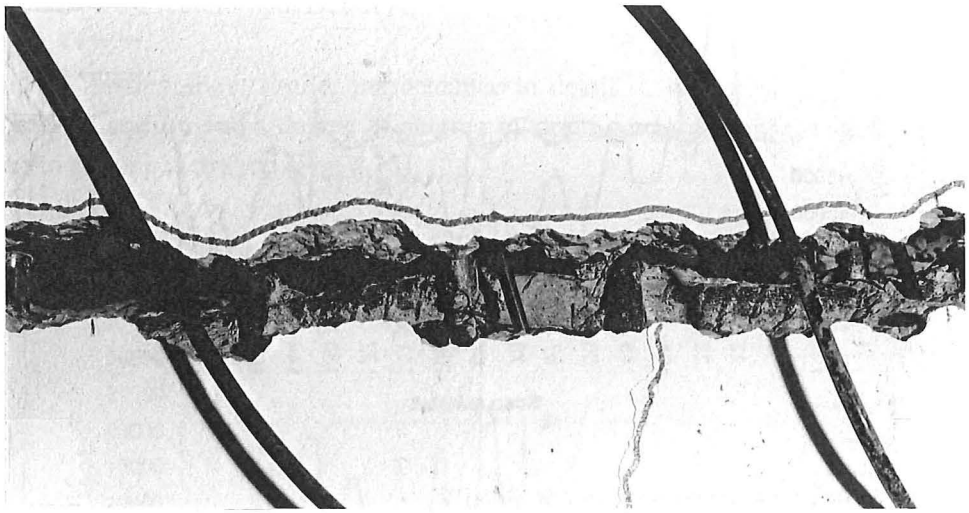

Fig. 4.19 Deformation (end of test) of HD20 bar acting as tie anchorage

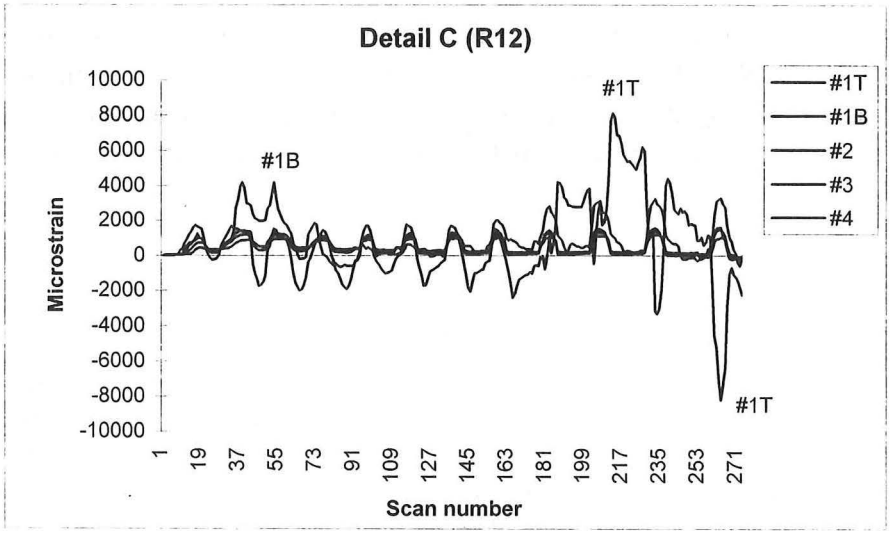

Fig. 4.20 Strain gauge recordings for Detail C

(e) Detail D (Fig. 4.13)

Although of short duration, the results from Detail D provide clear evidence of bar bond degradation and associated strain penetration effects that most specifically apply to plain round reinforcement (Fig. 4.21). The staged response increments at strain gauge stations occur in direct relation to embedded distances from the critical section, suggesting a systematic breakdown in bar bond under cyclic loading.

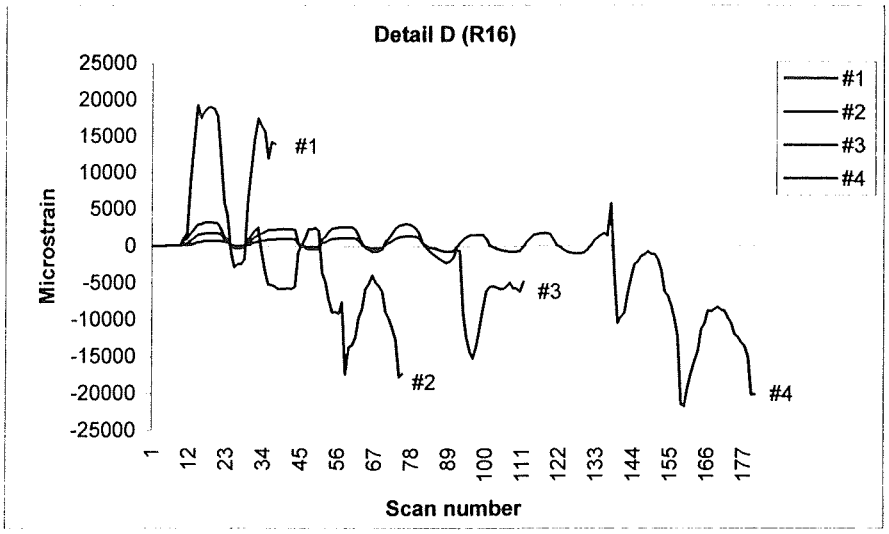

Fig. 4.21 Strain gauge recordings for Detail D

(f) Detail E (Fig. 4.13)

Detail E represented a horizontal tie placed centrally in the hollow core void, and is similar to a detail examined in earlier experiments [Mejia-McMaster and Park, 1994]. The prolonged response of gauge #1 (Fig. 4.22) was very beneficial in that it indicates a detail with sustained resistance to cyclic loading at large displacements. The increase in response magnitude towards the latter stages of testing further suggests that the detail retained a degree of axial stiffness in relation to the adjacent details.

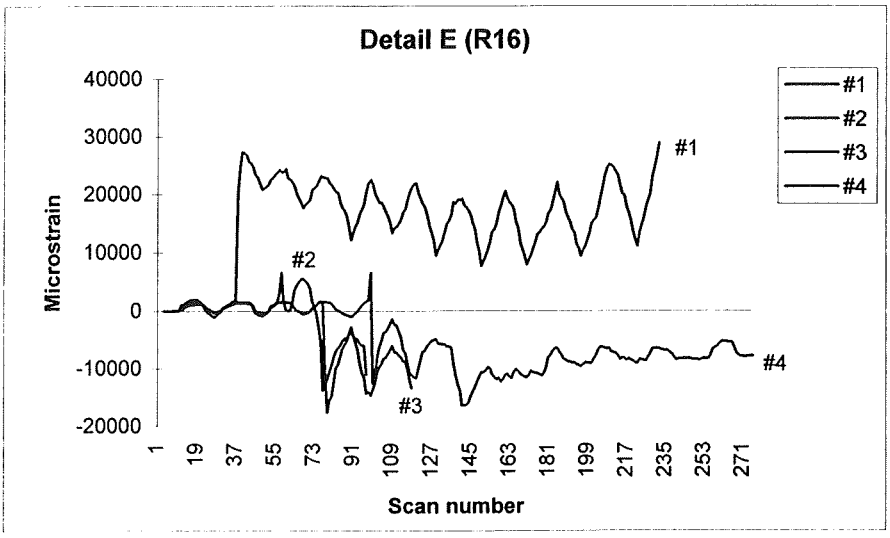

Fig. 4.22 Strain gauge recordings for Detail E

(g) Detail F (Fig. 4.13)

Dimensionally, Detail F is identical to Detail A. However, Detail F was placed under the top bar of the support block, and hence, was provided with a layer of confining reinforcement. Consequently, this detail did not experience the bar buckling and spalling of adjacent topping concrete that were a feature with Detail A.

The results of testing show similar performance to detail E, with positive response provided near the critical section and a degree of staging in strain gauge response relative to embedded length due to strain penetration (Fig. 4.23).

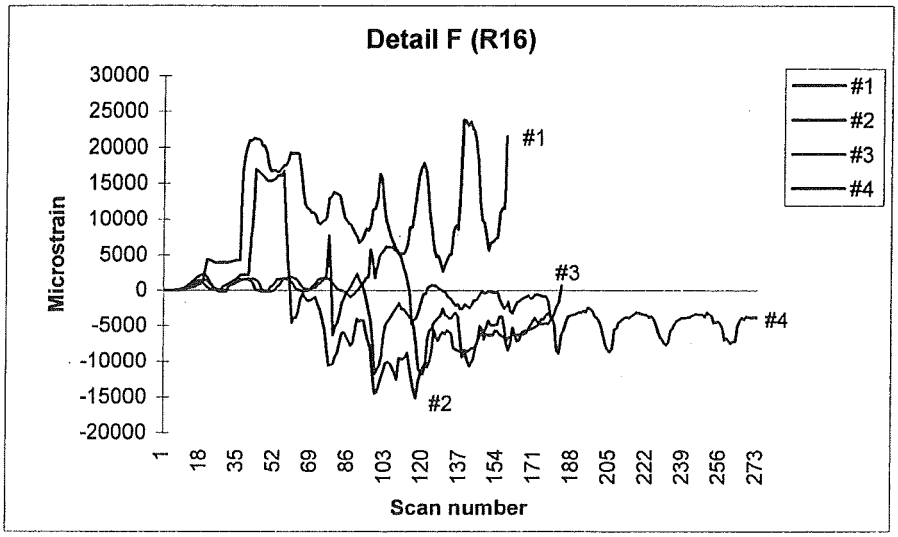

Fig. 4.23 Strain gauge recordings for Detail F

4.4 DISCUSSION ON TEST RESULTS

4.4.1 STARTER AND CONTINUITY BAR DETAIL (Test LOS 5)

It can be concluded from test LOS 5 that topping slab uplift may occur where flooring units are subjected to the combined effects of frame dilation and cyclic loading. It is certain that the characteristics and quantity of topping slab reinforcement will influence uplift tendencies, as will the tensile bond capacity exhibited between precast and composite concretes. It is evident that bond loss and separation had occurred between the precast and topping concrete surfaces well in advance of slab buckling. This is consistent with composite bond losses observed in the earlier LOS tests that involved similar support details subjected to monotonic loading.

The specimen tested may be considered to represent a lower bound, in that the bond surface of the precast hollow core unit exhibited a minimum of roughening and grouted edge keys were not incorporated. However, the topping slab uplift observed in this experiment was both severe

and immediate, suggesting that a positive means of uplift control is more necessary than preferential.

Whether uplift control can be achieved through roughening amplitude or grouted keys is debatable. In the author's opinion, tensile control achieved through the roughening amplitude of extruded concrete surfaces will be very limited. However, uplift restraint provided by edge key details will largely depend on maintaining construction joint integrity. It must be considered that edge keys usually represent only a 40 mm wide strip of plain concrete at 1.2 m centres, and are probably subject to physical degradation under two-way frame actions during a severe earthquake.

It has been observed (Tests LOS 2 and LOS 6) that the provision of cut-back hollow core flanges and grouted voids will greatly increase topping bond capacity in the support region. However, if the recommended detailing is not practicable, it is considered that either vertical ties or the inclusion of steel fibre reinforcement in the topping slab could provide some integrity across the horizontal plane of the edge key joints.

4.4.2 EMBEDDED TIE BAR DETAILS (Test LOS 6)

4.4.2.1 General

The main emphasis of test LOS 6 was to determine the comparative performance of plain bar details embedded in grouted hollow core voids. At the outset, it was considered that any of the details tested would be generally suitable for applications involving potential loss of support.

4.4.2.2 Detail A

The topping concrete spalling associated with Detail A was fully anticipated, although, its occurrence was of less significance than originally presumed. Essentially, the composite bond capacity afforded by removal of hollow core flanges appeared sufficient to control the progress of spalling that results from bar buckling. Also, the ready formation of a plastic hinge at the bar buckling node deferred axial forces by facilitating movement of the flooring unit. This mitigated the adverse effects of axial thrusts that may have acted to strip the bar from the topping slab, directly over the support beam.

From a different perspective, the bar at the buckling node would be subjected to considerable mechanical working under prolonged cyclic loading. Hence, the toughness properties of reinforcement may need to be taken into account if not to eventually affect the performance of this detail.

4.4.2.3 Detail B

Detail B provided no surprises and indicated that R12 paperclip details can afford sufficient ductility for loss of support applications. However, this detail was observed to buckle within the space of the critical crack opening. Therefore as expected, it appears that 12 mm diameter (and smaller) bar details might be prone to buckling at lower cyclic amplitudes.

4.4.2.4 Detail C

In order to gauge the effects of anchorage, Detail C (a shortened paperclip detail) was connected directly to the upper HD20 bar of the support block. Although the tie detail performed well, it is evident that considerable deformation of the anchorage bar is likely to result, especially where effective confinement is not available. Hence, Detail C may be unsuitable for applications that involve cyclic actions of the support member since induced bar deformations could promote the premature buckling of principal reinforcement.

4.4.2.5 Detail D

Detail D provided satisfactory performance, and gave clear indication of the effect of strain penetration that is required to achieve tie bar ductility.

4.4.2.6 Detail E

From the measured response and observations, Detail E provided perhaps the most suitable performance as a means of providing a ductile support tie. The detail, itself, is horizontal and embedded centrally in the hollow core void. Hence, it would seem well configured to sustain the type of loading regime placed on ductile support ties. It is evident that Detail E developed the required strain penetration, yet maintained stiffness toward the latter stages of testing. As such, bar buckling was not observed with this detail.

4.4.2.7 Detail F

Detail F is geometrically identical to Detail A, however, it was strategically placed below the top layer of reinforcement in the support block. It is evident that the top reinforcing layer to control bar buckling and spalling tendencies provided sufficient confinement. It is also considered that Detail F behaved in a similar manner to Detail E, but with a slightly more erratic response.

5

The Buckling of Topping Slabs

5.1 GENERAL

One of the most compelling observations from experiments involving precast flooring support is the effect of reinforcing details on composite topping behaviour. The tests that were reported in Chapter 3 indicate that diminishing composite bond strengths result when support details are displaced beyond their elastic limits. As reported in Chapter 4, a typical continuity bar detail subjected to in-elastic cyclic displacements experienced topping slab uplift via the buckling components of continuity reinforcement.

The primary consideration is that reinforcing bars are frequently placed in composite topping slabs and may play an important part in the overall design strategy for seismic resisting diaphragms. For instance, it is not uncommon in routine designs for appreciable volumes of small to medium sized bars (e.g., 10 mm to 20 mm diameter) to be placed in continuous bands within the topping slab to act as diaphragm chord ties (see section 2.3.2). Furthermore, trimmer bars are required in the vicinity of floor openings and minor drag bar configurations may be treated in the much the same manner as chord tie reinforcement.

Clearly, the greatest risk of topping slab buckling in seismic resisting diaphragms will occur in regions where concentrated forces arise. The in-plane forces that may be derived from plastic hinge development in beams and arch actions in diaphragms have been discussed in Section 2.3. There is a general requirement to examine of the influence of in-plane forces on the incidence of topping slab uplift.

Buckling analysis usually implies the development of effective length criteria based on classical Euler buckling theory. However, it is widely acknowledged [Young, 1989] that plate buckling stresses calculated by this method tend to over-estimate the buckling capacity of actual members. This discrepancy is further complicated with concrete as a base material, since the calculated slab buckling stresses can far exceed practical concrete crushing strengths.

The Euler buckling theory is founded on elastic response to concentric axial load and the premise that an orchestration of sine curves will develop. It is certainly an elegant solution, but is essentially defined by only one parameter: the assumption of a concordant elastic deflection profile. Hence, for applications involving plastically deformed concrete members it is difficult to fully reconcile the Euler buckling criterion with the actual mechanics, and it therefore requires fairly broad modifications for use in practical concrete design [Park and Paulay, 1975].

The most difficult aspect to resolve in the Euler buckling model is the profoundly elastic assumption of section flexural rigidity, EI. Although this notation has been strongly adhered to, it really has no rational basis for use in plastic member analyses. However, it is a convenient bench-mark from which to apply mostly empirical modifications to section properties.

In Section 2.2.1.3, an alternative method was presented for the rational estimation of flexural rigidity. Although the author is confident that the equivalent flexural rigidity (EI*) equation (Equation 2.40) has direct applications to concrete section analysis, its simple incorporation into the Euler equation for plastic buckling analysis would only concede to a single parameter model based on deflected shape. Although feasible, such an approach would be still depend on a method (probably empirical) for statistically weighting the often greatly varied effective flexural rigidity over the critical length.

As such, the equivalent flexural rigidity equation would appear more useful as a means for verifying the flexural rigidities used in existing formulae. However, it is considered that EI* could be employed in the Euler buckling approach to estimate the critical buckling stress of nominally elastic slender elements, and especially elements subjected to uniform bending moments (e.g., top-loaded tilt panel walls). A useful aspect of the EI* method is that it will indicate a decrease in flexural rigidity below EI_g in both the homogeneous and cracked states when (i) an amount of bending curvature is present and (ii) materials depart from linear stress-strain behaviour.

Alternative approaches to buckling are available, in which rational treatments of the base materials and structural element types are usually incorporated. One important method for the study of concrete wall stability has been developed and tested at the University of Canterbury [Goodsir, 1985]. This is a well-considered approach and it contains many aspects that are equally applicable to the present study, including plastic bending capacity and the effects of reinforcement.

However, it remains problematic in that the presumed curvature distribution of the Goodsir model is not directly applicable to the topping slabs in question. The deterministic requirement of a topping slab buckling analysis is the maximum permissible distance between two points of lateral restraint. A topping slab buckling failure will involve a mechanism of discrete plastic hinges (up to three hinges) of relatively short length, interspersed with comparatively long and unaffected portions of slab. Hence, the uniform radius of curvature over buckling length adopted by Goodsir may adequately define a buckling hinge length, but cannot be used to express the above multiple hinge mechanism. As such, the model best describes a localised buckling mode (generally) as opposed to a member buckling mode. The plastic hinge lengths of ductile structural walls, for which Goodsir's model was derived, are certainly long enough to accommodate the uniform curvature assumption. As a consequence, several design parameters based on this model have been incorporated into Chapter 12 of the New Zealand concrete structures design standard [Standards New Zealand, 1995].

5.2 DEVELOPMENT OF A SLAB BUCKLING MODEL

5.2.1 BUCKLING CRITERIA

5.2.1.1 General

As discussed above, there will be discrepancies between an assumed elastic deflection profile and the true deflection behaviour of any axially loaded concrete slab at buckling. Under the most favourable of conditions, the deflected profiles of reinforced concrete sections are mostly treated as estimates. Conversely, experience has shown that the equilibrium mechanics of concrete sections are very influential and have perhaps the greatest reliability in calculations. This important difference becomes even more distinct when the section is approaching its ultimate limit state.

A deflected shape parameter is fundamental in the development of a buckling model, and must describe a profile that is compatible with the behaviour of plastic failure mechanisms. From this perspective, it is considered that the deformation formats used in established methods of plastic analysis are equally applicable. However, integrated member stability also requires a parameter that can define the incipient point of buckling as a conclusive point of transition. Hence, this important additional parameter should function similarly in manner to the harmonic shape assumptions of the Euler model, yet be rigorously applicable to plasticity models.

5.2.1.2 Conservation of Energy

Energy methods are universal in their application to structures, being applicable in both elastic and plastic analysis. Consequently, these methods prove useful for concrete section analysis because they allow a unified approach when dealing with a material that may respond in both the elastic and plastic states.

It is considered that an element of structure can be regarded as either an isolated system, or at least a system that can be isolated in some manner. Since practical structural mechanics does not involve defined conditions of energy flow (as in the thermodynamic sense), it is reasonable to assume that no quantifiable amounts of energy will diffuse across boundaries of adjoining structural elements. This greatly simplifies the application of energy methods and the underlying conservation of energy principle. This principle may be stated as "the constancy of energy of an isolated system" in which "energy may be converted from one form to another, but is not created or destroyed" [Walker, 1995].

The conservation of energy principle would seem equally applicable to compression members at the incipient point of buckling. In a slender member (especially), the phenomenon of buckling implies a rapid transition from a compression-only state to a bending-only state. In real member collapse mechanisms, the compression-only state may involve linear deformations that are either elastic or elastic-plastic, whereas the bending-only state will primarily involve plasticity.

Hence, it is reasonable logic that for a rapidly buckling mechanism to substantially occur and remain consistent with the laws of mechanics, the existing quantity of stored strain energy "may be converted from one form (of energy) to another, but is not created or destroyed". Thus, the strain energy of force times linear displacement must either be converted into the strain energy of plastic bending moment times rotation, or be substantially transferred to some other energy form. Now, as buckling progresses toward collapse, the associated reduction in axial force potential is directly converted into increased bending rotation, since this is the sole resistance mechanism. Therefore, the assumed mode of conversion will feature strongly throughout the collapse process and must be regarded as the fundamental mode of energy conversion. On this basis, it is proposed that buckling is imminent at a stage when the stored quantity of strain energy due to axial compression U_c becomes equal the sum of strain energies U_b required to form a collapse mechanism containing n number of plastic hinges. Hence, written in terms of a simple energy balance, this may be expressed as:

$$U_c = \sum_n U_b \tag{5.1}$$

Because concrete members will usually exhibit plastic material response prior to buckling, the total strain energy must be related to individual stress-strain curves of concrete and steel reinforcement (see Figure 2.11):

$$U_c = \iint_{vol} f_c \, d\varepsilon \, dV + \iint_{vol} f_s \, d\varepsilon \, dV \tag{5.2}$$

The evaluation of bending moment plastic hinges is potentially more difficult than summations of strain energy under simple axial compression. Section geometry, reinforcement and loading configurations will certainly influence the nature and timing of hinge formation. One of the key issues is the point in the moment-curvature relationship at which plasticity accelerates, since this will also define the neutral axis depth applicable to section equilibrium in a buckling model. The differences that may occur in transition rates between elastic and plastic behaviour are illustrated by the moment-curvature relationships of Figures 5.1 and 5.2. In both cases, members are effectively subjected to axial compression via prestress forces.

Limiting the argument to topping slabs, it can be shown (Fig. 5.4) that even under substantial axial force a reasonably rapid transition will occur between elastic and plastic behaviour. Also as discussed, equivalent flexural rigidity (EI*) analysis will indicate a reduction in flexural rigidity under the dual conditions of curvature and departure from linear stress-strain response. Hence, for sections subjected to high axial compressive stress, the introduction of a small amount of bending curvature can sharply reduce the calculated EI* value.

A final consideration is the enhanced bending moment capacity of sections resisting axial compression. The increase in moment capacity over a member subjected to bending-only can be quite substantial. Figure 5.1 indicates that accurate estimates can be made of moment-curvature response by using established analysis techniques and realistic material properties. Since non-closure of cracks under cyclic actions will influence slab buckling, a conservative first estimate in design would be to adopt the bending-only capacity of the section (i.e., zero axial force).

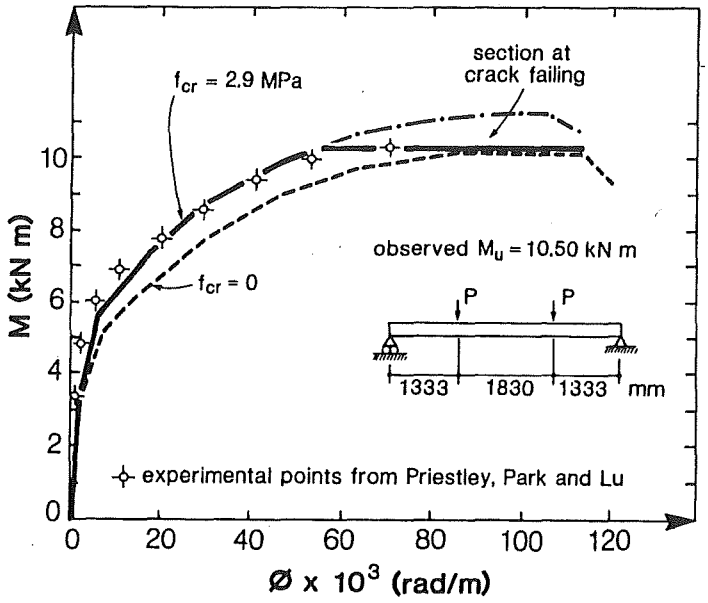

Fig. 5.1 Moment–curvature response of prestressed beam with slow transition between elastic and plastic behaviour [Collins and Mitchell, 1987]

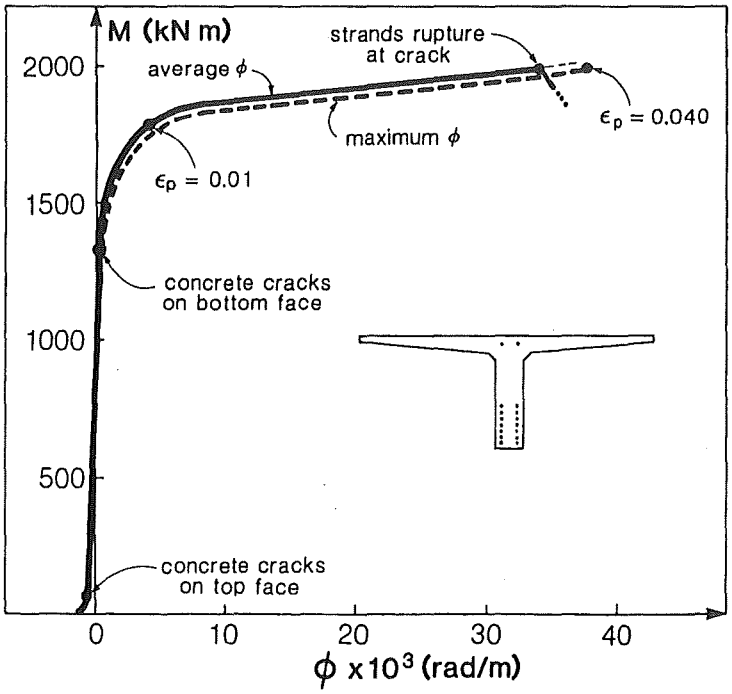

Fig. 5.2 Moment–curvature response of prestressed beam with rapid transition between elastic and plastic behaviour [Collins and Mitchell, 1987]

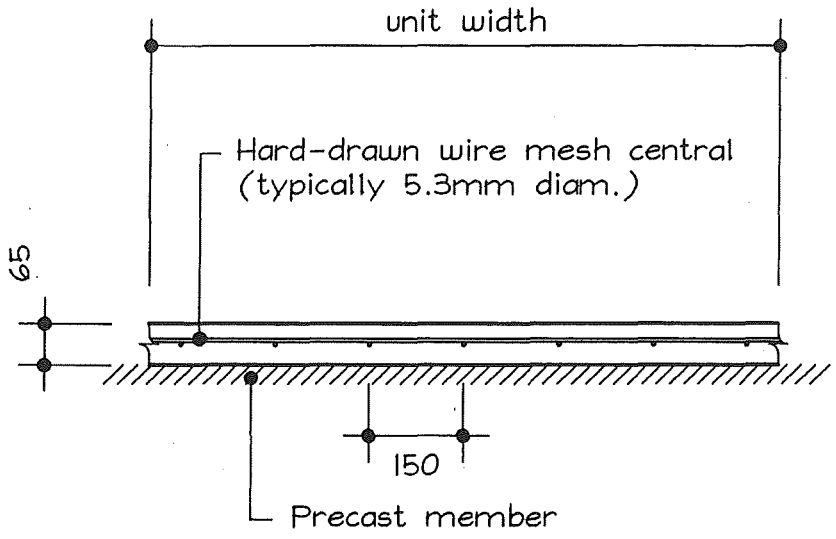

Fig. 5.3 Typical topping slab configuration

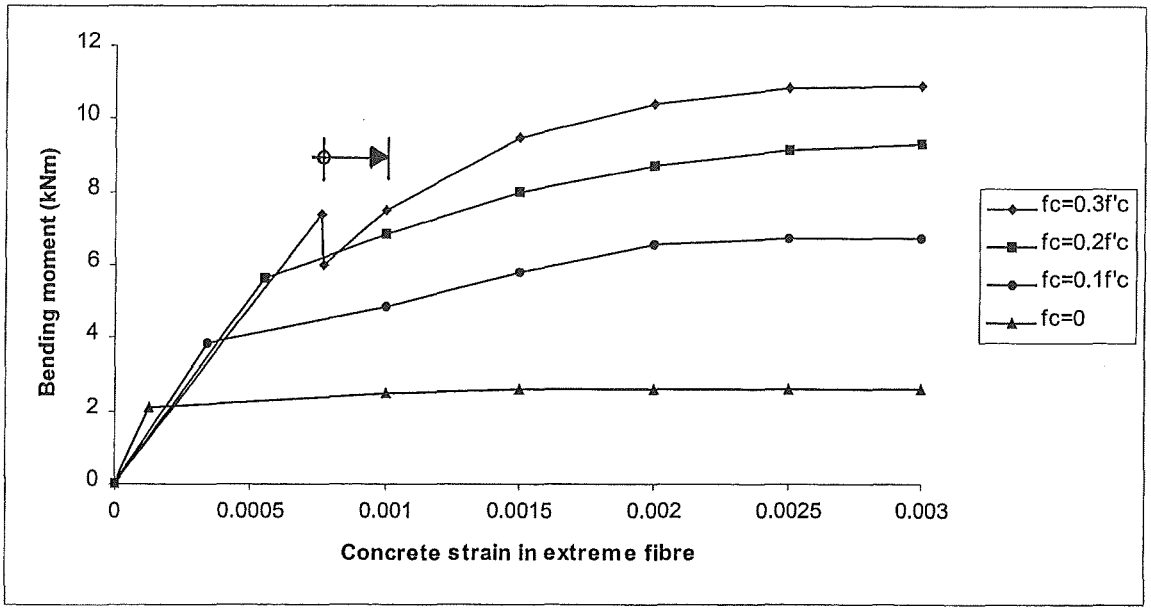

Fig. 5.4 Moment-curvature response of typical topping slab under varying levels of axial stress. The irregularity highlighted in the plot for $0.3f'_c$ axial compression (and edited from the other plots for clarity) occurs at the transition between uncracked and cracked section response. This is a common result for lightly reinforced members, indicating an accelerated plastic response due to sudden increase in curvature at a given bending moment.

The basic concept of column buckling is one of a slender prismatic member subjected to increasing axial force, until such a level of force is reached that sudden buckling occurs and collapse follows. With very slender members, where the Euler buckling criteria is most appropriate, a sudden (or snap-through) collapse pattern is generally expected. With members of decreasing slenderness, it is expected that an increasing degree of measurable axial displacement will occur before the onset of buckling. However, the members of broadest concern are usually neither very squat nor very slender, and it is reasonable premise that these members will exhibit an average-to-rapid loss of axial load resistance. Hence, it is considered that the relatively slender and lightly reinforced concrete topping slabs will exhibit such behaviour. The observations of test LOS 5 (reported in Chapter 3) and accelerated curvature response (see Fig. 5.4) are testimonial to this assumption.

5.2.1.3 Plastic Buckling Mechanism

The assumed shape at the onset of buckling is determined by the development of a plastic hinge mechanism. This developed mechanism will also be influenced by the conditions of restraint, whether end conditions are considered as pinned or fixed. The three conditions that may apply to a topping slab, and their associated plastic hinge mechanisms at buckling, are shown in Figure 5.5. In the slab buckling model, it is considered that the effects of cyclic loading will have caused sufficient loss in composite bond to nullify lateral bond restraint. This assumption is also supported by the test observations reported in Chapter 3.

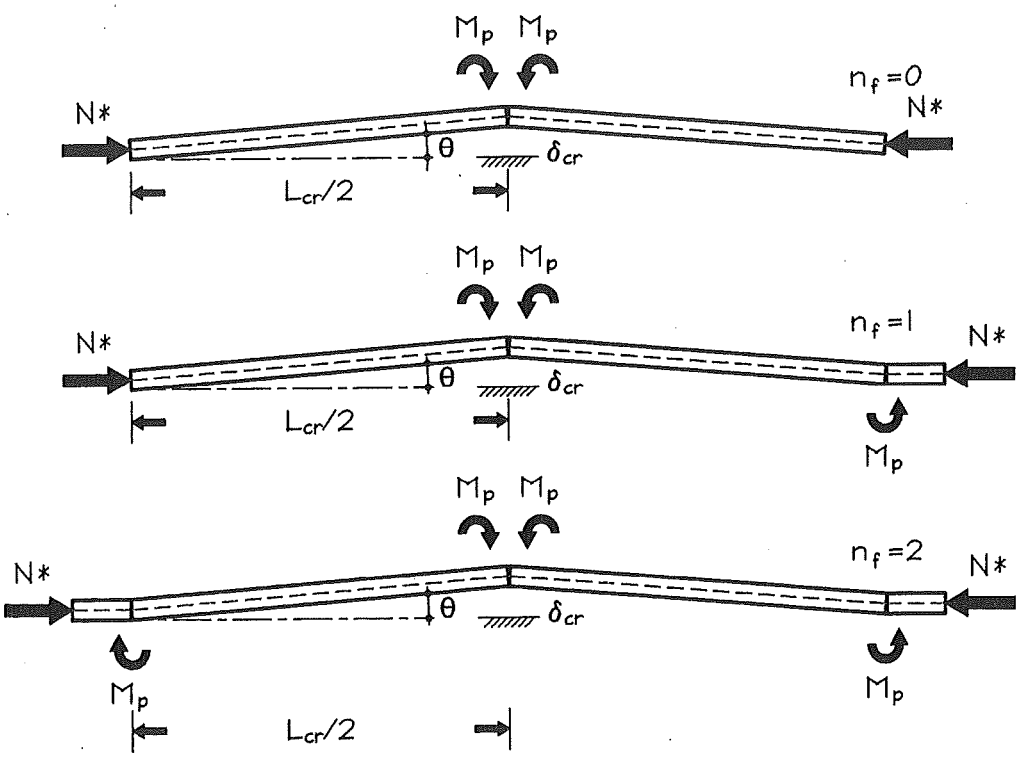

Fig. 5.5 Slab buckling mechanisms assumed in model

The fixed-fixed ($n_f = 2$) condition in Figure 5.5 is most relevant to practical situations that involve composite topping slabs.

In terms of plastic hinges and associated rotations, the sum of internal energy in the plastic hinge mechanism may be written as:

$$\sum_n U_b = \sum_n M_p \theta \tag{5.3}$$

For uniform moment capacities and with n_f equalling the number of fixed end conditions applicable to a length of slab that may buckle, combining into Equation 5.1 gives:

$$U_c = (n_f + 2) M_p \theta \tag{5.4}$$

With the reasonable assumption that a plastic hinge will form near the mid point of the buckling length, the mid-span displacement at collapse may be taken simply as moment M_p divided by design axial force N* (similarly as assumed in the Euler model). Hence:

$$\frac{M_p}{N^*} = \frac{\theta L_{cr}}{2} \quad \text{or} \quad \theta = \frac{2M_p}{N^* L_{cr}} \tag{5.5}$$

Substituting this expression for θ into Equation 5.4 gives:

$$U_c = 2(n_f + 2)\frac{M_p^2}{N^* L_{cr}} \tag{5.6}$$

Reverting to Equation 5.2, the strain energy due to axial deformation when expressed as the summation of concrete and steel components of a prismatic and uniformly reinforced topping slab gives:

$$U_c = (u_c A_c + u_s A_s) L_{cr} \tag{5.7}$$

where u_c and u_s are the individual strain energy densities of concrete and steel.

Assuming the characteristic stress-strain response of unconfined concrete, the strain energy density of concrete may be written as:

$$u_c = f'_c \int_0^{\varepsilon_c} \frac{2\varepsilon_c}{\varepsilon_o} - \left(\frac{\varepsilon_c}{\varepsilon_o}\right)^2 d\varepsilon \tag{5.8}$$

which gives:

$$u_c = \frac{f'_c \varepsilon_c^2}{\varepsilon_o}\left(1 - \frac{\varepsilon_c}{3\varepsilon_o}\right) \tag{5.9}$$

For prismatic concrete sections under axial compression, the strain corresponding to peak stress is often taken as $\varepsilon_0 = 0.002$. Hence, steel reinforcement with yield strength greater than 400 MPa is unlikely to reach the yield condition in compression. The use of higher grade steels such as Grade 430 reinforcement is increasingly common, and the yield strength of wire mesh will be at least 500 MPa.

For bonded reinforcement the compressive strain of steel will be equal to that of concrete, which gives the strain energy density of steel reinforcement as:

$$u_s = \frac{f_s^2}{2E_s} = \frac{\varepsilon_c^2 E_s}{2} \tag{5.10}$$

Therefore, combining Equations 5.9 and 5.10 into Equation 5.7 gives:

$$U_c = L_{cr}\varepsilon_c^2 \left[f'_c A_c \left(1 - \frac{\varepsilon_c}{3\varepsilon_0}\right) + \frac{E_s A_s}{2} \right] \tag{5.11}$$

and substituting Equation 5.11 into Equation 5.6 gives the general equation for critical buckling length L_{cr} as:

$$L_{cr} = M_p \sqrt{\frac{2(n_f + 2)}{N^* \varepsilon_c^2 \left[\frac{f'_c A_c}{\varepsilon_0} \left(1 - \frac{\varepsilon_c}{3\varepsilon_0}\right) + \frac{E_s A_s}{2} \right]}} \tag{5.12}$$

In most topping slabs, the contribution to total strain energy density from steel reinforcement is insignificant in practical terms, and may be ignored. Also, concrete strain ε_c can be expressed as a function of concrete stress f_c as follows:

$$\varepsilon_c = \varepsilon_0 \left(1 - \sqrt{1 - \frac{f_c}{f'_c}}\right) \tag{5.13}$$

and Equation 5.12 may be re-written as:

$$L_{cr} = \frac{M_p}{A_g} \sqrt{\frac{3(n_f + 2)}{\varepsilon_0 f_c f'_c \left[1 - \left(1 + \frac{f_c}{2f'_c}\right)\sqrt{1 - \frac{f_c}{f'_c}}\right]}} \tag{5.14}$$

As discussed, it is customary to adopt a concrete strain at peak stress of $\varepsilon_0 = 0.002$, giving:

$$L_{cr} = \frac{M_p}{A_g}\sqrt{\frac{1500\left(n_f + 2\right)}{f_c f'_c\left[1 - \left(1 + \frac{f_c}{2f'_c}\right)\sqrt{1 - \frac{f_c}{f'_c}}\right]}} \tag{5.15}$$

5.2.1.4 Practical Failure Criteria for Singly Reinforced Slabs

In recognition that reinforcement may contribute only a very small proportion of the total bending moment capacity, a further modification is especially applicable to singly reinforced slab members. Specifically, the reinforcement of axially compressed and singly reinforced slabs subjected to increasing bending curvature is likely to undergo a transition between compressive and tensile stress due to shifting neutral axis depths. Hence, there will be a point during the stage of accelerating bending curvature when reinforcement will provide nil contribution to bending capacity.

The above observation can be exaggerated to the case of an unreinforced (plain) concrete slab. In this situation, moment capacity will fully depend on distance between the centroids of concrete compression and the applied axial force, which is assumed to act through the slab centreline. In a practical sense, it is clear that slab localities would be severely prone to buckling failure from the instant that flexural cracking moment was exceeded. Hence, on the understanding that reinforcement may perform an insignificant and variable role, and that there will be other detrimental effects from non-closure of cracks etc., it is considered appropriate to use the flexural cracking moment M_{cr} as moment capacity for plain concrete slabs:

$$M_p = M_{cr} = \left(f_c + f_r\right)\frac{bh^2}{6} \tag{5.16}$$

where:

$$f_c = \frac{N^*}{A_g} \tag{5.17}$$

$$f_r = 0.8\sqrt{f'_c} \tag{5.18}$$

Furthermore, as the level of axial stress approaches the design crushing strength of concrete, the combined effects of compression and bending should not exceed the peak concrete strength value. The crushing strength of concrete in columns is usually taken as 85% of the test cylinder strength; the deviation being attributed to relative differences in the size and shape of columns, and segregation of fine aggregates at construction (which may be less critical for topping slabs) [Park and Paulay, 1975].

Therefore, it is considered that the effective crushing strength of concrete for use in the slab buckling model should also be taken as $0.85f'_c$, since this figure reflects the results of crushing tests and provides a practical margin for the added modulus of rupture f_r (see Equation 5.16). Substituting these values into Equation 5.15 yields the critical length equation for a slab member, where flexural actions are determined by the gross concrete section properties and flexural tensile strength:

$$L_{cr} = \frac{h}{6}\left(f_c + 0.8\sqrt{f'_c}\right)\sqrt{\frac{1500\left(n_f + 2\right)}{0.85f'_c f_c\left[1 - \left(1 + \frac{f_c}{1.7f'_c}\right)\sqrt{1 - \frac{f_c}{0.85f'_c}}\right]}} \qquad (5.19)$$

Alternatively, when moment capacity is derived from a more detailed section analysis:

$$L_{cr} = \frac{M_p}{A_g}\sqrt{\frac{1500\left(n_f + 2\right)}{0.85f'_c f_c\left[1 - \left(1 + \frac{f_c}{1.7f'_c}\right)\sqrt{1 - \frac{f_c}{0.85f'_c}}\right]}} \qquad (5.20)$$

Based on a 65 mm thick slab ($r \approx 19$ mm) of 25 MPa concrete, the critical buckling lengths as described by Equation 5.19 are shown in Figures 5.6, 5.7 and 5.8. The three common cases of braced compression members have been considered, namely pinned ends (free-free: $n_f = 0$, $k_e = 1.0$), fixed one end and pinned the other (fixed-free: $n_f = 1$, $k_e = 0.85$) or fixed both ends (fixed-fixed: $n_f = 2$, $k_e = 0.7$). The stated k_e values are effective length factors for the corresponding Euler buckling cases [Standards New Zealand, 1997]. For the calculation of Euler buckling strengths, column buckling stresses have been used, since plate buckling stresses according to Euler theory would exceed the concrete crushing strength by a factor of 14.

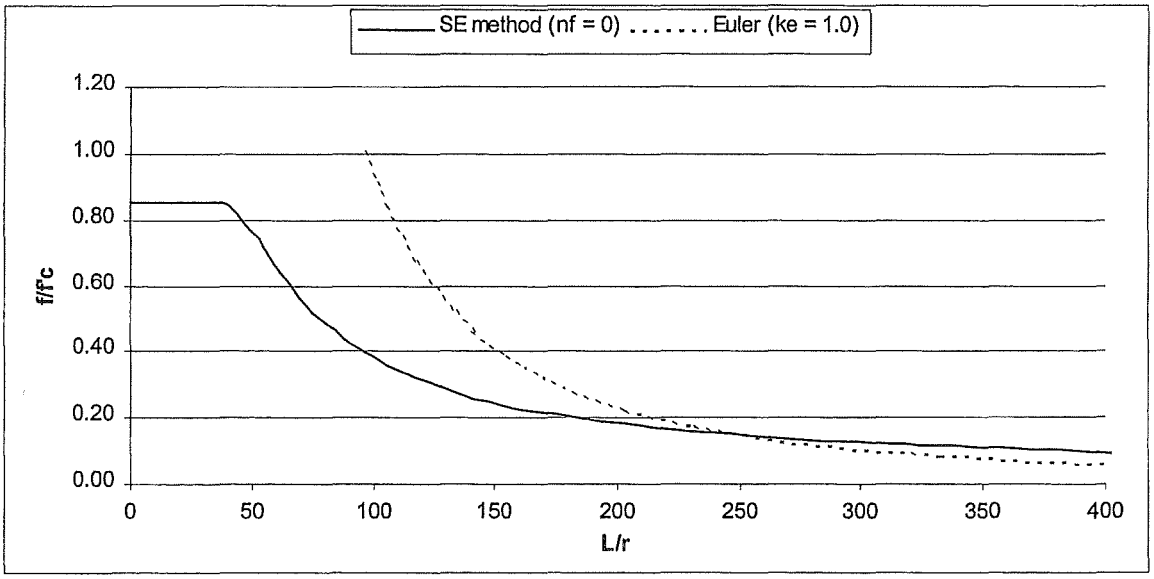

Fig. 5.6 Critical buckling slenderness ratio at proportion of concrete crushing strength (limited to $0.85f'_c$) for a braced strut with pinned ends.

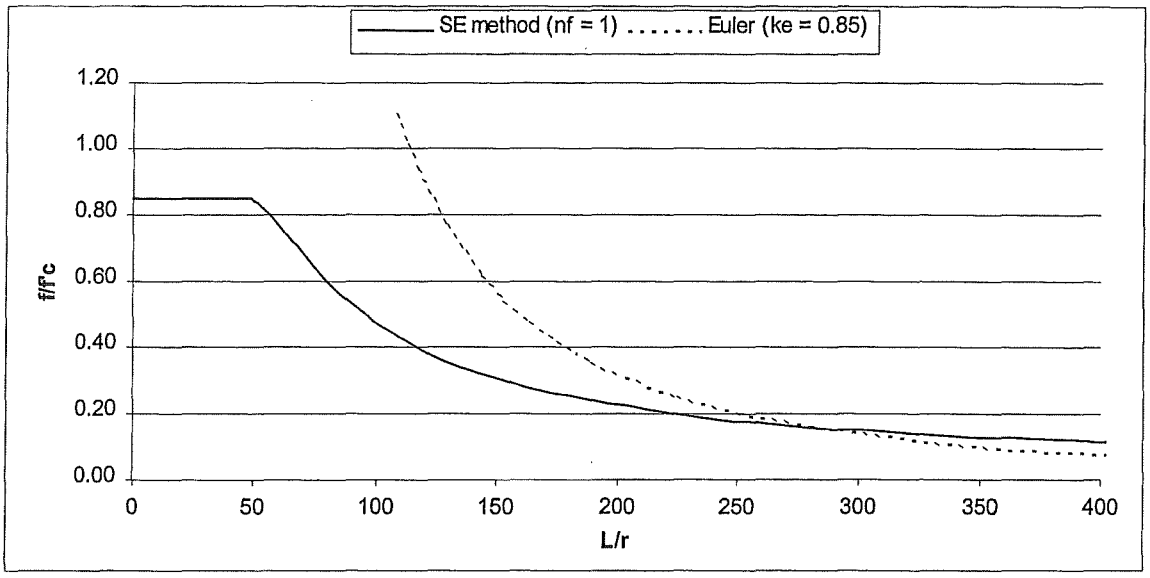

Fig. 5.7 Critical buckling slenderness ratio at proportion of concrete crushing strength (limited to $0.85f'_c$) for a braced strut with one pinned end and one fixed end.

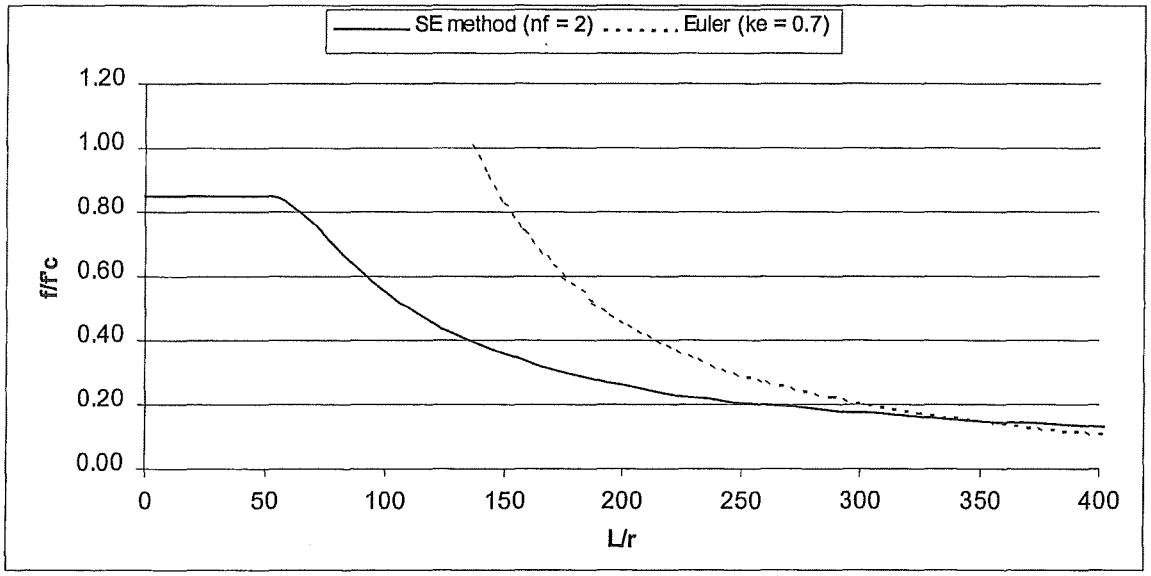

Fig. 5.8 Critical buckling slenderness ratio at proportion of concrete crushing strength (limited to $0.85f'_c$) for a braced strut with two fixed ends.

The effects of end fixity are shown in Figure 5.9. It is evident from Equation 5.19 that critical buckling lengths are proportional to the square root of the number of plastic hinges that must form to allow collapse, with $n_h = 4$ taken as maximum (i.e., $n_f + 2$). Furthermore, the general equation (Equation 5.12) may be simply adapted to the case of sway members, in that plastic hinges will only form at member ends. As such, the quantity of strain energy associated with $2 \cdot M_p \cdot \theta$ at the column mid-height will not be required, and by re-defining θ (see Equation 5.5), the numerator term under the square root sign in Equation 5.12 may be written as:

$$\frac{2}{2}(n_f + 0) = n_f \tag{5.21}$$

Hence, for a sway member with two pinned ends ($n_f = 0$), the collapse length is equal to zero (i.e., collapse is independent of buckling). Based on this observation, the effects of differing plastic hinge moment capacities may also be incorporated, since zero moment capacity may be interpreted as the least proportion of maximum moment capacity M_p. Therefore, the end fixity term may be replaced by a general summation, where n_θ is the number of plastic hinge rotations and the $M_{\theta(i)}$ terms are corresponding hinge moment capacities. Since hinge rotations are relative to their separation lengths at buckling, the length division factors are $\lambda = 1$ for sway members and $\lambda = 2$ for braced members, giving:

$$\frac{\lambda \sum_{n_\theta} M_{\theta_i}}{M_p} \tag{5.22}$$

where:

$$M_{\theta_i} \leq M_p \quad \text{and} \quad 0 \leq n_\theta \leq 4 \tag{5.23}$$

Therefore, the general expression for member buckling (Equation 5.12) may be written:

$$L_{cr} = \sqrt{\frac{\lambda M_p \sum_{n_\theta} M_{\theta_i}}{N^* \varepsilon_c^2 \left[\frac{f'_c A_c}{\varepsilon_0} \left(1 - \frac{\varepsilon_c}{3\varepsilon_o} \right) + \frac{E_s A_s}{2} \right]}} \tag{5.24}$$

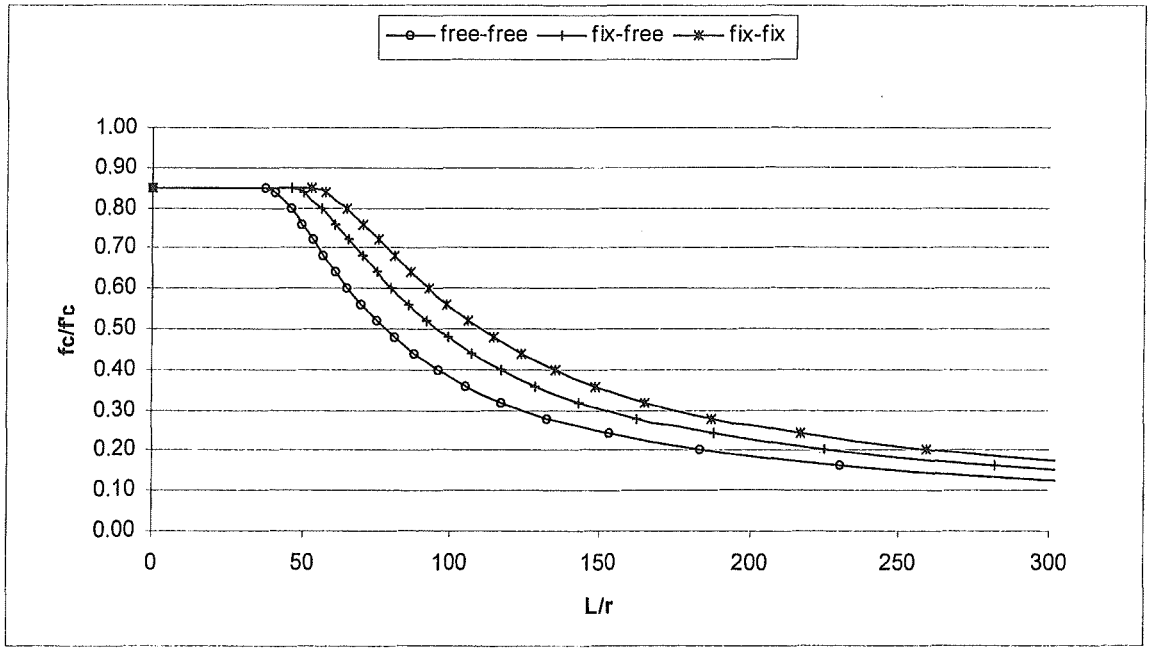

Fig. 5.9 Comparisons of critical slenderness ratios at proportion of concrete crushing strength (limited to $0.85f'_c$) for a 65mm slab with given end fixity and $\lambda = 2$

It is worth noting that for plastically deformed sway members, the length division factor used in Equation 5.24 may be taken greater than unity. This is because the characteristics of plastic hinges that develop in sway members are predisposed to the relative positions of bending inflection (see Section 2.2.1.4). Hence, it is conceivable that the effective length division factor may lie between $\lambda = 1$ for a complete column length and $\lambda = 2$ for two equal lengths between critical plastic hinges.

This and other plasticity effects are not considered further here, since the present buckling analysis is primarily directed at optimising the spacing of lateral restraints in topping slabs (i.e., braced member assumptions apply). However, the appropriate λ factors are ultimately determined from deflections associated with plastic hinge rotations, which may be estimated for actual sway members by the methods developed in Chapter 2 of this thesis.

To best determine the critical buckling lengths of slabs, an envelope of slenderness ratios should be constructed to allow for the transition between first cracking moment capacity and the plastic moment capacity assumed at failure (i.e., with concrete strain $\varepsilon_c = 0.003$). As mentioned earlier, the plastic moment capacity of a slab will reach a peak value under axial compression which is somewhat less than $0.85f'_c$. This is illustrated in Figure 5.10, where unlike the combined stresses assumption of elastic design, peak moment capacity may fall markedly under increasing axial compression.

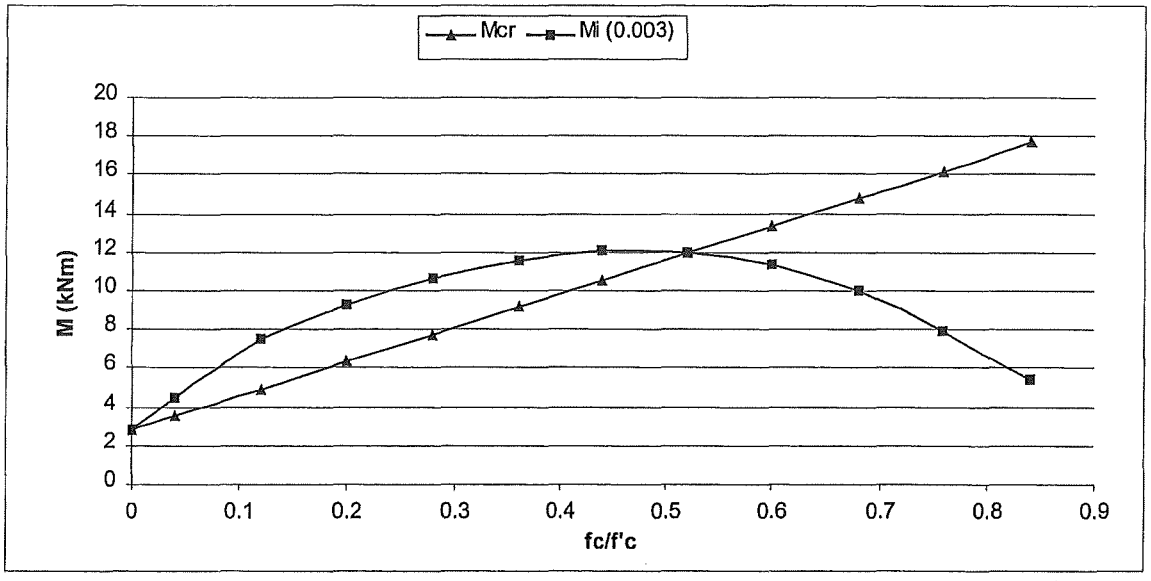

Fig. 5.10 Comparisons of bending moment capacities at first cracking (M_{cr} from elastic analysis) and M_i at a limiting concrete strain of $\varepsilon_c = 0.003$, for a 65 mm thick singly reinforced topping slab under axial compression

When plastic moment capacities M_i from Figure 5.10 are applied in Equation 5.20, the resulting slenderness ratios also reflect increased buckling length at lower axial loads, and decreased critical length at high axial load in relation to the M_{cr} envelope (Figure 5.11).

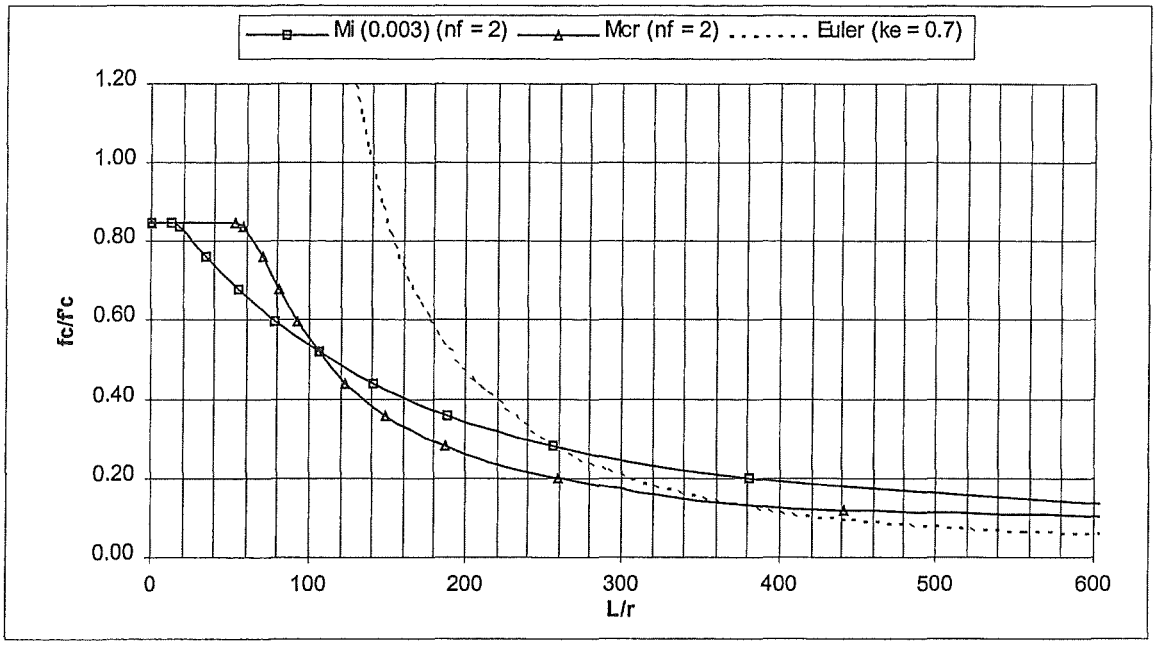

Fig. 5.11 Comparisons of critical buckling slenderness ratios at first cracking (M_{cr} from elastic analysis) and M_i at a limiting concrete strain of $\varepsilon_c = 0.003$, for a 65 mm thick singly reinforced topping slab.

By limiting the critical buckling slenderness L/r to the least value envelope given by Figure 5.11, it is evident that the Euler buckling model would determine the strength of very slender elements ($L/r \geq 360$). For elements of intermediate slenderness ($100 \leq L/r \leq 360$), the strain energy model (SE method) assuming elastic bending capacity (i.e., $M_p = M_{cr}$) would provide the least estimate, and for stocky elements ($L/r \leq 100$) the SE method assuming plastic moment capacity would govern.

In practice, the application of slab buckling length equations is appropriate for regions where sizeable in-plane forces might occur in floor diaphragms. These regions and the probable nature and magnitude of forces have been discussed in Section 2.3.

It is generally accepted that in-plane nodal forces arising from seismic actions will be distributed into both the topping and precast concrete sections. However, it is usual in design practice to assume that the topping slab alone will resist in-plane forces. Although this assumption may appear overly conservative, there are instances where edge-to-edge contact cannot be assumed between precast flooring members, thus deferring the transfer of compressive forces to the monolithic topping slab. A primary example of this is in typical flat slab and double tee floor construction, where the edges between precast members are unlikely to provide a reliable contact surface for the transfer of strutting forces. However, with flat slab and tee units, adequate surface roughening for composite bond is not difficult to achieve and ties may be readily incorporated.

The fundamental concern with topping uplift and buckling lies with extruded hollow core flooring, since the early breakdown of topping bond in laboratory tests was observed for extruded hollow core units without special surface roughening.

With regard to in-plane strutting forces, extruded hollow core flooring has the ready-made advantage of grouted shear keys that can facilitate the transfer of compression forces between adjacent members. Therefore, the situations that may require closer attention occur when (i) forces result from flexure as discussed in Section 2.3.1.2 and (ii) compression forces are generated under reverse seismic actions via chord tie reinforcement placed in the topping slab (see Section 2.3.2.2).

(a) Resistance to Flexure

Reverting to the example given in Section 2.3.1.2, a rational assessment can be made regarding the required spacing of topping ties to control slab buckling. The orthogonal over-strength bending moments M_{ox} and M_{oy} arise from concurrent plastic hinge formation during a severe seismic event. The resultant coupling force N_{oxy} has been derived from the vector sum of moments and the effective section depth jd. It is assumed that topping bond has degraded (as observed in experiments) and that the contribution of the topping slab must be considered as a stand-alone mechanism. The effective width of slab that resists N_{oxy} is taken as the diagonal distance between the plastic hinge lengths formed adjacent to the column faces (see Fig. 5.12).

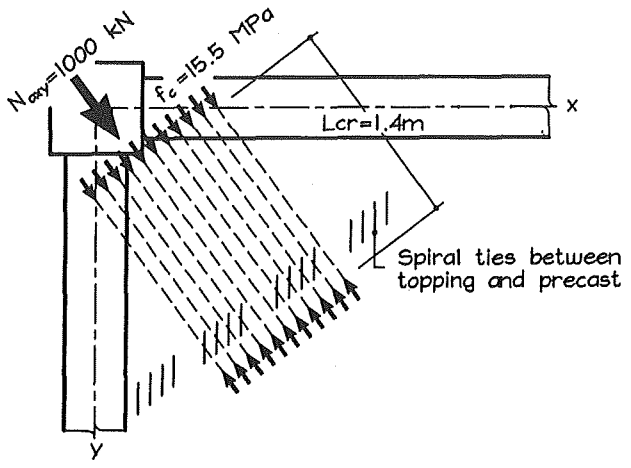

Fig. 5.12 Effective width of slab and critical buckling length for topping slab resistance to concurrent beam flexure at columns

Because the only effective reinforcement in the potential buckling zone is topping mesh, the critical slenderness may be conveniently taken straight from Figure 5.11. The axial stress as a proportion of f'_c is: 1000 kN / (25 MPa × (1000 × 65)mm2) = 0.62. Since this is greater than approximately $0.5f'_c$ the plastic moment capacity is applicable, giving a slenderness ratio of about 74. Hence, the critical buckling length is estimated as 74× 19 mm = 1.4 m, and a line of ties placed at say 0.85 × 1.4 = 1.2 m from the compression face should be considered.

(b) Resistance to Chord Forces

It is common in routine design for appreciable volumes of chord tie reinforcement to be placed in the topping slab near the supports and transverse to the span of precast flooring units. During a severe earthquake this band of reinforcement acts as a chord tie, thus controlling diaphragm actions and preventing the progress (unzipping) of cracks into the diaphragm along the joints between precast units (Fig. 5.13).

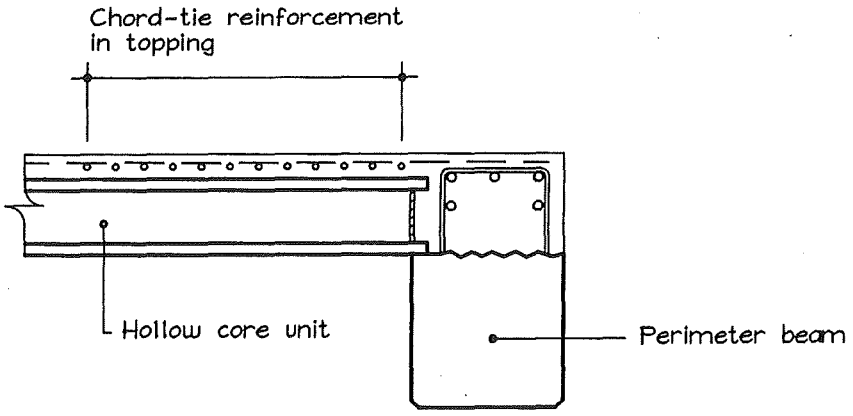

Fig. 5.13 Chord-tie reinforcement in the topping slabs of seismic resisting diaphragms

For chord-tie reinforcement to take effect, it must develop forces that are close to yield strength. Therefore, and depending on selected ductility factors, it is likely that some yielding of this reinforcement will occur during a strong earthquake. Hence, under cyclic response, it is reasonable to assume that the force of yielded bars will need to be resisted in compression by a topping slab with reduced composite bond.

In these situations, the volume of reinforcement should be taken into account. For example, if a unit (one metre) width of 65 mm slab has 12-H16 bars, then the force exerted on the slab face under compression is (12 × 201)mm^2 × 430 MPa = 1040 kN. Therefore, the concrete compression may be taken as approximately 1040 kN / (65 × 1000)mm^2 = 16 MPa. From Equation 5.13, this equates to an axial strain of $\varepsilon_c = 800\ \mu\varepsilon$ for 25 MPa concrete. Also, under 16 MPa compression and with reinforcement as above, the ideal moment capacity of the section at the limiting strain of $\varepsilon_u = 0.003$ is 11.2 kNm. Referring to Equation 5.24, the estimated critical length L_{cr} based on the common assumption of $\varepsilon_0 = 0.002$ is:

$$L_{cr} = \sqrt{\frac{2\times 11.2e^{6}\times\sum 44.8e^{6}}{1.04e^{6}\times\left(800e^{-6}\right)^{2}\times\left[\frac{25\times 62590}{0.002}\left(1-\frac{800e^{-6}}{3\times 0.002}\right)+\frac{200e^{3}\times 2410}{2}\right]}} = 1280\,\text{mm}$$

Therefore, in hollow core construction, ductile topping ties should be considered at each shear key (i.e., placed at 1.2 m centres) for the above volume of yielded chord-tie reinforcement.

5.3 BAR BUCKLING MODEL

5.3.1 BUCKLING CRITERIA

5.3.1.1 General

Based on rational material parameters, the buckling methodology developed in Section 5.2 for reinforced concrete members can likewise be applied to steel members. In particular, the response of reinforcing bars may be examined in a similar manner to slabs members in the preceding Section. The non-composite nature of typical steel members also allows for some simplifications in applying the developed principles.

5.3.1.2 Conservation of Energy

Proceeding as in Section 5.2.1.2, the sum of internal strain energy due to linear deformation is equated to the required strain energy in bending to allow a plastic collapse mechanism:

$$U_c = \sum_n U_b \tag{5.25}$$

Considering n_θ plastic hinge rotations (see Fig. 5.14), Equation 5.25 may be expanded to:

$$A_b L_{cr} \int_\varepsilon f_s \, d\varepsilon = n_\theta M_p \theta \tag{5.26}$$

where the rotation θ is likewise defined in accordance with Equation 5.5.

The integral of the LHS of Equation 5.26 gives the strain energy density of steel u_s, and is taken as the area under the characteristic stress-strain curve of the material. For the plastic buckling of steel, the material stress-strain response must be considered beyond yield strength.

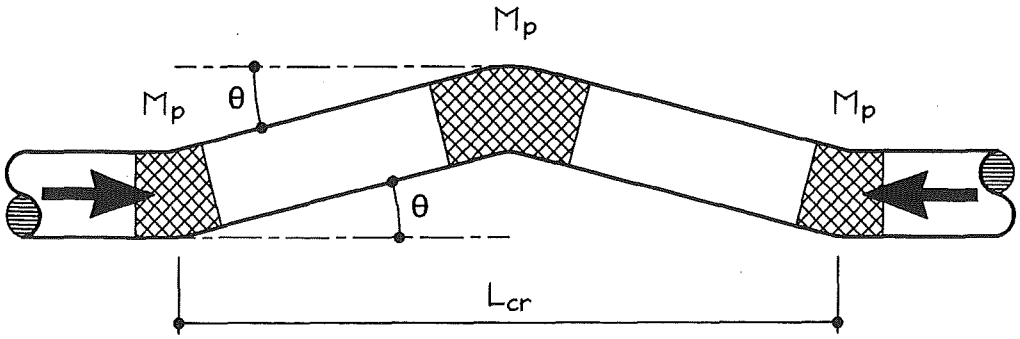

Fig. 5.14 Buckling model of steel bar

5.3.1.3 Equilibrium

The critical (equilibrium) displacement at buckling is taken as $\delta_{cr} = M_p/N^*$, which gives $\theta = \lambda \cdot M_p/N^* \cdot L_{cr}$. Therefore, the critical length may be written as:

$$L_{cr} = \sqrt{\frac{M_p^2 \lambda n_\theta}{N^* A_b u_s}} \tag{5.27}$$

For steels exhibiting a distinct yield plateau, strain energy density up to the point of strain hardening may be written:

$$u_s = f_s\left(\varepsilon_s - \frac{f_s}{2E_s}\right) \tag{5.28}$$

Observing that N^* is the product of $A_b \cdot f_s$, Equation 5.27 can therefore be simplified to:

$$L_{cr} = \frac{M_p}{N^*}\sqrt{\frac{\lambda n_\theta}{\varepsilon_s - \frac{f_s}{2E_s}}} \tag{5.29}$$

A further simplification may be made when f_s is less than the yield strength f_y (i.e., elastic buckling):

$$L_{cr} = \frac{M_e}{N^*}\sqrt{\frac{2E_s \lambda n_\theta}{f_s}} \tag{5.30}$$

As mentioned, the ratio of M_p/N^* in Equation 5.30 is the critical displacement. This value may be derived for the particular situation in accordance with axial load levels, initial member displacement and section geometry. The general equation may therefore be written:

$$L_{cr} = \delta_{cr}\sqrt{\frac{\lambda n_\theta}{\varepsilon_s - \frac{f_s}{2E_s}}} \tag{5.31}$$

Column buckling is imminent when the distance between the centroids of axial compression force and compression bending resistance has been exceeded at potential plastic hinge regions. Consequently, if both M_p and N^* in Equation 5.29 involve the material at yield strength (i.e., $f_s = f_y$) then the ratio will be that of plastic section modulus to cross section area, and therefore equal to the centroidal distance of the first moment of area about the neutral axis. Thus, for stocky members subject to plasticity, the critical displacement is:

$$\delta_p = \bar{y} = \frac{\sum A\bar{y}}{A} \tag{5.32}$$

For members subjected to elastic buckling, the critical displacement must also increase to reflect the (initially) elastic state of stress at the incipient point of buckling. Hence, the critical displacement value will vary between the respective centroids of plastic and elastic bending stress. As such, the radius of gyration may be taken as an intermediate value. Because the radius of gyration represents the area A pin-pointed at a distance r so that $A \cdot r^2 = I$, then the section modulus I/y must equal I/r, since this is also the fibre distance. Therefore, at equal stress, M_e / $N^* = A \cdot r^2 / A \cdot r = r$, and for elastic members of intermediate slenderness:

$$\delta_{ie} = r = \sqrt{\frac{I}{A}} \tag{5.33}$$

For slender members, the centroid of elastic bending stress is considered most appropriate. This is especially applicable to thin-walled hollow sections where the centre of bending resistance is concentrated near the section extreme fibre. Therefore for slender elastic members, the critical displacement may be taken as:

$$\delta_{se} = \bar{y} = \frac{M}{\sum \bar{\sigma} A} \tag{5.34}$$

Verification of the above equations are made by direct comparison with buckling slenderness ratios calculated in accordance with Chapter 6 of the Steel Structures Standard [Standards New Zealand, 1997]. In each case, the member is "compact" and has a form factor k_f of 1.0. For simplicity, the "compression member section constant" α_b has been taken as zero (0) in Table 6.3.3(2) of the standard. All members are assumed to be braced with pin-ends ($k_e = 1.0$). For the SE method and Euler buckling calculations, it is assumed that steel exhibits linear stress-strain response up to yield strength. The modulus of elasticity has been taken as 200 GPa.

For the SE method calculations, Equation 5.30 has been used with ratio M_e/N^* taken as the relevant δ_{cr} value given in Table 5.1 or 5.2. For braced pin-ended members, both n_θ and λ are equal to 2.0 (i.e, two plastic hinge rotations at mid-height, giving two corresponding length divisions).

Table 5.1 100 x 100 x 6 Square Hollow Section (Grade 350) (see Fig 5.15)

A (mm^2)	I (mm^4)	Z (mm^3)	S (mm^3)	$\delta_{ie} = r$ (mm)	δ_p (mm)	δ_{se} (mm)
2132	3.03 e^6	60.6 e^3	73.5 e^3	37.7	34.5	41.0

Table 5.2 86.6 x 86.6 Solid Square Section (Grade 250) (see Fig. 5.16)

A (mm^2)	I (mm^4)	Z (mm^3)	S (mm^3)	$\delta_{ie} = r$ (mm)	δ_p (mm)	δ_{se} (mm)
7500	4.688 e^6	108.25 e^3	162.38 e^3	25	21.7	28.9

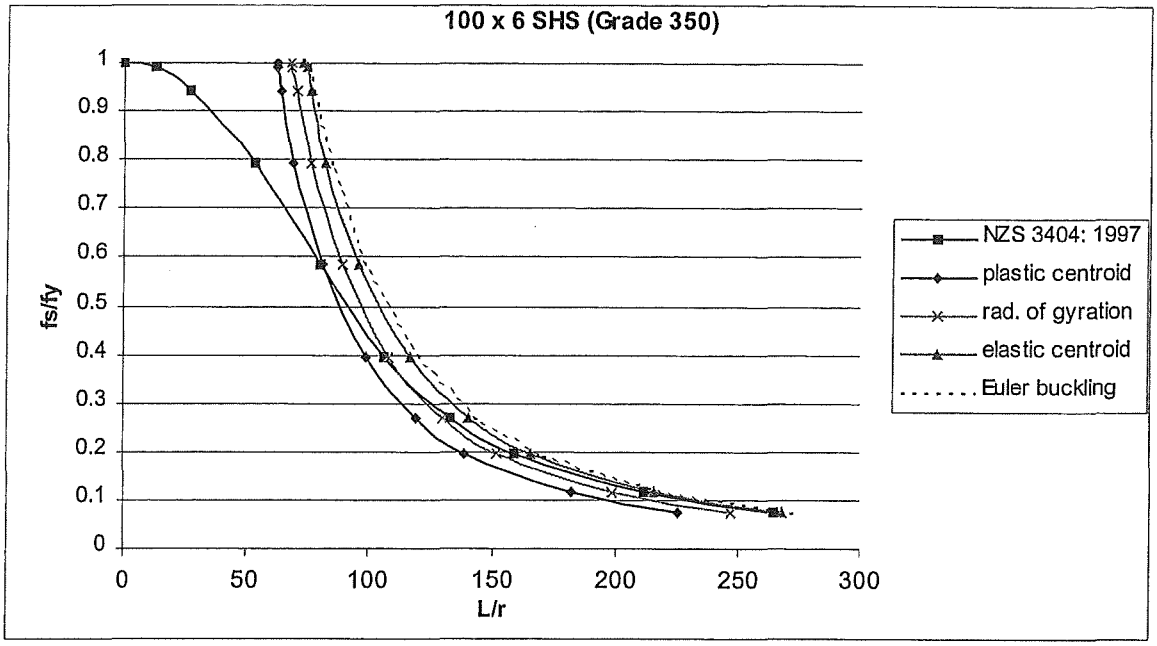

Fig. 5.15 Buckling slenderness ratios of a 100 x 6 Box Section (Grade 350) calculated in accordance with (i) NZS3404: 1997 (ii) the SE method for plastic, intermediate and elastic centroids, and (iii) classic Euler buckling theory

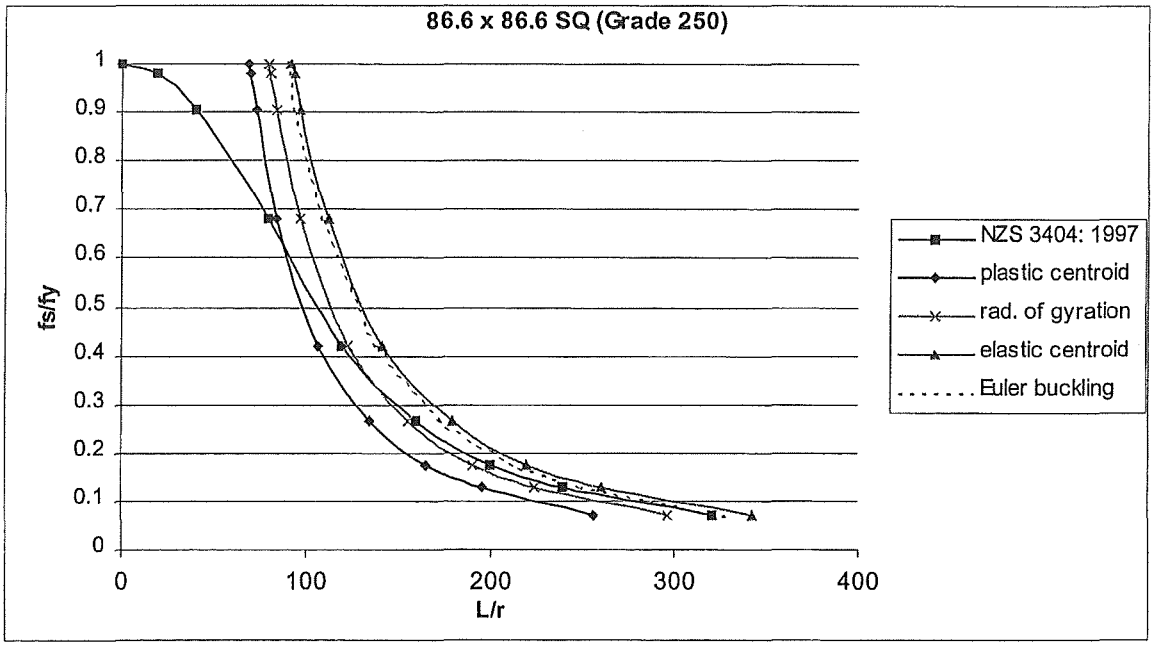

Fig. 5.16 Buckling slenderness ratios of a 86.6 x 86.6 Solid Square Section (Grade 250) calculated in accordance with (i) NZS3404: 1997 (ii) the SE method for plastic, intermediate and elastic centroids, and (iii) classic Euler buckling theory

It should be noted that the curve described by NZS3404: 1997 is based on Euler buckling theory, but with typical modifications for member class effects, increasing stockiness at reduced slenderness and initial deflections, etc [see Trahair and Bradford, 1988].

Assuming slender elastic behaviour, the SE method and classic Euler theory may be related by a simple expression. The critical buckling length according to Euler theory for braced pin-end members is:

$$L_{Ecr} = r\sqrt{\frac{\pi^2 E_s}{f_s}} \tag{5.35}$$

The corresponding critical length for braced pin-end slender elastic members by the SE method is:

$$L_{cr} = \delta_{se}\sqrt{\frac{8E_s}{f_s}} \tag{5.36}$$

Hence, the ratio between Euler buckling length and the SE method buckling length may be defined as a section constant:

$$\frac{L_{Ecr}}{L_{cr}} = \frac{r}{\delta_{se}}\sqrt{\frac{\pi^2}{8}} \tag{5.37}$$

In the preceding examples, the ratio described by Equation 5.37 is 1.02 for the 100 x 6 SHS and 0.97 for the 86.6 x 86.6 Solid Square Section.

However, despite the fact these theories may produce identical results, there are important conceptual differences between the two methods. Referring to the Equation 5.37, the radius of gyration r commonly employed in the Euler buckling theory is for convenience, being derived from the ratio of I/A that underlies the Euler theory. The radius of gyration applied in statics actually has limited physical meaning because it violates the parallel axis theorem.

Conversely, the critical displacement δ_{cr} in the SE method has important physical meaning, being the distance to the centroid of bending resistance applicable under the given state of stress. Hence, the critical displacement is an equilibrium requirement that will vary between elastic and plastic bending, and may be derived accordingly.

5.3.2 ELASTIC-PLASTIC TRANSITION

5.3.2.1 General

As demonstrated earlier, the underlying theory of the SE method does not limit the solution to tangent modulus theory or reduced modulus theory approximations for inelastic buckling. The underlying parameter is strain energy density, which may be rigorously derived for any stress-strain response. Hence, for typical mild steels that exhibit a distinct yield plateau (Lüders strain

region), the disappearance of an elastic modulus at yield ($E_s \rightarrow$ zero) has no impact on the validity of the theory.

5.3.2.2 The Bauschinger Effect

In seismic resisting reinforced concrete research, the cyclic stress-strain response of reinforcing steel has been the subject of much study. In particular, cyclic response and the induced Bauschinger effect has been examined in some detail, notably by Kent and Park, Thompson and Park, Spurr and Paulay, Mander et al, Tjokrodimuljo and Fenwick and Restrepo-Posada et al [see Park and Paulay, 1975: Restrepo-Posada, 1993].

The Bauschinger effect is important in that a reduced stiffness is experienced, and non-linear response develops at a strain much lower than the yield strain (Fig. 5.17). It is recognised that the Bauschinger effect likewise influences the behaviour of reinforced concrete members subjected to load reversals beyond the elastic range.

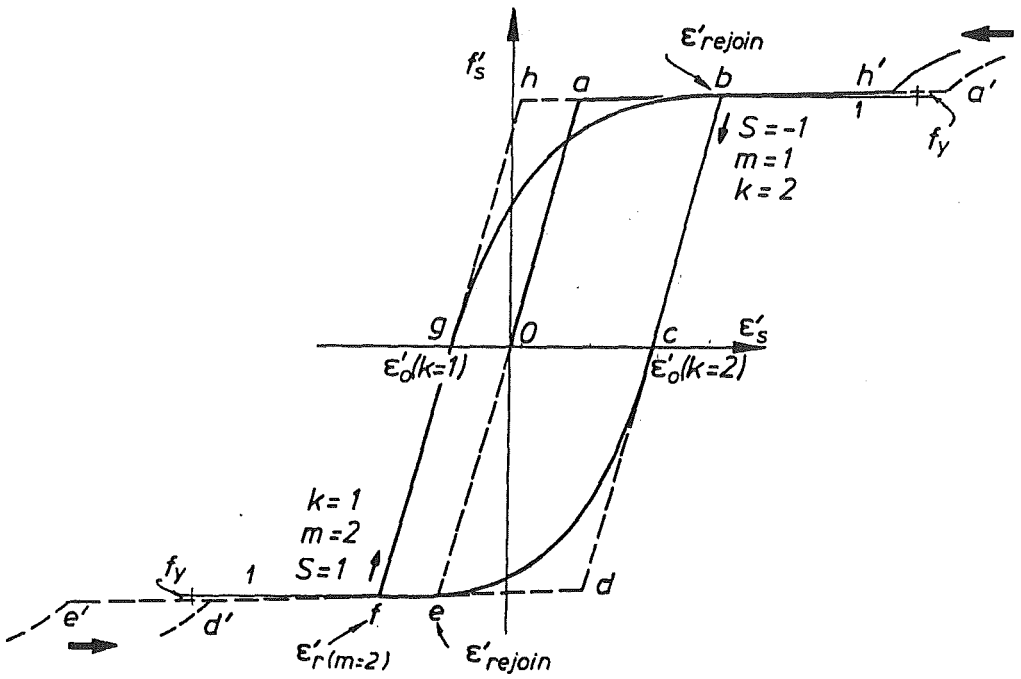

Fig. 5.17 Stress-strain behaviour in the yield plateau region, showing Bauschinger effect under load reversal [Restrepo-Posada, 1993]

Ultimately, the Bauschinger effect will reduce the buckling length of reinforcing bars where cover concrete has spalled under cyclic actions and effective confinement has not be provided. This may apply to regions of seismic resisting floor diaphragms where chord ties and drag bars constitute part of the force transfer system. In particular, these reinforcing details may coincide with (i.e., be connected to or lie adjacent to) the ductile structural elements where plasticity is expected to occur.

Taking Figure 5.16 as a typical example of softening response in the yield plateau range, a theoretical buckling envelope can be established for reinforcing bars in the transition between elastic and plastic response. The strain described by line c-g in Figure 5.16 corresponds with the point of zero stress and the rejoin point where yield stress is achieved. The magnitude of c-g is shown as approximately three times the monotonic loading yield strain, as indicated by lines o-a and o-e.

A simple but sufficiently accurate approximation is to treat the curves b-g and c-e as parabolic. As such, the parabolic stress equation normally assigned to unconfined concrete may be adapted to describe this curve and the associated strain energy density (see Equations 5.8, 5.9 and Figure 5.18). As discussed, the peak strain increment described by line c-g in Figure 5.16 is taken as three times the monotonic yield strain (i.e., $3 \cdot f_y/E_s$). Therefore $\varepsilon_0 = 3 \cdot \varepsilon_y$.

$$f_s = f_y \left[\frac{2\varepsilon_s}{\varepsilon_0} - \left(\frac{\varepsilon_s}{\varepsilon_0} \right)^2 \right] \tag{5.38}$$

and:

$$u_s = \frac{f_y \varepsilon_s^2}{\varepsilon_0} \left(1 - \frac{\varepsilon_s}{3\varepsilon_0} \right) \tag{5.39}$$

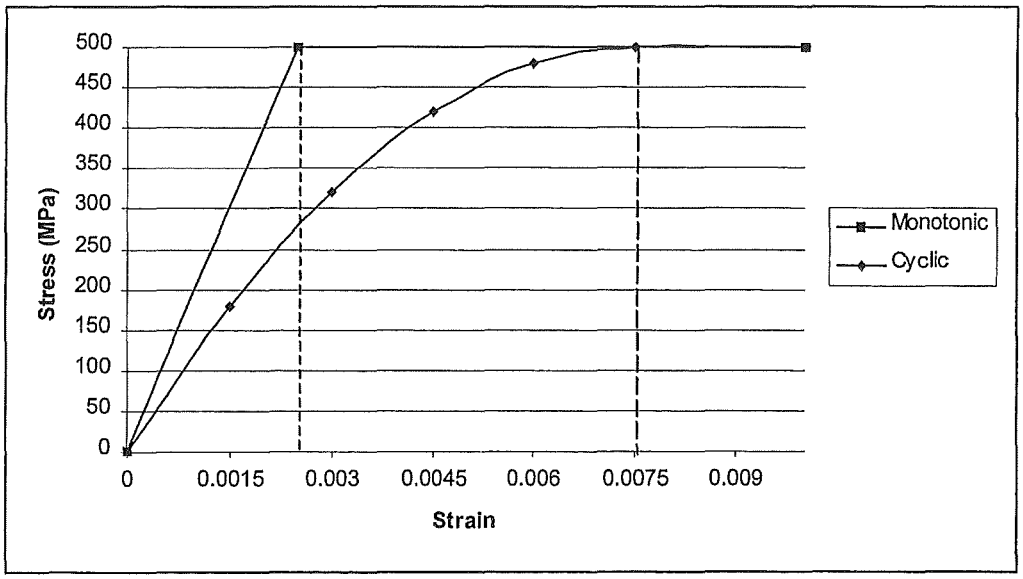

Fig. 5.18 Bauschinger effect approximated by parabolic relationship for yield plateau range (Equation 5.38), in comparison to monotonic stress-strain response

Table 5.3 Properties of reinforcing H16 (Grade 500) reinforcing bar

A_b (mm^2)	f_y (MPa)	δ_p (mm)	E_s (GPa)	ε_y	ε_o
201	500	3.4	200	0.0025	0.0075

For calculation of critical buckling length, Equation 5.27 may be written:

$$L_{cr} = \frac{M_p}{A_b}\sqrt{\frac{\lambda n_\theta}{f_s u_s}} \tag{5.40}$$

where M_p is equal to the product $S \cdot f_s$. Hence, for a round bar element, the ratio of M_p/A_b in Equation 5.40 may be written:

$$\frac{M_p}{A_b} = \delta_p f_s = \frac{2 d_b f_s}{3\pi} \tag{5.41}$$

For the buckling model, the bar element is assumed to be braced and have fixed ends:

$$\lambda = 2 \quad \text{and} \quad n_\theta = 4 \tag{5.42}$$

The buckling slenderness values (Fig. 5.19) are calculated from the figures in Table 5.4:

Table 5.4 Strain energy density under monotonic and cyclic loading between zero strain and $\varepsilon_o = 3 \cdot \varepsilon_y$ for H16 (Grade 500) bar

ε_s	f_s (monotonic) (MPa)	u_s (monotonic) (N/mm^2)	$\delta_p \cdot f_s$ (monotonic) (N/mm)	f_s (cyclic) (MPa)	u_s (cyclic) (N/mm^2)	$\delta_p \cdot f_s$ (cyclic) (N/mm)
0.0005	100	0.025	340	64	0.016	218
0.0010	200	0.100	680	124	0.064	422
0.0015	300	0.225	1020	180	0.140	612
0.0020	400	0.400	1360	231	0.243	785
0.0025	500	0.625	1700	278	0.370	945
0.0035	500	1.125	1700	358	0.690	1217
0.0040	500	1.375	1700	391	0.877	1329
0.0045	500	1.625	1700	420	1.080	1428
0.0050	500	1.875	1700	444	1.296	1510
0.0055	500	2.125	1700	464	1.524	1578
0.0060	500	2.375	1700	480	1.760	1632
0.0065	500	2.625	1700	491	2.003	1669
0.0070	500	2.875	1700	498	2.250	1693
0.0075	500	3.125	1700	500	2.500	1700

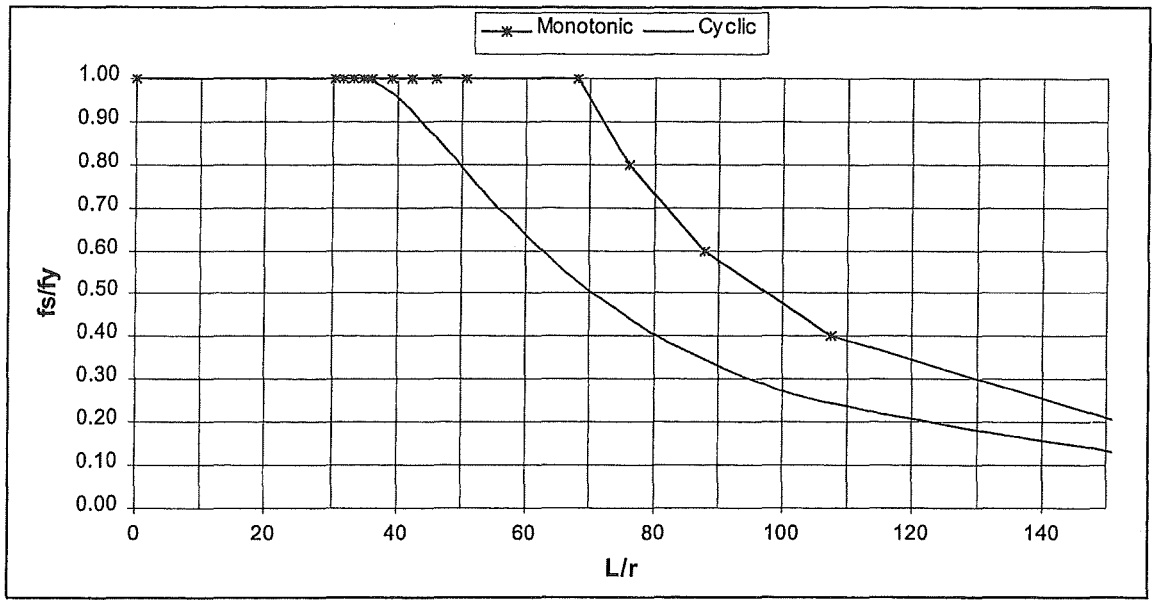

Fig. 5.19 Critical buckling slenderness ratios L/r for Grade 500 reinforcing bar under monotonic compression and cyclic compression incorporating the Bauschinger effect in the yield plateau range (see Fig. 5.18)

Although Table 5.4 specifically involves 16 mm bar, it will be noted that Figure 5.19 applies to all round bars exhibiting the stress-strain behaviour described by Figure 5.18, as the slenderness ratio is in linear proportion to the centroid distance δ_p. Also, the use of traditional terminology L/r is for comparison and convenience (since $r = d_b/4$). The plastic slenderness ratio L/δ_p (involving definable lengths) holds physical meaning within the model (Fig. 5.20).

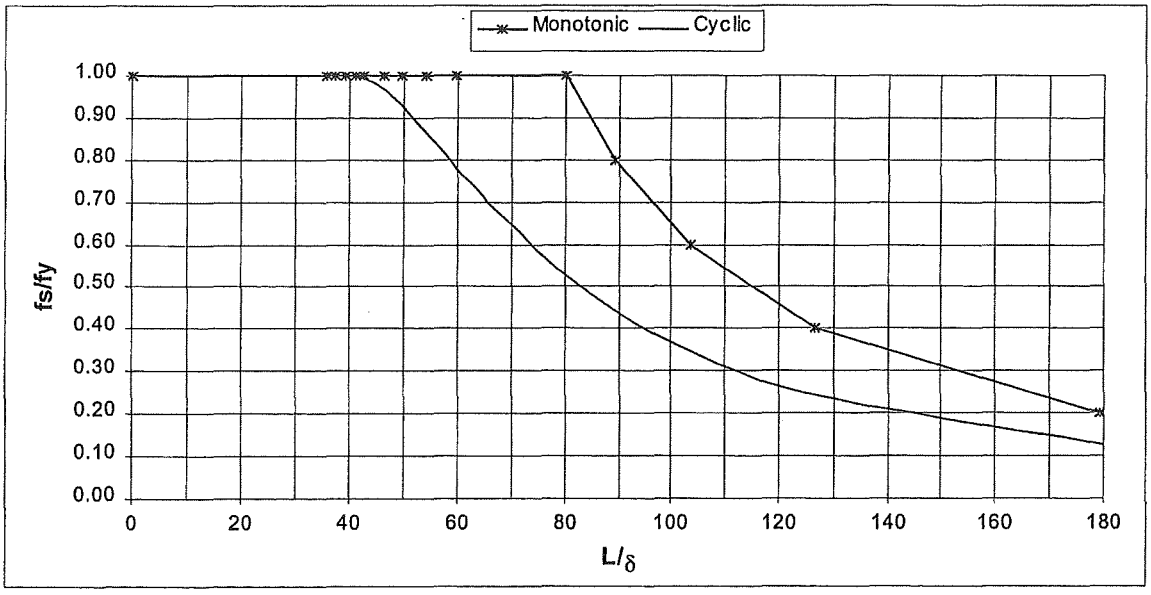

Fig. 5.20 Critical length displacement ratios L/δ for Grade 500 reinforcing bar under monotonic compression and cyclic compression incorporating the Bauschinger effect in the yield plateau range (see Figs 5.18 and 5.19)

5.3.2.3 Practical Buckling

It is widely recognised that the theoretical effective length factor of $k_e = 0.5$ for braced fixed-end members is unrealistic. This is because a degree of rotation is inevitable, thus weakening the sinusoidal deflected profile assumptions that are essential to the Euler theory. In structural steel design, where comparatively slender members are common, the minimum effective length factor for idealised end conditions is generally taken as not less than $k_e = 0.7$ (Fig. 5.21).

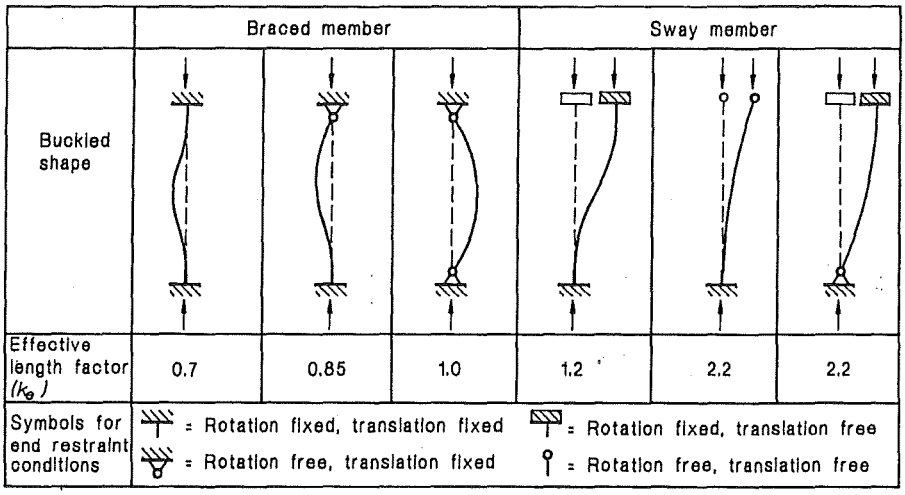

Fig. 5.21 Effective length factors for members with given conditions of end restraint [Standards New Zealand, 1997]

A final observation is to compare the slenderness ratio for monotonic loading calculated by the SE method, with that calculated from Euler theory modified by a suitable end condition constant. The Euler buckling stress was given by Equation 5.35 for the case of braced pin-end members. Since the braced pin-end member is the most fundamental case of Euler buckling, the end condition constant is simply taken as C = 1 (and is therefore ignored in Equation 5.35).

Considering the end condition constant C from a Mechanical Engineering perspective for the practical design of so-called Euler columns. It has been stated: "if liberal factors of safety are employed, and if the column load is accurately known, then a value of C not exceeding 1.2 for both ends fixed, or for one end rounded and one end fixed, is not unreasonable" [Shigley, 1986]. The theoretical and recommended C values for practical design are shown in Table 5.5:

Table 5.5 End Condition Constants for Euler Columns [Shigley, 1986]

Column end conditions	End-condition constant *C*		
	Theoretical value	Conservative value	Recommended value*
Fixed-free	$\frac{1}{4}$	$\frac{1}{4}$	$\frac{1}{4}$
Rounded-rounded	1	1	1
Fixed-rounded	2	1	1.2
Fixed-fixed	4	1	1.2

* To be used only with liberal factors of safety when the column load is accurately known.

The constant C is applied to Equation 5.43:

$$\frac{L_{Ecr}}{r} = \sqrt{\frac{C\pi^2 E_s}{f_s}} \tag{5.43}$$

The comparative slenderness ratios for Grade 500 steel bars calculated by the two methods (Equations 5.40 and 5.43 with C = 1.2) are shown in Figure 5.22 for bar stresses of 100, 200, 300, 400 and 500 MPa as shown in Table 5.4 for monotonic loading.

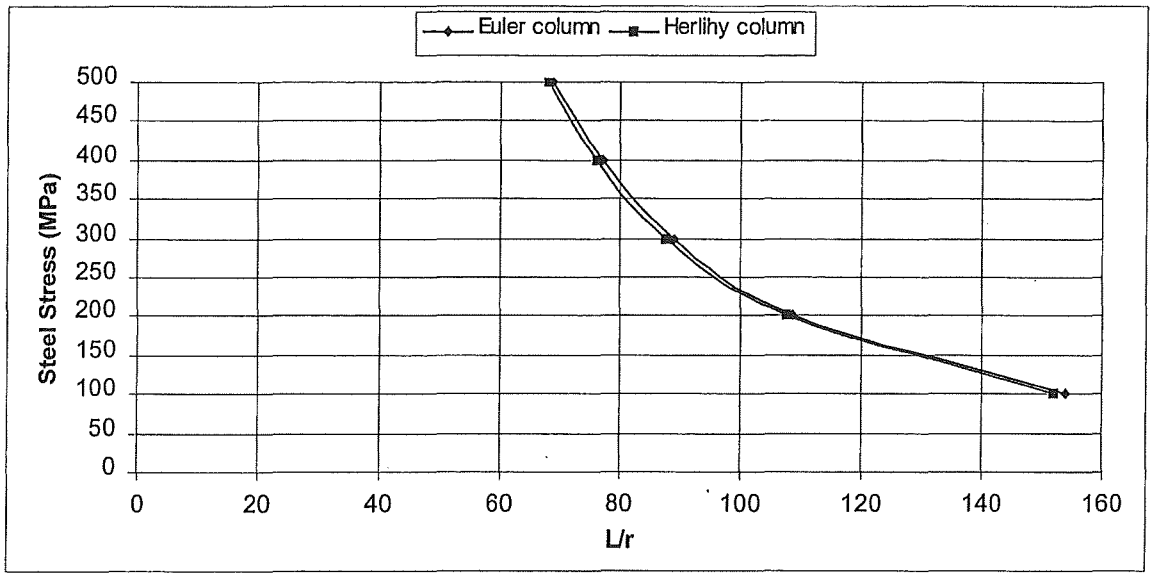

Fig. 5.22 Elastic critical slenderness ratios for Grade 500 round steel bars, calculated as Euler columns (with C = 1.2), and as Herlihy columns (by the SE method)

Referring to Figure 5.19, it is evident that a critical slenderness of about 30 ($7.5d_b$) is estimated for Grade 500 steel bars subjected to a compression strain of $3\varepsilon_y$ (0.75%) under cyclic loading. At $0.95f_y$ (475 MPa) the critical slenderness is estimated as 40 ($10d_b$) for bars subjected to the Baushinger effect. The comparative buckling slenderness for bars under monotonic loading to $0.95f_y$ is estimated as 70 ($17.5d_b$).

Therefore, for bars incorporated into regions of seismic resisting diaphragms where plasticity effects are expected during a severe earthquake, effective ties should be provided at $10d_b$ centres or less, depending on the anticipated level of plastic strain. It is apparent that the onset of strain hardening will increase both the quantities of f_s and u_s in Equation 5.40. This may effectively accelerate shortening of the critical buckling length, which is proportional to the dimensionless ratio:

$$\sqrt{\frac{f_s}{u_s}} \tag{5.44}$$

Hence, in simplest form, Equation 5.40 may be written:

$$L_{cr} = \delta_p \sqrt{\frac{f_s \lambda n_\theta}{u_s}} \tag{5.45}$$

A perfect-elastic perfect-plastic stress-strain behaviour has been used to calculate the buckling response of steel members as shown by Figures 5.15 and 5.16. Hence, the curves described by the SE method do not show a transition between the tangents of parabolic and horizontal lines. However, with higher-grade steels especially, an appreciable transition may occur between elastic and plastic behaviour under monotonic compression loading, similar in manner but less pronounced than described by the Bauschinger effect. Therefore, a transition of the type shown by Figure 5.19 for cyclically loaded bars would result for those steels, but initiating from a point on the monotonic loading curve.

As a consequence to the SE method buckling model, the following applies with regard to constructing a generalised design curve:

(i) Considering movement of the stress centroid between elastic and plastic bending resistance, the curve will vary between the critical displacements of slender elastic response (δ_{se}) and plastic response (δ_p) in direct proportion to the axial load ratio N^*/N_s. Thus, the design critical displacement δ^* may be written:

$$\delta^* = \delta_{se} - \frac{f_s}{f_y}\left(\delta_{se} - \delta_p\right) \tag{5.46}$$

and the design critical buckling length is defined as:

$$L_{cr} = \left(\delta_{se} - \frac{f_s}{f_y}\left(\delta_{se} - \delta_p\right)\right)\sqrt{\frac{f_s \lambda n_\theta}{u_s}} \tag{5.47}$$

(ii) The transition between parabolic and horizontal linear curves will initiate at the point of departure from initial elastic modulus, and become collinear with the horizontal line when yield stress had been achieved.

The curve that results from Equation 5.47 (yet unmodified for member effects) describes a buckling envelope very similar in appearance to the curve described by NZS 3404:1997, but with less conservative estimates of squat member buckling strengths. This is illustrated by Figure 5.23, where critical buckling lengths have been calculated for a 100 x 6 SHS (Grade 450) in accordance with Equation 5.47 and with strain energy densities u_s derived from Figure 5.24. The member is assumed to be braced with pin-ends ($k_e = 1$; both n_θ and $\lambda = 2$), and the section constant has been taken as $\alpha_b = 0$ in Table 6.6.3(2) of NZS 3404:1997.

Although hypothetical, the stress-strain relationship shown in Figure 5.24 is based on observed compression testing of steel bars. The relationship assumes a 0.15% proof stress, with departure from the initial elastic modulus commencing at $0.75f_y$ (337.5 MPa) and reaching yield stress at 0.375% strain. The strains corresponding to steel stress labels in figure 5.24 are 0.00169 (337.5), 0.0023 (414), 0.003 (443) and 0.00375 (450). From the above information, a sufficiently accurate estimate of strain energy density u_s can be made by area measurement.

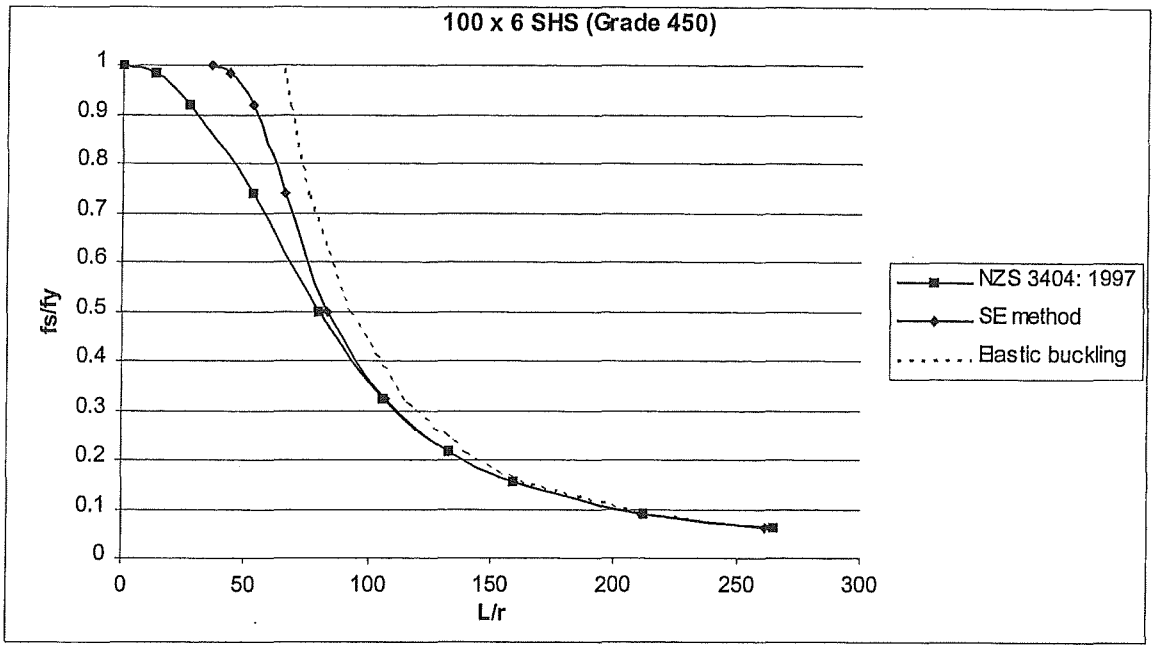

Fig. 5.23 Buckling slenderness ratios of a 100 x 6 Box Section (Grade 450) calculated in accordance with (i) NZS3404: 1997 and (ii) the SE method with allowance made for reducing critical displacement δ^* under increasing axial load and a reducing elastic modulus prior to yielding (see Fig. 5.24).

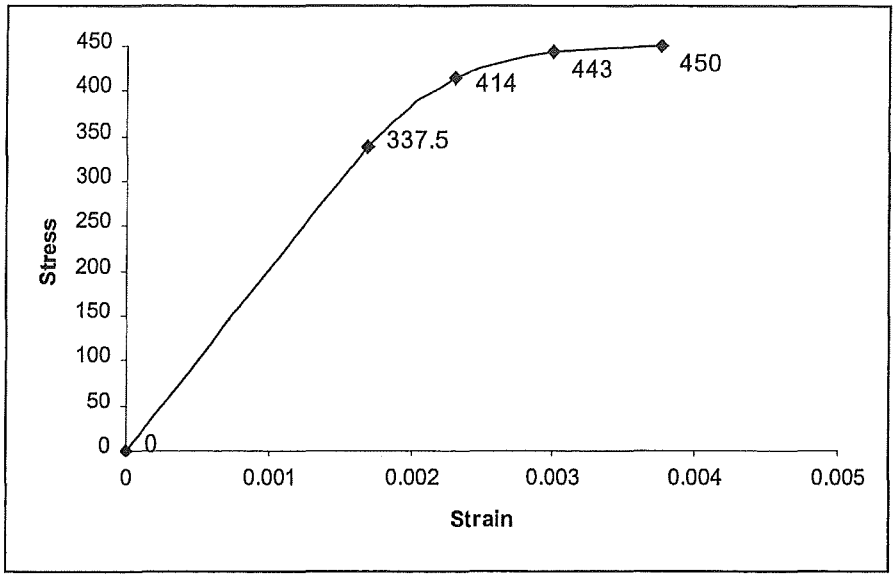

Fig. 5.24 Hypothetical stress-strain relationship, showing a reducing elastic modulus prior to yielding

5.4 CONCLUSIONS

5.4.1 GENERAL

In this Chapter, a general buckling theory has been proposed to facilitate the plasticity and composite section effects of reinforced concrete compression members. It is considered that the theory provides a more rational approach to buckling analysis than the traditional Euler theory, since equilibrium requirements and true material response may be incorporated into the solution. It is not possible to provide this level of amenity via the Euler solution, since mostly empirical notions of section stiffness response must be adopted.

Perhaps most importantly, the SE method theory principally requires knowledge of moment-curvature relationships in potential plastic hinges regions, which can now be ascertained with some accuracy. The regions away from plastic hinge locations do not exert a major influence within the theory. As such, the SE method is most adept for the analysis of ductile reinforced concrete members, since detailed modifications to the flexural rigidity EI in Euler theory must involve the entire member length in a mixture of guesswork and effort.

Members under combined actions of bending moment and compression have not been examined much beyond the effects of bending capacity on buckling length. However, it is considered that the underlying principle of energy balance must still apply, where the sum of strain energies due to compression U_c and bending U_b must equal the strain energy sum of a plastic collapse mechanism. Hence, Equation 5.1 may be more generally written as:

$$U_c + U_b = \sum_n U_p \qquad (5.48)$$

It is worth noting that there has been no empirical assumptions or adjustments used in the development of the SE method theory to this stage. Hence, Equation 5.47 (illustrated in Figure 5.23) is a primitive form of the critical buckling solution. Sufficient examples have been provided to validate the theory for use in both concrete and steel, elastic and plastic. Although an almost perfect correlation can be achieved with both pure and modified Euler theory (see Figures 5.15, 5.16, 5.22 and 5.23) it is important to note that the basis of the SE method theory is the conservation of energy principle, and is therefore quite separate from the Euler theory. Consequently, the SE method theory shares only one common assumption with the Euler theory: that bending moment is the product of force and displacement (i.e., the P-delta effect).

Some necessary assumptions have been made in the given examples. For instance, members have been considered as straight and free from residual stresses, etc. In the further development of a buckling theory, these effects would need to be closely examined. However, referring to Section 5.3.2.3, it is considered that modification by end condition constants (C in Equation 5.43) should not be applicable. This is because the development of plastic hinges essential to the SE method theory will be less sensitive to misalignments than the Euler theory. As such, the SE method theory simply requires that n_θ admissible plastic hinge rotations will form in order to satisfy equal energy principles, and allow member yield in accordance with statics.

5.4.2 CONCRETE SLABS

The critical buckling length of typical lightly reinforced slabs, calculated by the SE method, indicates that the buckling strength of very slender elements may be greater than predicted by the Euler theory (Fig. 5.11). This is the result of increased bending strength exhibited by concrete members resisting low-to-medium levels of axial compression. However, with increasing axial stress, the critical slenderness may decrease more significantly than estimated by elastic buckling assumptions.

The influence of bending response in the SE method is illustrated by Figure 5.11. Since the method incorporates the anticipated bending strength (see Fig. 5.10), the point of interception between elastic and ideal strengths at approximately $0.52f'_c$ in Figure 5.10 is reflected by the respective slenderness intercepts in Figure 5.11.

Likewise, the decreasing ideal moment capacity of highly compressed concrete members is reflected by the respective slenderness ratios in Figure 5.11. Hence, the SE method argues that a direct relationship exists between compression-bending interactions and the buckling strengths of reinforced concrete members.

From the analysis of typical slab configurations, it is concluded that designers must give some consideration to potential regions of buckling. This is especially the case when fully ductile behaviour may occur. From the developed buckling models, it is apparent that intense axial stress and cyclic actions will reduce the buckling capacity of these elements.

5.4.3 STEEL BARS

(a) Structural Steel Members

A précis analysis of structural steel members has been included, since the strong correlation with highly developed buckling methods given in modern steel design standards provides considerable validation of the SE method theory (Figures 5.15, 5.16 and 5.23). However, since modifications have not been made for specific member effects such as local buckling, the SE method estimates higher buckling strengths for squat members than the Standards method.

(b) Reinforcing Bars

As observed in test LOS 5, the buckling of topping slabs may be influenced by the behaviour of reinforcing steel. Under cyclic response, the associated softening response of steel bars (the Bauschinger effect) can result in non-closure of principle cracks. This effectively reduces the local bending capacity and facilitates slab buckling under lower levels of axial compression.

Examination of the Bauschinger effect indicates that a significant decrease in bar buckling lengths can be expected to occur under cyclic actions (see Fig. 5.19). Based on the parabolic

softening envelope of Equation 5.38 (see Fig. 5.18), Grade 500 bars reaching yield strength under cyclic strains up to $3 \cdot \varepsilon_y$, should be provided with lateral ties spaced at not more than $10 d_b$.

6

Composite Topping Bond

6.1 GENERAL

At the outset of testing, an initial estimate was made of the bond stress that could be resisted in shear between a composite topping and the clean surface of an as-extruded hollow core unit (Section 3.3.1.1). Although it was recognised that the hollow core surface was not intentionally roughened, experiments have indicated that the horizontal shear provisions for composite toppings may be conservative for units subjected to flexure and shear [Scott, 1973].

The 0.55 MPa provision of the design standard [Standards New Zealand, 1995] may be traced back to at least as far as ACI 318-63, where an ultimate strength design factor of 1.9 was permitted on a basic allowable stress of 40 psi (0.275 MPa) for clean and roughened surfaces. Hence, a basic ultimate strength value of 0.55 MPa (80 psi) was eventually adopted for the first New Zealand code of practice (NZS 3101: 1982).

However, the tests reported in Chapter 3 have highlighted that the horizontal shear strengths accorded by the design standards and associated literature are significantly more than the shear strengths observed under dilation type loading. The composite bond values reported in these documents are not disputed, but it is clear that they apply to the horizontal shear stresses arising from flexural actions (i.e., shear flow stresses) rather than direct horizontal shear.

It is considered that the deficit of shear strength results from the limited scope for stress redistribution to occur under a direct shear loading regime. By virtue of its name, direct shear involves the most fundamental concept of shearing; that of a definitive force acting tangentially to a planar surface of known area, so that strength is afforded by a near uniform distribution of shear stress. This concept certainly applies at the interface between topping slabs and precast flooring units in the support region.

To establish the direct shear capacity of topping-precast bond surfaces, a short series of tests were performed on precast surfaces, constructed with varying forms and amplitudes of surface roughening. These specimens were subjected to a direct shear force until failure of the bond surface (or specimen) occurred.

6.2 TEST METHODOLOGY

6.2.1 GENERAL PROCEDURE

Each test set-up was comprised of two precast components plus a cast-in-place topping. The precast components consisted of an anchor slab, which acted as a supporting element of structure, and a shear slab that acted a precast flooring unit. The cast-in-place topping effectively acted as a restraint between the two precast items, and with regard to the translating (shear) slab, the restraint force was resisted by composite bond.

6.2.2 DESCRIPTION OF TEST EQUIPMENT

6.2.2.1 General

The test equipment involved an actuating system in the form of two 43 tonne rams, linear strain potentiometers plus a pen plotter device. The potentiometers were configured so that force-displacement relationships could be traced throughout the test.

6.2.2.2 Test Set-up

The test rig set-up and components of the test are shown in Figures 6.1 and 6.2

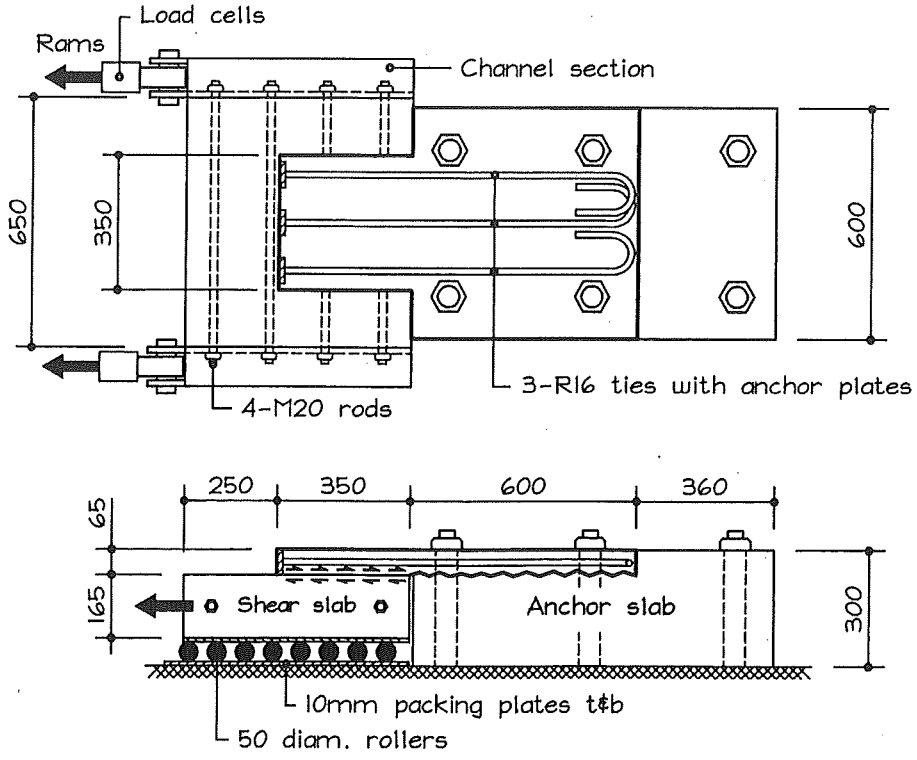

Fig. 6.1 Test set-up for establishment of composite bond strengths

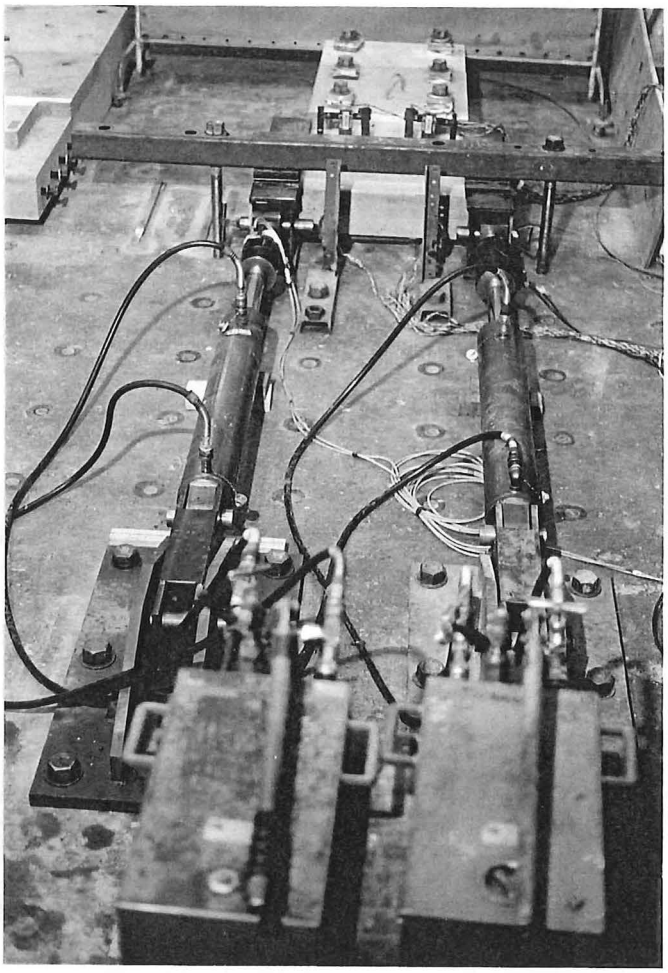

Fig. 6.2 View of test composite bond set-up

6.2.2.3 Horizontal Displacements

(a) Actuating System

Horizontal displacement was applied to the test specimens by two parallel acting hydraulic rams, as used for the LOS test series (see Figs 3.2). The rams were connected to the shear slabs via steel channel sections and four 20 mm threaded bars cast into the slab. The shear slabs were mounted on rollers on smooth levelled shim stock, to reduce the restrictive effects of an uneven surface.

(b) Measurements

Principal horizontal displacements were measured by placing two 20 mm linear displacement potentiometers against the end of the shear slab. The associated force measurements were taken directly from the load cells mounted between the rams and connection eyelets. These readings were bridged to a Watanabe X-Y pen plotter, and readings were also scanned to the Metrabyte logger unit.

6.2.3 MATERIALS AND CONSTRUCTION

6.2.3.1 General

The shear slabs were constructed at a precasting yard and the surfaces were roughed (where applicable) in accordance with standard construction practice.

6.2.3.2 Anchor Slabs

The anchor slabs were cast-in-place in the laboratory from 30 MPa concrete and moist cured for three days.

6.2.3.3 Shear Slabs

Table 6.1 Characteristics of shear slab concrete at testing

Design Strength (MPa)	Crushing Strength (MPa)	Splitting Strength (MPa)
45 at 28 days	47.7	3.5

At testing, the shear slab concrete achieved a cylinder splitting strength of $0.51\sqrt{f'_c}$.

The shear slabs were precast in a factory from concrete used in typical prestressed concrete manufacture. The bond surfaces were screeded level, followed by the relevant surface treatment.

The following bond interactions (times number tested) were considered (see Figs 6.3 to 6.7)

- Steel Trowel Finish (2) representing a smooth clean surface
- Wooden Float Finish (1) representing a textured clean surface
- Light Broom Finish (3) representing low-to-medium roughening with laitance
- Retarder + Water Blast (1) representing medium roughening amplitude free of laitance
- Medium Broom + Lightweight Topping (1) representing medium roughening with laitance, bonding with lightweight concrete topping

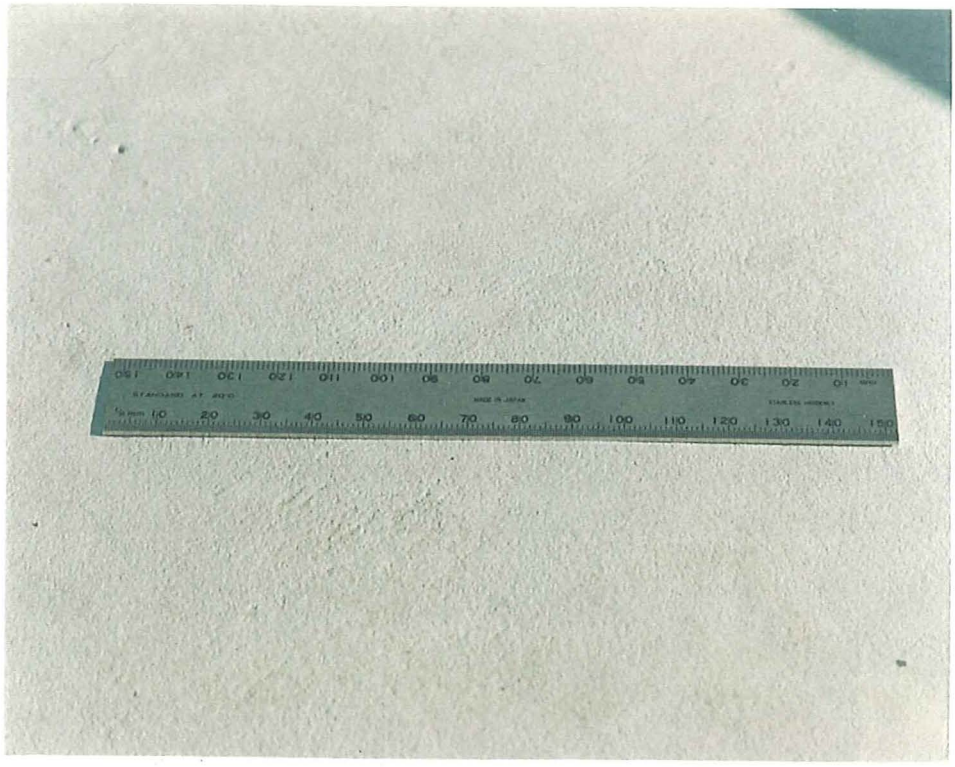

Fig. 6.3 Steel Trowel test surface

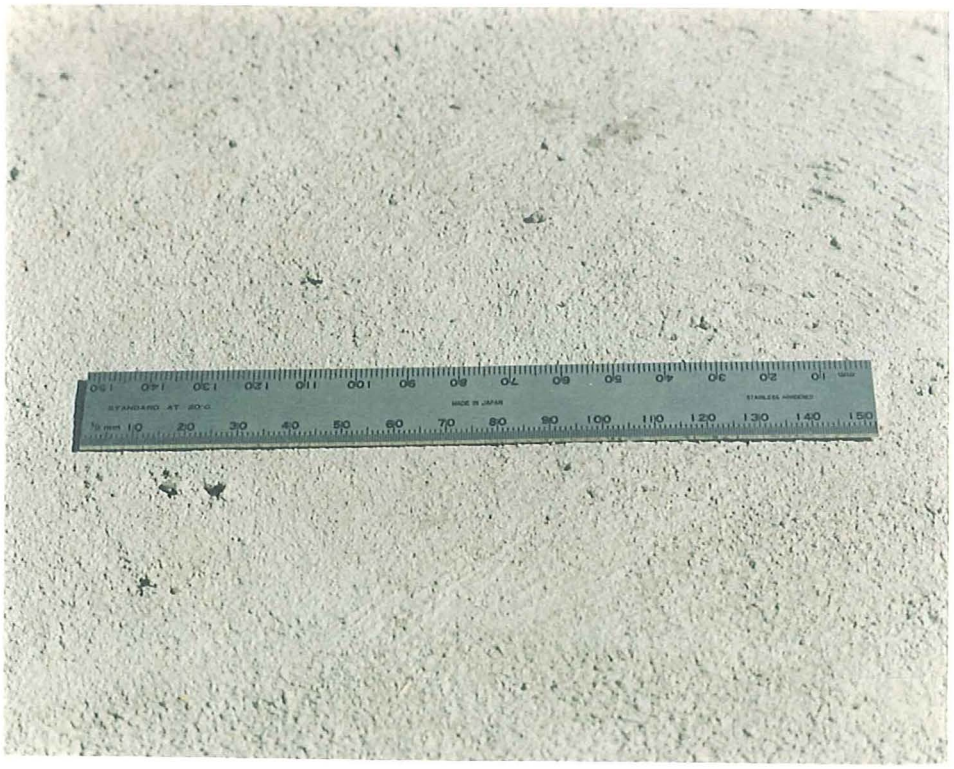

Fig. 6.4 Wooden Float test surface

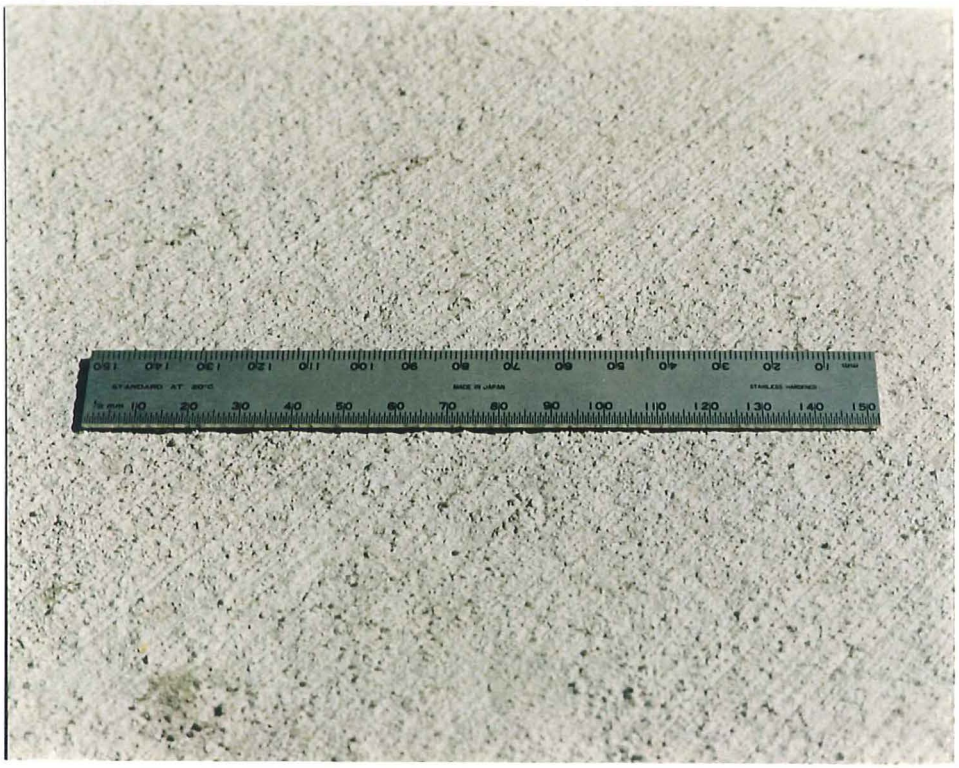

Fig. 6.5 Light Broom test surface

Fig. 6.6 Retarder + Water Blast test surface

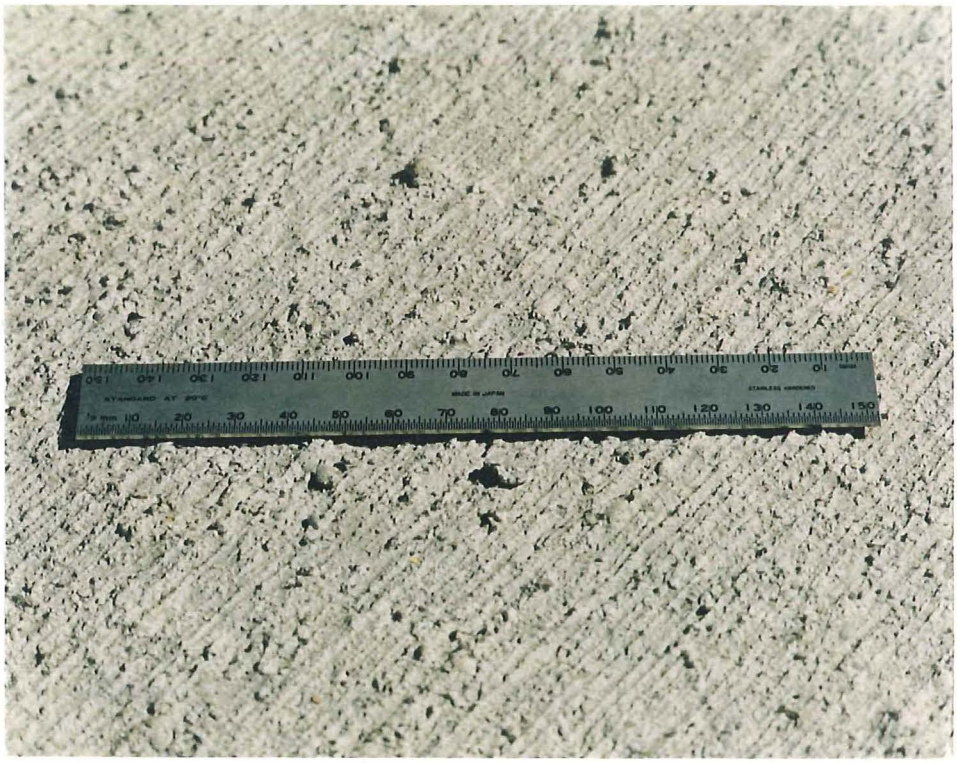

Fig. 6.7 Medium Broom + Lightweight Topping test surface

6.2.3.4 Cast-In-Place Topping Concrete

The precast surfaces were lightly dampened prior to placing of topping concrete. Moist curing was applied to the toppings for five days.

Table 6.2 Characteristics of cast-in-place topping concrete at testing

Design Strength (MPa)	Crushing Strength (MPa)	Splitting Strength (MPa)
25 at 28 days	24.3	2.8

At testing, the topping concrete achieved a cylinder splitting strength of $0.57\sqrt{f'_c}$.

The structural lightweight concrete was comprised of expanded clay shale (Liapor) lightweight aggregate and normal weight sands, with a target dry density of around 18 kN/m³.

Table 6.3 Characteristics of cast-in-place lightweight topping concrete at time of testing

Design Strength (MPa)	Crushing Strength (MPa)	Splitting Strength (MPa)
25 at 28 days	31.6	2.7

At testing, the lightweight topping concrete achieved a cylinder splitting strength of $0.49\sqrt{f'_c}$.

6.3 RESULTS OF EXPERIMENTS

6.3.1 BOND STRENGTH

6.3.1.1 General

The bond tests returned results that were generally consistent with expectations based on observation of earlier experiments and experience. The bond stress v_h was calculated as the average of horizontal force V_h divided by bond area A:

$$v_h = \frac{V_h}{A} \tag{6.1}$$

The shear slab extensions were continued beyond peak stress response for an approximate minimum of 10 mm. The graphed results are principally from logger data, with peak stress corrections taken from the X-Y plotter diagrams.

6.3.1.2 Steel Trowel Finish

Two specimens were examined, representing smooth clean surfaces in which adhesion between topping and precast concrete is influential. It is considered that these surfaces provide a reasonable comparison with those of as-extruded hollow core units used in the LOS testing series. The results of these tests are shown in Figures 6.8 and 6.9.

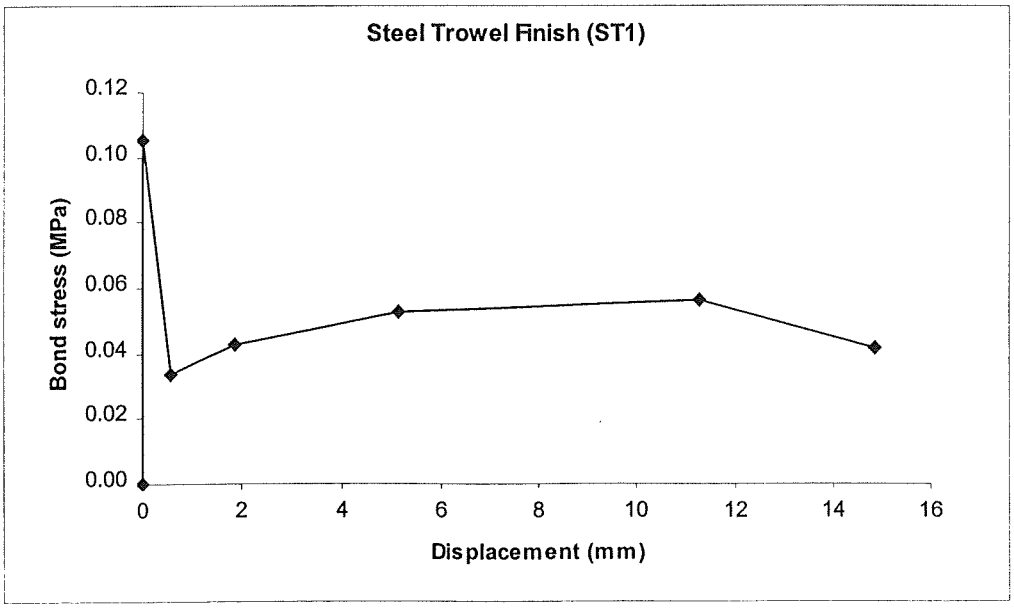

Fig. 6.8 Bond-displacement response of test ST1

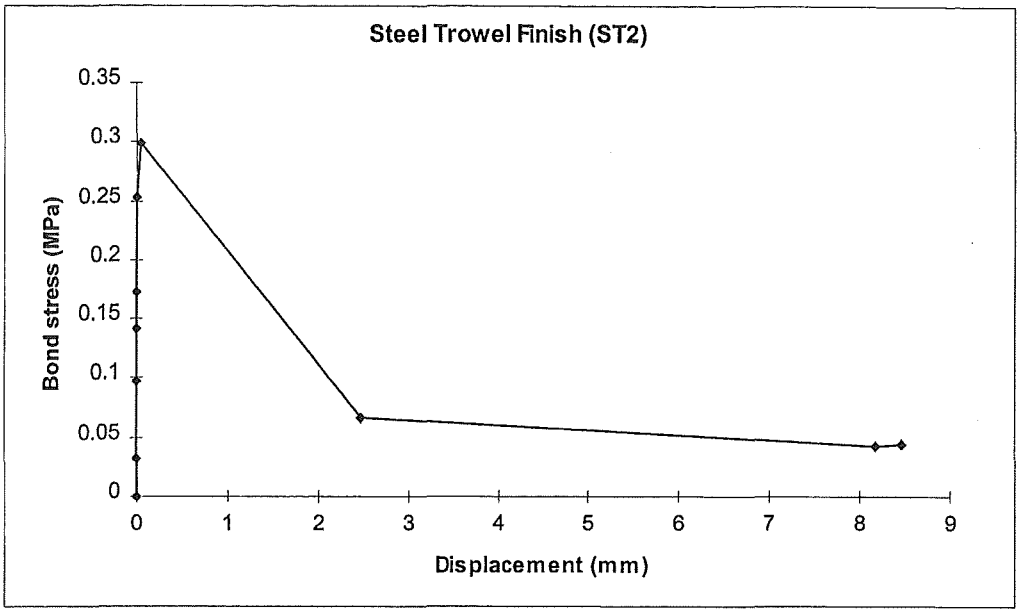

Fig. 6.9 Bond-displacement response of test ST2

6.3.1.3 Wooden Float Finish

One specimen was tested, representing a textured clean surface without deliberate roughening. The results of this test are shown in Figure 6.10.

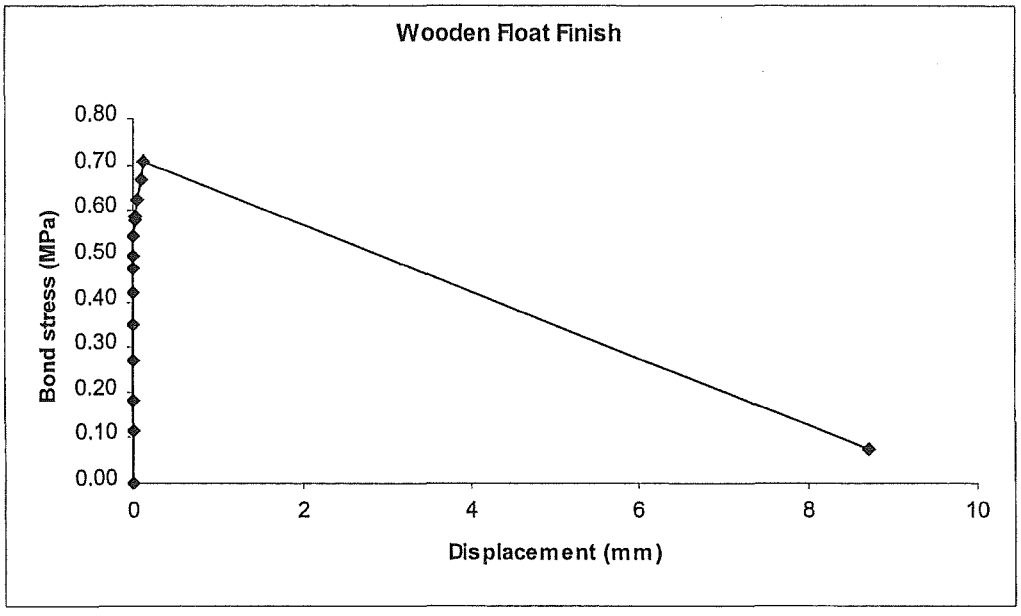

Fig. 6.10 Bond-displacement response of Wooden Float Finish test

6.3.1.4 Light Broom Finish

Three Light Broom specimens were tested, since the roughening amplitude is close to that achieved with broomed extruded hollow core units. The results of these tests are shown in Figures 6.11, 6.12 and 6.13.

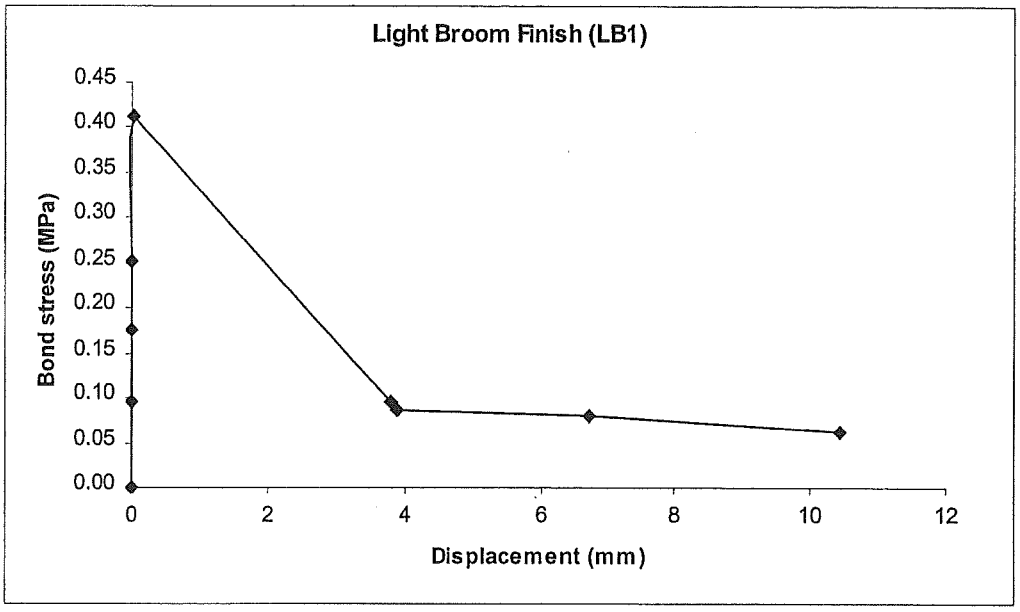

Fig. 6.11 Bond-displacement response of test LB1

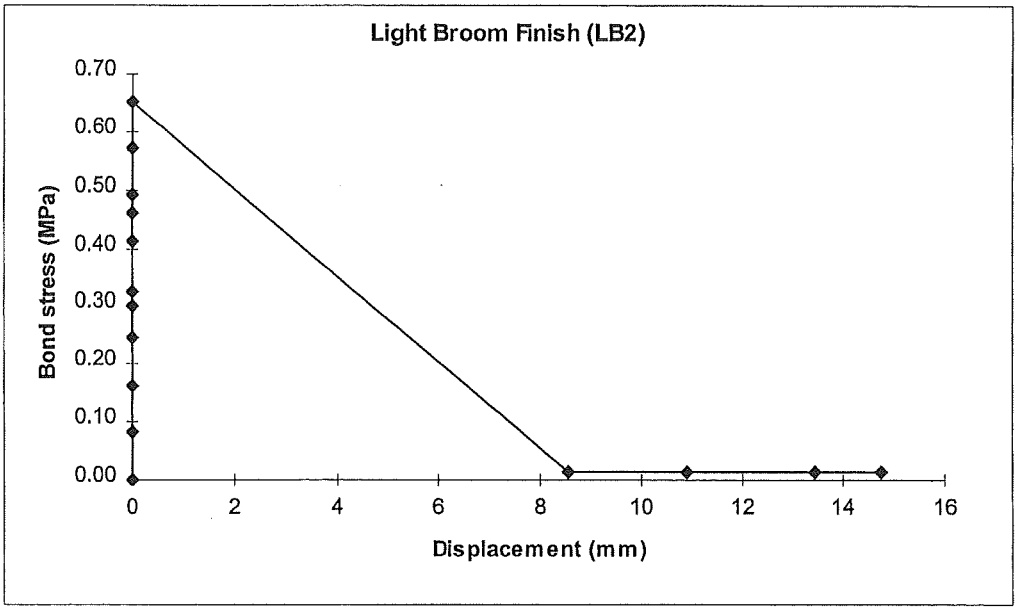

Fig. 6.12 Bond-displacement response of test LB2

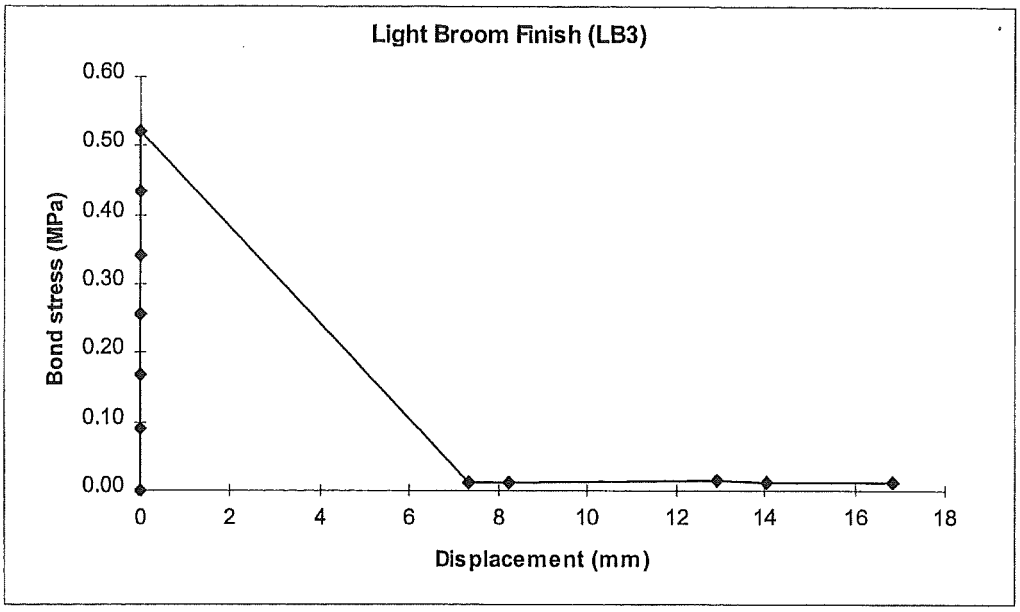

Fig. 6.13 Bond-displacement response of test LB3

6.3.1.5 Retarder + Water Blast Finish

This standard of finish is commonly used at construction joints in precast concrete. It is achieved by applying a retarding agent when the concrete surface is green, and subsequent water blasting when stripping strength has been achieved. The results of this bond test are shown in Figure 6.14:

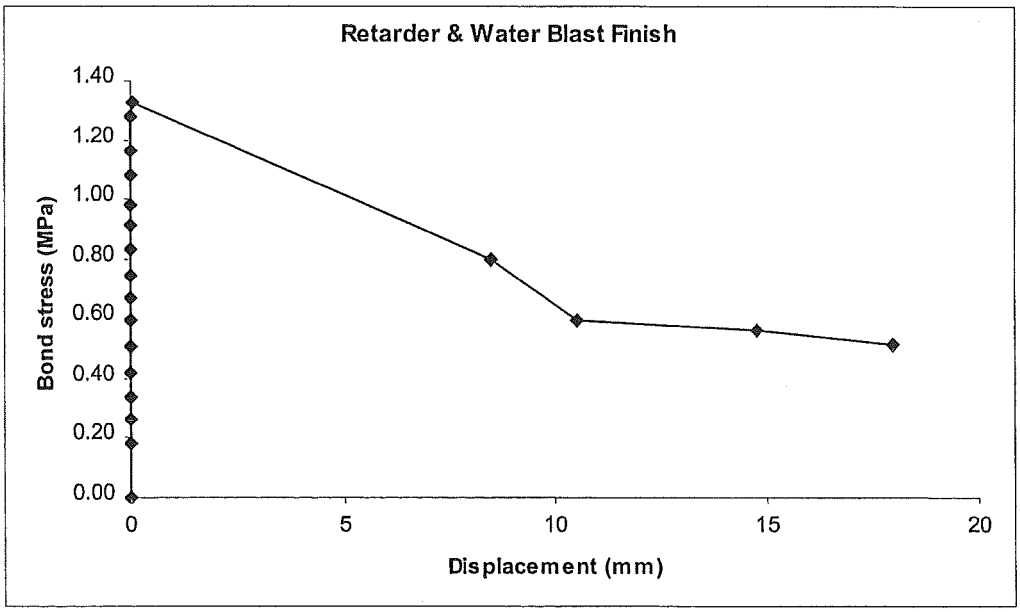

Fig. 6.14 Bond-displacement response of Retarder + Water Blast test

6.3.1.6 Medium Broom + Lightweight Topping

A structural lightweight concrete topping was placed over a medium broom surface. The results of this test are shown in Figure 6.15:

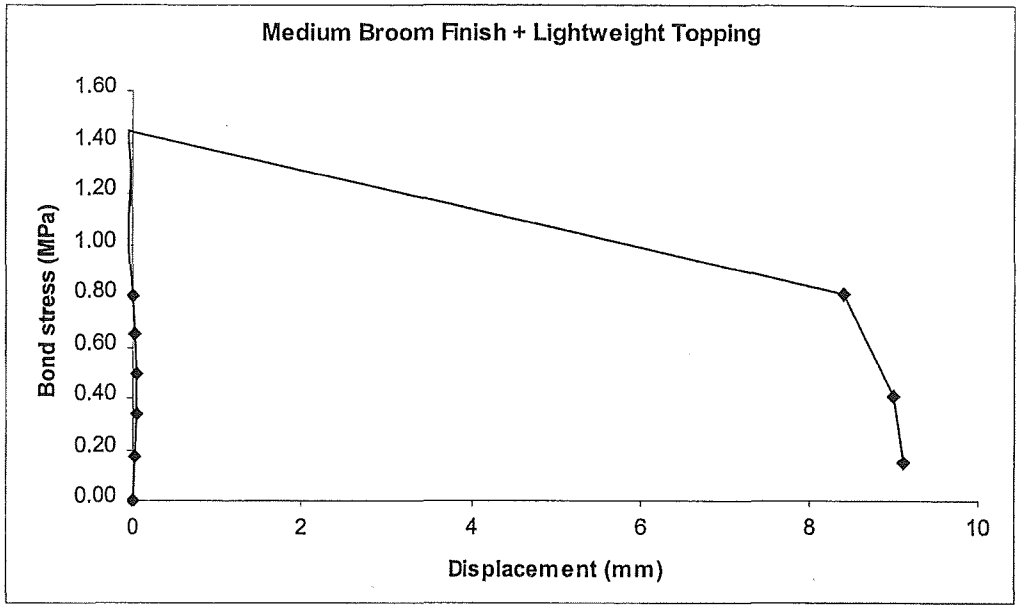

Fig.6.15 Bond-displacement response of Medium Broom + Lightweight Topping test

6.4 DISCUSSION ON TEST RESULTS

6.4.1 GENERAL

The direct shear test results give reasonable indications of composite topping bond strengths under dilation type loading. Furthermore, the tests verify that composite bond failure is very brittle and conclusive, with insignificant residual bond strengths being developed.

The observed test strengths would suggest that the surfaces listed in Section 6.2.3.3 could be generalised into three categories of direct shear bond strength (Table 6.4 and Fig. 6.16).

Table 6.4 Bond strength categories for surfaces under direct shear stress

Low Bond	Medium Bond	High Bond
Steel Trowel Finish	Light Broom Finish Wooden Float Finish	Medium Broom Finish Retarder + Water Blast Finish

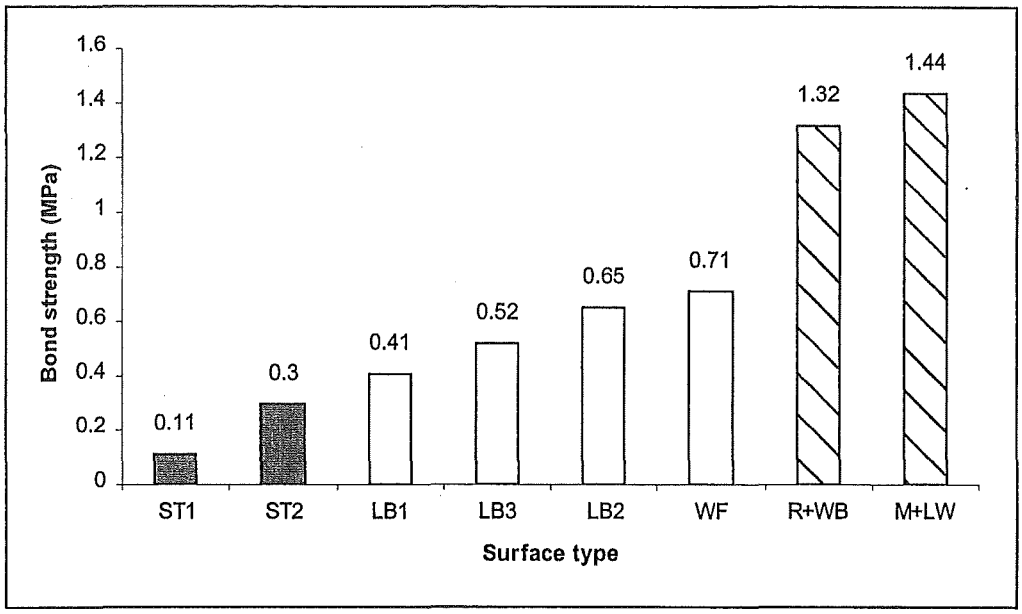

Fig. 6.16 Bond strengths in categories of Low, Medium and High Bond strength

6.4.2 STEEL TROWEL FINISH

It is clear from the tests that direct shear bond strengths of as-extruded surfaces are significantly lower than indicated by shear flow tests. This observation is entirely consistent with the early composite bond loss of LOS tests reported in Chapter 3. Hence, it is concluded that a degree of surface roughening must be provided for any precast flooring unit that may be subjected to dilation type loading.

6.4.3 LIGHT BROOM FINISH

This surface type is considered to represent the amplitude of roughening commonly achieved with broomed extruded hollow core units. It is difficult to achieve heavier amplitudes due to the tendency for upper surfaces of extruded sections to collapse under broom pressure. However, it is also possible that hollow core surfaces with light broom roughening will have superior bond strength than the test specimens due to lesser laitance associated with dry mix concrete. The test average is 0.53 MPa, and it is therefore feasible that with an appropriate capacity reduction factor, lightly broomed hollow core units will provide bond strengths that arecomparative to the 0.55 MPa specified in design standards.

6.4.4 WOODEN FLOAT FINISH

The textured surface of the wooden float surface produced a good level of bond strength. It is probable that this surface developed greater bond strength than the light broom surfaces due to comparable roughness but less prominent laitance. This is because brooming creates in a ridged roughing pattern with surface laitance appearing in the ridges, thus reducing shear strength.

6.4.5 RETARDER + WATER BLAST FINISH

In practice, this class of bond surface has shown to perform very well. In the test, full bond capacity was not achieved due to fracture of the shear slab, as is indicated in the residual shear region of Figure 6.14. Hence, it is almost certain that somewhat greater reliable bond strengths than shown can be achieved by this surface.

6.4.6 MEDIUM BROOM + LIGHTWEIGHT TOPPING

Due to considerably deeper striations resulting from a medium broom, much greater bond strength was achieved with this surface than with the light broom surfaces. It is important to note that the structural lightweight concrete topping did not appear to reduce bond strength. This is because the matrix contained a mixture of hard crusher and river sands, and since bond strength typically depends on the integrity of the cement/sand mortar fraction, lightweight coarse aggregates had no appreciable effect on composite bond strength.

6.5 CONCLUSIONS

The most important conclusion is that the bond surfaces of smooth "as-extruded" hollow core units, which have performed well in shear flow situations, are almost certain to perform badly in situations involving direct shear. Hence, where the effects of frame dilation are possible and support tie details depend on local composite bond strength, a degree of surface roughening must be applied to these surfaces.

From the results of testing, it appears that surface laitance has a significant mitigating effect on composite bond strength, and may be more influential than the amplitude of surface roughening. Hence, surfaces with appreciable roughening may not bond effectively if the brooming striations include an excess of laitance material. In production, this situation can arise when surface brooming is applied too early to wet or fatty mixes.

Bond surfaces that involve a hard interface (e.g., retarder and water blast surfaces) exhibit superior bond characteristics. These surfaces are almost totally impractical for precast floor unit production, however, the principle should be observed. It appears that a medium depth of brooming at the initial set stage would provide a satisfactory level of composite bond strength.

7

Cantilever Tests

7.1 GENERAL

Whether intentional or not, most seating connections between composite topped precast flooring and the support structure will develop an amount of bending moment resistance. In general, this has been a beneficial feature since it aids the serviceability of the composite floor and provides the type of structural continuum that is unique to concrete as an engineering material. There are very few known cases (although some do exist) where accidental carry-over of bending moments from precast floors to support elements has caused support member distress.

The proposed use of alternative support tie details as direct substitutions for traditional starter and continuity bar details may suggest that restraint associated with moment continuity will be affected. Hence, it was considered that the cantilever performance of hollow core slabs with composite topping and typical tie details (both traditional and proposed) should be tested for strength-rotation behaviour.

7.2 TEST METHODOLOGY

7.2.1 GENERAL PROCEDURE

The test set-up involved a 1.2 metre long section of 200 mm deep extruded hollow core unit with 65 mm composite topping, supported on a solid support (see Figs 7.1, 7.2 and 7.3). The support block was restrained against rotation and a vertical point load was applied near the end of floor cantilever. From this perspective the moment-rotation relationship was established, with concurrent bar strains data-logged from electrical resistance strain gauges attached to reinforcement.

Three specimens were constructed, representing one traditional deformed bar starter/continuity detail, and two embedded plain bar details. Topping mesh was provided, but terminated before the critical section so as not to influence bending strengths. To ensure that the critical section coincided with starting positions of strain gauges, a 10 mm deep crack inducing groove was formed in the topping at casting.

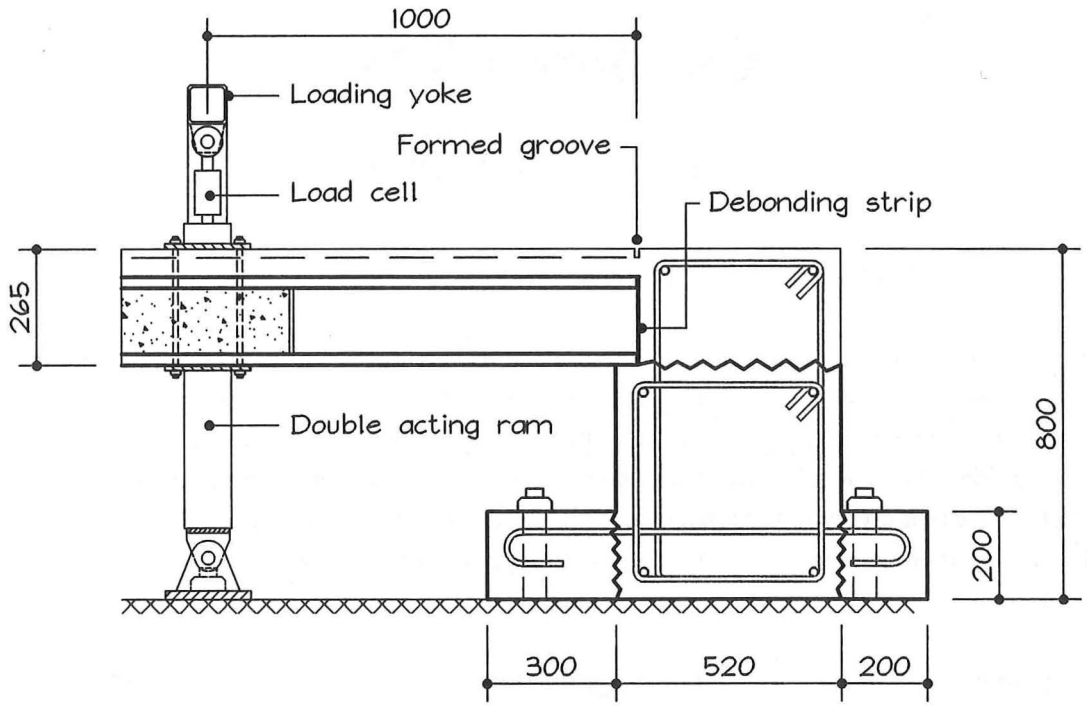

Fig. 7.1 Cantilever test set-up

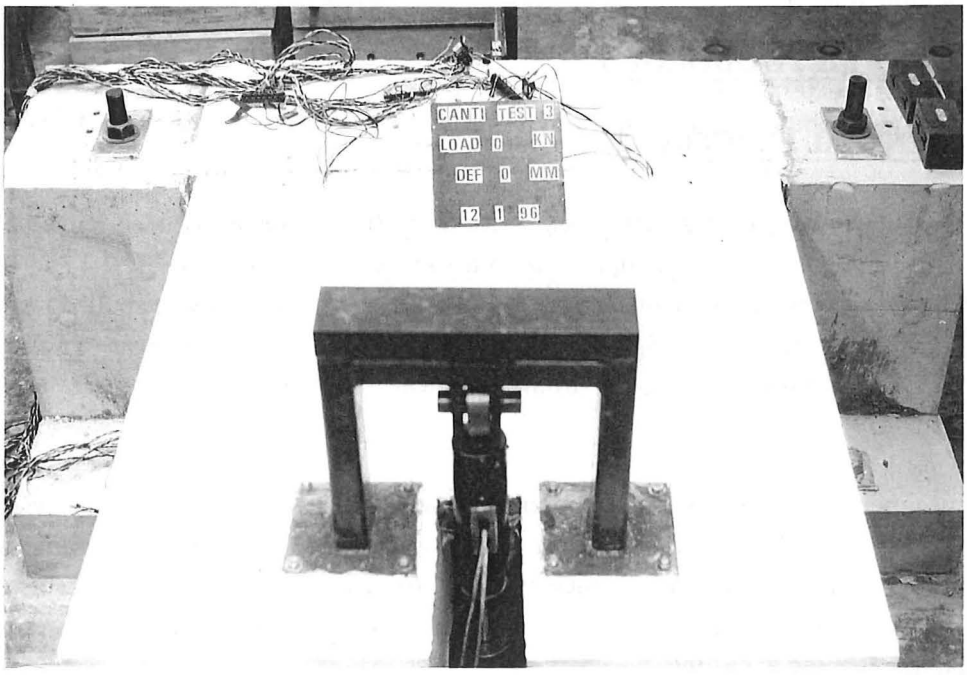

Fig 7.2 View of cantilever set-up prior to testing

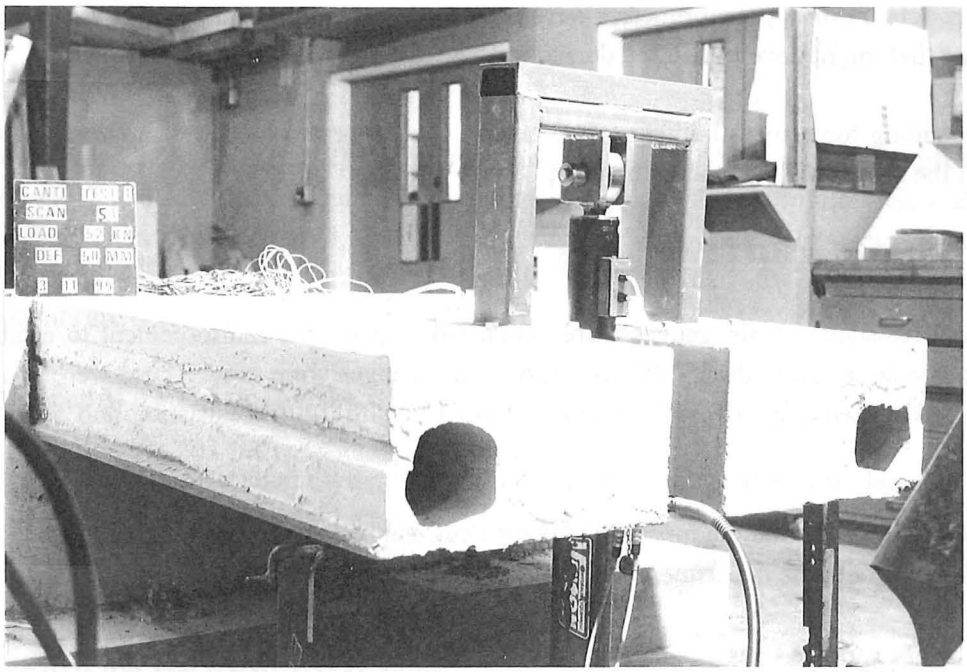

Fig. 7.3 View of deflected cantilever during test

7.2.2 DESCRIPTION OF TEST EQUIPMENT

7.2.2.1 General

Items of test equipment were either identical or similar to those used in earlier experiments. A small steel crosshead was constructed specifically for the tests, which was bolted to the top of the finished floor section. A pin connection was detailed to allow necessary rotation between the floor section and the hydraulic ram during testing.

7.2.2.2 Precast Support Beams

A precast concrete support beam was constructed for each test (see Fig. 7.1), with sufficient anchorage provided to resist the torsion induced by cantilever loading.

7.2.2.3 Vertical Force

(a) Actuating System

Vertical force was applied to the test specimens by a 20 tonne double-acting hydraulic ram swivel mounted to a steel crosshead (Fig. 7.1). The ram was operated via a hand pump.

(b) Measurements

Principal vertical displacements were measured by placing two 100 mm linear displacement potentiometers to the underside of the cantilever and coincident with the line of vertical force (see Fig. 7.1). Further potentiometers were placed against the support block to measure support rotations that might have transpired during testing.

Corresponding force measurements were taken via a calibrated load cell mounted between the stem of the ram and the connection eyelet.

7.2.2.4 Reinforcing Bar Strain Gauges

Electrical resistance strain gauges were connected to principal reinforcement to establish bar strain characteristics. Ordinary 3% extension strain gauges were used. These were supplied by Tokyo Sokki Kenkyujo Co. gauge type FLA-5-11, with 120Ω resistance and 5 mm gauge length.

Surface preparations and the method of fixing electrical resistance strain gauges was carried out in accordance with the departmental guidelines for these procedures [Hill, 1992].

7.2.2.5 Data Logger Unit

The load cell, potentiometers and strain gauges were all connected to the Metrabyte logger, which converted voltage changes caused by linear displacement into digital values. These values were recorded against respective scan numbers that were manually taken throughout the tests. At the conclusion of a test, the logged information was converted to an ASCII file that was then imported into Excel (spreadsheet program) for subsequent editing and data extraction.

7.2.3 MATERIALS AND CONSTRUCTION

7.2.3.1 General

The emphasis of this experimental programme was to reflect the general performance of pretensioned floor construction. The construction methods and curing was of a standard that might be expected on a well-supervised construction site.

7.2.3.2 Precast Pretensioned Hollow Core Units

Hollow core units were of the same type, dimensions and quality as described in Chapter 3.

7.2.3.3 Prestressing Strand

Prestressing strand properties were identical to those described in Section 3.2.3.3.

7.2.3.4 Cast-In-Place Topping Concrete

Topping concrete was selected and cured as described in Section 3.2.3.4.

7.2.3.5 Reinforcing Steel

(a) Starter/Continuity and Tie Bars

12 mm diameter Grade 430 (HD12) starter/continuity bars and 12 mm and 16 mm diameter Grade 300 (R12 and R16) plain round tie bars complying with the appropriate New Zealand standard [Standards New Zealand, 1989] were supplied cut and bent from recognised reinforcing steel merchants. The actual tensile characteristics of continuity and tie reinforcements are deferred to individual cantilever tests.

(b) Welded Wire Fabric (Mesh)

665 mesh (5.3 mm diameter) complying with the appropriate New Zealand standard [Standards New Zealand, 1975] was placed in the topping slab, but was not included in the principal crack region.

7.3 RESULTS OF EXPERIMENTS

7.3.1 CANTI-1

7.3.1.1 General

The initial cantilever test (Canti-1) was directed at a typical starter/continuity bar detail (Fig. 7.4). The floor configuration involved 65 mm of cast-in-place topping over a 200 mm hollow core extruded flooring unit. Four 12 mm diameter Grade 430 (HD12) starter/continuity bars were placed at 300 mm centres, and extended the full length of the cantilever slab. 665 mesh was placed over the hollow core unit and terminated before the end of the seating length.

7.3.1.2 Instrumentation

(a) Forces and Displacements

Forces and displacements were measured in accordance with the methods described in Section 7.2.2.

(b) Reinforcement

Standard 3% extension electrical resistance strain gauges (as described in Section 7.2.2) were employed on two items of starter reinforcement. These were configured so that a gauge was

situated directly over the induced cracking plane. The strain gauges were set at 50 mm centres away from the induced critical section (Fig. 7.5).

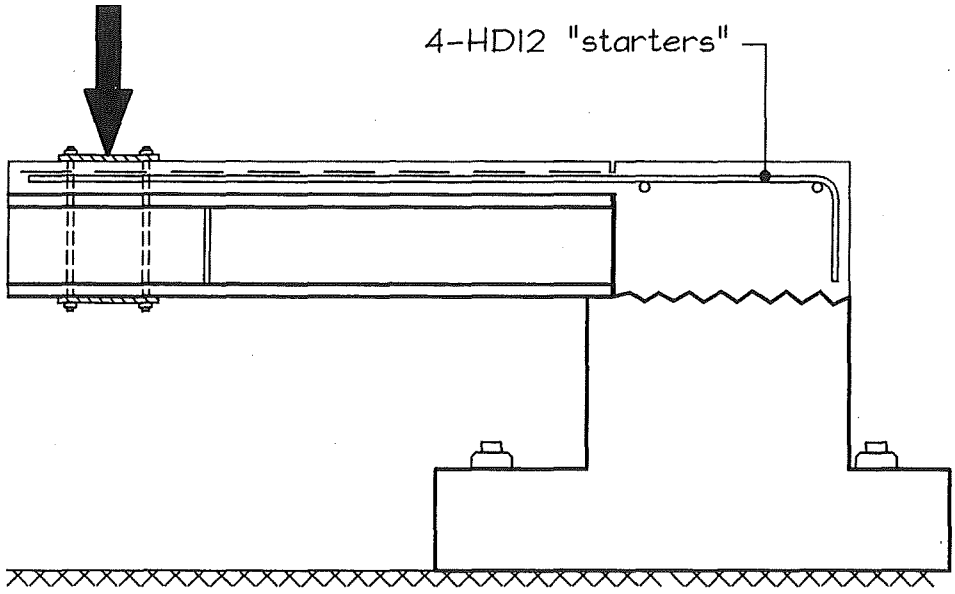

Fig. 7.4 Configuration of CANTI-1 test involving a typical starter/continuity bar detail

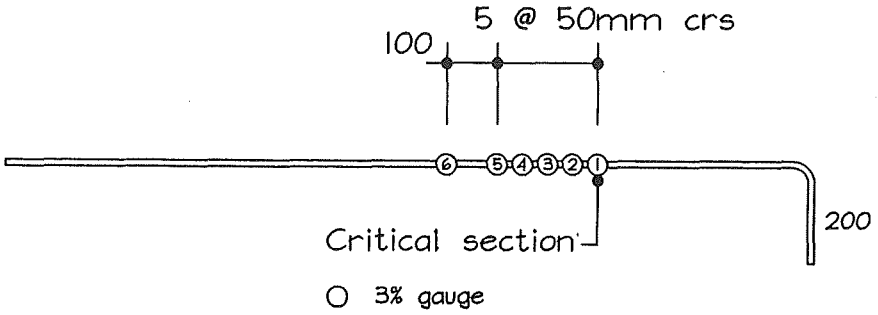

Fig. 7.5 Strain gauge positions on starter/continuity bars used in the CANTI-1 test

7.3.1.3 Cast-In-Place Topping Concrete

Concrete was ordered at a specified slump of 90 mm and accepted at a snatch sample slump of 110 mm (Table 7.1)

Table 7.1 Characteristics of cast-in-place topping concrete for CANTI-1 test

Design Strength (MPa)	Max. Aggregate Size (mm)	Ordered Slump (mm)	Received Slump (mm)	Test Strength (MPa)
25 at 28 days	19	90	110	34 at 28 days

7.3.1.4 Reinforcement

(a) 665 Mesh

The characteristics of hard drawn wire mesh were identical to those described in Table 3.2

(b) HD12 Continuity Bars

The tensile characteristics of HD12 bars were as described in Table 7.2

Table 7.2 Characteristics of HD12 starters used in CANTI-1 test

Avg. Yield Stress (MPa)	Avg. Strength at Fracture (MPa)	Avg. Strain at Fracture (%)
443	617	19.4

7.3.1.5 Results of Testing

The moment-rotation relationship (Fig. 7.6) shows an initially stiff elastic reaction with first cracking at 12.4 kNm. Moment capacity then increased to a distinct yield point at 39.7 kNm and 0.004 radians rotation. The moment capacity fell briefly to around 38 kNm, then gradually increased to a maximum of 51.9 kNm at 0.05 radians as the effects of strain hardening became apparent.

Based on the characteristic yield strength of bar, the calculated ideal bending strength with all bars yielded is around 43 kNm (d = 226 mm). Because significant plasticity occurred below this strength, it is evident that the yield strength of bars was not achieved in exact unison. The plots of the bar strain versus cantilever rotation (Figs 7.7 and 7.8) further support this assertion. These plots indicate that bar strains in the respective N and S gauge series developed in very different fashion. In the early stages, the S gauge series showed the greater strain response, but were dramatically superseded by the N gauge series as cantilever rotation increased.

On the strain-rotation plots, data points have been plotted to the termination point, where gauges had either failed or exceeded the gauge limit.

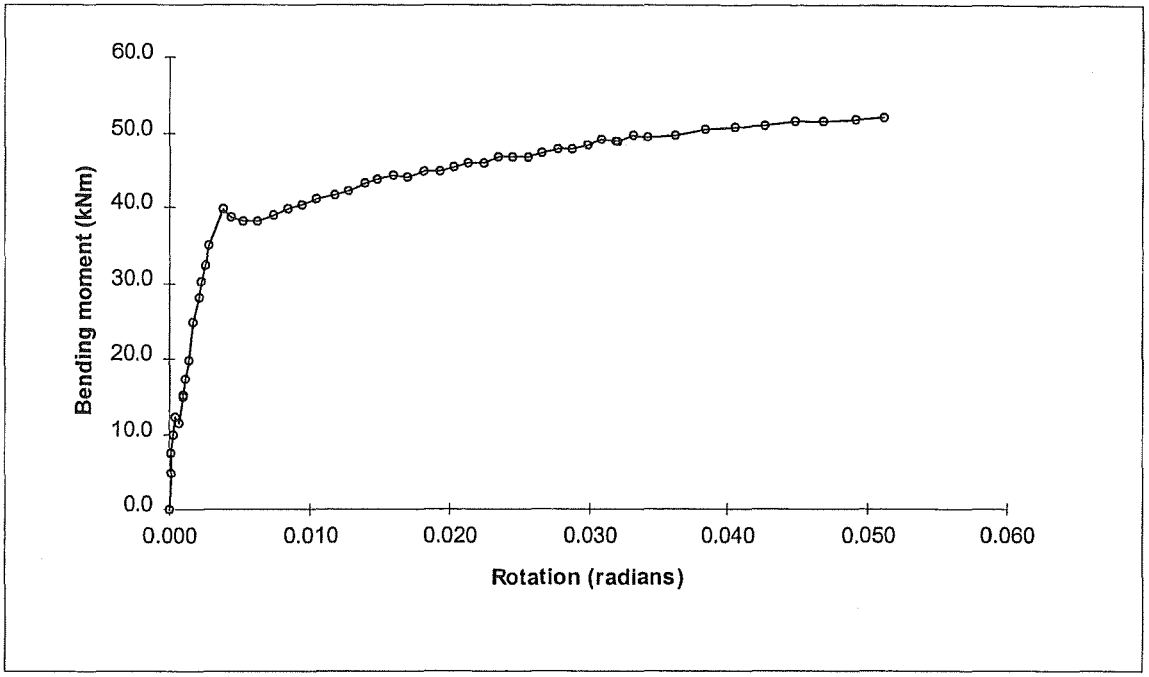

Fig. 7.6 Moment-rotation response of CANTI-1 test

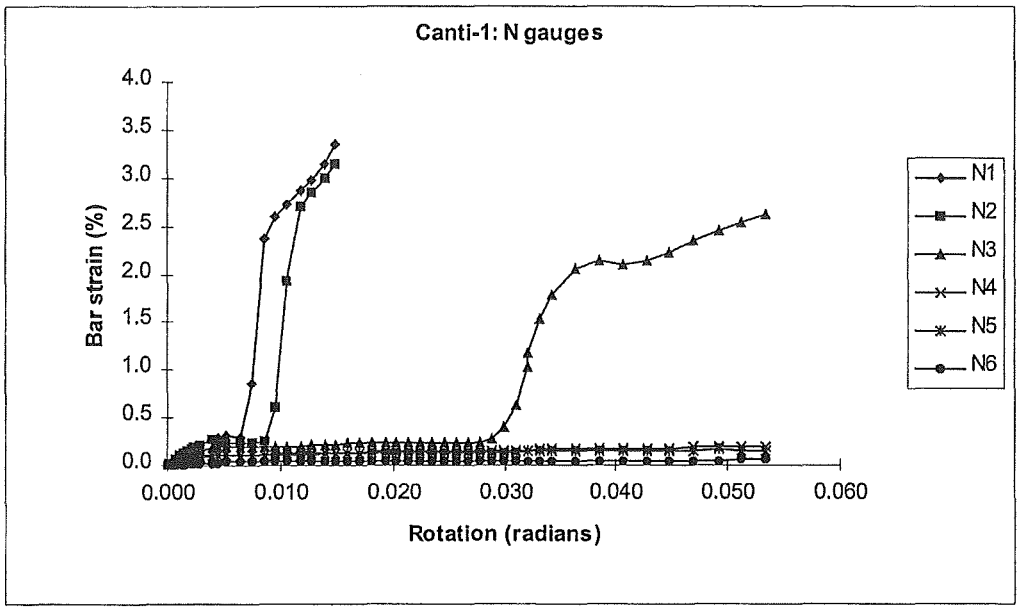

Fig. 7.7 Bar strain response of the N gauge series, showing dramatic strain increases at gauges N1 and N2 at approximately 0.015 radians, and a significant late response from gauge N3

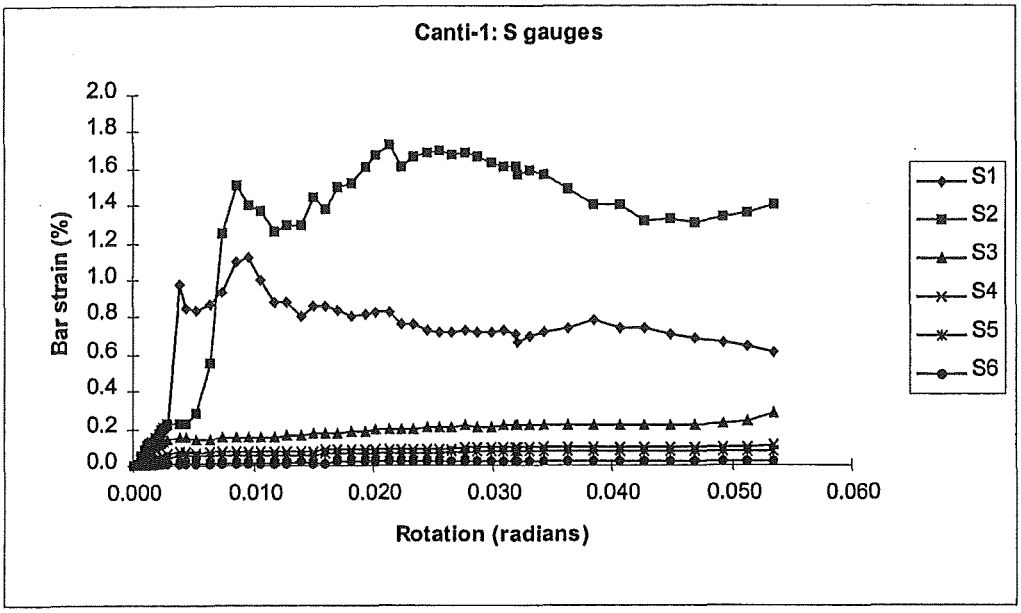

Fig. 7.8 Bar strain response of the S gauge series, showing greater early strain response than the N series gauges, but less in the latter stages of testing and limited contribution from gauge S3

Notable in both Figures 7.7 and 7.8 is the generally insignificant response of gauges number 3 and the almost negligible response of gauges number 4, 5 and 6. It must be appreciated that the number 3 gauges were located only 100 mm (8.3 bar diameters) away from the critical section.

Also notable in Figure 7.8 is the diminished response of gauge S1 with increasing rotation.

7.3.2 CANTI-2

7.3.2.1 General

The second cantilever test (CANTI-2) was directed at an embedded R16 tie detail that had performed satisfactorily in dilation tests (Fig. 7.9). The floor configuration involved 65 mm of cast-in-place topping over a 200 mm hollow core extruded flooring unit. Two 16 mm diameter Grade 300 (R16) tie bars were placed into cut out cores and grouted integrally with the topping concrete. 665 mesh was placed over the hollow core unit and terminated before the end of the seating length.

7.3.2.2 Instrumentation

(a) Forces and Displacements

Forces and displacements were measured in accordance with the methods described in Section 7.2.2.

(b) Reinforcement

Standard 3% extension electrical resistance strain gauges (as described in Section 7.2.2) were employed on the two items of tie reinforcement. These were configured so that a gauge was situated 25 mm either side of the induced cracking plane. The strain gauges were set at 50 mm centres away from the induced critical section (Fig. 7.10).

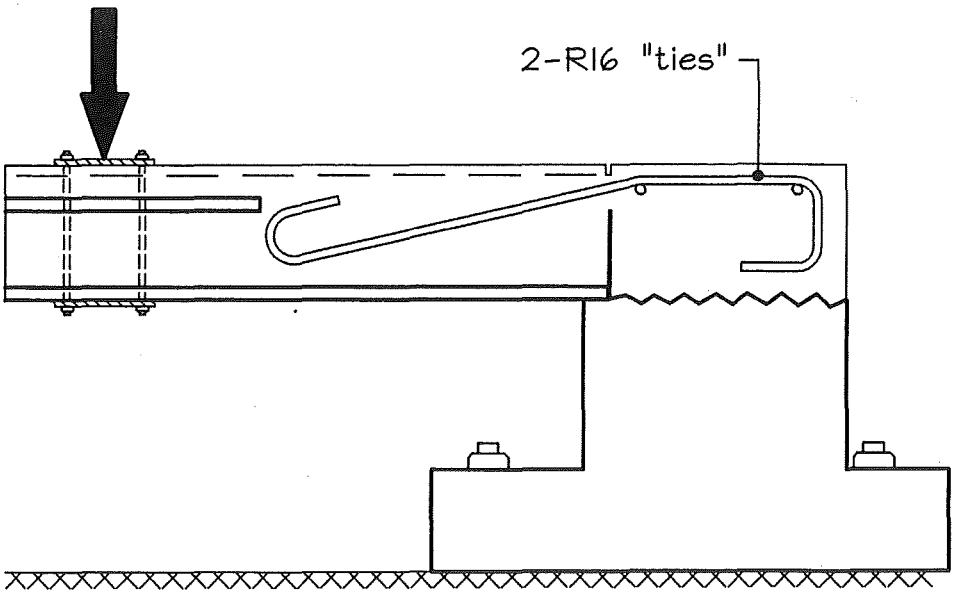

Fig. 7.9 Configuration of CANTI-2 test involving an embedded R16 tie detail

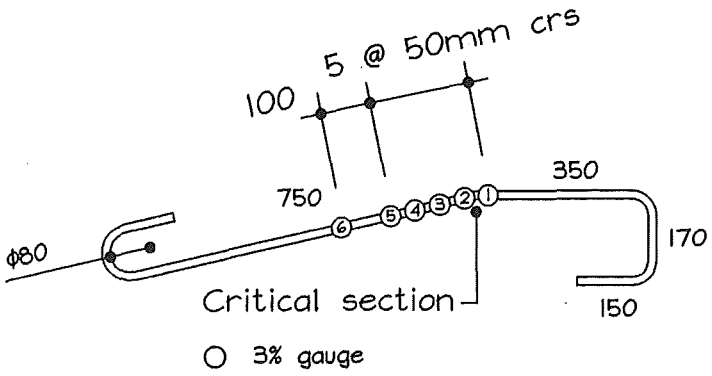

Fig. 7.10 Strain gauge positions on embedded R16 ties used in the CANTI-2 test

7.3.2.3 Cast-In-Place Topping Concrete

Concrete was ordered at a specified slump of 90 mm and accepted at a snatch sample slump of 125 mm (Table 7.3).

Table 7.3 Characteristics of cast-in-place topping concrete for CANTI-2 test

Design Strength (MPa)	Max. Aggregate Size (mm)	Ordered Slump (mm)	Received Slump (mm)	Test Strength (MPa)
30 at 28 days	13	90	125	28 at 17 days

7.3.2.4 Reinforcement

(a) 665 Mesh

The characteristics of hard drawn wire mesh were identical to those described in Table 3.2

(b) R16 Tie Bars

The tensile characteristics of R16 bars were as described in Table 7.4

Table 7.4 Characteristics of R16 tie bars used in CANTI-2 test

Avg. Yield Stress (MPa)	Avg. Strength at Fracture (MPa)	Avg. Strain at Fracture (%)
326	467	30.7

7.3.2.5 Results of Testing

The moment-rotation relationship (Fig. 7.11) shows an initially stiff elastic reaction with first cracking at 15.0 kNm, resulting in a softened response. Plastic behaviour commenced at around 22.5 kNm and rotation of 0.01 radians, followed by gradually increasing moment capacity as the effects of strain hardening became apparent.

Based on the characteristic yield strength of bar, the calculated ideal bending strength with both bars yielded is approximately 27 kNm (d = 217 mm). Similar to the CANTI-1 test, significant plasticity occurred below the calculated yield moment value. However, unlike CANTI-1 it is most likely that this resulted from a progressive decrease in effective depth due to bond loss over the inclined tie portion. Because the plain bar ties were inclined at 16 degrees to the horizontal, 50 mm of bond loss corresponds with a 14 mm reduction in effective depth. The plots of bar strain versus cantilever rotation (Figs 7.12 and 7.13) indicate that considerable

strain penetration occurred during the test, which supports the assertion of a reducing effective depth.

On the strain-rotation plots, data points have been plotted to the termination point, where gauges had either failed or exceeded the gauge limit.

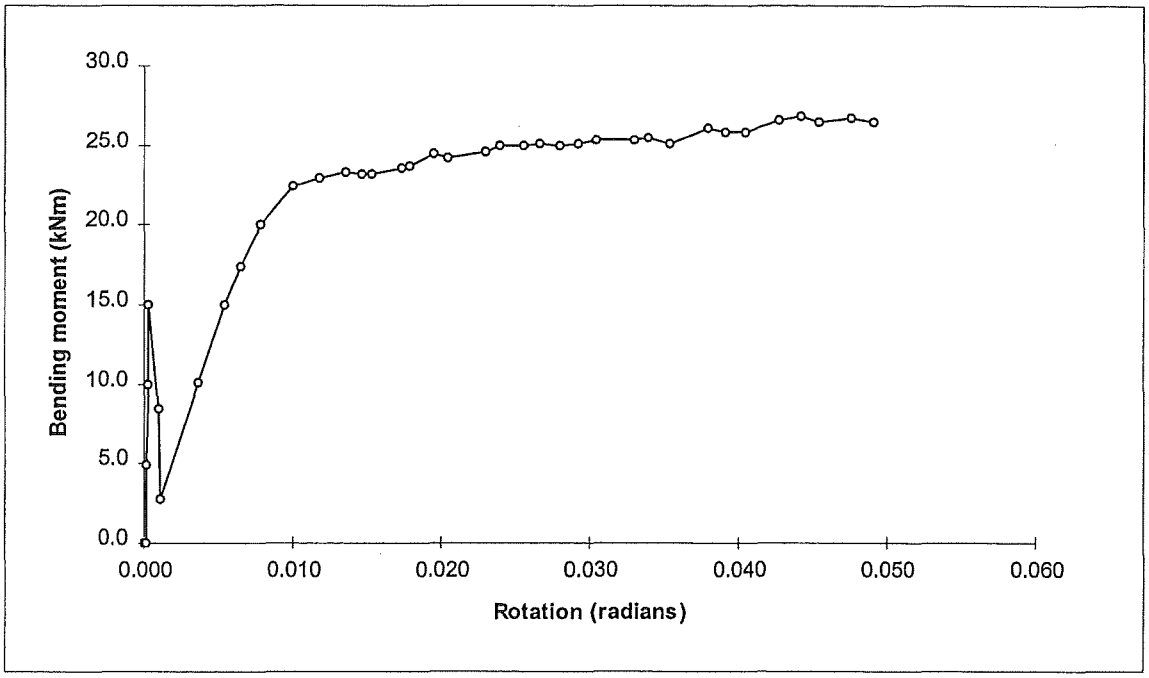

Fig. 7.11 Moment-rotation response of CANTI-2 test

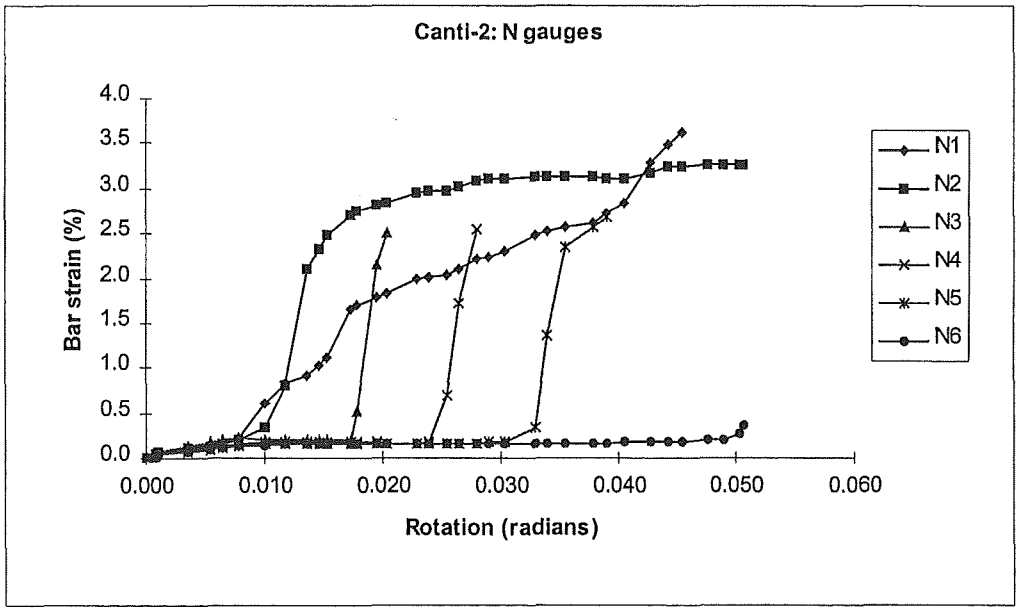

Fig. 7.12 Bar strain response of the N gauge series, showing the progression of strain penetration at gauges N3, N4 and N5

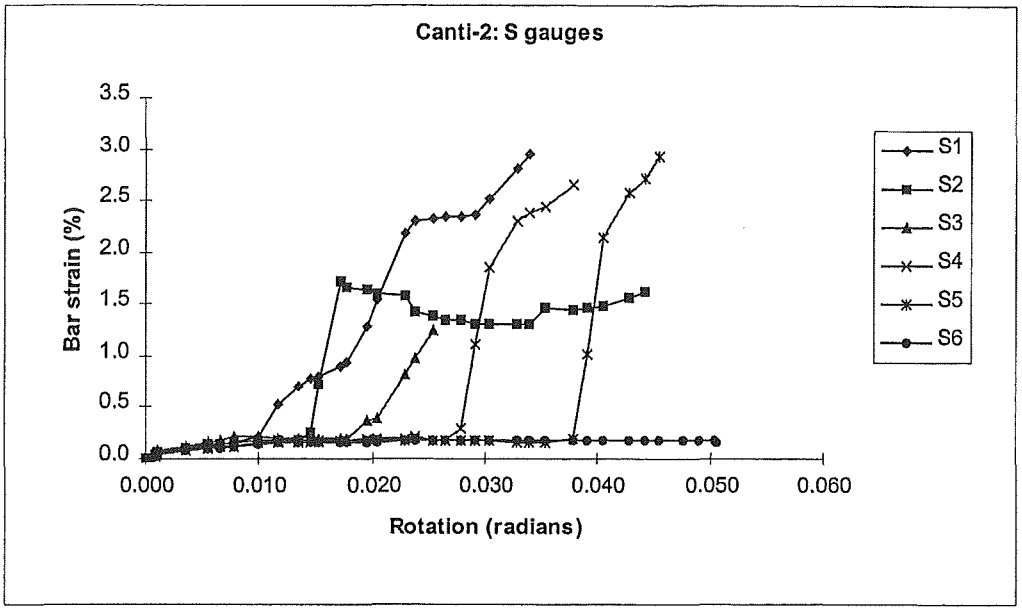

Fig. 7.13 Bar strain response of the S gauge series, showing the progression of strain penetration at gauges N3, N4 and N5

Notable in both Figures 7.12 and 7.13 is the delayed strain response at gauges 1 and 2, compared with rapid strain increases at gauges 3, 4 and 5.

7.3.3 CANTI-3

7.3.3.1 General

The third cantilever test (CANTI-3) was directed at an embedded R12 tie detail that were based on a proposed (paperclip) detail (Fig. 7.14). The floor configuration involved 65 mm of cast-in-place topping over a 200 mm hollow core extruded flooring unit. Four 12 mm diameter Grade 300 (R12) tie bars were placed into two cut-out cores (i.e., two bars per core) and grouted integrally with the topping concrete. 665 mesh was placed over the hollow core unit and terminated before the end of the seating length.

7.3.3.2 Instrumentation

(a) Forces and Displacements

Forces and displacements were measured in accordance with the methods described in Section 7.2.2.

(b) Reinforcement

Standard 3% extension electrical resistance strain gauges (as described in Section 7.2.2) were employed on two items of tie reinforcement. The configuration was such that two gauges were situated directly over the induced cracking plane (one on the top leg, one on the bottom). The strain gauges were set at 50 mm centres away from the induced critical section (Fig. 7.15)

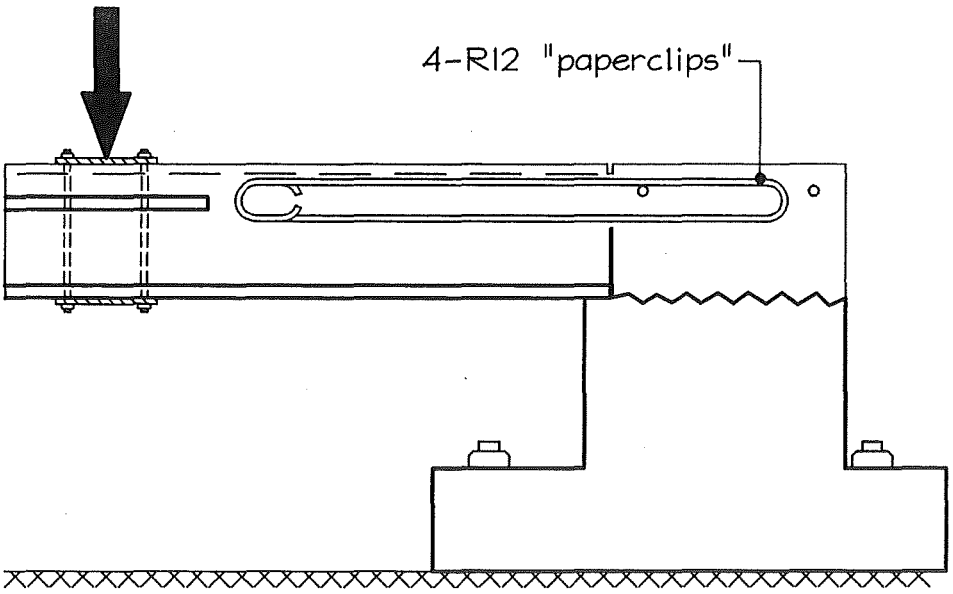

Fig. 7.14 Configuration of CANTI-3 test involving an embedded R12 tie detail

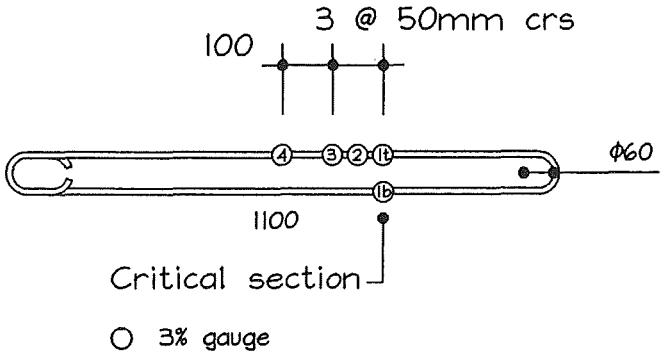

Fig. 7.15 Strain gauge positions on embedded R12 ties used in the CANTI-3 test

7.3.3.3 Cast-In-Place Topping Concrete

Concrete was ordered at a specified slump of 90 mm and accepted at a snatch sample slump of 125 mm (Table 7.5).

Table 7.5 Characteristics of cast-in-place topping concrete for CANTI-3 test

Design Strength (MPa)	Max. Aggregate Size (mm)	Ordered Slump (mm)	Received Slump (mm)	Test Strength (MPa)
25 at 28 days	13	90	135	24 at 20 days

7.3.3.4 Reinforcement

(a) 665 Mesh

The characteristics of hard drawn wire mesh were identical to those described in Table 3.2

(b) R12 Tie Bars

The tensile characteristics of R12 bars were as described in Table 7.6

Table 7.6 Characteristics of R12 tie bars used in CANTI-3 test

Avg. Yield Stress (MPa)	Avg. Strength at Fracture (MPa)	Avg. Strain at Fracture (%)
342	486	27.2

7.3.3.5 Results of Testing

The moment-rotation relationship (Fig. 7.16) shows an initially stiff elastic reaction with first cracking at 25.1 kNm, resulting in a softened response. Plastic behaviour commenced at around 48 kNm and rotation of 0.007 radians. The subsequent response involved almost perfect-plastic behaviour at an average 53.5 kNm over the remaining 80% of the test.

Based on the characteristic yield strength of bar, the calculated ideal first yield moment is approximately 46 kNm (d = 228 mm). Unlike the two prior tests, the calculated first yield moment was slightly lower than the actual test value. The plots of bar strain versus cantilever rotation (Figs 7.17 and 7.18) indicate that considerable strain penetration occurred during the test, which supports the assertion of a reducing effective depth.

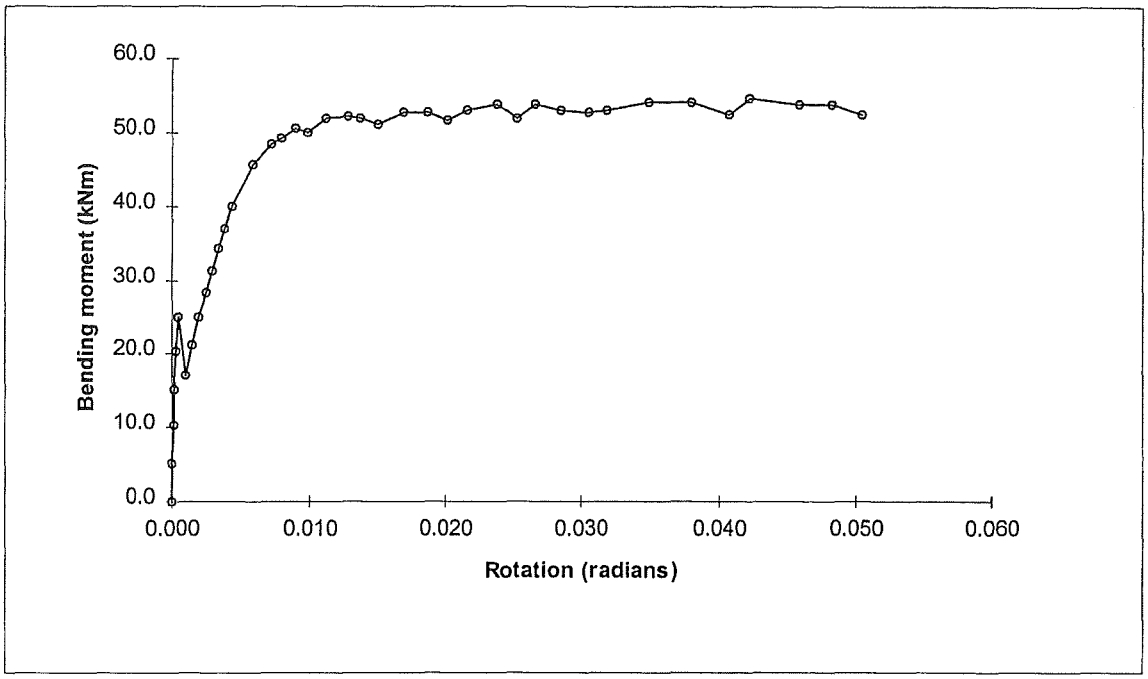

Fig. 7.16 Moment-rotation response of CANTI-3 test

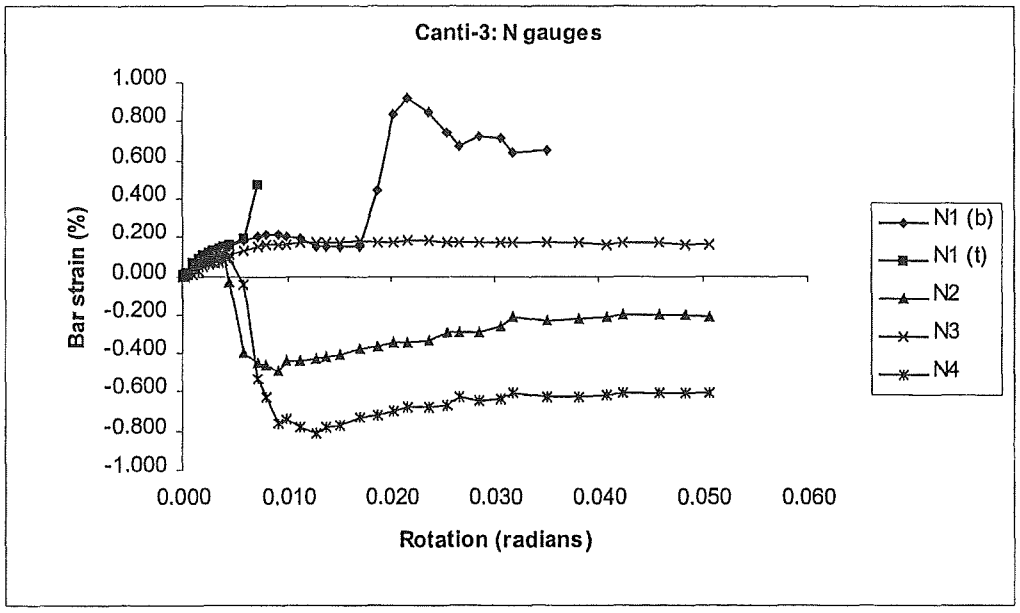

Fig. 7.17 Bar strain response of the N gauge series, showing an apparent strain transition at gauges N2 and N4

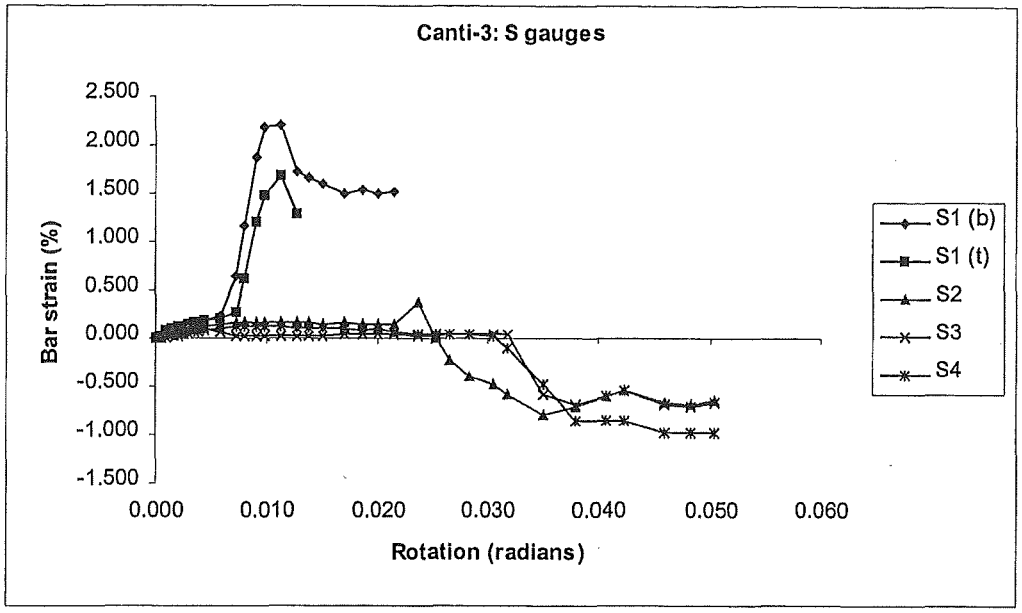

Fig. 7.18 Bar strain response of the S gauge series, showing an apparent strain transition at gauges S2, S3 and S4

Notable in both Figures 7.17 and 7.18 is the unanticipated behaviour at gauges 3, 4 and 5, showing apparent transitions from tensile to compressive strain under increasing rotation. These results are quite contrary to expectations; however, it is difficult to uniformly dismiss the data as a fundamental measurement error. For example, the strain transitions are gradual and seemingly independent of local gauge failure, and therefore cannot be simply linked to the instantaneous "zero shift" effect. Also, closer inspection suggests that distinct correlations exist between the slopes of plotted strain profiles at respective gauge positions such as N3 and N5 in Figure 7.17 and S3, S4 and S5 in Figure 7.18.

The phenomenon of a progressive strain transition in plain bar details is not unprecedented. An interesting feature of test LOS-6 (see Section 4.3.2) was the tendency towards an entirely compressive strain response at gauge locations remote from the critical section. From within the compressive strain domain, these gauges continued to reflect the externally applied cyclic forces, including the eventual diminishing response caused by the Bauschinger effect and bar buckling at the critical section. A characteristic evident in both the LOS-6 and CANTI-3 data is that the apparent compressive strain transition is most pronounced at gauges located furthest from the predominantly tensile critical section.

7.4 CALCULATED RESPONSE

7.4.1 GENERAL

The three details tested comprise a small representative sample of the possible combinations of support tie and starter/continuity details.

In general, typical continuity details involving deformed bars may vary slightly from the detail tested (CANTI-1) in that the quantity of reinforcement could differ. Conversely, support tie details involving plain bars may show significant variations, as influenced by support member configurations and strength requirements in the advent of support loss.

In order to quantify the performance of such details, comparisons are made between the theoretical and observed moment-rotation relationships of the three test specimens.

7.4.2 STRENGTH AND STIFFNESS

For the three test details, it is considered that moment-curvature relationships calculated up the point of reinforcement strain hardening is sufficient for comparison between theoretical and observed moment-rotation response. For the calculation of characteristic bending moments, the strain-equilibrium approach is used (as throughout this thesis), with converging neutral axis depths at a given value of concrete compressive strain.

In the prediction of rotational behaviour, the main difficulty lies in estimating effective plastic hinge lengths. In this instance, the method developed in Section 2.2.1.4 for estimation of effective plastic hinge lengths is utilised. In accordance with the calculated moment-curvature relationships, the method of Section 2.2.1.4 assumes the common parabolic relationship between unconfined concrete stress and compressive strain. Equation 2.52 from Section 2.2.1.4 is reproduced here, with the ratio of plastic hinge length l_p to shear-span z derived as:

$$\frac{\ell_p}{z} = \sqrt{\left(\frac{\Psi_p}{\Psi_\Delta} - 1\right)^2 + \frac{M_p}{3M_y\left(\frac{\varphi_p}{\varphi_y} - 1\right)}} - \left(\frac{\Psi_p}{\Psi_\Delta} - 1\right) \qquad (7.1)$$

and:

$$\Psi_\Delta = M_p(\varphi_p - \varphi_y) \qquad (7.2)$$

In the above expression, the strain energy per unit length Ψ_p corresponds with the plastic bending moment M_p at bending curvature ϕ_p. All other terms relate to the condition at first yield. Referring to Section 2.2.1.3, Ψ_p may be calculated as:

$$\Psi_p = \frac{b f_c' \varepsilon_c^3}{\varphi \varepsilon_0}\left(\frac{1}{3} - \frac{\varepsilon_c}{12\varepsilon_0}\right) + \sum_i A_s f_y\left(\varphi d - \varepsilon_c - \frac{\varepsilon_y}{2}\right) \quad (7.3)$$

As with the measured rotations, the theoretical rotations are simply calculated as deflection δ divided by shear span z, giving:

$$\theta_p = \frac{\varphi_y z}{3} + (\varphi_p - \varphi_y)\ell_p\left(1 - \frac{\ell_p}{2z}\right) \quad (7.4)$$

The theoretical bending moment capacities and matching rotations at selected values of concrete compressive strain are shown in Table 7.7.

Table 7.7 Calculated moment capacities, effective plastic hinge lengths and rotations of test specimens

$\varepsilon_s/\varepsilon_y$	ε_c	M_p (kNm)	M_y (kNm)	φ_p (θ/m)	φ_y (θ/m)	Ψ_p (kNm/m)	l_p (mm)	θ_p (m/m)
CANTI-1								
1.00	0.00039	43.18	43.18	0.01158	0.01157	0.2504	333	0.0039
2.46	0.0006	43.72	43.18	0.02679	0.01157	0.9111	258	0.0073
4.36	0.0008	44.06	43.18	0.04624	0.01157	1.766	215	0.0105
6.68	0.001	44.26	43.18	0.06993	0.01157	2.812	186	0.0137
CANTI-2								
1.00	0.00029	27.27	27.27	0.00893	0.00892	0.1219	333	0.0030
4.53	0.0006	27.71	27.27	0.03681	0.00892	0.8882	212	0.0083
7.96	0.0008	27.86	27.27	0.06349	0.00892	1.630	175	0.0117
12.06	0.001	27.96	27.27	0.09524	0.00892	2.516	150	0.0150
41.03	0.002	28.13	27.27	0.31750	0.00892	8.755	92	0.0299

$\varepsilon_s/\varepsilon_Y$	ε_c	M_p (kNm)	M_y (kNm)	φ_p (θ/m)	φ_y (θ/m)	Ψ_p (kNm/m)	l_p (mm)	θ_p (m/m)
CANTI-3								
1.00	0.00043	46.16	46.16	0.00944	0.00943	0.2186	332	0.0031
1.58	0.0006	54.22	46.16	0.01453	0.00943	0.4743	396	0.0047
2.76	0.0008	56.18	46.16	0.02432	0.00943	0.9249	412	0.0079
4.28	0.001	56.75	46.16	0.03663	0.00943	1.4883	414	0.0120
14.55	0.002	57.77	46.16	0.11830	0.00943	5.2774	410	0.0384

The calculated values from Table 7.7 are plotted against observed moment-rotation diagrams for tests CANTI-1, CANTI-2 and CANTI-3 respectively (Figures 7.19, 7.20 and 7.21):

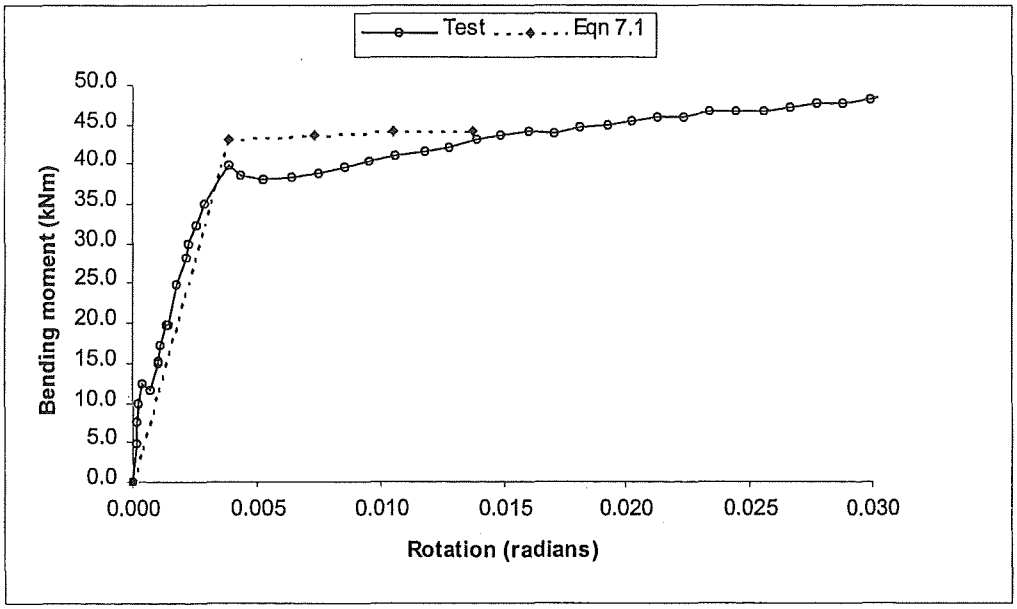

Fig. 7.19 Comparison between observed and theoretical rotational stiffness K_θ for test CANTI-1 (from Table 7.7)

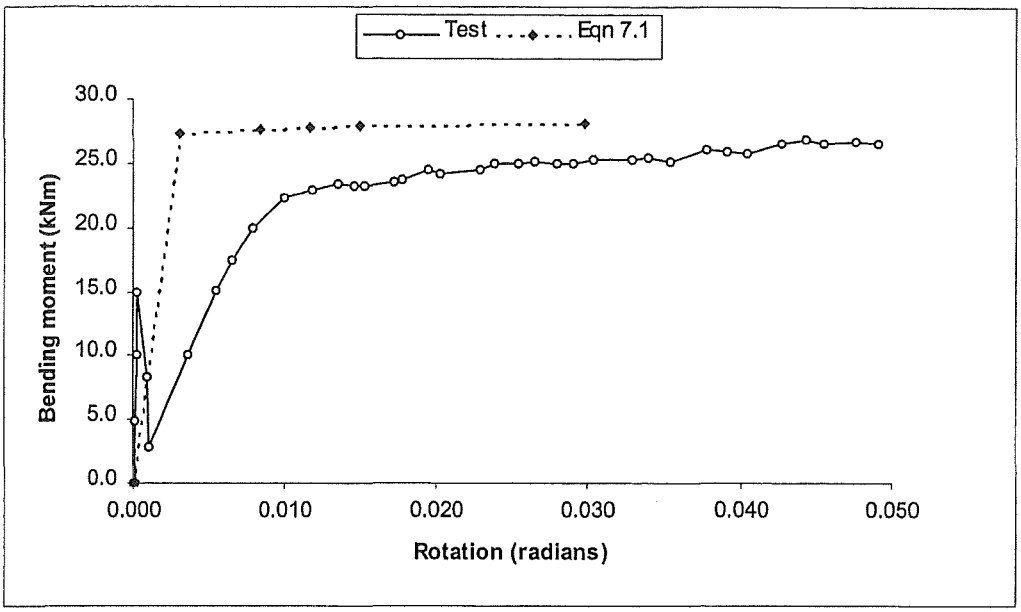

Fig. 7.20 Comparison between observed and theoretical rotational stiffness K_θ for test CANTI-2 (from Table 7.7)

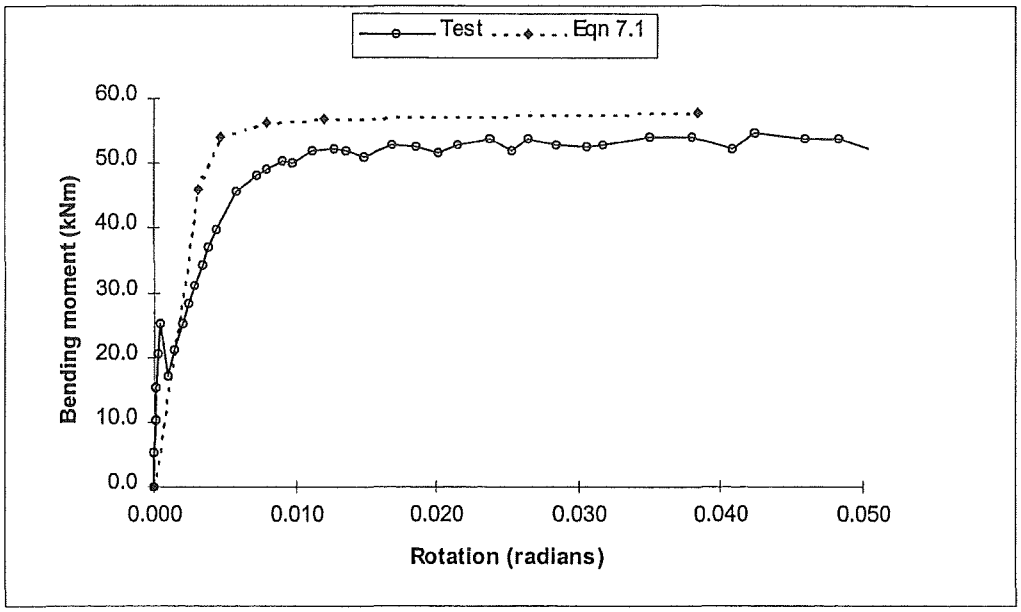

Fig. 7.21 Comparison between observed and theoretical rotational stiffness K_θ for test CANTI-3 (from Table 7.7)

7.5 APPLICATION OF TEST RESULTS

7.5.1 GENERAL

The cantilever tests have provided useful information on the characteristic strength, stiffness and bond behaviour of both the traditional starter/continuity bar and special plain bar details that have been advocated for hollow core floors in structures prone to dilation effects.

7.5.2 EFFECTIVE CONTINUITY

The comparative strength and stiffness of details is shown in Figure 7.22. From there, it is evident that the R12 "paperclip" detail of test CANTI-3 can provide very similar initial stiffness characteristics to the traditional starter/continuity detail of test CANTI-1, and significantly more post-yield strength. The secant stiffness values up to 40 kNm bending strength for the CANTI-1 and CANTI-3 tests were 10000 kNm/rad and 9000 kNm/rad respectively.

The R16 detail of test CANTI-2 exhibited good ductility, but clearly lacked the desired levels of initial stiffness and strength for efficient performance as a continuity detail. The secant stiffness value up to 20 kNm bending strength was 2500 kNm/rad.

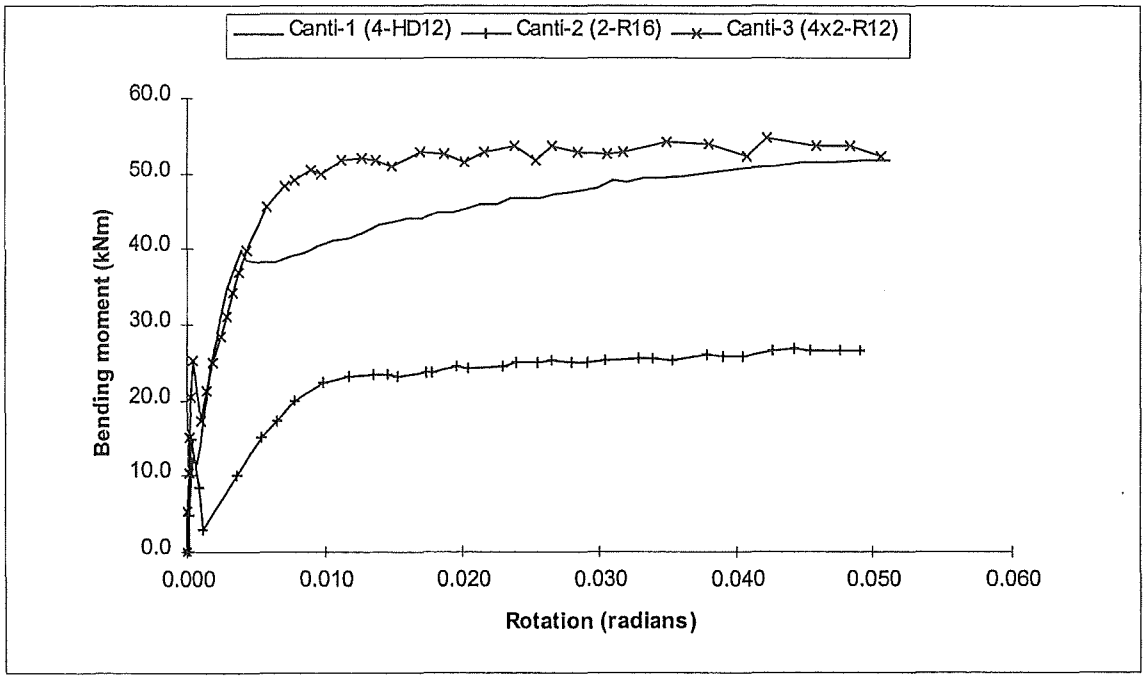

Fig. 7.22 Moment-rotation response of cantilever test details involving 200mm hollow core flooring with 65mm composite topping

The derived stiffness values may be incorporated into the analysis of flooring members for the determination of effective continuity moments under gravity loads. Referring to Figure 7.23, flexibility equations may be developed to include the rotational stiffness at supports i and j, as provided by the relative reinforcing detail. It is assumed that under gravity loads, a net clockwise rotation will result at support i (i.e., $-\theta_i$) and an anti-clockwise rotation at support j (i.e., $+\theta_j$), therefore:

$$\begin{aligned} +\frac{M_i L}{3EI} - \frac{M_j L}{6EI} - \rho_i + \theta_i &= 0 \\ -\frac{M_i L}{6EI} + \frac{M_j L}{3EI} + \rho_j - \theta_j &= 0 \end{aligned} \tag{7.5}$$

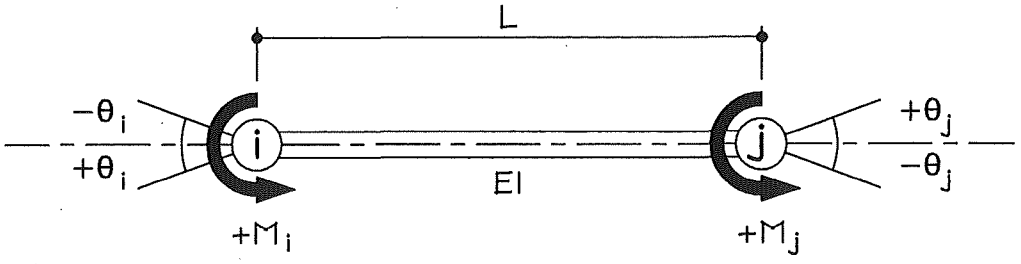

Fig. 7.23 Flexibility actions assumed in continuity analysis

In Equation 7.5, the terms ρ_i and ρ_j relate to the rotations caused at respective simple supports by the configuration of applied loads. For the common case of a uniformly distributed weight w per unit length (udl) acting over the entire span L:

$$|\rho_i| = |\rho_j| = \frac{wL^3}{24EI} \tag{7.6}$$

Also, the moment terms in Equation 7.5 can be written as the product of rotational stiffness and rotation, so that $M_i = K_{\theta i} \cdot \theta_i$, etc. Hence, Equation 7.5 becomes:

$$\begin{aligned} +\left(\frac{K_{\theta i} L}{3EI} + 1\right)\theta_i - \left(\frac{K_{\theta j} L}{6EI}\right)\theta_j &= \rho_i \\ -\left(\frac{K_{\theta i} L}{6EI}\right)\theta_i + \left(\frac{K_{\theta j} L}{3EI} + 1\right)\theta_j &= -\rho_j \end{aligned} \tag{7.7}$$

or in the form of a matrix equation:

$$\begin{bmatrix} \frac{K_{\theta i} L}{3EI} + 1 & -\frac{K_{\theta j} L}{6EI} \\ -\frac{K_{\theta i} L}{6EI} & \frac{K_{\theta j} L}{3EI} + 1 \end{bmatrix} \begin{Bmatrix} \theta_i \\ \theta_j \end{Bmatrix} = \begin{Bmatrix} \rho_i \\ -\rho_j \end{Bmatrix} \tag{7.8}$$

Of course, modern structural analysis programs implicitly solve these equations with direct assignment of rotational stiffness values. However, if there happens to be a power-up failure:

$$M_i = \frac{K_{\theta i} w L^3}{12} \cdot \frac{K_{\theta j} L + 6EI}{K_{\theta i} K_{\theta j} L^2 + 4EI\left[\left(K_{\theta i} + K_{\theta j}\right) L + 3EI\right]} \tag{7.9}$$

$$M_j = \frac{K_{\theta j} w L^3}{12} \cdot \frac{K_{\theta i} L + 6EI}{K_{\theta i} K_{\theta j} L^2 + 4EI\left[\left(K_{\theta i} + K_{\theta j}\right) L + 3EI\right]} \tag{7.10}$$

In Equations 7.9 and 7.10, M_i and M_j are considered as the negative bending reactions of a flooring unit of length L that supports a uniformly distributed load w.

Considering the practical design of a 200 mm deep hollow core unit with 65 mm topping in a car park building. The weight of unit plus topping is G = 4.0 kPa and the design floor load for car parking is Q = 2.5 kPa. The flooring units are not propped at construction, so that the continuity effect is mainly introduced under the superimposed live load. Normal volume changes such as creep and shrinkage occur in the flooring units, and promote the formation of topping cracks over supports. For the Ultimate Limit State under factored loads of 1.2G + 1.6Q, the applied load in addition to the self-weight of unit plus topping concrete (unrestrained at construction) is $w = [(1.2 - 1.0) \times 4.0 + 1.6 \times 2.5] = 4.8$ kPa ≈ 5.8 kN/m.

The properties of a typical hollow core flooring unit are given in Table 7.8, with the developed end moments relating to combinations of support tie details given in Table 7.9.

Table 7.8 Properties of 200 mm hollow core with 65 mm topping used in analysis (see Equations 7.9 and 7.10).

L (m)	w (kN/m)	EI (Nmm^2)	M* (mid-span) (kNm)
11.0	5.8	$40e^{12}$	159.7

Table 7.9 End continuity moments developed by support details, with the associated reduction in mid-span bending moments at the Ultimate Limit State.

$K_{\theta i}$ (kNm/rad)	$K_{\theta j}$ (kNm/rad)	M_i (kNm)	M_j (kNm)	Reduction in M* (%)
9000 (CANTI-3)	9000 (CANTI-3)	32.3	32.3	20.2
9000 (CANTI-3)	2500 (CANTI-2)	36.7	12.9	15.6
9000 (CANTI-3)	0 (NIL)	39.7	0	12.4
2500 (CANTI-2)	2500 (CANTI-2)	15.0	15.0	9.4
2500 (CANTI-2)	0 (NIL)	16.4	0	5.1

From Table 7.9, it is evident that reductions in mid-span moments of between 12% and 20% are reasonable for the given hollow core configuration incorporating CANTI-3 support details.

It is important that design for continuity in precast prestressed flooring is used with discretion, since successful continuity depends on physical contact between unit ends and the supports. Hence, volume change effects of creep and shrinkage will influence the development of continuity moments, and rotational stiffness in particular.

In this regard, it is generally considered that hollow core flooring is well suited to continuity development because extruded dry-mix concrete is a relatively stable material. However, with precast units manufactured from normal slump concrete, dimensional changes are more important. For example, single tee, double tee and prestressed joist units are all prone to creep effects under concentrated axial prestress.

A mixture of prestressing technique and selective use of continuity can mitigate the potentially adverse effects of creep shortening. For example, partial prestressing has proven to be advantageous in tee construction, and a judicious balance between axial prestress and continuity (where available) has proved satisfactory with shored joist construction.

In both tee and joist construction, it is apparent that excessive axial prestress is neither economical nor beneficial. For instance, there is a general tendency for the initial precamber of heat cured tee units to exceed deflection values calculated by purely elastic theory. Hence, even with partial prestressing, care needs to be taken with eventual cambers, and especially if the casting schedule is somewhat ahead of the delivery schedule (rare, but it still does happen).

In joist construction, limiting axial prestress will help control creep effects and therefore improve the efficiency of continuity development. Also, the composite section properties of shored joist flooring are considerably greater than the bare section properties of prestressed joists. Thus, topping concrete that incorporates creep restraint over the supports via continuity reinforcement should be considered as an initial control mechanism that gives long-term benefits.

7.6 DISCUSSION ON RESULTS

7.6.1 CHARACTERISTICS OF BAR BOND

The cantilever test details were comprised of three fairly distinct support tie configurations. In particular, the starter/continuity bar detail (CANTI-1) differed markedly from the other details because it involved typical use of deformed bars. The CANTI-2 and CANTI-3 tests both concerned plain bar details with proven ability as support ties under dilation actions. However, these details were also appreciably different, with the "paperclip" detail (CANTI-3) provided two legs of reinforcement at each tie location.

Hence, it is interesting to note that three substantially different details exhibited a general tendency for the strains associated with strain hardening to concentrate near the critical section. Thus, under pronounced rotations, the required bond lengths for each detail were generally quite short. This is clearly illustrated by the deformed bars of the CANTI-1 test, where it can be seen (Figures 7.7 and 7.8) that strain response beyond gauges N3 and S3 remained practically unchanged under increasing rotation. As such, the critical bar bond region for the deformed bars mostly occurred within 100 mm from the critical section.

The R16 bars of the CANTI-2 test detail naturally exhibited greater bond loss than the deformed bars of CANTI-1. The procession of bond loss is illustrated in Figures 7.12 and 7.13, where strain gauge response increased sharply at distinct rotation intervals. However, the effective bond development length was again quite short for such a detail. For example, gauges N4 and S4 were located only 125 mm from the critical section, yet exhibited an increased response at around 0.025 radians. This is more than four times the rotation associated with continuity moments at the ultimate limit state (see Table 7.8).

An interesting aspect of the CANTI-3 test was the apparent drift to from tension to compression strain at gauges situated away from the critical section. The exact cause of this phenomenon has not been verified, and could be the material of further research. However, it would, at the very least, seem to discount tensile bond demand at these locations. If the apparent sign shift of gauges is ignored, Figure 7.18 in particular indicates a concentrated strain profile, with gauges located only 50 mm and 100 mm from the critical section showing very limited response under pronounced rotation.

Based on the consistency of results, it is concluded that components of bending curvature may significantly influence the characteristic bond lengths of both plain and deformed reinforcing bars. This observation is supported by contemporary research at the University of Canterbury [Oliver, 1998]. In the testing of the "paperclip" support tie details, it was found that the friction component associated with the kinking of bars acted to restrict the bond lengths in plain bars. This is an important observation, since the success of support tie details in dilation loading situations depends on the ability of plain bars to slip within concrete and provide sufficient gauge length for extension compatibility.

It is now evident that the geometry of tie details may significantly influence the relationship between support rotation, strain penetration and rotational stiffness. As demonstrated in Chapter 4, the debonding of plain bars can be expected to occur under cyclic axial loading. With regard to bending, this result was also reflected in the CANTI-2 test by the conspicuous series of strain increments that occurred under increasing rotation (see Figures 7.12 and 7.13).

Tie details of the CANTI-2 and CANTI-3 varieties both exhibited strain penetration under cyclic axial loading. Therefore, the appreciably greater strain penetration exhibited by the CANTI-2 detail over the CANTI-3 detail under bending action is most likely attributable to inclined ties. Simple mechanics dictate that a completely vertical tie bar anchored between the points of support and load application would develop axial tensile force that is unaffected by support rotation. Hence, an inclined tie that is anchored within the shear span may also develop a proportion of axial force that is independent of bending interactions.

7.6.2 PREDICTED BEHAVIOUR

Comparisons between observed and theoretical moment-rotation behaviour are shown in Figures 7.19, 7.20 and 7.21. From there, it is evident that Equations 7.1 to 7.4 may allow reasonable predictions of effective plastic hinge lengths and resulting rotation response.

The most accurately predicted response is that of CANTI-1, which involved fully bonded deformed bars. The least accurately predicted response is that of CANTI-2, which involved a plain bar detail and considerable bond loss. The CANTI-3 detail involved plain bars with some bond loss, which is reflected in the general accuracy of the predicted response.

In both specimens that involved plain bars, it is clear that eventual bond loss and strain penetration under increasing rotations weakened the assumption of bonded reinforcement in the moment-curvature analysis. Hence, actual curvatures were greater than calculated curvatures, which is reflected in the "flattening" of the observed moment-rotation behaviours. This effect most pronounced with the CANTI-2 detail, which exhibited considerably more bond loss than the CANTI-3 detail.

It is evident that neither of the plain bar details exhibited enhanced bending strengths due to strain hardening of reinforcement, as is immediately apparent in the CANTI-1 test. This is most likely due to the described "flattening" effect of bond loss, since bar strains in excess of strain hardening were recorded at strain gauge locations.

Consequently, the moment-rotation behaviours predicted by Equation 7.1 would relate more closely to fully bonded (deformed bar) reinforcement under the same configurations. The predicted response of CANTI-1 (see Figure 7.19) is certainly sufficient for design purposes involving rotational stiffness with respect to continuity bars. It is considered that with small empirical modifications, the CANTI-3 detail may be similarly predicted.

7.7 CONCLUSIONS

From the observed and theoretical behaviour of the Cantilever tests, the following general conclusions are made:

The "paperclip" detail (CANTI-3) is able to achieve a level of rotational stiffness that is comparable to traditional deformed bar continuity details.

The rotational stiffness provided by CANTI-1 and CANTI-3 details are sufficient to provide useful levels of redistribution to mid-span bending moments.

Rotational stiffness can be predicted with reasonable accuracy by the analytical methods set out in Sections 2.2.1.3 and 2.2.1.4. However, the stiffness response of plain bar details will be affected by bond loss, which may limit the accuracy of the analytical method for predicting rotational stiffness.

Plain bar details with inclined legs may be particularly susceptible to bond loss, as indicated by progressions of strain development and relative rotational stiffness. This behaviour would limit their use as continuity details, but may enhance their performance as a support tie under dilation effects.

Strain gauge readings indicate that details may rely on relatively short bond lengths to achieve bending moment capacity at given stages. It is evident that the deformed bar detail (CANTI-1) required very short bond lengths from the critical section to achieve moment capacity over the entire test duration. It is considered that local friction effects may enhance bond and therefore reduce required bond lengths.

The strain gauge readings in the CANTI-3 test showed an apparent shift from tension to compression under increasing rotation. This phenomenon appears to be unrelated to the peculiarities of electronic equipment, since the transition is gradual, occurs at more than one gauge station and maintains a general empathy with the test procedure. Hence, the phenomenon should probably warrant further investigation. Nevertheless, it is unlikely that this observation exerted much influence on the particular test outcome, and it is not considered further here.

8

Reinforcing Bar Bond

8.1 GENERAL

An interesting and important observation from both this research and a contemporary study into flooring unit support [Oliver, 1998], is the apparent effect of tie bar kinking on reinforcing bar bond performance. In Section 7.4.3, generally diminished bond lengths were associated with continuity bending moments at flooring unit supports. In Oliver's work, the apparent bond due to friction in kinking bars was shown to be the most likely source of reduced extension capacity of plain round support tie bars. Oliver concluded thus: "Test results indicate that much of the inelastic strains developed by the bars may have been concentrated within the width of the cracked zone by friction forces that could have developed between the bar and the surrounding concrete at the face of the principle transverse crack". This conclusion is consistent with the findings from experimental research reported in this thesis.

It would be of little surprise to many that the minimum bond lengths of bars, as specified in design standards or codes of practice, are conservative for certain (albeit limited) applications. For instance, a simple comparison with concrete anchor technology will verify that a variety of successful anchorage systems rely on comparatively short bond lengths. In this regard, the very reliable mechanical anchors that employ "undercutting" mechanisms are certainly analogous in their application to plain round bars with hook returns. In both cases, the premature fracture of surface concrete is circumvented via bond loss over the shank length that terminates in a rigid embedded anchorage.

Hence, in terms of anchorage reliability, the concept of providing a debonded length is a defensible one. However, the present concern must lie with estimating the localised effects of friction on the viability of the debonded length. At this point, it is important to note that the described plain bars with hook ends are a prime example of friction development in lieu of pure bond, where the strength attributed to the anchorage is due to the bearing friction.

The following chapter examines a bond model that can allow for the components of friction forces, consistent with the combined actions that often exist in structural concrete members. Since the nature of bar bond is often quite variable and specific to member types and material conditions, emphasis is placed on the comparative effects of friction sources, within a hypothetical bar bond model.

8.2 DEVELOPMENT OF A BOND AND FRICTION MODEL

8.2.1 BOND AND FRICTION CRITERIA

8.2.1.1 General

The concept of reinforcing bar anchorage within a concrete mass has traditionally been related by strength development through pure bond stresses. As such, the concurrent transverse components of force acting on bars at critical (cracked) sections are not considered within the common bond model.

The friction effects from transverse forces may be particularly evident with support tie details, since these typically involve floor support derived from the significant kinking of small diameter reinforcement. From the first principles of bond analysis, it is immediately evident that smaller diameter bars require the least effective bond lengths. Based on an average bond strength $\bar{u}$ over length, the tensile force T of reinforcement is related to development length l_d :

$$T = A_b f_s = \bar{u} \Sigma o l_d \tag{8.1}$$

Therefore, the characteristic development length is related to the diameter d_b of reinforcement as:

$$l_d = \frac{d_b f_s}{4\bar{u}} \tag{8.2}$$

It is envisaged that the effects of friction will act to reduce the effective development length by enhancing the average effective bond stress.

8.2.1.2 Bar Bond

(a) Bond Strength

Straight lengths of plain round reinforcement invoke the most fundamental form of bond action, in which the developed strength depends on adhesion between the bar material and surrounding concrete. For plain bars with surface corrosion, bond strength is often significantly improved through friction that develops at the pitted bar surface. The forces of friction are, of course, most pronounced with deformed bars, where the bearing and shear forces associated with projecting ribs greatly increases the local "bond strength" [see Park and Paulay, 1975].

The bond strength between reinforcement and concrete is usually evaluated by bond stress-slip relationships. Associated forms of this test appear widely in research literature and design standards [Standards New Zealand, 1989]. The test bond-slip fundamentally involves measurement of bar slippage at an average bond stress, which is based on a relatively short bond length (see Fig. 8.1). The derived bond stress-slip relationship will typically show bond stress increasing at a decreasing rate under increments of applied force (Fig. 8.2).

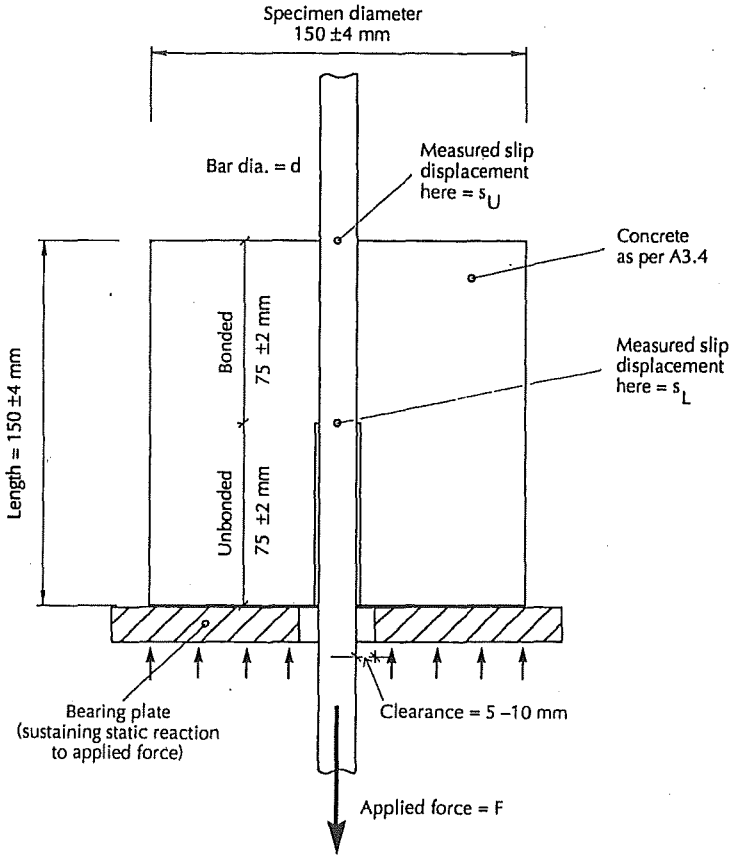

Fig. 8.1 Details of bond tests apparatus [Standards New Zealand, 1989]

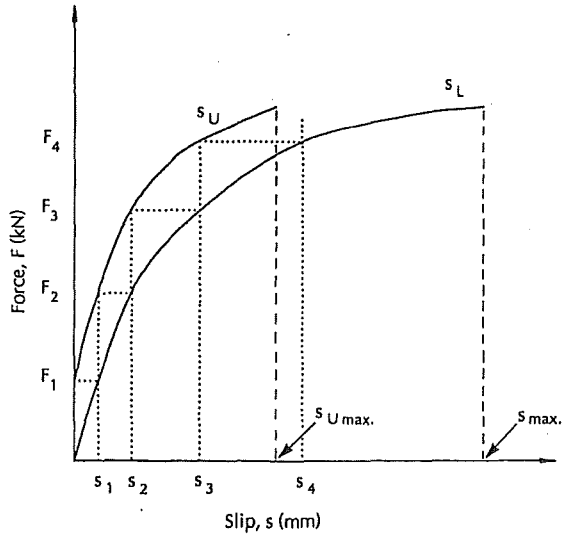

Fig. 8.2 Typical nominal shear (bond) versus slip diagram [Standards New Zealand, 1989]

The bond-slip diagram (Fig. 8.2) is often described by a power function, in which the maximum (or peak) bond stress τ_{max} is given at a corresponding nominal slip displacement s_1. Hence, the bond stress for a given slip s (for $s \leq s_1$) is calculated as:

$$\tau = \tau_{max}\left(\frac{s}{s_1}\right)^{\alpha} \tag{8.3}$$

where the coefficient α defines the curve shape, and may typically lie in the range $0 \leq \alpha \leq 1$. Typical parameters for deformed bars involving both confined and unconfined concrete and plain bars are shown in Table 8.1.

Table 8.1 Bond-slip parameters applicable to design in good bond conditions [CEB-FIP, 1990].

Bar profile	Concrete	τ_{max} (MPa)	s_1 (mm)	α
deformed	confined	$2.5\sqrt{f_{ck}}$	1.0	0.4
deformed	unconfined	$2.0\sqrt{f_{ck}}$	0.6	0.4
plain	all	$0.3\sqrt{f_{ck}}$	0.1	0.5

(b) Bond Capacity Function

In the proposed bond model, a bond capacity function $q_{(x)}$ is introduced. This function does not describe the required bond for strength development, but provides a shape function of bond capacity over the embedded length. Hence, under very low levels bar tension, it is assumed that a near uniform capacity will exist over the embedment length, and that progressive loading will reduce this capacity to zero at the loaded end. However, the capacity will be subject to less deterioration with increasing distance from the loaded end.

As such, the bond capacity function may be described by a power function, similar in appearance to equation 8.3, where the bond capacity q over embedment length L is given as:

$$q_{(x)} = q_u\left(\frac{x}{L}\right)^{n} \tag{8.4}$$

where q_u is the ultimate bond capacity, and the coefficient n is normally in the range $0 \leq n \leq 1$. The bond capacity envelopes described by equation 8.4 are shown in Figure 8.3.

It is considered that a number of factors, such as concrete condition, bar surface condition, degree of compaction, confinement and embedment length may all influence the value q_u. In this study, the bond capacity will be taken as an upper limit of bond strength for 10 mm plain round bars in ideal bond conditions.

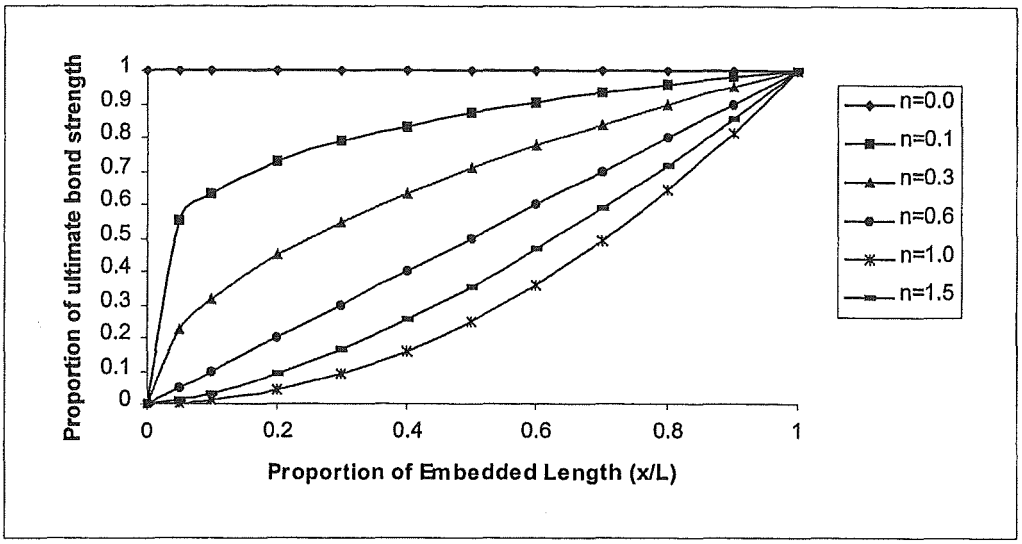

Fig. 8.3 Envelopes of bond capacity over embedment length, as described by Equation 8.4 with given values of the coefficient n

8.2.1.3 Friction from Shear

An embedded bar subjected to large shear displacements will resist shear forces by dowel action due to dowel kinking. Under the combined actions of shear and elongation, it is considered that friction associated with dowel action will affect the bond conditions in the vicinity of the critical section (see Fig. 8.4). As discussed, this is especially relevant to the small diameter support ties used in details to control seating failure.

In order to establish the extent of friction forces over a nominal bond length, the normal component of shear must be determined. In this regard, it is possible to estimate bearing stresses along an embedded length of dowel bar by using a beam on elastic foundation analogy [Elliott et al, 1992]. In Elliot's paper, it is considered that an embedded length of $8d_b$ is adequate to develop dowel action, and that compressive stress will be zero at around $2.5d_b$ from the critical section (i.e., the point of shear application).

Hence, by adopting a reasonable estimate of subgrade reaction (25 N/mm^3), the shear force distribution according to the Winkler theory [Young, 1989] for a 10 mm diameter bar is shown in Figure 8.5. It is evident from the analysis that the distance $2.5d_b$ is close to the point of zero stress and that $8d_b$ embedment is sufficient to develop shear strength. Also, and perhaps most importantly, this result appears to be fairly insensitive to the actual choice of subgrade reaction.

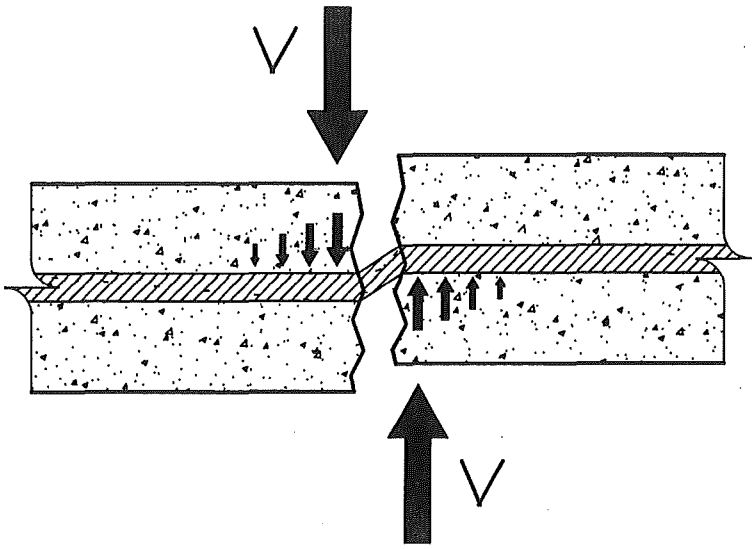

Fig. 8.4 Effect of bearing stresses on bar bond development

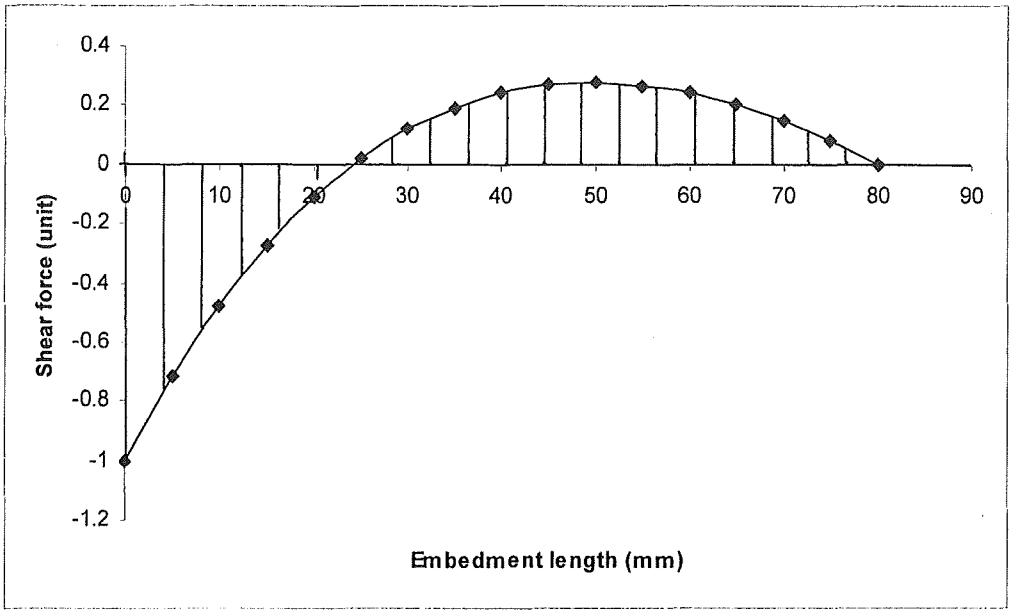

Fig. 8.5 Distribution of shear force, in accordance with Winkler beam theory, along a 10 mm diameter bar embedded 80 mm ($8d_b$) into concrete with a unit shear force applied at the critical section

The analytical solution to the curve in figure 8.5 involves a veritable cocktail of circular and hyperbolic functions. However, it is evident that a parabola will allow close approximation of the curve, and may be expressed in polynomial form:

$$V_{(x)} = V_0\left[5\left(\frac{x}{h}\right) - 5\left(\frac{x}{h}\right)^2 - 1\right] \qquad (8.5)$$

where V_0 is the shear force applied at the critical section and h is the effective embedment length, taken as 100 mm ($10d_b$).

8.2.1.4 Friction from Curvature

The concept of curvature bond is analogous to the frictional losses due to curvature in post tensioning operations. The bending curvature within a member will also result in angular changes to reinforcement. Therefore, the normal force component due to angular change will develop a friction force with the surrounding concrete. In this way, it is considered that curvature friction may provide bond in regions of constant moment, where the traditional expression for flexural bond (i.e., $V/\Sigma o_j d$) breaks down due to an absence of shear force.

8.2.1.5 Friction Coefficient

For smooth steel on concrete, the friction coefficient μ is usually taken as 0.7, and this figure is adopted for the proposed friction model. In tests conducted by Oliver [Oliver, 1998] involving 10 mm diameter plain bar, a friction coefficient of $\mu = 0.86$ was calculated from experimental results, and therefore compares well with the recommended value. It is considered that the friction coefficient of deformed bars would be at least twice the appropriate value for plain bars.

8.2.2 EQUILIBRIUM MODEL

8.2.2.1 General

In a bond model that includes the effects of friction forces, the actual interactions between bond and friction and the progressions of bond loss under load applications are likely to be extremely complex. In order to preserve simplicity in the proposed model, the combined effects of bond and friction resistance within a force equilibrium model are described by a single envelope of "effective" bond stress over the embedded bar length.

8.2.2.1 Equilibrium

An elemental length of reinforcing bar subjected to concurrent axial tension, shear force and curvature is shown in Figure 8.6.

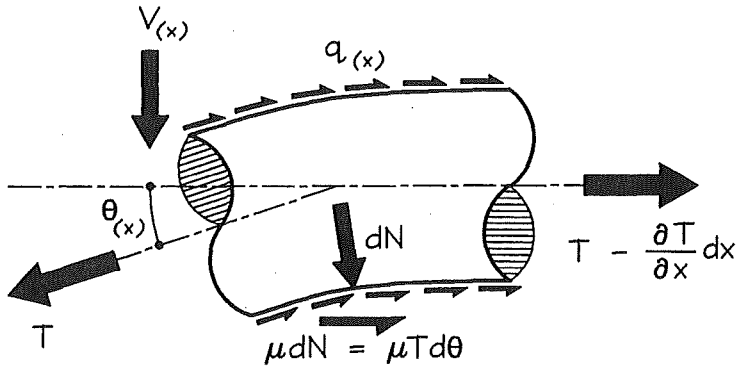

Fig. 8.6 Bond and friction forces acting on an element of reinforcing bar

Assuming that the tensile force T is resisted by bond and friction mechanisms, the differential equation of force equilibrium may be written:

$$T - \left(T + \frac{dT}{dx}dx\right) = \Sigma o\, q_{(x)}dx + \mu\left(dV + dN\right)_{(x)} \tag{8.6}$$

where Σo is the bar perimeter, $q_{(x)}$ is the bond capacity function according to Equation 8.4, μ is the friction coefficient, and $V_{(x)}$ and $N_{(x)}$ are the normal forces due to shear and curvature respectively. Furthermore, in terms of flexural bending, the normal differential force dN due to curvature may be written:

$$dN = T\,d\theta = T\varphi\,dx \tag{8.7}$$

and Equation 8.6 becomes:

$$-\frac{dT}{dx}dx = \Sigma o\, q_{(x)}dx + \mu\, dV_{(x)} + \mu T\varphi_{(x)}\,dx \tag{8.8}$$

In order to solve the differential equation, Equation 8.8 is written in dimensionless form:

$$\frac{dT}{T} = \frac{\Sigma o\, q_{(x)}}{T}\,dx + \frac{\mu}{T}\,dV_{(x)} + \mu\,\varphi_{(x)}\,dx \tag{8.9}$$

Equation 8.9 may be solved by separation of variables provided that the tension value T on the right hand side may be described as a constant that corresponds with the initial condition. This condition exists at x = 0, where T_0 is the bar tension at the critical section.

$$\frac{dT}{T_{(x=0)}} = -\left(\frac{\Sigma o\, q_{(x)}}{T_o}\, dx + \frac{\mu}{T_o}\, dV_{(x)} + \mu\, \varphi_{(x)}\, dx \right) \tag{8.10}$$

Integration of Equation 8.10 gives:

$$\ln T = -\left(\frac{\Sigma o}{T_o} \int q_{(x)}\, dx + \frac{\mu}{T_o}\, V_{(x)} + \mu \int \varphi_{(x)}\, dx \right) + C \tag{8.11}$$

where C is the arbitrary constant of integration.

8.2.2.3 Bond-Only Model

The common assumption of bar bond in response to direct axial tension is considered first. Thus ignoring friction effects, the first term of the RHS of Equation 8.11 is integrated and the relevant initial condition of $T = T_0$ at $x = 0$ is applied, so that:

$$\ln T_{(0)} = -\frac{\Sigma o\, L\, q_u}{T_o (n+1)} \left(\frac{x}{L} \right)^{n+1} + C \tag{8.12}$$

$$C = \ln T_{(0)} \tag{8.13}$$

which yields the solution for bar tension T as a function of embedded length x:

$$T_{(x)} = T_o \exp -\left[\frac{\Sigma o\, L\, q_u}{T_o (n+1)} \left(\frac{x}{L} \right)^{n+1} \right] \tag{8.14}$$

As discussed in Section 8.2.1.2, the bond stress $q_{(x)}$ described by Equation 8.4 is an envelope of bond capacity that may be influenced by such factors as reinforcing bar and concrete properties, confinement and loading regime. It is not the actual (effective) bond stress required to resist bar tension developed under a total embedment length L and selected envelope shape coefficient n, which will approach zero as length x approaches the total embedment length L. The effective bond stress envelope may be determined from the fundamental bar bond equation.

Referring to Equation 8.1, the variation of bar tension T with distance x may be written:

$$dT = \Sigma o\, u_{(x)}\, dx \tag{8.15}$$

Therefore, differentiating Equation 8.14 with respect to x and dividing by Σo gives the effective bond stress:

$$u_{(x)} = q_u\left(\frac{x}{L}\right)^n \exp-\left[\frac{\Sigma o\, L\, q_u}{T_o(n+1)}\left(\frac{x}{L}\right)^{n+1}\right] \qquad (8.16)$$

For a single round bar, the exponential function of Equations 8.14 and 8.16 may be simplified by reducing the terms Σo and T_o so that:

$$\exp-\left[\frac{4\,L\,q_u}{f_s\,d_b(n+1)}\left(\frac{x}{L}\right)^{n+1}\right] \qquad (8.17)$$

Based on Equations 8.4, 8.14 and 8.16, relationships between the assumed bond capacity envelope, derived tension forces and corresponding effective bond stresses are shown in Figures 8.8 to 8.11 for plain and deformed bars. In each case, the model has assumed a 10 mm diameter bar with good initial bond conditions (see Table 8.2) and varying degrees of bond capacity loss as described by Equation 8.4 (see Fig. 8.7). As such, a procession of bond loss may be modelled by increments of the coefficient n. Thus, the n = 0 condition represents undisturbed (uniform) bond capacity over the embedment length, characteristic of pre-yield bar tension. At the other extreme, the n = 2 condition represents considerable bond loss over the embedment length, characteristic of strain penetration effects under cyclic loading.

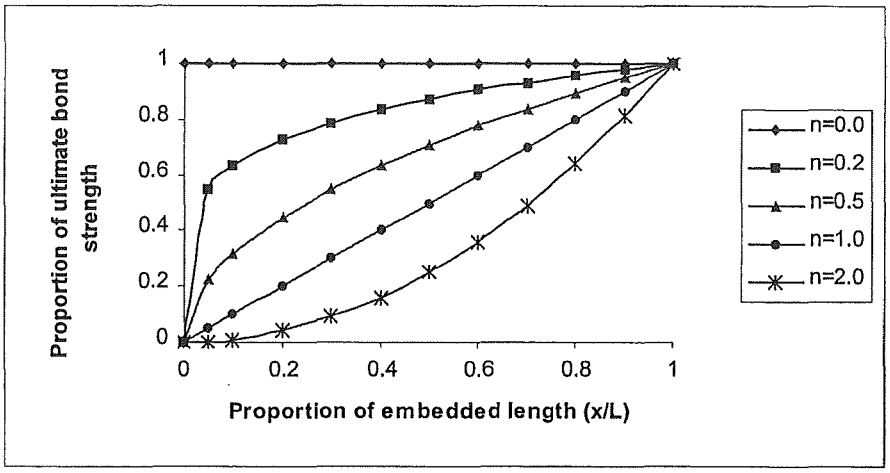

Fig. 8.7 Range of bond capacity shape coefficients n in Equation 8.4, for a 10 mm diameter bar embedded 600 mm into concrete.

Table 8.2 Characteristics of embedded bars corresponding with Figures 8.8 to 8.11

Bar profile	Size	T_0 (kN)	q_u (MPa)	L (mm)
plain	R10	23.6	4.0	600
deformed	D10	23.6	12.0	600

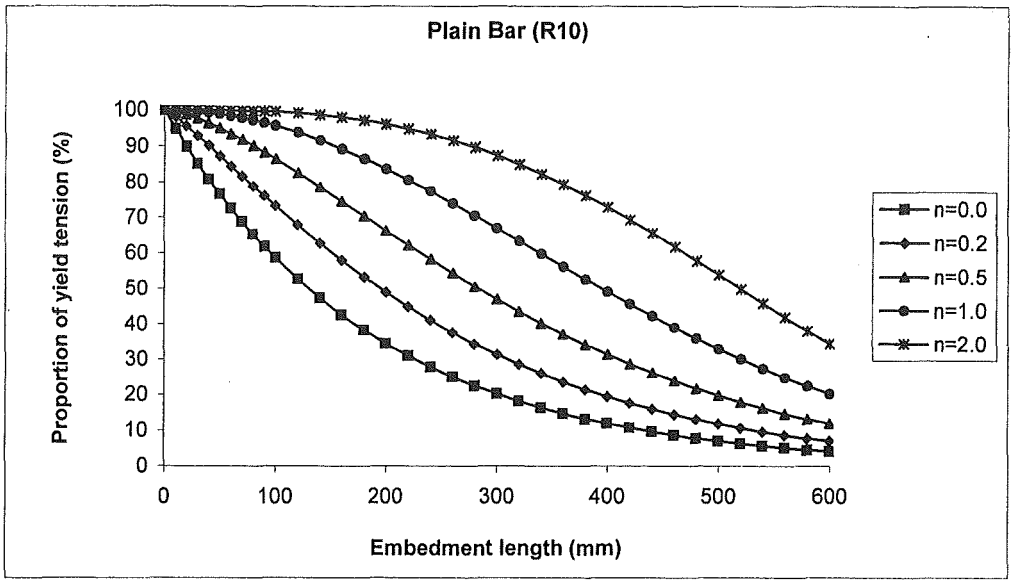

Fig. 8.8 Proportion of yield force T_o according to Equation 8.14, developed by a 10 mm plain round bar (Grade 300) over a 600 mm embedded length at bond capacity envelopes given in Figure 8.7 (increasing n corresponds with bond loss)

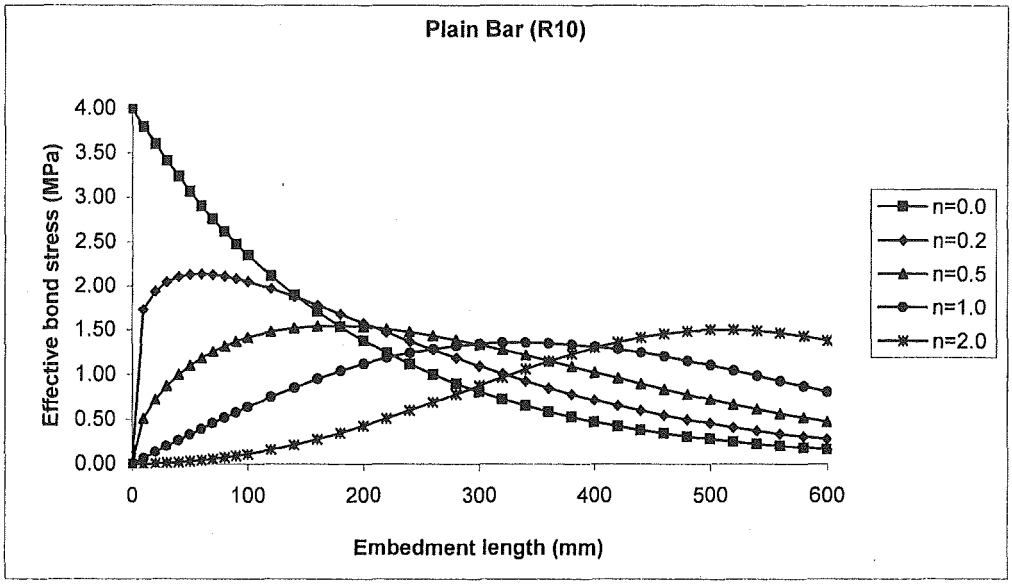

Fig. 8.9 Effective bond stress envelopes $u_{(x)}$ according to Equation 8.16, developed by a 10 mm plain round bar (Grade 300) over a 600mm embedded length at bond capacity envelopes given in Figure 8.7 (increasing n corresponds with bond loss)

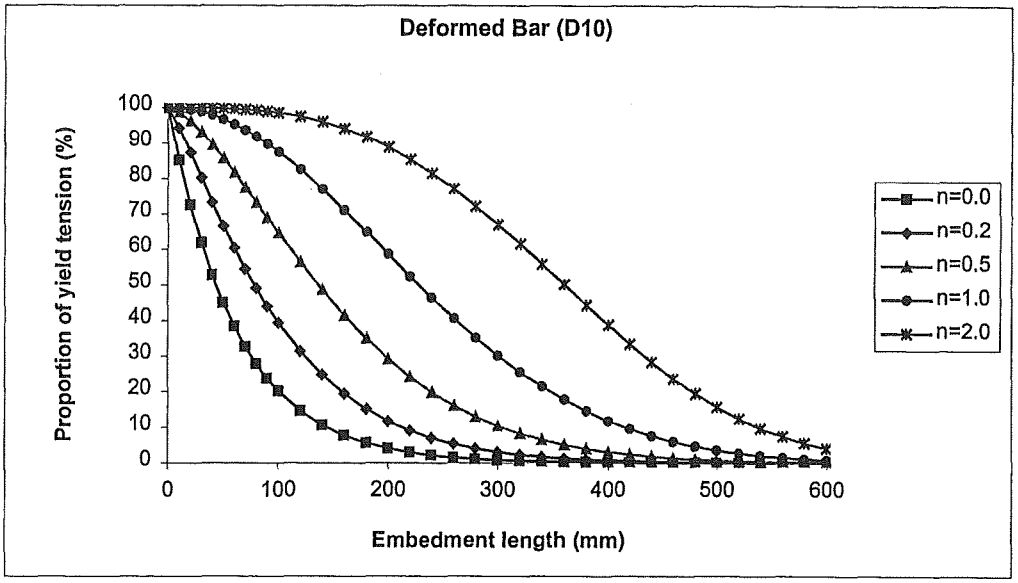

Fig. 8.10 Proportion of yield force T_o according to Equation 8.14, developed by a 10 mm deformed bar (Grade 300) over a 600 mm embedded length at bond capacity envelopes given in Figure 8.7 (increasing n corresponds with bond loss)

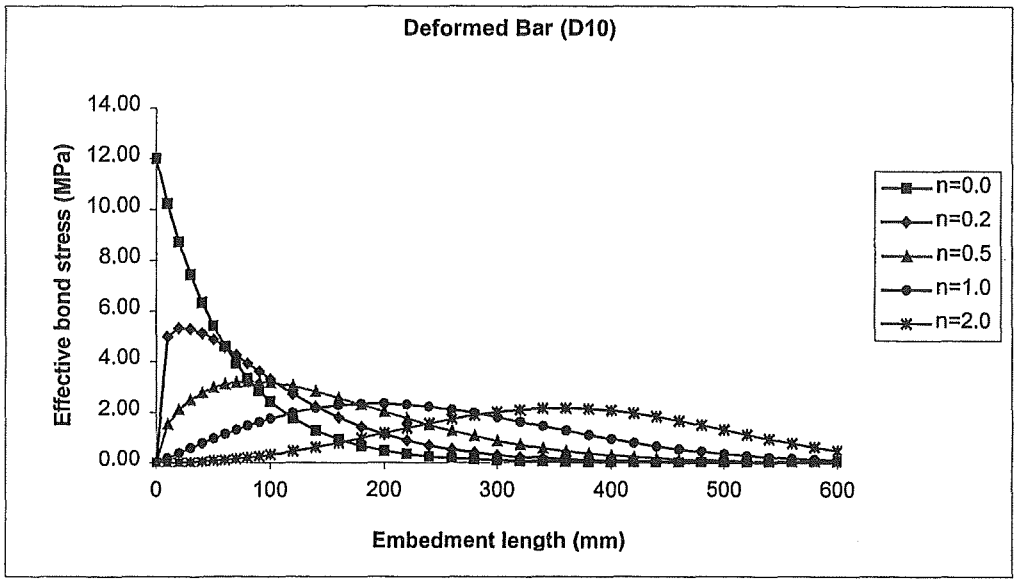

Fig. 8.11 Effective bond stress envelopes $u_{(x)}$ according to Equation 8.16, developed by a 10 mm deformed bar (Grade 300) over a 600 mm embedded length at bond capacity envelopes given in Figure 8.7 (increasing n corresponds with bond loss)

The bond capacity function $q_{(x)}$ is not limited to pull-out models, and may be adapted to the general cases of flexural bond and member axial tension. A simple example is to assume that the bond capacity between flexural or axial tension cracks can be described by a sine curve relationship (Fig. 8.12):

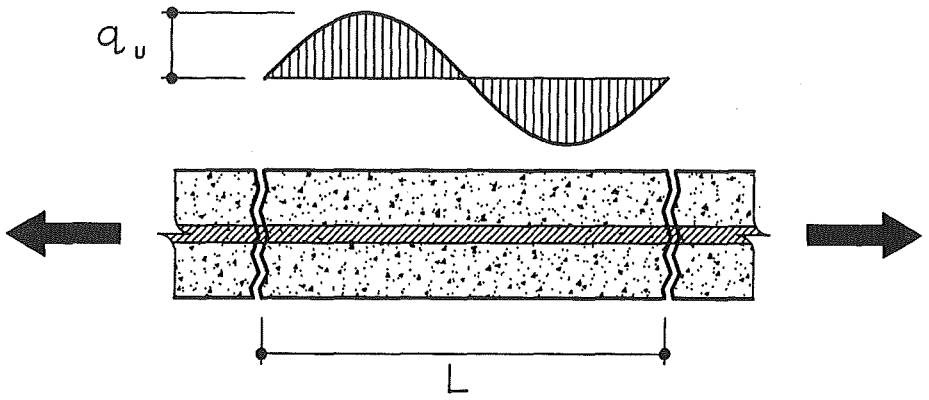

Fig. 8.12 Assumed distribution of bond capacity envelope between flexural cracks, relevant to direction of bar tension

Hence, the bond capacity is written:

$$q_{(x)} = q_u \sin\left(\frac{2\pi x}{L}\right) \tag{8.18}$$

Substituting Equation 8.18 into Equation 8.11, integrating and applying the initial condition of $T = T_0$ at $x = 0$ gives the solution for a round bar as:

$$T_{(x)} = T_0 \exp\left[\frac{2Lq_u}{\pi d_b f_s}\left(\cos\left(\frac{2\pi x}{L}\right) - 1\right)\right] \tag{8.19}$$

and the corresponding effective bond stress as:

$$u_{(x)} = q_u \sin\left(\frac{2\pi x}{L}\right) \exp\left[\frac{2Lq_u}{\pi d_b f_s}\left(\cos\left(\frac{2\pi x}{L}\right) - 1\right)\right] \tag{8.20}$$

Tension forces and effective bond stresses as described by Equations 8.19 and 8.20 and at varying values of ultimate bond capacity (see Table 8.3) are shown in Figures 8.13 and 8.14.

Table 8.3 Characteristics of longitudinal bar corresponding with Figures 8.13 and 8.14

Bar profile	Size	f_s (MPa)	q_u (MPa)	L (mm)
deformed	D10	300	0,2,4,8,16	300

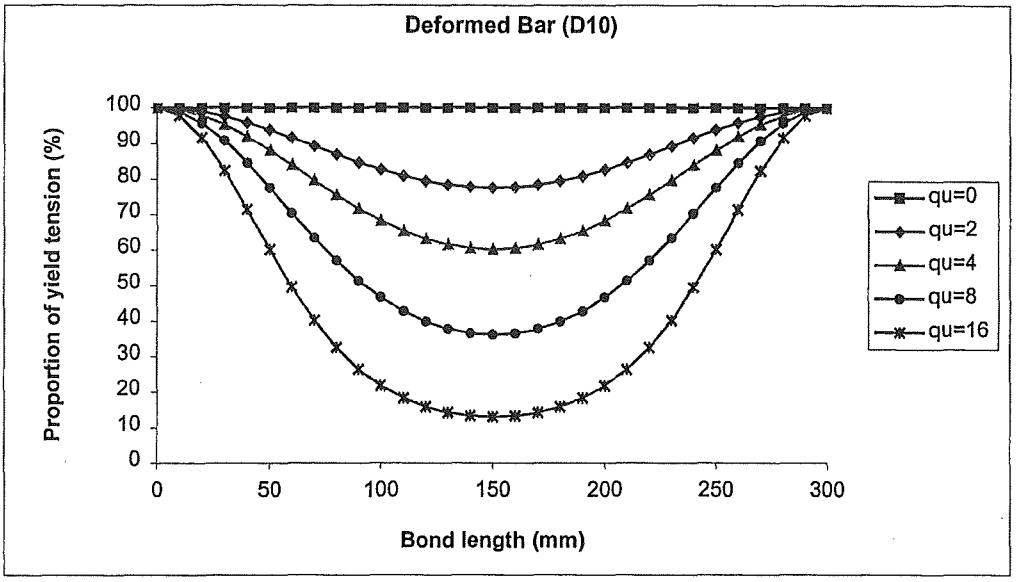

Fig. 8.13 Proportion of yield force T_0 according to Equation 8.19, developed by a 10 mm deformed bar (Grade 300) over of 300 mm bond length at the stated ultimate bond capacities

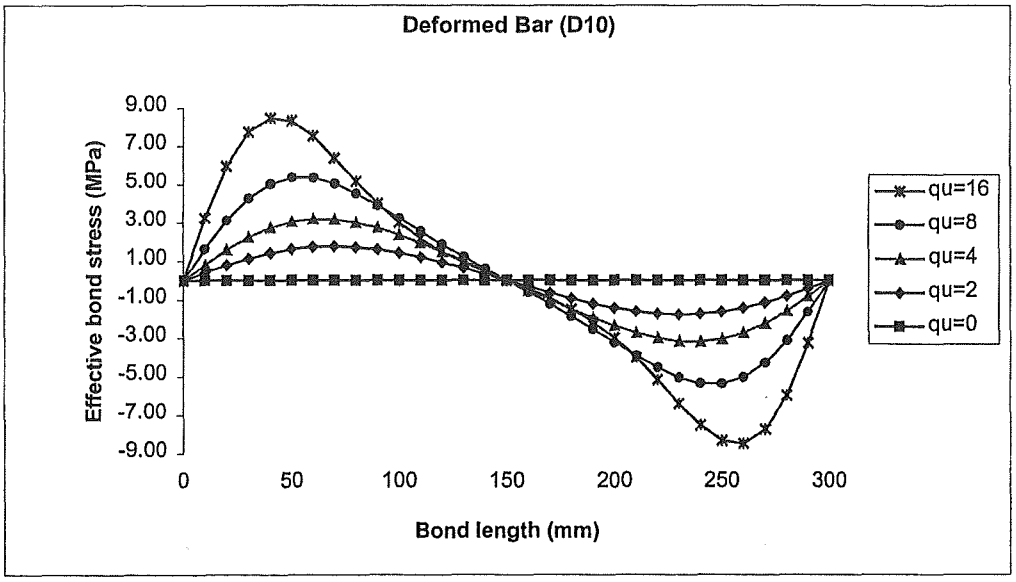

Fig. 8.14 Effective bond stress envelopes $u_{(x)}$ according to Equation 8.20, developed by a 10 mm deformed bar (Grade 300) over 300 mm of bond length at the stated ultimate bond capacities

8.2.3 FRICTION-BOND MODEL

8.2.3.1 General

At this point, the physical model involving the kinking of bars is revisited. For the particular case of support tie bars, it is considered that directly applied shear force will dominate local friction effects. Since the influence of curvature may feature less strongly in general, it will be ignored for the particular case of tie bar kinking.

Referring to Equations 8.4.and 8.5, and considering the initial condition of $T = T_o$ at $x = 0$ gives:

$$\ln T_{(0)} = -\frac{1}{T_o}\left\{\frac{\Sigma o\, L\, q_u}{(n+1)}\left(\frac{x}{L}\right)^{n+1} + \mu V_o\left[5\left(\frac{x}{h}\right) - 5\left(\frac{x}{h}\right)^2 - 1\right]\right\} + C \qquad (8.21)$$

$$C = \ln T_{(0)} - \frac{\mu}{T_o} V_o \qquad (8.22)$$

Combining Equations 8.21 and 8.22 gives the solution for reinforcing bar tension as a function of bond capacity, embedment length and shear force. In Equation 8.21, the absolute magnitude of shear force becomes applicable since friction developed between the bar and concrete is independent of the direction in which the shear force acts.

$$T_{(x)} = T_o \exp - \frac{\left[\frac{\Sigma o\, L\, q_u}{(n+1)}\left(\frac{x}{L}\right)^{n+1} + \frac{5\mu V_o \langle x\rangle}{h}\left(1 - \frac{\langle x\rangle}{h}\right)\right]}{T_o} \qquad (8.23)$$

and:

$$u_{(x)} = \left[q_u\left(\frac{x}{L}\right)^n + \frac{5\mu V_o}{\Sigma o\, h}\left(1 - \frac{2\langle x\rangle}{h}\right)\right] \exp - \frac{\left[\frac{\Sigma o\, L\, q_u}{(n+1)}\left(\frac{x}{L}\right)^{n+1} + \frac{5\mu V_o \langle x\rangle}{h}\left(1 - \frac{\langle x\rangle}{h}\right)\right]}{T_o} \qquad (8.24)$$

In the above expressions, angle brackets indicate that the contained value may not exceed $8d_b$ (80 mm), as prescribed by the shear force envelope of Equation 8.4 (see Fig. 8.5).

Tension forces and effective bond stresses according to Equations 8.23 and 8.24 at varying bar kinking angles ($\theta = 0°$, 10°, 20° and 30°) are shown in Figures 8.15 and 8.16, where shear force at the critical section $V_o = A_b f_y \cdot \sin\theta$ (see Fig. 8.6) and $T_o = A_b f_y$.

Table 8.4 Characteristics of embedded bars corresponding with Figures 8.8 to 8.11

Profile	Size	q_u (MPa)	μ	n	L (mm)	h (mm)
plain	R10	4.0	0.7	1.0	600	100

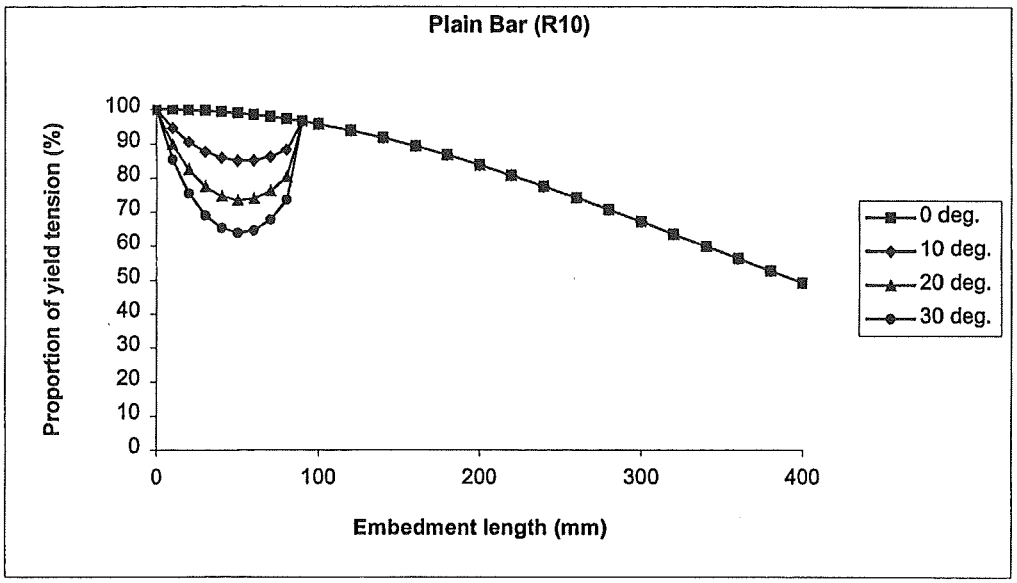

Fig. 8.15 Proportion of yield force T_0 according to Equation 8.23, developed on a 600 mm embedment length of 10 mm plain bar (Grade 300), showing influence of friction due to shear from bar kinking at given angles (see Fig. 8.6)

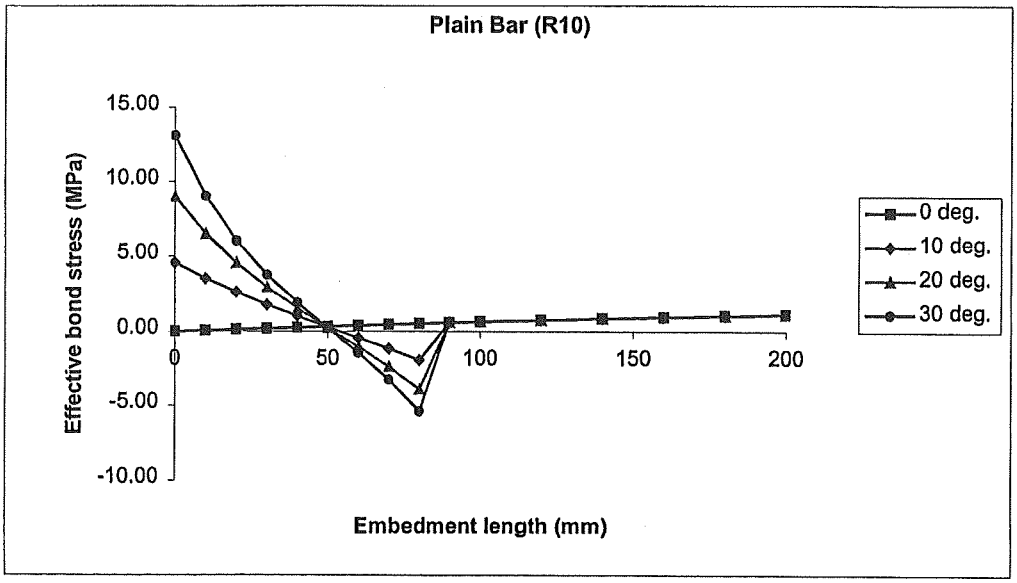

Fig. 8.16 Effective bond stress envelopes $u_{(x)}$ according to Equation 8.24, developed in the shear zone of a 10 mm plain bar (Grade 300), showing influence of friction due to shear from bar kinking at given angles (see Fig. 8.6)

Reverting to Equation 8.1, it is evident that for a bar kinking angle of 30 degrees in Figure 8.16, the average bond stress over the first 50 mm of embedment (i.e., approximately 6 MPa) is sufficient to develop 9.4 kN of tension, or 40% of the bar yield strength. Also, the summation of bond stress over embedded bar surface area (see Equation 8.15) will be marginally less than the total bar yield force T_0. Thus, the net tension demand over embedment length will equal the total tension at any point less the proportion of force developed through friction bond over the first 50 mm of embedment. As such, the net profile of bar tension demand over embedment length to resist T_0 is shown in figure 8.17.

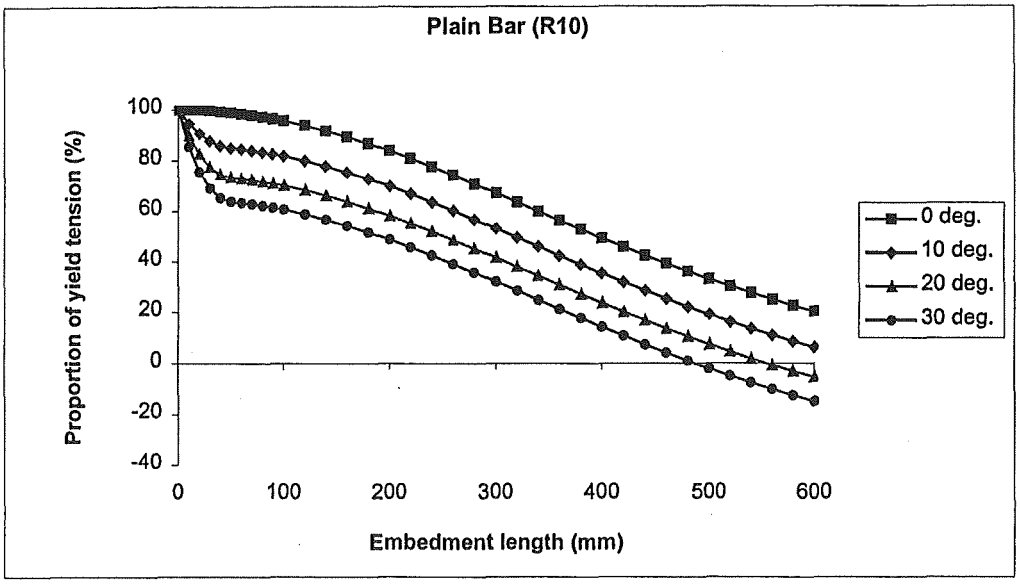

Fig. 8.17 Proportion of yield force T_0 developed on a 600 mm embedment length of 10 mm plain bar (Grade 300) after net deduction of force developed through friction from bar kinking at given angles

Figure 8.17 indicates that the effects of friction due to shear may have a significant influence on development lengths. For the case of the plain bar shown, an 80% reduction in yield force occurs at 600 mm embedment when $\theta = 0$ degrees. For the same bar, a 100% reduction in force is achieved at only 480 mm embedment when $\theta = 30$ degrees. Hence, the decreased effective bar anchorage length will directly limit the amount of extension available. For deformed bars, the above effect will be much more acute, resulting in significantly shorter development lengths and relatively large steel strains under dilation type loading (see Table 8.5, Figures 8.18 to 8.20).

Table 8.5 Characteristics of embedded bars corresponding with Figures 8.18 to 8.20

Profile	Size	q_u (MPa)	μ	n	L (mm)	h (mm)
deformed	D10	12.0	1.4	1.0	600	100

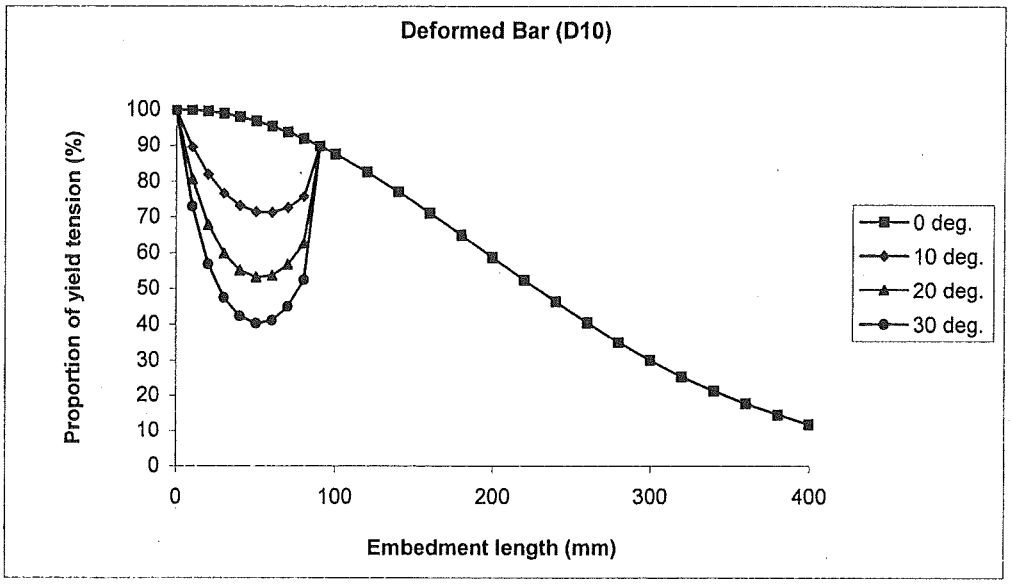

Fig. 8.18 Proportion of yield force T_0 according to Equation 8.23, developed by a 10 mm deformed bar (Grade 300) over a 600 mm embedded length, showing influence of friction due to shear from bar kinking at given angles (see Fig. 8.6)

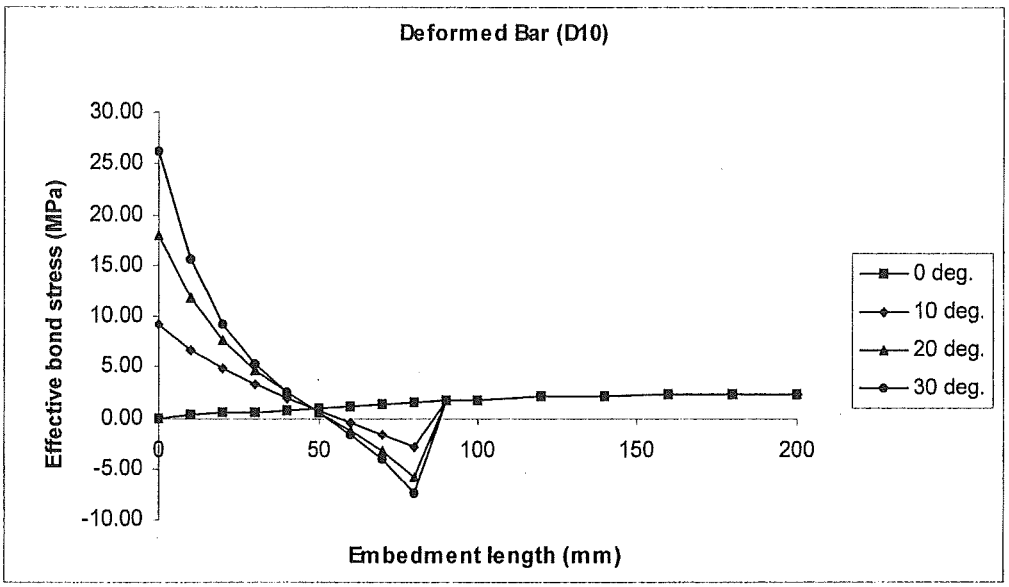

Fig. 8.19 Effective bond stress envelopes $u_{(x)}$ according to Equation 8.24, developed in the shear zone of a 10 mm deformed bar (Grade 300), showing influence of friction due to shear from bar kinking at given angles (see Fig. 8.6)

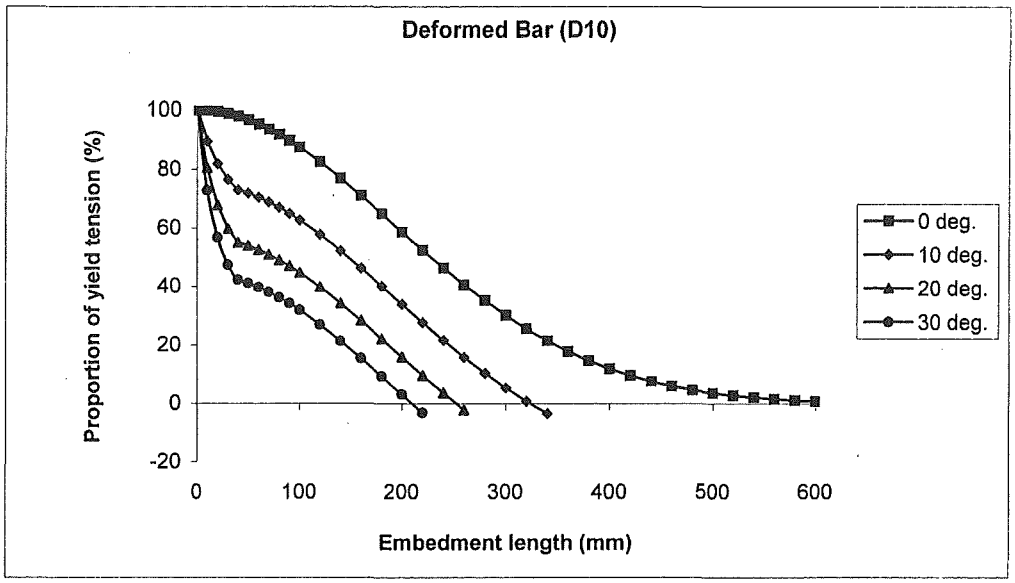

Fig. 8.20 Proportion of yield force T_0 developed by a 10 mm deformed bar (Grade 300) over a 600 mm embedded length after net deduction of force developed through friction from bar kinking at given angles

8.3 DISCUSSION ON RESULTS

8.3.1 COMPARISON WITH TEST RESULTS

The values given in Table 8.6 are extracted from recent research work on embedded support tie bars [Oliver, 1998]. As discussed earlier, the effects of friction were considered to have caused measurable reductions in tension force resisted by the embedded bar portion. These reductions are subsequently compared with estimated reductions, which are calculated in accordance with Equation 8.23.

Table 8.6 Horizontal force misclose observed during the testing of Unit 2 [Oliver, 1998: (Table 5.2)]

Horizontal Displacement (mm)	Applied Horizontal Force (kN) (1)	Measured Paperclip Force (kN) (2)	Continuity Bar Force (kN) (3)	Misclose (kN) (1) – (2) – (3)
20	333	106	204	23
30	135	110	Nil	25
45	141	110	Nil	28
47	139	113	Nil	26

From Table 8.6, the average force misclose may be taken as 25 kN. The associated shear force acting at the critical section was 29 kN. These two values were used by Oliver to calculate an effective friction coefficient between the plain bar reinforcement and surrounding concrete of $\mu = 25/29 = 0.86$.

Since the tested paperclip detail of Unit 2 involved four legs of R10 reinforcement, it is evident that an average initial tension force of $T_0 = 34$ kN and an average corresponding initial shear force of $V_0 = 7.25$ kN acted on each tie leg.

Inspection of Equation 8.24 and Figures 8.15 to 8.20 indicates that the critical bond length affected by shear force is 0.5h, (i.e., $5d_b$). Hence, the maximum reduced tension resulting from an introduction of shear force is equal to the value corresponding to $5d_b$ of embedment. If the critical shear bond length of $5d_b$ is adopted and cohesive bond is ignored (i.e., $q_u \rightarrow 0$) the expression for maximum reduced tension due to shear may be written as:

$$T_{(5d_b)} = T_o \exp - \frac{5\mu V_o}{4T_o} \qquad (8.25)$$

Substituting appropriate values derived from the experiment, the estimated reduced tension due to shear for Unit 2 is:

$$\frac{T_{(5d_b)}}{T_o} = \exp - \frac{5\times 0.86\times 7.25}{4\times 34} = 0.8$$

Referring to Table 8.6 and the difference between applied and measured horizontal forces, it is evident that the estimated 20% reduction to initial tension due to shear is comparable to the average observed reduction of 19.3%.

The estimated variation in reduced bar tension, with the initial bar tension ranging between nominal yield force and the ultimate tensile strength, is given in Table 8.7. For each case, the initial shear force and friction coefficient have been taken as constants.

Table 8.7 Relationship between initial bar tension T_0 and the maximum reduced tension due to shear force, T_{5db}.

Initial Bar Tension T_0 (kN)	Initial Shear Force V_0 (kN)	Friction Coefficient μ	Reduced Tension T_{5db} / T_o
23.5	7.25	0.86	0.72
27.0	7.25	0.86	0.75
31.0	7.25	0.86	0.78
34.8	7.25	0.86	0.80

8.4 CONCLUSIONS

8.4.1 GENERAL

The following general conclusions are made with regard to the bond theory presented in this chapter:

The friction-bond model assumes that friction effects, resulting from the normal components of direct shear and curvature, may significantly influence the nature of resistance to pullout forces.

In regions of constant bending moment, the friction-bond theory reasons that curvature friction (analogous to post-tension friction) may account for a proportion of the apparent bar bond.

Of the three bond modes considered (i.e., cohesive, direct shear and curvature friction), direct shear may be the singularly most influential source of effective bond in regions that involve dowel bar actions.

Based on the commonly assumed Winkler Beam analogy, the effective length of shear bond zone for a bar subjected to dowel action is five bar diameters ($5d_b$) from the critical section. At this distance, the maximum force reduction due to shear bond will have been achieved. In situations involving deformed bars, this distance may need to be increased somewhat to allow for concrete cone pullout (i.e., the so-called Goto effect).

When compared to test results involving plain tie bar details, the force misclose (i.e., the force reduction over embedment length) that results from friction effects may be estimated with reasonable accuracy.

9

Summary, Conclusions and Recommendations

9.1 GENERAL

A series of experiments were conducted with the intention of isolating various critical aspects of the support and continuity performance of hollow core flooring under (especially) seismic related forces. The main emphasis of testing has been to ascertain the capabilities of support details, specifically starter and tie bars, when subjected to the dilation type loadings associated with plastic hinge formation in support members.

The primary experimental programme involved six assemblages of hollow core flooring units with composite topping. These specimens exhibited variations in support tie details, and were loaded either monotonically and cyclically in order to test the hypotheses of inherent detail weaknesses under particular loading regimes.

Further experiments were conducted to determine more specific behaviour, such as composite topping bond capacity.

A sizeable introductory chapter is featured, in which the historical background of pretensioned flooring use is discussed. This is considered an important inclusion, since the current approach toward support detail design would appear more strongly influenced by a perceived history of performance than by way of substantiated test data.

A reasonable body of theory has been presented that examines the subjects of dynamics with stiffness degradation, elastic-plastic stiffness transition, effective plastic hinge lengths, frame sway compatibility, elastic-plastic buckling, rotational behaviour and bar bond. Although apparently diverse, it is considered that each aspect of theory presented may assist in one or more ways with the general analysis of flooring members and/or the interactions between flooring and ductile support members.

9.2 MONOTONIC DILATION

9.2.1 TYPICAL STARTER BAR DETAIL (Tests LOS 1, LOS 3, LOS 4)

Based on the evidence of testing full-scale specimens, the following is concluded for flooring members subjected to dilation type loading:

- Starter bar details are grossly inadequate for the purposes of maintaining a ductile tie connection between pretensioned flooring units and support members. Hence, starter details provide no control over the potential for loss of support and floor member collapse.

- For flooring members with relatively smooth bond surfaces (i.e., extruded hollow core), complete tensile fracture of the topping at the point of starter curtailment is almost certain. The topping fracture is accompanied by a rapid breakdown in composite bond strength between the topping slab and hollow core unit. It is likely that composite bond capacity will have begun to deteriorate prior to the sudden topping fracture.

- In fractured topping slabs that exhibit debonding, the onset of topping mesh fracture can be expected to occur at around 6 mm horizontal displacement. The tensile resistance of mesh will be fully depleted at about 20 mm displacement.

- When supported onto concrete members, it is likely that collapse of the hollow core unit will occur at a lesser horizontal displacement than the seating length due to spalling of support ledge concrete.

- In practice, the typical occurrence of chases and rebates in floor support regions are likely to exert considerable influence on the nature of topping and unit fracture.

9.2.2 HAIRPIN DETAIL (Test LOS 2)

Based on the evidence of a testing full-scale specimen, the following is concluded for flooring members subjected to dilation type loading:

- Support tie details involving bars embedded into the support and grouted into the hollow core voids can provide a controlled ductile response to dilation forces.

- From the test, it is apparent that efficient bond capacity associated with deformed bars can mitigate ductile capacity. Hence deformed bars are not well conditioned for situations where significant ductility may be required.

- Details involving removed hollow core flanges and fully grouted voids exhibit much improved topping bond capacity.

9.2.3 COMPOSITE TOPPING BOND

Based on the evidence of testing several direct shear specimens, the following is concluded for the bond surface condition of precast flooring members under monotonic dilation type loading:

- Smooth concrete surfaces subjected to direct shear developed (on average) only 37% of the minimum shear strength (0.55 MPa) required by the design standards. Hence, the results of shear flow experiments, on which composite bond capacity has been based, are not applicable to situations that involve direct shear.

9.2.4 CANTILEVER TESTS

Based on the evidence of testing three cantilever specimens, the following is concluded on the continuity performance of precast flooring members under rotational loading:

- Embedded tie bar details may be configured to develop end continuity moments of the same order of magnitude and rotational stiffness as conventional details.

- Due to reduced rotational stiffness that results from strain penetration, inclined plain bar details would appear the least favourable tie configuration for purposes of continuity development.

9.3 CYCLIC DILATION

9.3.1 TYPICAL CONTINUITY BAR DETAIL (Test LOS 5)

Based on the evidence of testing a full-scale specimen, the following is concluded for flooring members subjected to cyclic dilation type loading:

- For flooring members with relatively smooth bond surfaces (i.e., extruded hollow core), the mechanisms that facilitate topping slab uplift (buckling) may be expected to occur when typical quantities of continuity reinforcement are subjected to cyclic dilation type loading.

- Similar such mechanisms could develop in other parts of floor diaphragms where cyclic actions impose compression forces on yielded bars within topping slabs (e.g., chord-tie reinforcement).

- In the test specimen, buckling was observed to be both sudden and conclusive. It was evident that a considerable amount of topping bond degradation had occurred well in advance of slab buckling.

9.3.2 EMBEDDED TIE BAR DETAILS (Test LOS 6)

Based on the evidence of testing a full-scale specimen, the following is concluded for flooring members subjected to cyclic dilation type loading:

- Generally, the cyclic loading response of embedded plain bar details is excellent. For certain details (inclined ties), buckling may eventuate so that topping concrete is spalled and bar popping occurs. However, this effect is considered to be of little importance provided that some mechanical working of the bar is permissible.

- Similarly, smaller diameter tie bars (i.e., 12 mm and less) may be susceptible to buckling at low displacement cycles. Hence, the mechanical toughness of tie steel should be considered for these details.

- Removal of the top flange and grouting of cores would appear to effectively mitigate the problem of topping slab fracture and delamination.

- Considerable strain penetration may be observed when embedded plain bar details are subjected to cyclic loading.

- Directly connecting tie details to reinforcing elements of the support member should be avoided, since the impending lateral bar deformation may counteract the efficiency of confinement.

9.4 ANALYSIS

9.4.1 COMPOSITE BEAM-FLOOR ACTION

- Design information indicates that sufficient bond strength can exist between precast hollow core flooring and perimeter beams to develop the strength capacity of prestressing strands in tension flanges.

- Conventional section analysis indicates that the potential contribution to beam bending moment capacity from prestressing steel in tension flanges could be very significant.

- It is likely that the modular nature of precast flooring units will restrict the migration of tension flange cracks to the width of one precast unit.

- It is very likely that prestressed flooring units having thin flanges and open webs (e.g., tee units) would contribute considerably less to beam bending moment capacity.

- Compatibility analysis gives an estimate of the minimum beam lengths required to achieve prescribed structural rotations at limiting levels on concrete compression strain.

9.4.2 DIAPHRAGM FORCES AND SLAB BUCKLING

- The bending moment components of ductile beams in the vicinity of columns are almost certain to introduce large reaction (coupling) forces into adjacent floor planes.

- The conventional notion of uniformly distributed shear stresses acting along the peripheral elements of diaphragms is inconsequential when compared to nodal forces arising from the bending components of ductile support members.

- Buckling analysis indicates that topping slab regions subjected to large in-plane forces may be prone to buckling over relatively short distances if composite topping ties are not present and correct.

- Buckling analysis concludes that large diameter bars and/or concentrations of bars within topping slabs will reduce the critical buckling length, and therefore increase the required density of composite topping ties.

9.5 RECOMMENDATIONS FOR FUTURE RESEARCH

More information is required on the nature of frame dilation, and this must be determined largely by the physical testing of frame assemblages. However, it is warned that such testing will have limited meaning if the assemblages do not contain at least one module of pretensioned flooring unit. Clearly, there are very important and indivisible matters of composite beam-flooring interaction that need to be figured into the existing frame models.

With regard to the practical testing of diaphragm elements, it is considered that the logistically difficult task of testing full-size elements might not be necessary. It must be appreciated that strut and tie fields are also a partially notional concept, the same being subject to considerable spreading and redistribution within the floor slab. Rather, it is considered that the components of orthogonal bending, characteristic of ductile beams intersecting at corner columns, will induce perhaps the most definitive and plausible of all nodal (localised) reactions.

It is perceived that the following points should be closely examined in any such experiments:

- Contributions to beam strength and stiffness from adjacent flooring units, and the influence of adjacent flooring on the nature of beam plastic hinge development.

- The direct observation of dilation effects, with emphasis on the determination of practical dilation magnitudes in real structures and related design criteria.

For the general understanding of structural mechanics, various items of theory presented in this thesis should be examined, correlated with test data and developed further if appropriate. This would especially include the topics of elastic-plastic transition, rotational stiffness prediction and the plastic buckling theory.

References

ACI (1968), *ACI Manual Of Concrete Practice, Part 2,* American Concrete Institute, Detroit, Michigan, pp. 226-232.

ACI (1979), *Vibrations of Concrete Structures,* Publication SP-60, American Concrete Institute, Detroit, Michigan.

ACI 318-71 (1971), *ACI 318 Committee: Building Code Requirements for Reinforced Concrete*, American Concrete Institute, Detroit, Michigan.

Anderson A R and Anderson R G (1976), *An Assurance Criterion for Flexural Bond in Pretensioned Hollow Core Units,* ACI Journal, Vol. 73 August 1976, pp.457-464.

ATC-8 (1981), *Design of Prefabricated Concrete Buildings for Earthquake Loads*, Proceedings from Workshop ATC-8, Applied Technology Council, Berkeley, California.

Balázs, G L (1992), *Transfer Control of Prestressing Strands*, PCI Journal, November-December 1992, pp. 60-71.

Becker, J M and Sheppard, D A (1981), *Connections for Seismic Resistant Precast Concrete Structures*, Proceedings from Workshop ATC-8, Applied Technology Council, Berkeley, California, pp. 657-683.

Booth, E (Editor) (1994), *Concrete Structures in Earthquake Regions*, Concrete Design & Construction Series, Longman Scientific & Technical, Essex, England.

Bruggeling, A S G and Huyghe, G F (1991), *Prefabrication With Concrete*, A A Balkema, Rotterdam.

BS 8110: 1995 Handbook (1995), *Handbook to BS 8110: 1995, The Structural Use of Concrete,* Palladian Publications Ltd, London.

Building Industry Authority (1991), *The New Zealand Building Code,* Standards New Zealand, Wellington.

CEB (1991), *Vibration Problems in Structures (Practical Guidelines)*, Comité Euro-International du Béton, Bulletin D'Information No. 209.

CEB-FIP (1978), *Model Code for Concrete Structures,* Comité Euro-International du Béton-Fédération Internationale de la Précontrainte, FIP, 1978 (3rd Edition).

Lin, T Y and Burns, Ned H (1982), *Design of Prestressed Concrete Structures,* John Wiley & Sons, New York.

Mander, J B, Priestley, M J N and Park, R (1988), *Theoretical Stress-Strain Model For Confined Concrete*, Journal of Structural Engineering, ASCE, Vol 114, No. 8, August 1988, pp. 1804-1826.

Mejia-McMaster, J C and Park, R (1994), *Precast Concrete Hollow Core Floor Unit Support and Continuity,* Research Report 94/4, Department of Civil Engineering, University of Canterbury, Christchurch.

Neville, A M and Brooks, J J (1987), *Concrete Technology,* Longman Scientific and Technical, Longman Group, U.K.

NZCS (1983), *Applications of New Zealand Standard Code of Practice for the Design of Concrete Structures NZS 3101: 1982*, New Zealand Concrete Society, Technical Report No. 2.

NZCS-NZNSEE (1991), *Guidelines For the Use of Structural Precast Concrete in Buildings,* Joint Committees of the New Zealand Concrete Society and New Zealand National Society for Earthquake Engineering, Centre for Advanced Engineering, Christchurch.

NZNSEE (1994), *Bulletin Report on January 17 1994 Northridge Earthquake,* Bulletin of the New Zealand National Society of Earthquake Engineering, Vol. 27 No. 1, March 1994.

O'Grady, C R (1988), *Precast Cruciform Columns, H Frame and Precast Concrete Shear wall,* Proceedings, Pacific Concrete Conference, Auckland, Vol. 1, pp.345-354.

Oliver, S J (1998), *The Performance of Concrete Topped Precast Hollow Core Flooring Systems With and Without Dramix Steel Fibres Under Simulated Seismic Loading*, Master of Engineering Research Report, University of Canterbury, Christchurch.

Park R and Paulay T (1975), *Reinforced Concrete Structures*, John Wiley & Sons, New York.

Paulay T, Park, R and Phillips M H (1974), Horizontal Construction Joints in Cast-in-Place Reinforced Concrete, *Shear in Reinforced Concrete*, ACI Special Publication 42, Vol. 2, Detroit, pp. 599-616.

Paulay, T (1999), *Personal Communication at the University of Canterbury.*

Paulay, T and Priestley, M J N (1992), *Seismic Design of Reinforced Concrete and Masonry Buildings*, John Wiley and Sons, New York.

Paz, Mario (1985), *Structural Dynamics, Theory and Computation*, Second Edition, Van Nostrand Reinhold Company, New York.

Paz, Mario (1985), *Structural Dynamics, Theory and Computation*, Second Edition, Van Nostrand Reinhold Company, New York.

PCI (1981), *Reflections on the Beginnings of Prestressed Concrete in America,* Prestressed Concrete Institute, Chicago, Illinois.

PCI (1985), *Manual for Quality Control for Plants and Production of Precast and Prestressed Concrete Products*, Prestressed Concrete Institute, Chicago, Illinois.

Restrepo-Pasada, J I (1993), *Seismic Behaviour of Connections Between Precast Concrete Elements*, Ph.D thesis, Department of Civil Engineering, University of Canterbury, Christchurch.

Robertson, T W (1996), *The Strengthening of Auckland Town Hall*, Proceedings of NZNSEE Technical Conference, pp. 111-118.

Rosenthal, I (1978), *Full Scale Test of Continuous Prestressed Hollow Core Slab,* PCI Journal, May-June 1978, pp. 74-81.

SAA (1987), *AS 1311: Steel Tendons for Prestressed Concrete- 7 Wire Stress-Relieved Steel Strand for Tendons in Prestressed Concrete*, Standards Association of Australia.

SANZ (1968), *NZSR 32: Standard Recommendation for Prestressed Concrete,* Standards Association of New Zealand, Wellington.

SANZ (1982), *NZS 3101: Code of Practice for the Design of Concrete Structures, Parts 1 & 2 (Code & Commentary),* Standards Association of New Zealand, Wellington.

SANZ (1987), *NZS 3114: Specification for Concrete Surface Finishes*, Standards Association of New Zealand, Wellington.

Scott, N L (1973), *Performance of Precast Prestressed Hollow Core Slab with Composite Topping*, PCI Journal, March-April 1973, pp. 64-77.

Shigley, J E (1986), *Mechanical Engineering Design (First Metric Ed.)*, McGraw-Hill Book Co., New York.

Standards New Zealand (1975), *NZS 3422: Specification for Welded Wire Fabric of Drawn Steel Wire for Concrete Reinforcement*, Standards New Zealand, Wellington.

Standards New Zealand (1989), *NZS 3402: Steel Bars for the Reinforcement of Concrete*, Standards New Zealand, Wellington.

Standards New Zealand (1992), *NZS 4203: General Structural Design Loadings for Buildings, Parts 1 & 2 (Standard & Commentary),* Standards New Zealand, Wellington.

Standards New Zealand (1995), *NZS 3101: The Design of Concrete Structures, Parts 1 & 2 (Standard & Commentary),* Standards New Zealand, Wellington.

Standards New Zealand (1997), *NZS 3441: Steel structures Standard, Part 1 (Standard & Commentary),* Standards New Zealand, Wellington.

Stocker, M F and Sozen, M A (1970), *Bond Characteristics of Prestressing Strand,* University of Illinois, Engineering Experiment Station, Bulletin No. 503.

Thomas, G (1996), *Personal Communication with a Fire Engineer regarding FRR of Floors,* University of Canterbury, Christchurch.

Trahair N S and Bradford M A (1988), *The Behaviour and Design of Steel Structures (2nd Ed.),* Chapman & Hall Ltd, New York.

UBC:94 (1994), *Uniform Building Code,* Volume 2, Structural Engineering Design Provisions, International Conference of Building Officials, Whittier, California.

Walker, P (Ed.) (1995), *The Larousse Dictionary of Science and Technology,* Larousse plc, Edinburgh.

Wight, J K (Ed.) (1985), *Earthquake Effects on Reinforced Concrete Structures,* ACI Special Publication, SP 84.

Wood, B J (1988), *A Review of New Zealand Concrete Building* Structure, Proceedings, Pacific Concrete Conference, Auckland, Vol. 3, pp. 815-831.

Wyllie, Loring A and Filson John R (Ed.) (1989), *Armenian Earthquake Reconnaissance Report,* Earthquake Spectra, Earthquake Engineering Research Institute Supplement, August 1989, pp. 158-172.

Yee, Alfred A (1991), *Design Considerations for Precast Prestressed Concrete Building Structures in Seismic Areas.* PCI Journal, May-June 1991, pp.40-55.

Young, Warren C (1989), *Roarks Formulas for Stress and Strain (6th Edition),* McGraw-Hill Book Co, New York, pp. 200-201.

Zia, P and Mostafa, T (1977), *Development Length of Prestressing Strands,* PCI Journal, September-October 1977, pp. 54-65.